CERN-2008-005
CARE-Conf-08-004-HHH
25 August 2008

ORGANISATION EUROPEENNE POUR LA RECHERCHE NUCLEAIRE
CERN EUROPEAN ORGANIZATION FOR NUCLEAR RESEARCH

CARE-HHH-APD Workshop on

Finalizing the Roadmap for the Upgrade of the CERN & GSI Accelerator Complex

"BEAM'07"

CERN, Geneva, Switzerland, 1 - 5 October 2007

PROCEEDINGS

Editors:
W. Scandale
F. Zimmermann

GENEVA
2008

CERN – 300 copies – August 2008

ABSTRACT

This report contains the Proceedings of the CARE-HHH-APD Event BEAM'07, "Finalizing the Roadmap for the Upgrade of the CERN & GSI Accelerator Complex," which was held at CERN in Geneva, Switzerland, from 1 to 5 October 2007. BEAM'07 was primarily devoted to beam dynamics limitations for the two, or three, alternative baseline scenarios of the LHC luminosity upgrade and to critical design choices for the upgrade of the LHC injector complex at CERN and for the FAIR complex at GSI. It comprised five parts: (1) a Mini-Workshop on LHC+ Beam Performance, (2) a CERN-GSI Meeting on Collective Effects, (3) the Francesco Ruggiero Memorial Symposium, (4) a Mini-Workshop on the LHC Injectors Upgrade, and (5) the BEAM'07 Summaries.

Topics addressed in the first mini-workshop of BEAM'07 ranged from the luminosity performance reach of the upgraded LHC in different scenarios, over the generation and stability of the future LHC beams, the turnaround time, beam–beam effects, luminosity levelling methods, and beam–beam compensation techniques, to advanced collimation schemes.

The second mini-workshop of BEAM'07 and the integrated CERN-GSI meeting covered the superconducting proton linac (SPL), the PS2, and the upgraded SPS at CERN, as well as critical issues of the FAIR design. Here issues of electron cloud, space charge, beam impedance, the generation and the stability of future LHC beams in the PS and SPS, beam loss handling, and beam stability aspects for the FAIR rings were discussed.

At BEAM'07 inter-laboratory collaborations could be reinforced and valuable experiences from several other facilities were presented, including superconducting linac operation and laser stripping at SNS, ESS R&D, long-range beam–beam effects at RHIC, and luminosity-levelling attempts at the Tevatron.

PREFACE

The CARE-HHH-APD event BEAM'07 "Finalizing the Roadmap for the Upgrade of the LHC and GSI Accelerator Complex" was held at CERN from 1 to 5 October 2007. BEAM'07 was devoted to beam dynamics limitations for the two, or three, baseline scenarios of the LHC luminosity upgrade, and to critical design choices for the upgrade of the LHC injector complex at CERN and for the FAIR complex at GSI. A memorial symposium in the afternoon of 3 October was dedicated to Francesco Ruggiero and to his numerous contributions to accelerator physics.

Specifically, the CARE-HHH-APD BEAM'07 event comprised five parts:

1. **Mini-Workshop on LHC+ Beam Performance**, addressing beam parameters and upgrade scenarios, e.g. bunch spacing, operation with large Piwinki angle, luminosity performance;

2. **CERN-GSI bilateral Working Meeting on Collective Effects — Theory and Experiments**;

3. **Francesco Ruggiero Memorial Symposium**, with presentations by S. Berg, C. Biscari, O. Brüning, W. Chou, M. Furman, K. Hirata, A. Mostacci, L. Palumbo, S. Petracca, Q. Qin, W. Scandale, F. Zimmermann, and B. Zotter;

4. **Mini-Workshop on LHC Injectors Upgrade**, addressing SPL, PS2, and SPS enhancements; and

5. **BEAM'07 Summaries**.

BEAM'07 was attended by 88 participants from Europe, Asia, and the Americas, including 46 from CERN. Most of the workshop scope and programme were jointly drafted by the HHH-APD organizers Walter Scandale and Frank Zimmermann (both CERN), with additional input, for the Mini-Workshop on LHC+ Beam Performance, from Jean-Pierre Koutchouk (CERN), Wolfram Fischer (LARP-BNL), Vladimir Shiltsev (LARP-FNAL), Miguel Furman (LARP-LBNL), Uli Wienands (LARP-SLAC), and Kazuhito Ohmi (KEK) plus many others, and, for the Mini-Workshop on LHC Injectors Upgrade & FAIR, from Roland Garoby, Michael Benedikt, Elena Shaposhnikova (all CERN, PAF working group). Oliver Boine-Frankenheim (GSI) and Giovanni Rumolo (CERN) prepared the programme of the CERN-GSI bilateral Working Meeting on "Collective Effects — Theory and Experiments."

The first goal of BEAM'07 was to assess potential "show-stoppers" for the alternative LHC high-luminosity upgrade paths and to compare their respective luminosity performance reach. Topics addressed in pursuit of this goal included the beam–beam interaction in a regime of large Piwinski angle, the effects of a few long-range encounters at reduced separation, wire compensation, beam–beam compensation concepts, crab cavities, electron lenses, turnaround time, peak and average luminosities, luminosity levelling, machine protection and advanced collimation schemes. The presentations covered, for example, the experience with β^* levelling at

the Tevatron, a review of the turnaround time at various hadron and hadron–lepton colliders, experimental studies and conclusions from long-range beam–beam experiments at RHIC.

The second goal of BEAM'07 was to advance the designs of the LHC injector upgrade and of the GSI FAIR project. The discussion of the LHC injector upgrade centred on the superconducting proton linac (SPL), the PS2, and the necessary SPS enhancements. Critical issues of the FAIR design were also examined. Presentations concerning this second goal covered, among other topics, the CERN injector upgrade plans, the SNS operational experience, laser stripping, ESS R&D lessons and plans, pulsed superferric magnets, electron-cloud phenomena in the PS2 and SPS, instability issues for the CERN injectors and FAIR, the generation and stability of future LHC beams, space-charge and impedance effects, and the possible loss of Landau damping in the presence of a harmonic rf system.

The first half of the event was mainly allocated to beam dynamics and luminosity performance of the upgraded LHC, while the second half was devoted to the upgrade of the CERN and GSI accelerator complex.

Further information on the BEAM'07 Event can be accessed from its home web site, *http://care-hhh.web.cern.ch/CARE-HHH/BEAM07/.*

The proceedings are structured according to the twelve plenary sessions:

- Session 1-1: **Introduction and Overview** (convener W. Scandale)
- Sessions 1-2: **Beam–Beam Compensation Schemes** (convener J.-P. Koutchouk)
- Session 1-3: **Luminosity Performance** (convener V. Shiltsev)
- Sessions 1-4: **Advanced Collimation** (convener R. Assmann)
- Session 1-5: **LHC+ Beam Generation, Injector Upgrade & FAIR** (convener E. Shaposhnikova)
- Session 2-1: **Beam Losses, Halo Generation, and Collimation** (convener G. Rumolo)
- Session 2-2: **Space Charge and Instabilities** (convener O. Boine-Frankenheim)
- Session 3: **Francesco Ruggiero Memorial Symposium** (convener W. Scandale)
- Session 4-1: **Superconducting Proton Linac** (convener R. Garoby)
- Session 4-2: **PS2** (convener M. Benedikt)
- Session 4-3: **SPS Upgrade** (convener G. Arduini)
- Session 5: **BEAM'07 Summaries** (convener F. Zimmermann)

These proceedings have been published in paper and electronic form. The paper copy is in black and white; the electronic version contains colour pictures. Electronic copies can be retrieved through:
`http://care-hhh.web.cern.ch/CARE-HHH/BEAM07/Proceedings`

The compilation of these proceedings would not have been possible without the help of the conveners and speakers. The organizational support by the workshop secretary Evelyne Delucinge and Muriel Macchi is also gratefully acknowledged, as is the help of Lauriane Bueno for completing the final proceedings. In particular, we would like to thank all the participants for their stimulating contributions and lively discussions.

The BEAM'07 event was sponsored and supported by the European Community-Research Infrastructure Activity under the FP6 "Structuring the European Research Area" programme (CARE, contract number RII3-CT-2003-506395).

The BEAM'07 proceedings are dedicated to the memory of Francesco Ruggiero (1957-2007), who was instrumental in setting up and directing the CARE-HHH network and its APD work package.

Geneva, 1 July 2008

W. Scandale and F. Zimmermann

CONTENTS

[1)] A paper was not submitted to the proceedings. However, the slides presented are available in electronic form at *http://care-hhh.web.cern.ch/CARE-HHH/BEAM07*.

[2)] The same paper was submitted to the proceedings of the CARE-HHH-APD IR'07 workshop, *http://care-hhh.web.cern.ch/CARE-HHH/IR07*.

[3)] The slides presented are available in electronic form at *http://care-hhh.web.cern.ch/CARE-HHH/BEAM07*. A combined paper including the contents of this BEAM'07 presentation was submitted to the proceedings of the CARE-HHH-APD IR'07 workshop, *http://care-hhh.web.cern.ch/CARE-HHH/IR07*.

CERN-GSI Meeting on Collective Effects

[1)] A paper was not submitted to the proceedings. However, the slides presented are available in electronic form at *http://care-hhh.web.cern.ch/CARE-HHH/BEAM07*.

[1)] A paper was not submitted to the proceedings. However, the slides presented are available in electronic form at *http://care-hhh.web.cern.ch/CARE-HHH/BEAM07*.

[4)] A separate paper was not submitted to the proceedings. However, the contents of the slides is contained in the overview paper "Francesco Ruggiero 1957–2007" (pp. 121–137).

[5)] Q. Qin presented the slides prepared by W. Chou.

Mini-Workshop on LHC Injectors Upgrade

SESSION 1: SUPERCONDUCTING PROTON LINAC (convener: R. Garoby)

SESSION 2: PS2 (convener: M. Benedikt)

SESSION 3: SPS UPGRADE (convener: G. Arduini)

[1)] A paper was not submitted to the proceedings. However, the slides presented are available in electronic form at *http://care-hhh.web.cern.ch/CARE-HHH/BEAM07*.

BEAM'07 Summaries

(convener: F. Zimmermann)

[1] A paper was not submitted to the proceedings. However, the slides presented are available in electronic form at *http://care-hhh.web.cern.ch/CARE-HHH/BEAM07*.

[6] A separate paper was not submitted to the proceedings. However, the contents of the slides is contained in the combined paper "Scenarios for the LHC Upgrade" at the start of these proceedings (pp. 3). The same paper was also submitted to the proceedings of the CARE-HHH-APD IR'07 workshop, *http://care-hhh.web.cern.ch/CARE-HHH/IR07*.

Mini-Workshop on

LHC+ Beam Performance

Scenarios for the LHC Upgrade

W. Scandale, F. Zimmermann, CERN, Geneva, Switzerland

Abstract

The projected lifetime of the LHC low-beta quadrupoles, the evolution of the statistical error halving time, and the physics potential all call for an LHC luminosity upgrade by the middle of the coming decade. In the framework of the CARE-HHH network three principal scenarios have been developed for increasing the LHC peak luminosity by more than a factor of 10, to values above 10^{35} cm^{-2}s^{-1}. All scenarios imply a rebuilding of the high-luminosity interaction regions (IRs) in combination with a consistent change of beam parameters. However, their respective features, bunch structures, IR layouts, merits and challenges, and luminosity variation with β^* differ substantially. In all scenarios luminosity leveling during a store would be advantageous for the physics experiments. An injector upgrade must complement the upgrade measures in the LHC proper in order to provide the beam intensity and brightness needed as well as to reduce the LHC turnaround time for higher integrated luminosity.

1 MOTIVATION AND TIME FRAME

The Large Hadron Collider (LHC) will collide two proton beams with a centre-of-mass energy of 14 TeV at design and "ultimate" luminosities of 10^{34} cm^{-2}s^{-1} and 2.3×10^{34} cm^{-2}s^{-1}. The LHC proton beams will cross each other at the four detectors of the two high-luminosity experiments ATLAS and CMS, the B physics experiment LHCb, and the ion experiment ALICE. The LHC is set to explore an extremely rich physics landscape, spanning from the Higgs particle, over supersymmetry, extra dimensions, black holes, precision measurements of the top quark, the unitarity triangle, to the quark-gluon plasma [1].

Simple models for the LHC luminosity evolution over the first few years of operation [2] indicate that the IR quadrupoles may not survive for more than 8 years due to high radiation doses, and that already after 4–5 years of operation the halving time of the statistical error may exceed 5 years. Either consideration points out the need for an LHC luminosity upgrade around 2016. Actually there exists even a third reason for an LHC upgrade, which is extending the physics potential of the LHC: A ten-fold increase in the luminosity will increase the discovery range for new particles by about 25% in mass [1]. Detailed physics examples can be found in Ref. [3]. The particle-physicists' goal for the upgrade is to collect 3000 fb^{-1} per experiment in 3–4 years of data taking. Simlar upgrades were performed at previous hadron colliders, where, for example, the Tevatron upgrade has resulted in an integrated Run-II luminosity about 50 times larger than that of Run I.

The LHC upgrade could consist of a series of improvements, e.g. two stages – the first one consolidating the nominal performance and providing a luminosity of up to 3×10^{34} cm^{-2}s^{-1} and the second one increasing the luminosity by more than an order of magnitude from nominal, to values above 10^{35} cm^{-2}s^{-1}.

Possible LHC upgrade paths were first examined around 2001 [4]. They have been further developed by the CARE [5] HHH network [6], in collaboration with the US LARP [7].

2 LHC CHALLENGES

Three major challenges faced by the LHC are *collimation and machine protection* [8] including issues such as damage levels, quench thresholds, cleaning efficiency, and impedance; *electron cloud* [9] involving the heat load inside the cold magnets, instabilities, and emittance growth; and *beam-beam interaction* [10], including head-on effects, long-range collisions, weak-strong and strong-strong phenomena. All these effects tend to be more severe for an upgrade.

Another LHC challenge is related to the crossing angle, which, together with the finite bunch length ("hourglass effect"), introduces a geometric luminosity reduction factor [11]

$$R(\phi,\sigma_z,\beta^*) = \frac{1}{\sqrt{\pi}\sigma_z}\int_{-\infty}^{\infty} ds \left\{\frac{1}{1+\frac{s^2}{\beta^{*2}}} \exp\left(-\frac{s^2}{\sigma_z^2}\left\{1+\phi^2\frac{1}{1+\frac{s^2}{\beta^{*2}}}\right\}\right)\right\} \quad (1)$$

where β^* designates the IP beta function, σ_z the rms (Gaussian) bunch length, and $\phi \equiv \theta_c\sigma_z/(2\sigma_x^*)$ the so-called "Piwinski angle", with θ_c being the full crossing angle and σ_x^* the rms transverse beam size at the interaction point (IP).

For bunches much shorter than β^* the reduction factor (1) can be approximated as

$$R(\phi,\sigma_z,\beta^*) \approx R(\phi,0,\beta^*) \equiv R(\phi) = \frac{1}{\sqrt{1+\phi^2}} \quad (2)$$

The reduction factor $R(\phi)$ decreases steeply as ϕ is raised beyond nominal, e.g. for smaller β^* and larger crossing angle, as is illustrated in Fig. 1. The nominal LHC operates at $R(\phi) \approx= 0.84$.

If a crab cavity is present, Eq. (1) is modified to

$$R_{\rm cc}(\phi,\sigma_z,\beta^*) = \frac{1}{\sqrt{\pi}\sigma_z}\int_{-\infty}^{\infty}\left\{\frac{1}{1+\frac{s^2}{\beta^{*2}}}\exp\left[-\frac{s^2}{\sigma_z^2} -\frac{\theta_c^2(-k_{\rm cc}s+\sin(k_{\rm cc}s))^2}{4k_{\rm cc}^2\sigma_x^{*2}\left(1+\frac{s^2}{\beta^{*2}}\right)}\right]\right\}, \quad (3)$$

where $k_{\rm cc} \equiv 2\pi/\lambda_{\rm cc}$ denotes the wave number of the crab-cavity rf.

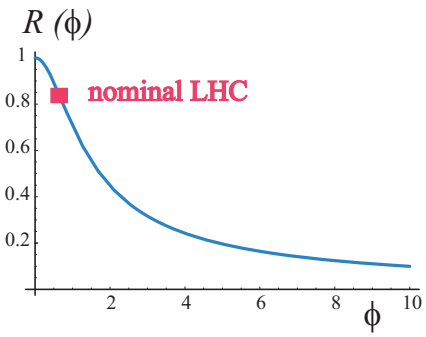

Figure 1: Geometric luminosity reduction factor $R(\phi)$ due to the crossing angle (2), as a function of the Piwinski angle ϕ. The nominal LHC operating point is also indicated.

3 BEAM PARAMETERS

The crossing angle reduces not only the luminosity, but also the beam-beam tune shift, and, thanks to this, for alternating planes of crossing at two interaction points (IPs), the luminosity can be expressed as [11]

$$L \approx \frac{f_{\rm rev}\gamma}{2r_p} n_b \frac{1}{\beta^*} N_b \; \Delta Q_{\rm bb} \; F_{\rm profile} F_{\rm hg} \; , \qquad (4)$$

where $\Delta Q_{\rm bb}$ denotes the total beam-beam tune shift, limited to about 0.01 according to experience at previous hadron colliders, $f_{\rm rev}$ the revolution frequency, N_b the number of protons per bunch, $F_{\rm profile}$ a form factor that depends on the longitudinal profile (about 1 for a Gaussian and $\sqrt{2}$ for a uniform profile) and $F_{\rm hg}$ the reduction factor due to the hourglass effect, which is relevant for bunch lengths comparable to, or smaller than, the IP beta function. In (4) the collision of two round beams has been assumed. Other variables are defined in Table 1, which compares parameters for the nominal and ultimate LHC with those for three upgrade scenarios (abbreviated "ES", "FCC" and "LPA"). The upgrade parameters in (4) which differ from the ultimate LHC configuration are $1/\beta^*$ ($\times 2$), N_b ($\times 2.9$), $\Delta Q_{\rm bb}$ ($\times 1.15$), $F_{\rm profile}$ ($\times\sqrt{2}$) and n_b ($\times 1/2$) for LPA, and $1/\beta^*$ ($\times 6.3$), $\Delta Q_{\rm bb}$ ($\times 1.25$) and $F_{\rm hg}$ ($\times 0.86$) in the ES or FCC schemes, yielding total increases in peak luminosity by factors of 15.5 and 10.6 above nominal, respectively.

Another important consideration for the upgrade is the luminosity lifetime, which can be written

$$\tau_{\rm lum} = \frac{1}{2}\frac{N_b}{\dot{N}_b} = \frac{n_b N_b}{L\sigma} = \frac{4\pi\epsilon\beta^*}{f_{\rm rev} N_b \sigma} \; . \qquad (5)$$

The luminosity lifetime is inversely proportional to the luminosity, or proportional to β^*. The lifetime can be increased only via a higher total beam current, proportional to $n_b N_b$. This implies either more bunches n_b (e.g. a previously considered scheme with 12.5-ns bunch spacing, which was ruled out at the CARE-HHH LUMI'06 workshop in view of excessive heat loads [12]) or a higher charge per bunch N_b, e.g. the LPA scheme. The effective luminosity lifetime can also be increased via "luminosity leveling," namely by suitably varying the beta function, the bunch length, or the crossing angle during a store.

4 EARLY SEPARATION SCHEME

In the **"early-separation" (ES) scenario** [13, 14, 15] one stays with the ultimate LHC beam, squeezes β^* down to about 0.1 m in ATLAS and CMS; and adds early-separation dipoles inside the detectors starting a few metres from the IP. Optionally, ES could also include a quadrupole doublet at about 13 m from the IP [16]. The ES scenario implies installation of new hardware inside the ATLAS and CMS detectors, as well as, most likely, the first ever hadron-beam crab cavities. The latter would gain a factor 2 to 5 in luminosity [15] by ensuring an effective Piwinski angle equal to zero. Their presence is assumed in Table 1. The maximum bunch intensity N_b is linked to the limit on the total beam-beam tune shift for two IPs, via $|\Delta Q_{\rm bb}| = N_b r_p \beta^*/(2\pi\gamma\sigma^{*2}) = N_b r_p/(2\pi(\gamma\epsilon))$, where σ^* denotes the transverse rms beam size at the IP. A maximum beam-beam tune shift of $|\Delta Q_{\rm tot}| = 0.01$ then translates into a maximum bunch population $N_b \approx 1.6 \times 10^{11}$. An IR layout for the ES scheme is sketched in Fig. 2.

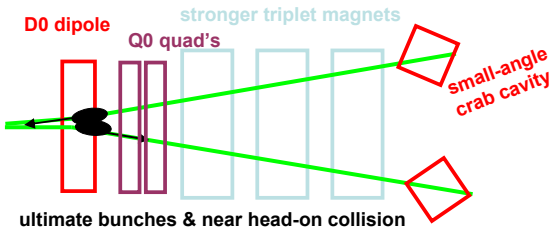

Figure 2: Possible interaction-region layout for the early-separation (ES) scheme, with highly squeezed optics ($\beta^* \approx 0.08$ m).

The merits of the ES scheme are the negligible effect of most long-range collisions thanks to the early separation, the absence of any geometric luminosity loss except for the hourglass effect, and no increase in the beam current beyond ultimate. Challenges include the early separation dipoles 'D0' deep inside the detector, the optional s.c. quadrupole doublet 'Q0', which would also be embedded, strong larger-aperture low-β quadrupoles based on Nb_3Sn, the use of crab cavities for hadron beams [17], the remaining 4 parasitic collisions at 4–5σ separation, a significant off-momentum beta beating (50% at $\delta = 3\times10^{-4}$), which may degrade the collimation efficiency plus low beam and luminosity lifetimes (proportional to β^*). Luminosity leveling via the crossing angle or crab voltage may alleviate this last concern [18].

Table 1: Parameters for the (1) nominal and (2) ultimate LHC compared with those for the three upgrade scenarios with (3) more strongly focused ultimate bunches at 25-ns spacing with either early separation and crab cavities [ES] or full crab crossing [FCC], and (4) longer intense flat bunches at 50-ns spacing in a regime of large Piwinski angle [LPA]. The numbers refer to the performance without luminosity leveling.

parameter	symbol	nominal	ultimate	ES or FCC	LPA
number of bunches	n_b	2808	2808	2808	1404
protons per bunch	N_b [10^{11}]	1.15	1.7	1.7	4.9
bunch spacing	$\Delta t_{\rm sep}$ [ns]	25	25	25	50
average current	I [A]	0.58	0.86	0.86	1.22
normalized transverse emittance	$\gamma\epsilon$ [μm]	3.75	3.75	3.75	3.75
longitudinal profile		Gaussian	Gaussian	Gaussian	uniform
rms bunch length	σ_z [cm]	7.55	7.55	7.55	11.8
beta function at IP1&5	β^* [m]	0.55	0.5	0.08	0.25
(effective) crossing angle	θ_c [μrad]	285	315	0	381
Piwinski angle	ϕ	0.4	0.75	0	2.01
hourglass factor	$F_{\rm hg}$	1.00	1.00	0.86	0.99
peak luminosity	$\hat{L}$ [10^{34} cm^{-2}s^{-1}]	1.0	2.3	15.5	10.6
events per crossing		19	44	294	403
rms length of luminous region	$\sigma_{\rm lum}$ [mm]	45	43	53	37
initial luminosity lifetime	$\tau_{\rm L}$ [h]	22.2	14.3	2.2	4.5
average luminosity ($T_{\rm ta} = 10$ h)	$L_{\rm av}$ [10^{34} cm^{-2}s^{-1}]	0.5	0.9	2.4	2.5
optimum run time ($T_{\rm ta} = 10$ h)	$T_{\rm run}$ [h]	21.2	17.0	6.6	9.5
average luminosity ($T_{\rm ta} = 5$ h)	$L_{\rm av}$ [10^{34} cm^{-2}s^{-1}]	0.6	1.2	3.6	3.5
optimum run time ($T_{\rm ta} = 5$ h)	$T_{\rm run}$ [h]	15.0	12.0	4.6	6.7
e-cloud heat load for $\delta_{\rm max} = 1.4$	$P_{\rm ec}$ [W/m]	1.07	1.04	1.0	0.4
e-cloud heat load for $\delta_{\rm max} = 1.3$	$P_{\rm ec}$ [W/m]	0.44	0.6	0.6	0.1
SR heat load	$P_{\rm SR}$ [W/m]	0.17	0.25	0.25	0.36
image-current heat load	$P_{\rm ic}$ [W/m]	0.15	0.33	0.33	0.70

Complementary Crab Cavities

In the ES scheme the geometric luminosity loss for a large crossing angle can be reduced either by bunch shortening rf or by crab cavity rf. It is instructive to compare the voltage required for the two cases [19].

The voltage required for bunch shortening is

$$V_{\rm rf} \approx \left[\frac{\epsilon_{||,\rm rms}^2 c^3 C\eta}{E_0 e\pi f_{\rm rf}}\right]\frac{1}{\sigma_z^4} \approx \left[\frac{\epsilon_{||,\rm rms}^2 c^3 C\eta}{E_0 e\pi f_{\rm rf}}\right]\frac{\theta_c^4}{\phi^4\ 16\ \sigma_x^{*\,4}}\ . \tag{6}$$

Equation (6) reveals an unfavorable scaling of the rf voltage with the 4th power of the crossing angle and the inverse 4th power of the IP beam size. The voltage can be decreased, to some extent, by reducing the longitudinal emittance (but limits come from intrabeam scattering, loss of Landau damping, and the injectors) and by increasing the rf frequency (the voltage scales inversely with the rf frequency).

By contrast, assuming horizontal crossing, the crab cavity voltage required is

$$V_{\rm cc} = \frac{cE_0\tan(\theta_c/2)}{e2\pi f_{\rm rf,cc}R_{12}} \approx \frac{cE_0}{e4\pi f_{\rm rf}R_{12}}\,\theta_c\ . \tag{7}$$

It is linearly proportional to the crossing angle and independent of the IP beam size. The voltage scales with $1/R_{12}$, where R_{12} is the (1,2) transport matrix element from the location of the crab cavity to the IP. As in the case of the bunch shortening rf, the crab-cavity voltage is also inversely proportional to the crab-rf frequency.

Figure 3 illustrates the voltages required for bunch shortening and for crab cavities, respectively, as a function of the crossing angle. The attractivity of crab cavities is evident. Figure 4 highlights the luminosity gain from a crab cavity for the ES and FCC schemes with an IP beta function β^* of 0.11 m. The residual $\sim$15% luminosity reduction at zero crossing angle is due to the hourglass effect, as β^* is comparable to the bunch length.

5 FULL CRAB CROSSING SCHEME

Crab cavities with sufficiently large total voltage could provide the same luminosity, and would allow for identical beam parameters, as the early separation (ES)) scheme, while avoiding the need for accelerator magnets inside the detectors. Possible beam parameters for such **"full crab crossing" (FCC) scenario** are identical to those of the ES scheme, as is indicated in Table 1. A corresponding IR layout is sketched in Fig. 5.

In the FCC scheme the crossing angle could be raised to any value supported by the triplet aperture and the crab-

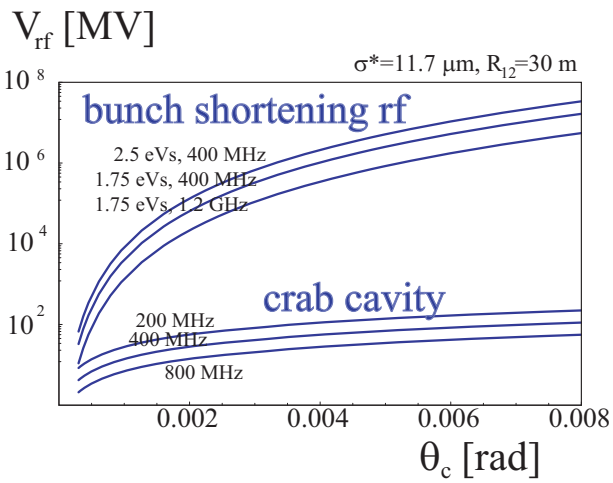

Figure 3: Bunch shortening rf voltage required to maintain a constant value $R(\phi) = 0.68$ and crab-cavity voltage as a function of the full crossing angle, for different rf frequencies and longitudinal emittances. The curves are computed from Eqs. (6) and (7). An IP beam size of 11.7 μm and $R_{12} = 30$ m from the crab cavity to the IP are assumed [19].

cavity system. For example, a transverse beam-beam separation of 8σ at the parasitic collisions is likely to be sufficient for avoiding performance degradation due to long-range beam-beam effects, provided a long-range wire compensation is also put in place.

The merits of the FCC scheme are the absence of any geometric luminosity loss except for the hourglass effect, no parasitic collisions at reduced separation, the absence of accelerator elements inside the detector, and no increase in the beam current beyond ultimate. A few of the ES challenges remain for FCC, namely the required strong larger-aperture low-β quadrupoles based on Nb_3Sn, the use of crab cavities for hadron beams (with 60% higher crab voltage than for ES), a significant off-momentum beta beating (50% at $\delta = 3 \times 10^{-4}$), plus low beam and luminosity lifetimes. Luminosity leveling via the crab voltage would be an option.

As an illustration, we consider an IP beta function $\beta^* = 0.08$ m, a crab cavity operating at 400 MHz and a typical (1,2) transport matrix element $R_{12} \approx 30$ m between the crab cavity and the IP. In this case the crossing angle needed for ES would be about 0.4 mrad (with 5σ separation), compared with 0.64 mrad for FCC (8σ separation). Using (7) these numbers translate into local crab-cavity voltages of 5.6 MV for ES and 9.0 MV for FCC. In other words, a 60% increase in the total crab voltage would be equivalent to the early-separation dipole.

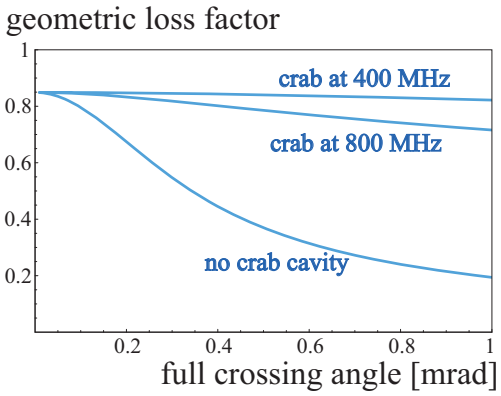

Figure 4: Luminosity reduction factor as a function of crossing angle without a crab cavity, and with a crab cavity operated at 400 MHz and 800 MHz, respectively, assuming $\beta^* = 0.11$ m. A crossing angle of 5 times the rms divergence (5 σ separation at the closest long-range encounters) would be 0.34 mrad, while 8σ separation at the closest parasitic encounters would translate to a 0.54-mrad crossing angle.

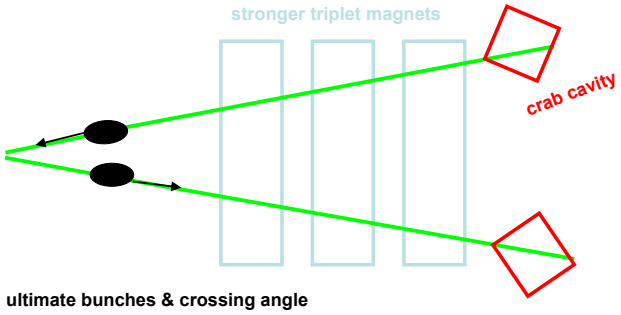

Figure 5: Possible interaction-region layout for the full crab-crossing (FCC) scheme, with highly squeezed optics ($\beta^* \approx 0.08$ m).

6 LARGE PIWINSKI ANGLE SCHEME

In the **"large Piwinski angle" (LPA) scenario** the bunch spacing is doubled, to 50 ns; longer, longitudinally flat, and more intense bunches are collided with a large Piwinski angle of $\phi \equiv \theta_c \sigma_z/(2\sigma^*) \approx 2$; the IP beta function is reduced by a more moderate factor of 2 to $\beta^* \approx 0.25$ m; and long-range beam-beam wire compensators [20] are installed upstream of the inner triplets. This regime of large ϕ and uniform bunch profile allows raising the bunch intensity N_b in (4) and thereby the luminosity, since lengthening the bunches in proportion to N_b maintains a constant value of $\Delta Q_{\rm bb}$. Figure 6 illustrates the IR layout for this upgrade option.

The merits of the LPA scheme are the absence of accelerator elements inside the detector, no crab cavities, reduced IR chromaticity, and relaxed IR quadrupoles. For

$\beta^* \approx 0.25$ m various possible optics solutions based on large-aperture NbTi quadrupoles exist [21], though the survival of the latter at high luminosity still remains to be demonstrated. Challenges are the operation with large Piwinski angle, unproven for hadron beams, the high bunch charge, in particular the beam production and acceleration through the SPS, the larger beam current, the (almost established) wire compensation, and an off-momentum beta beating of about 30% at $\delta = 3 \times 10^{-4}$. The level of off-momentum beta beating is about half that of the ES scheme, but approximately two times larger than for the nominal LHC, and likely to impact the collimation cleaning efficiency.

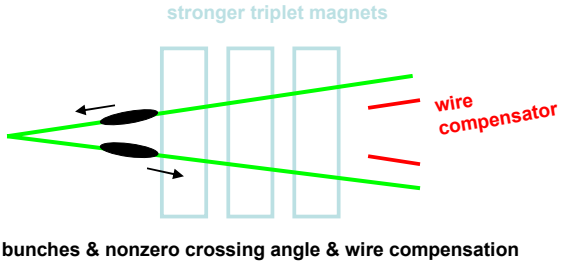

Figure 6: Interaction-region layout for large-Piwinski-angle (LPA) upgrade with an IP beta function of 0.25 m.

FLAT BUNCHES AND LARGE ϕ

The merits of longitudinally "flat" bunches and a large Piwinski angle can be unveiled more clearly by rewriting the luminosity expression in terms of the maximum beam-beam tune shift (which is taken to be the same and constant) for bunches with both Gaussian and uniform profiles.

As before and as appropriate for the LHC upgrade, we consider two interaction points (IPs) with alternating crossing. If the crossing angle is small, $\theta_c \ll 1$, the transverse IP beam size smaller than the bunch length, and the latter smaller than the IP beta function, $\sigma^* \ll \sigma_z \ll \beta^*$, and if furthermore the Piwinski angle is larger than 1, $\phi \gg 1$, the luminosity for bunches with Gaussian longitudinal profile can approximately be written [22]

$$L_{\rm gauss} \approx \frac{1}{2} \frac{f_{\rm rev} n_b \gamma}{r_p \beta^*} \Delta Q_{\rm bb} N_b \ , \qquad (8)$$

where $\Delta Q_{\rm bb}$ denotes the total linear beam-beam tune shift from the two interaction points, experienced at the center of the bunch.

Also for our second case of longitudinally "flat" bunches we assume a reasonably small crossing angle, $\theta_c \ll 1$. If in addition, the crossing angle is larger than the rms beam divergence, $\theta_c \gg \sqrt{\epsilon_N/(\gamma\beta^*)}$ (a logical requirement if the crossing angle is meant to separate the beams at the next parasitic encounter), and if the total bunch length l_b is larger than the effective extent of the beam intersection, $l_b \gg \sigma^*/\theta_c$, we can re-express the luminosity for bunches with flat longitudinal profile as [22]

$$L_{\rm flat} \approx \frac{1}{\sqrt{2}} \frac{f_{\rm rev} n_b \gamma}{r_p \beta^*} \Delta Q_{\rm bb} N_b \ . \qquad (9)$$

Comparison of (8) and (9) shows that, for the same number of particles per bunch N_b, and the same total tune shift from two IPs $\Delta Q_{\rm bb}$, the luminosity will be $\sqrt{2} \approx 1.4$ times higher with a "flat" distribution. The above assumptions were implicitly made when we earlier quoted the value of the form factor $F_{\rm profile}$ in (4).

As an additional merit, it is only in the regime of large Piwinski angle and for flat bunches that the number of particles N_b can be increased independently of the total tune shift $\Delta Q_{\rm bb}$, by lengthening the bunches.

7 CRAB WAIST COLLISIONS

All upgrade scenarios, LPA, ES and FCC, could conceivably be adapted for crab-waist collisions [23] by operating with flat beams with $\beta_x^* \gg \beta_y^*$, which would also make optimum use of the available aperture in the low-beta quadrupoles [24], and preferably with higher intensity and higher brightness. In addition, crab-waist collisions require a large Piwinski angle, such as the one for the LPA scheme, a small beta function comparable to σ_x^*/θ_c such as as for the ES or FCC scheme, and crab-waist sextupoles [25].

A possible approach for implementing crab-waist collisions at the LHC, therefore, is to adopt flat beams, combine some key ingredients of the ES, FCC and LPA schemes, and add suitable sextupoles in the IRs.

8 LUMINOSITY EVOLUTION

Figure 7 compares the luminosity evolution for the three scenarios. A turn-around time (the time between the end of a collision run and the start of the next collisions) of 5 h and the corresponding optimum run durations from Table 1 are assumed. The dashed lines indicate the respective time-averaged luminosities.

Without leveling the instantaneous luminosity decays as

$$L(t) = \frac{\hat{L}}{(1 + t/\tau_{\rm eff})^2} \ , \qquad (10)$$

with

$$\tau_{\rm eff} \equiv \frac{n_b N_b(0)}{\hat{L} \sigma_{\rm tot} n_{IP}} \qquad (11)$$

denoting the effective beam lifetime due to burn-off at the collision points, $\sigma_{\rm tot} \approx 100$ mb the relevant total cross section, n_{IP} the number of IPs, and $\hat{L}$ the initial peak luminosity. The optimum average luminosity is

$$L_{\rm av} = \frac{\hat{L} \tau_{\rm eff}}{(\tau_{\rm eff}^{1/2} + T_{\rm ta}^{1/2})^2} \ , \qquad (12)$$

where T_{ta} denotes the turn-around time. The optimum run time $T_{\rm run}$ is the geometric mean of effective lifetime and

turn-around time:

$$T_{\rm run} = \sqrt{\tau_{\rm eff} T_{\rm ta}} \, . \qquad (13)$$

In Fig. 7 it can be seen that the luminosity for the ES or FCC scenarios starts higher, but decays faster than for the LPA case, leading to shorter runs. The average luminosity values are nearly identical. The high initial peak luminosity for ES or FCC may not be useful for physics in view of possibly required set-up and tuning periods. On the other hand, the average event pile up for the ES and FCC options is about 30–40% lower than that for the LPA case, since there are twice as many bunches and collisions.

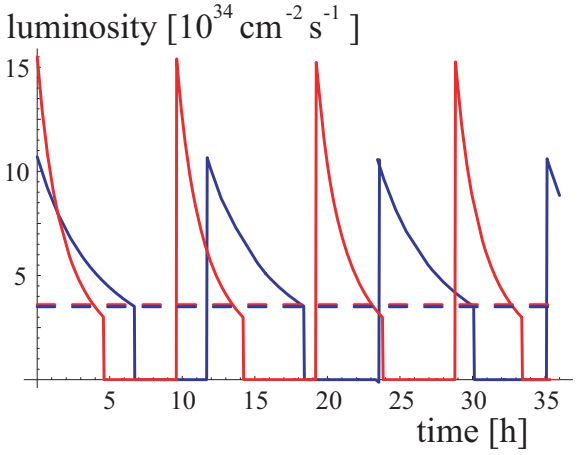

Figure 7: Ideal luminosity evolution without leveling for the ES or FCC (red) and LPA scenarios (blue), assuming the optimum run duration for a turn-around time of 5 h. The dashed lines indicate the corresponding time-averaged luminosities.

Smaller pile up at the start of a physics run, and higher luminosity at the end of each run would be desirable. Such luminosity leveling could be accomplished by dynamic β^* squeeze, crossing angle variation [18] for ES, or changes in the crab rf voltage for ES or FCC, and equally by dynamic β^* squeeze or via bunch-length reduction for LPA.

Leveling provides a constant luminosity, equal to L_0, and the beam intensity then decreases linearly with time t as

$$N_b = N_{b0} - \frac{L_0 \sigma_{\rm tot} n_{IP}}{n_b} t \, . \qquad (14)$$

The accessible intensity range $\Delta N_{b,\rm max}$ is limited, for example, by the range of the leveling variable, e.g. by the minimum value of β^*, so that the length of a run amounts to

$$T_{\rm run} = \frac{\Delta N_{b,\rm max} n_b}{L_0 \sigma_{\rm tot} n_{IP}} \, , \qquad (15)$$

and the average luminosity with leveling becomes

$$L_{\rm av,lev} = \frac{L_0}{1 + \Delta N_{b,\rm max} n_b T_{ta} / \left(L_0 \sigma_{\rm tot} n_{IP} \right)} \, . \qquad (16)$$

Table 2: Event rate, run time, and average luminosity for the three upgrade scenarios with leveling. Highlighted in bold are two promising examples.

	ES or FCC	LPA
events/crossing	300	300
optimum run time	N/A	2.5 h
av. luminosity [10^{34} cm^{-2}s^{-1}]	N/A	2.6
events/crossing	150	150
optimum run time	2.5 h	**14.8 h**
av. luminosity [10^{34} cm^{-2}s^{-1}]	2.6	2.9
events/crossing	75	75
optimum run time	**9.9 h**	26.4 h
av. luminosity [10^{34} cm^{-2}s^{-1}]	2.6	1.7

Table 2 compares event rates, run times, and average luminosity values achievable in the ES or FCC and LPA schemes. In case of β^* variation, the tune shift decreases during the store, while for leveling via the bunch length or crossing angle the tune shift increases. With leveling, the sensitivity of the average luminosity to the accessible range of the leveling parameter (β^*, bunch length or crossing angle) greatly depends on the chosen number of events per crossing, as is illustrated in Fig. 8.

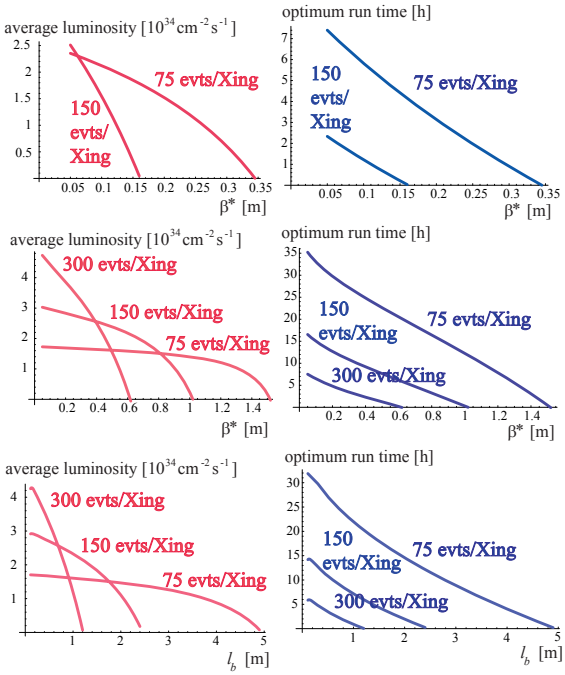

Figure 8: Average luminosity (left) and optimum run time (right) as a function of final β^* for ES or FCC with β^* leveling (top) and for LPA with β^* leveling (center), and as a function of l_b [total bunch length] for LPA with l_b leveling (bottom).

9 LUMINOSITY REACH

Figure 9 illustrates the dependence of the geometric luminosity reduction on the IP beta function. The two lower curves refer to a crossing angle of 9.5 or 5 times the rms IP beam divergence, respectively. The top curve represents both the early separation scheme with complementary crab cavity and also the full crab crossing scheme. The crab cavity restores most of the geometric overlap, except at very small β^* values, where the hourglass reduction becomes significant.

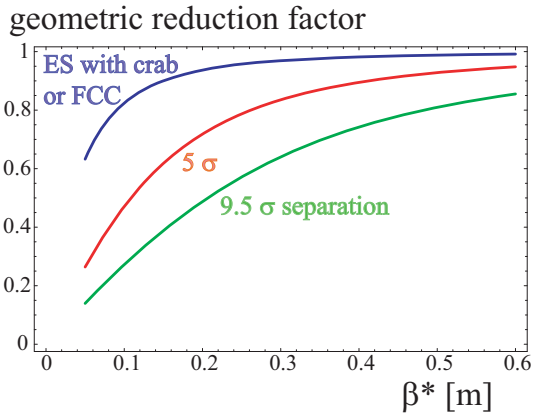

Figure 9: Geometric luminosity reduction as a function of β^* with 9.5σ (nominal) and 5σ separation (ES scheme without crab cavity) at the closest long-range encounters, as well as for arbitrary separation including crab crossing (ES with crab cavity or FCC).

Figure 10 shows the average luminosity as a function of β^* for four scenarios: the large-Piwinski angle (LPA) scheme, the early-separation (ES) scheme with either 9.5σ or 5σ beam-beam distance at the nearest long-range encounters if no crab cavity is employed, as well as ES with crab cavity or full crab crossing (FCC). The average luminosity shown is the ideal value (12), with an assumed turnaround time of 5 hours that could be provided by an upgraded LHC injector complex. For comparison, the average luminosities and β^* values corresponding to the nominal and the "ultimate" LHC with 10-h turnaround time are also indicated by plotting symbols.

The figure demonstrates that the performance of the ES scheme is considerably boosted by a crab cavity, but that both ES with crab cavity and FCC require β^* values below about 0.1 m in order to achieve the same average luminosity as obtained for the LPA scheme with a relaxed beta function of $\beta^* \approx 0.25$ m.

The LPA parameters in this example were chosen so that $|\Delta Q_{\rm tot}| \approx 0.011$ at $\beta^* \approx 0.25$ m. The magnitude of the LPA tune shift decreases if β^* is squeezed towards smaller values, a feature which could be exploited to further raise the integrated LPA luminosities for $\beta^* < 0.25$, e.g. by shortening the bunches. On the other hand, for constant normalized separation and constant bunch length, the total tune shift grows with increasing β^*, which may reduce the average LPA luminosity achievable for $\beta^* > 0.25$ m.

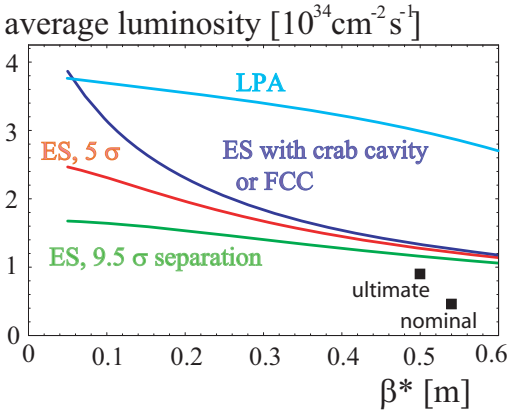

Figure 10: Average luminosity as a function of β^* for the large-Piwinski angle (LPA) scheme with a constant normalized separation of 8.5σ and a constant bunch length; for the early separation (ES) scheme with constant 9.5σ or 5σ separation and no crab cavity; and for ES with crab cavity or full crab crossing (FCC).

10 LHCB COMPATIBILITY

An upgrade of LHCb to Super-LHCb is planned, in order to exploit luminosities up to 2×10^{33} cm^{-2}s^{-1}, or 2% of the luminosity delivered to ATLAS and CMS. The LHCb detector is special due to its asymmetric location in the ring, which opens up a new possibility of supplying LHCb with its target possibility.

In the LPA case with 50-ns spacing between successive bunches in a train, we can arrange to have either collisions between the 50-ns bunches or no collisions at all in LHCb [27], depending on the distance in multiples of 25 ns which we choose between the various groups of bunch trains distributed around the ring. At 50-ns spacing, satellite bunches can be added in between the main bunches, as is illustrated in the bottom part of Fig. 11, displaying possible bunch patterns for various LHC configurations. Such satellites may be produced by asymmetric bunch splitting in the PS (possibly large fluctuation). In LHCb these satellites can be made to collide with main bunches at 25-ns time intervals. The intensity of the satellites should be lower than about 3×10^{10} protons per bunch in order to add less than 5% to the total tune shift and also to avoid electron-cloud problems. A beta function of about 3 m would result in the desired luminosity equivalent to 2×10^{33} cm^{2}s^{-1}. This value of β^* is easily possible with the present LHCb IR magnets and layout, which allows β^* squeezes down to 2 m [28].

For the ES or FCC scenarios with 25-ns bunch spacing, as well as for a different LPA filling with main-bunch collisions at LHCb, the resulting head-on collisions at Super-LHCb would contribute to the beam-beam tune shift of the

bunches colliding in ATLAS and CMS, which would lower the peak luminosity for the latter. Two ways out are (1) colliding only during the second half of each store when the beam-beam tune shifts from IP1 and 5 have sufficiently decreased below the beam-beam limit, or (2) introducing a transverse collision offset, albeit the latter raises concerns about offset stability, interference with collimation, poor beam lifetime, background etc. Requiring an LHCb contribution to the total tune shift of less than 10% implies transverse beam-beam offsets larger than 4.5σ, and $\beta^* \approx 0.08$ m, which is incompatible with the present LHCb IR configuration. For either option, the average luminosity delivered to Super-LHCb is considerably lower than for the LPA case with satellites.

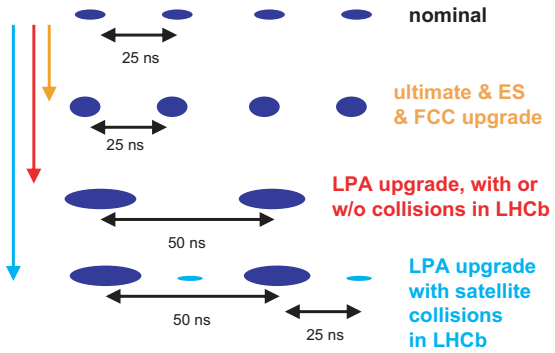

Figure 11: Bunch structures for nominal LHC, ultimate, ES or FCC upgrade, LPA upgrade, and LPA with satellite-bunch collisions at LHCb.

11 INJECTOR UPGRADE

An LHC injector upgrade is the central component of the CERN DG's White Papers [26]. The injector upgrade is already needed to produce the ultimate LHC beam (1.7×10^{11} protons per bunch with nominal beam emittance). In the context of the LHC upgrade, it will also provide a reduced turnaround time and, thereby, a higher integrated luminosity.

In order to provide the needed beam quality and intensity the existing 50-MeV proton Linac2 will be replaced by a 160-MeV "Linac4", and in the longer-term future extended by a 5-GeV s.c. proton linac (SPL). This will not only render the 1.4-GeV PS booster obsolete, but in addition it will raise the injection energy of the following storage ring PS2. The PS2 is a proposed successor of the present PS with twice the circumference and about twice the top energy (50 GeV). The next and last machine in the LHC injector chain is the Super Proton Synchrotron (SPS), which, though remaining, will be enhanced to cope with stronger electron-cloud effects and higher beam intensity.

The upgraded injector complex is designed to deliver to the LHC a beam with a maximum bunch intensity of 4×10^{11} at 25-ns bunch spacing. With this injector, the beam production for the ES scheme is straightforward. The LPA beam, requiring a slightly higher bunch population of 5×10^{11} at 50-ns bunch spacing, might be obtained by omitting the last double splitting in the PS, or in the future PS2 if the PS2 beam is still manipulated in a similar fashion as the present SPS. Numerous techniques for bunch flattening are at hand [29].

In the much longer term the SPS could be replaced by a higher-energy s.c. machine that would feed a higher-energy version of the LHC. R&D for an LHC energy upgrade is discussed in Refs. [30, 31], while the conceptual design for an energy tripler magnet can be found in [32].

12 CONCLUSIONS

We have presented three scenarios of the LHC luminosity upgrade, all promising a peak luminosity in excess of 10^{35} cm^{-2}s^{-1} with acceptable heat load and pile-up rate. Luminosity leveling should be seriously considered for the increased pile-up rates of the upgraded LHC, as it would provide a more regular flow of events at the possible expense of a moderate decrease in average luminosity.

The early separation (ES) and full crab-crossing (FCC) schemes both push β^*. ES requires slim magnets inside the detector, crab cavities, and Nb_3Sn quadrupoles. Also a "Q0" doublet inside the detector could optionally be added to achieve minimum β^* values. FCC requires 60% stronger crab cavities and wire compensation of residual long-range beam-beam effect. The ES and FCC schemes are particularly attractive if the total beam current in the LHC is limited. Luminosity leveling for ES and FCC can be realized by varying β^*, θ_c or the crab voltage. An open issue for ES is the effect of a few long-range collisions with reduced separation, which is avoided for FCC.

The large Piwinski angle (LPA) scheme entails fewer bunches of higher charge and an only moderately decreased β^*. It can conceivably be realized with NbTi magnet technology if necessary. The "Q0" doublet may also be an option for this scenario. LPA is more flexible in regard to collisions at LHCb. The LPA luminosity can be leveled by varying the bunch length or β^*. Open issues for LPA are the beam production, transport and acceleration through the SPS, and also hadron beam-beam effects at large Piwinski angle.

The off-energy beta beating compromises the collimation cleaning efficiency. This is a common concern for the three scenarios, but more severe for the lower β^* value of ES or FCC. The crab-waist scheme is yet another promising upgrade path that should further be explored for the LHC.

The first two or three years of LHC operation will clarify the severity of the electron cloud, long-range beam-beam collisions, collimator impedance, etc. On the same time scale, the first LHC physics results will indicate whether or not magnetic elements can be installed inside the detectors. Also around 2011, the LHC crab-cavity R&D, which — motivated by CARE-HHH discussions — is now being set up in a broad international collaboration, will have reached

a conclusion on the feasibility of LHC crab cavities and a solid cost estimate. The outcome from all these activities will finally decide the choice of the upgrade path.

13 ACKNOWLEDGEMENT

Many colleagues contributed to the ideas presented in this paper.

14 REFERENCES

[1] A. de Roeck, "Physics at the Next Colliders," Third National Turkish Accelerator Congress (UPHUK3), Bodrum, Turkey, 2007.

[2] J. Strait, private communication (2003).

[3] Physics Potential and Experimental Challenges of the LHC Luminosity Upgrade, F. Gianotti, M.L. Mangano, T. Virdee (conveners), CERN-TH/2002-078 (2002).

[4] O. Brüning et al, "LHC Luminosity and Energy Upgrade: A Feasibility Study," LHC-PROJECT-Report-626 (2002).

[5] *http://esgard.lal.in2p3.fr/Project/Activities/Current*

[6] *http://care-hhh.web.cern.ch/CARE-HHH*

[7] *http://www.agsrhichome.bnl.gov/LARP*

[8] *http://lhc-collimation-project.web.cern.c/lhc-collimation-project*

[9] *http://ab-abp-rlc.web.cern.ch/ab-abp-rlc-ecloud*

[10] *http://lhc-beam-beam.web.cern.ch/lhc-beam-beam*

[11] F. Ruggiero, F. Zimmermann, "Luminosity Optimization Near the Beam-Beam Limit by Increasing Bunch Length or Crossing Angle," PRST-AB 5, 061001 (2002).

[12] L. Tavian, "Cryogenic Limits," CARE-HHH LUMI'06 workshop, Valencia, 16–20 October 2006; *http://care-hhh.web.cern.ch/CARE-HHH/LUMI-06/*; and W. Scandale, F. Zimmermann, "IR Ranking Proposal and New Beam Parameter Sets for the LHC Upgrade — The View of HHH," Proc. CARE-HHH LUMI'06, Valencia, CERN Yellow Report CERN-2007-002, p. 99 (2006)

[13] J.-P. Koutchouk, "Possible Quadrupole-First Options with $\beta^* \leq 0.25$ m," Proc. CARE-HHH LHC-LUMI-05, Arcidosso, CERN Yellow Report CERN-2006-008, p. 41 (2006)

[14] J.-P. Koutchouk, "Strong Focusing Insertion Solutions for the LHC Luminosity Upgrade," Proc. CARE-HHH LHC-LUMI-06, Valencia, CERN Yellow Report CERN-2007-002, p. 43 (2007)

[15] E. Todesco, R.W. Assmann, J.-P. Koutchouk, E. Metral, G. Sterbini, F. Zimmermann, R. De Maria, "A Concept for the LHC Luminosity Upgrade Based on Strong Beta* Reduction Combined with a Minimized Geomtrical Luminosity Loss Factor," PAC'07, Albuquerque (2007).

[16] E. Laface et al, private communication; see also E. Laface, "Q0 Status," CARE-HHH IR07 workshop, Frascati, 6-8.11.2007, *http://care-hhh.web.cern.ch/CARE-HHH/IR07*

[17] R. Calaga, K. Akai, K. Ohmi, K. Oide, U. Dorda, R. Tomas, F. Zimmermann, "Small Angle Crab Compensation for LHC IR Upgrade," PAC'07, Albuquerque (2007).

[18] G. Sterbini, J.-P. Koutchouk, "A Luminosity Leveling Method for LHC Luminosity Upgrade Using an Early Separation Scheme," LHC-Project-Note-403 (2007).

[19] F. Zimmermann, U. Dorda, "Progress of Beam-Beam Compensation Schemes," Proc. CARE-HHH-APD Workshop LUMI'05, Arcidosso, CERN Yellow Report CERN-2006-008, p. 55 (2005).

[20] U. Dorda, W. Fischer, V.D. Shiltsev, F. Zimmermann, "LHC Beam-Beam Compensation Using Wires and Electron Lenses," PAC'07, Albuquerque (2007).

[21] O. Brüning, R. De Maria, R. Ostojic, "Low Gradient, Large Aperture IR Upgrade Options for the LHC Compatible with Nb-Ti Magnet Technology," LHC-PROJECT-Report-1008 (2007).

[22] F. Ruggiero, G. Rumolo, F. Zimmermann, Y. Papaphilippou, "Beam Dynamics Studies for Uniform (Hollow) Bunches or Super-Bunches in the LHC: Beam-Beam Effects, Electron Cloud, Longitudinal Dynamics, and Intrabeam Scattering," Proc. RPIA2002, Tsukuba, Japan, CERN-LHC-Project-Report-627 and KEK Proceedings 2002-30 (2002)

[23] P. Raimondi, "New Developments in Super B Factories," Proc. PAC'07, Albuquerque (2007).

[24] S. Fartoukh, "Flat Beam Optics," LHC MAC, 16.06.2006 *http://cern.ch/mgt-lhcmac*

[25] P. Raimondi, M. Zobov, D. Shatilov, "Beam-Beam Simulations for Particle Factories with Crabbed Waist," Proc. PAC'07, Albuquerque (2007).

[26] CERN DG White Papers, June 2006.

[27] M. Ferro-Luzzi, private communication, January 2008.

[28] W. Herr, Y. Papahilippou, "Alternative Running Scenarios for the LHCb Experiment," LHC-Project-Report-2009 (2007).

[29] F. Zimmermann, "Generation and Stability of Intense Long Flat Bunches," CARE-HHH BEAM'07, CERN, 1-5 October 2007, *http://care-hhh.web.cern.ch/CARE-HHH/IR07*, these proceedings (2008).

[30] LBNL S.c. Magnet Program Newsletter, no. 2 "HD-1 Sets New Dipole Field Record" (2003).

[31] *http://lt.tnw.utwente.nl/project.php?projectid=9*

[32] P. McIntyre et al, "On the Feasibility of a Tripler Upgrade for LHC," PAC'05, Knoxville (2005).

SUMMARY OF THE LARP MINI-WORKSHOP ON BEAM-BEAM COMPENSATION 2007*

W. Fischer (BNL), O. Brüning, J.-P. Koutchouk, F. Zimmermann (CERN), T. Sen, V. Shiltsev (FNAL), K. Ohmi, (KEK), M. Furman (LBNL), Y. Cai, A. Chao (SLAC)

INTRODUCTION

The LARP Mini-Workshop on Beam-Beam Compensation 2007 was held at SLAC, 2-4 July 2007. It was attended by 33 participants from 10 institutions in Asia, Europe, and America. 26 presentations were given, while more than one third of the time was allocated to discussions. The workshop web site is Ref. [1]. The workshop's main focus was on long-range and head-on beam-beam compensation, with a view towards application in the LHC. Other topics included the beam-beam performance of previous, existing and future circular colliders; beam-beam simulations; new operating modes, theory, and unexplained phenomena. This summary is also published as Ref. [2].

PERORMANCE OF CIRCULAR COLLIDERS, SIMULATIONS, AND THEORY

The expected LHC beam-beam performance was presented by F. Zimmermann, CERN. In the nominal LHC there will be 4 experiments. In 3 of them the beams collide head-on, at the fourth they are separated by 5 σ. In each of the four interaction regions the bunches also experience 30 long-range interactions. Half of these are at an average separation of 9.5 σ, and are expected to have a significant impact on the beam dynamics. The other half is expected to have little impact. To alleviate the impact of long-range interactions, the LHC beams collide under a crossing angle of approximately 300 μrad. This puts the LHC in a new operating regime for hadron colliders, where the long-range interactions lead to the emergence of a "diffusive aperture", namely a threshold in the betatron amplitude at which the transverse diffusion rate increases by orders of magnitude. The total beam-beam induced tune spread is expected to be 0.010-0.012 for the nominal beam paramters (25% of this is contributed from long-range interactions), and up to 0.015-0.017 for the ultimate beam parameters. In light of the new challenges, the operating experience of other colliders was reviewed.

The B-factories KEKB and PEP-II were presented by K. Ohmi, KEK. These machines have delivered record luminosities above $10^{34}\text{cm}^{-2}\text{s}^{-1}$, and in both machines beam-beam effects are a dominant luminosity limit, typically leading to beam size blow-up. Beam-beam parameters of up to 0.132 have been reached in PEP-II, and up to 0.175 in KEKB. With such strong beam-beam interactions, the interplay with a number of other machine properties is important, such as working point (both machines operate near the half integer resonance), global linear optics errors, local optics errors at the IP, chromatic optics errors, sources of noise, static and dynamic offsets at the IP, feedback noise, and electron clouds.

A. Valishev, FNAL, summarized the Tevatron beam-beam performance. In this machine long-range beam-beam effects at injection cause 5-10% proton beam loss. At store, long-range interactions had caused beam lifetime deterioration and emittance increases. These effects could be reduced in 2006 through the implementation of a new separation scheme ("helix"), leading to a 16% increase in luminosity lifetime. Currently the dominant beam-beam effects in stores are proton beam losses due to head-on interactions. The antiproton losses are almost entirely due to burn-off. The total beam-beam induced tune shift reached 0.026 for the antiprotons, and 0.016 for the protons. To increase the luminosity further, a working point near the half integer is considered, which does require a correction of the momentum dependency of the β-functions. Such a correction is also expected to be beneficial at the current working point.

In RHIC proton operation the total beam-beam induced tune spread reached 0.012, with 2 head-on collisions and no long-range interactions. (For heavy ions the beam-beam parameter is 2.5 times smaller.) With this about 10% of the luminosity decays exponentially with a lifetime of 0.3 h, the remainder has a lifetime of 12 h. A number of effects reduce the luminosity lifetime in conjunction with beam-beam effects. Nonlinear chromaticity induces a tune spread of approximately 0.003. A correction was implemented in 2007, but not yet tested with protons. 10 Hz triplet vibrations lead to offset modulations at the IP, for which an orbit feedback became operational in 2007. A modification of the triplet assemblies is under study to eliminate the 10 Hz vibrations at the source. A new 9 MHz rf system will become operational in 2008, allowing to match the proton bunches longitudinally at injection, leading to a smaller hour-glass effect (currently 23% at the beginning of stores). A new working point near the integer resonance will be tested in 2008, as presented by C. Montag, BNL. Simulations show a better dynamic aperture and a larger tolerance against tune errors. The implementation requires an improved orbit and beta-beat correction.

Simulations for hadron colliders are still challenging, since time scales of interest (hours) can still not easily be reached with large numbers of particles (tens of thousands) using a detailed model (like element-by-element with magnetic errors).
A. Kabel, SLAC, pursued the question of what we can learn from beam-beam simulations in proton machines, with examples from his code PLIBB. The code had been developed to calculate beam lifetimes for the Tevatron. He concluded that the calculation of observable quantities may now be within reach. A. Valishev, FNAL, showed simulations that explain and predict beam-beam effects in the Tevatron, using the code LIFETRACK [3]. Problems investigated were the bunch-by-bunch variations (due to the PACMAN effect) in orbit, tune, emittance growth, and chromaticity, as well as the effect of different helix settings. For time scales up to 5 min, the code has been shown to have predictive power, for longer time scales less so. J. Qiang, LBNL, showed strong-strong simulations for RHIC and the LHC obtained with his code BeamBeam3D, including emittance growth rates for different beam separations, and tunes in RHIC, and emittance growth rates for mismatched and offset beams in the LHC.

K. Ohmi, KEK, discussed the recent experience with crab crossing in KEKB, the first time such a scheme has been used in a collider. The KEKB beams meet under an angle of 22 mrad, and strong-strong simulations suggest that the beam-beam parameter can be increased by a factor 2 with crab crossing. So far the crab cavities were shown to actually tilt the beams in the expected manner, and they were operated at beam currents up to 1.3 A for the positrons, and 0.7 A for the electrons, although no absolute luminosity increase has been obtained yet (the specific luminosity did increase by about 15%). An rf phase fluctuation of 20 s period was observed in high current operation, and only with colliding beam.

Y. Alexahin, FNAL, reviewed coherent effects in hadron colliders. These are well established in e^+e^--colliders but were not important in the SPS collider or the Tevatron in the past (the ISR had seen some coherent effects but with their continuous beams of very high current and small beam-beam parameter the ISR situation was quite different from today's hadron colliders in a number of ways). About a decade ago, Alexahin and Gareyte had raised the possibility of an instability arising because the coherent π-mode tune created through the strong-strong beam coupling lies outside the incoherent beam-beam spectrum. π-mode tunes were observed later in RHIC, although only with an external excitation. Coherent beam-beam coupling lowered the TMCI threshold in LEP, and it leads to instability at low chromaticities in the Tevatron and RHIC. A number of suppression mechanisms were proposed including a break in the symmetry, and active damping.

Y.Cai, SLAC, presented unexplained phenomena in lepton machines. For example, currently it is not understood why the beam-beam parameter can be increased near the half integer working point to the values that have been observed. Some bunches, typically at the beginning of a PEP-II train "flipped" and were found to have very short lifetimes. The achieved vertical beam-beam parameter follows approximately a $\lambda^{-0.4}$ scaling, where λ is the damping decrements. While single bunch effects are generally well understood with simulations, this is less so with multiple bunches and in the presence of one or several other strong effects (such as ions, electron clouds, or other nonlinearities).

T. Pieloni, CERN and EPFL Lausanne, showed tune spectra calculated for the LHC, using COMBI. These are computed to predict bunch-by-bunch differences, and investigate beam-beam effects for different operational scenarios. In RHIC tune spectra were measured with colliding proton bunches, and compared to the calculated spectra. Taking into account that the RHIC BTFs are currently measuring predominantly the most intense bunches (i.e. bunches with only 1 head-on collision instead of 2 for most of the bunches), a good agreement for both the total tune spread, and the number of peaks in the spectrum was found.

LONG-RANGE BEAM-BEAM COMPENSATION

Long-range beam-beam interactions are important in the Tevatron (70 per turn, distributed), and the LHC (30 per IR, localized). In RHIC there are nominally no long-range beam-beam interactions at store, but up to 12 can be generated for machine experiments. Long-range interactions, in conjunction with other effects, have also limited the performance of e^+e^- colliders such as DAΦNE (24 in main IR), KEKB (4 in IR), and PEP II (2 in IR). General strategies to mitigate the effect of long-range beam-beam interactions are a reduction of their number, or and increase in the beam separation. This can be done with early separation schemes using dipoles (as in RHIC, or an LHC upgrade scheme proposed by J.-P. Koutchouk and G. Sterbini, CERN), or
via larger crossing angles. Another way to reduce long-range beam-beam effects is to compensate the field of the opposite beam by a magnetic field of opposite sign, that can be generated with either an electron beam (proposed for the Tevatron by V. Shiltsev) or a wire (proposed for the LHC by J.-P. Koutchouk). Such a compensation scheme appears to be practical only if the long-range interactions are localized around an IR, and a location for a compensator can be found with a phase advance only a few degrees away from the average betatron phase of the nearby long-range interactions. Space for long-range wire compensators is reserved in the LHC, and the compensation was shown to increase the dynamic aperture by about 2 σ both for the nominal LHC and for a

possible upgrade, as shown by U. Dorda, CERN. A number of other important tests have been made so far.

Two wires were installed next to each other in the SPS in 2002 for beam test. Three types of signal were used in previous experiments: beam lifetime and background, final emittance, and scraper retraction. The beam lifetime scales with the 5^{th} power of the distance between beam and wire. In 2004 two new movable units with three wires each were installed, only 2.6º away in betatron phase from the single-wire units, which is the same phase advance as between long-range collisions and wire in the LHC, to test the efficiency of the compensation, and different crossing schemes by means of two wires. Open questions from these tests were shown by F. Zimmermann, CERN. These include the scaling from the SPS to the LHC, discrepancies between measured and simulated dynamic aperture and beam lifetime, the breakdown of the 2-wire compensation at certain tunes, and the lifetime scaling with the wire distance to the beam (this is found to be different for the SPS, Tevatron and RHIC). Some of the SPS measurements were affected by the relatively short beam lifetime, which is only 5-10 min at 26 GeV/c.

In the e^+e^--collider DAΦNE the beam and luminosity lifetime could be improved with a combination of octupoles and long-range wire compensator, as shown by C. Milardi, LNF-INFN. This is the first time that long-range beam-beam compensation was demonstrated in an operating collider. In DAΦNE there are 24 long-range beam-beam interactions in the main IR. The compensating wires, built and installed in 2005, are outside the vacuum chamber, in-between the two beams, 4.9 m from the IP, and allow for a partial compensation of the long-range interactions. The observed beam lifetime improvements could be reproduced with the code LIFETRACK [2]. In the future a new vacuum chamber will be installed in the interaction region, by which all but two long-range interactions will be eliminated.

In RHIC there are nominally no long-range interactions in store, but up to 12 per turn can be generated for accelerator experiments. In the last two years the effect of a single long-range interaction was tested at injection and at store, where it was found that distances as small as 4 σ at store are needed to create visible beam losses under normal operating conditions. Last year, a vertically movable wire with an integrated strength of up to 125 A·m was installed in each of the RHIC rings. The experiments this year, presented by N. Abreu, BNL, measured loss rates of Au beams at 100 GeV/nucleon as a function of wire current and distance to the beam. The RHIC measurements complement the earlier SPS measurements, with the beam conditions of an actual collider ring and a good base beam lifetime. Simulations of the RHIC were done by U. Dorda, CERN, H.J. Kim and T. Sen, FNAL, and A. Kabel, SLAC. These aim to reproduce general features of the measured data, such as the onset of increased beam losses at certain wire distances and strengths. In some cases, a remarkably good agreement has been found but the simulation work is still ongoing. For next year, it is planned to test the compensation of a single long-range beam-beam interaction in RHIC with proton beams. In the LHC different bunches have different long-range interactions, and an optimum compensation requires that the wire current changes from bunch-to-bunch. This is technically challenging, and was discussed by U. Dorda, CERN.

HEAD-ON BEAM-BEAM COMPENSATION

The compensation of the head-on beam-beam effect can only be done with an electron beam that creates the same amplitude dependent force like the opposite beam, which typically has an approximately Gaussian profile.

A head-on compensation scheme was tested in DCI [4] with four beams (two e^+ and two e^- beams). However, due to coherent beam-beam effects, the space-charge compensation of the beam-beam effect did not work as expected. In hadron colliders, with much smaller beam-beam parameters, such strong coherent effects are not expected to be a problem. Head-on beam-beam compensation had been proposed for the SSC by E. Tsyganov, now at UT Southwestern, and his co-workers. E. Tsyganov reviewed this work at the workshop.

W. Scandale and F. Zimmermann, CERN, presented the possible LHC luminosity gain from an electron lens. Together with an injector upgrade an electron lens may be able to double the beam brightness under collision conditions. For the LHC ultimate beam parameters, and assuming no increase in the total beam intensity, this would result in 20% more average luminosity since the initial luminosity lifetime with head-on compensation would be only 7 h, half of the lifetime without the compensation. Head-on compensation would yield larger gains if the ultimate beam parameters had not yet been reached.

Much progress has been made with operating electron lenses in the Tevatron, presented by V. Kamerdzhiev, FNAL. The 2 Tevatron electron lenses were used for the compensation of beam-beam effects of colliding antiproton and, recently, in proton beams with energies of 980 GeV. They have been shown to improve the proton beam lifetime by us much as a factor of 2.3 under operating conditions. The compensation effect was most prominent in a few bunches (3-6 out of 36 total) having the largest tune shifts due to the PACMAN effect. Although this compensation is mostly due a fast tune shift, not a reduction in the tune spread needed for head-on compensation, it shows that electron lenses can improve the performance of an actual collider without creating emittance growth or other harmful effects for the beam.

At RHIC an effort has started, presented by Y. Luo, BNL, to investigate the benefits of an electron lens in simulations, and to define the hardware parameters of an electron lens, taking advantage of the EBIS [5] technology. The simulations aim to show by how much the beam-beam parameter can be increased with an electron lens. It is planned to conclude the simulation effort in about a year. With a positive outcome, a decision could be made for the construction of an electron lens at RHIC, which would then also become a test bed for such a device in the LHC.

The possible uses of electron lenses in the LHC were explored in more detail by V. Shiltsev, FNAL. Not only could these lenses be used as a head-on beam-beam compensator, potentially doubling the luminosity, they could also be used to create a stabilizing tune spread if needed, as a soft hollow collimator, and as a soft beam conditioner eliminating satellite bunches. By now a task has been created within LARP to investigate the configuration details of electron lenses, and to define the main parameters for possible electron lenses in the LHC.

REFERENCES

[1] Workshop website: www-conf.slac.Stanford.edu/larp/
[2] Submitted to ICFA Beam Dynamics Newsletter No. 44, BNL C-A/AP/291 (2007).
[3] D. Shatilov, Part. Acc. 52, 65 (1991).
[4] G. Arzelia et al., Proc. 8th Int. Conf. High Energy Acc. (1971); H. Zyngier, AIP Proc. 57 (1979); Ya.S Derbenev, 3rd All Union Conf. On Acc. (1972); E. Keil, Proc. 3rd ICFA Beam Dyn. Workshop (1989).
[5] J. Alessi et al., PAC07 (2007).

ELECTRON LENSES FOR COMPENSATION OF BEAM-BEAM EFFECTS: TEVATRON, RHIC, LHC

V.Shiltsev (Fermilab) for the *LHC Electron Lens* team

Abstract

Since previous BEAM'06 workshop a year ago, significant progress has been made in the field of beam-beam compensation (BBC) – it has been experimentally demonstrated that both Tevatron Electron Lenses (TEL) significantly improve proton and luminosity lifetimes in high-luminosity stores. This article summarizes these results and discusses prospects of the BBC in Tevatron, RHIC and LHC.

INTRODUCTION

Essentially, an electron lens is very stable ~2mm diameter and 2m long, very straight cylinder of about 10^{12} electrons with kinetic energy of 5 to 10kV, immersed in 3T longitudinal magnetic field for stability reasons. Such a charged cylinder generates up to 0.3MV/m radial electric field attracting protons. For such kind of "controlled electron cloud" one can control charge density, diameter, length, transverse position, timing, velocity, shape, angle, direction – that makes it quite a versatile tool.

The figure of merit for eLens space charge action is the tune shift it induces [1]:

$$dQ_{x,y} = \mp \frac{\beta_{x,y}}{2\pi} \cdot \frac{1 \pm \beta_e}{\beta_e} \cdot \frac{J_e \cdot L_e \cdot r_p}{e \cdot c \cdot a_e^2 \cdot \gamma_p} \qquad (1)$$

where J_e is the current. For example, the 1st Tevatron Electron Lens TEL1 can move the tune of 980 GeV protons by about 0.01, i.e. it's is a very strong instrument. Note that because in many applications the size of the electron beam a_e should be equal or proportional to the rms size of high-energy beam, the tune shift Eq.(1) is independent on the machine parameters and scales as (J_e/*normalized emittance)*. Therefore, eLens tuneshifts in RHIC, Tevatron and LHC should be about the same for the same J_e of few Amperes.

Two electron lenses were built and installed in the Tevatron and have proven themselves safe for operations: first, for abort gap cleaning (for >5 years in 24/7 operation since 2002), and, more recently, for beam-beam compensation itself.

BBC BY TEVATRON ELECTRON LENSES

We follow Ref.[2] in description of the demonstration of BBC in Tevatron. One of the most detrimental effects of the beam-beam interaction in the Tevatron is the significant attrition rate of protons due to their interaction with the antiproton bunches in the main IPs (B0 and D0) and due to numerous long-range interactions. The effect is especially large at the beginning of the HEP stores where the positive proton tune shift due to focusing by antiprotons at the main IPs can reach ξ=0.016-0.020. Fig. 3 shows a typical distribution of proton loss rates at the beginning of an HEP store. In the Tevatron, 36 bunches in each beam are arranged in 3 trains of 12 bunches separated by 2.6 μs long abort gaps. Proton bunches #12, 24, and 36 at the end of each bunch train typically lose about 9% of their intensity per hour while other bunches lose only (4-6)% /hr. These losses are a very significant part of the total luminosity decay rate of about 20% per hour (again, at the beginning of the high luminosity stores). The losses due to inelastic proton-antiproton interactions at the two main IPs are much smaller (1.1–1.5%/hr). Fig.1 shows large bunch-to-bunch variations in the beam-beam induced proton losses within each bunch train but similar rates for equivalent bunches, e.g. #12, 24, and 36.

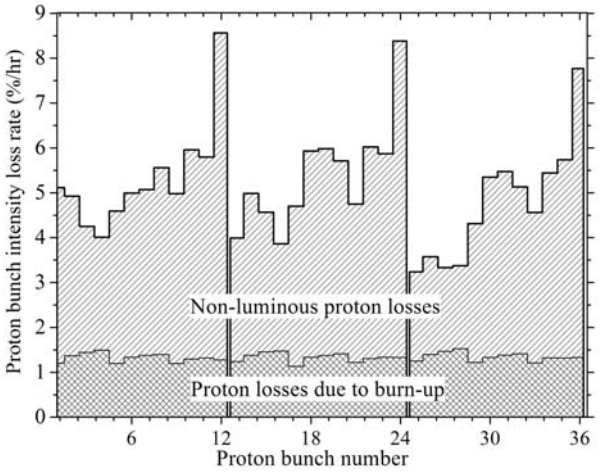

Figure 1: Proton-bunch intensity loss rates at the beginning of the Tevatron store #5155, Dec. 30, 2006, with initial luminosity $2.5 \cdot 10^{32}$ cm^{-2} s^{-1}.

In the BBC demonstration experiment, we centered and timed the electron beam of the A11 TEL2 onto bunch #12 without affecting any other bunches. When the TEL2 peak current was increased to J=0.6A, corresponding to the vertical tune shift of $dQ=0.0015$, the lifetime $\tau=N/(dN/dt)$ of bunch #12 went up to 26.6 hours from about 12 hours - see Fig.2 At the same time, the lifetime of bunch #36, an equivalent bunch in the third bunch train, remained low and did not change significantly (at 13.4 hours lifetime). When the TEL2 current was turned off for fifteen minutes, the lifetimes of both bunches were, as expected, nearly identical (16 hours). The TEL2 was then turned on again, and once again the lifetime for bunch #12 improved significantly to 43 hours while

bunch #36 stayed poor at 23.5 hours. This experiment demonstrates a factor of two improvement in the proton lifetime due to compensation of beam-beam effects with the TEL.

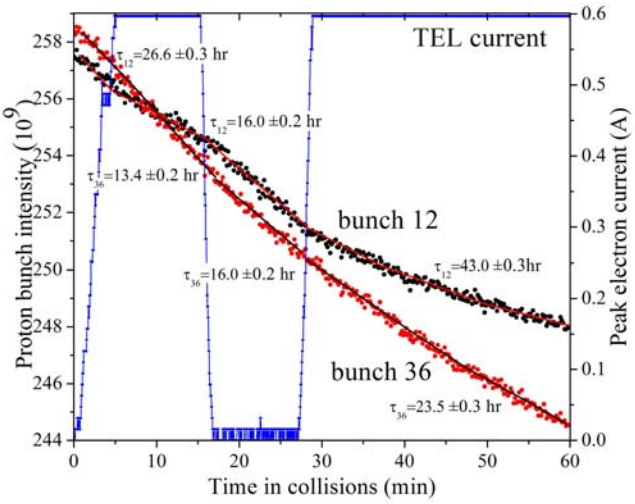

Figure 2: Proton-bunch intensity loss rates at the beginning of the Tevatron store #5119, Dec. 12, 2006, with initial luminosity $2.5 \cdot 10^{32}$ cm^{-2} s^{-1}.

Another electron lens, TEL1 (installed at the location of high horizontal beta-function, and therefore, shifting mostly horizontal tune) has demonstrated similar effect. Besides reduction of the intensity loss, the lenses improve luminosity lifetime by as much as 12% and therefore can increase luminosity integral per HEP store.

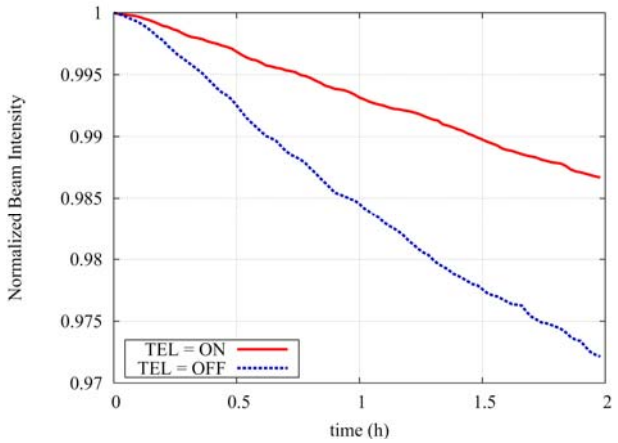

Figure 3: LIFETRAC simulations of the Tevatron proton bunch intensity with TEL off(blue line) and on (red).

Positive effect of the TEL2 on proton lifetime has been observed in the LIFETRAC tracking code simulations as well [3] – see Fig.3. Though high proton losses in the Tevatron are due to a complex combination of head-on and long-range effects, the TEL-induced lifetime improvement is thought to be mainly due to the long-range beam-beam tune shift compensation. Compensation of the non-linear effects due to head-on collisions awaits further experiments.

HEAD-ON BBC IN LHC

Currently, it is believed that beam-beam effects with nominal beam-beam parameter of ~ 0.003 per IP will not limit operation of the LHC with 3 IPs.On the other hand, operation with twice or more protons per bunch may be necessary if the total beam power will need to be limited by other considerations (e.g. collimation system efficiency or electron cloud). In that case, both head-on and long-range beam-beam interactions are expected to be unbearable.

According to [1], a complete compression of head-on tune footprint is possible if the number of electrons in the electron is $N_e = N_{ip} N_p /(1+\beta_e)$. For the LHC parameters $N_p = 2.3\ 10^{11}$, and four head-on interaction points $N_{ip} = 4$, so for 10 kV electrons ($\beta = 0.2$) one needs $N_e = 8.8\ 10^{11}$, or about 2.4A DC, and the electron transverse beam profile which exactly matches the proton beam profile (presumed to be Gaussian with an rms sigma of 0.3-1.0 mm depending on location of LEL). Head-on beam-beam compensation together with "wire" long-range beam-beam compensation [4] could be used to compress total footprint to an acceptable value as shown in Fig. 4 from [5]. Therefore, the electron lenses combined with current carrying wires for long-range beam-beam compensation are believed to allow to reach higher collider luminosities without significant increase of particle loss rates or emittance growth rates.

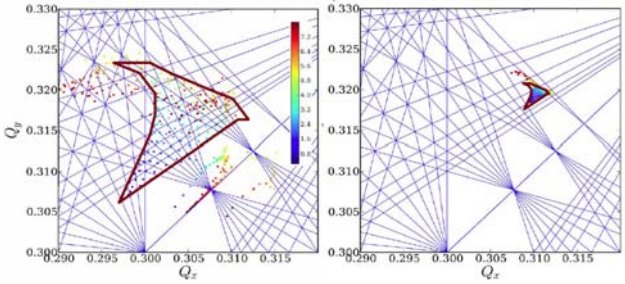

Figure 4: LHC footprint reduction by electron lens for full head on compensation by electron lenses and long-range compensation by wires. Left plot - the LHC with beams with *Np*=2.3e11/bunch and no e-lens, right – with beam-beam compensation provided by wires and head-on LELs ([5], courtesy of U.Dorda).

A 70 m long drift section between D1 and D2 dipoles has been proposed as a possible location for the LEL (LHC Electron Lenses). Optical functions of the LHC collider lattice with β^*=55cm are presented in Fig.5 from [6]. Advantages of that location are large proton beam size (1.1mm) that makes easier electron beam compression needed to match the proton profile, almost equal beta-functions, very small dispersion and close to 90 degree phase advance from the main IPs (which are about 110 m away).

The most important questions needed to specify the LEL parameters include whether full tune-spread compensation neede whatsoever and how may it affect single- and multi-bunch coherent stability. What is optimal degree of the head-on compensation? For example, it is thought to be necessary to avoid "footprint folding" which usually leads to faster diffusion.

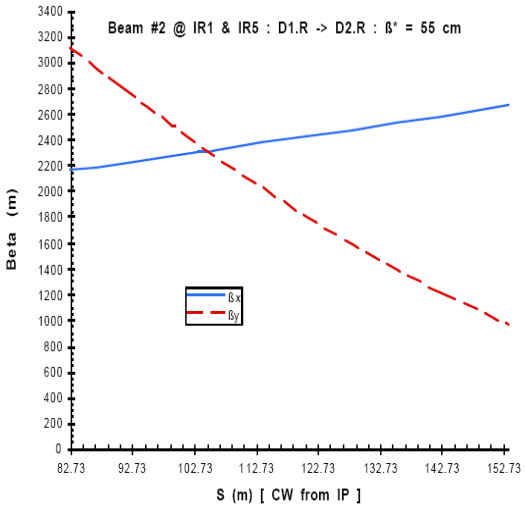

Figure 5: LHC optical functions at the proposed LEL location.

It may be very possible the LELs will need to be used only for particle compensation – e.g. to the maximum tolerable tunespread of $dQ\_spread = 0.010$. It has been pointed out that there are strong arguments for a better coherent beam-beam stability if the tunespread is compensated to the level of $dQ\_spread=0.003$ [7]. Similar questions are posed by a team of BNL researchers exploring possibility of the head-on BBC with electron lenses in RHIC [8].

Yet another possibility to consider is the use of electron beam for long-range beam-beam compensation, as a kind of "electron wire". It will work the way similar to copper wires [4] but can be placed much closer to the beam. Indeed, the copper wire can be placed only in the shadow of collimators and thus can be employed only for reasonable beam-beam separation of about 5-7σ or more.

The Electron Lens can act as "electron wire" at any separation; in addition, it is quite easy to vary the eLens current with 375ns rise time and f_r =439kHz. The requirement of integrated current of 80Am can be satisfied by using longer e-beam (6-8 m). If only long-range tune shift compensation is needed, then a head-on elens can be used. In that case, the e-beam length and current need to be about the same as in the Tevatron Electron Lenses.

SUMMARY, NEXT STEPS

In summary, experimental demonstration of compensation of the beam-beam effects in the Tevatron with use of electron lenses (which double proton beam lifetime in high-luminosity HEP stores, as reported in Ref.[1]) has greatly increased interest to the idea of using similar lenses for BBC in LHC. Seems that head-on BBC with electron lens(es) combined with long-range wire compensation is the most promising method.

Extensive theoretical studies and numerical tracking of the electron lenses for BBC in LHC are needed before undertaking expensive hardware R&D. We are at the very beginning of the systematic studies in that direction. A new task "LHC Electron Lenses" has been created within US LARP. Design, fabrication and tests of electron gun with Gaussian current profile is planned as well. Significant efforts on the same compensation method in RHIC has been started in BNL , and one should hope that they will be of importance for the LHC considerations.

This presentation summarizes discussions on the subject of the Electron Lens Beam-Beam Compensation among a group of interested people including Yu.Alexahin, V. Kamerzdhiev, J.Johnstone, T.Sen (FNAL), W. Fischer and Y.Luo (BNL), F. Zimmermann, J.P. Koutchouk and U.Dorda (CERN).

REFERENCES

[1] V.Shiltsev, *et al.* , *Phys. Rev. ST Accel. Beams* **2**, 071001 (1999).
[2] V.Shiltsev, *et al.* , *Phys. Rev. Lett.* **99** 244810 (2007)
[3] V.Kamerdzhiev, *et al.*, *Proc. IEEE PAC 2007 (Albuquerque, NM, USA)*, p.1703.
[4] J.P.Koutchouk, in *Proc. PAC'2001, Chicago,* p.1681.
[5] U.Dorda, *et al*, *et al.*, *Proc. IEEE PAC 2007(Albuquerque, NM, USA)*, p.1589.
[6] J.Johnstone, LARP-doc-560 (2007)
[7] Yu.Alexahin, presented at the Workshop on Beam-Beam Compensation (July 2007, SLAC)
[8] Y.Luo, W.Fischer, presented at the Workshop on Beam-Beam Compensation (July 2007, SLAC)

BEAM-BEAM WITH A FEW LONG RANGE ENCOUNTERS AT SHORT DISTANCE*

N. P. Abreu, Brookhaven National Laboratory, Upton NY 11973

Abstract

The high nominal luminosity of the LHC requires a large number of bunches spaced by about 25 ns. To prevent more than one head-on collision in each interaction region, a total crossing angle of 0.285 mrad is necessary, and the bunches experience around 30 long range (LR) interactions per IP with at mean separation of 9.5 σ. For the LHC luminosity upgrade, there are two possible scenarios: the early separation scheme and low Piwinski angle (LPA) scheme. In the early separation scheme, a few long range interactions need to be tolerated, this paper the discuss the possibility of having a few LR encounters at a minimum separation smaller than the 9 σ, and present observations from other hadron machines with a smaller beam separation.

INTRODUCTION

In the LHC there is a total 120 LR interactions with 30 LR per interaction point. In simulations these interactions create a diffusive aperture around 6 σ. In order to overcome this aperture limitation and also increase the luminosity two different scenarios were propose: the early separation scheme and the LPA scheme with LR wires compensators.

In the early separation scheme a dipole (D0) is installed at a distance between 2 and 9.5 meters from the IP. With this setup the crossing angle would be zero (in the case of 2 meters separation) or reduced (in the case of the 9.5 m separation) which would lead to a gain in luminosity of 110% or 65 % respectively. However both setups reduce the nominal minimum bunch separation around the IP from 9.5 σ to between 3 to 5 σ. Simulations show that these few LR encounters does not reduce the diffusive aperture.

In the second scheme, more indicated for long bunches with 50 ns spacing, a wire is installed near each IP to compensate for the LR interactions. This setup could compensate for the tunes changes due to the LR and simulations show that it could increase the diffusive aperture by 1 up to 2 σ.

Given the two possible upgrades scenarios it is important to know whether a few long-range encounters could be accepted without limiting the lifetime or the dynamic aperture. A possible investigation of the effect is to look into the limitations of other hadron machines like Tevatron, RHIC and SPS with a few LR interactions and/or the wire compensators. A description of the RHIC wire experiments is also shown and comparison with simulation results is presented

*Work supported by US Department of Energy.
#nabreu@bnl.gov

OBSERVATIONS OF A FEW LONG RANGE INTERACTIONS AT THE TEVATRON

In the Tevatron each bunch experiences 70 LR interactions at each turn. Different from the other colliders, these interactions are distributed around the machine and not localized in the interaction regions. There are 138 locations where these interactions can take place and the sequence of 72 out of 138 is different for each bunch, hence the effects changes from bunch to bunch. These parasitic collisions limit the dynamic aperture and lifetime, and thereby the luminosity.

Experience shows that a minimum separation smaller than 5-6 σ causes losses there are unacceptable. The emittance blow-up cause by the beam-beam interactions is reduced by increased that Helix field and thus increasing the minimum separation from 4 σ to 6 σ (Figure 1).

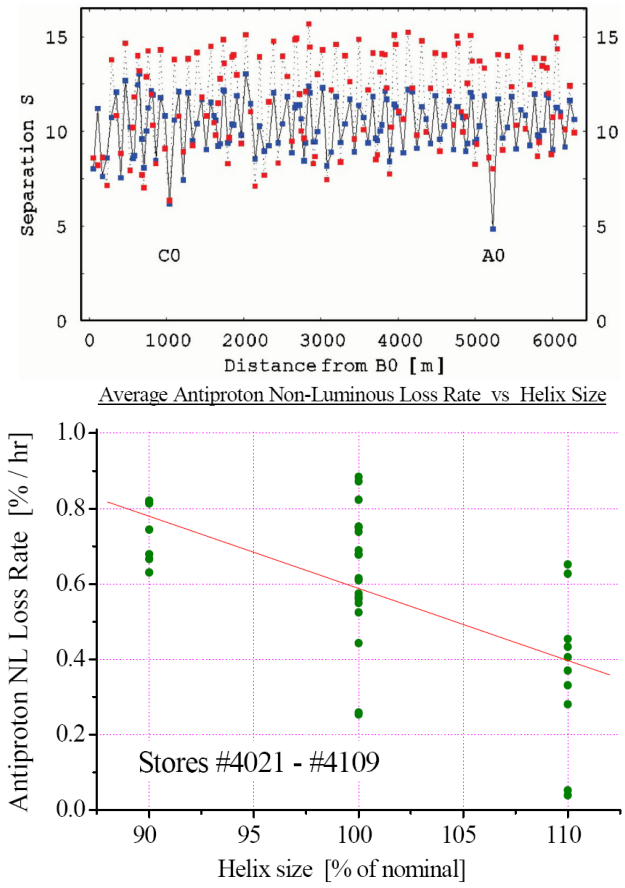

Figure 1: Increase in the Helix separation field increases the minimum separation from 4 to 6 σ [5] (top), and increase in the antiproton lifetime [3] (bottom).

WIRE EXPERIMENTS AT THE SPS

There are two sets of wires already installed is the SPS that can create LR-like interactions. Experiments with that wire show that an excitation corresponding to 9 LR-like encounters at 4.3 σ and the ultimate bunch charge did not show any observable beam loss. It is possible to correct the effect of one set of wires with the second set, as shown in Figure 2, indicating the ability to compensate for LR interactions.

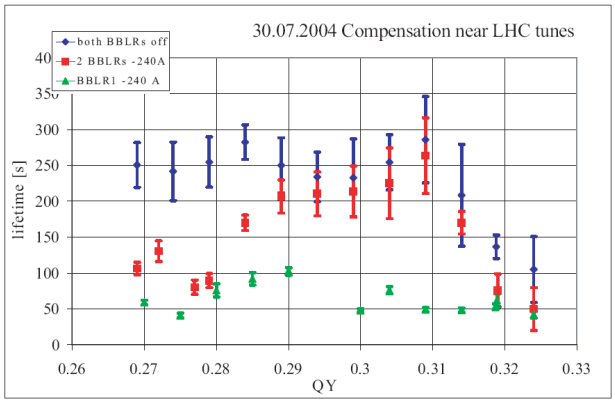

Figure 2: Experiments at the CERN SPS indicating that it is possible to compensate for LR-like interactions wire the wires [6].

EXPERIMENTS AT RHIC

Like in the LHC, LR interactions in RHIC are localized in the IRs, but with a bunch spacing of 108 ns (currently nominal operation) there are no LR interactions under current operations conditions. For eRHIC a bunch spacing of 72 ns is considered which would lead to 2 LR interactions per IP.

Experiment with one long range interaction

Experiments where performed with protons at 100 GeV and the beam were driven near a resonance in order to enhance the effect of the LR interaction and the Yellow beam was moved closer to the Blue beam. As shown in Figure 3, losses start around 4 σ.

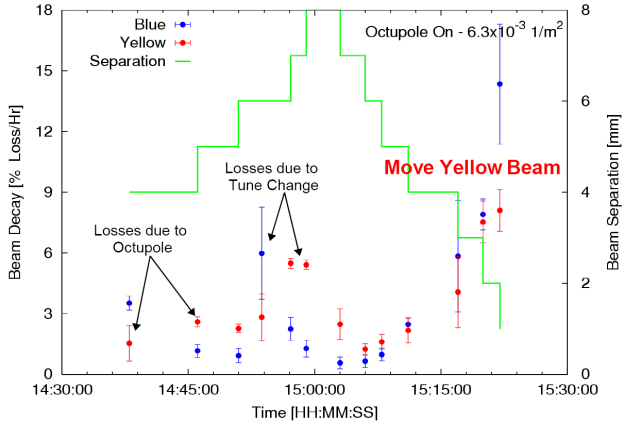

Figure 3: Experiment at RHIC with 1 LR interaction. The Yellow beam was moved towards the Blue beam. The losses start at a separation of 4 σ.

We also simulate this 1 LR interaction at 5 σ separation comparing the effect on the diffusive aperture with the nominal tunes and the ones used at the experiment (Figure 4) showing that for the nominal operation the diffusive aperture is around 10 σ. We also simulate the diffusion as a function of the minimum separation (Figure 5).

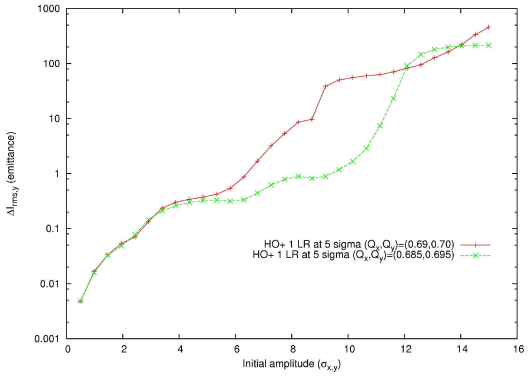

Figure 4: Simulations of 1 LR interaction in RHIC with the nominal tunes and the tunes used in the experiment showing the diffusive border at 10 σ and 5 σ respectively.

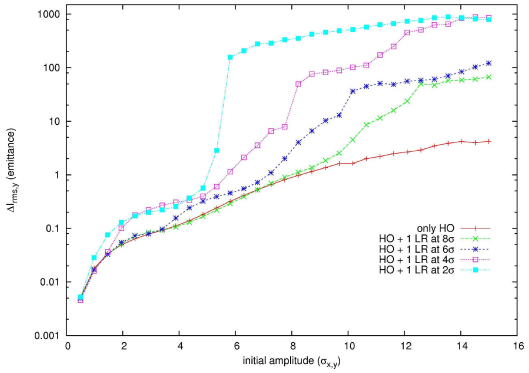

Figure 5: Simulations of 1 LR interaction in RHIC as a function of the beam minimum separation.

Experiments with the wire

In 2006 a set of compensators were installed in RHIC and a set of experiments were carried out at the Au 2007 run at top energy (100 GeV/nucleon). The integrated strength of the wires is: 12.5 Am (=1 LR) and 125 Am (=10 LR). Figure 5 show the schematics of the wires installed in RHIC.

In the experiments we moved the wire towards the beam and measured the losses. The experiments where done using the nominal tunes where we could observe the onset of losses around 5 σ for the Blue beam; and with the tunes swapped when we observed losses around 5 σ for the Yellow beam and 8-9 σ for the Blue beam.

Simulation results indicate that the lifetime has a strong correlation with the wire current and also there a reasonable agreement with the onset of chaos and the

diffusive border measured for the 12.5A case [7], as is shown in Figure 8.

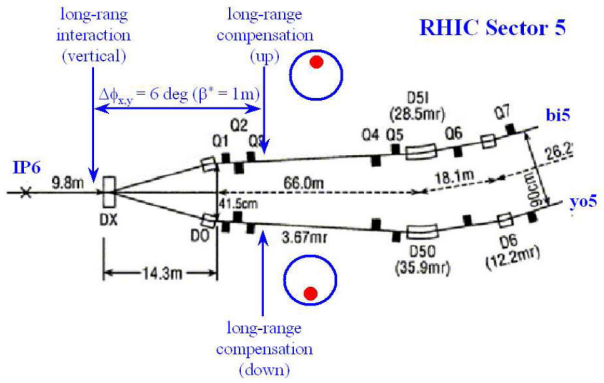

Figure 6: Setup of the wires in RHIC.

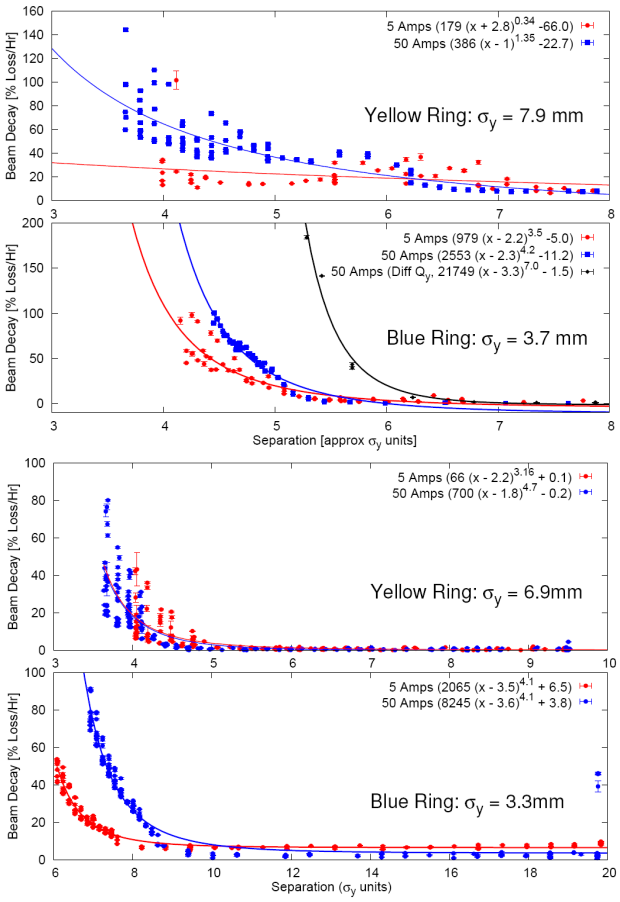

Figure 7: Wire experiments in RHIC. Nominal tunes (top) and tunes swapped (bottom) [7].

CONCLUSION

In the early separation scheme for LHC, the beam has up to 3 LR encounters at a minimum separation of 5 σ. The experience from other hadron colliders can be summarized as:

- Tevatron: 70 LR encounters at a mean separation of 9 σ. Losses start for a minimum separation of 5-6 σ.
- SPS: wire experiments show no observable losses for 9 LR-like interactions at 4.5 σ and for 120 LR-like interactions losses start at 9 σ.
- RHIC: 1 LR interaction show onset of losses at 4 σ. Wire experiments show that losses are very sensitive to the working point and start between 5 and 9 σ separation.

Simulations for the RHIC experiments show agreement with the experimental results and LHC simulations show that the wire compensator should increase the diffusive aperture by 1 to 2 σ, and that a few LR encounters at 5.5 σ does not affect the diffusive aperture.

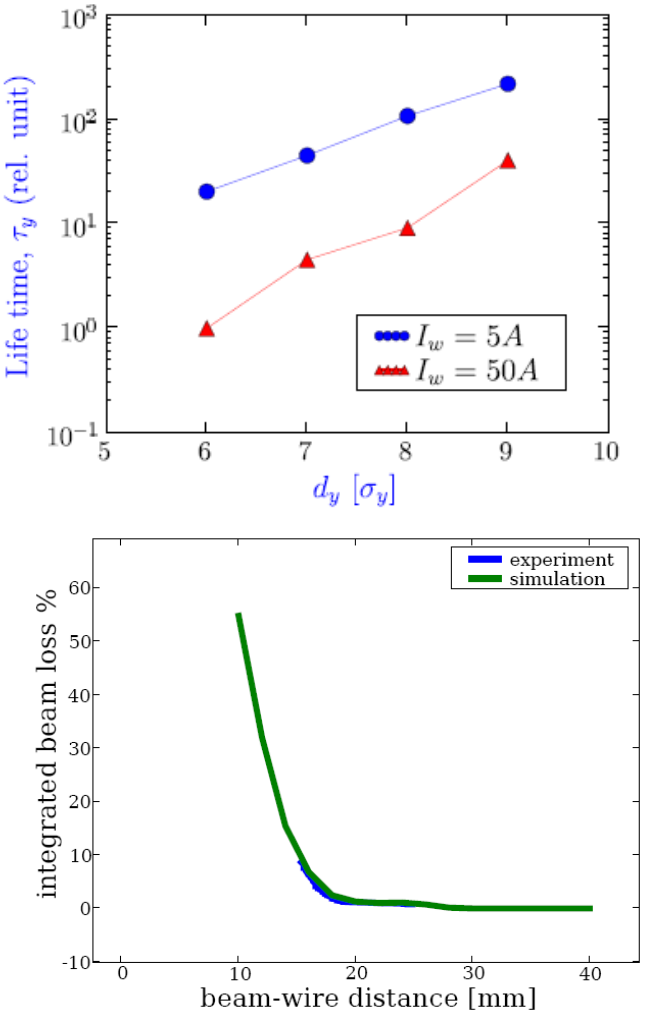

Figure 8: Simulations of the wire experiments in RHIC. Lifetime show a strong dependence with the wire current (top) and for the 12.5 Am case there is a very good agreement between the onset of chaos calculated and the onset of losses measured (bottom) [7].

ACKNOWLEDGEMENTS

I would like to thank W. Fischer, R. Calaga and G. Robert-Demolaize for discussions and feedback.

REFERENCES

[1] J.-P. Koutchouk, G. Sterbini, An early beam separation scheme for the LHC luminosity upgrade, p. 2137, EPAC06

[2] Y. Papaphilippou and F. Zimmermann, Weak-strong ebam-beam simulations for the Large Hadron Collider, PRST-AB vol.2 104001 (1999).

[3] V. Kamerdzhiev, BB Compensation with Tevatron Electron Lenses, LARP Mini-workshop at SLAC, July 2007, http://www-conf.slac.stanford.edu/larp/.

[4] A. Valishev, Tevatron BB Phenomena and Counter Measures, LARP Mini-workshop at SLAC, July 2007, http://www-conf.slac.stanford.edu/larp/.

[5] V. Shiltsev, *et al.*, Beam-beam effects in Tevatron PSRT-AB vol.8 101001 (2005).

[6] F. Zimmermann *et al*. Experiments on the LHC long-range bema-beam compensation and crossing scheme at the CERN SPS in 2004, p. 686, PAC05.

[7] W. Fischer, *et al.*, Experiments with a DC wire in RHIC, p. 1859, PAC07.

Study of beam-beam interaction with a large Piwinski angle at LHC

K. Ohmi *
KEK, 1-1 Oho, Tsukuba, 305-0801, Japan

Abstract

Collision with a large Piwinski angle is one of the update scenarios of LHC toward the luminosity 10^{35} cm^{-2}s^{-1}. The large Piwinski angle is realized by a small beta function at the collision point and longer bunch length. The Piwinski angle is increased from 0.6 to 2 in the scenario. The bunch population is increased so as to keep the beam-beam parameter.

The beam-beam performance is degraded by crossing angle which induces additional nonlinear terms due to a symmetry breaking of the collision especially for the high beam-beam parameter. Effect of crossing angle for the nominal LHC design and the large Piwinski angle scheme are studied.

INTRODUCTION

We discuss effects of crossing angle in LHC and its upgrade plans. Piwinski angle for horizontal crossing is defined by

$$\phi = \frac{\theta\sigma_z}{\sigma_x}. \tag{1}$$

where θ, σ_z and σ_x are a half crossing angle, bunch length and horizontal beam size, respectively. The nominal LHC is $\theta = 140$ μrad, $\sigma_z = 7$ cm and $\sigma_x = 17$ μm, thus the Piwinski angle is $\phi = 0.6$.

The crossing angle induces [7] various nonlinear terms, which degrade the luminosity performance. The large Piwinski angle scheme $\phi = 2$ expects linear luminosity increase for the bunch population without increasing the beam-beam parameter. We study the beam-beam performance for the crossing collision in the nominal design and upgrade options using computer simulations.

EFFECT OF CROSSING ANGLE

Lorentz transformation is used so that the two beams move completely opposite direction. Electro-magnetic field is formed in the perpendicular to the moving direction, thus colliding beam experiences the electro-magnetic field in the perpendicular to the moving direction [1, 2, 3]. This feature simplifies treatment of the beam-beam force. The schematic view is seen in Figure 1.

The Lorentz transformation from the laboratory frame to the head-on frame ($\mathcal{M}_L$) is given for a half crossing angle θ by [3]

$$x^* = \tan\theta z + \left(1 + \frac{p_x^*}{p_s^*}\sin\theta\right)x$$

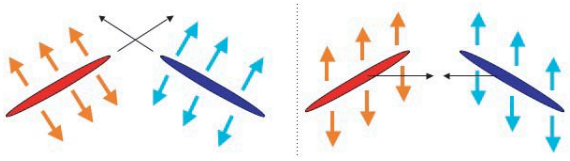

Figure 1: Collision in the laboratory and head-on frame. Light blue and orange arrows display the electric field line of the colliding bunches. Black arrow displays the traveling direction of the bunches.

$$\begin{aligned} y^* &= y + \sin\theta\frac{p_y^*}{p_s^*}x \\ z^* &= \frac{z}{\cos\theta} - \frac{H^*}{p_s^*}\sin\theta x \\ p_x^* &= \frac{p_x - \tan\theta H}{\cos\theta} \\ p_y^* &= \frac{p_y}{\cos\theta} \\ p_z^* &= p_z - \tan\theta p_x + \tan^2\theta H, \end{aligned} \tag{2}$$

where

$$H = (1+p_z) - \sqrt{(1+p_z)^2 - p_x^2 - p_y^2}$$

$$p_s = \sqrt{(1+p_z)^2 - p_x^2 - p_y^2}.$$

A star designates a dynamical variable in the head-on frame. H^* and p_s^* are $H(\boldsymbol{p}^*)$ and $p_s(\boldsymbol{p}^*)$, respectively. Note that the x^* and y^* axes are defined in the same direction for both beams, while the s^* axis is defined in opposite directions, since the two beams travel in opposite directions.

The linear part of the transformation is expressed by a matrix

$$M_L = \begin{pmatrix} 1 & 0 & 0 & 0 & \tan\theta & 0 \\ 0 & 1/\cos\theta & 0 & 0 & 0 & 0 \\ 0 & 0 & 1 & 0 & 0 & 0 \\ 0 & 0 & 0 & 1/\cos\theta & 0 & 0 \\ 0 & 0 & 0 & 0 & 1/\cos\theta & 0 \\ 0 & -\tan\theta & 0 & 0 & 0 & 1 \end{pmatrix}. \tag{3}$$

These transformations, Eqs.(2) and (3), are not symplectic. In fact, the determinant of the transfer matrix M_L is not 1, but $\cos^{-3}\theta$. This is not a problem because the inverse factor of $\cos^3\theta$ is applied by the inverse transformation. This is due to the fact that the Lorenz transformation is not symplectic for the accelerator coordinate, because the Hamiltonian is divided by a reference momentum. Needless to say, the Lorentz transformation is symplectic for the

physical coordinate, thus the transformations, Eqs.(2) and (3), are symplectic in the physical coordinate. The adiabatic damping is the concept in the accelerator coordinate. This discussion can be applied to the nonlinear transformation of Eq.(2) [4].

SIMULATION FOR NOMINAL LHC

We first evaluate luminosity for the nominal LHC using weak-strong and strong-strong simulations. Crossing angle induces linear $x - z$ coupling, with the result that the beam distribution diffuses and the luminosity degrades [4]. The diffusion rate strongly depends on the beam-beam parameter. For electron-positron colliders, the diffusion rate is faster than radiation damping rate $> 10^{-4}$/turn for $\xi > 0.05$. Here damping rate of LHC is the order of one day 10^9 turns and the luminosity life time is expected 10^9 turns. Tolerable diffusion rate or luminosity decrement is 10^{-9}/turn. The simulations was carried out during $\sim 10^6$ turns in this paper. The decrement of 10^{-3} should be cared to predict the luminosity life time of 10^9 turns.

Figure 2 shows evolution of the beam-size and luminosity given by the weak-strong and strong-strong simulation for the nominal bunch population. Plot (a) depicts beam size evolution given by the weak-strong and strong-strong simulations. A bunch is sliced in 10 pieces along its length in the weak-strong simulation. Macro-particles of 10^4 was used in the weak-strong simulation. The beam size of the weak beam is averaged in each 100 turns. No emittance growth nor luminosity degradation were seen in the weak-strong simulation.

Two dimensional model is used for the strong-strong simulation to save the calculation time. This approximation may give optimistic results. However an emittance growth is seen in the strong-strong simulation. The emittance growth is considered by numerical noise of macro-particle statistics. Macro-particles of 10^6 are used the simulation. The statistical noise of collision offset (0.1%) can be introduced collision by collision in the simulation [5]. Needless to say, the weak-strong simulation is noise free. Plot (b) depicts luminosity evolution for the nominal, twice and 4 times bunch populations. Luminosity degradations are 10^{-9}, 5×10^{-9} and 3×10^{-8} in one turn, respectively. If we believe this result, the bunch population is limited to the nominal value by the beam-beam effect. Here we consider this degradation is due to the numerical noise again. More discussions for noises in macro-particle simulations are seen in Ref.[6]. We use only the weak-strong simulation hereafter.

Figure 3 shows the luminosity degradation for $2\times$, $4\times$, $6\times$ and $8\times$ more bunch populations than the nominal value. The red and green lines depict the evolution of the luminosity zero or finite crossing angle. In the nominal bunch population, there was no difference between zero and finite crossing angle. The difference was visible for more than 6 times population. Anyway, the nominal LHC is no problem for finite crossing angle.

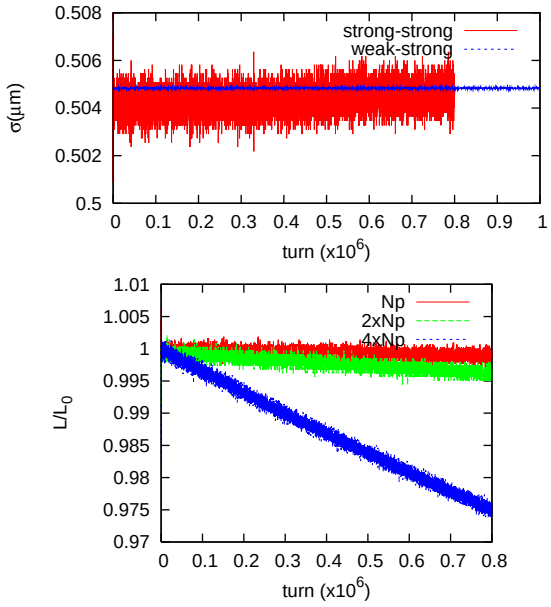

Figure 2: Beam size increment and luminosity decrement given by the strong-strong simulation.

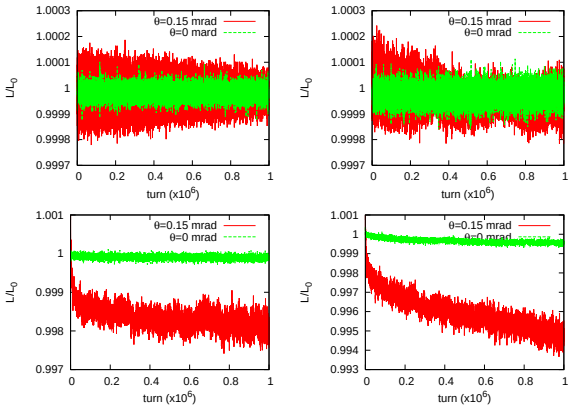

Figure 3: Luminosity degradation due to the crossing angle given by the weak-strong simulation. Plots (a)-(d) depicts for $2\times$, $4\times$, $6\times$ and $8\times$ more bunch population than the nominal value, respectively.

LARGE PIWINSKI ANGLE OPTION

We study a large Piwinski angle option for LHC. Table 1 [8] shows parameter list of the large Piwinski angle options. The Piwinski angle $\phi = 2$ is realized in the first option with long flat bunch, a half beta and 5 times bunch population. The angle $\phi = 3$ is realized in the second option with a quarter low beta and 2 times bunch population. In this paper we study the first scheme (LPA1).

LHC has two collision points. Both of the two collision points are designed so as horizontal-horizontal crossing in the nominal design. Hybrid crossing, in which horizontal and vertical crossing[9] are adopted for the two interaction points, can be considered for the upgrade plan. The tune spread due to the nonlinear beam-beam interaction is

narrower for the hybrid crossing than the nominal crossing. The horizontal crossing induces the nonlinear terms xy^2 while vertical crossing induces skew terms x^2y. This means the hybrid crossing induces more resonances than the nominal crossing. It is very difficult which is better the two cases, less resonance with wider tune spread, or more resonances with narrower resonances. The answer depends on the case by case, operating point, beam-beam parameter and so on. Simulation only gives the answer.

The nominal crossing induces the same nonlinear interactions at the two interaction point. This means some nonlinear terms can be cancelled depending on the betatron phase difference. In the hybrid crossing, some terms can be cancelled but terms with different symmetry (parity) can not be cancelled.

Table 1: Basic parameters of LHC nominal and large Piwinski angle option. * The bunch length is total length with a flat longitudinal distribution.

variable	nominal	LPA-1	LPA-2
circumference (m)		26,658	
beam energy (TeV)		7	
bunch population (10^{11})	1.15	4.9	2.5
half crossing angle (mrad)	0.14	0.19	-
beta function at IP (m)	0.55	0.25	0.14
emittance (m)		5.07×10^{-10}	
beam-beam tune shift	0.0033		
bunch length (cm)	7	41*	7.5
synchrotron tune, ν_s		0.0019	
betatron tune, $\nu_{x(y)}$		63.31/59.32	
revolution frequency		10^9/day	
Piwinski angle ϕ	0.4	2	3
luminosity ($\mathrm{cm}^{-2}\mathrm{s}^{-1}$)	1	10	

Simulation for the nominal and hybrid crossings

The weak-strong simulation was executed to study the large Piwinski angle scheme. The number of the longitudinal slices are increased for proportional to the Piwinski angle. We show examples of the nominal and hybrid crossings. It should be emphasized that the results depend on the betatron phase difference between two IP. Here the phase difference is chosen to be $\Delta\psi = 0.2 \times 2\pi$ for both of x-y plane. The parasitic interactions are included in the simulation.

Figure 4 shows the simulation results for $N_p = 4.9 \times 10^{11}$ with including 7 parasitic collisions both side of upstream and down stream of the collision point. Plots (a), (b) and (c) depict the evolution of luminosity and beam size, and beam particle distribution in x-y plane after 10^6 revolutions, respectively. Red and green lines are turn by turn beam size and its average during 100 turns. Luminosity does not change, while the beam size fluctuates for the revolutions. It is seen that some particles have a large amplitude in the final distribution (c).

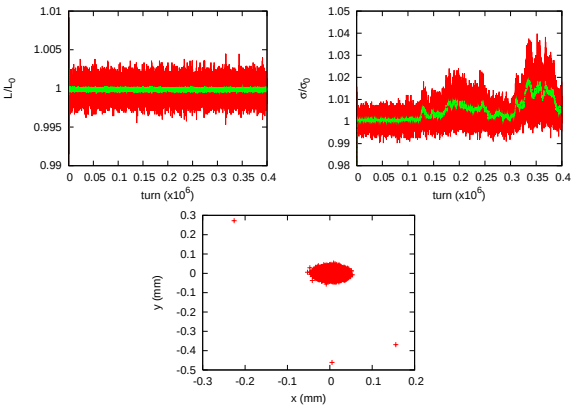

Figure 4: $N_p = 4.9 \times 10^{11}$ Evolution of (a) luminosity and (b)beam size. (c) Beam particle distribution in x-y plane after 10^6 revolutions.

A higher bunch population, $N_p = 6 \times 10^{11}$ was tried to make clear the luminosity degradation and emittance growth. Figure 5 shows the simulation results for $N_p = 6 \times 10^{11}$ with including 7 parasitic collisions each side. Again the luminosity does not degrade, but beam size increases faster than that of the nominal population, $N_p = 4.9 \times 10^{11}$. More particles have large amplitudes in the final distributions.

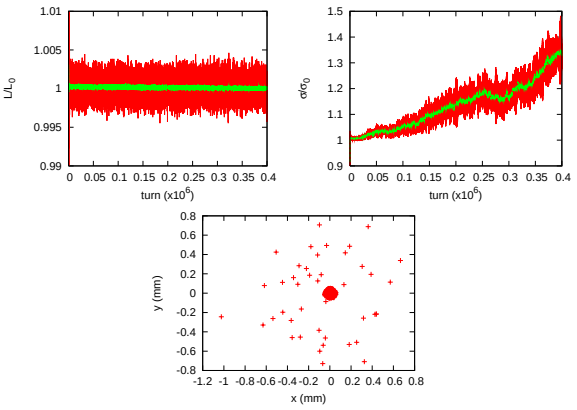

Figure 5: $N_p = 6 \times 10^{11}$ Evolution of (a) luminosity and (b)beam size. (c) Beam particle distribution in x-y plane after 10^6 revolutions.

We next cut off the parasitic interactions to understand why particles have large amplitudes. Figure 6 shows the simulation results for $N_p = 6 \times 10^{11}$ without parasitic collisions.

The same simulation was carried out for the nominal collision scheme, horizontal-horizontal. Emittance growth and luminosity degradation were not seen in the nominal collision. We would like to say the tune spread is not universal parameter to characterize the emittance growth and/or beam-beam performance, and we do not conclude

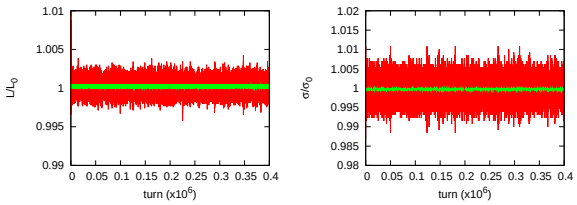

Figure 6: $N_p = 6 \times 10^{11}$ Evolution of (a) luminosity and (b)beam size. (c) Beam particle distribution in x-y plane after 10^6 revolutions.

that the nominal collision scheme is better than the hybrid scheme in this example.

Taylor map analysis for the nominal and hybrid crossings

Nonlinear terms in one turn map depend on the collision scheme; the nominal or hybrid crossing, or betatron phase difference between the two interaction points. The beam-beam interaction can be expanded by Taylor polynomial for the dynamic variables. The one turn map including two interaction points and two linear arcs is represented by Taylor polynomial. The one turn map characterizes resonance behaviors of the beam particles. For example, $x^n y^m$ term in the map, $\exp(-a : x^n y^m :)$, drives resonances of $n\nu_x \pm m\nu_y$. Details of the analysis is seen in Ref. [7] We discuss nonlinear terms up to 4-th order in this paper. Higher order terms may be important for proton rings without radiation damping. Further studies will be done elsewhere.

Figure 7 shows the coefficient of x^4 term of the beam-beam interaction as a function of the betatron phase difference between the two interaction points. The coefficient for the nominal crossing is small than that for hybrid crossing. This means the x^4 term is weakened by long bunch collision in the horizontal plane, perhaps. The coefficient has peaks for the phase difference of 0.3 and 0.8. The total tune is $(\nu_x, \nu_y) = (0.31, 0.32)$. The phase difference is another arc is 0.5 or 1 at the peaks, respectively.

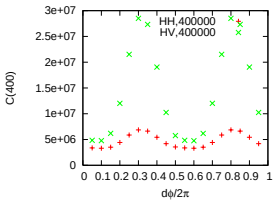

Figure 7: Coefficient of x^4 term for the betatron phase difference between the two interaction points. Red (HH) and green (HV) lines are for the horizontal-horizontal crossing adn horizontal-vertical crossing, respectively.

Figure 8 shows the coefficients of x^3z, y^3z and related terms. y^3z terms are very small for the nominal crossing, because the terms are suppressed by symmetry of the horizontal-horizontal crossing.

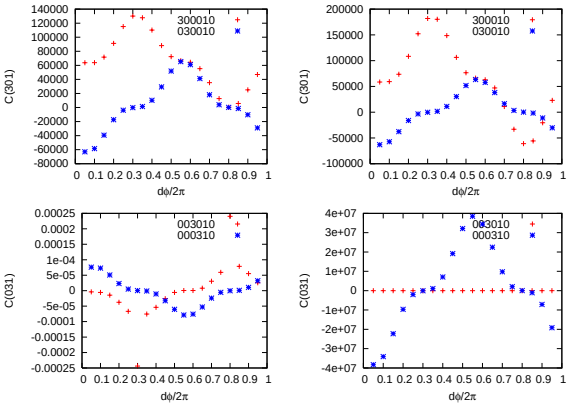

Figure 8: Coefficients of x^3z and y^3z terms of the beam-beam interaction. (a) x^3z (300010) and p_x^3z (030010) for the horizontal-horizontal crossing. (b) x^3z (300010) and p_x^3z (030010) for the horizontal-vertical crossing. (c) y^3z (003010) and p_y^3z (000310) for the horizontal-horizontal crossing. (d) y^3z (003010) and p_y^3z (000310) for the horizontal-vertical crossing.

Figure 9 shows the coefficients of x^2yz, xy^2z and related terms. xy^2z terms are very small for the nominal crossing, because the terms are suppressed by symmetry of the horizontal-horizontal crossing.

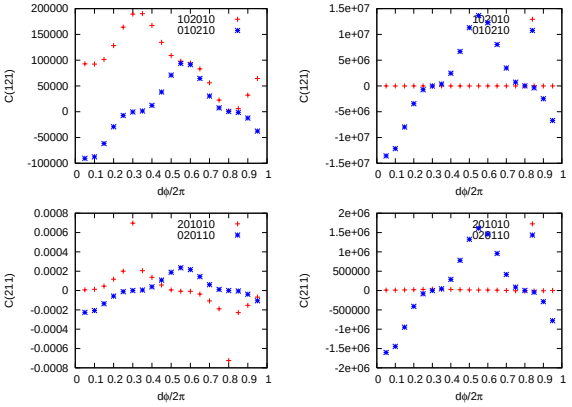

Figure 9: Coefficients of xy^2z and x^2yz terms of the beam-beam interaction. (a) xy^2z (102010) and $p_xp_y^2z$ (010210) for the horizontal-horizontal crossing. (b) xy^2z (102010) and $p_xp_y^2z$ (010210) for the horizontal-vertical crossing. (c) x^2yz (201010) and $p_x^2p_yz$ (020110) for the horizontal-horizontal crossing. (d) x^2yz (201010) and $p_x^2p_yz$ (020110) for the horizontal-vertical crossing.

SUMMARY

Effect of crossing angle are evaluated for the nominal LHC. The weak-strong simulation showed a visible luminosity degradation in a day for 6 times higher bunch population: that is, there is no problem for the nominal de-

sign. The strong-strong simulation gave luminosity degradation stronger than that of the weak-strong simulation. This degradation is considered due to numerical noise of macro-particle statistics at present.

High Piwinski angle scheme with a half beta and twice longer bunch length was investigated. The simulation included 7 parasitic interactions both of upstream and downstream of the collision point. Two type of collision scheme for two collision points, the nominal horizontal-horizontal crossing and the hybrid horizontal-vertical crossing, was studied. An example for each scheme was investigated with the weak-strong simulation. The hybrid crossing gave a halo formation due to the parasitic interactions in this example. We should not conclude that the nominal collision scheme is better than the hybrid scheme in this example.

Preliminary results for Taylor map analysis of the beam-beam interactions were presented. Nonlinear terms depending on the symmetry (parity) of the colliding system appear in the map. The nominal crossing gives a wide tune spread but less resonance term, while the hybrid crossing gives a narrow tune spread but more resonance terms. It is difficult to say simply which is better; depending on the operating point, betatron phase difference between the two interaction points.

ACKNOWLEDGEMENT

The author thanks to K. Takayama and F. Zimmermann for fruitful discussions.

REFERENCES

[1] J. Augustin, Orsay Report, No 36-69 (1969).

[2] K. Oide and K. Yokoya, Phys. Rev. A40, 315 (1989).

[3] K. Hirata, Phys. Rev. Lett. 74, 2228 (1995).

[4] K. Ohmi et al., Phys. Rev. ST-AB 7,104401 (2004).

[5] K. Ohmi et al., Proceedings of PAC07 (2007).

[6] K. Ohmi, Proceedings of ECLOUD07, KEK proceedings 2007-10, 189 (2007)

[7] K. Ohmi et al., Proceedings of PAC07 (2007).

[8] F. Zimmermann, Proceedings of PAC07 (2007).

[9] K. Takayama et al., Phys. Rev. Lett. 88, 144801 (2002).

[10] F. Ruggiero and F. Zimmermann, Phys. Rev. ST-AB 5, 061001 (2002).

Luminosity leveling with angle

G. Sterbini, J.-P. Koutchouk

Abstract

The very high luminosity foreseen for the LHC luminosity upgrade entails in all cases a significant luminosity decrease during a few hours run. We present in this note a new method of luminosity leveling, based on the on-line adjustment of the crossing angle, while keeping the optics unchanged. It is implemented using the D0 dipole of a possible Early Separation Scheme and an orbit corrector. The whole bump is confined in the experimental drift space. It should be operationally simple as it avoids most complicated side effects that other leveling principles would produce.

INTRODUCTION AND CONCEPT

The LHC luminosity upgrade aims at increasing significantly the peak and average LHC luminosity [1]. In all scenarios, the decay of the luminosity due to the beam-beam interaction becomes dominant over other mechanisms and very significant as compared to the nominal LHC parameters. This is particularly true for the most efficient and economical scenarios where the luminosity increase is obtained by other means than a beam current increase. A large variation of the luminosity over a few hours run shows many drawbacks, both for the detectors and the machine components. From the machine point of view the main issues are the peak and average power deposition in the superconducting triplets and ancillary magnets. To prevent a quench, it has to be designed for the maximum instantaneous luminosity. The present knowledge shows that the capability of Nb-Ti appears significantly exceeded while the Nb_3Sn technology could face it though with additional improvements of the shielding efficiency. For the experiment itself, the high initial peak luminosity produces a higher multiplicity and a stronger background. To cope with it, either the detector has to be designed for the peak multiplicity that is significantly above the design goals of the present detectors or a fraction of the running time will not be used efficiently for data taking.

An answer to this challenge is luminosity leveling. It is traditionally proposed to adjust in real time the beam size at the crossing point to obtain this result. The authors ignore whether this was ever made operational in practice. While a modulation of the focusing is indeed a priori simple in principle, it shows a large potential of side effects that is bound to make it delicate in practice: when the focusing is modified, its chromatic correction has to be adjusted. As it is not locally corrected, all the lattice sextupoles have to be ramped, with unwanted feed-down effects on the betatron tunes and closed orbit all around the machine, including in the collimation sections. Likewise, the modification of the β-function at the place where it reaches its maximum requires strictly local correction of alignment or tilt imperfections, rarely obtained in practice, resulting, e.g. in closed orbit distortions propagating to the whole machine. In the LHC the situation is further complicated by the presence of a crossing angle that extends up to Q4/Q5 and that create feed-down effects depending on the detail of the optics, of the imperfections and of their correction strategy or capability. While this method is certainly not impossible, its complexity may require a long time (i.e. integrated luminosity) to make it operational.

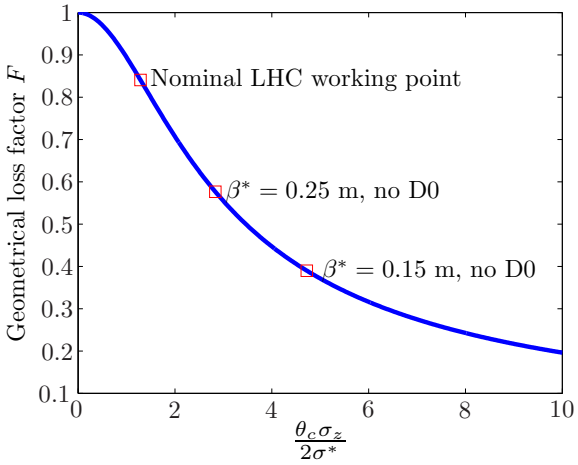

Figure 1: The geometrical loss factor as function of the Pinwiski parameter.

The early separation scheme proposed to modify the beam crossing layout [3] potentially allows another approach to luminosity leveling that appears much easier to implement. The principle is to adjust the crossing angle in real-time with an adjustment of the beam trajectories only in the experimental straight section between the left and right Q1 quadrupoles. In this way advantage is made of the significant influence of the crossing angle or rather geometrical loss factor F on the luminosity, as shown on Figure and Equation 1

$$F \approx \frac{1}{\sqrt{1+\left(\frac{\theta_c \sigma_z}{2\sigma^*}\right)^2}} \qquad (1)$$

where θ_c is the full crossing angle, σ_z is the RMS bunch length and σ^* is the RMS beam size at the IP (in the round beam hypothesis). All the side-effects met when modulating the focusing and introduced before are suppressed. Other side effects are nevertheless present:

- a modulation of the length of the luminous region
- a modulation of the beam-beam tune shift, always toward lower values
- a modulation of the excitation of beam-beam driven synchro-betatron resonances.

The two former issues are discussed in this note while the latter is a general issue for the luminosity upgrade that goes beyond this study.

This method assumes that, in addition to the early separation dipoles that would be embedded in the detectors, a standard closed orbit corrector is installed ideally in front of Q1 towards the IP.

THE LUMINOSITY LIFETIME

In order to describe the evolution of the luminosity we numerically implement a simple model assuming that the luminosity will be dominated by the three following mechanisms

- the protons burning
- the intra beam scattering
- the rest gas scattering.

As shown in the following the previous phenomena are coupled.

The protons burning

The equation that describes the proton burning is

$$\dot{N_b}(t) = -\frac{\sigma\, n_{exp}}{n_b} L(t) \tag{2}$$

where $N_b(t)$ is the number of protons per bunch, n_b is the number of the bunches, n_{exp} the number of experiments considered at the luminosity $L(t)$ and σ is the p–p cross-section. In the following we assume $n_{exp} = 2$ and $\sigma = 80$ mbarn [1].

The intra beam scattering

The equation that describes the intra beam scattering is [2]

$$\dot{\epsilon}(t) = \frac{1}{\tau_{IBS}} \frac{N_b(t)}{N_{IBS}} \epsilon(t) \tag{3}$$

where $\epsilon(t)$ is the beam emittance, τ_{IBS} is the time constant for intra beam scattering relative to N_{IBS} protons per bunch, $N_b(t)$ is the number of protons per bunch considered. In the following we assume $\tau_{IBS} = 91.3$ h at $N_{IBS} = 1.15\ 10^{11}$ [1].

The rest gas scattering

The equation that describes the rest gas scattering is [2]

$$\dot{N_b}(t) = -\frac{n_b}{\tau_{RGS} N_{RGS} n_{RGS}} {N_b}^2(t) \tag{4}$$

where τ_{RBS} is the time constant for rest gas scattering relative to N_{RBS} protons per bunch and n_{RBS} bunches, $N_b(t)$ and n_b is respectively the number of protons per bunch and the number of bunches considered. In the following we assume $\tau_{RGS} = 78.35$ h, $N_{RGS} = 1.15\ 10^{11}$ and $n_{RGS} = 2808$ [1].

THE LUMINOSITY LEVELING INSERTION

In order to vary **locally** the crossing angle we propose to install one dipole and one orbit corrector between the IP and the triplet. The baseline crossing angle bumps extends beyond Q5: if we use this bump for leveling, the beam closed orbit in the quadrupoles will change with similar drawbacks as using a variable β^*. We performed the computations in the thin dipole approximation: the dipole is at l_1 from the IP and the orbit corrector at l_2. The angular kicks that should be provided by the two magnets in order to close the bump can be easily obtained by geometrical considerations:

$$\begin{aligned} \theta_1 &= atan\left(\frac{l_2\, tan(\frac{\theta_{tripl}}{2}) - l_1\, tan(\frac{\theta_c}{2})}{l_2 - l_1}\right) - \frac{\theta_c}{2} \\ \theta_2 &= \frac{\theta_{tripl}}{2} - \frac{\theta_c}{2} - \theta_1 \end{aligned}$$

where θ_{tripl} is the angle between the beams in the triplet needed to preserve the $9.5\ \sigma$ separation. The inequality $l_1 < l_2 \leq l^*$ should be respected. In the following we assume that $l_1 = 6$ m and $l_2 = 19$ m: this choice is just a starting point. The dipole position (l_1) is crucial since it determines the number of parasitic encounters at reduced distance: this has to be chosen keeping in mind the integrability issues in the detector areas and the beam stability constraint (hopefully to be confirmed by experimental results). In any case the dipole cannot approach the IP more than 3.5 m due to the inner detector presence: in the 25 ns time spacing scenario at least one parasitic encounter would occur at reduced distance.

THE DYNAMIC RANGE OF THE θ_C

We found two mechanisms that limit the θ_c range. The minimum θ_c is constrained by the encounters at reduced distance: after some preliminary experimental results, we propose that the minimum distance should be consider equal to half the nominal that is to say around $5\ \sigma$. Reducing it below this threshold we assume that strong compensation should be implemented. The maximum θ_c is limited by possible synchro-betatron resonances: this problem should be addressed in a general study.

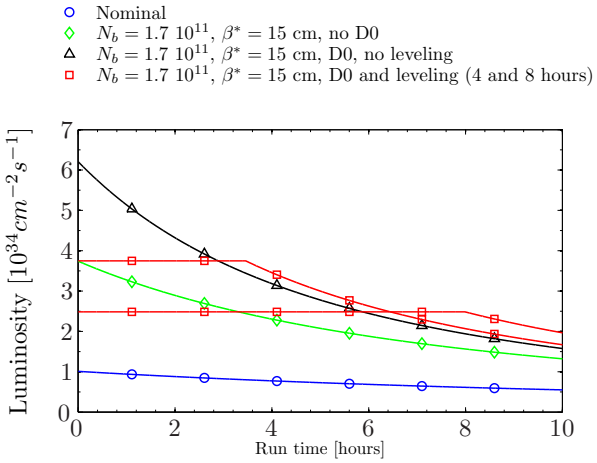

Figure 2: The luminosity behavior during the run time.

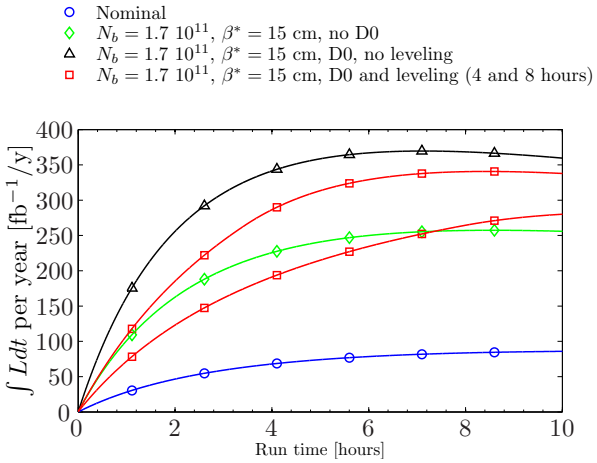

Figure 3: The integrated luminosity in a year considering 200 working days and 5 h of turn-around-time.

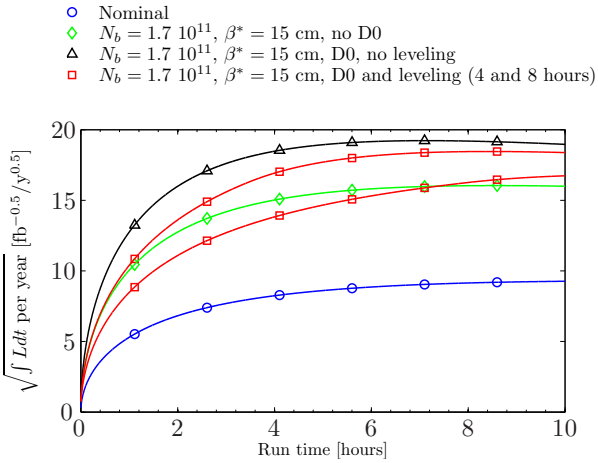

Figure 4: The square root of the integrated luminosity considering 200 working days and 5 h of turn-around-time.

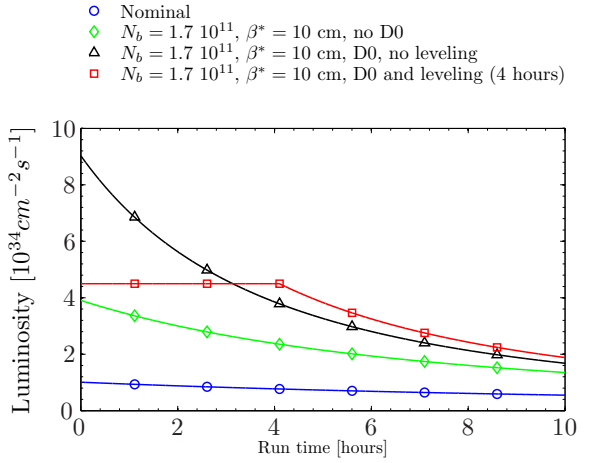

Figure 5: The luminosity behavior during the run time.

SCENARIOS, PERFORMANCE AND SIDE EFFECTS

Scenarios and Performance

In the following we present a possible scenario of upgrade considering a $\beta^* = 0.15$ m at the ultimate current ($n_b = 2808$ and $N_b = 1.7\ 10^{11}$) and therefore a bunch spacing of 25 ns. The former is just one scenario among others with the only aim to provide an example.

In Figure 2 we show the luminosity behavior during the run in different configurations. Without implementing the D0 (or alternative solutions that reduce the crossing angle, such as Crab cavities) the gain in peak luminosity is about a factor 4. With the D0 and a fixed crossing angle we reach a factor 6; with the leveling, partially reducing the integrated luminosity, we reduce the peak luminosity of a factor 2. In Figure 3 we show the integrated luminosity achievable considering our model and in Figure 4 its square root. It is evident that we reduced the peak luminosity with a cost in term of integrated luminosity. However our computation of the integrated luminosity is simplistic: it assumes 100% efficiency in using the collisions at all times and a luminosity decay only due to the above mentioned well defined sources. The apparent loss of luminosity due to leveling may well be overestimated.

To analyze the scheme potential in presence of even more challenging scenario we can look at the Figures 5 and 6. Here we consider the ultimate current, a $\beta^* = 0.10$ m and and the minimum distance between the beams of $3.3\,\sigma$. To reach that configuration without impacting on the beam lifetime strong compensation scheme are probably needed (electron lenses) or the use of weak crab cavities as auxiliary system of the D0's task. The peak luminosity and the integrated luminosity are summarized in Table 1: for the computation of the integrated luminosity we assumed 200 working days per year and a turn-around-time of 5 h (we

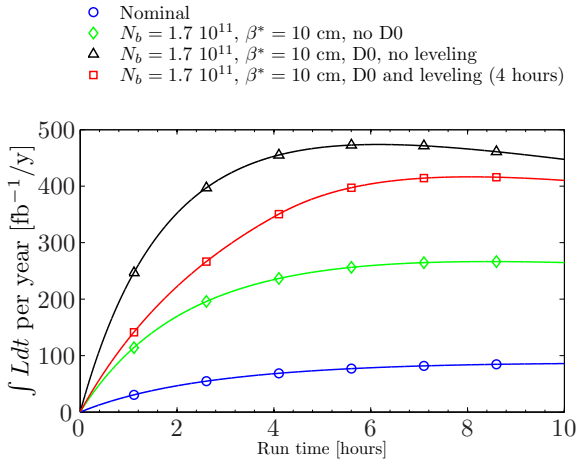

Figure 6: The integrated luminosity in a year considering 200 working days and 5 h of turn-around-time.

Table 1: Performances in term of luminosity (L) of the different schemes

		Integrated L [fb^{-1}]
Nominal scenario		86.37
$\beta^* = 0.15$ m	no D0	257.37
$\beta^* = 0.15$ m	D0, no leveling	369.65
$\beta^* = 0.15$ m	D0 and leveling	340.70
$\beta^* = 0.10$ m	no D0	266.49
$\beta^* = 0.10$ m	D0, no leveling	473.87
$\beta^* = 0.10$ m	D0 and leveling	416.54

consider as turn-around-time the distance in time between the beam dumping and the first collisions).

In the following we always consider the more conservative scenario with ultimate current, $\beta^* = 0.15$ cm and $4.75\ \sigma$ minimum separation.

The leveling will modify the crossing angle and consequently the geometrical loss factor during the run as described in Figure 10 and 11.

The requested integrated magnetic field on the dipole and the orbit corrector is shown in Figure 12 and 13 respectively.

We plotted in Figure 14 and 15 the evolution of the beam current and of the beam normalized emittance.

Side effects

In the previous section we underline the fact that using a leveling we have the advantage of reducing the peak luminosity with the drawback of losing some integrated luminosity. We have to stress that this is a result obtained from simple models: it doesn't take into account effect that can be dominant in real life. For instance the first parts of the run can be dedicated to the tuning of machine setup or of experimental instrumentation: therefore cannot be considered as useful luminosity. In any case the hardware needed for the leveling is definitely compatible with the run that doesn't change the crossing angle.

A very important aspect to investigate is the required distance between the beams (Figure 7): the impact of the reduced distance at parasitic encounters should be hopefully addressed with an experiment at RHIC. An other possible

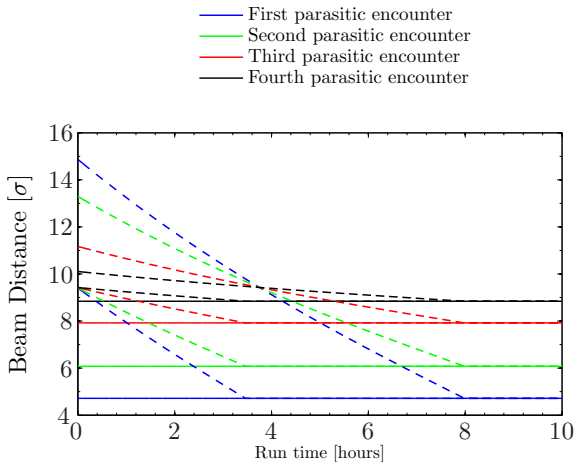

Figure 7: The distance between the beams at the first four encounters with the D0 without leveling (*solid line*) and with leveling (*dotted line*).

drawback is the change of longitudinal size σ_{lum} of the luminous region [4]

$$\frac{1}{\sigma_{lum}} \approx \sqrt{\frac{2}{\sigma_z^2} + \frac{\theta_c^2}{2\,\sigma^{*2}}} \tag{5}$$

that is to say

$$\sigma_{lum} \approx \frac{\sigma_z}{\sqrt{2}}\,F. \tag{6}$$

As shown in Figure 8 the leveling has a significant impact that ought to be investigated.

On the other hand in Figure 9 the tune shift ξ due to the head on

$$\xi = \frac{N_b r_p}{4\pi\epsilon_n}\,F \tag{7}$$

where N_b is the number of protons per bunch, r_p is the classical radius of the proton, ϵ_n in the beam normalized emittance and F the geometrical loss factor. It seems that the impact of the leveling on the head-on tune shift is not more severe than in the other configurations that do not implement the Early Separation Scheme.

CONCLUSION

In this work we presented the concept and the performance of a leveling scheme for the LHC luminosity upgrade. With the early separation scheme it is possible to vary the crossing angle between the beams during the run: there is no impact on the optics of the machine itself. In general, limiting the peak luminosity has some negative

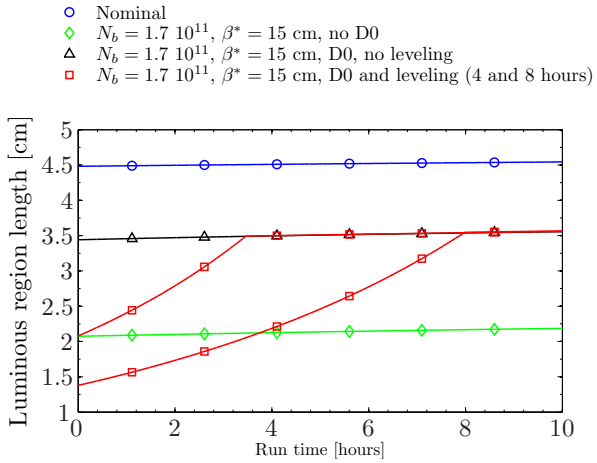

Figure 8: The luminous region size during the run time.

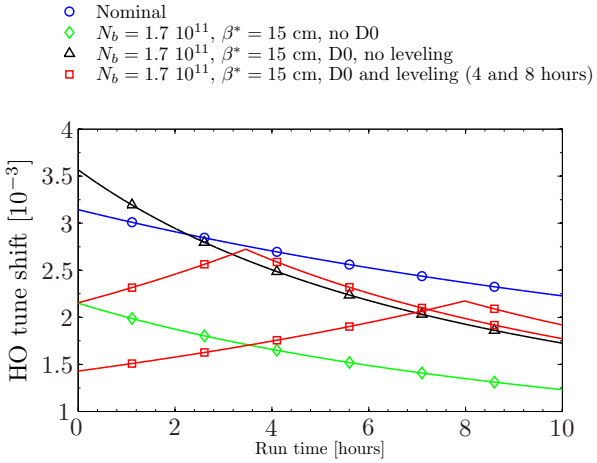

Figure 9: The HO tune shift during the run time.

impact on the integrated luminosity: the early separation scheme gives a lot of flexibility that can be adjusted to the experiments' needs. From first discussions there seems to be not significant problems with respect to the luminous region length and the HO tune shift, while synchro-betatron resonances still have to be addressed in a more general framework.

REFERENCES

[1] O. Brüning and al., *"LHC Luminosity and Energy Upgrade: a Feasibility Study"*, LHC Project Report 626, December 2002, Geneva.

[2] A.W. Chao and M. Tigner, *"Handbook of Accelerator Physics and Engineering"*, World Scientific Publishing Co. Pte. Ltd. , 2006.

[3] J.-P. Koutchouk and G. Sterbini, *"An Early Beam Separation Scheme for the LHC Luminosity Upgrade"*, EPAC06 Proceedings, Edinburgh.

[4] F. Zimmermann and W. Scandale, *"Two scenarios for the LHC Luminosity Upgrade"*, PAF/POFPA meeting, 13 February 2007, CERN.

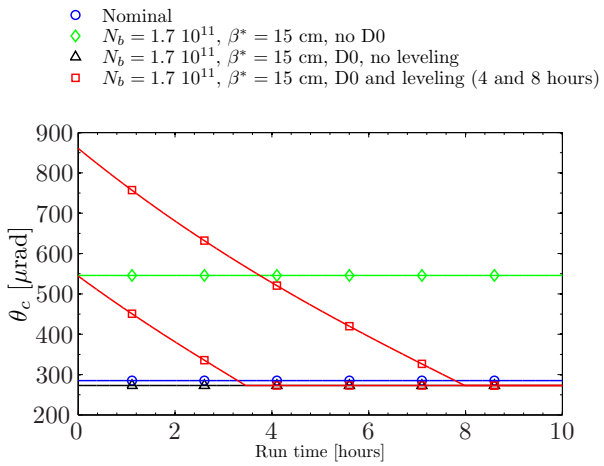

Figure 10: The θ_c behavior during the run time.

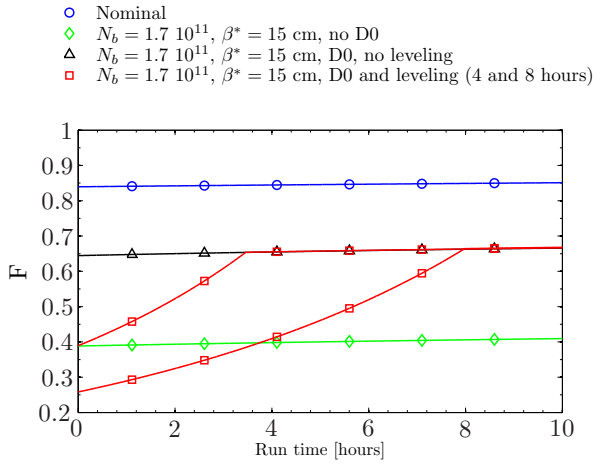

Figure 11: The geometrical loss factor during the run time.

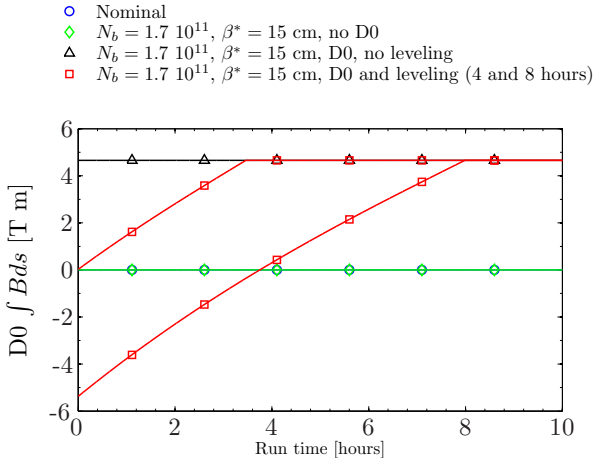

Figure 12: The integrated magnetic field request on the D0.

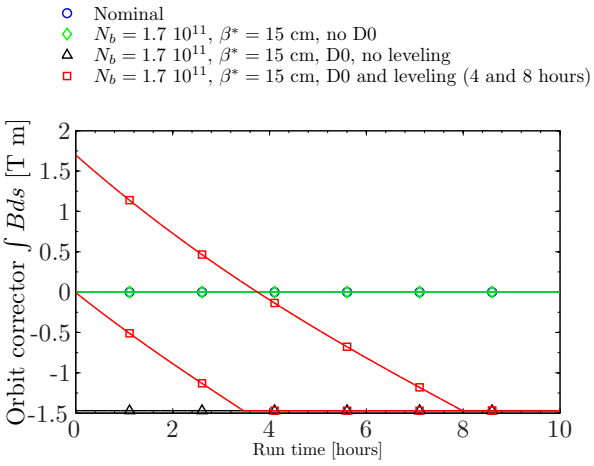

Figure 13: The integrated magnetic field request on the orbit corrector.

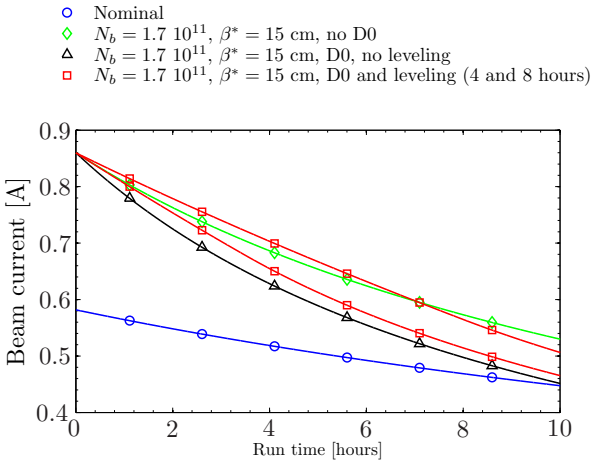

Figure 14: The current behavior during the run time.

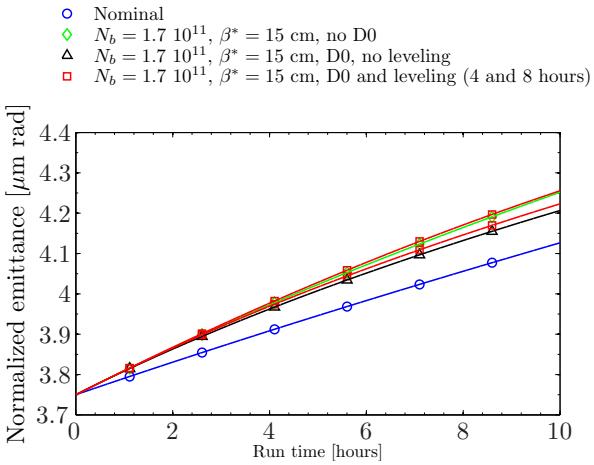

Figure 15: The beam normalized emittance during the run time.

TURNAROUND TIME IN MODERN HADRON COLLIDERS & STORE-LENGTH OPTIMIZATION

O. Brüning, CERN, Geneva, Switzerland

Abstract

The paper presents a review of the average accelerator turnaround time in existing superconducting hadron machines (HERA at DESY@, RHIC at BNL§ and the TEVATRON at FNAL&). Based on the past experience with these previous hadron accelerators the paper aims at a best guess estimate for an initial and optimum turnaround time in the LHC during the first year of operation and for routine operation after the machine commissioning.

@: Data on the operational experience with the HERA machine has been kindly made available by Bernhard Holzer from DESY.

$: Data on the operational experience with the RHIC machine has been kindly made available by Wolfram Fischer from BNL.

&: Data on the operational experience with the Tevatron machine has been kindly made available by Vladimir Shiltsev from FNAL and retrieved from the Tevatron operation Internet pages:
http://www-bd.fnal.gov/pplot/index.html.

We acknowledge the support of the European Community-Research Infrastructure Activity under the FP6 "Structuring the European Research Area" programme
(CARE, contract number RII3-CT-2003-506395)

1. INTRODUCTION

In the following we define the turnaround time of an accelerator storage ring as the time between the end of one and the start of the next physics run. For an accelerator storage ring the measurement of the turnaround time starts with the beam at top energy of the accelerator and comprises the ramp down of the magnet system to the injection energy settings after the beam extraction, the time required for setting up the machine for the next injection, the time required for injecting new beams into the machine, the time required for the beam acceleration (ramp), the optics transition for the physics run (squeeze) and the time required for adjusting the beam conditions so that the detectors can start again data taking. The minimum theoretical turnaround time ($T_{turnaround,min}$) for the LHC amounts to approximately 70 minutes and is defined by the following contributions [1]:

- Ca. 18 minutes for reducing the magnet strength from the required values during the physics run operation at top energy to the required magnet strength at the pre-injection plateau ('ramp down') assuming a maximum ramp speed of 10A per second in the main LHC magnet circuits. In order to minimize the dynamic magnet field errors during the injection and acceleration process and to assure that the magnetic field does not change the Hysteris branch at the start of the beam acceleration, the magnet current is first reduced to values slightly below the actually required strength for the beam injection ('pre-injection plateau') and then increased again to the values required for the beam injection.
- Ca. 15 minutes steady magnet powering at the 'pre-injection plateau'.
- Ca. 15 minutes for increasing the magnet strength from the 'pre-injection plateau' to the actual injection settings.
- Ca. 8 minutes for machine adjustments with low intensity 'pilot beams' (assuming 6 injection shots per LHC beam).
- Ca. 7 minutes for the actual filling of the LHC with nominal beams.
- Ca. 28 minutes for increasing the magnet current from the strength required for beam injection to the required values required for physics operation at top energy ('ramp up'). The 'ramp-up' of the magnet current takes slightly longer than the 'ramp down' because the ramp rate is optimized at each acceleration stage for minimizing the dynamic field errors in the main magnets. At the beginning of the ramp the magnet current follows a parabolic current variation with time, followed first by an exponential and then a linear variation with time and a final parabolic round off at top energy. The ramp down without beam features on the other hand only a linear variation of the magnet current with time.
- Ca. 15 minutes for the optics transition to the physics configuration ('optics squeeze'). Due to aperture limitations inside the magnets next to the Interaction Point (IP) the optics configuration for physics operation can only be adjusted at top energy when the beam size has shrunk due to the acceleration damping.

Some of the above estimates are only best guesses for the minimum required time. For example, the time required for adjusting the machine with pilot beams at injection energy and the optics squeeze at top energy depend a lot on the machine reproducibility, which can only be quantified with machine operation.

The actual required time for larger in real operation due to required additional adjustments (e.g. beam based fine tuning of the collimator jaws). Figure 1 shows basic magnet cycle for the LHC [1].

Figure 1: The LHC magnet cycle during nominal operation.

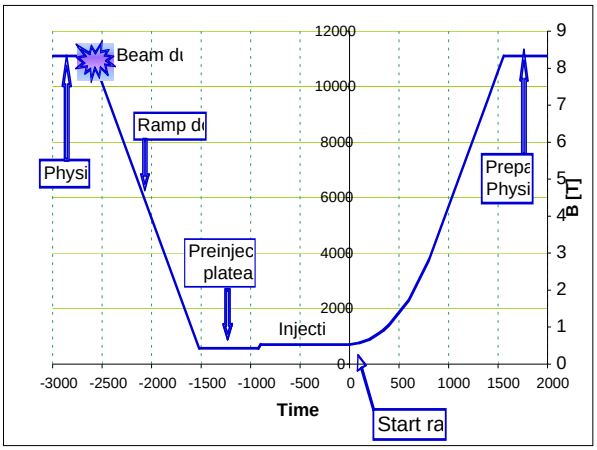

The minimum machine turnaround time defines an important input parameter for calculating the maximum attainable integrated luminosity of a collider complex. Equation 1 yields the total integrated luminosity in a collider as a function of the collider turnaround time and the luminosity lifetime [2].

$$\hat{L} = R \cdot M \cdot (24 \cdot 60^2) \cdot L_0 \cdot \frac{\tau_{L,tot}[h]}{T_{run}[h] + T_{turnaround}[h]} \cdot \left[1 - e^{-T/\tau_{L,tot}}\right] \quad (1)$$

$$\hat{L} = R \cdot M \cdot (24 \cdot 60^2) \cdot L_0 \cdot f(T, \tau) \quad (2)$$

T_{run} specifies the run time for physics data taking, $T_{turnaround}$ the collider turnaround time, L_0 the initial luminosity (expressed in cm-2 sec-1), and $t_{L,tot}$ the luminosity lifetime, M the number of scheduled days of physics operation and 'R' the overall collider efficiency. Using an exponential approximation for the luminosity decay, the luminosity lifetime is approximately 15h for the nominal LHC beam parameters and reduces to approximately 10h for the ultimate beam parameters [2]. In both cases, the luminosity lifetime is dominated by the beam losses due to the beam collisions at the IP. Increasing the initial luminosity beyond the nominal and 'ultimate' luminosity values ($L_{nominal}$ = 1.0 1034 cm-2 sec-1 and $L_{ultimate}$ = 2.3 1034 cm-2 sec-1) results therefore in a rapidly decreasing luminosity lifetime. Depending on the upgrade solution, it decreases to 2.2h or 4.5h for the two Phase 2 upgrade scenarios under study for the LHC [3]. Table 1 summarizes the main LHC machine parameters for the nominal and ultimate performance as well as for the two upgrade options that are currently studied for pushing the LHC machine peak luminosity above 10^{35} cm^{-2} sec^{-1}. Table 2 shows the ratio of average to peak luminosity as a function of luminosity lifetime and turnaround time assuming an optimum run length for each fill (function 'f' in Equation (2)). One clearly recognizes that the ratio of integrated to peak luminosity decreases significantly if the machine turnaround time becomes significantly longer than the luminosity lifetime. Transforming an increase in peak luminosity into a gain in integrated luminosity therefore requires a machine turnaround time, which is comparable or shorter to the luminosity lifetime.

Table 1: The nominal, ultimate and Phase 2 upgrade machine parameters for the LHC [3].

parameter	nominal	ultimate	25ns	50ns
Protons per bunch	$1.15\ 10^{11}$	$1.7\ 10^{11}$	$1.7\ 10^{11}$	$4.9\ 10^{11}$
Total beam current	0.58 A	0.86 A	0.86 A	1.22 A
Longitudinal bunch profile	Gauss	Gauss	Gauss	Flat
β^* at the IPs	0.55m	0.5m	0.08m	0.25m
Full crossing angle at the IPs	285µrad	315µrad	0µrad	381µrad
Peak luminosity [cm^{-2} sec^{-1}]	$1\ 10^{34}$	$2.3\ 10^{34}$	$15.5\ 10^{34}$	$10.7\ 10^{34}$
Peak events per crossing	19	44	294	403
Initial luminosity lifetime	25h	14h	2.2h	4.5h
Stored beam energy	370MJ	550MJ	550MJ	780MJ
Additional requirements	-	-	Large aperture triplet magnets	Large aperture triplet magnets
			Efficient / radiation hard absorbers	Efficient / radiation hard absorbers
			D0	Wire compensators
			Crab cavities	

Table 2: The ratio of average to peak luminosity as a function of luminosity lifetime and machine turnaround time (function 'f' in Equation (2)).

$T_{turnaround}$ [h] / τ_{lumi} [h]	1	6	10	20
2.5	0.46	0.20	0.14	0.09
10	0.66	0.39	0.32	0.22
15	0.70	0.46	0.38	0.28
19	0.73	0.5	0.42	0.31

The assumption of an optimum run length clearly provides an optimistic estimate as the optimum run length depends on the machine turnaround time which is only precisely known once the machine starts the next physics run. Table 3 shows the optimum run lengths for various luminosity lifetimes and machine turnaround times.

Table 3: The optimum run length for various luminosity lifetimes and machine turnaround times.

T_{turn} / τ_{lumi}	1h	6h	10h	20h
2.5h	2h	4h	5h	6h
10h	4h	9h	11.5h	15h
15h	5h	12h	15h	20h
19h	5.5h	13h	16.5h	22h

Figure 2 shows the integrated luminosity for a turnaround time of 10h and a luminosity lifetime of 10h as a function of the run length. One recognizes how the integrated luminosity decreases if the run length becomes too short, e.g. due to an unscheduled run abort due to a technical fault in the collider equipment, or too long, e.g. if there is a fault in the injector complex and a new fill cannot be prepared at the requested moment or if a too large value had been assumed for the turnaround time.

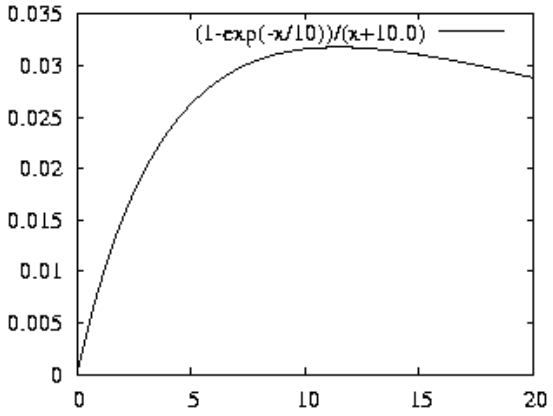

Figure 2: The integrated luminosity as a function of the run length for a luminosity lifetime of 10h and a turnaround time of 10h in arbitrary units.

2. OPERATIONAL MACHINE TURNAROUND TIME VERSUS MINIMUM THEORETICAL MACHINE TURNAROUND TIME

The average machine turnaround time can be significantly larger than the theoretical minimal turnaround time of a collider storage ring. This is particularly true if the machine performance is pushed to its maximum and the operating margins are reduced. An estimate for the operational machine turnaround time during routine operation is therefore the prerequisite for estimating the potential performance reach of the LHC in terms of integrated luminosity for various luminosity values. Faults generating a long interruption time (long compared to the optimum run length) essentially reduce the scheduled operation time and can be accounted for by an overall collider efficiency 'R'.

$$\hat{L} = R \cdot M \cdot (24 \cdot 60^2) \cdot L_0 \cdot f(T, \tau) \qquad (3)$$

In the following we will therefore discard all interruptions of the machine operation that are longer than a given threshold value. This cut depends on the machine under investigation and will be specified separately for each studied case.

Faults creating a short interruption time result either in a non-optimum run length if the fault occurs during a physics run, or in prolonged effective machine turnaround times if the fault occurs during the preparation of a new fill.

3. EXPERIENCE FROM EXISTING HADRON COLLIDER STORAGE RINGS

In the following we will look at the operational experience from existing hadron storage rings and compare their operational average and minimum turnaround times to their theoretical values. We will look at three machines (RHIC at BNL, Tevatron at FNAL and HERA at DESY) and discuss the main reasons for operation failures.

3.1 Tevatron at FNAL

Table 4 shows the planned Tevatron machine parameters for RunII from the technical design report [4] and Table 5 shows the main beam parameters from the operational experience with RunII [5]. The operational minimum turnaround time and average store length are approximately twice as long as the planned parameters.

Table 4: The planned Tevatron machine parameters for RunII [4].

Planned RunII parameters	**Value**
Minimum theoretical turnaround time	1 hour
Nominal proton beam intensity	36 x 27 10^{10} ppb
Nominal anti-proton intensity	36 x 3.1 10^{10} ppb
Nominal initial luminosity	86 10^{30} cm^{-2} sec^{-1}
Theoretical beam lifetime	τ > 13 hours
Store length	12 hours

Table 5: The operational Tevatron machine parameters for the 2007 RunII [5].

RunII parameters in operation	**Value**
Minimum operational turnaround time [6]	2.5 hours
Proton beam intensity	36 x 26 10^{10} ppb
Anti-proton intensity	36 x 6.1 10^{10} ppb
Average initial luminosity	186 10^{30} cm^{-2} sec^{-1}
Average Store length	21.3 hours
Average set-up time	2.4 hours

The Tevatron featured a total of 1292 stores during its first 6 years of operation. 932 of these 1292 stores were intentionally terminated with an average store length of 22.4 hours. 360 stores ended due to failures with an average store length of 10.23 hours. The top 10 causes for unintentional run terminations were:

- Problems related to the cryogenic system: 49 cases ➔ 13%
- Lightening and thunder storms: 40 cases ➔ 11%
- Problems with the quench protection system: 33 cases ➔ 9%
- Problems with the controls: 29 cases ➔ 8%
- Problems with the beam separators: 25 cases ➔ 7%
- RF problems: 25 cases ➔ 7%
- Problems related to the low b quadrupoles: 24 cases ➔ 7%
- Corrector magnet problems: 20 cases ➔ 5.5%
- Human errors: 20 cases ➔ 5.5%
- Power converter problems: 20 cases ➔ 5.5%

One can expect most of the above failure causes also for the operation of the LHC. Figures 3 and 4 show the efficiency of the machine expressed in time spend in physics and average store hours per week averaged of the full fiscal year respectively for the 2007 run [5]. The above statistics is compatible with M = 365 and R = 0.6 in Equations (1) and (2) and corresponds well to the experience from the RHIC operation. Figure 5 shows the occurrence of various turnaround times between two consecutive fills [6] in form of a histogram. Figures 6 and 7 show the average turnaround time as a function of store umber without and with the application of a 36h cut respectively. The minimum operational turnaround time is approximately 2.5 hours and is therefore, after 6 years of Run II operation, ca. 2.5 times larger than the minimum theoretical turnaround time. The average operational turnaround time is ca. 8 hours and approximately 8 times larger than the minimum theoretical turnaround time. The average store length in 2007 operation was 21 hours and the average machine setup time amounted to ca. 2.4 hours.

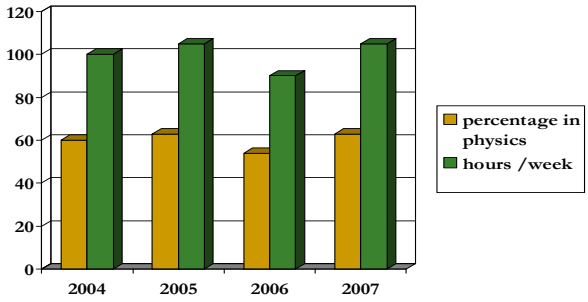

Figure 3: Machine efficiency expressed in time spent in physics operation in hours per week and percentage per calendar time.

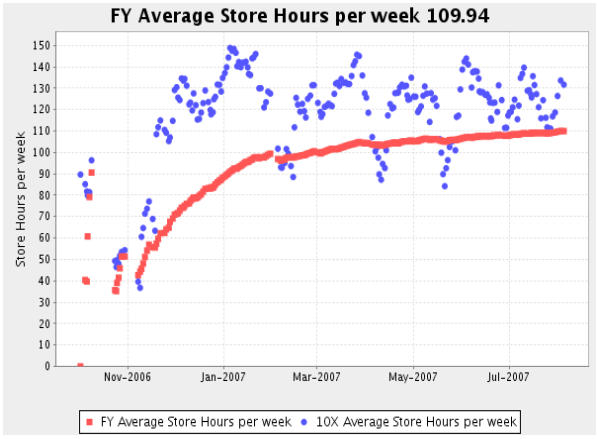

Figure 4: Average store hours per week averaged over the full fiscal year [5].

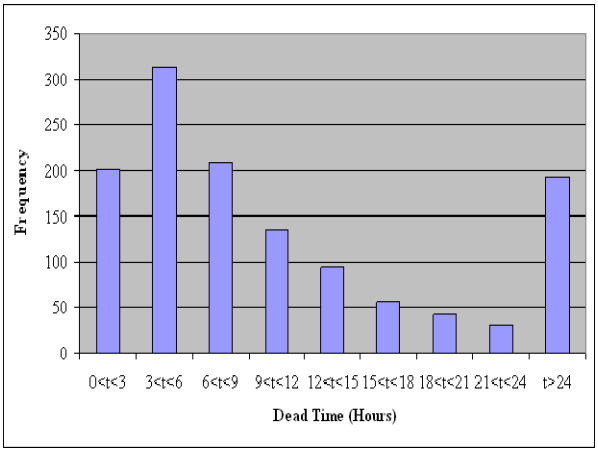

Figure 5: Time between two consecutive fills of the Tevatron [6].

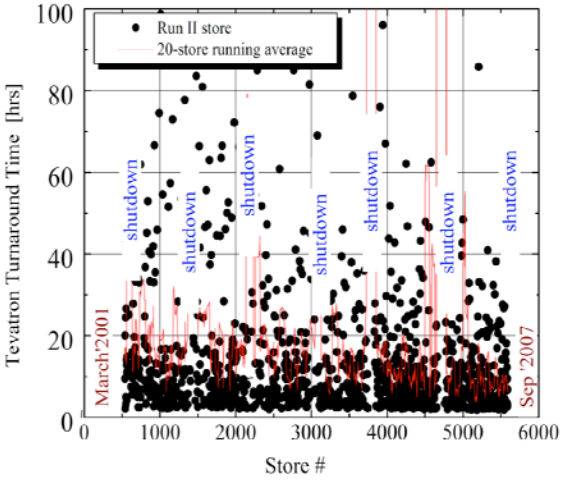

Figure 6: The Tevatron turnaround time as a function of store number.

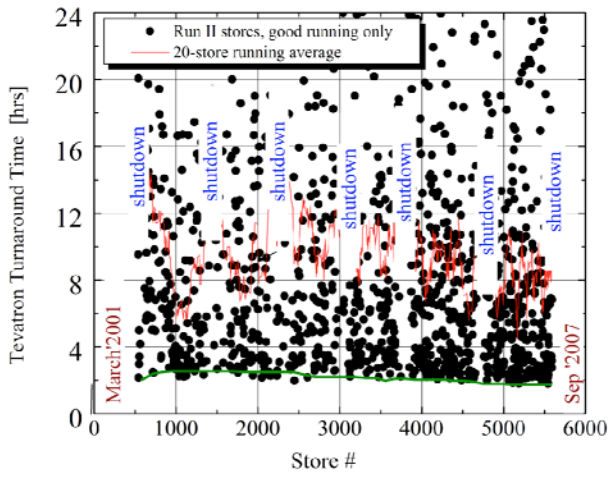

Figure 7: The Tevatron turnaround time as a function of store number with a cut of 36h

Table 6: Summary of the key observations from the Tevatron operation.

Parameter	Value
Minimum theoretical turnaround time	1 hours
Minimum operational turnaround time	2.5 hours
Average operational turnaround time	8 hours
Machine efficiency in percent of calendar time spent in physics operation.	60%
Average Store length	21 hours

Table 6 summarizes the main observations from the Tevatron operational experience.

3.2 HERA AT DESY

Table 7 and 8 show the main machine parameters for the HERA I and HERA II run periods [7]. The minimum theoretical turnaround time consists of 35 minutes filling time (defined by the cycle of the PETRA machine) plus 2 times 30 minutes for ramping the magnets up and down.

Table 7: The main HERA machine parameters for HERA I operation.

HERA I parameters	Value
Minimum theoretical turnaround time	1.5 hour
Nominal proton beam intensity	180 x 7.3 10^{10} ppb
Nominal electron beam intensity	180 x 3.7 10^{10} ppb
Nominal initial luminosity	17.8 10^{30} cm^{-2} sec^{-1}
Theoretical beam lifetime	t > 1000 hours
Store length	Ca. 10 hours

Table 8: The main HERA machine parameters for HERA II operation.

HERA II parameters	Value
Minimum theoretical turnaround time	1.5 hour
Nominal proton beam intensity	180 x 10.3 10^{10} ppb
Nominal electron beam intensity	180 x 4.3 10^{10} ppb
Nominal initial luminosity	75.8 10^{30} cm^{-2} sec^{-1}
Theoretical beam lifetime	t > 340 hours
Store length	Ca. 14 hours

Figures 8 and 9 show examples for the machine reliability from the 2006 operation. The left-hand side of Figure 8 shows a series of unscheduled proton beam losses that were caused by a variety of unforeseen beam losses (e.g. beam showers in the collimation sections and fast (ms time scale) beam losses. The right-hand side of Figure 8 shows fills of a regular operation period. The left-hand side of Figure 9 shows a series of operation failures due to technical problems (cryogenic problems, power failure and quench alarms during beam injection). The right-hand side of Figure 9 shows again regular fills corresponding to a normal operation period. Figure 10 shows the overall machine efficiency during the 2000 operation. The average machine efficiency of ca. 55% corresponds well to the operational experience from RHIC and Tevatron. Figure 11 gives a statistics of the most frequent reasons for an interruption of the HERA operation and Figure 12 shows the corresponding failure time in operation days [7]. In total HERA featured 115 physics stores in the 2006 operation requiring 164 proton and 185 electron injections. During the 2006 operation period HERA featured a total of 230 faults. The average store length amounted to 7.4 hours with a minimum store time of 0.16 hours and a maximum sore length of 14 hours. Figure 13 shows the distribution of various operation modes for HERA during the 2006 run. Ca. 50% of the operation time was spent in luminosity operation and ca. 25% of the operation time was lost due to faults. Ca. 13% of the operation time was required for filling the HERA machine with new beams.

The most frequent interruptions are caused by:

- Problems with operation ('Bedienung'): 40 cases ➔ 17%.
- Problems with the electron RF ('eHF'): 35 cases ➔ 15%.
- Problems with power supplies: 29 cases ➔ 13%.
- Problems created by beam losses ('Strahlverlust'): 19 cases ➔ 8%.
- Problems related to controls ('MSK'): 18 cases ➔ 8%.
- Problems related to the injector complex: 13 cases ➔ 6%.
- Problems related to the proton RF: 9 cases ➔ 4%.
- Problems related to super conducting cavities: 7 cases ➔ 3%.
- Problems related to the quench protection system: 7 cases ➔ 3%.
- Problems related to beam instrumentation: 7 cases ➔ 3%.

Most of the above fault types can also be expected for the LHC operation (except for problems related to the electron RF system).

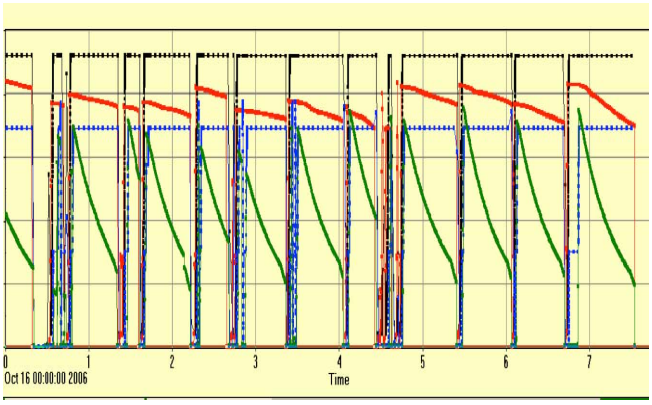

Figure 8: HERA operation in week 46 in 2006 [7].

The left-hand side shows a series of unscheduled proton beam losses that were caused by unforeseen beam losses (e.g. beam showers in the collimation sections and fast (ms time scale) beam losses). The right-hand side shows fills of a regular operation period.

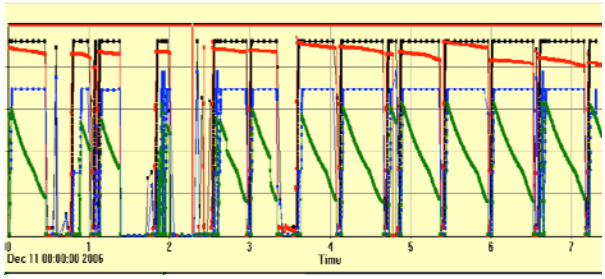

Figure 9: HERA operation in week 50 in 2006 [7].

The left-hand side shows a series of operation failures due to technical problems (cryogenic problems, power failure and quench alarms during beam injection). The right-hand shows regular fills corresponding to a normal operation period.

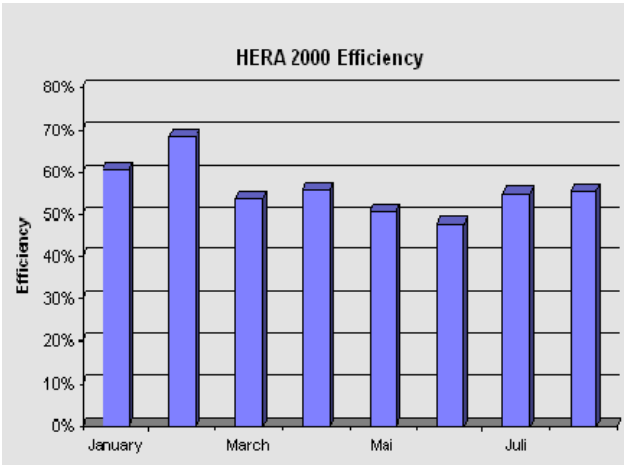

Figure 10: The HERA machine efficiency during the 2000 operation.

In addition to the loss of total operation time, the faults and beam aborts result in a significant increase of the average machine turnaround time. For example, the operational experience from the 2005 run showed that, even after 10 years of experience, the HERA operation featured on average 2.5 faults per luminosity run and required 1.8 proton injections and 1.6 electron injections per successful luminosity fill [8]. Taking further into account that a fault in the 2005 operation lasted on average 2.5 hours and that the preparation of the proton and electron fills required on average 1.43 hours and 0.83 hours for the proton and electron beams respectively, one obtains an average machine turnaround time of 10.2 hours for the 2005 run [9].

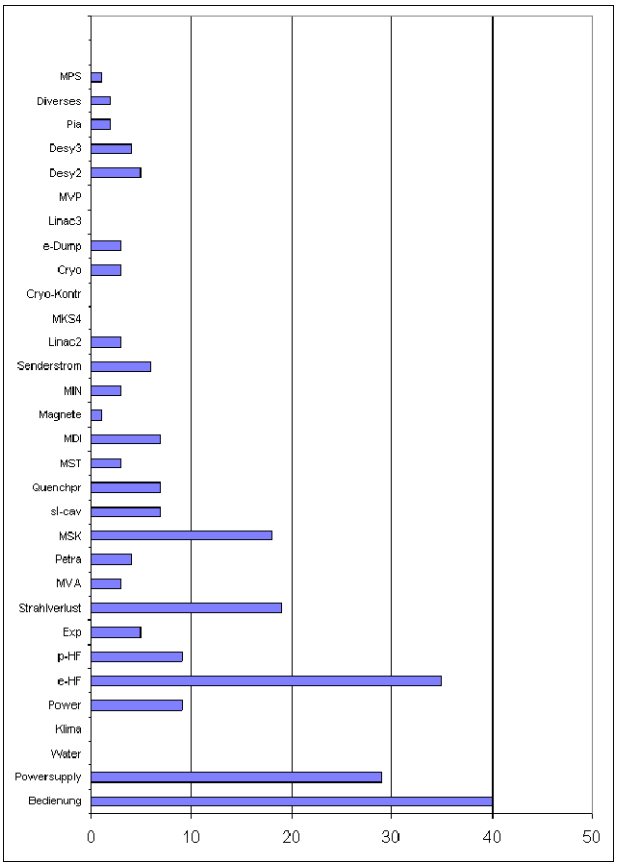

Figure 11: The most frequent reasons for an interruption of the HERA operation in the 2006 run period.

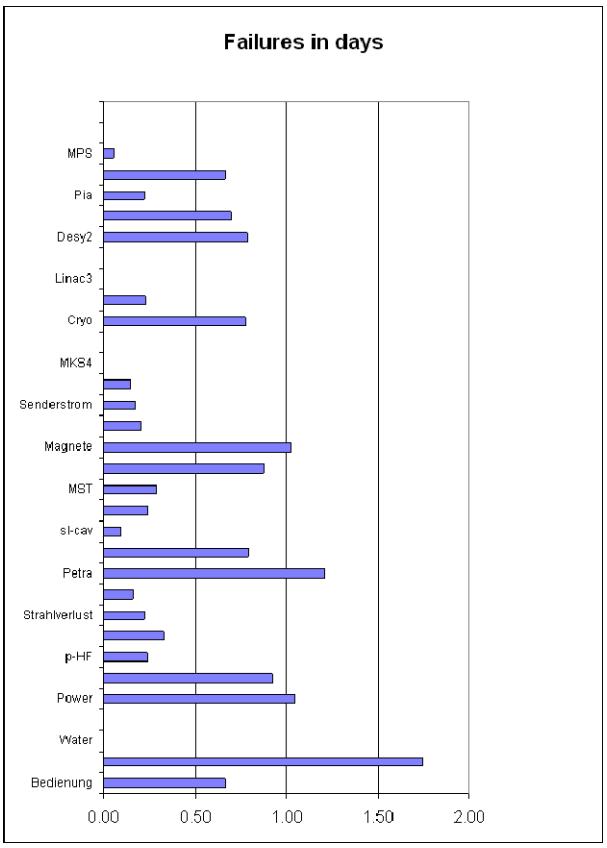

Figure 12: The total machine down time for various causes of for an interruption of the HERA operation in the 2006 run period.

This average machine turnaround time is approximately 6 times larger than the minimum theoretical turnaround time. The minimum operational turnaround time amounts to ca. 2.5 hours and is therefore ca. 1.7 times the theoretical minimum time.

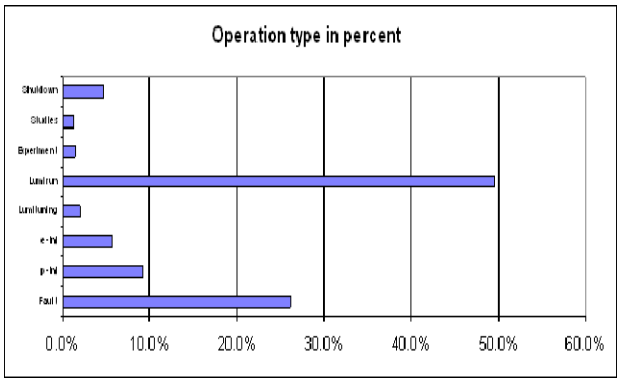

Figure 13: The distribution of various operation modes for HERA during the 2006 run.

Ca. 50% of the 2006 operation time was spent in luminosity operation and ca. 25% of the operation time

was lost due to faults. Ca. 13% of the operation time was required for filling the HERA machine with new beams.

Table 9 summarizes the main observations from the HERA operational experience.

Table 9: Summary of the key observations from the HERA operation.

Parameter	Value
Minimum theoretical turnaround time	1.5 hours
Minimum operational turnaround time	2.5 hours
Average operational turnaround time	10.2 hours
Machine efficiency in percent of calendar time spent in physics operation.	55%
Average Store length	10 to 14 hours

3.3 RHIC at BNL

The RHIC collider operates in two different modes: operation with polarized proton collisions and operation with ion-ion collisions. The beam parameters are different for the two operation modes and we list the relevant values separately for both modes.

Table 10 lists the main parameters of the RHIC collider as given in [9]. The commissioning assumption for RHIC was a store length of 10h and a turnaround time of much less than 1h. Figure 14 shows the operational time in physics operation (store time) in RHIC for various calendar years and operation modes as a fraction of the full calendar time. The machine operation improved over the first 4 years from ca. 25% of the calendar year to ca. 50% in the following years. The above statistics is compatible with M = 365 and R = 0.5 in Equations (1) and (2). Figure 15 shows the operational machine turnaround time in RHIC for various runs.

The average turnaround time was ca. 23 times the theoretical minimum value and ca. 5 times the operational minimum value after 4 years of operation. Figure 15 shows the data without and with a cut of 5h where at cut of 5h implies that all machine turnaround times larger than 5h have been discarded for the calculation of the average operational turnaround time (resulting only in a reduction of the time the machine spend in physics operation). The average turnaround time was approximately 1.9h in the Run4 and Run6 operation assuming a 5h cut for the data and 8h for the first years of operation without a cut. The minimum operational turnaround time was ca 1h for Run2 and Run3 and ca. 0.4h for the last 4 years

Table 10: The minimum theoretical and operational machine turnaround times and key beam parameters for the two main RHIC operation modes as defined in [9] before RHIC was commissioned. The luminosity values of the 2006 and 2007 runs exceed the above luminosity values by a factor 2 (p-p) to 5 (Au-Au). The average store length refers to the experience from the 2007 / 2008 operation.

Parameter	p-p	Au-Au
Minimum theoretical turnaround time	5min	5min
Minimum operational turnaround time	24min	24min
Nominal beam intensity	60 x 10^{11} ppb	60 x 10^{9}ipb
Nominal initial luminosity	1.5 10^{31} cm^{-2} sec^{-1}	8 10^{26} cm^{-2} sec^{-1}
Theoretical beam lifetime (2 experiments)	t = 1000h	t = 20h
Operational beam lifetime	t = 50h	t = 30h (stoch. cooling)
Ion luminosity lifetime (dominated by IBS)	-	t= 2h
Average store length	7.2h	4.6h

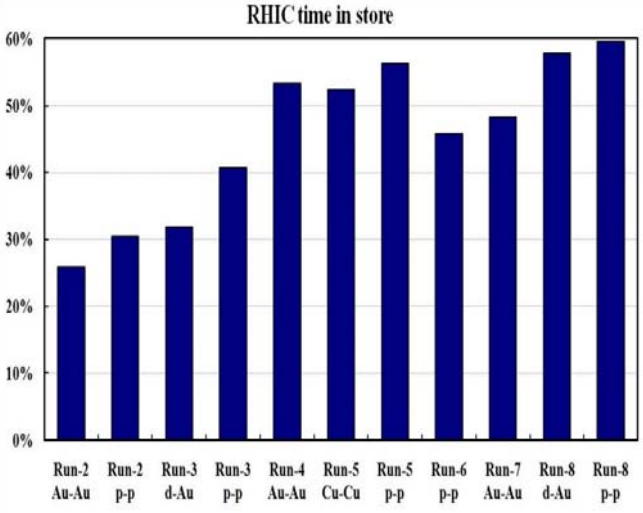

Figure 14: The operational store time in RHIC for various runs from 2002 to 2008 in percentage of the full calendar year. The above statistics is compatible with M = 365 and R = 0.3 and R = 0.6 in Equations (1) and (2) during the first and last years of operation respectively.

Both values are significantly larger than the theoretical minimum turnaround time of 5 minutes. The minimum operational turnaround time was approximately 12 times the theoretical value during the first 4 years of operation and ca. 5 times the theoretical value during the last years of operation.

Among other things, the longer operational turnaround times are mainly caused by aborted ramps due to beam loss monitor readings during the optics squeeze, equipment failure and injection tuning. One can expect all the above problems also for the LHC operation. The machine operation uses the average operational turnaround time for calculating the optimum store length. Table 11 summarizes the main observations from the RHIC operational experience.

Table 11: Summary of the key observations from the RHIC operation

Parameter	Value
Minimum theoretical turnaround time	5 minutes
Minimum operational turnaround time	24 minutes
Average operational turnaround time	114 minutes
Machine efficiency in percent of calendar time spent in physics operation	60%
Average Store length (p-p / Au-Au) [10]	7.2 hours/ 4.6 hours

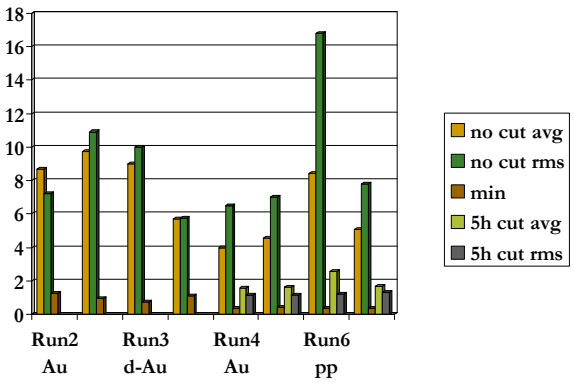

Figure 15: The operational machine turnaround time in RHIC in hours for various runs.

4. SUMMARY

4.1 Findings from the operational experience in existing Hadron colliders

Table 12 summarizes the main observations from the Tevatron, HERA and RHIC operation.

All analyzed hadron colliders have, after several years of operation, an operational efficiency (time in physics / calendar time) of ca. 60%. It therefore seems reasonable to assume for the nominal LHC operation well after the commissioning a similar figure:

$$\hat{L} = R \cdot M \cdot (24 \cdot 60^2) \cdot L_0 \cdot f(T, \tau) \qquad (6)$$

with M = 365 and R = 0.6 and 'f' given in Table (2). During the first years of operation the collider efficiency can be significantly lower. For example, RHIC featured an efficiency of R = 0.3 during its first three years of operation. It seems therefore reasonable to assume also for the LHC for the first year of operation M = 365 and R = 0.3.

All analyzed hadron colliders did not reach their minimum theoretical turnaround time. The main reasons for the required longer minimum operational turnaround times are the need for injection tuning:

- The Tevatron achieved a minimum operational turnaround time that is 2.5 times the minimum theoretical value.
- HERA achieved a minimum operational turnaround time that is 1.5 times the minimum theoretical value.
- RHIC achieved a minimum operational turnaround time that is 12 times the minimum theoretical value.

The case of the RHIC collider is a bit special as the theoretical machine turnaround time (ca. 5min) is much shorter than the minimum theoretical turnaround time in the other colliders and much shorter than the average run length. Reducing the minimum operational turnaround time in RHIC further below the achieved value of 24 minutes will not have a large impact on the overall integrated luminosity and has therefore not been pursued with high priority in the RHIC operation. We will therefore use for RHIC the ratio between average and minimum turnaround time when we compare in the following it's performance with that of the other hadron colliders.

Table 12: Summary of the key observations from the Tevatron, HERA and RHIC operation

Parameter	Tevatron	HERA	RHIC
Minimum theoretical turnaround time	60 minutes	90 minutes	5 minutes
Minimum operational turnaround time	150 minutes	150 minutes	24 minutes
Average operational turnaround time	480 minutes	612 minutes	114 minutes
Machine efficiency in percent of calendar time spent in physics operation	60%	55%	60%
Average Store length (from last years of proton operation)	21 hours	14 hours	7.2 hours

Due to beam aborts during the store preparation, all analyzed hadron colliders feature on average turnaround times, which are significantly larger than the minimum operational turnaround times:

- The Tevatron achieved on average an operational turnaround time that is 8 times it's minimum theoretical and 3 times it's operational minimum turnaround time.
- HERA achieved on average an operational turnaround time that is 7 times it's minimum theoretical and 4 times it's operational minimum turnaround time.
- RHIC achieved on average an operational turnaround time that is 23 times it's minimum theoretical value and 5 times it's minimum operational turnaround time.

The LHC has a minimum theoretical turnaround time of 1.2 hours and, based on the operational experience of HERA, it seems reasonable to assume an average operational turnaround time of seven times it's minimum theoretical value ($T_{turnaround}$ = 10 hours) during the first years of operation. Using the experience from the Tevatron (an average turnaround time that is 20 times the theoretical minimum value) or RHIC (an average turnaround time that is 23 times the theoretical minimum value) would lead to even longer average turnaround times for the LHC.

4.2 Implications for the LHC performance during the first year of operation

During the first years of operation the collider efficiency can be significantly lower (e.g. R = 0.3 in the case of RHIC). Assuming a peak luminosity of $L = 2\ 10^{33}$ cm^{-2} sec^{-1} for the LHC during the first year of operation (limit for the operation without Phase II collimation system and dump dilution kickers [11]), using M = 365, R = 0.3 and assuming an average turnaround time of 10 hours with a beam lifetime of 20 hours one obtains from Table 2: $f = 0.42$. Inserting this value into Equation (6) yields a total integrated luminosity of

$$4.6\ fbarn^{-1} \tag{7}$$

per year.

4.3 Implications for Nominal LHC Performance

Inserting the nominal peak luminosity of the LHC, R = 0.6 and assuming again an average turnaround time of 10 hours and a beam lifetime of 20 hours one obtains an integrated luminosity of

$$46\ fbarn^{-1} \tag{8}$$

per year of operation.

4.4 Implications for the nominal performance with a fully commissioned machine

Each transition from one accelerator generation to the next achieved a reduction of the ratio between minimum theoretical and average operational machine turnaround time (for RHIC we use the minimum operational turnaround time instead of the minimum theoretical value). For the transition from the Tevatron to HERA the ratio improved from 8 to 6 and from HERA to RHIC from 6 to 5. After several years of operation one might hope to obtain a similar improvement in the ratio between theoretical minimum and average turnaround time as has been achieved between the last two accelerator generations. An improvement of the ratio by approximately 20% with respect to the RHIC experience implies a factor 4 between the theoretical minimum and operational average turnaround times of a fully commissioned LHC machine. In other words, one could hope for an average machine turnaround time of 5 hours after several years of machine operation. Table 2 yields for a luminosity lifetime of 20 hours and a machine turnaround time of 5 hours: $f = 0.5$ and therefore an integrated luminosity of:

$$55\ fbarn^{-1} \tag{9}$$

per year of operation.

However, this assumption neglects the fact that all colliders discussed in this paper are much smaller and less complex than the LHC machine. It is therefore far from obvious that one can hope to actually obtain the same level of improvement from RHIC to the LHC as has been achieved from the Tevatron to HERA for example. On the contrary, given the much smaller operational margins and larger machine complexity of the LHC compared to HERA, one might even question if one can actually achieve a similarly good performance of the LHC in terms of ratio between average operational to minimum theoretical machine turnaround time as has been achieved in the Tevatron and HERA operation.

4.5 Implications for the upgraded LHC performance with a tenfold increase in the peak luminosity

Looking at the ratio of integrated to peak luminosity given in Table 2, it becomes clear that an operation with luminosity lifetimes below 3 hours, as required for the Phase 2 luminosity upgrade scenarios of the LHC [3], becomes only efficient if the average machine turnaround time can be clearly kept below 6 hours. For example, Table 2 yields for a luminosity lifetime of 2.5 hours and an average machine turnaround time of 6 hours: f = 0.2. Inserting this value into Equation (6) and assuming again M = 365 and R = 0.6 yields a total integrated luminosity of

$$378\ fbarn^{-1} \qquad (10)$$

per year.

Using instead a machine turnaround time of 10 hours, Table (2) yields: $f = 0.14$.which implies a luminosity loss of 30% with respect to the value given in (10). Efforts for minimizing the machine turnaround time (renovation and upgrade of the LHC injector complex and an efficient beam collimation system) are therefore the prerequisites for an LHC luminosity upgrade that aims at a ten fold increase of the integrated.

REFERENCES

[1] 'Mike Lamont, Commissioning the complete normal cycle', Chamonix XII.
CERN-AB-2003-008 ADM
[2] LHC Design Report, Volume 1: The LHC Main Ring, CERN-2004-003, June 2004.
[3] Proceedings of the LUMI'06 CARE HHH workshop, Valencia, Spain, September 2006.
[4] http://www-bdfnal.gov/doereview02/RunIIBTDR.pdf
[5] http://www-bd.fnal.gov/pplot/index.html
[6] Courtesy of Cons Gattuso, FNAL.
[7] Courtesy of Bernhard Holzer, DESY.
[8] M. Bieler, LUMI'05, Arcidosse Italy 2005
[9] S, Peggs, RHIC AP115
[10] W. Fischer, BNL.
[11] R. Bailey
http://lhccwg.web.cern.ch/lhccwg/Bibliography/Commissioning%20stages.ppt

ELECTRON LENSES FOR PARTICLE COLLIMATION IN LHC

V.Shiltsev, FNAL, P.O.Box 500, Batavia, IL 60510, U.S.A.

Abstract

Electron Lenses built and installed in Tevatron have proven themselves as safe and very reliable instruments which can be effectively used in hadron collider operation for a number of applications, including compensation of beam-beam effects [1], DC beam removal from abort gaps [2], as a diagnostic tool. In this presentation we – following original proposal [3] – consider in more detail a possibility of using electron lenses with hollow electron beam for ion and proton collimation in LHC.

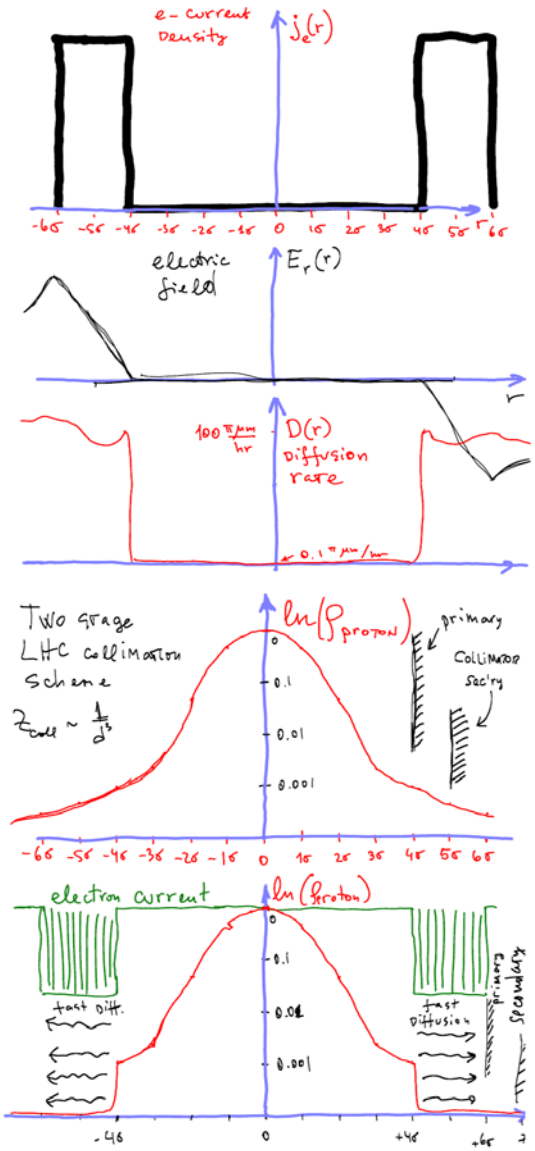

Figure 1: (top – bottom) current distribution in the e-lens for collimation; electric field and diffusion speed; cartoon of the particle distribution during halo removal by hollow beam e-lens.

HOLLOW ELECTRON BEAM FOR LHC COLLIMATION

As depicted in Fig.1, an ideal round hollow electron beam has no electric or magnetic field inside and strongly nonlinear fields outside. The non-linear field components significantly enhance transverse diffusion of high-energy particles in a storage ring with betatron amplitudes larger than e-beam size, as experimentally demonstrated in the beam studies with Tevatron Electron Lenses (see Fig.6 in Ref.[4]).

The speed of diffusion of the large amplitude particles can be greatly enhanced if the electron current varies in sync with betatron oscillations or at the nearest non-linear resonance line. The hollow e-beam can serve as primary collimator or as an enchancer – a device for faster delivery of halo particles to secondary collimators which can be then placed further from the primary one and the beam itself – see cartoon in Fig.1. Hollow eLens also offers a viable solution for a primary collimator of the LHC ion beam, because such an electromagnetic collimator does not break an ion into fragments (as any primary collimator made of usual material would do). In that case, the hollow e-beam systems would have to be installed to replace the current primary LHC collimators.

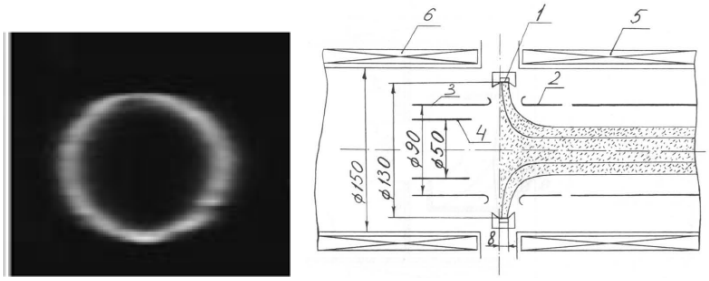

Figure 2: (a) hollow electron beam [5]; (b) cylindrical electron gun tested in [6].

Hollow electron beams are widely used in electron cooling devices [5,6] and corresponding electron guns have been developed and extensively tested – see Fig. 2.

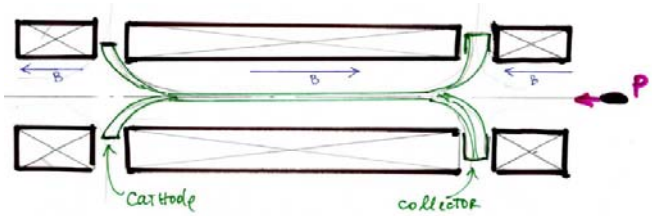

Figure 3: Electron lens configuration for collimation

Fig.3 presents possible system configuration which is needed for generation of the axially symmetric hollow electron beam for LHC collimation. Main parameters of the hollow electron beam system needed for EM collimation of ions and/or protons are presented in the Table below:

Maximum current	10-50 A
Ring cathode radius/width	25 mm/ 6 mm
Magnetic Field on Cathode	1-2 kG
Current density on cathode	j_e=1-5 A/mm^2
β–functions @ e-IR location	$\beta_x = \beta_y$ =2300 m
Beam radius/width @e-IR	Hollow 4.4mm/1.1mm
Main solenoid filed	B_m=3.2T if B_{cath}=1kG
Electron beam energy	10-20 kV
Regime of operation/ voltage	~3 kHz *sin*-modulation
Electron beam length	2(4)m
e-beam radius in/out	1.5 mm / 2 mm
Magnetic fields in collector	1kG→0kG
Ring collector radius/width	25 mm/ 12-30 mm
Beam power in collector	P_{coll}=20-50 kW

For comparison, TEL electron beam parameters are j_e=6 A/mm^2, B_m=6.5T, P_{coll}=50kW – i.e. the hollow beam parameters are not very far from those already achieved.

MODELING

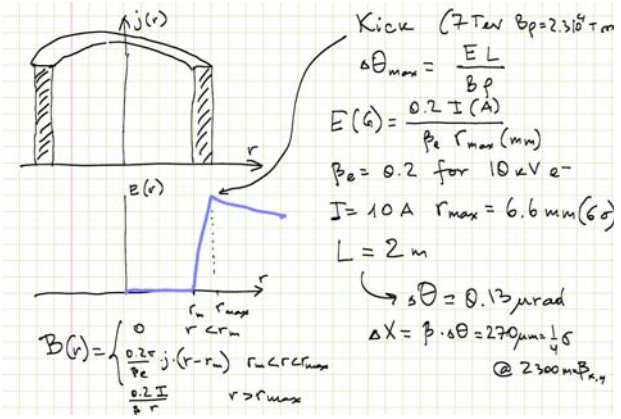

Figure 4: Cartoon of the hollow e-collimator used in the modelling.

Fig.4 above shows geometry of the radially symmetric hollow beam used in the modelling. It also presents estimate of the dipole kick produced by such a beam with 10 A of current for a 7TeV particle outside its outer bound at 6σ (6.6 mm) radius – it is about 0.13 μrad or 270 μm in amplitude. For comparison, the rms angle due to particle scattering in 1 m long carbon jaw of the LHC primary collimator is about 4.5 μrad. Advantage of the e-Collimator is that it does not destroy any particle and can in principle act over many (say, thousands) turns. In that case, every time when particle appears beyond the boundary of the electron beam, it gets a radial kick – as schematically depicted in Fig.5.

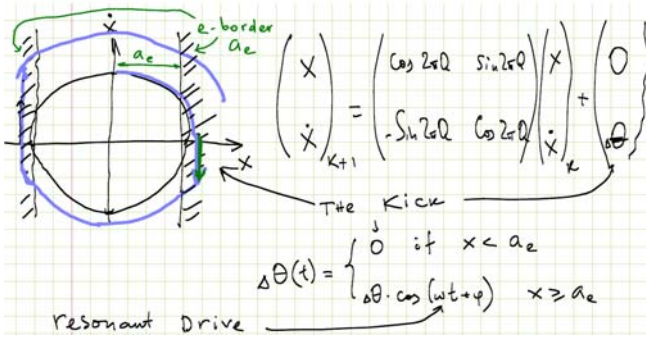

Figure 5: Phase space dynamics of the hollow e-beam collimation

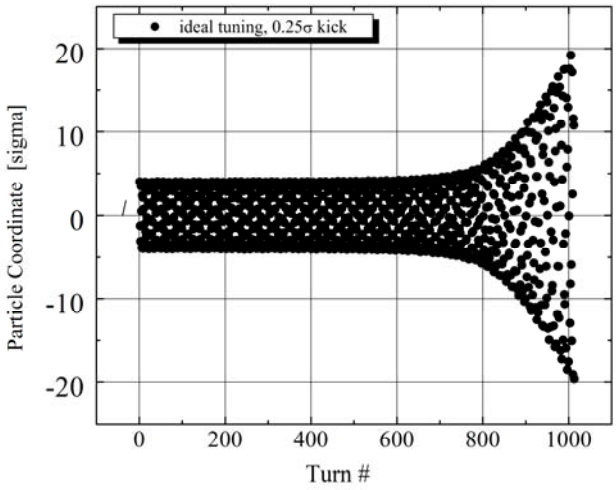

Figure 6: Particle motion driven by hollow e-beam with maximum kick of 0.25σ, in sync and in phase with betatron motion with tune *Q=0.31*.

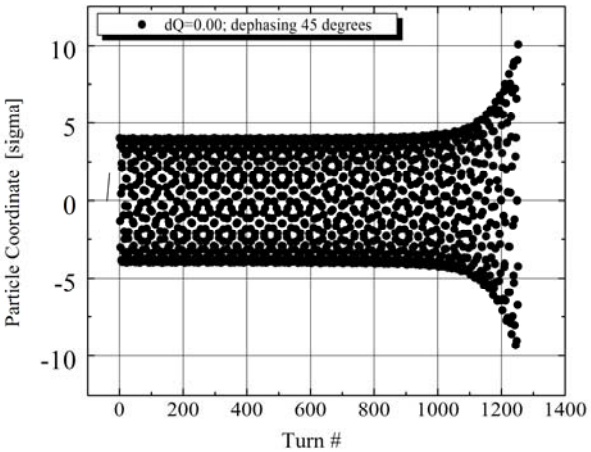

Figure 7: same as in Fig.6 but with 45 degree phase shift between e-current and particle betatron oscillations.

In the very first simulation run, presented in Fig.6, a particle which initially intercepted the e-wall boundary by

0.1σ has been driven resonantly to amplitudes as large as 10-20σ in less than 1000 turns (0.1 sec of real time in the LHC). Maximum strength of the e-beam kick is equal 0.25σ, electron current is modulated in phase with betatron motion of the particle, tune equal to *Q=0.31*. Next Fig.7 shows that even if the phase difference between e-current waveform and particles oscillations is as large as 45 degrees, the particle still achieves large amplitudes in 1000-1200 turns. At 90 degrees of the phase difference, the particle will see zero electron current and get no kick.

Due to natural tune spread (induced by beam-beam, or due to synchrotron motion), one should not worry about exact synchronization of frequency and phase with all the particles. Electron beam modulation frequency can be set close to the frequencies of interest (e.g, frequency of 4σ particles) or may cover a band of frequencies. Fig. 8 and 9 show resonant increase of particle amplitude in the case of significant frequency difference between the particle and the electron beam drive *dQ=0.002* and *dQ=0.005*, correspondingly.

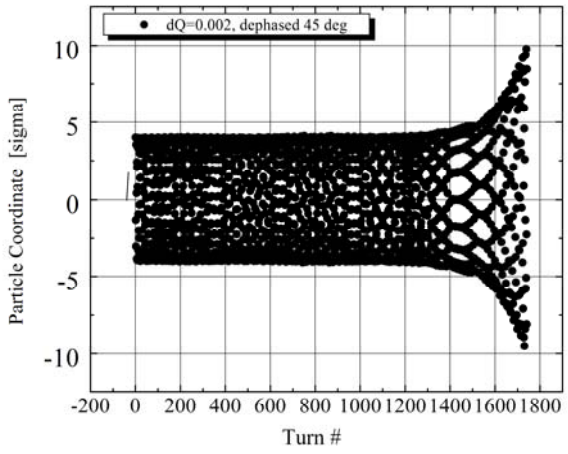

Figure 8: same as in Fig.7, with tune difference *dQ=0.002*.

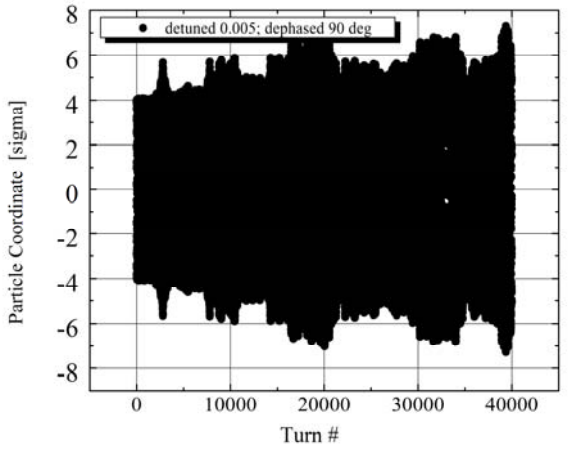

Figure 9: same as in Fig.7, with tune difference *dQ=0.005*.

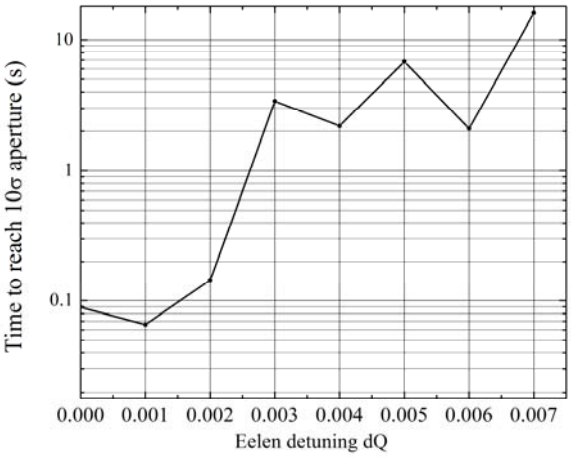

Figure 10: Collimation time (time needed to reach 10σ amplitude) vs detuning parameter *dQ*.

Figure 10 shows that the time needed (in the simulations) to reach 10σ amplitude grows with the dutuning and reaches 10 seconds for *dQ=0.007*. For most optimal operation, one can envision detuning not exceeding *dQ=0.002* which collimates (drives particles out on aperture set by secondary collimators) in about 0.1 seconds. Obviously, with larger e-beam current – and kicks – the collimation time can be reduced to shorter values as shown in Fig.11. If the secondary collimators are set closer to the beam – say 6-8σ - then, the time will be shorter, too.

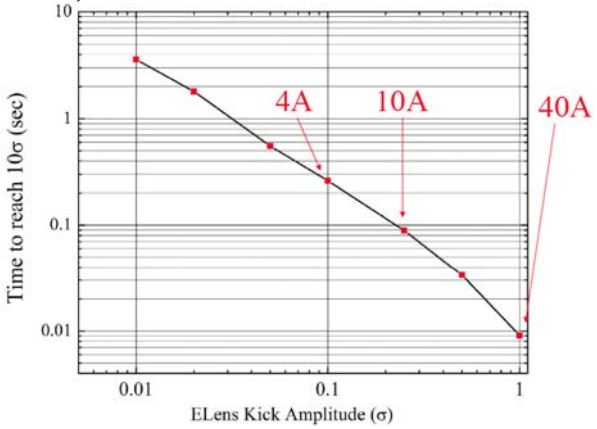

Figure 11: Collimation time (time needed to reach 10σ amplitude) vs maximum electron beam kick.

DISCUSSION, SUMMARY

So far, the hollow electron beam idea looks promising for improve the LHC collimation system: a) the e-beam technology is developed and well tested in the Tevatron Electron Lenses; b) reliability of such a system has been proven by years of operation under a hardon collider conditions; c) there is just electro-magnetic, no nuclear, interaction in the e-collimators which can work for ions and protons; d) as shown above, e-collimators seem to be strong enough to clean fast – its cleaning time (0.1-30 sec) is much faster than the diffusion time (1000's sec); e)

e-collimators are "refreshable", no beam incident can damage the electron beam the way it can damage metal or carbon jaws in conventional systems; f) because of that, no expensive damage diagnostics is need; g) collimator's size/position are controlled by magnetic fields, therefore, no mechanical system (movers, etc) is needed.

Another foreseeable advantage of the hollow e-beam is that it cleans (removes) halo smoothly over many turns – and because of that the system will not be sensitive to orbit motion. It also promises very smooth known radiation levels on secondary collimators and in the HEP detectors. As an example, Tevatron D0 and CDF detectors enjoy smooth abort gap loss rates smoothed by TELs.

As initially reported in Ref.[2], accumulation of the DC beam particles in the Tevatron could be dangerous because of quenches on abort. TELs effectively prevent that and are used in 24/7 operation. Figure 12 shows an example of a simple experiment at the end of HEP store. In this figure, the T:IBEAM is the total beam current in the Tevatron, C:FBIPNG is the total bunched-beam current, the T:L1COLI is the average electron current in TEL1 and C:B0RATI is the abort gap loss rate as reported by the CDF detector. When the TEL was turned off (red trace), the abort gap loss rate started to grow after about 10min and the loss spikes appeared. To clean out of the DC beam in the abort gap, the dipole beam-beam kick is used to excite particle oscillations resonantly which eventually increase oscillation amplitude until the particle get lost on a limited aperture. Therefore, when the TEL was turned on, a chunk of the DC beam intensity was quickly lost so that T:IBEAM had shown a beam loss (green curve) while the lifetime of bunch beam T: FBIPNG did not change. There was also a huge spike in the abort gap counter indicating that the DC beam in the abort gap has been cleaned out by the TEL. Then the loss rate in the abort gap returned back to a steady state level, without big spikes. Excitation of a 7th order or 3rd order resonances (*Q=0.583* or *Q=0.600*) has been found the most effective for the DC beam removal by electron lenses in Tevatron.

In various discussions, it was proposed to consider more suitable locations for the e-collimator, e.g., betatron or/and momentum cleaning long straight sections where most of the Phase I collimators are located now (instead of the space between D1 and D2 with very large beta-functions). These locations don't have very large beta-functions, so consequently, beam size is factor of 3-4 smaller and hollow electron beam size (which is some 4-5σ inner radius) has to be smaller, too. Compression ratio of the electron beam emitted by a ring cathode should be proportionally higher, that call for higher ratio of the magnetic field in the interaction region and on the cathode B_m/B_{cath}. Minimum field on the cathode depends on the electron current density (the field should be high enough to keep electron beam stable against its own space-charge forces). Maximum field in main solenoid is limited by technology (and is about 12-15T) and available radial space between two beams. Though these changes – needed to achiev higher B_m/B_{cath} ratio – will make e-collimatort quite different from TELs (compared to the high-beta location elens), electron beam formation and dynamics as well as magnet design could be addressed in straightforward simulations.

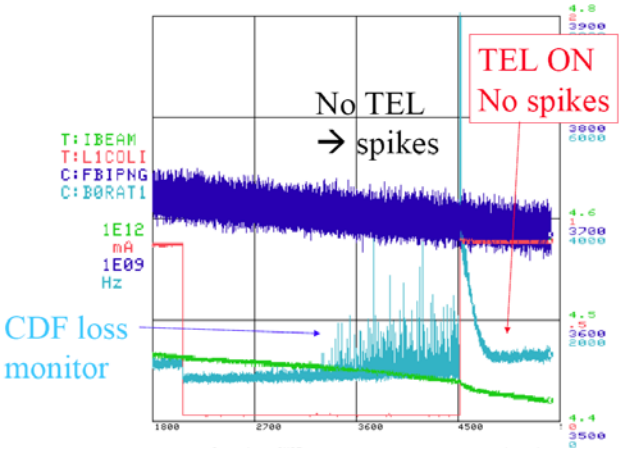

Figure 12: Beam intensity and abort gap losses during a HEP store. TEL1 was turned off and then on.

Another concern to address in simulations is axial symmetry of the electron current density distribution which is required for particles inside the electron tube to stay intact. One can see three effects/possibilities to avoid generation of dipole imperfections leading to the transverse emittance blowup of core particles: a) a set of control sector electrodes can be set near the cathode which can be used for slow or fast correction of the symmetry; b) under action of its own SC field, the electron beam rotates due to **E×B** drift – and that enforces the symmetry; c) the betatron frequency of the core particles is different from the frequency of the halo particles – the effect is especially big at collisions – so, setting electron beam modulation frequency far enough from the core but close to the halo tune will effectively reduce the effect on low amplitude particles.

In summary, proton or ion collimation with hollow electron beams looks very promising, it should be considered in detail, as it may complement conventional system and does not disintegrate ions.

ACKNOWLEDGEMENTS

The author is indebted to N.Mokhov and V.Kamerdzhiev (FNAL), R.Assmann, V.Previtale, F. Zimmermann, W.Scandale and R.Schmidt (CERN) for useful discussions on the possible use of hollow electron beams in the LHC collimation system.

REFERENCES

[1] V.Shiltsev, *et al.* , *Phys. Rev. Lett.* **99** 244810 (2007)
[2] X.L.Zhang, *et al.*, *Proc. IEEE PAC 2003 (Portland, OR, USA)*, p.1778

[3] V.Shiltsev, in *Proc. BEAM'06 (Valencia, Spain)*, Yellow Report CERN-2007-002
[4] K.Bishofberger *et al, Proc. IEEE PAC 2003 (Portland, OR, USA*, p. 57.
[5] A.Bubley, *et.al*., *Instruments and Experimental Techniques*, v.49, No.1 (2006), p.83.
[6] A.Sharapa, A.Shemyakin, *NIM-A* 336 (1993), pp.6-11.

ULTIMATE LHC BEAM

G. Arduini, CERN, Geneva, Switzerland

Abstract

The present status of the nominal LHC beam in the LHC injector complex and the limitations towards the achievement of the ultimate brightness are outlined.

INTRODUCTION

The schematic layout of the LHC Hadron Injector Complex with the corresponding kinetic energy range is shown in Fig. 1. In the following only the circular proton injectors will be considered.

The beam parameters for the nominal and ultimate LHC beams are listed in Table 1 for all the circular LHC Injectors at injection and at extraction. The bunch population of the ultimate LHC beam is approximately 50% higher than that of the nominal LHC beam while the transverse and longitudinal emittances are the same. This implies that the longitudinal and transverse brightness of the ultimate LHC beam are 50% higher than those of the nominal beam.

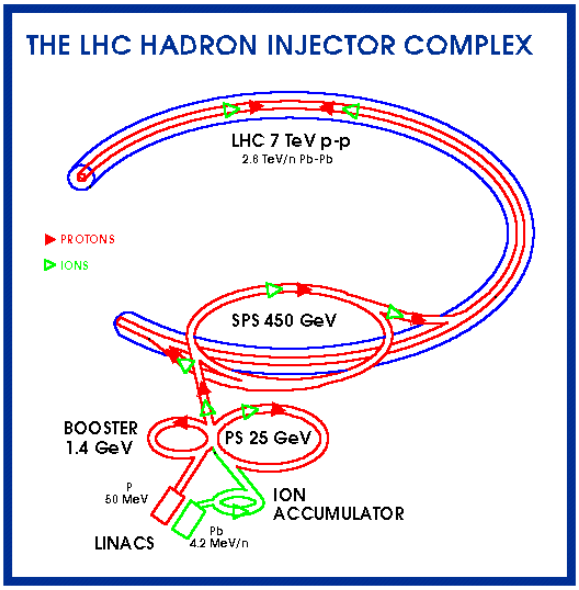

Figure 1. The LHC Hadron Injector Complex. Proton beams are indicated in red while Ion beams are indicated in green.

	PSB@inj	PSB@extr	PS@inj	PS@extr	SPS@inj	SPS@extr
p [GeV/c]	0.31	2.14	2.14	26	26	450
K [GeV]	0.050	1.4	1.4	25.08	25.08	449.06
T_{rev} [μs]	1.67	0.572	2.29	2.1	23.07	23.05
Q (H/V)	4.3/4.45	4.2/4.2	6.22/6.25		26.13/26.18	
γ_{tr}	4.15		6.11		22.83	
bunches/ring	0-1	0-1	6	72	2-4×72	2-4×72
N_b [10^{11} p]	13.8/**20.4**	13.8/**20.4**	13.8/**20.4**	1.15/**1.7**	1.15/**1.7**	1.15/**1.7**
ΔT_{bunch} [ns]	-	-	326.88	24.97	24.97	24.95
τ_b [ns]	571	190	190	4	4	<2
$\varepsilon^*_{H,V}$ [μm]	-	<2.5	-	<3	-	<3.5
ε_L [eV.s]	~0.7	1.4	1.4	0.35	0.35	<0.8

Table 1. Main design parameters of the LHC Nominal and Ultimate (in bold when different from nominal ones) beams [1].

PS BOOSTER

The present performance of the PS Booster for the LHC beam is summarized in Fig. 2 showing the measured normalized vertical and horizontal transverse emittances as a function of the bunch population at extraction. The full green and orange vertical lines indicate the nominal and ultimate bunch populations while the dashed green vertical line indicates the required bunch population in order to achieve the nominal bunch population at the SPS extraction taking into account the losses occurring in the PS and in the SPS. These losses amount to approximately 10-15 %. The blue horizontal line represents the design transverse emittance. The measured data for each of the 4 PSB ring is presented together with the average over the 4 rings. Although the nominal design parameters have been fully achieved the ultimate ones are not within reach at present.

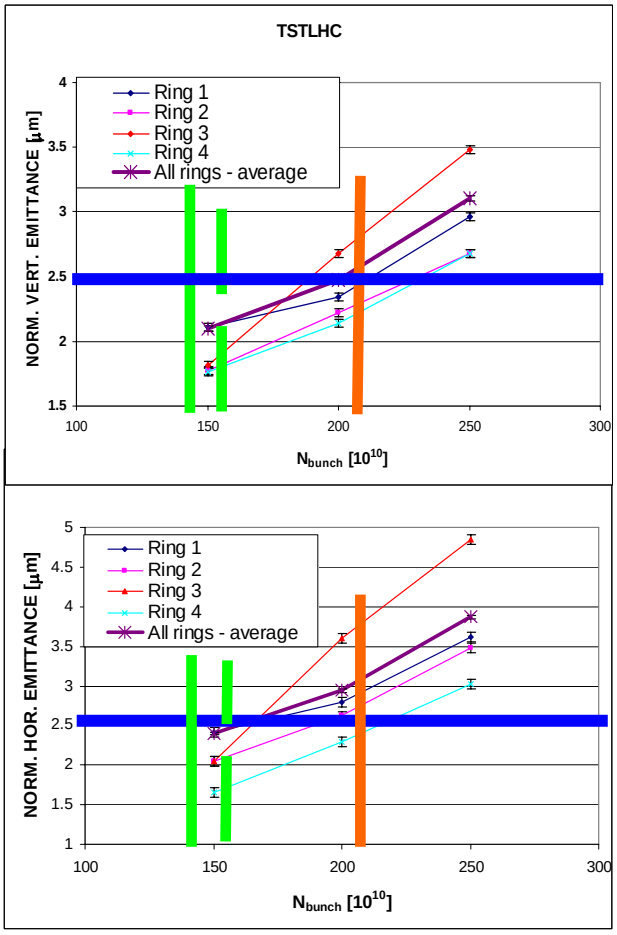

Figure 2. Measured normalized vertical (top) and horizontal (bottom) emittance vs. bunch population for the LHC beam at extraction from the PS Booster. Courtesy of K. Hanke and B. Mikulec.

Space charge is considered to be the main limitation for the achievement of ultimate performance in the PS Booster [2]. The injection at 160 MeV with the LINAC4 should reduce the space charge limit at injection by a factor two [3][4]. A reduction of the losses in the PS and SPS is also mandatory in order to relax the requirements in terms of brightness to the PS Booster.

PS

LHC beams with bunch population close to 1.5×10^{11} p have already been produced in the PS, nevertheless two potential limitations in the road towards ultimate performance have been evidenced [2]:

- space charge;
- electron cloud instability at extraction.

Space Charge

Double-batch injection has been implemented in the PS for the LHC beam (Fig. 3) in order to keep the space charge tune spread at injection in the PSB below 0.5. As a consequence of that the first injected batch remains for 1.2 s at PS injection momentum limiting the maximum acceptable space-charge tune spread in the PS to approximately 0.25.

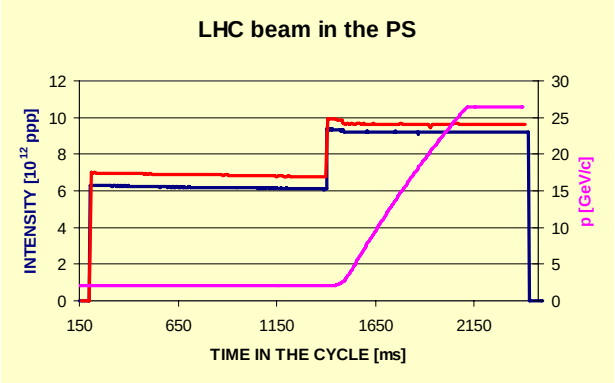

Figure 3. Double batch injection for the LHC beam in the PS. Approximately 3% losses are observed during the 1.2 s long injection plateau. Courtesy of E. Métral.

Space charge and synchrotron motion induce periodic tune modulation and trapping-de-trapping on resonance islands leading to halo and losses [5][6]. This could explain low energy losses observed in the PS (Fig. 3).

This explanation is consistent with the observation that losses are affecting mainly shorter and/or more intense bunches and are normally involving particles with larger momentum offsets (Fig. 4).

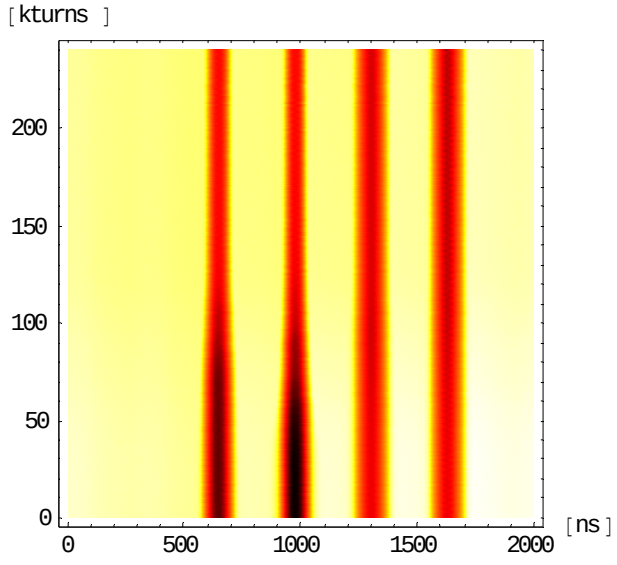

Figure 4: Density plot of the bunch profiles of the four bunches of the first PSB batch injected in the PS as measured with a wall current monitor as a function of the turn number. The most intense bunches are mainly affected by losses and their bunch length is decreasing. Courtesy of S. Hancock and E. Métral.

A higher injection energy and/or single batch injection could help in minimizing these effects.

Electron Cloud Instability

A horizontal instability with a rise-time of about 1 ms has been observed for the nominal LHC beam at top energy after the last bunch splitting leading to the 25 ns bunch spacing [7][8]. At nominal bunch population the beam becomes unstable for a total bunch length shorter than 12 ns (Fig. 5) which is close (within 10 %) to the typical bunch length of the beam few ms before extraction. For a bunch length of 12 ns the threshold bunch population is approximately 0.6×10^{11} p (i.e. approximately half the nominal bunch population).

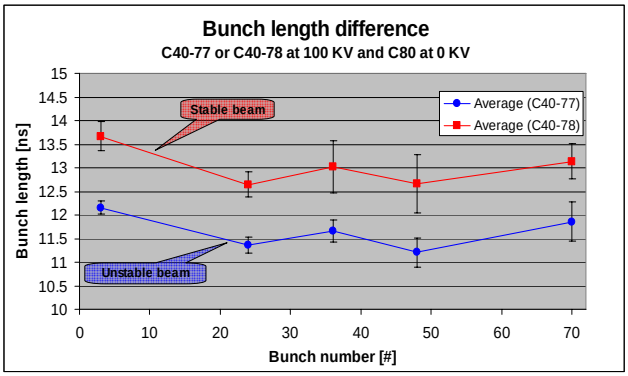

Figure 5: Measured full bunch length along the LHC beam bunch train for two different configurations of the 40 MHz RF system in the PS leading to different bunch lengths by approximately 10% because of a voltage calibration error in one of the cavities. The beam is transversally unstable when the bunches are shorter than 12 ns (blue dots). Courtesy of E. Métral and R. Steerenberg.

Studies are ongoing to better understand the electron-cloud build-up in the PS and possible solutions are being investigated. These include:

- a different RF programme to compress the bunch length to ~ 4ns before extraction to the SPS;
- the possibility of using the transverse feedback to damp this instability.

SPS

Design longitudinal (ε_L<0.8 eV.s) and transverse (ε^*_H=3.0±0.3 μm and ε^*_V =3.6±0.3 μm) parameters have been achieved in the SPS for the nominal LHC beam at extraction energy although no margin exists in particular for the vertical emittance. The main limitations towards the achievement of ultimate performance in the SPS are [2][9]:

- Fast Vertical Single Bunch Instability at injection due to machine impedance;
- Electron Cloud effects.

Fast Vertical Instability

A fast single-bunch vertical instability develops in the SPS right after injection at 26 GeV/c for bunch populations larger than 0.6×10^{11} p if the longitudinal emittance of the beam is smaller than 0.2 eV.s [10]. Figure 6 (left) shows the loss occurring few ms after injection for a single LHC bunch with nominal population (~ 1.2×10^{11} p) and low longitudinal emittance (~ 0.2 eV.s, to be compared with the design value of 0.35 eV.s). The RF voltage for that experiment was close to 600 kV which corresponds to a synchrotron period of 7.1 ms. The loss occurs when the bunch length is minimum (i.e. when the peak intensity is maximum).

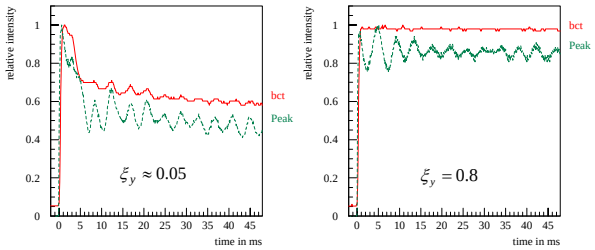

Figure 6: Measured relative bunch intensity (normalized to the value at injection) vs. time in the SPS machine for two values of the vertical chromaticity. bct stands for beam current transformer and Peak stands for peak intensity. Courtesy of H. Burkhardt.

The characteristics of the instability are typical of a Transverse Mode Coupling Instability (TMCI) and experimental and simulation studies are ongoing to better characterize it [11][12].
Simulation studies performed with the HEADTAIL code [13] taking into account the measured SPS broad-band impedance, space charge and the rectangular cross-section of most of the SPS apertures indicate that the threshold of this instability for the LHC beam parameters and operating conditions should be close to the ultimate bunch population.

High chromaticity (see Fig. 6) and high capture voltage have proved to be affective in suppressing this instability but both of them result in larger tune spread and therefore in a lower lifetime and losses.

Possible cures for the TMC instability are:

- identification of the impedance sources and reduction of their transverse impedance;
- operation far from transition (this would be the case if the injection energy of the SPS would be increased as foreseen with the PS2 upgrade [3][14]).

A measurement and simulation campaign to identify the major remaining sources of transverse impedance has started and it is reviewed in [15].

Electron Cloud Effects

Electron multipacting and electron cloud build-up along the bunch train have been observed with the LHC beam [16]. Above the threshold for the onset of electron multipacting (typically $N_{th}=0.2\times10^{11}$ p/bunch in the SPS arcs after a machine shut-down) transverse instabilities develop along the batch, starting from the tail and

progressing to the head of the batch, and resulting in strong emittance blow-up and in beam losses, mainly affecting the tail of the batch.

An increase in the threshold bunch population required to induce multipacting can be obtained by reducing the SEY of the vacuum chamber surface by electron bombardment induced by the beam ("scrubbing"). This process has been thoroughly studied at CERN [17] and it has been observed in the SPS [16]. By scrubbing the SPS vacuum chamber with the nominal LHC beam the thresholds for the onset of the beam-induced multipacting can be increased from 0.3×10^{11} p/bunch to 0.8×10^{11} p/bunch in the arcs which are covering approximately 70% of the SPS circumference.

Experience shows that the electron cloud activity cannot be suppressed completely by scrubbing and the final threshold intensities and SEY depend on the operational conditions of the machine.

In the horizontal plane the electron cloud instability manifests as a coupled bunch instability in which low order coupled-bunch modes (up to few MHz) are excited and can be damped by means of the transverse feedback.

The vertical electron cloud instability is of single bunch type. The instability mainly affects the tail of the bunch train and the rise time is decreasing with increasing bunch population N_b (the maximum amplitude of oscillation, corresponding to the machine physical aperture, is reached in about 600 turns for $N_b=0.3\times10^{11}$ p and in 300 turns for 0.5×10^{11} p). A vertical motion inside the bunch at frequencies of about 700 MHz has been observed which can be associated with the electron oscillation frequency and possibly with an additional external impedance (Fig. 7).

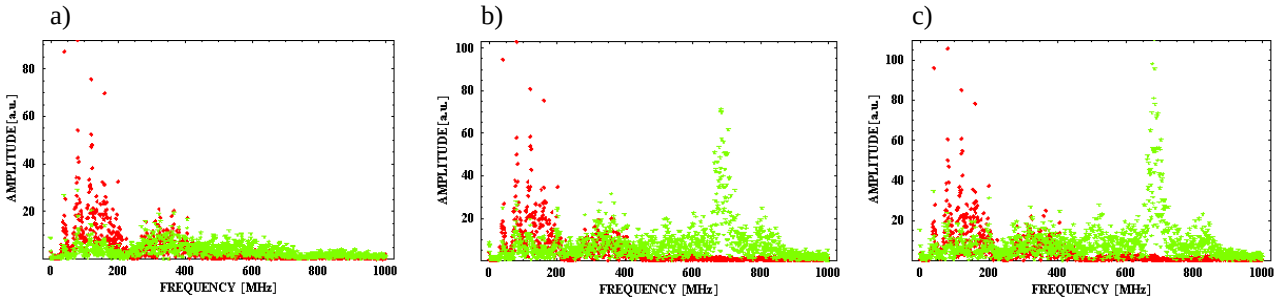

Figure 7. Fourier spectra of the sum (red) and delta (green) signals from a wideband vertical pick-up for the leading (a) bunch of the LHC bunch train and for bunch number 15 (b) and 39 (c). $N_b= 0.8\times10^{11}$ before scrubbing (when the threshold bunch population for the onset of electron multipacting is 0.2×10^{11} p) [16].

The observed single-bunch instability cannot be damped by the transverse feedback that can only detect and correct dipole modes. Running at high chromaticity (ξ_V>0.4-0.5) is the only cure found so far to fight the electron cloud instability but the lifetime of the nominal LHC beam at the injection plateau has been observed to be limited to less than 10 minutes as a result of that. Recently it has been proposed (G. Franchetti, E. Métral, F. Zimmermann) that the limited lifetime and the incoherent emittance blow-up could be the result of the strongly time-varying non-linear fields generated by the pinching of the electron-cloud during the bunch passage [18][19]. Indirect measurements of the non-linear fields generated by the electron cloud along the bunch train have been performed and are reported in [16]. No evident cure has been found so far for these phenomena induced by the electron cloud. Their impact can only be reduced but not suppressed by beam scrubbing.

No detailed measurement of the momentum dependence of the growth rate of the electron-cloud vertical dependence exists. Recent simulations seem to indicate that the threshold for the onset of this instability decreases with increasing energy for constant normalized transverse emittance, longitudinal emittance and bunch length [20]. A series of experiments has started in the SPS to verify the scaling predicted by simulations [21].

A possible radical solution would be to suppress the electron cloud build-up by coating the vacuum chambers with coatings with low Secondary Electron Yield or by inserting clearing electrodes. An experimantal programme is being set-up in this respect in the SPS [22][23].

SUMMARY AND CONCLUSIONS

The nominal LHC beam is at the performance limit of the LHC injectors. Space charge in the PSB limits the maximum bunch intensity within nominal transverse emittances to ~75 % of the ultimate bunch population. No sizeable margin exists for the operation above the nominal LHC beam in the PS and even more in the SPS. The main limitations towards the achievement of the ultimate LHC beam performance in the injectors have been briefly reviewed. Studies and experiments have started to address the PS & SPS limitations above the nominal and towards the ultimate beam but they need to be intensified. This will require the allocation of manpower and machine time.

A re-optimization of the design parameters for the LHC beam in the LHC Injector chain (keeping fixed the parameters at extraction from the SPS) based on the

operational experience gained in the LHC Injectors with the LHC beam might be also beneficial as suggested by E. Métral at the workshop.

ACKNOWLEDGEMENTS

I would like to thank K. Hanke, S. Hancock, E. Métral, B. Mikulec, G. Rumolo, E. Shaposhnikova, B. Spataro (INFN-LNF), R. Steerenberg who provided me with most of the information presented here and for the interesting discussions during the preparation of the presentation and at the workshop.

REFERENCES

[1] M. Benedikt, P. Collier, V. Mertens, J. Poole, K. Schindl eds., "LHC Design Report vol. 3: The LHC Injector Chain", CERN-2004-003 - V-3.

[2] G. Arduini, "Intensity (and Brightness) Limitations in the LHC Proton Injectors", Proceedings of the Third CARE-HHH-APD Workshop - LHC-LUMI-06, Valencia, Spain, 16-20 Oct 2006, CERN 2007-002, p. 159-169.

[3] R. Garoby, "LHC injector upgrade plan", these Proceedings.

[4] M. Vretenar, "LINAC4", these Proceedings.

[5] G. Franchetti, I. Hofmann, M. Giovannozzi, M. Martini, E. Métral, "Space charge and octupole driven resonance trapping observed at the CERN Proton Synchrotron", PRST-AB 6, 124201 (2003).

[6] E. Métral, G. Franchetti, M. Giovannozzi, I. Hofmann, M. Martini and R. Steerenberg, "Observation of octupole driven resonance phenomena with space charge at the CERN Proton Synchrotron", NIM A 561 (2006) 257-265.

[7] R. Cappi et al., "Electron cloud build-up and related instability in the CERN Proton Synchrotron", PRST-AB, 5, 094401 (2002).

[8] R. Steerenberg, G. Arduini, E. Benedetto, A. Blas, W. Höfle, E. Métral, M. Morvillo, C. Rossi, G. Rumolo, "Nominal LHC Beam Instability Observations in the CERN Proton Synchrotron", Proceedings of PAC 2007, Albuquerque, New Mexico, USA, 25 – 29 June 2007, C. Petit-Jean-Genaz Ed., p. 4222-4224.

[9] E. Shaposhnikova, "SPS Challenges", these Proceedings.

[10] G. Arduini, T. Bohl, H. Burkhardt, E. Métral, G. Rumolo, B. Salvant, "Fast Vertical Single-bunch Instability at Injection in the CERN SPS - An Update", Proceedings of PAC 2007, Albuquerque, New Mexico, USA, 25 – 29 June 2007, C. Petit-Jean-Genaz Ed., p. 4162-4164 and references therein.

[11] E. Métral, G. Arduini, T. Bohl, H. Burkhardt, G. Rumolo, "The Fast Vertical Single-bunch Instability after Injection into the CERN Super Proton Synchrotron", EPAC 2006, Edimburgh, Scotland, pp. 2913-2915.

[12] B. Salvant, "TMCI studies with HEADTAIL & MOSES", these Proceedings.

[13] G. Rumolo, F. Zimmermann, "Practical user guide for HEADTAIL", CERN-SL-Note-2002-036 AP. G. Rumolo, F. Zimmermann, "Electron cloud simulations: beam instabilities and wakefields", PRST-AB 5, 121002 (2002). See also: http://proj-headtail-code.web.cern.ch/proj-headtail-code/ .

[14] Y. Papaphilippou, "Optics Considerations for PS2", these Proceedings.

[15] E. Métral, "SPS Impedance", these Proceedings.

[16] G. Arduini, T. Bohl, K. Cornelis, W. Höfle, E. Métral, F. Zimmermann, "Beam Observations with electron Cloud in the CERN PS&SPS Complex", CERN-2005-001, pp. 31-47 and references therein.

[17] B. Henrist, N. Hilleret, C. Scheuerlein, M. Taborelli, G. Vorlaufer, "The Variation of the Secondary Electron Yield and of the Desorption Yield of Copper under Electron Bombardment: Origin and Impact on the Conditioning of LHC", EPAC 2002, Paris, France, pp. 2553-2555.

[18] E. Benedetto, G. Franchetti and F. Zimmermann, "Incoherent Effects of Electron Cloud in Proton Storage Rings", Phys. Rev. Lett. 97 (2006) 034801.

[19] G. Franchetti, "Incoherent space charge and e-cloud effects", these Proceedings.

[20] G. Rumolo, E. Métral, E. Shaposhnikova, "SPS Performance with PS2", Proceedings of LHC-LUMI-06, Valencia, Spain, 16-20 October 2006, CERN-2007-002, pp. 129-134.

[21] G. Rumolo, "Experimental studies on SPS e-cloud", these Proceedings.

[22] S. Calatroni, P. Chiggiato, M. Taborelli, "SPS chamber upgrade: TiN coating", these Proceedings.

[23] F. Caspers, T. Kroyer, "Clearing electrodes: Past experience, technological aspects and potential", these Proceedings.

GENERATION AND STABILITY OF INTENSE LONG FLAT BUNCHES

F. Zimmermann and Ibon Santiago Gonzalez*, CERN, Geneva, Switzerland

Abstract

This report surveys possible schemes for producing long, "flat", intense bunches of about 5×10^{11} protons spaced by 50 ns, as are required by one of the proposed LHC upgrade scenarios. It also examines potential intensity limitations and instability thresholds for such beams.

THE ISSUE

The "large Piwinski angle" (LPA) scenario of the LHC upgrade [1] requires bunches of 5×10^{11} protons, spaced by 50 ns, with a flat longitudinal profile.

For demonstrating the feasibility of such upgrade path, the following questions must be addressed:

- How and where can such intense bunches be generated?
- How and where can they be made flat?
- Do these bunches remain stable and do they preserve their longitudinally flat shape?

This paper attempts to take a first look at the above questions.

GENERATION OF INTENSE BUNCHES

For the LPA scheme we should produce bunches of about 5×10^{11} protons at 50 ns spacing in the LHC. The Superconducting Proton Linac (SPL) and the PS2 are being designed to deliver 4×10^{11} protons per bunch at 25 ns spacing, which corresponds to the expected space charge limit at PS2 injection. Therefore, generating an intensity of 4×10^{11} protons per bunch at 50 ns spacing is easy with SPL and PS2, by injecting only every second bunch from the linac into the PS2. The higher bunch intensity $\sim 5.5 \times 10^{11}$ needed for LPE (with some margin for downstream losses) may be reached by one of the following methods:

- raising the SPL energy by about 17%;
- bunch merging at PS2 extraction;
- slip stacking in the SPS; or
- slip stacking in the LHC.

Raising the SPL energy would have implications on the linac length or linac gradient required. Bunch merging or slip stacking could result in increased beam losses and activation problems. Depending on where these longitudinal bunch manipulations are performed, additional RF systems will be required in the PS2, the SPS or the LHC itself.

STABILITY OF INTENSE BUNCHES

In the SPS intensity limits for LPA arise from the Transverse Mode Coupling Instability (TMCI) and from a longitudinal coupled bunch instability, while electron cloud is not expected to be a problem at 50-ns bunch spacing [1].

The effective transverse SPS single-bunch broad-band impedance $|Z_y^{BB}|$ for a 0.5 rms bunch length has been about 23 MΩ/m in 2006 and 2007. This value was inferred from the measured vertical tune shift (see Fig. 1) and head-tail growth rate as a function of intensity or chromaticity, respectively [2, 3]. The measurement uncertainty is 10-20%. Changes from one year to the next of up to 30% were found to well track the removal or addition of high-impedance components, e.g. kicker magnets, and to be close to expectation [2, 3].

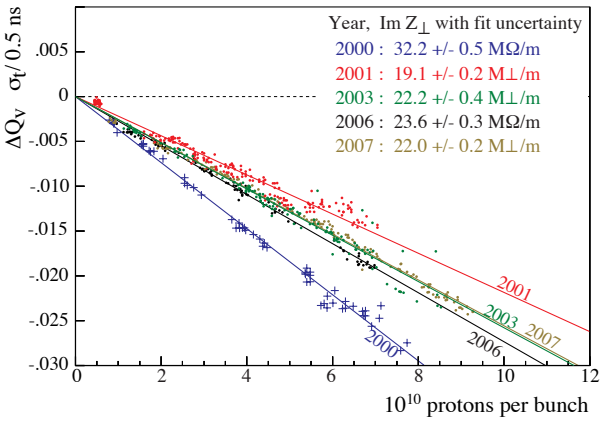

Figure 1: Vertical betatron tune as a function of intensity measured at the SPS in various years [3].

The Transverse Mode Coupling Instability is observed with a proton beam at the SPS [4, 5]. The measured threshold intensity is well described by the theoretical expression [4]

$$N_{b,thr} \approx \frac{8\pi Q_y \epsilon_{||}}{e^2 c} \frac{f_{rev}}{|Z_y^{BB}|} \left(1 + \frac{f_\xi}{f_r}\right) , \qquad (1)$$

Where $\epsilon_{||}$ denotes the longitudinal rms emittance, Q_y the betatron tune, e the electron charge, c the speed of light, f_r the effective broadband resonator frequency, $\eta \equiv (1/\gamma^2 - \alpha_C)$ the slippage factor, and $f_\xi = Q'\omega_0/\eta$ the chromatic

* On leave from University of the Basque Country, Bilbao, Spain

frequency shift (where ω_0 denotes the angular revolution frequency).

With the present typical longitudinal emittance of $\epsilon_{||} \approx 0.2$ eVs, Eq. (1) predicts the TMCI threshold for $N_{b,thr} \approx 10^{11}$ protons at a beam energy of 26 GeV, which is consistent with the experimental results, but about a factor 2 higher than the threshold simulated by the code HEADTAIL [5] without space charge, as is illustrated in Fig. 2. The difference between observed and simulated thresholds decreases if space-charge effects are included in the simulation [6].

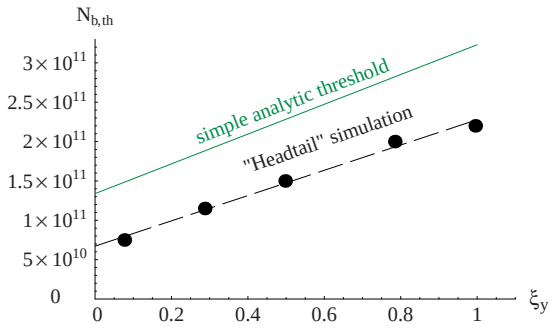

Figure 2: Instability thresholds according to Eq. (1) and from simulations with the code HEADTAIL as a function of vertical chromaticity [5].

In view of the reasonable consistency with the experiments, we can apply (1) to extrapolate the threshold that we should expect for intense bunches in the PS2. Tripling the longitudinal emittance will increase the threshold three times. Raising the injection energy from 26 GeV in the present SPS to 50 GeV for injection from a PS2, will increase the magnitude of the slippage factor, $|\eta|$ by a factor 2.5, and, finally, operating with a chromaticity of $Q' \approx 10$ will give another factor of 2. Putting everything together, we expect that the TMCI threshold in the SPS can easily be shifted towards 1.5×10^{12}, far above our target value of 5.5×10^{11} protons per bunch.

A concern related to TMCI will arise, however, if we decide to flatten the bunches by means of a higher harmonic RF system, since the TMCI threshold may go to zero in such a case [7].

The longitudinal broadband impedance of the SPS is estimated from the measured shift of the quadrupole oscillation frequency with bunch intensity [9]. In 2007 a value $Z/n \approx 10\ \Omega$ was obtained [8], as is illustrated in Fig. 3. The longitudinal broadband impedance can lead to a loss of Landau damping against coupled-bunch instabilities. Figure 4 shows how the threshold for coupled-bunch instabilities decreases with increasing beam energy in the SPS. Without the stabilizing third harmonic 800-MHz system the threshold at top energy is only $N_{b,thr} \approx 2 \times 10^{10}$ ($N_{b,thr} \approx 1.3 \times 10^{11}$ at injection). With the 800 MHz system turned on in "bunch shortening mode" the instability occurs only on the SPS flat top, up to nominal intensities ($N_b \approx 1.2 \times 10^{11}$) [9]. The beam can be further stabilized by a controlled blow up of the longitudinal emittance, since the threshold increases roughly in proportion to $\epsilon_{||}^2$ [9].

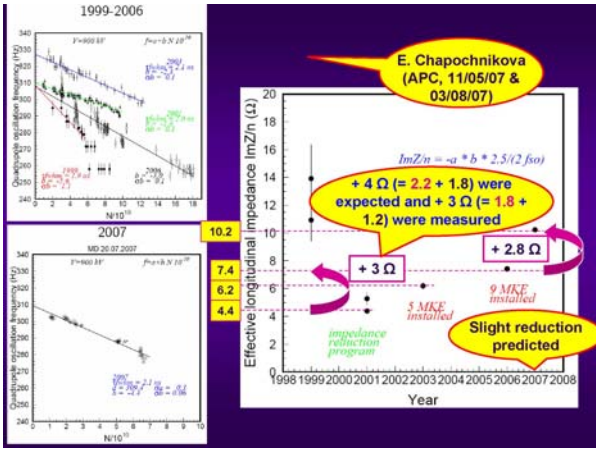

Figure 3: Quadrupole oscillation frequency in the SPS as a function of intensity in various years (left) and the inferred effective longitudinal impedance Z/n versus the year (right) (E. Metral, E. Shaposhnikova et al.) [8].

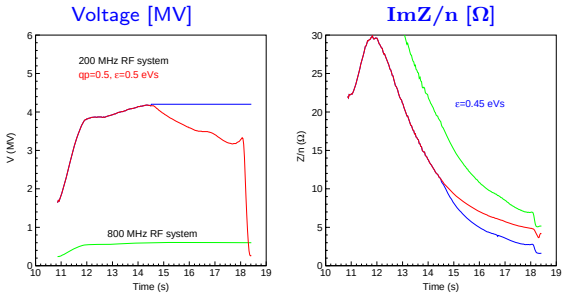

Figure 4: RF voltage programmes for the 200-MHz and 800-MHz systems as a function of time during the SPS cycle (left) and the corresponding longitudinal instability thresholds (right) (E. Shaposhnikova) [8].

HOW TO MAKE "FLAT" BUNCHES?

This question was already studied in depth by J.-P. Delahaye and co-workers in 1980 [10], who distinguished two basic approaches: (1) a modification of the beam distribution, or (2) a change of potential.

Either in the LHC itself or in its injector complex several techniques are available:

- 2nd harmonic debuncher in the linac (J.-P. Delahaye et al, 1980 [10], Fig. 5);
- empty bucket deposition in debunched beam (J.-P. Delahaye et al 1980 [10], A. Blas et al, 2000 [11], Fig. 6);

- higher harmonic cavity (J.-P.Delahaye et al, 1980 [10], Fig. 7);
- blow up by modulation near f_s together with a higher frequency RF near the harmonic frequency (R. Garoby, S. Hancock, 1994 [12], Fig. 8);
- the recombination with an empty bucket using a double harmonic RF system (C. Carli, M. Chanel, 2001 [13, 14], Fig. 9);
- the redistribution of phase space using a double harmonic RF system (C. Carli, M. Chanel, 2001 [13, 14], Figs. 10 and 11);
- RF phase jump (RHIC [15], Fig. 12)
- injection of band-limited noise (E. Shaposhnikova).

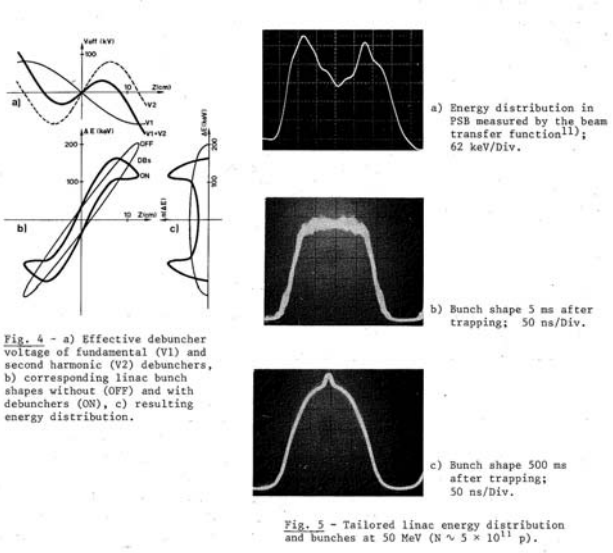

Fig. 4 - a) Effective debuncher voltage of fundamental (V1) and second harmonic (V2) debunchers, b) corresponding linac bunch shapes without (OFF) and with debunchers (ON), c) resulting energy distribution.

Fig. 5 - Tailored linac energy distribution and bunches at 50 MeV (N ~ 5 × 10^{11} p).

Figure 5: Example for bunch flattening by second harmonic linac debuncher (J.-P. Delahaye et al, 1980 [10]).

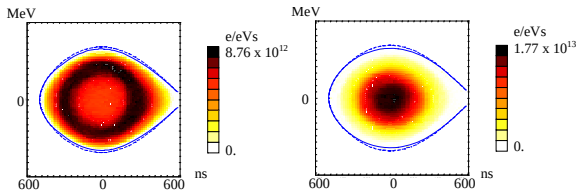

To the left, a flat bunch of 7.4×10^{12} protons and, to the right, a normal bunch of the same intensity. Note the different density scales.

Figure 6: Example for bunch flattening by empty bucket deposition (A. Blas et al, 2000 [11]).

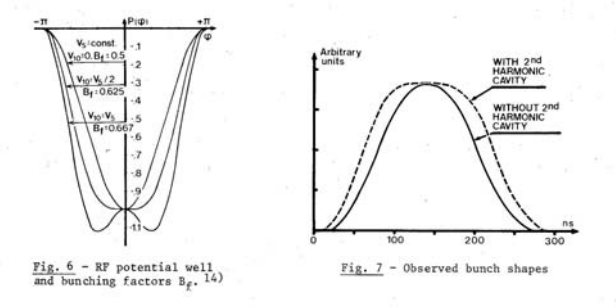

Fig. 6 - RF potential well and bunching factors B_f. [14]

Fig. 7 - Observed bunch shapes

Table 4 - Typical intensities per pulse accelerated in ring 3 (in units of 10^{12} p).

RF voltage	Injection (50 MeV)	After capture	At 200 MeV
Fundamental (V_5) only	9.6	6.3	5.9
2nd-harmonic (V_{10}) added (V_{10} = 0.5 V_5)	9.8	7.8	7.2

Figure 7: Example for bunch flattening by second harmonic ring cavity (J.-P. Delahaye et al 1980 [10]).

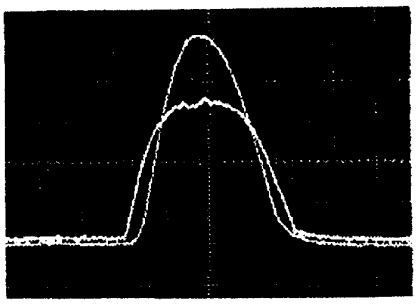

50 ns/div.

Figure 8: Example for bunch flattening by blow up via modulation near f_s together with higher harmonic RF (S. Garoby, S. Hancock, 1994 [12]).

ARE "FLAT" BUNCHES STABLE?

We look at four different aspects of this problem:

- Landau damping for a double RF system;
- Landau damping for a flat bunch in a single RF system;
- stability of hollow bunches with RF & phase loop; and
- the effect of intrabeam scattering.

Landau Damping for a Double RF System

By a double harmonic RF system the bunches can be either lengthened or shortened, depending on the relative phase of the higher harmonic RF wave with respect to the fundamental RF wave. The bunch lengthening mode would also lead to flatter bunches. Therefore this would be the ideal operation mode for our purpose of producing long flat bunches at the LHC. However, there is a problem, pointed out by E. Shaposhnikova [9, 16, 17]. Namely in the bunch

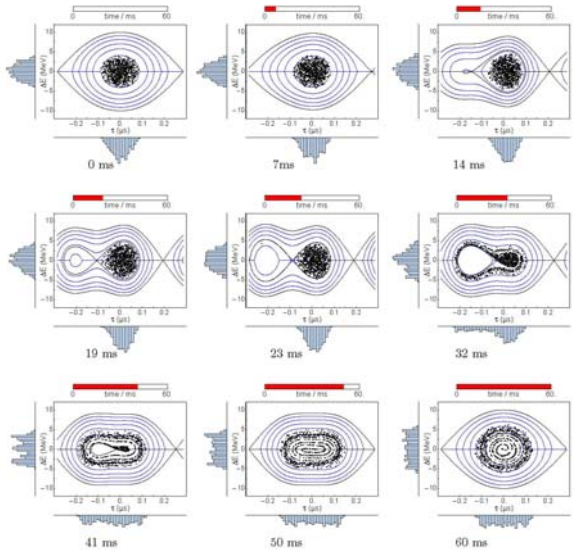

Figure 4: *Blow-up by recombination of a bunch with an empty bucket with improved adiabaticity at small amplitudes. Simulated phase space portraits at different times during the process, with RF parameters versus time plotted in Figure 3.*

Figure 9: Simulation example for bunch flattening by recombination with an empty bucket: empty phase space is inserted close to the bucket center (C. Carli, M. Chanel, 2001 [13, 14]).

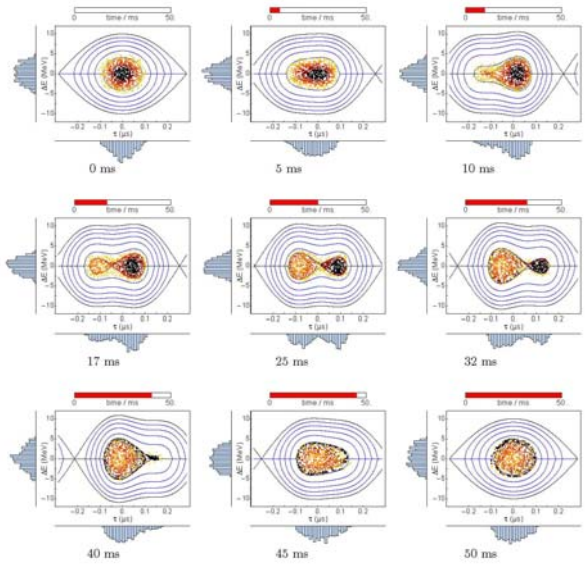

Figure 6: *Redistribution of phase space surfaces to create hollow bunches. Simulated phase space portraits at different times during the process, with RF parameters versus time plotted in Figure 5.*

Figure 10: Simulation example for bunch flattening by redistribution of phase-space surfaces: high-density region and periphery are exchanged (C. Carli, M. Chanel, 2001 [13, 14]).

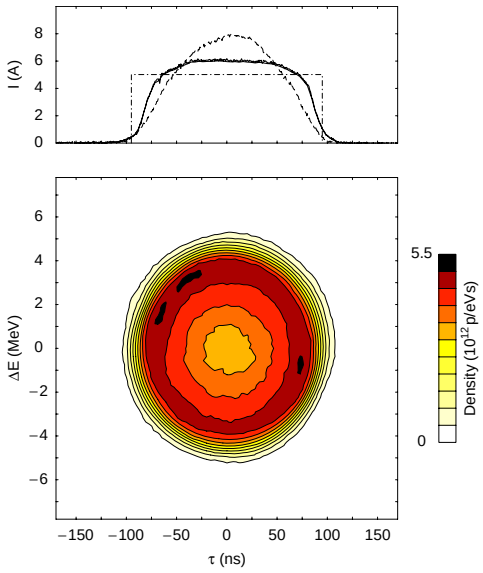

Figure 11: Example for bunch flattening by redistribution of phase-space surfaces: measurement with 6×10^{12} protons per bunch in the PS Booster (C. Carli, M. Chanel, 2001 [13, 14]).

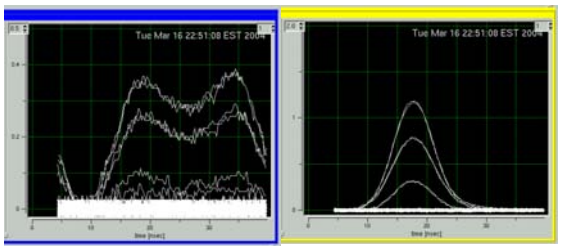

Figure 12: Example for bunch flattening by RF phase jump in RHIC: gold beam, store at 100 GeV/u with h=360 RF system; no collision, no Landau cavity, no dampers, no kickers; hollow beam in the RHIC blue ring, created by RF phase jump, compared with a normal beam in the yellow ring (J. Wei et al [15]).

lengthening mode a critical value of the longitudinal emittance exists above which the bunches do no longer self-stabilize. This critical value is related to the longitudinal oscillation amplitude (or action I) at which the synchrotron tune assumes its maximum value, or $\omega'(I) = 0$, and where Landau damping is lost. Figure 13 compares the variation of the synchrotron tune with amplitude for a single RF system with the one for a double RF in either bunch lengthening or bunch shortening mode. A pronounced maximum of the synchrotron tune at an intermediate amplitude is found only for the bunch lengthening configuration. This extremum inside the beam distribution lies at the origin of the latent beam instability for this case.

Indeed, at the CERN SPS large coherent signals were

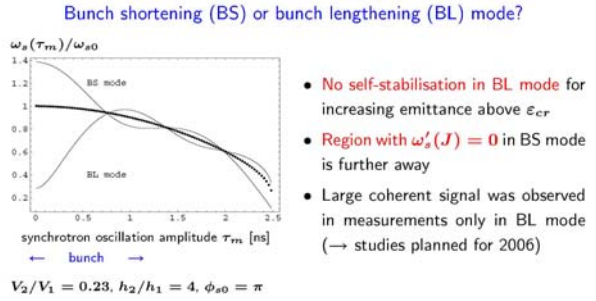

Figure 13: The SPS synchrotron tune as a function of longitudinal oscillation amplitude for a single RF system and for a double RF system in bunch shortening (BS) or bunch lengthening mode (BL); the synchrotron tune is normalized to the central tune for the single RF system. The voltage ration of double harmonic or single harmonic RF is 0.23. The second RF system operates at 4 times the base frequency (800 and 200 MHz, respectively) [9].

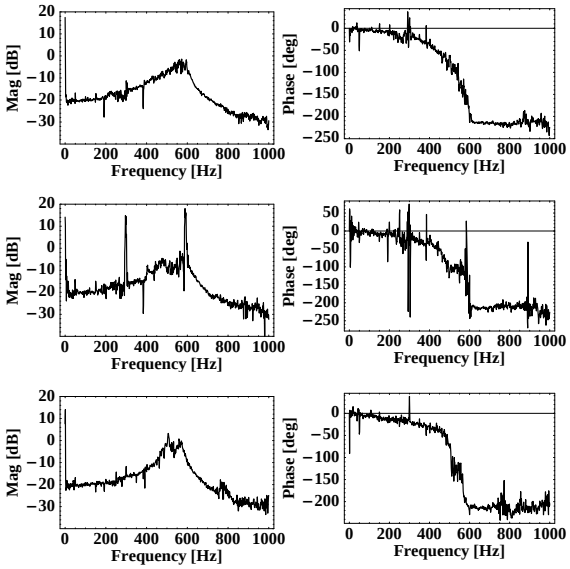

Figure 14: Longitudinal amplitude (left) and phase response (right) of the CERN SPS beam as a function of excitation frequency for a single RF system (top), for a double RF system in bunch lengthening mode (center) and for a double RF system in bunch shortening mode (bottom); the beam transfer function measurement for the bunch lengthening mode shows a strong coherent response at an excitation frequency corresponding to the synchrotron-oscillation amplitude at which $\omega_s'(I) = 0$ [9, 16].

observed in beam measurements only when the double harmonic RF was active in bunch lengthening mode. The loss of Landau damping for this 'bad' phasing of the higher harmonic RF is also evidenced by SPS beam-transfer function measurements, illustrated in Fig. 14. Figure 15, also from the SPS, presents detailed images of the bunch shape evolution with a double RF system, which reveal the creation of shoulders in regions where the distribution function F_0 has zero derivative, $dF_0/dJ = 0$, corresponding to the regions with maximum synchrotron tune.

The HEADTAIL programme [18] was recently upgraded by G. Rumolo, in order to model the SPS situation with a double RF system [19]. A higher order harmonic cavity element has become available, which can be switched on and ramped. The extended code was tested for present SPS parameters with a combination of 200-MHz and 800-MHz cavities. The HEADTAIL simulations can now predict the SPS bunch shapes for a double RF system operated in either bunch lengthening or bunch shortening mode. Preliminary results are displayed in Fig. 16.

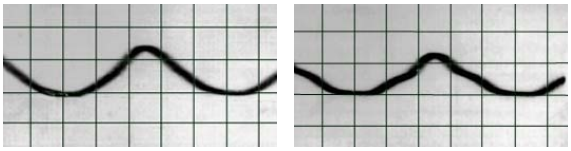

Figure 15: Bunch profiles at the beginning (left) and end (right) of a 10 min. SPS coast at 120 GeV/c in bunch lengthening mode, revealing the development of shoulders [16].

Landau Damping for Flat Bunches and Single RF

Flat distributions can be obtained from the Ruggiero-Berg class of generalized parabolic distributions [20]

$$\lambda(z) = \frac{n(n+1)\Gamma(n)}{\hat{\tau}\sqrt{\pi}\Gamma(n+\frac{3}{2})}\left(1+\frac{r^2}{\hat{\tau}^2}\right)^{n+\frac{1}{2}} \quad \text{for } 0 < z < \hat{\tau}\ , \tag{2}$$

by taking the limit $n =\!\!\rightarrow -1/2$, where r denotes the radial coordinate in longitudinal phase space. Examples of this and various other Berg-Ruggiero parabolic-like distributions as well as an alternative better behaved flat distribution à la Furman [21] (including its Abel transform [22]) are illustrated in Fig. 17, both as (projected) longitudinal density in physical space and as radial density in phase space [23]. The calculation in [23] extended earlier Landau-damping considerations of Refs. [24, 25, 26] to longitudinally flat beams.

From the phase-space density the Landau-damping stability limit in the complex tune-shift plane can be calculated using Sacherer's dispersion relation [23, 24]. Examples for elliptical and flat distributions in the Ruggiero-Berg parametrization are displayed in Fig. 18. The direction relevant for finding the tune-shift threshold with space charge below transition (e.g. for the PS) or with an inductive impedance above transition (e.g. for the SPC or LHC) is towards the right. Table 1 summarizes the coherent tune shift stability limits for various different distributions. This table and Fig. 18 demonstrate that flat bunches in a single

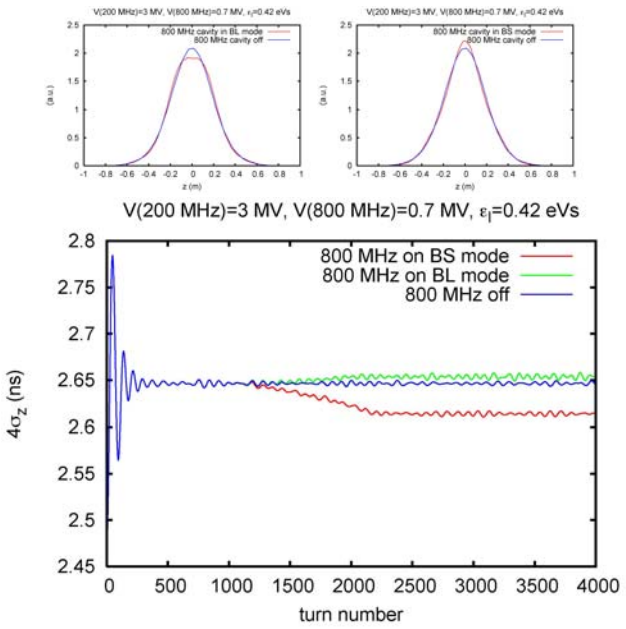

Figure 16: HEADTAIL simulation results for the SPS. The bunch shape with an 800-MHz 3rd harmonic system in bunch lengthening mode compared with the Gaussian shape of a single harmonic RF (top left); the same for the bunch shortening mode (top right); and the 4σ bunch length as a function of turn number for a single RF system and a double RF system in either one of the two operation modes [19].

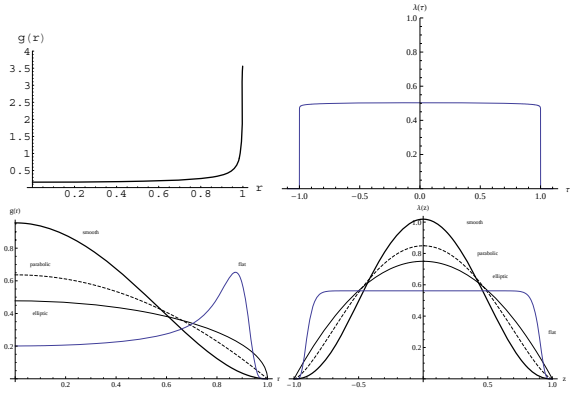

Figure 17: Radial phase space density (left) and longitudinal profile (right) for a flat distribution as limiting case of Ruggiero-Berg class of parabolic distributions (top) as well as for various other quasi-parabolic disttribution functions and another smoother flat distribution à la M. Furman (bottom) [23].

RF system are more stable than any of the considered types of non-flat bunches.

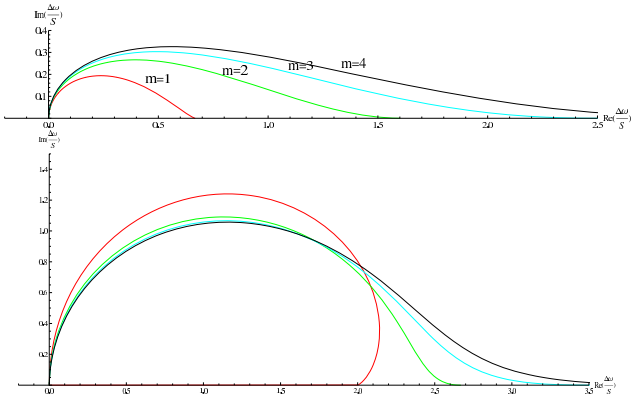

Figure 18: Stability diagrams computed from the Sacherer dispersion relation [24, 23] in the complex tune shift plane, normalized to the bunch synchrotron frequency spread S, for an elliptical distribution with $n = 1/2$ (top) and a flat distribution with $n = -1/2$ (bottom), considering dipole $m = 1$), quadrupolar ($m = 2$) and higher order modes of oscillation [23].

Table 1: Coherent tune shift stability thresholds of the lowest four modes for various longitudinal distributions normalized to the total synchrotron-frequency spread S [23]; $m = 1$ refers to the dipole mode, $m = 2$ to the quadrupolar one, etc.

distribution	n	$\frac{\Delta\omega_1}{S}$	$\frac{\Delta\omega_2}{S}$	$\frac{\Delta\omega_3}{S}$	$\frac{\Delta\omega_4}{S}$
smooth	2	0.33	1	1.8	2.67
parabolic	1	0.5	0.33	2.25	3.2
elliptic	1/2	0.67	1.6	2.57	3.56
flat	$-1/2$	2	2.67	3.6	4.57
flat (Furman)	N/A	1.58	2.13	2.90	3.71

Flat Bunches with Single RF and Phase Loop

Flat or hollow bunches stored in a ring with a single RF can become unstable if an RF phase loop is active [11]. Some pertinent observations from the PS Booster [11] are shown in Fig. 19.

The stability of regular and hollow bunches in single RF systems with RF phase loop was studied by A. Blas, S. Koscielniak et al [11, 27]. These authors considered several typical distributions shown in Fig. 20 (top) and calculated the corresponding Nyquist-Bode stability diagrams of the longitudinal beam-transfer functions (BTF) including phase loop (bottom pictures in Fig. 20). The reference points for the BTF are defined in Fig. 21. An ordinary BTF shows 0 phase lag in the limit of low frequency and a -180 degree shift at high frequencies, passing through -90 de-

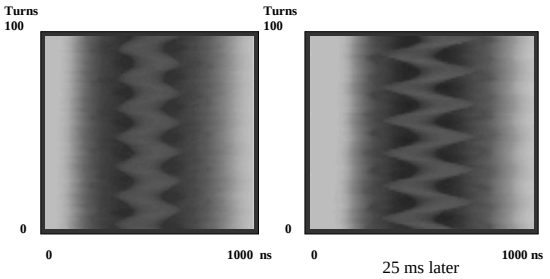

Figure 19: Unstable hollow bunches observed in the CERN PS with both a single RF and active phase loop. The right picture was taken 25 ms after the left [11].

gree between these two extremes. For hollow bunches the derivative of the distribution function is positive for small amplitudes. An additional -90 degree phase change arises from the residue term of the dispersion integral [27]. For significantly hollow bunches, there is a further -90 degree phase change (yielding a total of -360 degree) which is contributed by the principal value of the dispersion integral [27]. A simple interpretation of these findings is that the hollow bunch represents the sum of a positive and a (smaller) negative bunch. The BTF of the negative bunch is simply -1 times that of a positive bunch, and so it has a phase response of $+180$ degree at low frequency and $+0$ degree at high frequency. The phase response of the sum can either lag or lead the excitation. S. Koscielniak concluded that some hollow beams must become unstable when the phase loop is closed; however, the stability and growth rate depend on the degree of hollowness. Figures 22 and 23 illustrate the transition of the BTF from a stable "flat" bunch to an unstable significantly "hollow" bunch.

Longitudinal Emittance Blow Up

In various stages in the LHC accelerator chain (PS Booster, SPS, LHC) the longitudinal emittance is blown up to increase Landau damping and to stabilize the beam. For example, at injection (450 GeV) into the LHC the longitudinal emittance is $0.6-1.0$ eVs. This emittance is blown up during the ramp to reach a value of 2.5 eVs at 7 TeV [28]. In the SPS, the longitudinal emittance of the injected beam at 26 GeV amounts to 0.35 eVs, and it is increased to 0.6 eVs at 450 GeV [29]. All longitudinal emittance numbers here are defined as 4π times the rms energy spread time the rms bunch length, as is customary in the CERN RF group.

It is important to note that the longitudinal blow up during the acceleration of the SPS and the LHC could render useless any prior bunch shaping. Against this background, future more elaborate studies are likely to conclude that the bunch flattening should best be performed in the LHC itself, and ideally at top energy or as part of the longitudinal blow up.

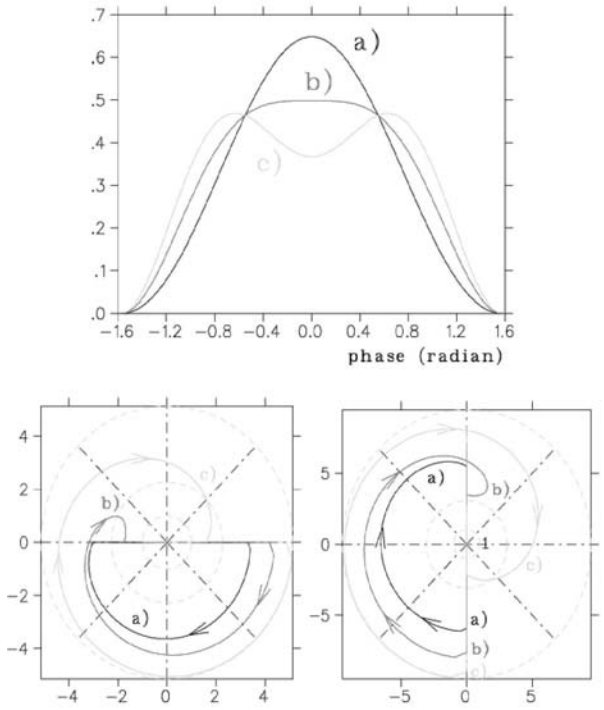

Figure 20: Three different longitudinal distributions for which the stability with RF phase loop was studied (top), and the Nyquist-Bode diagrams of the beam-transfer functions for the same three distributions (bottom). The left picture corresponds to point "1)", the right picture to point "2)" of the phase-loop diagram in Fig. 21. In case of the hollow distribution c the path in the polar diagram surrounds the point $+1$ once in a clockwise sense which indicates instability, while a beam with the flat distribution b is still stable. [11].

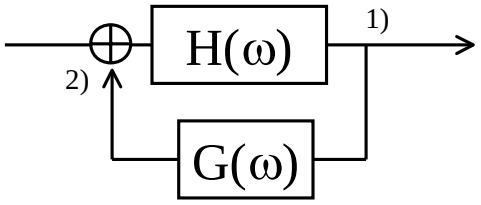

Figure 21: Transfer function diagram in frequency domain for the definition of points "1)" and "2)" used in Fig. 20; $H(\omega)$ denotes the open-loop beam transfer function, and $G(\omega)$ is the phase loop.

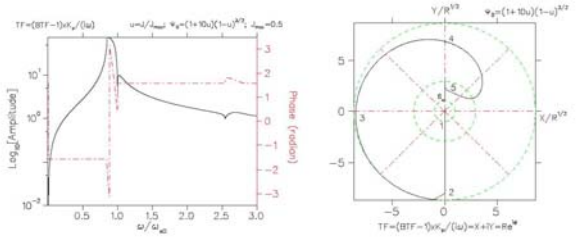

Figure 12: Amplitude/phase and polar plots of the transfer function with phase loop for $\Psi_0 \propto (0.1 + J)(\bar{J} - J)^{3/2}$. The gain $K_p = 3\Omega_s$ per radian.

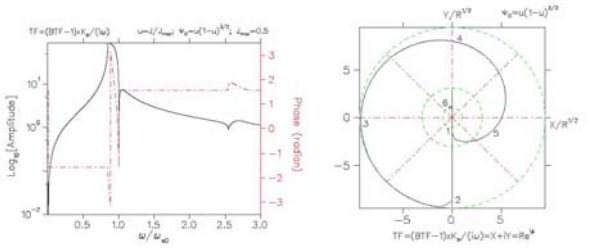

Figure 13: Amplitude/phase and polar plots of the transfer function with phase loop for $\Psi_0 \propto J(\bar{J} - J)^{3/2}$. The gain $K_p = 3\Omega_s$ per radian.

Figure 22: Beam transfer functions in amplitude-phase (left) and Nyquist-Bode representation (right) of a slightly hollow stable bunch (top) and of a significantly hollow unstable bunch (bottom) [27].

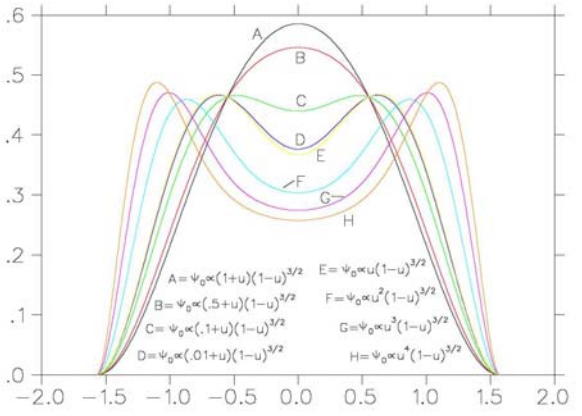

Figure 1: Bunch shapes arising from various phase space distribution functions Ψ_0.

Figure 23: Bunch shapes arising from various phase distribution functions Ψ_0 as indicated; the distribution C is stable while D and E are unstable [27].

Intrabeam Scattering for Flat or Hollow Bunches

We finally address the question whether intrabeam scattering (IBS) could destroy the flat or hollow profile. Machine experiments at, and simulations for, RHIC provide a first tentative answer, noting that IBS is a much stronger effect in RHIC than in the LHC. Figure 24 compares the time evolution of the longitudinal profile for a normal and a hollow beam, as observed in a dedicated RHIC experiment. The former retained its Gaussian-like shape, with increasing rms size, while, after 30 minutes, the hollow beam profile showed a reduction in the depth of its central hole, but was still "flat". Simulations of the profile evolution due to IBS conducted with the code BBFP ("Bunched Beam Fokker-Planck Solver" [31]) are in good agreement with the experimental observations; see Fig. 25 [30]. The IBS calculation in BBFP is performed in action variables. Figure 26 illustrates the calculated time evolution of the density in the longitudinal action space for both hollow and Gaussian beam profiles in RHIC over an interval of 1 h. The BBFP results in terms of action are easily converted to the longitudinal phase and momentum planes.

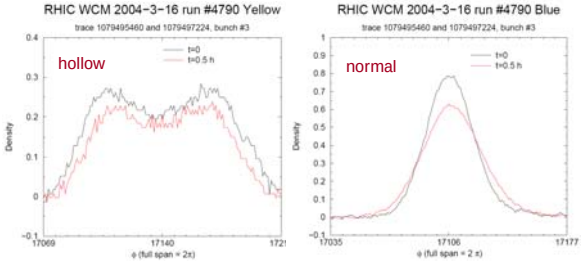

Figure 24: Beam profile evolution for a hollow beam (left) and for a normal beam (right) observed in RHIC; the two curves correspond to the initial profile and to the profile measured after 30 minutes (in red), respectively [30].

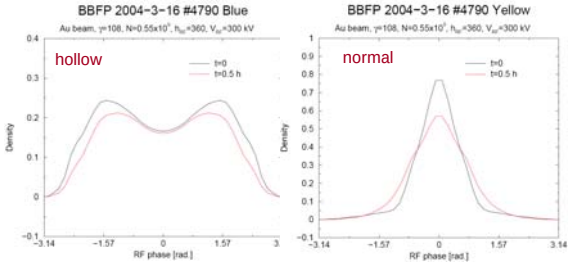

Figure 25: Beam profile evolution for a hollow beam (left) and for a normal beam (right) due to IBS simulated for the beam parameters of the RHIC experiment in Fig. 24; the two curves again correspond to the initial profile and to the profile measured after 30 minutes (in red), respectively [30].

CONCLUSIONS AND OUTLOOK

A concrete scheme for generating the 50-ns LPA beam of an LHC upgrade is still being called for. Several bunch flattening techniques are available and could be applied in various CERN machines. Flat bunches in a single RF system are strongly Landau damped. A double RF system may, however, lead to the loss of Landau damping if the beam distribution extends to the region where $\omega_s(I) = 0$. The ensuing loss of Landau damping is accompanied by the

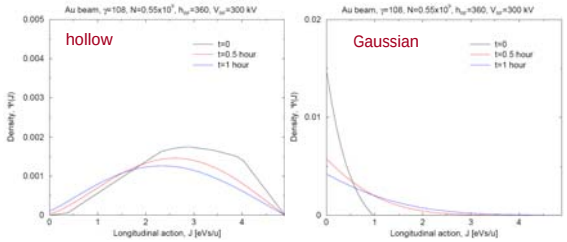

Figure 26: Density evolution in terms of longitudinal action for a hollow beam (left) and for a normal beam (right) due to IBS in RHIC over an interval of 1 h [30].

formation of "shoulders" in the longitudinal profile and by coherent signals. Significantly flat, or hollow, bunches can also become unstable in a single RF system in the presence of an RF phase loop.

The next steps will include (1) further machine studies on beam stability and lifetime in a double RF system, (2) machine studies on flat bunch stability and beam evolution in a single RF system, (3) machine studies on flat-bunch generation, (4) continued analytical studies of Landau damping; (5) simulations with the HEADTAIL and BBFP codes; (6) the development of a detailed strategy to generate intense long flat 50-ns bunches in LHC [in which machine, and by which method(s)?], and (7) the implications for the RF systems in one or several of the upgraded CERN accelerators.

ACKNOWLEDGMENTS

We warmly thank Michael Benedikt, Christian Carli, Steven Hancock, Elias Metral, Yannis Papaphilippou, Giovanni Rumolo, Elena Shaposhnikova, and Jie Wei for helpful discussions. The support of the European Community-Research Infrastructure Initiative under the FP6 "Structuring the European Research Area" programme (CARE, contract number RII3-CT-2003-506395) is gratefully acknowledged.

REFERENCES

[1] F. Zimmermann, "LHC Upgrade Scenarios," PAC2007, Albuquerque (2007).

[2] H. Burkhardt, G. Rumolo, F. Zimmermann, "Coherent Beam Oscillations and Transverse Impedance in the SPS," EPAC 2002 Paris (2002).

[3] H. Burkhardt, "SPS Transverse Impedance Measurements," CERN APC 17.08.2007.

[4] E. Metral, "Stability Criteria for High-Intensity Single-Bunch Beams in Synchrotrons," EPAC 2002 Paris (2002).

[5] H. Burkhardt et al, "Observation of a Fast Single-Bunch Transverse Instability on Protons in the SPS," EPAC 2004 Lucerne (2004).

[6] E. Metral et al, "The Fast Vertical Single-Bunch Instability after Injection into the CERN Super Proton Synchrotron," EPAC 2006 Edinburgh (2006).

[7] Y.H. Chin, "Transverse Mode Coupling Instability in a Double RF System, " Part. Acc. 45: 209, CERN-SL-93-03-AP (1993).

[8] E. Metral, "The SPS Impedance Budget," CERN SPS Upgrade Meeting, 21.08.2007.

[9] E. Shaposhnikova, "Studies of Beam Behavior in Double RF System," CERN APC 06.06.2007.

[10] J.-P. Delahaye et al, "Shaping of Proton Distribution for Raising the Space Charge of the CERN PS Booster," 11th HEACC, Geneva, 1980

[11] A. Blas, S. Hancock, M. Lindroos, S. Koscielniak, "Hollow Bunch Distributions at High Intensity in the PS Booster," EPAC 2000, Vienna (2000).

[12] R. Garoby, S. Hancock, "New Techniques for Tailoring Longitudinal Density in a Proton Synchrotron," EPAC 94, London (1994).

[13] C. Carli, "Creation of Hollow Bunches using a Double Harmonic RF System", CERN/PS 2001-073 (AE) (2001).

[14] C. Carli and M. Chanel, "New Methods to Create Hollow Bunches," Proc. HB2002, Batavia, AIP CP642, CERN-PS-2002-035-AE (2002)

[15] J. Wei, "IBS Theories, Codes, and Benchmarking", IBS'07 workshop, Daresbury (2007).

[16] E. Shaposhnikova et al, "Beam Transfer Functions and Beam Stabilisation in a Double RF System," PAC2005 Knoxville

[17] E. Shaposhnikova, "Bunched Beam Transfer Matrices in Single and Double RF systems," CERN SL/94-19-RF (1994).

[18] G. Rumolo, F. Zimmermann, "Practical User Guide for HEADTAIL," CERN SL-Note-2002-036-AP (2002).

[19] G. Rumolo, private communication, 07.08.2007

[20] F. Ruggiero, S. Berg, "Stability Diagrams for Landau Damping," PAC'97 Vancouver (1997)

[21] M.A. Furman, "E-Cloud in PS2, PS+, SPS+," Proceedings LHC-LUMI-06, CERN-2007-002, CARE-Conf-07-004-HHH (2007).

[22] P.W. Krempel, "The Abel-Type Integral Transformation and Its Application to Density Distributions of Particle Beams," MPS/Int.BR/74-1 (1974).

[23] I. Santiago Gonzalez, "Loss of Longitudinal Landau Damping in the LHC Injectors," CERN-AB-Note-2008-001, CARE-NOTE-2007-012-HHH (2007).

[24] F.J. Sacherer, "A Longitudinal Stability Criterion for Bunched Beams," CERN/MPS/BR 73-1, IEEE Tr. NS 20, 3, 825 (1973).

[25] E. Metral, "Longitudinal Bunched Beam Coherent Modes: From Stability to Instability and Inversely," CERN-AB-2004-002 (ABP).

[26] K.Y. Ng, "Comments on Landau Damping due to Synchrotron Frequency Spread," FERMILAB-FN-0762-AD (2005).

[27] S. Koscielniak, "Transfer Functions of Hollow Bunches," TRI-DN-99-25 (1999).

[28] E. Shaposhnikova, "Longitudinal Phenomena during the LHC Cycle," Chamonix XI, CERN-SL-2001-003 DI (2001).

[29] E. Shaposhnikova, "Longitudinal Stability of the LHC Beam in the SPS," CERN SL-Note-2001-035-HRF, 2001.

[30] J. Wei, "IBS Theories, Codes, and Benchmarking," IBS07 workshop, Daresbury (2007).

[31] Information on the BBFP code can be found in the CARE-HHH code web repository; see *http://oraweb.cern.ch:9000/pls/hhh/code_website.disp_allcat*. The code is available from the author.

SLIP STACKING*

K. Seiya, B. Chase, J. Dey, P. Joireman, I. Kourbanis, J. Reid, Fermilab, Batavia, IL 60510, U.S.A.

Abstract

Slip stacking has been onperational at Fermilab Main Injector (MI) since December 2004. The proton beam intensity for the anti proton production was increased by 70% with the stacking scheme. We plan to use it also for the Numi operation which is providing beams to the MINOS neutrino experiment. [1]

OPERATION STATUS

The MI sends protons with the energy of 120GeV to a pbar target and the Numi beam line in one MI cycle of 1.8 sec. Total 7 batches were injected from Booster at 8GeV, where one batch contained 84 bunches. The first two batches were merged into one batch by slip stacking and the other 5 batches were injected after the stacking process was completed as shown in Figure 1 and 2. There were one double-density batch going to the pbar target, and 5 single-density batches for the Numi in the MI at 8GeV. They were accelerated to 120 GeV at one cycle. The Booster cycle is 66.6msec and the MI cycle is 1.6sec at the minimum, so that accelerating 7 batches together increases beam efficiency effectively in the MI. The intensity for the pbar target is 9.0e12 and for Numi beam line is 22e12 particles per pulse (ppp) on the current operation.

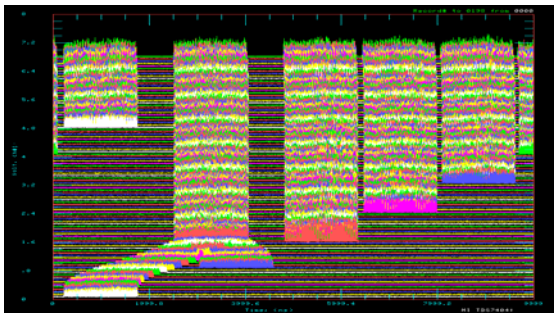

Figure 1: Mountain range plots with wall current monitor signals at 8GeV. The horizontal scale is 10μsec and the MI revolution is ~11μsec.

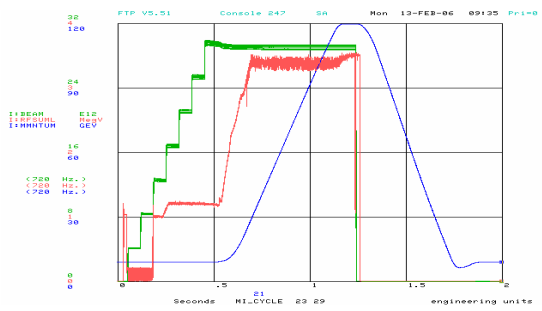

Figure 2: Total beam intensity in the MI (green), RF voltage (red) and momentum (blue).

SLIP STACKING

In the slip stacking the beam at higher energy and the beam at lower energy are slipping each other, and they are captured by one rf bucket when they are lined up longitudinally.

RF system and MI momentum aperture

Two different rf frequencies were used for the slip stacking process. The MI has 18 53MHz rf cavities of three are driven at one frequency (lower) and three other at another frequency (higher). The rest of the cavities were off but were compensating for the beam loading effects. [2] The momentum aperture of MI is about +/- 1.0% so that the frequency can be changed by +/- 3000Hz from the central frequency. [3]

Table 1: The MI parameters

Harmonic number	588
RF frequency at injection	52811400 Hz
Transition Gamma	21.6
Kinetic energy at injection	8 GeV

Frequency curves and frequency separation

The frequency separation between higher and lower frequencies was studied by measurements and simulation. [3] In the case of the emittance of 0.08eV-sec and rf voltage of 60kV, the frequency separation of more than 1200Hz was necessary to avoid an emittance blow-up. Since a beam emittance depends on the beam intensity, the parameters were optimized by measurements of beam losses at high intensity. The frequency separation kept at 1400Hz with the RF voltage of 110kV in the operation. Both higher and lower frequency beams were captured with central frequency rf voltage of 1MV when they were at the same longitudinal location as shown in Figure 3.

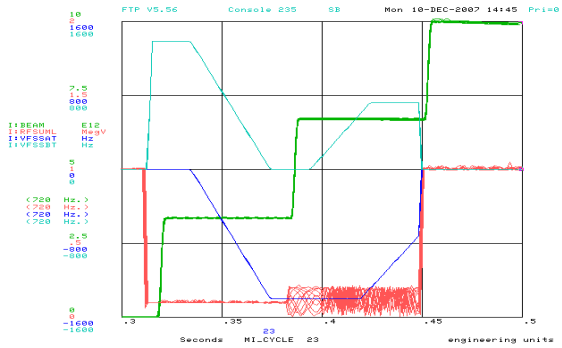

Figure 3: Higher (cyan) and lower (blue) rf frequencies, total beam intensity (green) and total rf voltage (red).

*Operated by Fermilab Research Alliance, LLC under Contract No. DE-AC02-07CH11359 with the United States Department of Energy.

#kiyomi@fnal.gov

Bucket acceptance for Slip stacking

The bucket size was estimated by particle simulations with applying two frequency rf voltages. [4] All particles were located on the bucket trajectory of central frequency rf at input. Because the higher frequency rf was applied, only the particles shown in Figure 4 was able to stay in the bucket after 120msec. The bucket acceptance with current operational parameters was +/-5 nsec in the phase and +/- 7.5 MeV in the energy directions in order to avoid beam loss.

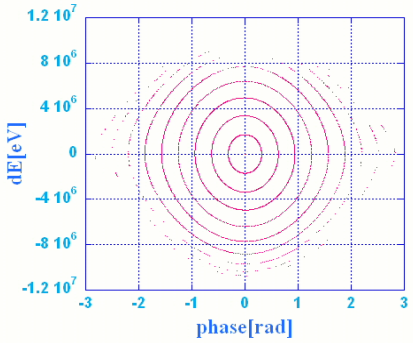

Figure 4: Bucket acceptance with rf voltage of 110kV and frequency separation of 1400Hz.

Emittance growth

A longitudinal emittance per bunch of 0.12 eV-sec with momentum spread of +/-9.4 MeV was measured at injection with the intensity of 4.23e12 ppp out of Booster. The longitudinal phase space was measured at recapture time and shown in Figure 5 (left). Figure 5(right) shows the phase space at recapture by simulation using the same injection emittance as measurements. The emittance at recapture was measured to be 0.35 eV-sec agreeing the simulation. There was no unexpected emittance blow-up during slip stacking on operation with beam loading compensation according to the specification. [2]

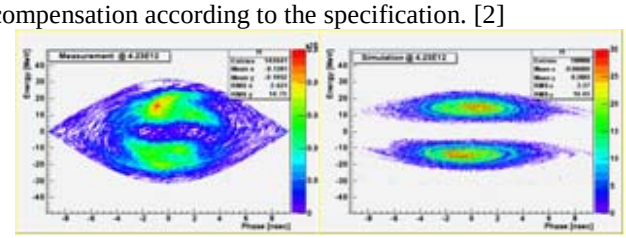

Figure 5: Phase space tomography at recapture time on measurement (left) and simulation (right).

MULTI BATCH SLIP STACKING

The slip stacking scheme was extended for the "Proton plan" project in order to increase intensity for the Numi operation. Eleven batches will be injected from the Booster to the MI. One slip stacking batch is going to the pbar target, while four doubled batches and one single batch are going to the Numi beam line. Total beam power is expected to increase from 300 to 400kW with repetition rate of 2.2sec. The intensity for the pbar target will stay at 8.0 - 9.0E12 ppp and that for the Numi will be increased to 36.0E12 ppp. The total beam loss has to be less than 5%.

Multi batch slip stacking and Status of studies

Multi batch slip stacking uses two different frequencies as shown in Figure 6. The multi batch slip stacking scheme was already verified in the mountain range plots of the whole process was shown in Figure 7. Beams were sent to the pbar and NuMI targets with intensity of 8.2E12 (Pbar) and 30E12 (Numi) with an efficiency of 95.5%. A record intensity of 4.6E13 ppp was accelerated to 120 GeV as shown in Figure 8.

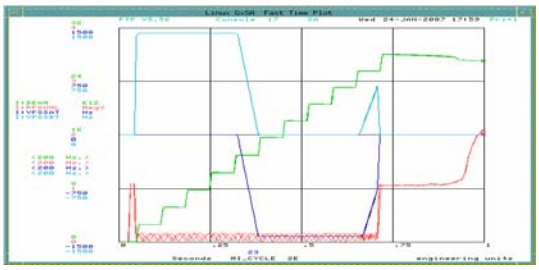

Figure 6: Higher rf frequency (cyan), lower rf frequency (blue), total beam intensity (green) and total rf voltage (red) on multi batch slip stacking.

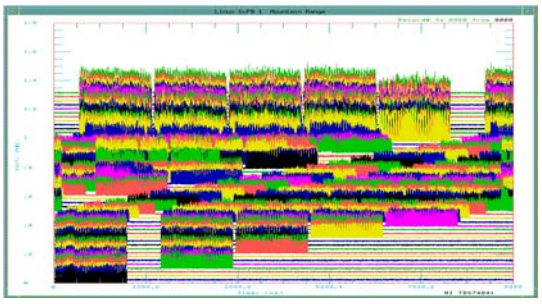

Figure 7: Mountain range plots with wall current monitor signals at 8GeV of multi batch slip stacking. The horizontal scale is 10μsec.

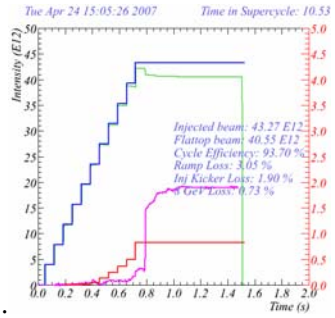

Figure 8: Total intensity injected from Booster (blue) and total intensity in the MI (green).

BEAM LOSSES IN MULTI BATCH SLIP STACKING

Beam losses in the multi batch slip stacking were studied by measurements and simulations. [5] Four different categories of beam losses were identified:

- Injection kicker gap loss.
- Loss at beginning of acceleration.
- Extraction kicker gap loss.

- 8 GeV life time loss.

The first three losses were created by longitudinal motion. Longitudinal particle simulations were carried out with rf parameters. The last one was created by transverse effects and has not been simulated yet.

Emittance measurements at different intensities

The longitudinal emittance was measured by using phase space tomography of wall current monitor signals at injection. The tomography pictures for three different intensities from Booster are shown in Figure 9. At the highest intensity of 4.3e12 ppp the phase space distribution is varying from pulse to pulse as shown in Figure 10. The distributions of energy and phase were fit to Gaussian, and two sigma were listed in Table2.

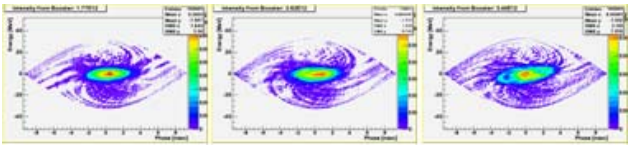

Figure 9: Tomography with intensity of 1.77(left), 2.65(middle) and 3.44 e12 ppp(right).

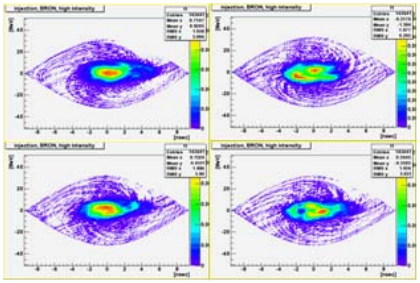

Figure 10: Tomography with intensity of 4.23E12 ppp for four different pulses.

Table 2: Measured beam size at different intensities

intensity	Energy spread	Bunch length
1.77e12 ppp	+/-6.88MeV	+/-2.94nsec
2.65e12 ppp	+/-7.62MeV	+/-3.36nsec
3.44e12 ppp	+/-8.99MeV	+/-3.56nsec
4.23e12 ppp	+/-9.37MeV	+/-3.58nsec

Measurement and Simulation results for the beam loss

The longitudinal particle simulation was curried out in order to estimate injection kicker gap loss and acceleration ramp loss with the emittances listed in the table2. The Figure 11 shows the results of measurements and simulations as a function of intensity. The simulation results are following those of measurements. The measurements at 4.23 ppp were changing from pulse to pulse because of the emittance at injection as shown in Figure 11. Figure 12 shows simulation of extraction kicker gap losses on the left and right side of the batch going to the pbar target. The losses on the right side are higher than the left, which agrees with what was measured by the WCM signal at the MI extraction. The three losses depend on the beam size at injection.

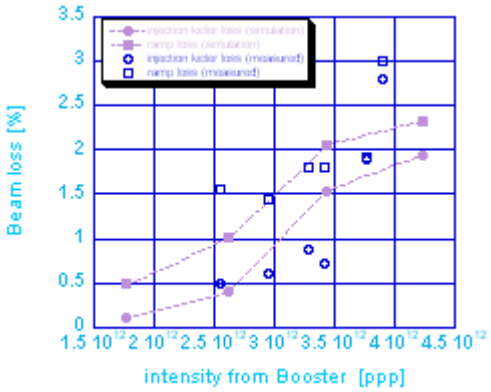

Figure 11: Simulation (blue) and Measurement (purple) results on injection kicker gap loss and loss(circle) at the beginning of acceleration(square).

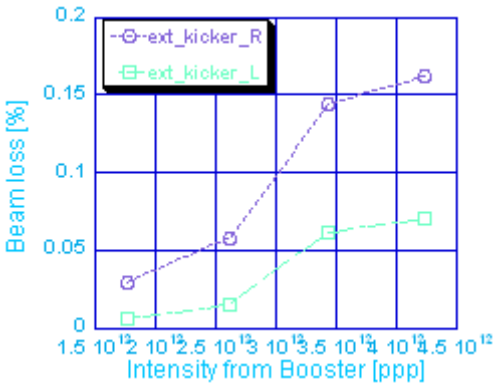

Figure 12: Simulation results on extraction kicker gap loss in the left (purple) and right (cyan) side of the pbar batch.

SUMMARY

Slip stacking is in operation for pbar stacking since December 2004. Multi batch slip stacking scheme has been verified and sent beam to the pbar and NuMI targets. Beam loss issues have been studies with measurements and simulations. The results shows to require small emittance beam at injection to lower beam loss.

REFERENCES

[1] I. Kourbanis, "Present and future high energy accelerator for Neutrino experiment", Particle Accelerator Conference (PAC 07), Albuquerque, New Mexico, Jun 2007.

[2] J. Dey, et al, "53 MHz Beam Loading Compensation for Slip Stacking in the Fermilab Main Injector", PAC05, Knoxville, May 2005.

[3] K. Koba, "Slip Stacking at Low Intensity – Status of the Beam Studies", MI-0294

[4] K. Seiya, et al, "Progress in Slip stacking and barrier bucket", HB2006 ICFA Workshop, Japan, June 2006.

[5] K. Seiya et al,, "Multi-batch slip stacking in the Main Injector at Fermilab", PAC 07, Albuquerque, New Mexico, Jun 2007.

CERN-GSI Meeting on Collective Effects

BEAM LOSSES IN THE PS DURING CT EXTRACTION

S. Gilardoni[@], J. Barranco[#], CERN, Geneva, Switzerland.

Abstract

The proton beams used for the fixed target physics at the SPS are extracted from the PS at 14 GeV/c in five turns, using a technique called Continuous Transfer (CT). During this extraction, large losses are observed in straight sections were the machine aperture should be large enough to accommodate the circulating beam without any loss. These losses are due to particles scattered by the electrostatic septum used to slice the beam and defocused by a quadrupole used during the extraction. Simulations and experimental results are presented.

INTRODUCTION

The proton beams used for the fixed target physics at the SPS (Super Proton Synchrotron) are extracted from the PS (Proton Synchrotron) at 14 GeV/c in five turns using a technique called Continuous Transfer (CT)[1]. During this extraction, large losses are observed in straight sections were the machine aperture should be large enough to accommodate the circulating beam without any loss. These losses are due to particles scattered by the electrostatic septum used to slice the beam and defocused by a quadrupole used during the extraction. These losses limit the maximum intensity deliverable to the SPS for fixed target physics, like for the CERN to Gran Sasso (CNGS) neutrino program, because of the large irradiation of the site outside the PS tunnel and at the CERN fence.

Simulation and experimental results are presented as update of the study of [2].

CONTINUOUS TRANSFER: CT EXTRACTION

During the CT extraction, the horizontal tune of the PS is set to 6.25, namely to obtain a phase advance per turn of 90°. In such conditions, a part of the proton beam is pushed by a slow and a fast bumps beyond the blade of an electrostatic septum. The sliced beam that receives the kick of the electrostatic septum is extracted during the current machine turn, while the rest is extracted with the same mechanism within the next 4 turns. The different bumps are set in such a way that the five beam slices feature the same intensity.

Among the different elements of the PS, which is composed by 100 combined-function magnets arranged in a FDODF lattice and interleaved by 100 straight sections (SS, numbered from SS00 to SS99), the ones used for the CT extraction are (see Fig. 1):

- Slow bump (BSW31) around the electrostatic septum, created by two magnets in SS27 and SS35, and used together with the two fast kickers (BFA9 and BFA21) to push the beam beyond the electrostatic septum.
- The electrostatic septum (SEH31) used to impart an extra kick to the beam slice for the extraction.
- The slow bump (BSW16 composed of four magnets in SS12, SS14, SS20 and SS22 respectively) used to direct the beam, together with the magnetic septum (SMH16), in the transfer line towards the SPS.
- Two quadrupoles located in SS25 and SS05, which form the QKE16, used to distort the optics of the machine between them hence having a large horizontal beta at the septum SEH31 and practically zero dispersion, as shown in Fig. 2.

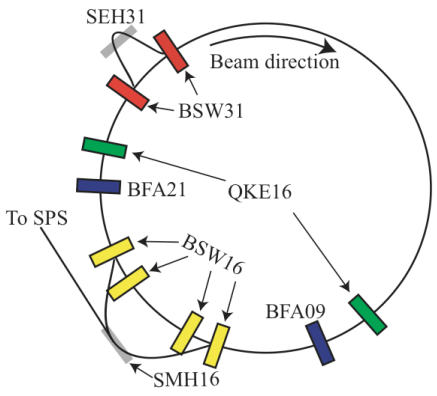

Figure 1: Scheme of different elements used during the CT extraction.

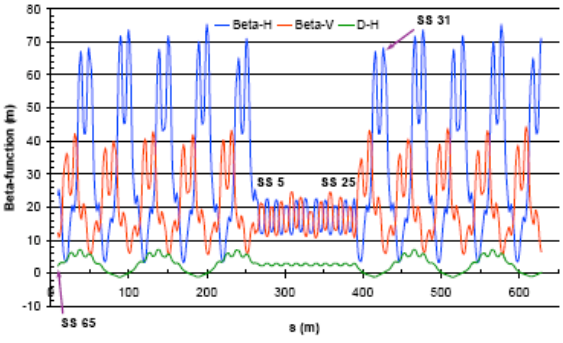

Figure 2: PS optics perturbed by the QKE16 during the CT extraction [11].

During the slicing/extraction process losses are observed, as expected, downstream of SS31 and in the extraction region around the SS16, as shown in Fig. 3. However, losses are present also in non-expected SS, like in the injection region, from SS39 to SS46, and

[@] Simone.Gilardoni@cern.ch
[#] PhD student at Universitat Politècnica de Catalunya, Barcelona, Spain

under the so called the PS-Bridge, between SS05 and SS10.

The machine shielding around the mentioned sections is not sufficient, causing large irradiation outside the PS tunnel, and hence limiting the maximum intensity deliverable to the SPS.

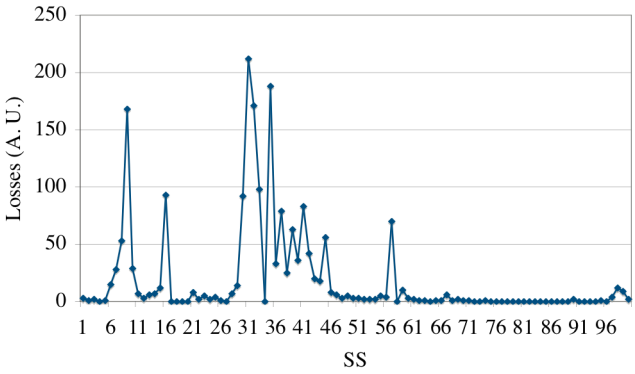

Figure 3: Beam loss pattern as recorded by the ACEM detectors for a moderate intensity CNGS beam.

The beam loss monitor system

The beam loss monitor (BLM) system is composed by 100 ACEM detectors (Aluminium Cathode Electron Multiplier [3]) mounted on top of the main magnets. Due to the position chosen in the past (the system dates back to the middle '80s) and the large variation of the signal with the primary proton energy, it is practically impossible to correlate the amount of protons lost in the machine with the signal recorded by the BLMs. Most of the losses in the PS are in the horizontal plane, whereas the BLMs are mounted on top of the bulky iron yoke of the main magnets (see Fig. 4), just after each SS. Since some straight sections are composed by a simple beam pipe, while some others are completely filled by magnetic elements, particles lost in different SS will create a very different secondary shower reaching the loss detectors.

To complicate even more the picture, the BLMs are installed on different sides of the main magnets, in some sections facing the inside of the ring, sometimes the outside, following the quasi-regular pattern of the four magnet types which compose the PS lattice. For these reasons, the BLM system is used during operation to detect malfunctioning of the machine, more than as a real protection system, obtained by comparing online a given loss pattern with the reference one.

The pattern of the losses observed with the system can tell something about the region where the losses occurs, whereas it is not possible for example to deduce the ratio of beam lost between two different sections of the machine. It is not even possible to deduce if the loss is produced in one of the main magnets or in the straight sections, being the BLM mounted at the entrance of the magnet unit.

Figure 4: PS main magnet units. The ACEM BLM detectors are the orange cylinders mounted on top of the magnets.

The aim of the simulations presented in the following is to reproduce qualitatively the observed loss pattern but not to quantify the beam loss detected by the BLMs. This would require a detailed simulation of the secondary shower developing in a large fraction of the main magnets, and goes beyond the purpose of this study.

Loss mechanism: principle and simulations

During the pulsing of the extraction elements, losses are identified in SS05-SS10 during the rise of the BSW31, before actually the beam is sent completely beyond the SEH31 to be sliced. This would indicate that the particles lost are the results of the interaction of the circulating beam with the about 150 μm thick, 1.8 m long Molybdenum septum blade. The multiple scattering introduced by the blade material results in an extra angular kick to the particles, which then follow a large amplitude orbit, so large that when they arrive at the location of the quadrupole in SS05 they are basically extracted.

Two simulations have been developed to understand this loss mechanism. The goal of the simulations is to reproduce qualitatively the observed loss pattern, but also to prove that the simulations are precise enough to predict a possible alleviation of the problem. The goal is also to prove that these tools could be used in the future for the study of losses in low energy synchrotrons like the PS2 [4].

Two methods have been implemented:

- The interaction of the circulating beam with the septum blade is simulated by the MARS[5] Monte Carlo code. The scattered particles are then tracked in the PS lattice and a simplified aperture model using MAD8[6]. This simulation does not take into account the fast bumps and consider only one turn.
- The interaction with the septum blade is modelled using K2[7] and the tracking is performed by SIXTRACK[8,9]; K2 is a Monte Carlo interaction module developed for the LHC collimation studies, hence the physics has been adapted for the PS energies. A bunch of particles is tracked through a thin lens lattice (generated by MADX[10]), undergo scattering processes in the septum blade (K2) and, finally loss locations are determined by means of an external program and the detailed aperture model. Some approximation introduced by the thin-lens model had to be corrected: the high order terms of edge effects in fact are not symplectic in thin lens. Thin multipoles were included and tune and chromaticity matching were performed to take into account correctly the end-field effects of the main magnets. This simulation tracks particles on the five extraction turns, considering also the fast bumps.

Simulation Results

Fig. 5 and Fig. 6 present the results for the two simulations. The patterns of the losses versus the SS are qualitatively very similar, even though the two

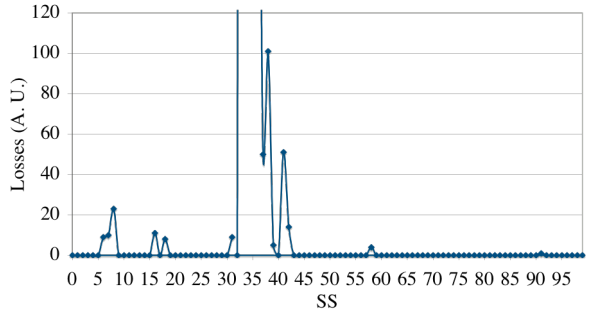

Figure 5: Simulated losses with simplified method versus SS. The vertical scale represents the number of proton lost per section non-normalised by the number of primary protons.

simulations do not have the same normalisation. An eventual discrepancy in the simulated pick ratio with respect to the BLM data is not surprising.

As described in the previous section, the BLM system is not meant to provide precise data about the amount of proton lost, whereas the results of the simulation is a pure counting of protons which hit the machine aperture.

Other discrepancies might be due to the fact that in reality the scattered particles might re-interact with other aperture restrictions in the machine and being furthermore deviated, whereas in the simulation those supplementary restrictions are considered as pure absorbing surfaces. Moreover, the simulations do not take into account the propagation of the secondary particle shower, which might displace the maximum of the losses by one or two SS.

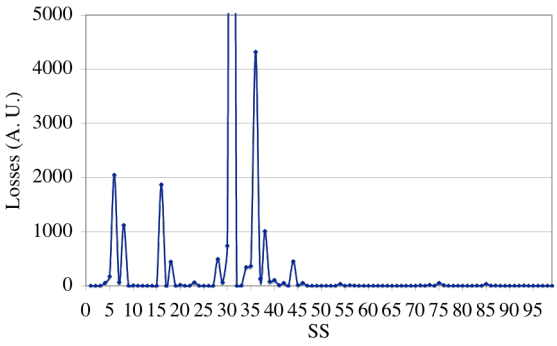

Figure 6: Simulated losses with more refined method versus SS. The vertical scale represents the number of proton lost per section non-normalised by the number of primary protons.

Considering all of this, the simulation is precise for prediction of the losses within ±1 SS with respect to what the BLMs will detect.

LOSSES DISPLACEMENT

Since it has been shown that the two simulations confirm the loss mechanisms, it is impossible to avoid these kind of losses without changing completely the extraction scheme, like it is foreseen in the future Multi Turn Extraction (MTE, see [11]). The only viable solution is to displace the losses in a better-shielded part of the machine, where the tunnel radiation shield thickness is enough. This can be done, as shown by

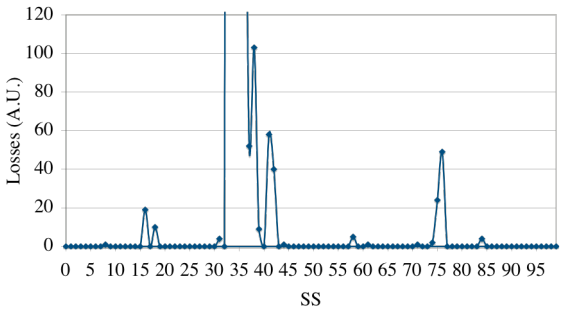

Figure 7: Simulated losses with the simplified method with the losses displaced thanks to the new quadrupole.

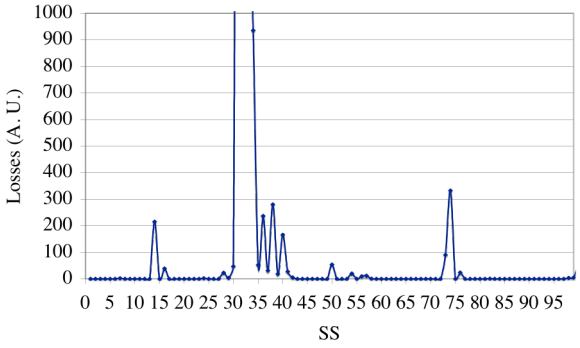

Figure 8: Simulated losses with more refined method with the losses displaced thanks to the new quadrupole.

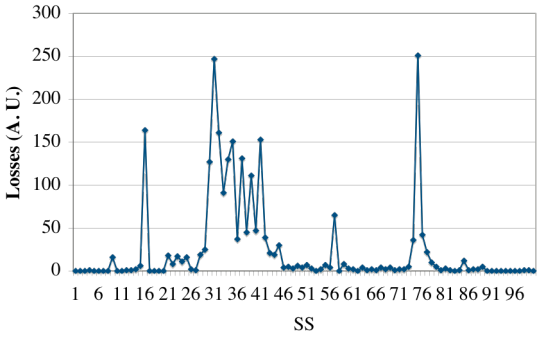

Figure 9: Measured losses displaced thanks to the new quadrupole.

simulations (see Fig. 7 and Fig. 8), by installing a new quadrupole in SS73, 4π in phase advance before the quadrupole in SS05. The new extraction scheme would be then unchanged, apart that instead of powering the QKE16, one should power the quadrupole in SS25 and the one in SS73. This should remove completely the losses in SS05-SS10 and bring them in SS73-SS78. During the shutdown 2006-2007 a set of new quadrupoles has been installed, in such a way that four quadrupoles could be available for the extraction. Tests powering the quadrupoles in SS25 and SS73 confirmed the simulation prediction.

As shown in Fig. 9, in fact, the losses appear to be displaced in the predicted sections, without changing the extraction efficiency. Actually, this new extraction configuration has been retained for the 2007 run, in particular during the high intensity operation with 2200e10 proton per pulse extracted for the CNGS and the SFTPRO (Fixed Target Physics at the SPS) beams, and it will be used for the 2008 run.

A further optimisation has been done by powering the four available quadrupoles at the same time, the group SS25-SS73 at full current while the group SS25-SS05 at one third of the nominal one. This, as predicted by simulations, results in the sharing of the losses between SS05-SS10 and SS73-SS78, as shown by the small peak appearing in SS09 in Fig. 9. Moreover, it has been experimentally observed that the extraction efficiency improved, thanks probably to a large beam envelope at the septum location.

CONCLUSIONS

Losses during CT extraction from the PS are generated by the beam interaction with the electrostatic septum used to slice the beam in 5 turns. These losses cannot be avoided but only displaced in sections of the machine further away from the CERN fence and where the tunnel radiation shielding is more effective.

Simulations and experiments confirm the mechanism of losses and the loss pattern observed. The proposed scheme to displace the losses, once implemented, showed to be well in agreement with the simulations, with the losses moved in the predicted locations.

New simulation tools developed using SIXTRACK and K2 adapted to low energy synchrotrons plus the proper aperture model show to be suitable for the study of the mentioned losses.

ACKNOWLEDGMENTS

The authors are thankful: to the PS operation team for the support during the experimental measurements, to G. Arduini, M. Giovannozzi, B. Jeanneret and Y. Papaphilippou for the fruitful discussion, to O. Berrig for providing the detailed aperture model of the PS, to R. Brown, S. Baird, the AB/PO and AB/CO CERN groups for implementing the new quadrupole configuration.

REFERENCES

[1] C. Bovet et al., "The fast shaving ejection for beam transfer from the CPS to the CERN 300 GeV machine", PAC1973, edited by D. W. Dupen (IEEE, New York, 1973).

[2] J. Barranco et al., "Beam loss map simulations and measurements in the CERN PS", PAC07

[3] V. Agoritsas et al., "A microprocessor-based system for continuous monitoring of radiation levels around the CERN PS and PSB accelerators", NIMA 247 (1986), 44-49

[4] W. Baartmann et al, "Optics considerations for the PS2", PAC07, Albuquerque, USA

[5] N.V. Mokhov, Fermilab-FN-628 (1995). O.E. Krivosheev, N.V. Mokhov, Fermilab-Conf-00/181 (2000). N.V. Mokhov, Fermilab-Conf-03/053 (2003). N.V. Mokhov, K.K. Gudima, C.C. James et al.,Fermilab-Conf-04/053(2004). http://www-ap.fnal.gov/MARS/

[6] http://mad.web.cern.ch/mad/mad8web/mad8.html

[7] T. Trenkler, J.B. Jeanneret, "K2: A Software Package evaluating Collimation Systems in

Circular Colliders (Manual)", SL/Note 94-105 (AP)
[8] F. Schmidt, "SixTrack. User's Reference Manual", CERN/SL/94-56(AP)
[9] G. Robert-Demolaize et al., "A New Version of Sixtrack with Collimation and Aperture Interface", CERN-AB-2005-033
[10] H. Grote, F. Schmidt, 2003 PAC Conference. MADX webpage http://mad.home.cern.ch
[11] Giovannozzi, Massimo (ed.) et al. , "The CERN PS multi-turn extraction based on beam splitting in stable islands of transverse phase space : Design Report", CERN-2006-01

ION AND PROTON LOSS PATTERNS AT THE SPS AND LHC

R. Bruce, R. Assmann, G. Bellodi, C. Bracco, H.H. Braun, S. Gilardoni,
J.M. Jowett, S. Redaelli, T. Weiler, CERN, Geneva, Switzerland

Abstract

The collimation system of the LHC, primarily designed for proton operation, must function safely also with $^{208}\mathrm{Pb}^{82+}$ions. However, the particle-matter interaction in a collimator is different for heavy ions and protons. Heavy ions are subject to nuclear fragmentation, which creates a spectrum of secondary particles exiting the collimators with a Z/A ratio different from the nominal beam. These particles could be lost in a superconducting magnet and the induced heating might cause a quench. The program ICOSIM has previously been used to simulate these losses in the LHC. In this article, we present a benchmark of ICOSIM, using measured proton and ion loss maps in the SPS, and find a good qualitative agreement. We also make a quantitative comparison where the showers of the lost particles are simulated with the FLUKA code in the full magnet geometry. Here a discrepancy of a factor 3.8 is found. Estimation of expected uncertainties continues.

INTRODUCTION

The LHC requires a very efficient collimation system, since the beams have higher intensities than ever before and at the same time the superconducting magnets are very sensitive to heating and might thus quench due to lost beam particles. This is achieved with a two-stage collimation system [1, 2]: Short primary collimators intercept halo particles and give them an angular kick caused by multiple scattering, so that they, possibly several turns later, are intercepted by the longer secondary collimators where they deposit their energy through a hadronic shower. Both primary and secondary collimators are made of graphite because of its low stopping power and good heat transfer characteristics. This system has been primarily designed to meet the tight requirements for proton operation.

However, the LHC will also collide $^{208}\mathrm{Pb}^{82+}$ion beams during approximately one month per year, and necessary precautions have to be made for heavy ion operation in order to make sure that beam losses are within acceptable limits. The main parameters of the $^{208}\mathrm{Pb}^{82+}$and proton beams are summarized in Tab. 1. Although the stored energy in the $^{208}\mathrm{Pb}^{82+}$beam is only 3.81 MJ, compared to the 350 MJ in the proton beam, the ion collimation efficiency is much lower [3]. This is caused by the different particle-matter interaction in the collimator jaws. The nuclear interaction length is 2.2 cm for 2.76 TeV/nucleon $^{208}\mathrm{Pb}^{82+}$ions in graphite as opposed to 38.1 cm for 7 TeV protons, although multiple scattering angles are very similar. The nuclear interactions, together with electromagnetic dissociation, split up the nucleus into smaller fragments. This means that the ions have a high probability of fragmenting in the primary collimator before they have obtained the necessary angular deviation to be intercepted by the secondary jaws.

Table 1: LHC beam parameters for $^{208}\mathrm{Pb}^{82+}$and p^{+} operation (nominal collision).

	$^{208}\mathrm{Pb}^{82+}$ions	Protons
Energy per nucleon	2.76 TeV	7 TeV
Number of bunches	592	2808
Particles per bunch	7×10^7	1.15×10^{11}
Bunch spacing	100 ns	25 ns
Peak luminosity	10^{27} cm^{-2} s^{-1}	10^{34} cm^{-2} s^{-1}
Stored beam energy	3.81 MJ	350 MJ

The fragmented ions leaving the primary collimator have different Z/A ratios, and thus different magnetic rigidities equivalent to a fractional momentum deviation of

$$\delta = \frac{AZ_0}{A_0 Z} - 1 \tag{1}$$

with A_0 and Z_0 being the mass and charge numbers of the nominal beam. Therefore, these ions follow the locally generated dispersion function d_x from the primary collimator and are lost where the horizontal aperture A_x satisfies

$$A_x = \delta d_x. \tag{2}$$

This is likely to happen outside the warm regions of the LHC, where the dispersion has grown sufficiently large. It is therefore vital to have a good quantitative understanding of these processes, in order to ensure safe operation of the LHC uninterrupted by magnet quenches.

THE ICOSIM CODE

In order to simulate the particle propagation through the LHC lattice, linked with particle-matter interactions in the collimators, a specialized code, ICOSIM [3], has been developed. ICOSIM creates an initial beam distribution that is tracked through a lattice read in from optics files and aperture tables created by MAD-X [4]. Particles are tracked using a linear matrix formalism but chromatic effects at leading order and sextupoles in thin kick approximation are also included. Beam acceleration is not taken into account, since the RF synchrotron oscillation period is about 500 turns at collision.

ICOSIM has a simple built-in Monte-Carlo code for simulating the interactions in the collimator, including

multiple scattering (described by a Gaussian approximation, see Chap. 23 in Ref. [5]), ionization through the Bethe-Bloch formula, nuclear fragmentation and electromagnetic dissociation. The last two processes are simulated through tabulated cross sections calculated with the abrasion-ablation [6] and RELDIS [7] models.

We have also implemented the possibility of treating the collimator interactions in an external Monte-Carlo code, which performs the transport through the collimator geometry and gives residual particles back to the tracking. Both FLUKA [8, 9] and MARS [10] have been used with similar results. These codes include more complete physics but slow down the tracking considerably. Linking with an external Monte-Carlo program is necessary when simulating proton interactions, since the built-in physics models of ICOSIM only handle ions.

RESULTS FOR THE LHC

The simulated LHC ion loss maps from ICOSIM have been presented elsewhere [3, 11, 12]. Here we will give a short summary.

An example of the loss pattern at top energy found downstream of IR7 (betatron cleaning region) is shown in Fig. 1. This simulation was done using standard settings (primary collimators at 6 σ, secondary at 7 σ and tertiary at 10 σ). Also the TCLA absorbers were included.

ICOSIM first calculates only relative magnitudes of the losses at different positions in the machine. To find the expected heating power this loss map is normalized by the beam intensity (as given in Tab. 1) and the beam life time, which is of course not well known. As a worst-case estimate the minimum allowed life time of 12 minutes was used.

It is clear that the expected heating power from beam losses well exceeds 8.5 W/m, which is an estimate of the average quench limit according to Ref. [13]. However, the quench limit depends also on factors such as magnet type and distribution of the beam losses within a given magnet and is thus not well known. There are ongoing studies on this in the AT department at CERN.

At top energy, a collimation inefficiency of 4-5% was found (defined as ratio of the number of particles lost on the aperture over the number stopped in the collimators at a particular turn of the machine), which is several orders of magnitude higher than the required value for the proton beam [14]. Similar results were found for beam 1 and 2. At injection energy the heating power is lower by a factor 20-50 which, together with the fact that the quench limit is higher, should mean that these beam losses are within acceptable limits.

Apart from the already mentioned uncertainty in the quench limit, and the uncertainty in the assumed beam lifetime, there are other factors which might introduce errors in the final result. The nuclear cross sections for ion-matter interaction in the collimators might have up to 50% error margins, and there is also an uncertainty in the impact distribution of the beam particles on the collimators, since the beam dynamics of the halo is not well known.

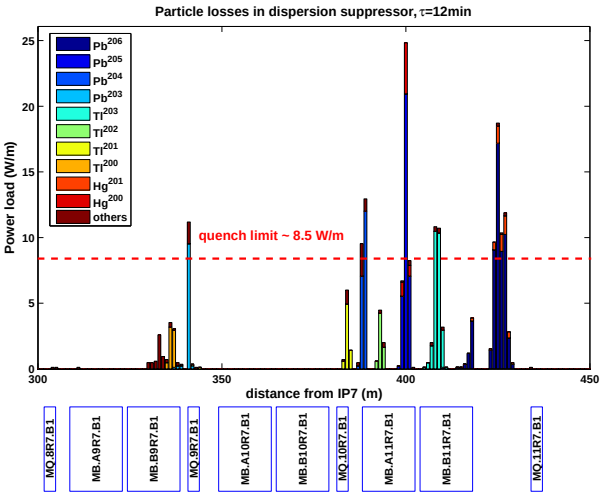

Figure 1: (color online) The loss map form ICOSIM for the dispersion suppressor after IP7 in the LHC. The estimated quench level from Ref. [13] is indicated.

Because of these uncertainties in the ICOSIM result, a benchmark of the code is needed; we describe this in the following sections.

PROTON BENCHMARK IN THE SPS

At CERN, the two possible ways of testing the ICOSIM results are with proton or $^{208}\mathrm{Pb}^{82+}$ion beams in the SPS, using a prototype secondary LHC collimator, which has been installed in LSS5 [15]. The aperture and the lattice within the vicinity of the installation are shown in Fig. 2. The collimator consists of two graphite jaws, which can be moved independently to collimate the beam in the horizontal plane. This was done during circulating beam operation, and the induced beam losses were recorded by the 216 beam loss monitors (BLMs) placed around the ring.

In this section we describe the results of the measurements with proton beams, and in the next section we describe corresponding measurements with ions. Data were collected during proton operation in dedicated MD sessions in 2006 and 2007 with 270 GeV coasting beam. Typical collimator steps ranged from a few hundred micrometers up to a mm, although some larger steps up to a cm were performed.

A typical example of a recorded loss map from September 2007 is shown in Fig. 3, together with the corresponding simulated loss map from ICOSIM linked with MARS. The detector background, consisting of noise and other beam losses that are not caused by the collimator movement, had to be subtracted. As background we used the loss map from the machine cycle before the collimator movement. A similar approach was already used in Ref. [15] to benchmark simulation results from the SixTrack code.

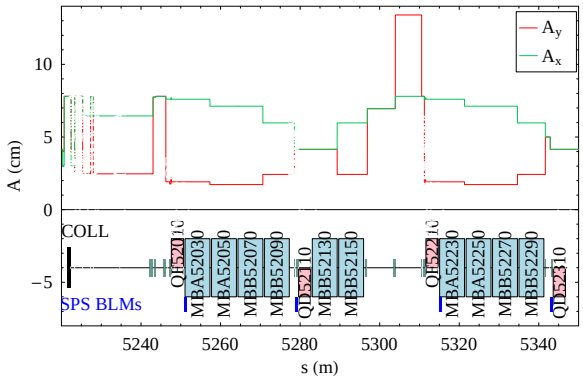

Figure 2: (color online) The aperture and beamline of the SPS just downstream of the LHC prototype collimator. Also the locations of the BLMs are indicated.

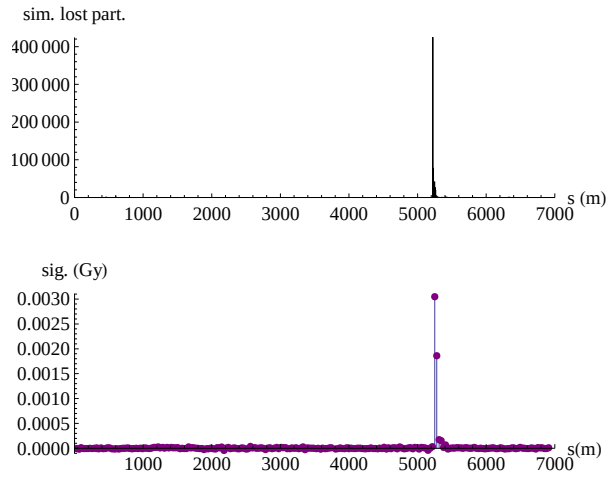

Figure 3: Simulated ICOSIM (top) and measured (bottom) proton loss map for the whole SPS ring. The collimator is located at $s = 5222$ m, just before the large loss peak.

As might be expected, the main loss location is just downstream of the collimator, which is very well reproduced by the simulation. In order to make a quantitative comparison with data, we need to consider the actual magnitude of the BLM signals. This can not be directly inferred from the ICOSIM loss maps, although we can make a rough estimate by simply counting the number of protons lost close to each BLM. In Fig. 4 the normalized average measured signal of the four closest BLMs after the collimator is shown, together with the number of particles impacting within a 2 m interval before each chamber. As can be seen, the simulated ratio between the two highest locations agrees very well with measurements.

It was found in the measurements that the ratio between these four signals was almost independent of the collimator movement—when a larger fraction of the beam is scraped away, the losses increase correspondingly, keeping this ratio. This is shown for the BLM with the highest signal (BL520 at $s = 5250$ m) in Fig. 5. Here we show the BLM signal as a function of the decay in beam current for several different collimator movements. It can be seen from the figure that this is an approximately linear function, except when the BLM begins to saturate. This motivates why we can use the average ratio in Fig. 4.

In a general case this linear assumption might be false—a simple example of this is changing the angles of the collimator jaws and thereby the effective length travelled by the particles inside the collimator. This changes the ratio of particles lost in the collimator and the ring. In the measurements considered here however, the jaws were approximately centered around the beam. The linear behaviour is also confirmed by ICOSIM simulations, which show that the relative loss pattern stays approximately constant regardless of the distance to which the jaws are moved in.

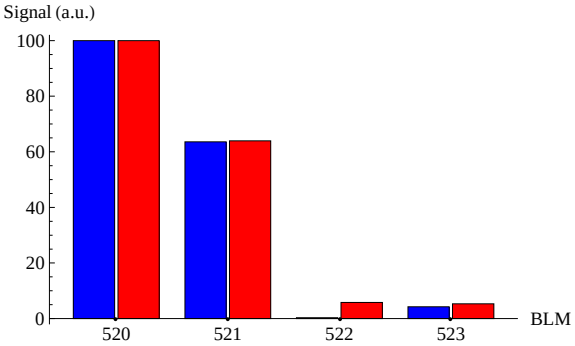

Figure 4: (color online) Average measured loss map with background subtracted over several cycles (light gray, red online) and simulated number of protons lost within a 2 m interval before each BLM (dark gray, blue online) normalized to the highest peak for the four BLMs closest to the collimator downstream.

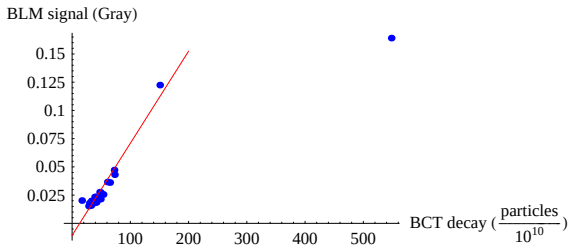

Figure 5: The highest BLM signal, from monitor BL520, as a function of the measured decay in beam current during several different collimator movements. Except for the last point to the right, where the BLM is likely to be saturated, the behaviour is approximately linear. A straight line has been plotted to guide the eye.

The smaller loss peaks in other parts of the ring were fluctuating in a seemingly random pattern between different measurements. This could be for instance due to orbit variations. In some of the measured loss maps, the second largest peak was found at $s \approx 600$ m, corresponding to the

second largest peak also in the simulation. An example of a measured and a simulated loss map for this part of the machine is shown in Fig. 6. There is also a simulated loss at $s \approx 460$ m, which could not be measured. However, the next BLM after this loss location is 15 m downstream, meaning that it might not detect these losses.

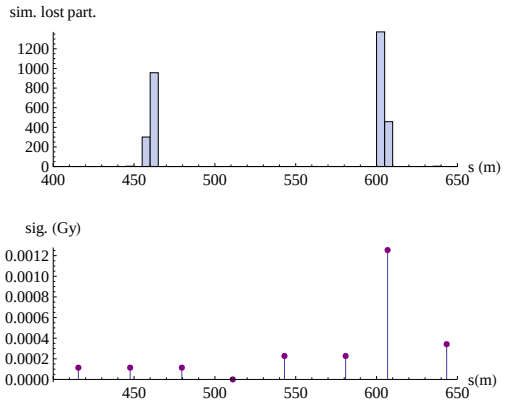

Figure 6: Simulated ICOSIM (top) and measured (bottom) proton loss map for the first part of the SPS ring.

Furthermore, smaller loss peaks were sometimes detected at $s \approx 5920$ m and 1660 m, which were not reproduced by simulations, and at $s \approx 5410$ m, which was well reproduced. A small loss peak was predicted but not measured at $s \approx 6340$ m. However, in the earlier measurements in Ref. [15], losses were detected also in this area. Generally, the loss map from ICOSIM shows a qualitatively similar behaviour to the SixTrack simulations presented in Ref. [15].

The BLM signals depend not only on the number of particles lost nearby, but also on the impact distribution of the lost particles and the amount and type of material they have to traverse before reaching the monitor. At some BLMs, with less nearby material, particles lost far away may cause a signal, while BLMs that are well shielded by magnetic elements may only see small traces of the showers caused by the closest losses. In order to accurately simulate this, the particle-matter interaction of the lost particles need to be taken into account. Thus the 3D geometry of the magnetic elements around the monitor BL520 (closest to the collimator, 30 m downstream of it) was implemented in FLUKA, as illustrated in Fig. 7. The magnetic field in the quadrupole magnet was neglected. The momenta and impact coordinates on the inside of the vacuum pipe of all particles within 10 m distance of the collimator were recorded in ICOSIM and fed as starting conditions into FLUKA and the resulting energy deposition in the N_2 gas was recorded and converted to dose in Gy. It was found from the simulations that the signal on the monitor BL520 is 0.15 mGy per 10^{10} lost particles. Comparing with measurements, the average ratio between signal and BCT current decay was found to be 0.57 mGy per 10^{10} lost particles, which is a factor 3.8 higher than simulations. This error could be due to several factors. Apart from the systematic uncertainty in the shower simulation, and the uncertainty in the distribution of the impacting lost particles, the measurements themselves showed variations between different MDs. A detailed error estimate is ongoing work.

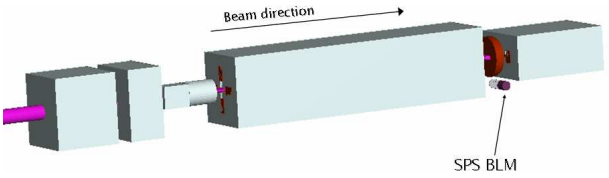

Figure 7: (color online) The geometry as implemented in FLUKA around the monitor BL520, which is located around 30 m downstream of the collimator in the SPS.

ION BENCHMARK IN THE SPS

Measurements similar to the ones described above were also carried out using coasting $^{208}\mathrm{Pb}^{82+}$ion beams at 106.4 GeV/nucleon in the SPS in late 2007. The beam was again scraped by the collimator to induce losses in typical steps between 200 μm up to a mm. From ICOSIM loss maps, it was found that the protons are lost mainly due to angular deviations induced by the collimator, while the ions are lost due to the change in magnetic rigidity, δ, caused by fragmentation. Ions that have changed their magnetic rigidity are deterministically lost where the locally generated dispersion from the collimator and the aperture satisfy Eq. 2. This is shown in Fig. 8, where several dispersive horizontal orbits starting at the collimator are shown, for typical values of δ. It is clear from the figure that all fragments within the range $-0.09 < \delta < -0.14$ are lost at the same aperture limitation ($s = 5277$ m).

This corresponds to a large fraction of the lost fragments, and since the monitor BL521 is located only 2 m downstream of this position with almost no shielding material in between, this monitor is expected to show a high signal when ion beams are scraped with the collimator. The simulated and measured loss maps show that this is indeed the case. As can be seen in Fig. 9, showing the loss pattern for the whole ring, and Fig. 10, showing the four BLMs closest downstream of the collimator, BL521 has a signal much higher than BL520, which is closest to the collimator and where the maximum was found for protons. This is a significant qualitative difference between ion and proton operation, which is found both in simulations and measurements.

In order to verify the loss pattern quantitatively, FLUKA simulations of the particle showers should be done also for ions. We intend to do this in the future.

CONCLUSION AND OUTLOOK

We have presented preliminary results of simulated and measured beam losses in the SPS for protons and

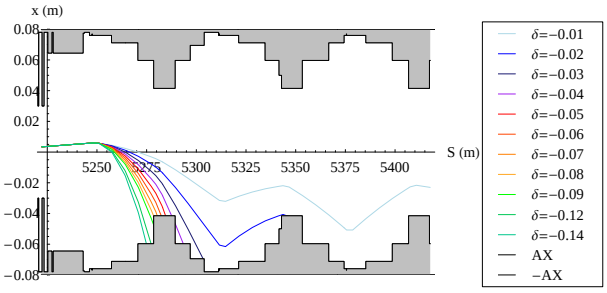

Figure 8: (color online) Dispersive orbits of fragmented ions coming out of one of the collimator jaws, shown together with the aperture. A large fraction of the total losses occur at the aperture limitation at $s = 5277$ m.

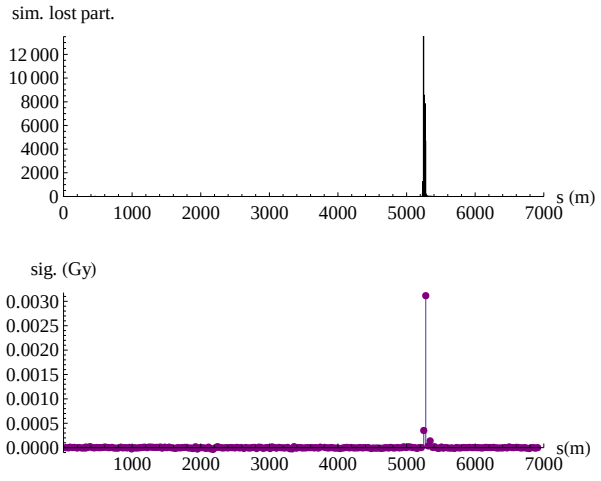

Figure 9: Simulated ICOSIM (top) and measured (bottom) $^{208}\mathrm{Pb}^{82+}$ loss map for the whole SPS ring.

$^{208}\mathrm{Pb}^{82+}$ ions caused by movements of the collimator. In terms of comparing the ratio between different loss locations, the simulated loss patterns from ICOSIM agree well with the measured ones. However, the FLUKA simulation of the signal from proton losses in the detector with the highest signal deviated by a factor 3.8 from the measured signal. A detailed error analysis is ongoing.

We found a significant difference between the loss patterns for $^{208}\mathrm{Pb}^{82+}$ ions and protons, with the maximum signal occurring at different locations, which is well understood and reproduced by ICOSIM. This is a valuable benchmark of the ICOSIM simulations carried out for the LHC.

In order to better quantify the comparison, further FLUKA simulations of the expected BLM signal for ions should be carried out. Also other monitors than BL520 should be simulated for both particle species to make a more complete analysis. This work is planned for the future.

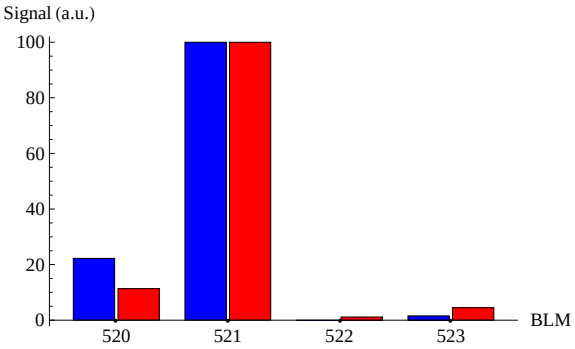

Figure 10: (color online) Average measured loss map with background subtracted over several cycles (light gray, red online) and simulated number of nucleons (number of ions$\times A_{\mathrm{ion}}$) lost within a 2 m interval before each BLM (dark gray, blue online) normalized to the highest peak for the four BLMs closest to the collimator downstream.

ACKNOWLEDGEMENTS

We would like to thank the BLM team (B. Dehning, E.B. Holzer, D. Kramer, M. Stockner, C. Zamantzas et al) and the machine operators of the SPS for indispensable help with carrying out the measurements, and D. Mangluki and G. Arduini for setting up the ion beam in the SPS.

REFERENCES

[1] J. B. Jeanneret. Optics of a two-stage collimation system. *Phys. Rev. ST Accel. Beams*, 1(8):081001, 1998.

[2] R. Assmann et al. An improved collimation system for the LHC. *Proc. of the European Particle Accelerator Conf. 2004, Lucerne, Switzerland*, page 536, 2004.

[3] H.H. Braun. Collimation of Heavy Ion Beams in the LHC. *Proc. of the European Particle Accelerator Conf. 2004, Lucerne, Switzerland*, page 551, 2004.

[4] `http://cern.ch/mad/`.

[5] S. Eidelman *et al*. Review of Particle Physics. *Physics Letters B*, 592:1+, 2004.

[6] J.-J. Gaimard and K.H. Schmidt. Review of Particle Physics. *Nucl. Phys. A*, 531:709, 1991.

[7] I.A. Pshenichnov *et al*. Mutual heavy ion dissociation in peripheral collisions at ultrarelativistic energies. *Phys. Rev. C*, 64:024903, 2001.

[8] A. Fasso *et al.* FLUKA: a multi-particle transport code. *CERN Report CERN-2005-10*, 2005.

[9] A. Fasso *et al.* The physics models of FLUKA: status and recent developments. *Proc. of the Computing in High Energy and Nuclear Physics 2003 Conf., La Jolla*, 2003.

[10] `http://www-ap.fnal.gov/MARS/`.

[11] R. Bruce et al. Monitoring Heavy-Ion Beam Losses in the LHC. *Proc. of the European Particle Accelerator Conf. 2006, Edinburgh, Scotland*, page 544, 2006.

[12] G. Bellodi et al. Beam loss monitors for heavy ion operation. *LHC Project Note 402, CERN*, 2007.

[13] J.B. Jeanneret et al. Quench levels and transient beam losses in LHC magnets. *LHC Project Report 44*, 1996.

[14] R. Assmann et al. Expected performance and beam-based optimization of the LHC collimation system. *Proc. of the European Particle Accelerator Conf. 2004, Lucerne, Switzerland*, page 1825, 2004.

[15] S. Redaelli et al. Comparison between measured and simulated beam loss patterns in thc CERN SPS. *Proc. of the European Particle Accelerator Conf. 2006, Edinburgh, Scotland*, page 1810, 2006.

Analysis of resonances induced by the SIS–18 electron cooler*

S. Sorge†, O. Boine-Frankenheim, and G. Franchetti, GSI, Darmstadt, Germany

Abstract

Besides beam cooling, an electron cooler also acts as a non-linear optical element. This may lead to the excitation of resonances possibly resulting in an increase of the beam emittance. The aim of this work is the calculation of resonances driven by the electron space charge field in the cooler installed in the SIS heavy ion synchrotron at GSI Darmstadt. For our calculations, we used a numerical model consisting of a rotation matrix representing the ideal lattice together with a non-linear transverse kick element representing the electron cooler. Within this model, we studied the dominant resonance lines resulting from the interaction with the cooler.

INTRODUCTION

The space charge field in an electron cooler acts as a non-linear optical element in the lattice of a storage ring. This may lead to the excitation of additional ring resonances. Depending on the machine working point these resonances cause emittance growth and an effective heating of the beam, as it was observed e.g. in the CELSIUS cooler storage ring [1].

Electron cooling at medium energies will play an essential role in the proposed FAIR storage rings [2]. Electron cooling is already available to improve the beam quality of the intense ion beams at low energy in the existing SIS synchrotron. On the other hand, the transverse tune shift and spread due to the direct space charge force plays an important role at low or medium energies. The resonances excited by the non-linear space charge field of the cooler electron can potentially limit the reachable beam intensity and quality.

In this work, we calculated the resonances driven by the electron space charge field in the cooler installed in the SIS–18 heavy ion synchrotron at GSI Darmstadt. This theoretical study provides the necessary information for dedicated measurements of cooler induced resonances and effects in SIS.

MODEL

In our calculations we used a simple model consisting of a rotation matrix providing the phase advance of the lattice of SIS–18 and a non-linear transverse kick introducing the force of the electron cooler in thin lens approximation. The coordinates of a particle after the $(n+1)$-st revolution are calculated from those of the n-th revolution by

$$\begin{pmatrix} z_{n+1} \\ z_{n+1}^{'} \end{pmatrix} = \begin{pmatrix} \cos 2\pi\nu_z & \hat{\beta}_z \sin 2\pi\nu_z \\ -\frac{1}{\hat{\beta}_z}\sin 2\pi\nu_z & \cos 2\pi\nu_z \end{pmatrix} \times \begin{pmatrix} z_n \\ z_n^{'} + \Delta z^{'}(x_n, y_n) \end{pmatrix} \quad (1)$$

with $z = x, y$. Here, ν_z is the bare tune of the lattice, $\hat{\beta}_z$ is the unperturbed beta function in z direction at the location of the electron cooler, and

$$\Delta z^{'}(x,y) = \frac{q q^{'} N^{'}}{2\pi\varepsilon_0 m_0 c^2 \beta_0^2 \gamma_0^3} \frac{z}{R^2} \int_0^R \mathrm{d}r \; r \; n_0(r) \quad (2)$$

with $R = \sqrt{x^2 + y^2}$ is the transverse momentum kick depending on both spatial directions x, y. Here, we applied a radial shape of the electron beam $n_0(r)$ having a constant density in the centre and a thin edge region being characteristic for an electron cooler as shown in figure 1. The parameters used in the calculations are given in table 1.

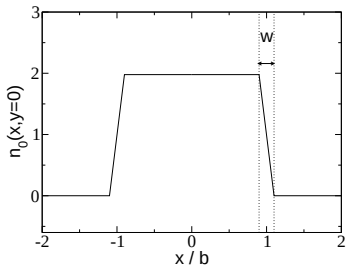

Figure 1: Normalised charge density profile used for the electron beam as provided by the beambeam element of MAD-X as a function of x for $y = 0$. An edge layer with a width $w = 0.01\ b$ was used in the calculations.

Particle	U^{73+}
Injection energy E	$11.4\ \mathrm{MeV/u}$
Relativistic factors $\beta_0,\ \gamma_0$	$0.15,\ 1.01$
Cooling length L_{cool}	3 m
Electron current I_e	0.3 A
Cathode radius r_{cath}	12.7 mm
Adiab. expansion factor f_E: used, (range)	$3,\ (1 \ldots 8)$
Electron beam radius ($b = r_{\mathrm{cath}}\sqrt{f_E}$)	22 mm
Beta function in the cooler ($\hat{\beta}_x,\ \hat{\beta}_y$)	8 m, 15 m

Table 1: Parameter of SIS–18 used in the calculations and taken from [3] and [4].

* Work supported by the European Community RESEARCH INFRASTRUCTURES ACTION under the FP6 programme: Structuring the European Research Area - Specific Support Action - DESIGN STUDY (contract 515873 - DIRACsecondary-Beams)

† S.Sorge@gsi.de

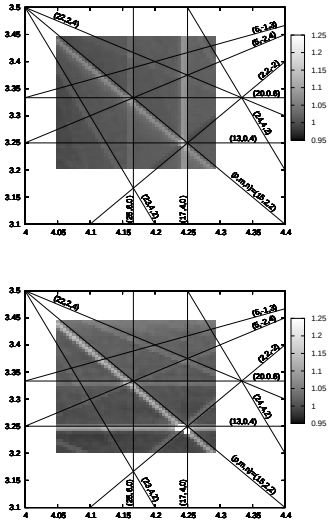

Figure 2: Relative rms beam width in x and y direction, upper and lower picture, respectively, depending on ν_x and ν_y (x and y axis in both figures). The colour scale is within $w_{\rm rel} \leq 1$ (dark grey) and $w_{\rm rel} \geq 1.25$ (white).

RESULTS

To make the positions of the resonances visible, the relative rms beam width was calculated as a function of the tune values ν_x, ν_y of the rotation matrix.

We explored for resonances the range given by $\nu_x \in [4.05, 4.3]$ and $\nu_y \in [3.2, 3.45]$, which is near the working point $(\nu_x, \nu_y) = (4.2, 3.4)$ [3], and which does not contain a half integer resonance. On the other hand, it was shown in [1] within an analytic model, that an electron cooler with a round electron beam excites only resonances of even order, where, additionally, the resonances strength decreases with increasing order. Hence, we searched only for resonances of order 4 and 6. Figure 2 shows the positions of the resonances found in the $\nu_x - \nu_y -$ plane. The black lines denote the positions of the resonances given by the condition

$$p = m\nu_x + n\nu_y. \tag{3}$$

So, all resonances found in our scan could be identified, and they show a quite reasonable behaviour. We found, that only sum resonances and uncoupled resonances lead to an increase of the beam width.

Figure 3 shows the relative beam width depending on the vertical tune. So, one can see, that the beam width is enhanced up to a factor 1.5 under the conditions considered, what is not visible in figure 2 due to the resolution.

In both figures, one can see, that the regions of enhanced beam width are always slightly shifted to smaller values compared to the lines defined by the resonance condition (3). This is because, in contrast to the lattice non-linearities, the electron cooler provides a finite linear tune shift in addition to the non-linear part.

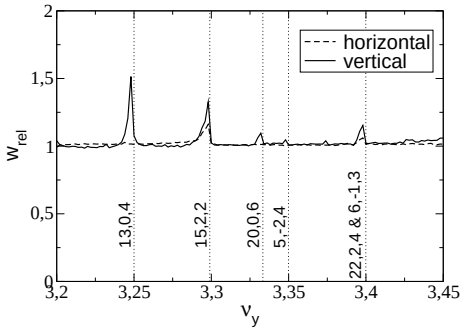

Figure 3: Relative beam width as a function of the vertical tune within the range $\nu_y \in [3.1, 3.45]$ for a fix horizontal tune $\nu_x = 4.2$. So, this figure is an extract of figure 2.

SUMMARY

We studied the resonances generated by the space charge force of the electron beam in the SIS–18 cooler. The initial rms radius of the ion beam was adjusted to the radius of the electron beam. Resonances up to the 6th order could be identified. Furthermore, we could qualitatively reproduce the dependency of the resonance width on the resonance order as given by an analytic model in reference [1]. Within that model, the widths of the resonances driven by a transverse momentum kick representing an electron cooler are given as integrals over the angle variable of the betatron motion. It predicts that the resonance width decreased, when the order of a the resonances is enhanced. A quantitative reproduction of the beam width using an analytic model was possible only for the half integer resonance, see [6].

The motivation for this work was, that the resonances are an additional possible constraint for the choice of the tune, because they could limit the extension of the space charge tune spread due to the self fields of the beam and therefore leading to the reduction of the space charge limit.

Additionally, there are many resonances driven by the non-linearities of the lattice in the real SIS, see e.g. [5]. In contrast to them, the resonances driven by the electron cooler do not lead to a beam loss, but to an increase of the beam with. Furthermore, the non-linearities and the cooler drive partially the same resonances. So, a major task of forthcoming studies will be to distinguish between the effects of both sources of resonances. Hence, further theoretical studies are necessary to investigate, the interplay of both sources of resonances and, that subject will also be an important task within measurements of the resonances driven by the electron cooler of SIS–18.

This work is presented in more detail in [6].

REFERENCES

[1] V. Ziemann, "Resonances driven by the electric field of the electron cooler", TSL Note 98-43

[2] FAIR Baseline Technical Report Sept. 2006, GSI

[3] B. Franczak, Parameter list of SIS–18, GSI-SIS-TN / 87-13, September 10, 1987

[4] L. Groening, "Untersuchung zur Elektronenkühlung und Rekombination hochgeladener Ionen am Schwerionensynchrotron SIS", GSI Dissertation 98-20, November 1998

[5] G. Franchetti, P. Schuett, T. Hoffmann, G. Rumolo, and A. Franchi, "Mapping of resonances in SIS18", GSI-Acc-Note-2005-02-001

[6] S. Sorge, O. Boine-Frankenheim, and G. Franchetti, Proc. of COOL, Bad Kreuznach 2007, see `http://bel.gsi.de/cool07/PAPER/WEM103.PDF`

RESONANCE TRAPPING, STOCHASTIC DIFFUSION AND INCOHERENT EMITTANCE GROWTH INDUCED BY STRUCTURED ELECTRON-CLOUD PINCH

G. Franchetti, GSI Darmstadt, Germany; F. Zimmermann, CERN Geneva, Switzerland

Abstract

When a bunch passes through an electron cloud, the transverse electron density distribution is enhanced and modulated in time as a consequence of the motion of individual electrons under the action of the nonlinear beam field. The effect of this "structured" electron pinch together with the synchrotron motion of beam particles leads to an incoherent emittance growth via the excitation and repeated crossing of resonances, that can give rise to either stochastic "scattering" ("diffusion") or trapping. We study these effects via a toy model of an idealized pinch, and present applications to the CERN SPS and the GSI SIS100.

LANDSCAPE

It is well known that the excitation of nonlinear resonances by magnet errors, space charge or beam-beam interaction in conjunction with tune modulation can lead to stochastic diffusion, resonance trapping and emittance growth in hadron storage rings. Already in the 1950s the change of a particle's oscillation amplitude due to a single "fast" resonance crossing was calculated by Schoch [1] following earlier work by mathematicians. In the 1970s A. Chao and M. Month stressed the complementary possibility of adiabatically trapping particles in resonance islands, and transporting them, via a slow tune modulation, towards larger amplitudes [2]. Since the times of Schoch, Month or Chao, several novel theoretical approaches for describing the effect of tune modulation have been developed in the field of nonlinear dynamics, e.g., a theory of "modulational diffusion" by Chirikov, Vivaldi, Lieberman and co-workers [3]. Following the above pioneers, over many decades numerous theoretical and experimental studies were conducted on the combined effects of tune modulation and nonlinear forces in accelerators. A review of these phenomena in regard to beam-beam interaction, including estimates of diffusion rates, was delivered by L. Evans in a school for the SPS collider [4]. A review of related diffusion mechanisms in regard to nonlinear magnetic field errors was also published more than 10 years ago [5]. An extrapolation of the dynamic aperture due to field errors in the presence of tune modulation was derived by a Bologna-CERN collaboration [6]. Later, the interplay of direct space charge and tune modulation was studied for the LHC [7]. In 1999 M.A. Furman and A.A. Zholents pointed out, for the first time, that the "pinch" of an electron cloud during a bunch passage induces a tune shift changing along the bunch, which together with synchrotron motion excites synchro-betatron resonances [8]. The phenomenon considered was found not to be a strong effect for the PEP-II B factory. At about the same time, K. Oide also hypothesized about an incoherent electron-cloud effect, as a possible explanation for the vertical beam-size blow up that was observed at the KEKB positron ring. The KEKB beam blow up was however soon explained in theory and simulations by a TMC-like fast head-tail instability [9], an explanation which was afterwards confirmed experimentally [10]. Nevertheless some KEKB data suggest that even below the threshold of the fast instability a small "incoherent" blow up occurs [11]. The detailed distribution of the pinched electron cloud inside a KEKB positron bunch and the resulting large incoherent tune shift, computed in 2000 [12], suggest a possible explanation. In 2001 the incoherent tune shift due to an electron cloud at the end of a bunch passage was also estimated for the LHC proton beam in the PS, SPS and LHC [13]. An analytical few-particle model, including the tune shift from space charge and from electron cloud (with a simplified "linear" pinch), plus synchrotron motion, was developed by G. Rumolo *et al.* [14], following a suggestion by K. Cornelis. In a 2002 memorandum K. Ohmi discussed the incoherent electron-cloud effect, emphasizing its similarity to the incoherent effect of space charge [15]. He later compared this effect with a linear stopband resonance due to a quadrupole error [16]. In 2003, the tune footprint created by the pinched electron cloud was calculated via frequency maps, revealing several resonances which would potentially contribute to an incoherent emittance growth [17]. Accompanying longer-term tracking simulations showed a strong dependence of the emittance growth on the synchrotron tune. Also, in 2004, E. Benedetto *et al.* presented an analytical calculation of the electron-induced incoherent tune shift as a function of the longitudinal and transverse beam-particle position along the bunch, assuming that this tune shift could be responsible for incoherent emittance growth [18, 19]. Incoherent space-charge effects in high-intensity high-brightness beams have become more relevant with the advent of new projects such as FAIR [20]. In preparation of FAIR, these effects have been studied in an extensive experimental campaign at CERN [21], which was accompanied by several numerical benchmarking studies [22]. The main outcome of this campaign is that a particle may indeed be trapped in a resonance when the latter is crossed, as predicted by Chao and Month more than 30 years earlier. The resonance crossing and trapping is particularly relevant in bunched beams where particles, due to space charge, may periodically be subjected to a resonance crossing via the synchrotron motion.

ELECTRON RESONANCES

In September 2004 some analogies were drawn between resonance-trapping phenomena for space charge invoked to explain the beam losses observed during the PS measurement campaign, and beam losses seen at the SPS, which could be due to space charge or electron cloud, during discussions at CERN by E. Metral, E. Shaposhnikova, and G. Arduini, in connection with the ICFA-HB2004 workshop [23]. Inspired by the remarkable similarities of incoherent space charge effects and incoherent electron cloud effects, that had already been exploited by G. Rumolo *et al.* [14] and by K. Ohmi [15], the CARE-HHH 2004 workshop established a close collaboration between CERN, GSI, and KEK [24], which culminated in the use of an analytical electron-pinch model all around the ring for detailed long-term tracking studies of the SPS and LHC [25], and in an alternative description and interpretation put forward by K. Ohmi and K. Oide, who refer to it as "6-dimensional Arnold diffusion" [26]. The pinching of the electron cloud, either in a field-free region or in magnetic field, leads to a complicated structure with a series of higher density regions, which are successively emerging on the beam axis, at various longitudinal positions along the bunch. The regions of peak density are a result of the transverse oscillatory electron motion. After its formation on axis, each high-density region soon splits into two, on either side of the beam. During the later part of the bunch passage, the two newly generated electron "stripes" are then moving outward, away from the transverse bunch center. Such electron structures were first obtained from an analytical model of the pinch for a round beam without magnetic field [18, 19] and later reproduced in detailed pinch simulations with the HEADTAIL code [27] for various beam and magnetic field conditions [28]. The presence of an electron stripe and its transverse distance from the bunch center depends on the longitudinal coordinate z describing the longitudinal position along the bunch with respect to a co-moving reference particle. Therefore, there exists a correlation between the electron-cloud field experienced by a beam particle and its longitudinal position in the bunch. Via the synchrotron motion this dependence translates into a tune modulation, a mechanism that is familiar from space charge. In numerical simulations the long-term effect of a localized pinched electron cloud is a non-negligible emittance growth [24], which vanishes if the longitudinal motion of the particles in the bunch is artificially frozen [25]. Unfortunately a fully self consistent simulation of a bunched beam interacting with a pinching electron cloud all around a storage ring is prohibitively CPU time consuming, for typical storage times of a rings like the SPS or the LHC which range from 20 minutes to several hours in real time. As a remedy we may employ the simplifying assumption that the electron pinch identically repeats on each successive bunch passage through the same or equivalent location. However, even with this assumption the number of turns which can be explored is relatively small [25]. In an attempt to overcome this difficulty and to unravel the mechanisms of the slow emittance growth, a further simplified analytical model of the pinched electron cloud was constructed based on the principle of electron charge conservation and assuming that the pinch increases linearly along the bunch. For the purpose of comparison, this simplified model was also implemented in the PIC code HEADTAIL and over 5000 turns and 10000 turns a simulation benchmarking has been performed [25]. Other benchmarking efforts were reported in Ref. [29]. However, up to now, in the "frozen models" of the electron cloud, the presence of the electron "stripes" was completely ignored. In this paper, we address the effect of the pinch structure on the beam dynamics. We adopt a simplified model in order to gain a first qualitative and semi-quantitative understanding of the role of the electron "stripes" on the beam dynamics.

"STRIPES" PINCH MODEL

The pinch of the electron cloud gives rise to the formation of a certain number of "stripes" [18, 19]. The morphology of each electron stripe is quite complex, and the effect of the stripe on the beam dynamics is difficult to assess. We simplify the problem by considering idealized electron stripes formed mainly in the horizontal direction and extending infinitely in the vertical plane (Fig. 1). This simplification is a reasonable approximation for the pinch occurring with a flat beam in a vertical magnetic field [28], and it allows for a straightforward analytical description of the electric field. The picture shows an example of three electron stripes modeled by straight walls of uniform electron density ρ_e. The change of the hori-

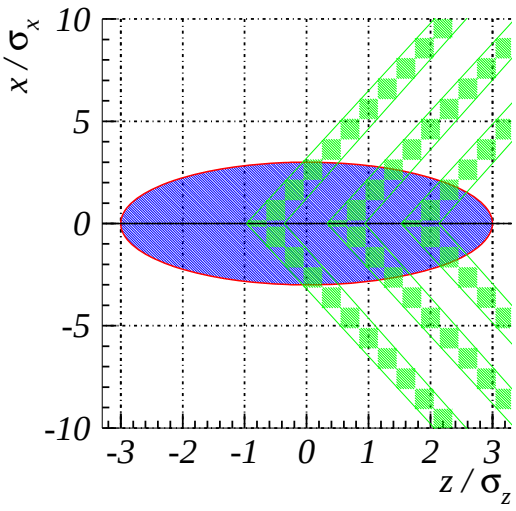

Figure 1: Schematic of a one-dimensional model of electron-cloud stripes in the bunch reference frame. Indicated in blue is the $x - z$ area occupied by a bunch. The electron stripes are shown as green bands.

zontal stripe location with location z is taken to be small, i.e. $\theta \equiv dx/dz|_{\rm stripe} \ll 1$. The electron density of our model is chosen as constant inside the stripes and zero outside, namely

$$\rho(x) = \begin{cases} 0 & \text{if} \quad 0 < |x| < R_1 - \Delta R \\ \rho_e & \text{if} \quad R_1 - \Delta R < |x| < R_1 \\ 0 & \text{if} \quad R_1 < |x| \end{cases} \qquad (1)$$

where ΔR denotes the x-thickness of the stripe, and R_1 is the outer horizontal border of the electron wall. In this approximation the electric field is readily computed via Gauss's law, and we find that the electric field is absent inside the stripes (i.e. for $|x| < R_1 - \Delta R$), and constant outside the stripes (i.e. for $|x| > R_1$). At each z, the total electric field E_x is the composition of the electric field produced by all individual electron stripes which are present. We denote by z_p the start position of a new pair of two stripes. In our model, electrons belonging to the same stripe are found on the bunch axis over the longitudinal region $(z_p, z_p + \Delta R/\theta)$. This short region correspond to a maximum of the pinch.

Consider a ring with a highly localized electron cloud described by a single interaction point (IP) between the electrons and the beam. In such case, the density ρ_e can be related to the detuning produced at the center of the pinch, via the relation

$$\Delta Q_{x,ec1} \approx \frac{\beta_{x,IP}}{4\pi} \frac{e\rho_e}{\epsilon_0} \frac{q}{p_0 v_0} \Delta s \ , \qquad (2)$$

where $\beta_{x,IP}$ designates the beta function at the IP, ϵ_0 the vacuum permittivity, ρ_e the EC density within a stripe, q the charge of the beam particle, e the electron charge, p_0 the beam particle's longitudinal momentum, v_0 its longitudinal velocity, and Δs the longitudinal extent of the electron cloud. If many IPs are present in the ring and the detuning from each IP is small, then the global detuning is the sum of the individual detuning contributions from all IPs. If the detuning from the individual IPs is too strong (or the betatron tune close to an integer or half integer), higher order term enter into the evaluation of the total EC detuning. Note that Eq. (2) is valid only for particles experiencing linear electron forces at the location of the pinch. For particles at larger amplitudes (e.g. $|x| > \Delta R$), or at different longitudinal locations (in the bunch reference frame) the expression for the detuning is more complicated. In the model of Fig. 1 each stripe intersects the axis at an angle $\theta = 3.33\sigma_x/\sigma_z$, the x-thickness of the stripe is $\Delta R = 1\sigma_x$, and the three stripes have their pinch maxima located at the positions $z_p = -1\sigma_z$, $0.3\sigma_z$, and $1.5\sigma_z$, respectively.

DETUNING AT LARGE AMPLITUDE

We consider the model of Fig. 1 where a single electron stripe produces a detuning of $\Delta Q_{x,ec1} = 0.02$. The density ρ_e is set via Eq. (2). We take a test particle at the longitudinal position of the pinch $z = -0.9\sigma_z$ (in the bunch reference frame). If the linear oscillation amplitude of a particle is large, i.e. $X \equiv \sqrt{2I_x\beta_{x,IP}} \gg R_1$ (with I_x denoting the classical action variable, equal to half the Courant-Snyder invariant), the detuning is mainly determined by the effect of the electric field outside the stripes. In spite of the fact that the electric field is constant here, the detuning decreases for larger oscillation amplitudes as the integrated effect of the electron field gets smaller compared with the natural betatron motion. An analytic approximation of the detuning, valid for $X \gg R_1$ is (see Appendix)

$$\Delta Q_{x,ec1,o}(I_x) = \frac{4}{\pi} \frac{R_1 \Delta Q_{x,ec1}}{\sqrt{2\beta_{x,IP} I_x}}. \qquad (3)$$

In Fig. 2a we compare results from Eq. (3) with numerical evaluations of the tune and find an excellent agreement.

The situation can be more complicated if the test particle has a small or moderate oscillation amplitude and is located at a longitudinal position in the bunch where $R_1 > \Delta R$. In this case for a particle with a maximum amplitude $X < R_1 - \Delta R$, the tune will equal the unperturbed betatron tune as no electron force is present on the inner side of the electron stripe. If $X > R_1$ the particle will spend part of its time outside the stripe, and part of it inside. Therefore the resulting detuning will be somewhat reduced with respect to the case where $X \approx R_1$ (e.g. see Fig. 2a). However, for $X \gg R_1$ the particle will stay mostly outside the stripe, and therefore the detuning will approach the prediction of Eq. (3) where we substitute R_1 with ΔR. We can recognize this effect in Fig. 2b, where at large amplitudes the analytic curve (red) converges towards the numerical one (black). The green area represents the region of the stripe which at $z = -0.4\sigma_z$ is located between 1 and $2\sigma_x$ [and between -2 and -1 σ_x]. If the test

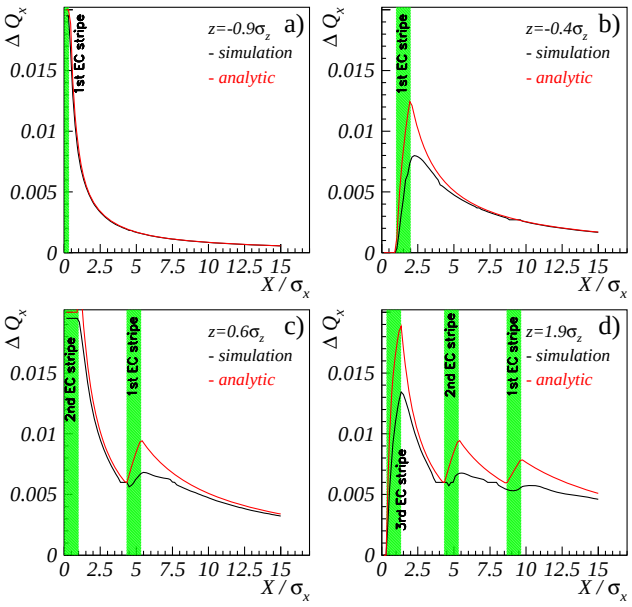

Figure 2: Detuning induced by the electron stripe model of Fig. 1 at several longitudinal positions along the bunch.

particle is situated at a longitudinal position and has a transverse amplitude such that two stripes are intercepted in the course of its oscillation the resulting detuning is the composition of the detuning induced by each of the two stripes (see Fig. 2c). In Fig. 2d at $z = 1.9\sigma_z$ all three stripes are present. The overall effect is a significant residual detuning at large transverse amplitude $(X = 15\sigma_x)$ whereas the latter was practically zero at the pinch location of the first stripe (Fig. 2a). These numerical examples allow us to conclude that:

- The presence of electron stripes creates a detuning proportional to $1/\sqrt{I_x}$ at large amplitudes.
- The varying horizontal position (or the 'slope') of the stripes introduces a z-dependence of the detuning with transverse amplitude which is analogous to the dependence of the detuning produced by space charge in high intensity bunches [30].
- The presence of multiple stripes creates a complex dependence of the detuning on the coordinates (z, x) and it reduces the decrease of the electron-cloud induced detuning with transverse amplitude.

PARTICLE DYNAMICS IN PRESENCE OF ELECTRON CLOUD STRIPES

We here discuss the single particle dynamics in presence of 1-dimensional electron stripes at a single IP (modeled as in Fig. 1). Our example accelerator is described by a smooth approximation, and we assume the typical tunes of the SPS: $Q_x = 26.185$, and $Q_y = 26.136$. For the sake of example, we select an electron density ρ_e which gives rise to an electron detuning of $\Delta Q_{x,ec1} = 0.1$. The presence of a single IP excites all resonances whose driving terms are present in the electron-induced force. On this occasion we note that the electron force is constant everywhere but within the stripe, and represents a strong nonlinearity which excites all harmonics. The dynamical properties of this system are better understood by studying the Poincaré sections of the frozen system, i.e. without synchrotron motion. We take the start particles at $z = -0.9\sigma_z$, i.e. at the location of the first pinch. In Fig. 3a the presence of 5 filled islands and 5 empty ones suggest that a 10th order resonance is excited by 1 IP. In Fig. 3b we show the beam particle detuning as a function of the particle amplitude X. The presence of islands is detected by the flat region in the tune curve. When we launch the test particles at a different longitudinal position, for example at $z = -0.6\sigma_z$ see Fig. 3c, the 5 occupied islands are located further outward than in Fig. 3a. This is reminiscent of what happens for bunched beams that are space-charge dominated. However, the reason why the islands move outward is different: In high intensity bunches dominated by space charge the islands are located outward for small $|z|$ because the space charge is larger close to the bunch center, hence the detuning increases at the center. In the present example instead,

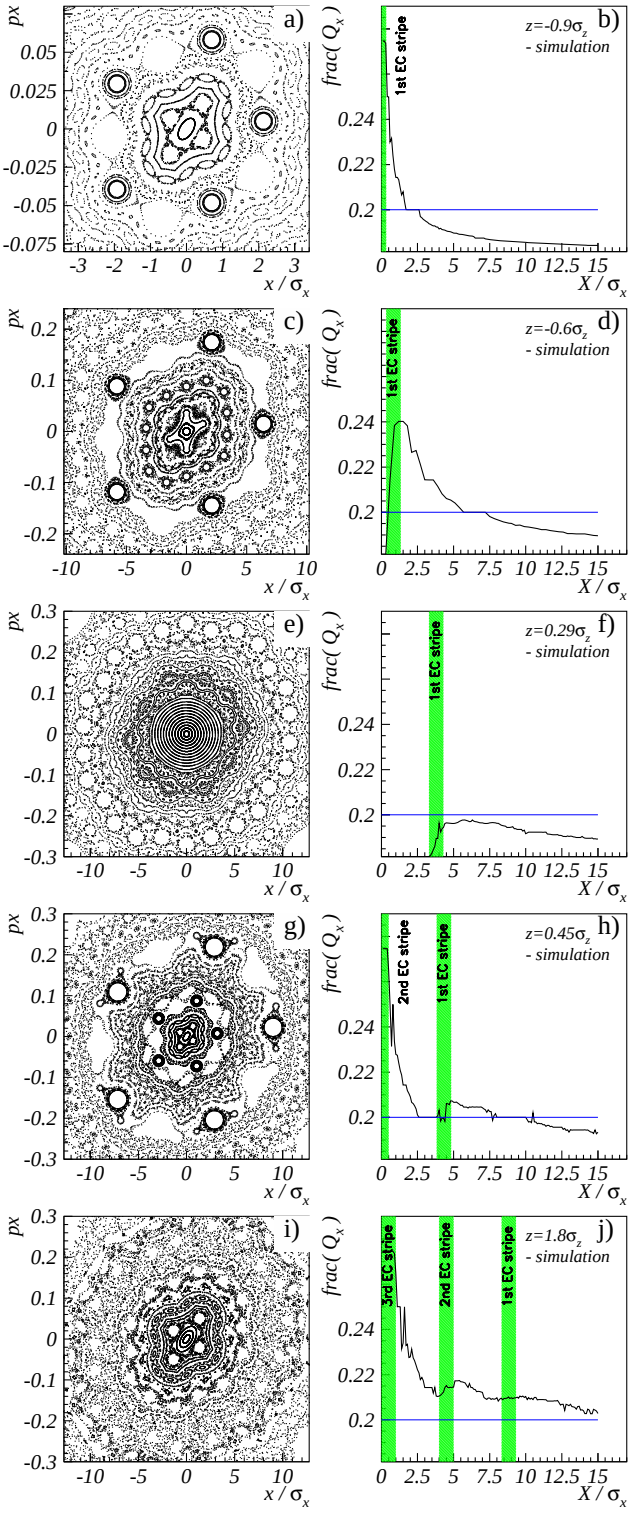

Figure 3: Transverse phase space (left) and nonlinear tune (right) for test particles at several transverse and longitudinal locations.

at $z = -0.6\sigma_z$, the electron stripes are located further outward (at $x = 1.33\sigma_x$) than for $z = -0.9\sigma_z$, but since there now are more electrons inside the stripe (which builds up from $z = -1.0\sigma_z$ to $z = -0.7\sigma_z$) the net result is an increase in the detuning. This is visible in Fig. 2a where $\Delta Q_{x,ec} = 1.67 \times 10^{-3}$, at $X = 5\sigma_x$ while in Fig. 2b at $X = 5\sigma_x$ the detuning is $\Delta Q_{x,ec} = 4.74 \times 10^{-3}$. The increased electron detuning pushes the islands outward, but when the stripes are far from the origin, and for particle amplitudes close to the stripes the increase of the detuning is compensated by the increase of the area inside the stripes. Globally this compensation leads to a decrease of the detuning which can be seen in Fig. 3f, where at $X = 5\sigma_x$ the detuning is smaller than in Fig. 3d. Note that in this last case (Fig. 3f), the tunes of the test particles stay below the 10th order resonance, and therefore 10th order islands no longer appear in phase space. Also visible in Fig. 3e is a peculiarity of our model in which electron forces are absent inside the electron stripes, namely that the inner region of the phase space here exhibits completely unperturbed Courant-Snyder ellipses. When the second electron stripe emerges, at $z = 0.45\sigma_z$ (Figs. 3g,h), the detuning is strongly enhanced close to the origin, and more weakly increased further away, but the overall effect is that the test particle tune crosses the 5th order resonance at two positions, namely at $X = 3.5\sigma_x$ and at $X = 9\sigma_x$. This is reflected in Fig. 3g by the presence of two chains of five islands. This additive effect of the electron stripes on the detuning is found at all longitudinal positions. In particular, at $z = 1.8\sigma_z$ we observe that the tunes $\Delta Q_{x,ec}$ always lie above the 5th order resonance for all values of X and therefore no 10th or 5th order island is found (see Figs. 3i,j). In other words, for intense bunched beams, the electron stripes introduce an $x - z$ correlation in the position of the transverse islands, which are self generated and strongly excited due to the concentration of electrons at a single interaction point.

TRAPPING ON RESONANCE CROSSING

In the previous section we uncovered several analogies between the pinched electron cloud and space-charge effects for intense bunched beams. We now explore if a shift of the tune across the 10th order resonance may induce particle trapping in the presence of an electron pinch as is the case for space charge. There is one important difference: For space-charge dominated intense bunched beams, the resonance is normally excited by a nonlinear driving term of the optical lattice, whereas in the case of the electron pinch the resonance driving term is provided by the electron stripes themselves. In the simulation, we first induce a resonance crossing by varying the accelerator tune $Q_{x,0}$ over 10^4 turns from 26.185 to 26.22, so that we intersect the resonance $10Q_x = 262$. We launch a test beam particle of initial coordinates $x = 2\sigma_x$, $z = -0.95\sigma_z$, and $p_x = p_z = 0$ so that only the effect of the 1st stripe is included. Then we simulate the resonance crossing, keeping the synchrotron motion of our particle frozen. Here the speed of the crossing is intentionally chosen to be much smaller than what it might be for a real bunched beam, as the trapping is facilitated if adiabatic conditions are met. The electron density of the stripe is adjusted via Eq. (3) so that it creates a detuning of $\Delta Q_{x,ec1} = 0.1$. In Figs. 4a,b

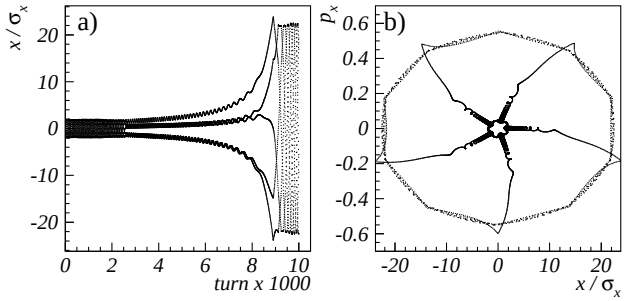

Figure 4: Crossing of the 10th order resonance by varying $Q_{x,0}$.

we show the particle amplitude versus the number of turns. The trapping is evident. Note that the particle is escaping towards infinity very fast when the tune is on the resonance, and finally a de-trapping takes place leaving the particle at a very large transverse amplitude, in this example at $X \approx 20\sigma_x$. This result strongly depends on the speed of the resonance crossing: the slower the crossing the larger is the amplitude gain, consistent with the theory of Schoch [1]. This dependence is similar to what was shown in Refs. [31, 32, 33] for high-intensity bunched beams with space charge. Figure 5 presents a detail of the trapping with a typical spiraling of the particle in phase space, following the outward moving islands.

The second fundamental type of resonance crossing occurs when the bare tune $Q_{x,0}$ is fixed, but the particle is allowed to longitudinally oscillate according to the synchrotron motion. The dynamics of this case is much more complex as the particles travel through different longitudinal sections of the bunch for which the electron stripes vary in number and position. As a first step to approach this problem we consider the single passage through a resonance over half a synchrotron oscillation. We set the synchrotron period equal to 2×10^4 turns and take a test particle located at the head of the bunch with initial coordinates: $x = 2\sigma_x, z = -3\sigma_z, p_x = p_z = 0$. The density of the electron-cloud is again adopted to produce a detuning of $\Delta Q_{x,ec1} = 0.1$ at the pinch location. The tunes of the ring are those of the SPS: $Q_{x,0} = 26.185, Q_{y,0} = 26.136$. In Fig. 6a we present the motion of the test particle in the $x - z$ plane. The motion appears to be regular until $z \approx -1\sigma_z$ is reached, where the first electron stripe is encountered. Following this, the motion ceases to be regular, but trapping does not yet occur as the important islands are still well inside the particle orbit. An island trapping takes place only at $z \simeq -0.35\sigma_z$. The trapping is evidenced in Fig. 6b by the 5 arms leaving the inner,

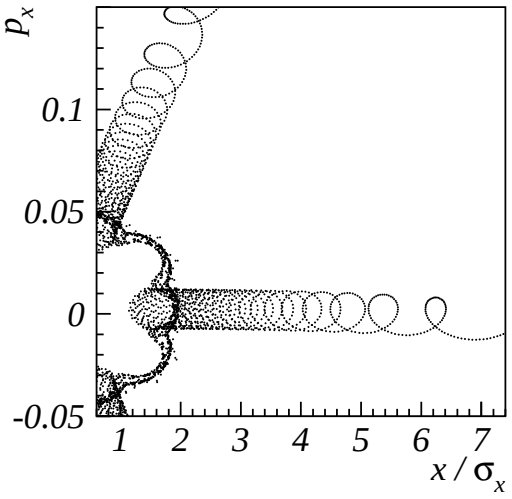

Figure 5: Detail of Fig. 4b: particle trapping induced by electron-cloud stripes.

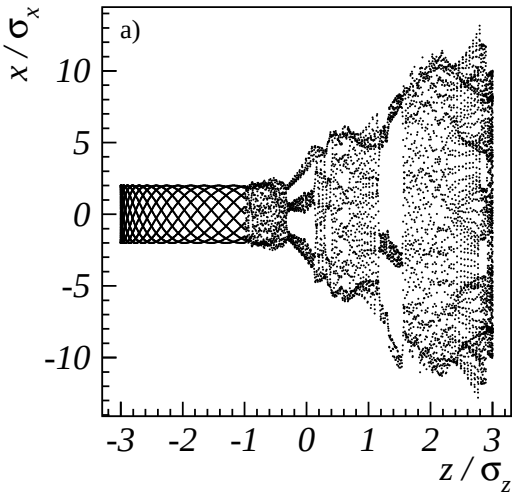

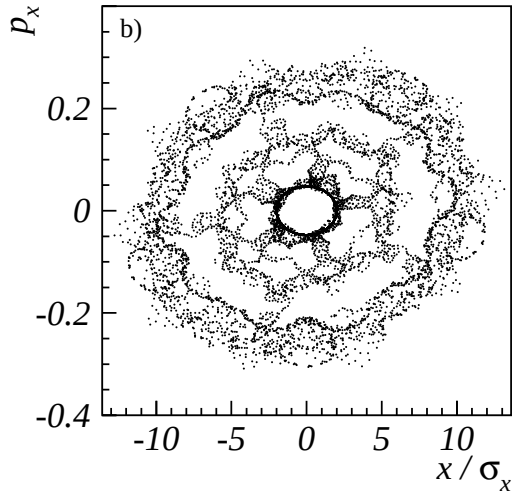

Figure 6: Crossing of the 10th order resonance in half a synchrotron period.

smaller deformed ellipse. Also, due to a stroboscopic effect, the same trapping is signaled by 3 arms in Fig. 6a. A de-trapping occurs at $z \simeq 0.1\sigma_z$, from when on the islands no longer intercept the particle orbit. In particular the resonance is not crossed anymore by our particle in the region $z = [0.15, ..., 0.25]\sigma_z$, whereas in the following interval $z = [0.25, .., 0.3]\sigma_z$ the islands disappear entirely and the particle executes a nearly regular betatron motion. Both these effects are visible in Fig. 6a, where the three arms vanish. Then, islands are newly formed at $z \geq 0.3\sigma_z$, namely two or three chains of 10th order islands (see Fig. 3g). Our tracked particle is located between the inner and outer island chains. The outer chain does not intercept the particle orbit, while the inner smaller chain of islands never succeeds in crossing the particle orbit: for $z > 0.46\sigma_z$ the detuning is already so large that the particle tune is moved above the 10th order resonance. Consequently in the region $z = [0.4, ..., 1.2]\sigma_z$, the particle mainly undergoes chaotic betatron-like motion. Note, however, that the further outward the electron stripes are located, the weaker becomes the electron-induced detuning. At $z \simeq 1\sigma_z$ the reduction of the detuning is such that the test particle again assumes a tune on the 10th order resonance. A "trapping" now takes place (see the stroboscopic effect in $1.2\sigma_z < z \lesssim 1.5\sigma_z$). When the third electron stripe commences, at $z = 1.5\sigma_z$, the detuning rises again, eliminating all 10th order islands. This is visible in Fig. 6a by the irregular motion in the interval $1.5\sigma_z < z < 2.3\sigma_z$. For $z > 2.3\sigma_z$ the electron-induced detuning shrinks again and the 10th order islands reappear, but no full trapping takes place. The partial trapping of this phase is visible by a weak signature of some stroboscopic effect in Fig. 6a, in the region $2.3\sigma_z < z < 3\sigma_z$. This last part of the particle's motion corresponds to the outer halo in Fig. 6b.

EXAMPLE APPLICATIONS

The aim of the previous section was to demonstrate that trapping by electron stripes is possible. However, in normal operating conditions, most synchrotrons work in the "non adiabatic" regime, with longitudinal oscillations much faster that in the previous examples. The fast longitudinal oscillations create a complicated dynamical situation, where resonance trapping is dominated by "scattering" [34] (see also the original discussion of fast resonance crossing by Schoch [1]). We now apply our toy model for

the electron stripes described in Fig. 1 to the SPS ring assuming a realistic longitudinal frequency $Q_{z,0} = 1/168$. Figure 7a presents the simulated emittance growth for 120 electron-cloud interactions equally distributed around the SPS ring. In Fig. 7b there are 744 electron-cloud interactions, one for each dipole according to the SPS structure. The total electron-induced detuning is again chosen equal to 0.1. Note the asymmetric response of the beam growth for a swapping of the horizontal and vertical tunes as a consequence of the crossing or non crossing of the 10th order resonance. In spite of the different number of interactions, the beam response is comparable in the two pictures. In Fig. 7b the emittance growth is slightly smaller than in Fig. 7a as the smaller number of interaction points excites the 10th order resonance more strongly. In all these simulations we assumed a zero chromaticity, a linear lattice, and an accelerator optics modelled in smooth approximation.

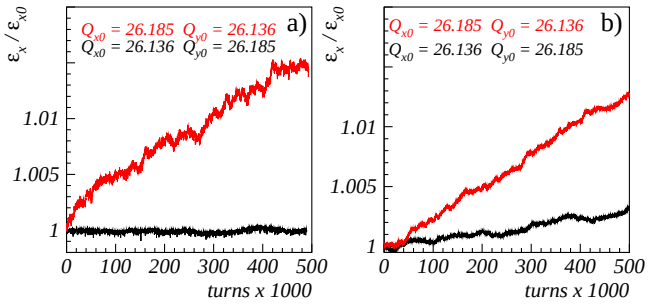

Figure 7: Example application to the SPS: a) electron IPs uniformly distributed around the circumference; b) one electron IP for each of the 744 dipoles in the SPS lattice.

We also applied this modeling of electron stripes to the future SIS100 ring at the GSI, even though the occurrence of an electron cloud at SIS100 is not yet fully assessed [35]. Figure 8a shows the simulated emittance growth during 120×10^3 turns, and Fig. 8b the accompanying halo development. The working points are $Q_{x,0} = 18.84, Q_{y,0} = 18.73$, and the longitudinal tune is $Q_{z,0} = 10^{-3}$. A more detailed discussion of the SIS100 parameters and the associated space-charge issues can be found in Ref. [36]. The results of our simulation show an emittance increase by 12%, and the fraction of halo particles outside $3\sigma_x$ exceeding 2%. Though these results appear acceptable compared with the beam-loss budget, a complete evaluation of the actual electron-cloud density expected in SIS100 still remains to be carried out.

CONCLUSION

The study presented in this report demonstrates that the morphological fine structure of the electron-cloud pinch plays an important role in creating the amplitude dependent detuning responsible for island migration and consequent particle trapping. Differently from the space-charge induced resonance trapping, the multiple stripes formed by the electron cloud induce multiple resonance crossings due to slow synchrotron motion. The complexity of the dynamics is fully illustrated by Fig. 6 where in half a synchrotron period the trapping and diffusion regimes alternate several times. We expect that a refined modeling of the electron stripes will create an even more complex dynamics which renders the reliable prediction of long term emittance growth a challenging endeavour indeed.

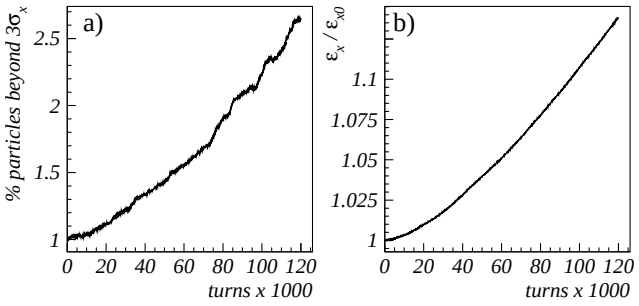

Figure 8: Application of the one dimensional electron stripe model to SIS100. a) emittance increase; b) % of particles beyond $3\sigma_x$. In this simulations the total electron-induced detuning is chosen equal to 0.1.

ACKNOWLEDGMENT

We acknowledge the support of the European Community-Research Infrastructure Initiative under the FP6 "Structuring the European Research Area" programme (CARE, contract number RII3-CT-2003-506395).

APPENDIX

The detuning created by one localized EC kick can be computed as follows. Consider the beam-particle motion in a section of the storage ring where the beam-electron interaction is located. In this section let the beta function be $\beta_{x,IP}$, and for simplicity adopt a smooth approximation with $\alpha_{x,IP} \approx 0$. In Courant-Snyder variables the particle's phase-space coordinates then are $\hat{x} = \sqrt{2I_x}\cos(\theta_x)$, and $\hat{x}' = \sqrt{2I_x}\sin(\theta_x)$, with θ_x denoting the betatron phase of the particle and I_x the classical action variable. The average shift in the betatron phase advance after N turns, due to the additional deflections $\Delta x_i'$ ($i = 1, ..., N$) experienced at a single beam-electron interaction point on successive turns, is

$$\Delta\theta_x = \frac{1}{N}\sum_{i=1}^{N} \frac{\sqrt{\beta_{x,IP}}\Delta x_i' \cos(\theta_{x,i})}{\sqrt{2I_x}} , \qquad (4)$$

where $\theta_{x,i}$ denotes the betatron phase on turn i. In Eq. (4) we assume that the invariant I_x remains constant, i.e. we exclude any resonant effect, or, in other words, we are averaging over a number of turns N sufficiently small that the growth of I_x is negligible, but large enough for phase averages to make sense. For applying Eq. (4) to the effect of

the pinched electrons, we first note that, in our toy model, the EC electric field E_x inside the emerging stripes close to the center of the pinch z_p, is given by

$$E_{ec,x} = -\frac{e\rho_e}{\epsilon_0} x \ . \tag{5}$$

Inserting the resulting deflection $\Delta x'$, which is also linear in the offset x, into Eq. (4) the calculation reduces to an average over the term $\cos^2(\theta_{x,i})$ which can be estimated analytically using the aforementioned assumptions. We then find that one IP for a particle with small transverse amplitude will give rise to the detuning

$$\Delta Q_{x,ec1} = \frac{\beta_{x,IP}}{4\pi} \frac{e\rho_e}{\epsilon_0} \frac{q}{p_0 v_0} \Delta s \ . \tag{6}$$

We can therefore express the density of a stripe as a function of the EC detuning in the pinch as

$$\rho_e = \epsilon_0 \frac{4\pi}{\beta_{x,IP}} \frac{\Delta Q_{x,ec1}}{\Delta s} \frac{p_0 v_0}{eq} \ . \tag{7}$$

For a particle at large transverse amplitude with respect to the stripe location $R_1 > \Delta R$, we can approximate the electron field as

$$E_{x,o} = -\frac{e\rho_e}{\epsilon_0} \Delta R \ \mathrm{sign}(\hat{x}). \tag{8}$$

and again apply Eq. (4). In the expression (8) we do not distinguish between the inside of the stripe (where $E_x = 0$) and the outside (where the field is constant) because, for large betatron amplitudes, the inside of the stripe occupies only a small fraction of the area spanned by the particle motion, which will not significantly contribute to the overall detuning. By combining Eq. (8) and Eq. (4) the detuning at large amplitudes becomes

$$\Delta Q_{x,ec1,o} = \frac{1}{\pi^2} \sqrt{\beta_{x,IP}} \left(\frac{e\rho_e}{\epsilon_0} \frac{q}{p_0 v_0} \Delta s \right) \frac{\Delta R}{\sqrt{2 I_x}} \ , \tag{9}$$

and inserting ρ_e from Eq. (7) we finally obtain the equation for the tune shift. Note that if $0 < R_1 < \Delta R$ then we substitute ΔR with R_1 and obtain Eq. (3).

REFERENCES

[1] A. Schoch, "Theory of Linear and Non-Linear Perturbations of Betatron Oscillations in Alternating Gradient Synchrotrons," CERN 57-21 (Proton Synchrotron Division), Section 14 (1958).

[2] A. Chao and M. Month, "Particle Trapping during Passage Through a High-Order Nonlinear Resonance," Nuclear Instruments Methods **121**, p. 129 (1974).

[3] B.V. Chirikov, M.A. Lieberman, D.L. Shepelyansky, F.M. Vivaldi, "A Theory of Modulational Diffusion," Physica D, **14**, 3, 289–304 (1985).

[4] L.R. Evans, "The Beam-Beam Interaction," CERN Accelerator School 'Antiprotons for Colliding Beam Facilities', CERN October 1983, CERN **84-15**, p. 319 (1984).

[5] F. Zimmermann, "Transverse Proton Diffusion," Particle Accelerators **49**, 67–104 (1995).

[6] M. Giovannozzi, W. Scandale, E. Todesco, "Dynamic Aperture Extrapolation in the Presence of Tune Modulation," Phys. Rev. E **57**, 3432–3443 (1997).

[7] F. Ruggiero, F. Zimmermann, "Consequences of the Direct Space Charge Effect for Dynamic Aperture and Tail Formation in the LHC," PAC'99 New York, vol. **4**, 2626 (1999).

[8] M.A. Furman and A.A. Zholents, "Incoherent Effects driven by the Electron Cloud," PAC 99 New York, Vol. **3**, 1794 (1999).

[9] K. Ohmi and F. Zimmermann, "Head-Tail Instability Caused by Electron Cloud in Positron Storage Rings," Phys. Rev. Letters **85**, 3821 (2000).

[10] J. Flanagan *et al.*, "Observaton of Vertical Betatron Sideband due to Electron Clouds in the KEKB LER," Phys. Rev. Letters **94**:054801 (2005).

[11] H. Fukuma *et al.*, "Study of Vertical Beam Blowup in KEKB Low Energy Ring," Proc. HEACC 2001 Tsukuba *http://conference.kek.jp/heacc2001/*

[12] F. Zimmermann, H. Fukuma, K. Ohmi, CERN-SL-Note-2000-061, November 2000.

[13] F. Zimmermann, "Electron Cloud Simulations: An Update," Proc. Chamonix XI, p. 144, CERN-SL-2001-003-DI (2001).

[14] G. Rumolo, F. Zimmermann, "Electron-Cloud Instability with Space Charge or Beam Beam", 3rd paper in 'Contributions of the SL-AP Group to the Two-Stream Instabilities Workshop,' CERN-SL-2001-067 (2001).

[15] K. Ohmi, "Single Bunch Electron Cloud Instability for a Round Beam," Memorandum, November 2002; see *http://ab-abp-rlc-ecloud.web.cern.ch/ab-abp-rlc-ecloud*

[16] K. Ohmi, "Single Bunch Electron Cloud Instability for a Round Beam II," Memorandum, December 2002, see *http://ab-abp-rlc-ecloud.web.cern.ch/ab-abp-rlc-ecloud*

[17] E. Benedetto *et al.*, "Transverse 'Monopole' Instability driven by Electron Cloud?," PAC 2003, Portland (2003).

[18] E. Benedetto and F. Zimmermann, "Analysis of the Electron Pinch during a Bunch Passage," Proceedings ECLOUD'04, Napa April 2004, CERN Report CERN-2005-001, p. 81 (2005).

[19] E. Benedetto and F. Zimmermann, "Dynamics of the Electron Pinch and Incoherent Tune Shift Induced by Electron Cloud," Proc. of EPAC'04, Lucerne, Switzerland, WEPLT009, p. 1834 (2004).

[20] D. Kraemer, Proc. EPAC 2007, THXAB02, p. 2598; P. Spiller, Proc. HB2006 ICFA Workshop, Tsukuba, Japan, 29 May – 2 June 2006, MOBP02, p. 24.

[21] G. Franchetti *et al.*, Phys. Rev. ST Accel. Beams **6**, 124201 (2003); E. Metral *et al.*, NIM A **561**, 257 (2006).

[22] G. Franchetti, I. Hofmann, Proc. HB2006 ICFA Workshop, Tsukuba, Japan 29 May - 2 June 2006, WEAX01, p. 167; ed. H. Sako (2006).

[23] E. Metral, E. Shaposhnikova, G. Arduini, private communication (2006).

[24] E. Benedetto *et al.*, "Emittance growth caused by electron cloud below the "fast TMCI" threshold: numerical noise or true physics?," PAC2005 Knoxville, USA, p. 1344 (2005).

[25] E. Benedetto, G. Franchetti, F. Zimmermann, Phys. Rev. Lett., **97**, 034801 (2006).

[26] K. Ohmi, K. Oide, "Chaos and Emittance Growth due to Nonlinear Interactions in a Circular Accelerator," Phys. Rev. ST Accel. Beams **10**:014401 (2007).

[27] G. Rumolo, F. Zimmermann "Practical User Guide for HEADTAIL," SL-Note-2002-036-AP (2002).

[28] E. Benedetto, "Emittance Growth Induced by Electron Cloud in Proton Storage Rings," PhD Thesis Politecnico di Torino (2006).

[29] E. Benedetto *et al.*, "Modeling Incoherent Electron-Cloud Effects," Proc. of PAC'07, Albuquerque, New Mexico, USA. THPAN075, p. 3393 (2007).

[30] G. Franchetti et al, "Long-Term Simulations of Space Charge and Beam Loss Observed in the CERN PS," Proc. ICFA Workshop HB2004, Bensheim, Germany 18-22 October 2004, eds. I. Hofmann, J.-M. Lagniel, and R.W. Hasse, AIP **773**, 137 (2004).

[31] G. Franchetti, "Recent Developments in Understanding Beam Loss in High-Intensity Synchrotrons," Proc. of PAC'07, Albuquerque, New Mexico, USA. TUZAAB02, p. 794 (2007).

[32] I. Hofmann and G. Franchetti, "Scaling Laws for Space-Charge Driven Resonances," Proc. of PAC'07, Albuquerque, New Mexico, USA. THPAN017, p. 3259 (2007).

[33] S.Y. Lee *et al.*, New J. Phys. **8** (2006) 291; S.Y. Lee, Phys. Rev. Lett. **97**, 104801 (2006).

[34] A.I. Neishtadt, "Scattering by Resonances," Celestial Mech. Dyn. Astronomy, vol. **65**, p. 1–20 (1997).

[35] G. Rumolo and O. Boine-Frankenheim, "Study of Electron Cloud Formation and Instability in SIS," Internal note, GSI-Acc-Note-2003-10-001, (2003).

[36] G. Franchetti *et al.*, "Space charge and electron clouds issues", Proc. of LHC Lumi 2006, October 16-20 2006, Valencia, Spain. p. 192 (2006).

LOSS MAPS OF RHIC*

G. Robert-Demolaize, A. Drees, BNL, Upton, NY 11973, USA

Abstract

State-of-the-art tracking tools were recently developed at CERN to study the cleaning efficiency of the Large Hadron Collider (LHC) collimation system [1]. These tools are fully transportable, meaning that any accelerator lattice that includes a collimation system can be simulated. Each of the two Relativistic Heavy Ion Collider (RHIC) [2] beam lines features a multi-stage collimation system, therefore dedicated datasets from RHIC operations with proton beams can be used to benchmark the tracking codes and assess the accuracy of the predicted hot spots along the LHC.

INTRODUCTION

Simulations were performed with an extended version of the well-established SixTrack code to predict the cleaning efficiency of the LHC multi-stage collimation system [3, 4]. The primary goal of this system is to minimize the risks of beam-induced quenches, especially for all sensitive magnets (e.g. the triplet quadrupoles) in the high luminosity experimental insertions. The trajectories recorded from the tracking code can be compared to a detailed aperture model of the machine [5], and longitudinal beam loss maps similar to the one shown in Figure 1 are then obtained for different machine setups (i.e. beam energy, collimator openings or orbit perturbation).

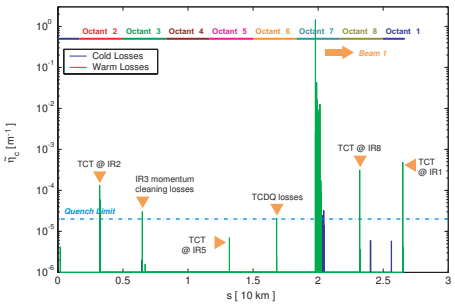

Figure 1: Sample simulated longitudinal beam loss map in the LHC Top Energy case.

These studies also have an impact on how the machine protection system will be set-up for operations. The simulated loss maps can identify possible hot spots along the beam lines, which helps installing beam loss monitors (BLMs) appropriately. It then becomes important to check how accurate the predictions are, both for the locations and the relative amplitudes of losses. To do so, one needs to reproduce real machine conditions of a lattice using collimators and compare the simulated loss map with measurements from BLMs. This can be done with data taken in the RHIC machine during one of its proton runs.

RHIC is a circular accelerator made of two individual beam lines (Blue and Yellow) with 6 common regions, 4 of which are dedicated to experiments. Figure 2 shows a schematic layout of RHIC. The machine was designed to run both gold ions and protons, but other species have also been injected over the course of operations (e.g. copper ions and deuterons). The data considered in this paper was taken during the 2005 proton run, whose parameters are listed in Table 1.

Table 1: Main RHIC parameters for the FY05 $p^+ - p^+$ run.

Number of bunches	111
Protons per bunch	2.0×10^{11}
E_{store} [GeV]	100
Working point Q_x, Q_y	0.690/0.685
ϵ_N [μm]	20.0
L_{peak} [cm^2.s^{-1}]	10^{30}
β^* STAR,PHENIX [m]	0.9
β^* IR10, IR4 [m]	10.0
β^* IR12 [m]	5.0
β^* IR2 [m]	3.0

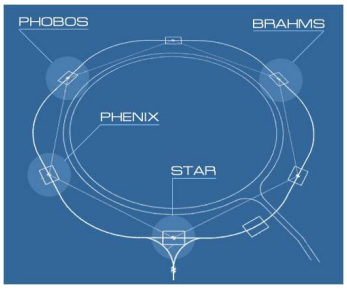

Figure 2: Schematic of the RHIC layout and its experiments.

The RHIC collimation system is made of 1 primary and 3 secondary collimators for each beam line that only intercept one side of the beam per transverse plane. As a comparison, in the LHC case one counts 4 primary and 16 secondary collimators per beam in IR7 which feature 2 parallel jaws per transverse plane. As shown in Figure 3, the RHIC primary jaw is L-shaped, allowing to collimate in both transverse planes at the same time. These elements are located around the PHENIX experiment and aim at minimizing the background level in all experimental insertions.

* Work supported by the U.S. Department of Energy

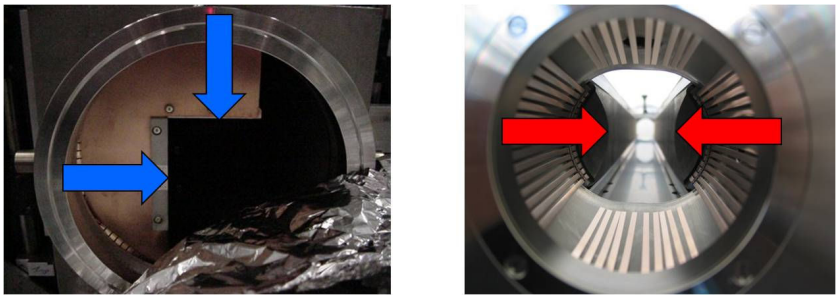

Figure 3: Comparison of mechanical layouts between the RHIC primary scraper (left) and a LHC horizontal collimator (right).

REQUIRED TRACKING TOOLS

Dedicated data sets were taken by moving the RHIC collimators close to the beam, with all relevant informations (jaw positions, closed orbit, BLMs signal) being logged during the entire operation. One then needs to:

- get the lattice and optics files corresponding to the machine conditions at the time of the measurements,
- simulate the trajectories of protons impacting on collimators using the actual collimator openings in the input files,
- compare these trajectories with a detailed aperture model of the RHIC beam lines.

Numerical models of the machine are obtained via the MAD-X code. An online model is used to store the magnet strengths into a file after each succsesful ramp, allowing to reproduce realistic machine conditions (i.e. tunes and β^* mainly). An outdated aperture model was available from previous collimation studies [6], that is not compatible with the output from SixTrack. The computing resources should also allow tracking large particle ensembles, i.e. at least 2×10^5 particles per job.

A new RHIC aperture model is therefore required, that must include all modifications since the original model. Most of the available database files only list the transverse dimensions at the beginning or the end of a given element; to obtain accurate beam loss maps, the aperture database should include the complete description along that element. As for the LHC studies, the new RHIC model is split into 10 cm bins in order to be as close as possible to the real shape of all elements. The model must also match the simulated lattice, hence the aperture database needs to be compared with the MAD-X lattice in order to find any element that was either moved, removed or replaced. Finally, all collimator tanks are taken as drift spaces, since the corresponding aperture restrictions are applied in the tracking routines.

Some machine elements needed more details than others, especially close to the interaction points. Figure 4 shows an example of how a DX separation magnet can be modeled. These separation elements ensure the transition from two separate vacuum pipes into a common pipe in which both pass each other. While the transverse opening in the common area is larger than the single vacuum pipe, neither beam actually travels through the center of the common transition region: as indicated in Figure 4, there is a closed-orbit offset that sets the beam closer to the aperture limits. For practical reasons, the DX elements (along with all elements that feature this orbit offset) have their aperture data given with the center of the pipe as reference, and the orbit offest for each 10 cm bin along the element is included in a separate column. When checking for beam losses, the aperture program adds the orbit offset to the recorded coordinates along the considered element.

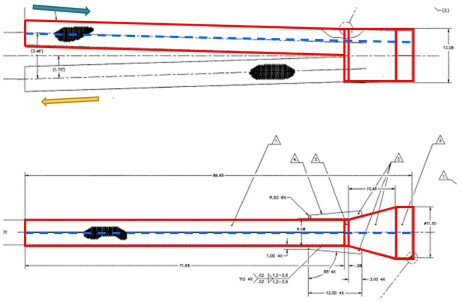

Figure 4: Top view (top) and side view (bottom) of a RHIC DX separation magnet. The red solid lines show how the transverse openings of this element were inserted in the new RHIC aperture model following a block method. The dashed line represents the linear approximation of the closed-orbit followed by the blue beam going from left to right through the element.

MEASUREMENTS VS. PREDICTIONS

The following presents the results of comparison between measurements taken during the FY05 $p^+ - p^+$ run and the corresponding simulations. The data was collected on April 28, 2005 during the fill #06981 for the Blue beam. Figure 5 shows the movements and positions of the collimator jaws that are reproduced in the tracking tools. The beam loss maps obtained from the tracking code are then compared to the longitudinal loss locations as indicated in the BLM signal. A sample map of the logged BLM signal can aslo be seen in Figure 5: the horizontal axis stands for the s location around the machine and the vertical axis gives the time of the measurement. The intensity of the sig-

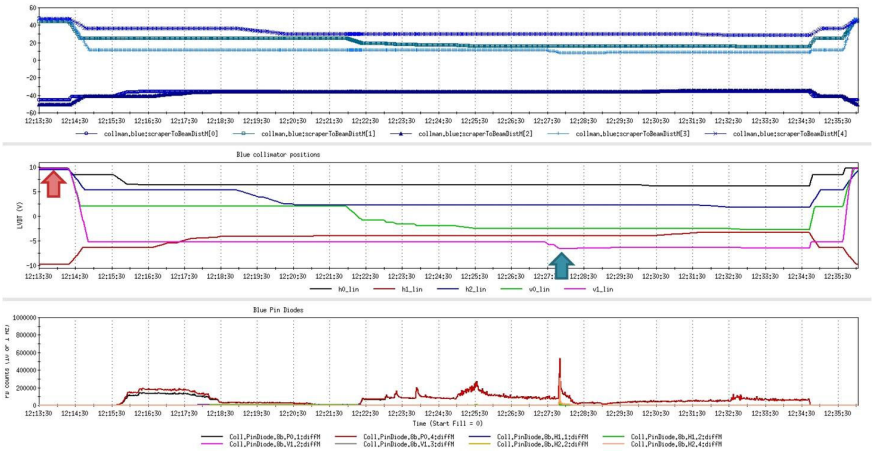

Figure 5: Collimator jaw positions in millimeters (top) and LVDT arbitrary units (middle) compared to the pin diode signals (bottom) versus time. Data is taken once the beam is at store. The red arrow points to the reference position "all out" of the collimator jaws for the BLM signal. The green arrow points to the "all in" position of the collimator jaws that are used for the tracking.

nal from each loss monitor is then displayed in color bins, with red indicating the highest value. The data shown in Figure 6 illustrates the goal of the RHIC collimation system: once the beam is at store, collimators should be set into positions that would minimize beam losses occuring at the triplet magnets located in the high luminosity insertions (the STAR experiment in this example). This would lower the background levels in the detectors and improve significantly the signal-to-noise ratio.

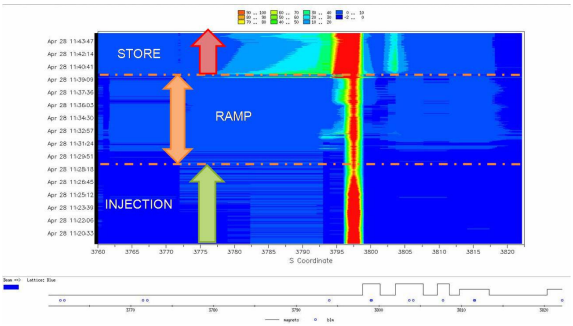

Figure 6: Zoom of the RHIC BLM data around the triplet magnet upstream of the STAR experiment following the Blue beam. Beam losses are increased coming into the triplet when the beam is at store. A schematic of the beam line is included below the BLM signal as a reference; the locations of each triplet quadrupoles are given by the rectangular shapes.

Preliminary simulated loss maps around the RHIC Blue beam line are shown in Figure 7. The impact parameter on the primary collimator was taken as 5 μm. Each transverse planes was tracked separatelyl; tracking results are then presentend individually (horizontal plane on top, vertical on bottom) so as to correlate the loss patterns with the collimation planes. The BLM data is also shown for comparison and corresponds to the difference in the intensity of the signal at each loss monitor between the collimator positions "all out" (red arrow in Figure 5) and "all in" (green arrow in Figure 5).

One can see from Figure 7 that the predicted loss locations actually match most of the peaks in the BLM signal all around the machine. This strengthens the accuracy of prediction of the tracking tools developped for LHC collimation studies. Figure 8 shows details of these results around the collimation region. Losses seen at the triplet magnet upstream of the collimation system are due to some of the halo protons that were scattered by the collimators and managed to travel around the machine for nearly a full turn. These protons face an aperture bottleneck at the triplet quadrupoles since β^* in IR8 is squeezed down to 0.9 m for higher luminosity. This also explains the peaks in Figure 7 for IR2 and IR6 (low β^* insertions too, see Table 1), both for the BLM signal and the simulated loss maps. It is also worth noticing that the BLM data can be much higher than the simulated loss peaks in IR8. In Figure 8, the BLM signal around 700m is dominated by the showering of secondary particles from the collimator jaws, while the tracking tools are designed to show the locations where the protons scattered by the collimation system are lost. One would then have to use some additional numerical models to generate the showers induced by the proton-matter inelastic interactions in each collimator jaw, and include the results in the simulated loss maps.

When looking at the loss pattern given by the BLM data, there are a few locations that are not predicted by the simulations. Figure 9 shows the details of the beam losses around IR10. The peak in the loss monitor signal around 1320 m corresponds to losses taking place at an abort kicker magnet (Blue Kicker Abort, BKA): these losses are known to occur during regular RHIC operations and are not collimation related. Losses detected by BLMs at a focusing quadrupole (labeled QF in Figure 9) in the arc downstream of IR10 are still investigated.

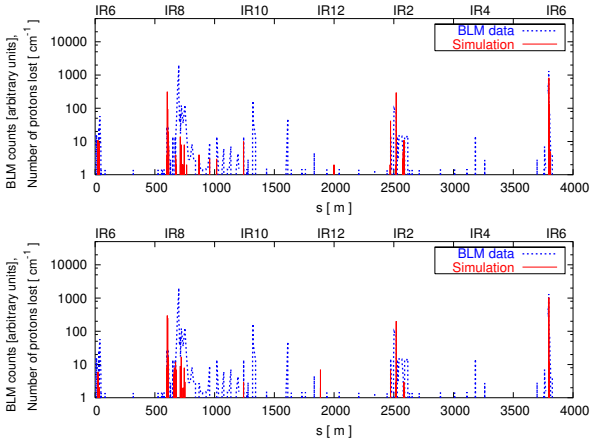

Figure 7: Comparison between RHIC BLM measurements and simulated loss maps due to beam impacts on the horizontal (top) and vertical (bottom) primary collimator jaw for the Blue beam, circulating from left to right. The solid lines show the number of protons lost per 10 cm bins obtained from the tracking tools; the dashed lines represent the BLM signal as measured in the machine.

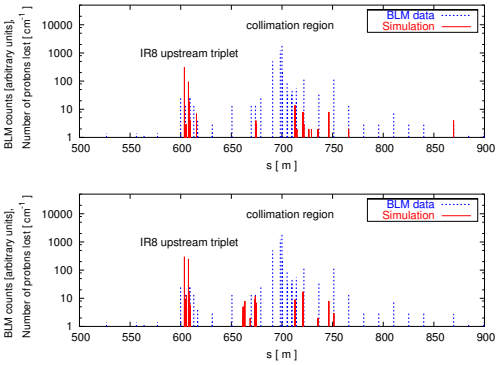

Figure 8: Zoom of the simulated loss maps and BLM signal around the collimation region following the Blue beam. In addition to the peaks downstream of the collimators, beam losses can be spotted at the triplet magnet upstream of the collimators.

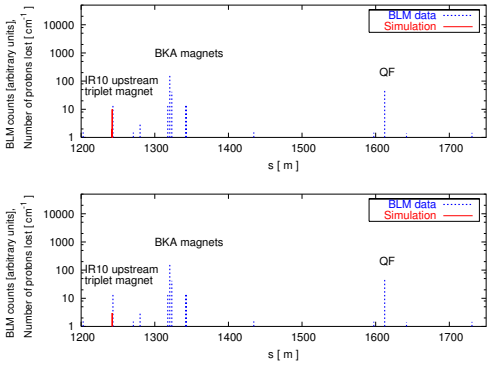

Figure 9: Zoom of the simulated loss maps and BLM signal around IR10 following the Blue beam. Beam losses can be spotted at the triplet magnet upstream of IP10 and at the Blue Kicker Abort (BKA) magnet.

CONCLUSION

Simulations were performed for the RHIC collimation system using machine optics given by live measurements. With an updated aperture model, it was possible to compare the predicted proton loss locations with the measured BLM signal obtained with a dedicated set of collimator positions: there is a good agreement between the tracking tools and the real data on the locations of the losses around the machine. On that aspect, the code is successfully benchmarked.

Work is currently ongoing to check for the quantitative agreement between predicitons and measurements. This includes running the previous simulations with higher statistics as well as the analysis of the inelastic scattering processes taking place in the collimator jaws, that could explain the discrepancy in the amplitude of the losses in regions located a couple hundred meters downstream of the collimation insertion.

REFERENCES

[1] "LHC Design Report", Volume I, Ch. 18, CERN, 2004

[2] http://www.agsrhichome.bnl.gov/NT-share/rhicdm/00_toc1i.htm, BNL, October 2000

[3] G. Robert-Demolaize, R. Assmann, S. Redaelli, F. Schmidt: "A new version of SixTrack with collimation and aperture interface", Proc. PAC 2005.

[4] G. Robert-Demolaize: "Design and performance optimization of the LHC collimation system", CERN-LHC-PROJECT-REPORT-981, 2006.

[5] S. Redaelli: "LHC aperture and commissioning of the collimation system", Proc. Chamonix 2005.

[6] Raymond Patrick Fliller III: "The Crystal Collimation System of the Relativistic Heavy Ion Collider", Ph. D. thesis, State University of New York at Stony Brook, see also BNL CAD/AP Note C-A/AP/#170, 2004.

INFLUENCE OF UNIFORM ELECTRON CLOUDS ON THE COUPLING IMPEDANCE*

A.M. Al-Khateeb, Yarmouk University, Irbid, Jordan,
R.W. Hasse, O. Boine-Frankenheim, GSI Darmstadt, Darmstadt, Germany

Abstract

The contribution to the longitudinal coupling impedance from an electron cloud in the form of a uniformly distributed non-neutral plasma of electrons is investigated analytically. The beam-pipe is assumed to be of circular cross section with a thick resistive wall. The beam charge distribution is uniform in the transverse direction. The electron contribution to the charge and current densities are obtained from the collective electron response to the beam passage through the pipe. We obtain the radial differential equation governing the field variation in the presence of the electron background and a general closed formula for the longitudinal coupling impedance is derived. The depletion of the coupling impedance with the density of the electron cloud is discussed for the examples of GSI SIS-18 and SIS-100, CERN SPS and PS, and the KEKB LER, and conditions for the minimum excitation frequency as a function of the electron density are derived. Furthermore, the case of over-dense plasmas is also studied.

INTRODUCTION

During the recent years clouds of electrons have been found in circular accelerators with high energy high current ion beams which evidently are created by protons (or ions) hitting the walls in the dipoles or elsewhere. In the walls avalanches of electrons are generated which give rise to clouds of electrons. The ion charges disturb the original beam and give rise to instabilities.

Examples where such instabilities were observed are the KEKB Low Energy Ring (LER) [1], and the CERN Proton Synchrotron (PS) [2] and Super Proton Synchrotron (SPS) [3], and at the Relativistic Heavy Ion Collider (RHIC) [4]. For a review see Zimmermann [5]; the CERN webpage on electron clouds (EC) [6], and for recent simulations see ref. [7, 8]. The instabilities manifest themselves in single bunches due to multiple transitions of a bunch through the EC [5, 7]. In the SPS the single-bunch instability affects the last two thirds of the batch. Also, vertical instabilities have been observed of single bunch nature, its growth rate depending on intensity. The vertical instability seems to be enhanced by the machine impedance around $600\cdots800$ MHz. On the other hand, the wake-field generated by the EC may influence the low density region between heads and tails of the bunches, see e.g. ref. [8]. This, in turn, results in a fast horizontal coupled bunch instability of low order that may be cured by a feedback system.

[1]Proc. Beam07 CARE-HHH-APD Workshop, CERN, 1-5 Oct. 2007

In the SPS as well as in the LER electron cloud densities of $n_{\rm ec} = 10^{11}\cdots10^{12}$ m^{-3} have been detected. The EC, however, not only generates a wake-field but it also modifies the impedance coming from coupling of the beam to the resistive wall.

In the present paper we study this effect by simply assuming a homogeneous EC of density $n_{\rm ec}$ spreading all over the interior of the aperture which holds the charged particle beam. Here the EC acts like shielding the beam which, in turn, gives rise to a depletion of the coupling impedances. This depletion then is calculated as a function of the electron cloud plasma frequency $\omega_{\rm ec}$, namely,

$$\omega_{\rm ec} = \sqrt{\frac{n_{\rm ec}e^2}{m_{\rm e}\epsilon_0}}\ , \qquad (1)$$

where $m_{\rm e}$ is the electron mass, e is the elementary charge, and ϵ_0 is the permittivity of free space. For the electron densities given above the electron plasma frequencies are of the order of $f_{\rm ec} = \omega_{\rm ec}/2\pi$ = $1\cdots10$ MHz. It turns out that this is effect is governed by the ratio $\omega_{\rm ec}/\omega$ with ω being the excitation frequency. The results are applied to the circular machines CERN SPS and PS, KEKB LER and GSI SIS-18 and the proposed SIS-100. As a stability criterion for low energy machines $\omega_{\rm ec}/\omega \lesssim 0.5$ must be fulfilled but for the high energy machines $\omega_{\rm ec}/\omega \ll 1$ is necessary. Qualitatively, hence, we see that for low frequencies the appearance of instabilities is favoured by electron clouds. In the next sections we will study this effect quantitatively.

ELECTRON CLOUD CONTRIBUTION TO THE SOURCES

Consider the motion of a rotationally symmetric lamina of particles of radius a and total charge Q in a smooth cylindrical pipe of radius b and circumference L. The beam moves in this nonneutral plasma with a constant longitudinal velocity $\vec{v}_b = \beta c\hat{z}$ along the z axis through a uniform electron background of density $n_{\rm ec}$ electrons per unit volume which fills the whole pipe up to radius b, each of mass $m_{\rm e}$, and of charge $-e$. The total (effective) current $\vec{J}$ and charge $\rho(\vec{r},t)$ densities are defined as follows,

$$\vec{J}(\vec{r},t) = \vec{j}_0 + \vec{j}_{\rm e}\ , \qquad (2)$$
$$\rho = \rho_0 + \rho_{\rm e}\ .$$

In following along the lines Mulsers oscillator model [9], the current $\vec{j}_0$ and charge ρ_0 densities in eq. (2) are those associated with the streaming motion of the beam particles, whereas $\vec{j}_{\rm e}$ and $\rho_{\rm e}$ are the collective current and charge

densities due to the coupling between the background electrons and the excited electric fields in the cylindrical pipe. For cold, collisionless, unmagnetized electron background, the electron equation of motion in the effective electromagnetic field is,

$$\frac{d\vec{j}_{\rm e}}{dt} = \frac{e^2 n_{0ec}}{m_{\rm e}}\,\vec{E} - \frac{e}{m_{\rm e}}\,\vec{j}_{\rm e}\times\vec{B}\,. \tag{3}$$

Fourier transforming in time, for the transverse magnetic (TM) modes of lower order $\ell = 0$ corresponding to axially symmetric transverse beam charge distribution, and by ignoring the $\vec{E}\times\vec{B}$ drift of the electron background, we obtain the following simple expression for the effective induced EC current density, namely,

$$\vec{j}_{\rm e} = \frac{i\omega e^2 n_{0ec}}{m_{\rm e}\omega^2}\,\vec{E}\,, \tag{4}$$

$$\frac{\partial^2\rho_{\rm e}}{\partial t^2} + \vec{\nabla}\cdot\frac{d\vec{j}_{\rm e}(\vec{r},t)}{dt} = \frac{\partial^2\rho_{\rm e}}{\partial t^2} + \frac{e^2 n_{0ec}}{m}\,\vec{\nabla}\cdot\vec{E}(\vec{r},t) = 0\,.$$

Upon using Faraday's and Ampere's laws, the wave equations satisfied by the magnetic induction $\vec{B}$ and the electric field $\vec{E}$ in nonconducting media with $\epsilon = \epsilon_0$ and $\mu = \mu_0$ are,

$$\nabla^2\vec{B}(\vec{r},t) - \frac{1}{c^2}\frac{\partial^2\vec{B}(\vec{r},t)}{\partial t^2} = -\mu_0\vec{\nabla}\times\vec{J}(\vec{r},t), \tag{5}$$

$$\nabla^2\vec{E}(\vec{r},t) - \frac{1}{c^2}\frac{\partial^2\vec{E}(\vec{r},t)}{\partial t^2} = \mu_0\frac{\partial\vec{J}(\vec{r},t)}{\partial t} + \frac{\vec{\nabla}\rho(\vec{r},t)}{\epsilon_0}\,.$$

For a beam with uniform distribution moving along z, and using $\omega = k_z v$ we get

$$\vec{J}(r,z,\omega) = \left(\frac{Q}{\pi a^2}\,e^{ik_z z}\,\hat{z} + i\frac{e^2 n_{0ec}}{m\omega}\,\vec{E}(r,z,\omega)\right), \tag{6}$$

$$\rho(r,z,\omega) = \left(\frac{Q}{\pi a^2\beta c}\,e^{ik_z z} + \frac{e^2 n_{0ec}}{m\omega^2}\,\vec{\nabla}\cdot\vec{E}(r,z,\omega)\right),$$

with $E_z(r,z,\omega)$ having the same z dependence such that $E_z(r,z,\omega) = E_z(r,\omega)\;e^{ik_z z}$. as well as $\rho(r,z,\omega)$ and $J_z(r,z,\omega)$. Due to the axial symmetry, the only non-vanishing field components excited by the beam are $E_z(r,\omega)$, $E_r(r,\omega)$ and $B_\theta(r,\omega)$. Fourier transforming eq. (5) and by accounting for TM modes only we get,

$$\left(\nabla_\perp^2 - k_z^2\right)\vec{E}(r,z,\omega) + \frac{\omega^2}{c^2}\,\vec{E}(r,z,\omega) =$$

$$\frac{ik_z Q\,e^{ik_z z}}{\epsilon_0\pi a^2\beta c\gamma_0^2}\,\hat{z} - i\omega\mu_0\vec{j}_{\rm e} + \frac{\omega_{\rm ec}^2}{\omega^2}\,\vec{\nabla}\left[\vec{\nabla}\cdot\vec{E}(r,z,\omega)\right], \tag{7}$$

where $\nabla_\perp^2$ is the transverse Laplacian operator, and γ is the relativistic factor defined as $\gamma_0^{-2} = 1-\beta^2$. By making use of the Maxwell's curl equations, the relations between the longitudinal electric field component $E_z(r,z,\omega)$ and the transverse components $E_r(r,z,\omega)$ and $B_\theta(r,z,\omega)$ are as follows,

$$E_r(r,\omega) = \frac{-i}{k_z\left(1-\beta^2\varepsilon_{\rm ec}\right)}\,\frac{{\rm d}E_z}{{\rm d}r}\,, \tag{8}$$

$$B_\theta(r,\omega) = -\frac{i\omega\mu_0\epsilon_0\epsilon_{\rm ec}}{k_z^2\left(1-\beta^2\varepsilon_{\rm ec}\right)}\,\frac{dE_z}{{\rm d}r}\,,$$

where the longitudinal dielectric function

$$\varepsilon_{\rm ec} = 1 - \frac{\omega_{\rm ec}^2}{\omega^2} \tag{9}$$

has been introduced. the z-component of $\vec{\nabla}[\vec{\nabla}\cdot\vec{E}(r,z,\omega)]$ on the right hand side of eq. (7) is rewritten in cylindrical coordinates as

$$\frac{\partial}{\partial z}\left[\vec{\nabla}\cdot\vec{E}(r,z,\omega)\right] = \left[\frac{1}{1-\beta^2\varepsilon_{\rm ec}}\frac{\partial^2}{\partial r^2} - k_z^2\right]E_z(r,\omega)\;e^{ik_z z}.$$

Also, using $\omega = k_z\beta c$ eqs. (7) for the excited electric field component E_z become,

$$\left(1 - \frac{\omega_{\rm ec}^2}{\omega^2}\,\frac{1}{1-\beta^2\varepsilon_{\rm ec}}\right)\frac{{\rm d}^2E_z(r,\omega)}{{\rm d}r^2} + \frac{1}{r}\frac{{\rm d}E_z(r,\omega)}{{\rm d}r} - \frac{k_z^2\varepsilon_{\rm ec}}{\gamma_0^2}\,E_z(r,\omega) = \frac{ik_z Q\Theta(a-r)}{\epsilon_0\pi a^2\beta c\gamma_0^2}, \tag{10}$$

where Θ stands for Heaviside unit step function. Within the conducting wall of coductivity S, we have the following equation for E_z,

$$\left[\frac{{\rm d}^2}{{\rm d}r^2} + \frac{1}{r}\frac{\rm d}{{\rm d}r} - \frac{k_z^2}{\underline{\gamma}^2}\right]E_z(r,\omega) = 0\,, \quad b\le r<\infty, \tag{11}$$

where the modified relativistic factor due to the conductivity reads

$$\underline{\gamma} = \frac{\gamma_0}{\sqrt{1 - i\mu_0\omega S\gamma_0^2/k_z^2}}\,. \tag{12}$$

SOLUTION OF THE DIFFERENTIAL EQUATION

To solve the homogeneous part of eq. (10), we follow ref. [10]. Introducing the following parameters,

$$\alpha = \frac{\omega_{\rm ec}^2}{\omega^2}\,\frac{1}{1-\beta^2\varepsilon_{\rm ec}},$$

$$\nu = \frac{\alpha/2}{1-\alpha},$$

$$\sigma_{\rm ec}^2 = \frac{k_z^2}{\gamma_0^2}\,\frac{\varepsilon_{\rm ec}}{1-\alpha} = \frac{k_z^2}{\gamma_0^2}\,\varepsilon_{\rm ec}(2\nu+1)\,,$$

and assuming a solution of the form $E_z = r^{-\nu}\,V(r)$, the homogeneous part of eq. (10) reduces to the differential equation of the modified cylindrical Bessel equation for $V(r)$, namely,

$$r^2V''(r) + \left(r - \sigma_{\rm ec}^2 r^2 - \nu^2\right)\,V(r) = 0\,. \tag{13}$$

Accordingly, the overall regular general solutions are expressed in terms of first kind I_ν and second kind K_ν modified cylindrical Bessel functions as follows,

$$E_z(r,\omega) = \begin{cases} A_1\, r^{-\nu}\, I_\nu(\sigma_{\rm ec} r) - i\dfrac{Q}{\pi a^2 \epsilon_0 \varepsilon_{\rm ec} k_z \beta c} & 0 \le r \le a \\ A_2\, r^{-\nu}\, I_\nu(\sigma_{\rm ec} r) + A_3\, r^{-\nu}\, K_\nu(\sigma_{\rm ec} r) & a \le r \le b \\ A_4\, K_0(\underline{\sigma} r) & b \le r < \infty \end{cases}$$

whith $\underline{\sigma} = k_z/\underline{\gamma}$.

The electromagnetic field components $E_r^{(\rm p,co)}$ and $B_\theta^{(\rm p,co)}$ in plasma and conducting wall regions are to be obtained from the corresponding $E_z^{(\rm p,co)}$ as follows,

$$E_r^{(\rm p)}(r,\omega) = \frac{1}{ik_z\,(1-\beta^2\epsilon_{\rm ec})}\,\frac{{\rm d}E_z^{(\rm p)}}{{\rm d}r}\ ,$$
$$B_\theta^{(\rm p)}(r,\omega) = \frac{\omega\mu_0\epsilon_0\epsilon_{\rm ec}}{ik_z^2\,(1-\beta^2\varepsilon_{\rm ec})}\,\frac{{\rm d}E_z^{(\rm p)}}{{\rm d}r}\ , \qquad (14)$$

$$E_r^{(\rm co)}(r,\omega) = \frac{\underline{\gamma}^2}{ik_z}\,\frac{{\rm d}E_z^{(\rm co)}}{{\rm d}r}\ ,$$
$$B_\theta^{(\rm co)}(r,\omega) = \frac{\omega\mu_0\epsilon_0\underline{\gamma}^2}{ik_z^2}\,\frac{{\rm d}E_z^{(\rm co)}}{{\rm d}r}\ . \qquad (15)$$

Accordingly, the field component E_r becomes as follows,

$$E_r(r,\omega) = \begin{cases} \dfrac{\sigma_{\rm ec}\, r^{-\nu}}{ik_z(1-\beta^2\varepsilon_{\rm ec})}\, A_1\, I_{\nu+1}(\sigma_{\rm ec} r) & r \le a\ , \\ \dfrac{\sigma_{\rm ec}\, r^{-\nu}}{ik_z(1-\beta^2\varepsilon_{\rm ec})} \times & \\ [A_2\, I_{\nu+1}(\sigma_{\rm ec} r) - A_3\, K_{\nu+1}(\sigma_{\rm ec} r)] & a \le r \le b \\ i\underline{\gamma}\, A_4\, K_1(\underline{\sigma} r). & b \le r < \infty \end{cases}$$

The integration constants are determined from the boundary conditions at $r = a$ and $r = b$, namely, the continuity of E_z and B_θ at $r = a$ and at $r = b$. Upon applying these boundary conditions, we obtain the following integration constants,

$$A_1 = -\left[\frac{K_{\nu+1}(\sigma_{\rm ec} a)}{I_{\nu+1}(\sigma_{\rm ec} a)} + \frac{K_\nu(\sigma_{\rm ec} b) - \eta_{\rm ec}\, K_{\nu+1}(\sigma_{\rm ec} b)}{I_\nu(\sigma_{\rm ec} b) + \eta_{\rm ec}\, I_{\nu+1}(\sigma_{\rm ec} b)}\right] A_3,$$
$$A_3 = \frac{Q a^\nu \sigma_{\rm ec} a}{i\pi a^2 \epsilon_0 \varepsilon_{\rm ec} k_z \beta c}\, I_{\nu+1}(\sigma_{\rm ec} a),$$
$$\eta_{\rm ec} = \frac{K_0(\underline{\sigma} b)}{K_1(\underline{\sigma} b)}\,\frac{\omega\epsilon_0\varepsilon_{\rm ec}}{i\underline{\gamma}(S - i\omega\epsilon_0)}\,\frac{\sigma_{\rm ec}}{k_z(1-\beta_0^2\varepsilon_{\rm ec})},$$
$$\eta = \frac{\omega\epsilon_0\gamma_0}{i\underline{\gamma}\,(S - i\omega\epsilon_0)}.$$

COUPLING IMPEDANCE

The current densities are defined in equation (6),

$$j_{z,b}(r,\omega) = \frac{Q}{\pi a^2}\ ,$$
$$j_{z,e}(r,\omega) = \frac{i\epsilon_0\,\omega_{\rm ec}^2}{\omega}\,E_z(r,\omega)\ ,$$
$$j_{r,e}(r,\omega) = \frac{i\epsilon_0\,\omega_{\rm ec}^2}{\omega}\,E_r(r,\omega). \qquad (16)$$

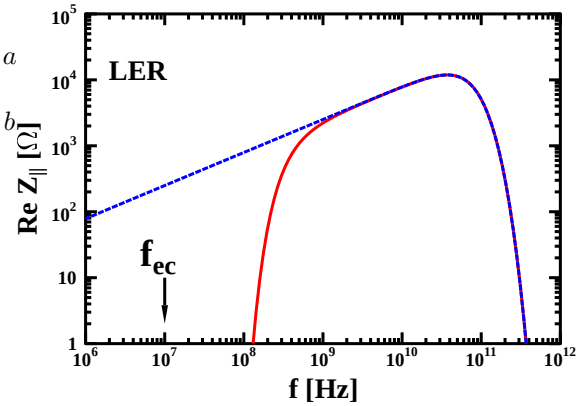

Figure 1: Dependence of the real part of the longitudinal resistive wall impedance on the excitation frequency for $f_{\rm ec} = 10$ MHz. (KEKB LER). The blue dotted line shows the impedance without electron cloud and the full red line with EC.

The longitudinal coupling impedance for the beam monopole source term is obtained as follows,

$$Z_\parallel(\omega) = -\frac{1}{Q^2}\int_\Omega E_z(\vec{r},\omega)\cdot j_b^*(\vec{r},\omega)\,{\rm d}^3 r$$
$$= -\frac{2L}{Qa^2}\int_0^a \left[A_1\frac{I_\nu(\sigma_1 r)}{r^\nu} - i\frac{Q}{\pi a^2\epsilon_0\varepsilon_{\rm ec}k_z\beta c}\right] r{\rm d}r, \quad (17)$$

where L is the circumference of the ring. This integral can be solved to yield the closed form expression

$$Z_\parallel(\omega) = -\frac{2L}{Qa^2}\left[A_1\left(\frac{I_{\nu-1}(\sigma_{\rm ec}a)}{\sigma_{\rm ec}a^{\nu-1}} - \frac{\sigma_{\rm ec}^{\nu-2}}{2^{\nu-1}\Gamma(\nu)}\right) - i\frac{Q}{\pi a^2\epsilon_0\varepsilon_{\rm ec}k_z\beta c}\,\frac{a^2}{2}\right]. \qquad (18)$$

For $\omega_{\rm ec} = 0$, the impedance above reduces into the known form [10]

$$Z_\parallel(\omega) = i\,\frac{nZ_0}{2\beta\gamma^2}\,\frac{4\gamma_0^2}{k_z^2 a^2}\left[1 - 2I_1^2(\sigma_0 a)F\right] \qquad (19)$$

with the constant

$$F = \frac{K_1(\sigma_0 a)}{I_1(\sigma_0 a)} + \frac{K_0(\sigma_0 b) - \eta\dfrac{K_0(\underline{\sigma} b)}{K_1(\underline{\sigma} b)}K_1(\sigma_0 b)}{I_0(\sigma_0 b) + \eta\dfrac{K_0(\underline{\sigma} b)}{K_1(\underline{\sigma} b)}I_1(\sigma_0 b)}.$$

NUMERICAL EXAMPLES AND DISCUSSION

The longitudinal coupling impedances above are calculated for various circular machines with idealized machine parameters and different strengths of the electron cloud density. In Fig. 1 at the example of the KEKB LER with the assumed electron plasma frequency of 10 MHz is shown the real part of the coupling impedance with (full red

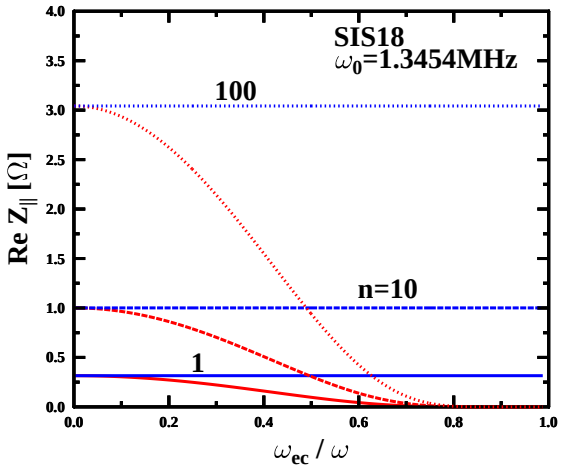

Figure 2: Dependence of the real part of the longitudinal resistive wall impedance on the ratio of electron cloud plasma frequency to excitation frequency $\omega = n\omega_0$ (GSI–SIS18). The blue lines show the impedance for $\omega_{ec} = 0$ and n indicates the harmonic number.

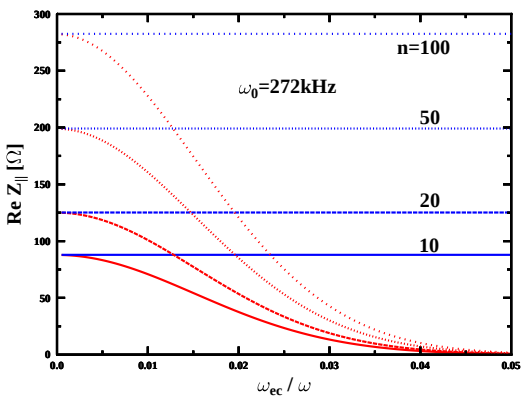

Figure 3: Same as Fig. 2 but for the CERN SPS. Note the change of scale of the abscissa.

line) and without (blue dotted line) presence of the electron cloud. The coupling impedance is depleted for all excitation frequencies up to about 500 MHz, i.e. almost two orders of magnitude above the EC plasma frequency. Similarly, in Fig. 2 for SIS18 and Fig. 3 for SPS is shown the dependence of the real part of the longitudinal coupling impedance on the electron cloud plasma frequency ω_{ec} (or $f = \omega_{ec}/2\pi$) for various excitation frequencies $f = nf_0$, where n is the harmonic number and f_0 is the revolution frequency. Due to the dependence of the dielectric function in eq. (9) on ω_{ec}/ω (or f_{ec}/f) this ratio is chosen. They exhibit a decrease of the real part of the resistive–wall impedance with increasing EC density due to the plasma shielding of the wall, and therefore a reduction in the current induced by the beam in the wall of beam–pipe. Equivalently, the coupling impedance increases with increasing excitation frequency.

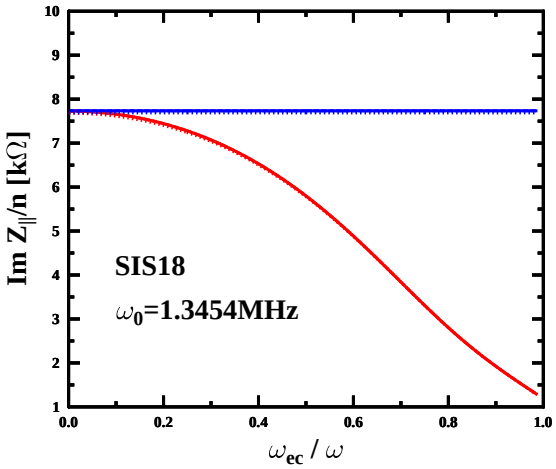

Figure 4: Comparison between the imaginary parts of the longitudinal resistive wall impedance per harmonic (GSI–SIS18) with and without electron cloud. Same notation as in Fig. 2.

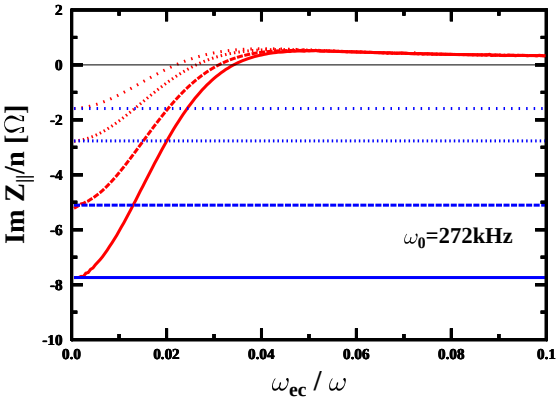

Figure 5: Imaginary part of the longitudinal resistive wall impedance per harmonic (CERN SPS).

Analogously, in Fig. 4 for SIS18 and Fig. 5 for SPS are shown the imaginary parts. In contrast to the real part, the total imaginary part consists of two parts, the resitive wall and the space charge $Z_{||}(\omega_{ec} = 0, S = \infty)$ contributions. Here the total imaginary part of the coupling impedance for SIS18 (space charge + resistive–wall) is positive according to our physical conventions (negative imaginary in engineering conventions), and therefore the EC as a whole acts as a capacitive medium for all frequencies such that $\omega > \omega_{ec}$. Its resistive wall part, however, is negative, thus inductive.

For excitation frequencies below the plasma frequency the EC will act as an inductive medium with negative imaginary part. For the SPS, on the other hand, the imaginary part is negative and turns capacitive only in the presence of strong electron fields.

Using a simple analogy, we can explain the above properties of the impedance in the presence of the EC. The total current in the electron cloud region is composed of dis-

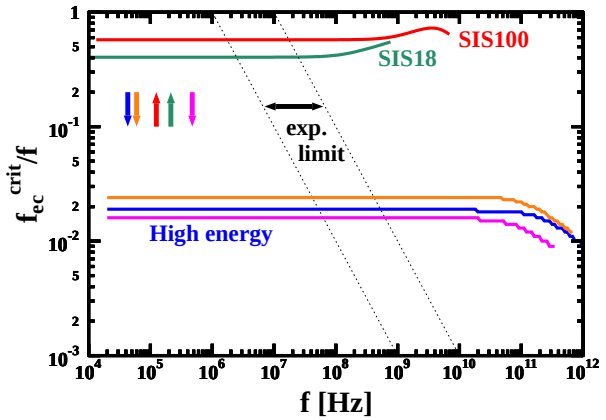

Figure 6: Fraction of critical electron cloud frequency where the longitudinal resistive wall impedance is half depleted as compared to the excitation frequency. The dahed lines idicates the measured value of electron cloud density of 10^{12} m^{-3} and 10^{11} m^{-3} in the SPS and LER. The arrows point to the respective revolution frequencies.

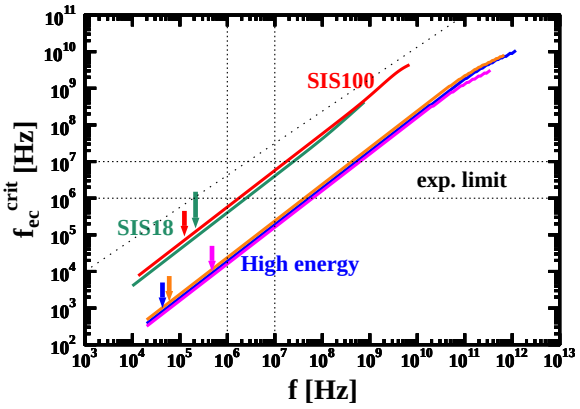

Figure 7: Same as Fig. 6 but critical electron cloud frequency vs. frequency

placement and EC currents (plasma), respectively,

$$\vec{J}(\vec{k},\omega) = -i\,\omega\,C_{\rm ec}\,\vec{E} - \frac{1}{i\omega\,L_{\rm ec}}\,\vec{E}.$$

Here $C_{\rm ec} = \epsilon_0$ ist the capacitance per unit length and $L_{\rm ec} = m_{\rm e}/n_{\rm ec}e^2$ is the inductance times unit length. We introduce the Plasma (Electric) Impedivity $\hat{z}_{\rm e}$ as follows,

$$\vec{E} = \hat{z}_{\rm e}\,\vec{J},\quad \hat{z}_{\rm e} = -\frac{i\omega\,L_{\rm ec}}{1-\omega^2\,C_{\rm ec}L_{\rm ec}},$$
$$\omega_{\rm ec} = \frac{1}{\sqrt{L_{\rm ec}C_{\rm ec}}} = \sqrt{n_{\rm ec}e^2/m\epsilon_0}.$$

As can be seen from the expression for $\hat{z}_{\rm e}$, the EC act as a capacitive plasma for $\omega > \omega_{\rm ec}$, and as inductive plasma for $\omega < \omega_{\rm ec}$. By ignoring Joule heating of the electron cloud (energy loss due to collisions), there will be a total cancellation between displacement and plasma currents at mode frequencies such that $\omega = \omega_{\rm ec}$, namely, $\vec{J}(\vec{r},\omega) = \vec{J}_D + \vec{J}_{\rm ec} = 0$.

There is a striking difference between the results for the low energy machines SIS18, SIS100 and the high energy machines SPS, PS, and LER. namely that the latter deplete their impedance for EC plasma frequencies already of the order of 2% of the excitation frequency whereas this ratio is about 50% for the SIS18. This behaviour is studied systematically for all machines under consideration and the critical ratios $\omega_{\rm ec}^{\rm crit}/\omega = f_{\rm ec}^{\rm crit}/f$ are extracted where $\omega_{\rm ec}/\omega$ fall of to 50% from their original values. These ratios are shown in Fig. 6. Experimental EC densities measured in SPS and LER are in the range $n_{\rm ec} = 10^{11}\cdots10^{12}$ m^{-3}, indicated by the dotted lines in Figs. 6, 7. This means that instabilities in the low energy machines are expected for frequencies below $2\cdots20$ MHz whereas in the high energy machines instabilities are expected in a much wider frequency range below $50\cdots500$ MHz. Fig. 7 shows the same as Fig. 6 but as the critical electron cloud density vs. excitation frequency.

SURFACE-WAVE-SUSTAINED MODES

Electromagnetic waves cannot propagate in an overdense plasma if the plasma frequency is larger than the excitation frequency, $\omega_{\rm ec} > \omega$, i.e. when the beam is completely shielded by the electromagnetic field of the electron cloud. Then the waves are reflected at the conducting surface due to the skin effect and become evanescent waves. Their penetration depth corresponds roughly to the skin depth $\delta_s \approx c(\omega_{\rm ec}^2-\omega^2)^{-1/2}$. This may give rise to heating a plasma rather than damping it. The waves then do not travel any more in the radial direction but rather propagate along the plasma surface. The wave energy is then transferred to the plasma by the evanescent wave which enters the plasma perpendicular to its surface and decays exponentially with the skin depth. Due to the heating process, the real part of the impedance becomes negative. This transfer mechanism allows to support over-dense plasmas with electron plasma frequencies beyond the excitation frequency. For even higher excitation frequencies, $\omega_{\rm ec}/\omega > \sqrt{2}$, these waves do not propagate any more along the surface bur are rather overdamped in the longitudinal direction. Such overdamped surface waves have been studied e.g. in ref. [11].

Our analysis for a relatively weak beam ($\gamma = 1.0122$) in SIS18 shown in Figs. 8,9 indicates that one can distinguish three regions of a beam embedded in an overdamped plasmas: (i) No waves exist for $1 < \omega_{\rm ec}/\omega \lesssim 1.05$; (ii) In the intermediate region of evanescent waves, $1.05 \lesssim \omega_{\rm ec}/\omega \lesssim \sqrt{2}$ the real part of the impedance is negative and the imaginary part is positive, thus capacitive due to the strong magnetic field; (iii) Overdamped surface waves $\omega_{\rm ec}/\omega > \sqrt{2}$ with positive real part and negative imaginary part exist for $\omega_{\rm ec}/\omega > \sqrt{2}$ in analogy to the case of $\omega > \omega_{\rm ec}^{\rm crit}$ of the previous chapter The latter two regions are separated by a resonance transition. Due to the presence of the weak beam the critical value $\sqrt{2}$ is only shifted slightly. An case of more intense beams it is shifted substantially to higher values.

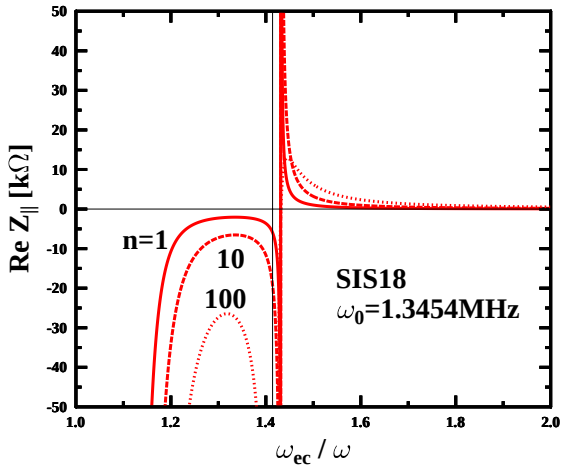

Figure 8: Same as Fig. 2 but for $\omega_{\rm ec} > \omega$. The thin vertical line points to the ower limit of surface waves $\omega_{\rm ec}/\omega = \sqrt{2}$ (SIS18).

SUMMARY AND OUTLOOK

The effect of shielding of a beam by a homogeneous electron cloud on the coupling impedance has been calculated as a function of the electon cloud density. It has been found that the depletion of the coupling impedance is complete not as expected at the excitation frequency corresponding to the plasma frequency of the EC but, for high energy circular machines, already for much lower electron cloud densities.

The theory does not yet account for resonance effects at the singularity at $\omega = \omega_{\rm ec}$. The calculations, hence, must be extended to include Joule heating by losses from the imaginary part of ω and to small excitation frequencies $\omega < \omega_{\rm ec}$.

The same theory can also serve for the calculation of modifications of the electric field of the beam due to the presence of an electron cooler. The electron beams of present electron coolers generate amperes of current and, hence, shield the beam substantially.

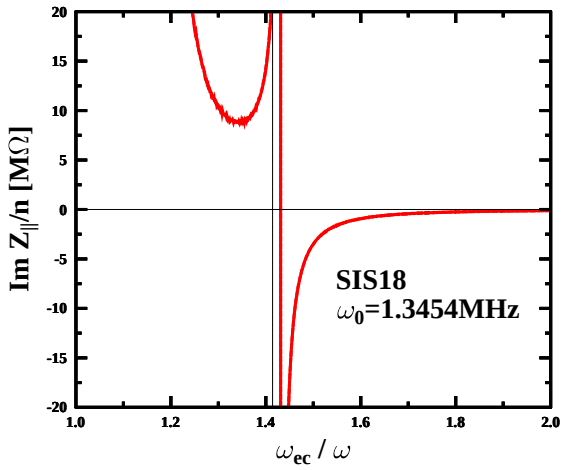

Figure 9: Same as Fig. 4 but for $\omega_{\rm ec} > \omega$ (SIS18).

ACKNOWLEDGMENTS

One of us (A.A.) thanks the Fair Accelerator Theory Group of GSI Darmstadt for frequent invitations. He also likes to thank the Council of Scientific Research of Yarmouk University, Irbid, Jordan, for supporting this work by the grant 8/2007. He also likes to thank the Arab Fund for Economic and Social Development (AFESD, State of Kuwait) for the financial support of his stay at GSI-Darmstadt (Germany) via their Fellowship Award. We also acknowledge the support of the European Community *Research Infrastructures Action* under the FP6 programme: Structuring the European Research Area - Specific Support Action - Design Study (contract 515873 - DIRAC-secondary-Beams).

REFERENCES

[1] F. Zimmermann, *Electron-Cloud Studies for the Low Energy Ring of KEKB*, CERN-SL-Note-2000-004 AP.

[2] M. Giovannozzi, Métral, G. Rumolo, and F. Zimmermann, Phys. Rev. ST Accel. Beams **6** (2003) 010101.

[3] G. Rumolo, A. Z. Ghalam, T. Katsouleas, C. K. Huang, V. K. Decyk, C. Ren, W. B. Mori F. Zimmermann, and F. Ruggiero, Phys. Rev. ST Accel. Beams **6** (2003) 081002.

[4] W. Fischer, J.M. Brennan, M. Blaskiewicz, and T. Satogata, Proc. ECLOUD'02 Workshop, CERN, 15-18 April 2002, CERN Yellow Report CERN-2002-001.

[5] F. Zimmermann, Phys. Rev. ST Accel. Beams **7** (2004) 124801.

[6] *http://ab-abp-rlc.web.cern.ch/ab-abp-rlc-ecloud.*

[7] G. Rumolo and F. Zimmermann, Phys. Rev. ST Accel. Beams **5** (2002) 121002.

[8] G. Rumolo and Métral, Proc. 9th Int. Computational Accelerator Physics Conference, Oct. 2-6, 2006, Chamonix Mont-Blanc, France, ICAP06, *http://accelconf.web.cern.ch, MOA2IS02.*

[9] P. Mulser, *High Power Laser-Matter Interaction*, Springer, Berlin 2006

[10] A.M. Al - Khateeb, O. Boine-Frankenheim, R.W. Hasse, and I. Hofmann, Phys. Rev. E **71**, 026501-1 (2005).

[11] A. Boardman, *Electromagnetic Surface Waves*, Wiley, N.Y. 1982.

BENCHMARK OF ACCSIM-ORBIT CODES FOR SPACE CHARGE AND ELECTRON-LENS COMPENSATION

Masamitsu Aiba, CERN, Geneva, Switzerland

Abstract

Numerical simulation is a possible approach to evaluate and to understand space charge effects in the CERN injector chain for the LHC. Several codes to simulate space charge effects have been developed, and we performed a benchmark of ACCSIM [1] and ORBIT [2] in this study. The study is highly motivated since beam losses and/or deteriorations in beam quality due to space charge effects are not negligible or sometimes considerable in the complex, especially in the Proton Synchrotron Booster. We also discuss a possibility of compensation of space charge effects by applying "electron-lens".

INTRODUCTION

Beam losses and/or deteriorations in beam quality due to space charge effects are not negligible or sometimes considerable in the CERN injector chain, especially in the Proton Synchrotron Booster (PSB). A lot of efforts both from experimental side [3] and analytical/simulation side [4] have been made in order to ensure the best use of injectors toward the LHC. Historically in CERN, the ACCSIM code has been employed for space charge simulation studies. A benchmark study using the ORBIT code has been started to confirm the results from ACCSIM and to profit from the advantages of ORBIT such as the capability of parallel processing. Although this kind of benchmark has been already performed [5], it is still worth to benchmark the two codes using the specific machine parameters of the PSB in which the tune spread is unusually large (up to ~0.5 for high intensity beams and more than 0.3 for LHC type beams discussed here) and overlap with the low order resonances.

We also discuss the compensation of space charge effects by applying a so-called "electron-lens". A new module for ORBIT to introduce electron-lens has been developed. Preliminary results with the module are presented and discussed.

BENCHMARK

Benchmark condition

For the benchmark, a simplified PSB lattice that has 16 identical cells excluding injection bumps is employed. No field error and no alignment error are assumed in the lattice. We assume a proton beam with the kinetic energy of 160 MeV and the intensity of 3.25×10^{12}, which will be provided by the coming Linac4. The beam parameters are summarized in Table 1.

Both ACCSIM and ORBIT are based on the so-called Particle-In-Cell (PIC) method to calculate space charge forces. Simulation parameters such as the number of grids and the number of macro particles should then be carefully determined to minimize numerical noises. In ACCSIM simulations, these parameters have been well defined. We therefore discuss the results from ORBIT for various simulation parameters.

Table 1: Beam parameters for benchmark

*For the benchmark simulations presented here, the beam is captured with an RF system of h=1 with 8kV, whereas in the real machine an RF system of h=2 is used for bunch flattening.

**Coasting beam is used for electron-lens compensation study.

Parameter	**Value**
Kinetic energy	160 MeV
Intensity	3.25×10^{12} proton/ring
Initial transverse distribution	Gaussian / Elliptic
Transverse emittance	2.5 πmm-mrad. r.m.s. normalized
Initial longitudinal profile	Parabolic (bunched)* / Flat (coasting)**
Longitudinal emittance for bunched beam	0.9 eV-s

Results

The emittance evolutions for the parameters listed in Table 1 are shown in Fig. 1.

For Gaussian distribution, the emittance evolution does not depend significantly on the number of grid points, and we see rather good agreement between ACCSIM and ORBIT.

For elliptic distribution, especially the vertical emittance growth is sensitive to the number of grid points in ORBIT, and we see a sudden blow-up in vertical emittance. This sudden blow-up is due to generation of halo particles, which is observed both in ACCSIM and ORBIT. It is, however, too small to produce a visible change in r.m.s. emittance in ACCSIM. It is difficult to reproduce such an incoherent motion with different codes. In conclusion, both codes give us fairly similar picture but we have to be careful when we discuss incoherent motions like of halo particles.

Actually, the number of particles of 10^5 is the limit in ACCSIM. Though it is possible to increase it by small modification of the source code, it is practical limit in single processing with the present computation capability. On the other hand, ORBIT could simulate more and more particles with parallel processing. Figure 2 shows emittance evolutions for elliptic distribution and various number of particles.

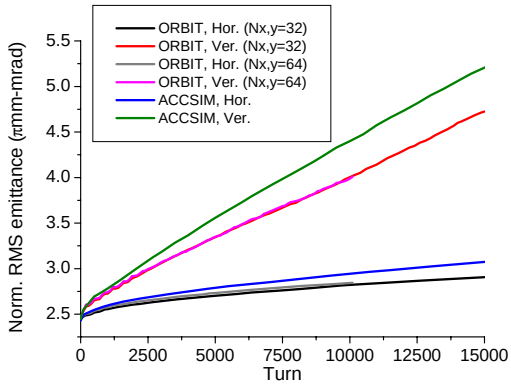

(a) Gaussian distribution, Np=99999

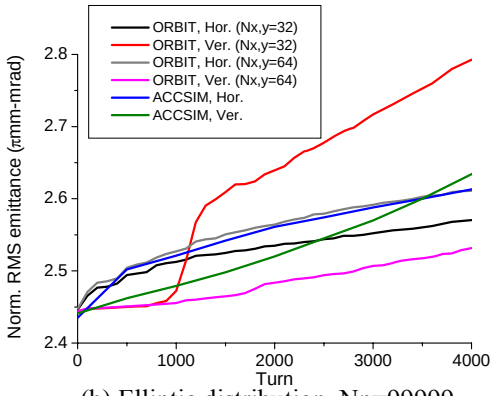

(b) Elliptic distribution, Np=99999

Figure 1: Emittance evolutions for Gaussian and elliptic initial distribution. Np is the number of macro particles and Nx,y is the number of grid points. (The ACCSIM results are taken from simulations carried out by M. Martini [4])

The number of particle of 10^5 seems not enough in this case, and the emittance evolutions shows signs of convergence with more than 5×10^5 particles.

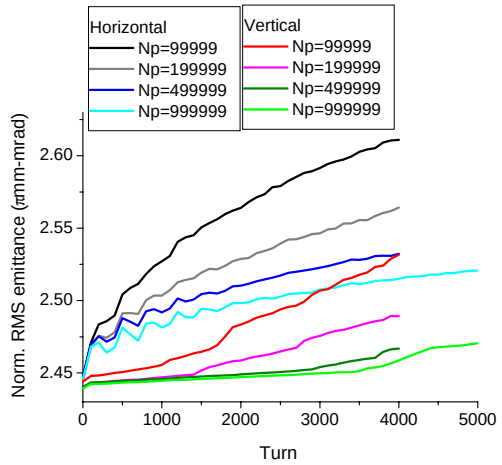

Figure 2: Emittance evolutions with ORBIT for elliptic distribution and for various numbers of macro particles, Np=99999~999999. Nx,y=64.

ELECTRON-LENS COMPENSATION

The idea of electron-lens compensation [6] is to neutralize space charge potential by applying electron-lens (electron beam) to proton beam or possibly to positive ion beam. Ideally the transverse beam profile in the lens should be the same to the one of proton beam to compensate not only linear tune shift but also nonlinear tune spread. Longitudinal profile in the lens is discussed later but it is obvious that the speed of electrons can be different from that of protons, and the energy of electron-lens is generally the order of 1~10 keV.

Localized electron-lens

Since it is impossible to apply electron-lens all over the ring, the electron-lens(es) will be localized longitudinally. The device to generate electron-lens will be a similar to a (low energy) electron cooler. The space charge force due to proton beam and localized electron-lens is sketched in Figure 3.

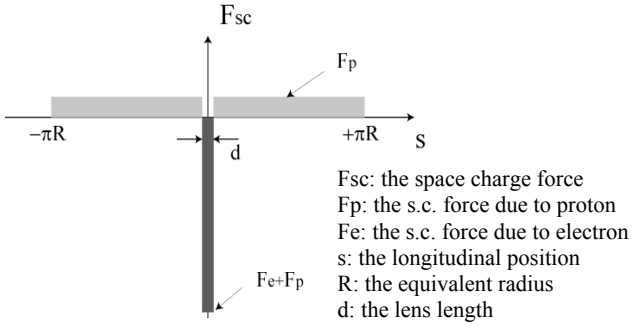

Figure 3: Space charge force with localized electron-lens.

For further convenience, we introduce the following definitions to estimate a required lens current. Since the betatron tune is a consequence of focusing force over the ring, tune shift and tune spread are expected to be compensate perfectly when the following equation is fulfilled for both horizontal and vertical plane,

$$\int_0^{2\pi R} (F_p / \beta + F_e / \beta) ds = 0, \qquad (1)$$

where β is the horizontal or vertical beta function, which is introduced to take into account effective focusing force. When a costing proton beam is assumed, the transverse densities of proton and electron would be

$$\rho_e(r) = A\rho_p(r), \qquad (2)$$

with

$$A = \frac{2\pi R}{d} \frac{1-\beta_p{}^2}{1 \pm \beta_e \beta_p}, \qquad (3)$$

where β_p and β_e is the relativistic beta for proton and electron, respectively. Equation (2) means the transverse profile of election beam matches to the proton beam profile. The sign in the denominator depends on the direction of electron beam: it is positive when the electron beam has opposite direction to the proton beam. With Eq.

(3), a required electron current will be a few amperes for the beam of Table 1.

Specifically in the PSB, the proton bunch length (~100 m) will be much longer than the electron lens since the straight section is ~2.5 m. A pulsed electron lens could be applicable to follow the longitudinal profile of proton beam as sketched in Figure 4. Equations (1) and (2) will be fulfilled at one time by applying the pulse-lens.

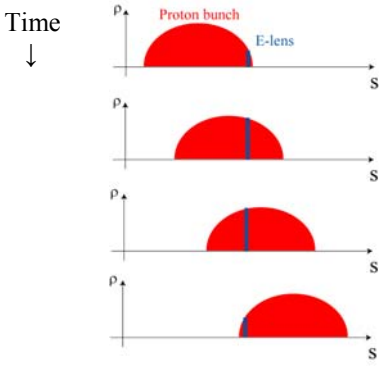

Figure 4: Pulse electron-lens

Modelling of electron-lens

A new ORBIT module to introduce electron-lens has been developed and is under testing. The ORBIT code is written in C++ programming language. Thus it is possible to add user-defined modules without changing the original code (modules).

We introduce the space charge force due to electron-lens through analytical formulae. In other words, we assume the transverse profile of electron beam does not change due to the interaction with proton beam. At this moment, the lens current is constant in time (DC-lens).

The longitudinal force due to electron-lens is ignored in the module since this would be justified by taking into account a cancellation of deceleration and acceleration at the entrance and the exit of electron-lens.

Tune spread and emittance evolution

Tune spread is expected to shrink when the electron-lens compensation is applied. To confirm this fact, tune spread is simulated with the module described above. Four electron-lenses with ~2 m long are installed into the PSB lattice so that the super periodicity will be four. The beam parameters listed in Table 1 is again employed, and the results are shown in Fig. 5.

It is seen in Fig. 5(a) that the tune spread is effectively compensated by applying electron-lenses. We confirm the advantage of compensation in principle. In Fig. 5(b), the tune spread of bunched beam cannot be compensated because the electron-lenses are DC-lens at this moment.

Beam emittance directly represents beam quality, and its evolution is practically important to know and to measure the impact of space charge effects. Several simulation results of emittance evolution are shown in Fig. 6.

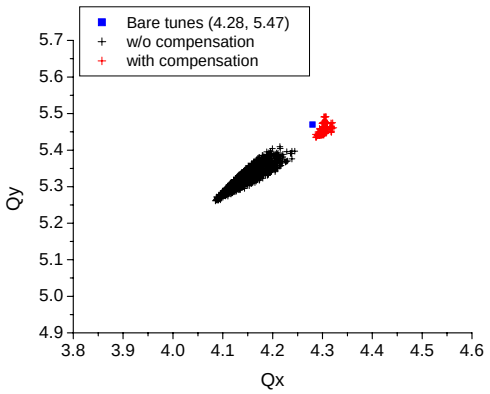

(a) Coasting beam

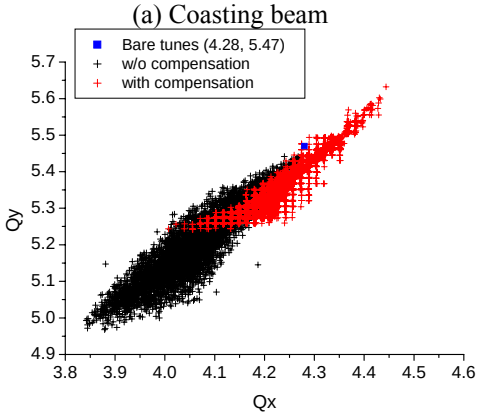

(b) Bunched beam

Figure 5: Tune spread with or without electron lenses.

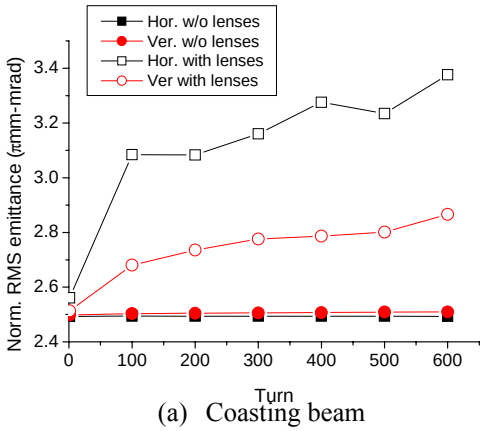

(a) Coasting beam

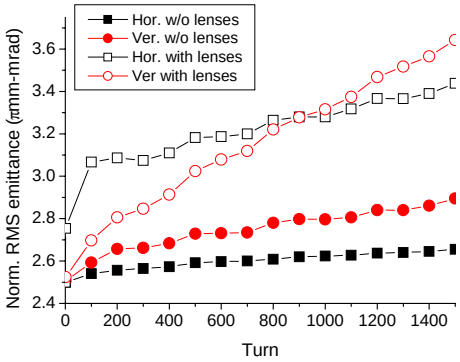

(b) Bunched beam

Figure 6: Emittance evolutions with or without electron-lenses.

In the coasting beam, the beam emittances are almost constant as shown in Fig. 6(a) because there seems no obvious source of emittance growth. The beam emittances, however, grow when the electron-lenses are applied. This might be due to the resonances excited by the focusing force of electron-lenses.

Once an rf voltage is applied to the beam, that is, in the bunched beam, the longitudinal motion results in a source of emittance growth. The space charge force depends on line density, and thus incoherent tunes changes in accordance with longitudinal motion. The particles would then experience resonance crossings. Consequently, the beam emittances could growth as shown in Fig. 6(b).

The DC-lenses cannot compensate tune spread of bunched beam but can reduce linear tune shift. As shown in Fig 5(b), the linear tune shift does not cross Qx=4, which is a fourth order structure resonance, when the electron-lenses are applied. At least the crossing of Qx=4 is avoided but the horizontal emittance growth as well as vertical one are enhanced due to electron-lenses.

Unfortunately, all of present results shows that emittance growth is enhanced due to electron lens. However, it would be too early to deny the possibility of electron-lens compensation with the preliminary results shown here. It would be worth trying a pulse-lens, various number of lenses, various operation points as well as different ring and so on.

SUMMARY

A benchmark study of ACCSIM and ORBIT codes has been performed for the PSB ring with 160 MeV beam which will be provided by the coming Linac4. Both codes give us fairly similar picture but we have to be careful when we discuss incoherent motions like of halo particles. We also investigated a possibility of space charge compensation by applying electron-lens. A new ORBIT module to introduce electron-lens has been developed and is under testing. We confirmed that tune shift and tune spread could be compensated by applying electron-lens. Although the preliminary results shows that emittance growth is enhanced due to electron lens, it would be worth trying a pulse-lens, various number of lenses, various operation points as well as different ring and so on.

ACKNOWLEDGEMENTS

The active support by Drs. S. Cousineau and A. Shishlo for ORBIT code was very helpful. I would like to thank to Dr. R. Garoby for introducing me to the study of electron-lens compensation. The frequent discussions with Drs. G. Arduini, C. Carli, M. Chanel, A. Franchi, F. Gerigk, M. Martini, M. Meddahi and F. Zimmermann were valuable and encouraging.

REFERENCES

[1] F. Jones, "Users' guide to ACSSIM", TRIUMF Design Notes, TRI-DN-90-17 (1900), http://www.triumf.ca/compserv/accsim.html
[2] J. D. Galambos et. al.," The ORBIT User's Manual", http://www.sns.gov/APGroup/Codes/Codes.html
[3] M. Chanel, this conference
[4] M. Martini, note in preparation
[5] S. Cousineau, "SIMULATION TOOLS FOR HIGH INTENSITY RINGS", Proc. of PAC'03, pp259-263 (2003)
[6] A. V. Burov, G. W. Foster and V. D. Shiltsev, "Space-Charge Compensation in Proton Booster", Proc. of PAC'01, pp2896-2898 (2001)

SPACE CHARGE MEASUREMENTS AT THE PSB

Michel Chanel, CERN, Geneva, Switzerland

Abstract

The PS Booster (PSB) is an accelerator working under very high space charge during the first part of its cycle. After the change of tune, it was necessary to revisit the space charge effects to try to understand and possibly improve the situation. In addition, the Linac2 will be replaced by the Linac4 providing an H^- injection in the PSB at 160 MeV. This energy is chosen to reduce by a factor 2 the space charge effect with the same beam characteristics. It was then needed to make some measurements at this energy, not only to find the limits but also to benchmark some simulation with available programs [1].

THE PSB, INJECTION AND ACCELERATION

The PS Booster [2] is composed of four superposed rings. The lattice is a sequence of sixteen periods BFoDoFoB. The PSB is feed with protons by the LINAC2 at 50 MeV through a classical multi-turn injection (thin magnetic septum and decreasing local bump). A maximum of 13 turns are injected from the 160 mA proton beam leading to more then 1.4 10^{13} protons circulating into the PSB (injection efficiency~70%). During the injection the magnetic field is already varying at a rate of 0.5 T/s. Then the beam is immediately bunched with a two harmonic system [3] (h=1+h=2) providing the best possible bunching factor (Bf~0.5) to decrease the space charge effects (see Tomoscope [4] on figure 1). The beam is finally accelerated to 1400 MeV in 530ms. During the first 30-40 ms, part of the beam is lost due to large Laslett tune shift (ΔQ_0~-0.5), tune spread and coherent tune shift (ΔQ_c~-0.15). To compensate for these shifts, the tune is set to (Qh=4.28, Qv=4.60) during the injection process (figure 2) and restored back to the operational tune (Qh=4.17, Qv=4.23) in about 150 ms. It allows most of the particles to stay within an area of the tune diagram free of dangerous resonances (integer, coupling or excited by space charge). To limit the losses, all the resonances which could affect the particles movement are compensated at the best, even the second order, 2 Qv=9. Nevertheless, about 25% of the particles injected are lost during the first part of acceleration. The performances obtained so far are indicated in table 1 and figure 3.

Table 1: PSB performances

N accelerated to 1.4 GeV	1.02	10^{13} p/ring
Normalised emittances (H/V)	12/7	μm(1σ)
Brightness for high intensity beams (N/ε*)	0.8	10^{12}/μm
Beam for LHC (nominal/ultimate)	1.7/2.5	10^{12} p/ring
Brightness for LHC beam (nominal/ultimate)	0.6/0.7	10^{12}/μm

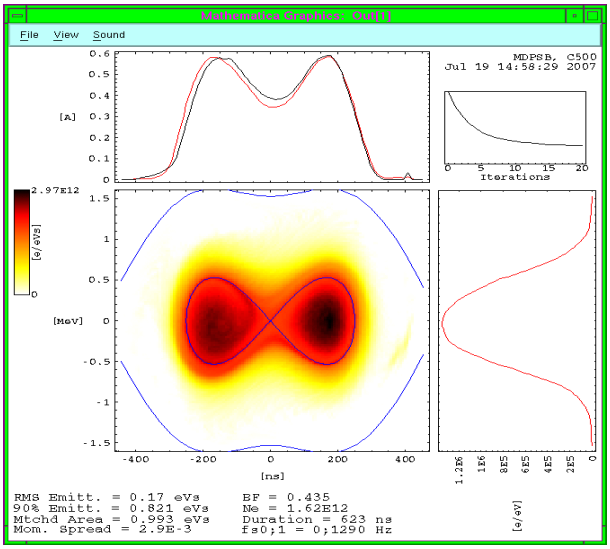

Figure 1: Tomoscope representation of the longitudinal phase space and projected distributions.

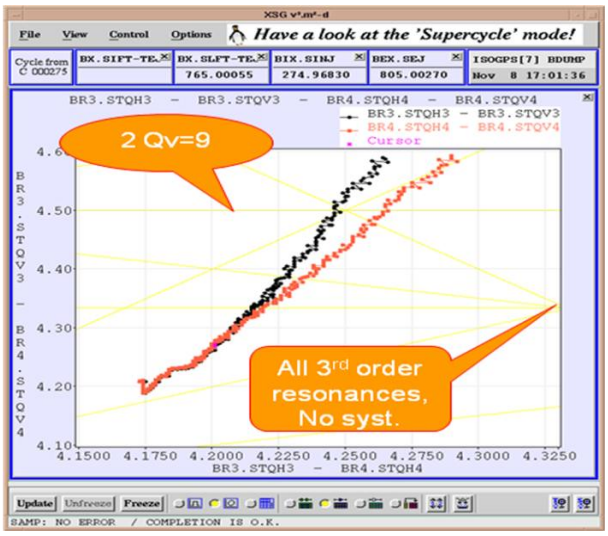

Figure 2: Tune diagram showing the dynamic tune along acceleration for rings 3 and 4

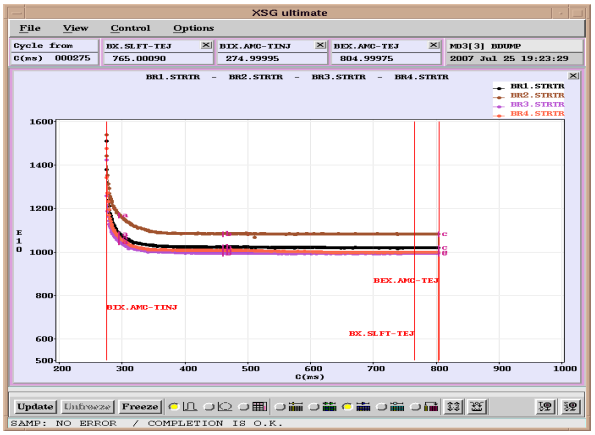

Figure 3: Number of protons accelerated for the 4 PSB rings

MEASUREMENTS

Due to the extreme conditions for the particles at the beginning of acceleration, it was decided to perform measurements of the beam characteristics varying different parameters, like tune, intensity and density. The tools used where:

- A sieve in the injection line which allows the reduction of the Linac2 proton beam density by a factor 5 to 6.
- Transformers in the machine to measure the currents.
- Tomoscope to evaluate the longitudinal emittances and the momentum distribution.
- Wire scanners in the machine to measure the emittances. They were not operational for some of the measurements.
- Semgrids in the extraction line to measure the emittances after acceleration and extraction.

The first measurements concerned the emittances obtained for different number of turns injected with and without sieve.

As the PSB machine will be fed in 2012 by the Linac4 [5], it was important to observe the beam behaviour on a 160 MeV flat top after acceleration from 50 MeV. The effect of the integer resonances was studied at this energy as the beam was particularly stable compared to a 50MeV flat top,

EMITTANCES WITH AND WITHOUT SIEVE

The emittances, after acceleration and extraction, were measured for 1 to 13 turns injected with and without the sieve (Figure 4). In the horizontal plane there is no effect of the sieve while the vertical emittance is strongly affected (a factor 2 at high intensities).

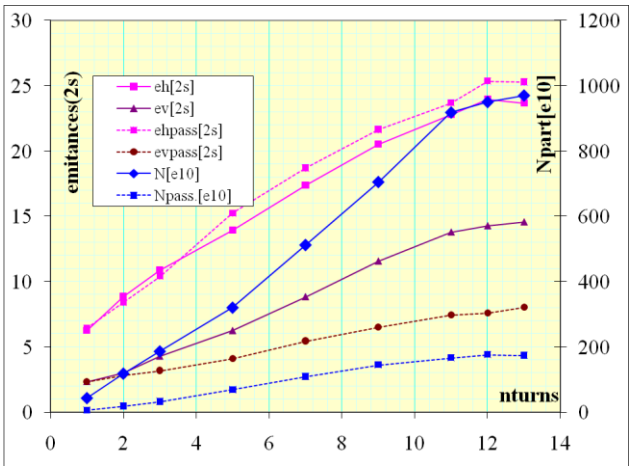

Figure 4: Emittances and number of particles accelerated and extracted versus number of turns injected without (plain) and with sieve (dashed)

Then we compute using the usual Laslett formulae and the measured parameters the tune under space charge for the zero-amplitude particle (the one which is the most affected by the space charge). We also extrapolated this zero-amplitude tune to the case where the emittances are the one obtained with sieve and the number of particles is the one without the sieve (Figure 5). We observe that the linear coupling resonance and possibly the integer resonances are responsible for the vertical emittance increase. It should be noted that the vertical emittance obtained without the sieve corresponds to the vertical acceptance of the PSB at low energy.

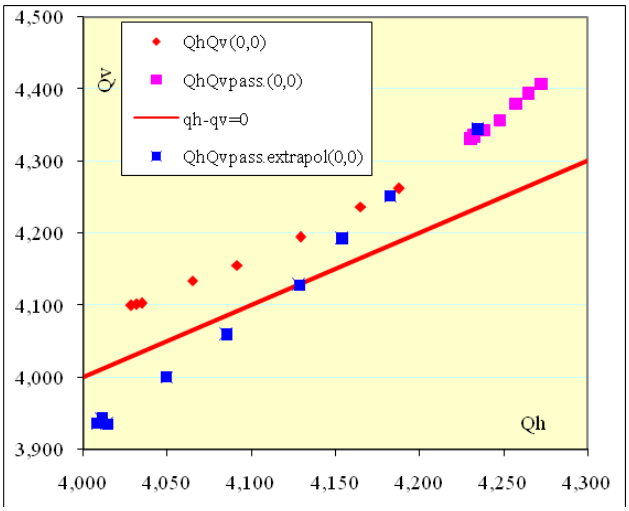

Figure 5: Tunes for particles having oscillations of zero amplitude at the start of acceleration. Red lozenges: without sieve; magenta square: with sieve; blue square: computed with the number of particles without sieve and the emittances with sieve. The red curve is the linear coupling resonance Qh–Qv=0.

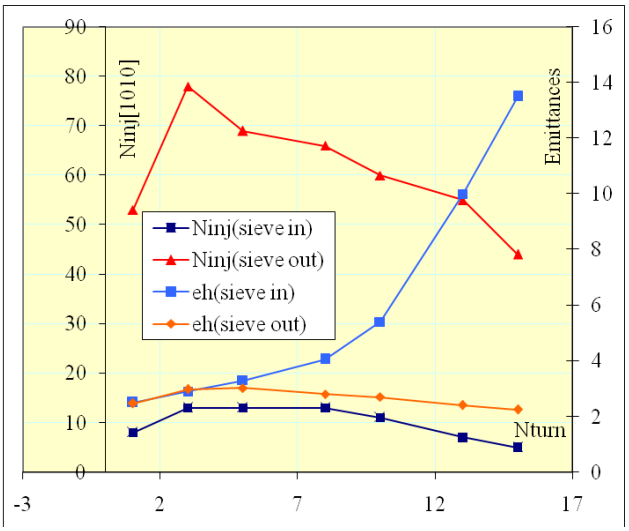

Figure 6: Injection of one turn with the same oscillations as the injected turn number 1 to 14, with and without the sieve.

We have also very often observed that, for only turn injected, the obtained emittance was very much related to the Linac2 emittance and not affected by the large horizontal oscillations during the injection process. To verify this observation, we have injected one turn with horizontal oscillation corresponding to the first, second...thirteenth turn, and with and without sieve (Figure 6). With the sieve, the final horizontal emittance increases indicating a filamentation in phase space. At the contrary, without the sieve, the final emittance is the same whatever is the original injection oscillation. This can be interpreted as a frozen phase space by the space charge forces, which don't allow filamentation. The beam is then a rigid body which oscillates for long time until the oscillation is damped through the interaction with the environment. Long damping time was also observed during the measurements. In term of beam stability, it is interpreted as large space charge impedance which drives the beam close to instability. Fortunately, the PSB is working below transition which helps the beam to not undergo instabilities through this process.

BEAM ACCELERATED TO 160 MeV

The beam was accelerated from 50MeV to 160MeV in the same way the acceleration to 1.4GeV, except for the last part just prior to the flattop. The beam was also partly decelerated back to 50MeV. It was possible to accelerated and maintain 1.08 10^{13} protons along the 200ms flattop with only small evolution of the beam emittances and number of particles (case 1). To evaluate the limits of the space charge, the second harmonic cavity voltage was first set to 2kV (instead of 8kV)(case 2) and then 8kV(case 3) but in phase with h=1 instead of being normally out of phase (Table 2).

Table 2: beam evolution along the 160MeV flattop depending of the bunch characteristics. Note that density is the bunch relative bunch peak density.

cases	1	2	3	units
V(h=1)	8	8	8	kV
V(h=2)	8	2	8	kV
Relative phase	π	π	0	rad
Qh	4.21	4.21	4.21	
Qv	4.35	4.35	4.35	
density	1	1.35	1.64	
N begin ft	1.05	1.05	1.03	10^{13} p
$\varepsilon_h/\varepsilon_v$ (2 σ)beg.	100/47	91/45	126/47	πmmmrad
N end ft	1.05	0.99	0.9	
$\varepsilon_h/\varepsilon_v$ (2 σ)end	93/52	91/53	133/48	πmmmrad

First, we should note that the normalised emittances are larger (a factor 1.2) than the emittances obtained when the beam is directly accelerated to 1.4 GeV. It surely means that, arriving on the flattop, the emittances have increased due to the proximity of several resonances. In the case 1, along the flat top only the vertical emittance increases, indicating a possible coupling effect leading to small losses. The case 2 is very similar to case 1 despite the loss increase. This indicates a possible 35% bunch peak density margin. To minimize the losses for case 3, the vertical tune was increased to 4.46. Nevertheless, the horizontal emittance and the losses are much larger than for the other cases. It was possible to restore the same horizontal emittance as for cases 1 and 2, but at the expense of the losses along the flattop. In conclusion, it is possible to further increase the peak density, but probably not more than 35%, with the same beam characteristics. Nevertheless, the resonances compensation at 160MeV should be reviewed to possibly increase the margin.

INTEGER RESONANCES

During the above measurements, it appears that the coupling resonances (Qh-Qv=0) and the integer resonances play an important role when the beam is under strong space charge. To understand these phenomena, we have changed the tune, approaching the integer resonances and finally crossing them. We have recorded the number of particles, the evolution of emittances and orbit. These measurements were taken on a 160MeV flattop as the beam with high number of particles is much more stable. Again, we compared the measurements with and without sieve.

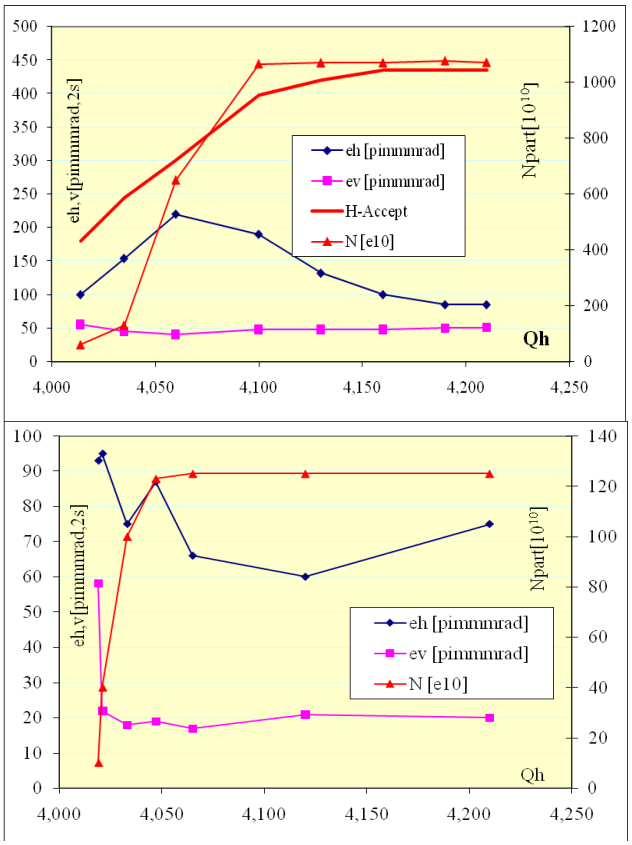

Figure 7: Evolution of different beam parameters when the horizontal working point is moved toward the integer resonance Qh=4. Top: without sieve i.e. high intensity beam; bottom: sieve in, lower intensity and ~5 times less beam density.

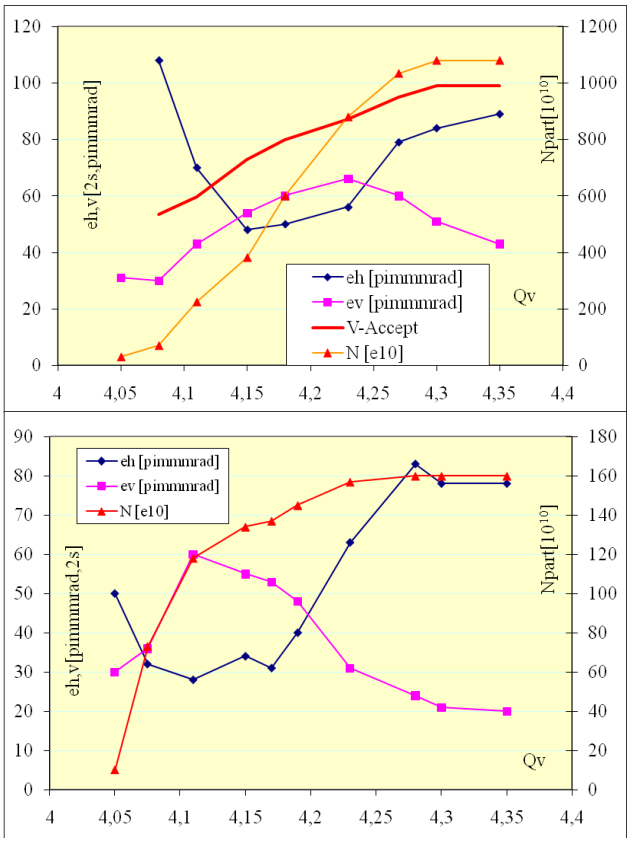

Figure 8: Evolution of different beam parameters when the vertical working point is moved toward the integer resonance Qv=4. Top: without sieve i.e. high intensity beam; bottom: sieve in.

Resonance Qh=4

While keeping the vertical tune at 4.30, the horizontal tune is moved to the resonance Qh=4. We observe(Figure 7] that the horizontal emittance is first growing up to a maximum value (~200 πmmmrad) while the peak to peak orbit increases, and then reducing the horizontal acceptance. Losses occur when the dynamical acceptance is reached. Note the constant difference between the 2 sigma's emittance and the machine acceptance computed from the mechanical aperture, the peak orbit and the lattice Twiss parameters. When the sieve is inserted into the injection line, the losses start at a later time, i.e. closer to the integer resonance. The emittance increase is not as important as for the strong space charge case (without sieve). It probably means that the integer resonance is also excited by the octupole's like effect derived from high density beam (in addition, at the PSB, the resonance 4 Qh=16 is a systematic resonance). The effect of the horizontal integer resonance has been used to send to the PS a beam with a larger horizontal emittance, easing the island formation for the 5 turn's extraction [6].

Resonance Qv=4

While keeping the horizontal tune to 4.21, the vertical tune is moved to the resonance Qv=4. On the way, the working point crosses the coupling resonance Qh-Qv=0. During this crossing, emittances are exchanged (at least partially), and then losses occur {Figure 8] as the vertical emittance reaches the vertical acceptance. Otherwise, the same conclusions as for the horizontal plane can be drawn. In the strong space charge regime, the two resonance effects are mixed which renders the analysis more difficult.

OUTLOOK

The measurements have shown a very large orbit increase when approaching the resonance. Then a program has been launched to better correct this orbit during the coming shut down by displacement of quadrupoles.

We have also seen interesting evolutions of the distributions. This has to be measured systematically and compared with simulations, trying to find corrective solutions.

CONCLUSIONS

We have extensively measured the beam behaviour in the PS Booster and tried to disentangle different observed effects. The strong space charge doesn't allow filamentation which is one of the reasons for the easiness we have had to produce the small emittances for LHC in the PSB, despite a multiturn injection. The tune diagram space is just sufficient at 160 MeV to allow a beam of allow 10^{13} protons having emittances suitable for the PS to survive for long time on a flat top. Of course the problematic could be different if the beam is accelerated as soon it is injected.

ACKNOWLEGMENT

This work has been the fruit of strong collaboration with the PSB operation crew, the support of G. Arduini and continuous discussions with C. Carli.

REFERENCES

[1] M. Aïba, these proceedings.

[2] M. Benedikt (Editor), The PS Complex as Proton Pre-Injector for the LHC – Design and Implementation Report, CERN 2000-003, Geneva, 2000.

[3] J. P. Delahaye et al, Shaping the Proton Distribution for Raising the Space-Charge of the CERN PS Booster, Proc. of the 11th Conference on High Energy Accelerators, Geneva (1980),pp299-304.

[4] S. Hancock, P. Knaus, M. Lindroos, Tomographic measurements of longitudinal phase space density. European Particle Accelerator Conference, Stockholm, Sweden, 1998, pp. 1520-1522

[5] R. Garoby, G. Bellodi, F. Gerigk, K. Hanke, A.M. Lombardi, M. Pasini, C. Rossi, E.Z. Sargsyan, M. Vretenar, Linac4, a New Injector for the CERN PS Booster. Proc. Of EPAC 2006, Edinburg, Scotland

[6] S. Gilardoni, M. Giovannozzi, M. Martini, E. Métral, P. Scaramuzzi, R. Steerenberg, and A.-S. Müller, Experimental evidence of adiabatic splitting of charged particle beams using stable islands of transverse phase space, Phys. Rev. ST Accel. Beams 9, 104001 (2006)

TRANSVERSE MODE COUPLING INSTABILITY IN THE SPS: *HEADTAIL* SIMULATIONS AND *MOSES* CALCULATIONS

B. Salvant, EPFL, Lausanne, Switzerland
E. Métral, G. Rumolo, R. Tomás, CERN, Geneva, Switzerland

Abstract

Since 2003, single bunches of protons with high intensity (~ 1.2 10^{11} protons) and low longitudinal emittance (~ 0.2 eVs) have been observed to suffer from heavy losses in less than one synchrotron period after injection at 26 GeV/c in the CERN Super Proton Synchrotron (SPS) when the vertical chromaticity is corrected ($\xi_y \sim 0$). Understanding the mechanisms underlying this instability is crucial to assess the feasibility of an anticipated upgrade of the SPS, which requires bunches of 4 10^{11} protons. Analytical calculations and particle tracking simulations had already agreed in predicting the intensity threshold of a fast instability. The aim of the present paper is to present a sensitive frequency analysis of the HEADTAIL simulations output using SUSSIX, which brought to light the fine structure of the mode spectrum of the bunch coherent motion. Coupling between the azimuthal modes "-2" and "-3" was clearly observed to be the reason for this fast instability.

INTRODUCTION

A campaign for the reduction of the SPS impedance took place between 1999 and 2001 to allow high-intensity LHC-type beams to be accelerated in the SPS without suffering from longitudinal microwave instability [1]. Subsequent measurements in 2003 [2] and 2006 [3] showed that the SPS intensity is now limited by a fast vertical single bunch instability at injection energy (p = 26 GeV/c) if the bunch longitudinal emittance is low ($\varepsilon_L \sim 0.2$ eVs), and the vertical chromaticity is corrected ($\xi_y \sim 0$).

This vertical instability presented the signature of a Transverse Mode Coupling Instability (TMCI): (i) The resulting heavy losses appeared within less than a synchrotron period; (ii) they could be avoided if the vertical chromaticity was increased ($\xi_y = 0.8$); and (iii) a travelling-wave pattern propagating from the head to the tail of the bunch could be observed on the data recorded on the SPS "HeadTail" monitor [4].

Calculating the coherent bunched-beam modes with the MOSES code [5] and simulating the coherent behaviour of a single bunch with the HEADTAIL code [6] agree in predicting the intensity threshold of a single bunch interacting with a broadband (BB) transverse impedance [4].

In the following, further frequency analysis of the bunch spectrum of the HEADTAIL simulation output is performed and compared with the bunch mode spectrum predicted by MOSES for a round chamber. The more realistic case of a flat chamber is then addressed, along with studies of the effect of linear coupling on the instability threshold.

ANALYTICAL CALCULATIONS WITH MOSES FOR A ROUND CHAMBER

MOSES v3.3 is used to generate the bunch mode spectrum as a function of bunch intensity, for a bunch interacting with a transverse broadband impedance of a round structure. The parameters are listed in Table 1. Horizontal and vertical planes are equivalent in this section.

Table 1: MOSES calculation parameters

Parameter Name	**Value**	**Unit**
Betatron tune spread	0	
Synchrotron tune (Q_s)	3.24 10^{-3}	
Beam energy	26	GeV
Rms bunch length	21	cm
Beta function	40	m
Revolution frequency	4.33 10^{-2}	MHz
Momentum compaction factor	1.92 10^{-3}	
Linear chromaticity ($\xi_x = \xi_y$)	0	
Impedance resonant frequency	1	GHz
Impedance at resonance frequency	10	MΩ/m
Quality factor	1	

Tune shift of the bunch coherent modes

The tune shift $Re(Q - Q_x)$ with respect to the 0-current-tune Q_x is normalized to the synchrotron tune Q_s to identify each of the bunch azimuthal modes, and is plotted as a function of bunch intensity (I_b) in Fig. 1.

The azimuthal modes of the bunch are observed to separate into several radial modes, which shift with their own pace as the bunch intensity is increased. Some azimuthal modes are observed to couple, in particular modes "0" and "-1" at $I_b = 0.3$ mA, which also decouple if the bunch current is increased further. Modes "-1" and "-2", as well as modes "-2" and "-3" also couple between $I_b = 0.45$ mA and $I_b = 0.5$ mA.

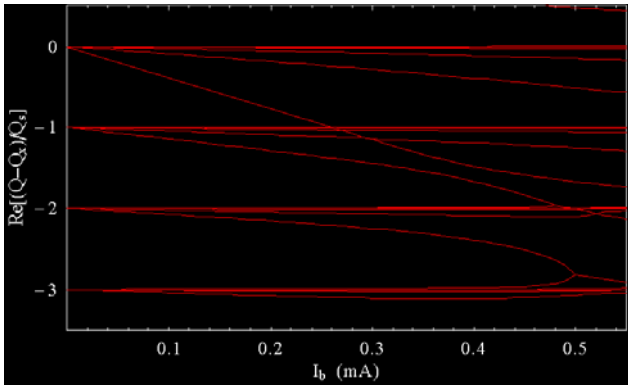

Figure 1: Zoom of the normalised real part of the mode spectrum of the bunch (from azimuthal mode "0" to azimuthal mode "-3") as a function of the bunch intensity (I_b) calculated with MOSES (see Table 1).

Growth rate

The instability growth rate τ is derived from the imaginary part of the normalized mode spectrum, and displayed in Fig. 2.

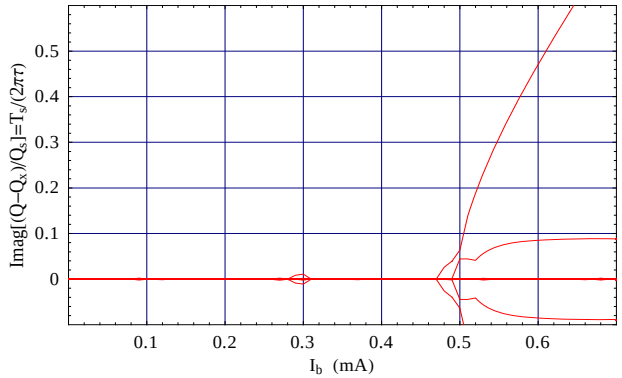

Figure 2: Imaginary part of the normalized mode spectrum of the bunch as a function of the bunch intensity (I_b) calculated with MOSES (see Table 1).

The growth rate is observed to be particularly significant for large beam intensities (I_b > 0.47 mA). Taking into account the observations on the real part of the mode spectrum, it can be concluded that this instability growth rate is due to coupling between azimuthal modes "-1" and "-2" from I_b = 0.47 mA, followed by an even stronger coupling between azimuthal modes "-2" and "-3" from I_b = 0.5 mA.

The coupling observed between modes "0" and "-1" at I_b = 0.3 mA on Fig. 1 leads to a smaller growth rate on Fig. 2. This growth rate vanishes as soon as the two modes decouple.

From these observations, it can be concluded that the instability modelled by MOSES in these conditions is the result of the coupling of transverse modes, and therefore can be referred to as a TMCI.

SIMULATIONS WITH HEADTAIL FOR A ROUND CHAMBER

The HEADTAIL code was used to simulate the interaction of a low longitudinal emittance bunch of macroparticles with a transverse impedance modelled as a broadband resonator. The main simulation parameters are given in Table 2, and are chosen to reproduce the situation modelled by MOSES in the previous section. The transverse tunes (Q_x, Q_y) are set to the working point used in the past. Q_x and Q_y have since been exchanged to enhance the lifetime. Also, assumptions include no space charge, no amplitude detuning, a linearized RF bucket, and a "frozen" wake field – i.e. the wake field is only calculated for the first turn, and remains unchanged for all remaining turns. This approximation holds because (i) the bunch is assumed to be well matched to the bucket and (ii) no longitudinal impedance is included in the simulation. In this section, the chamber is round, so horizontal and vertical planes are again equivalent.

Table 2: Main HEADTAIL simulation parameters

Parameter	**Symbol**	**Value**	**Unit**
Circumference	L	6911	m
Number of bunches		1	
Relativistic Gamma		27.7286	
Initial Rms beam sizes	σ_x, σ_y	1.8	mm
Horizontal Tune	Q_x	26.185	
Vertical Tune	Q_y	26.13	
Linear chromaticities	$\xi_{x,y}$	0 / 0	
Initial rms Bunch length	σ_z	0.21	m
Initial Longitudinal Momentum spread (rms)	σ_p / p_0	$9.3\ 10^{-4}$	
Synchrotron Tune	Q_s	$3.24\ 10^{-3}$	
Cavity Harmonic Number		4620	
Momentum Compaction Factor		$1.92\ 10^{-3}$	
BB shunt impedance		10	MΩ/m
BB resonant frequency		1	GHz
BB quality factor		1	
Kick amplitude (in x and y)		0.9	mm
Average Beta function	β_x, β_y	40	m

Growth rate

The instability growth rate is calculated from the exponential growth of the amplitude of the bunch centroid oscillations as a function of time. The growth rate as a function of bunch intensity calculated from the output of the HEADTAIL simulations is compared with MOSES results in Fig. 3.

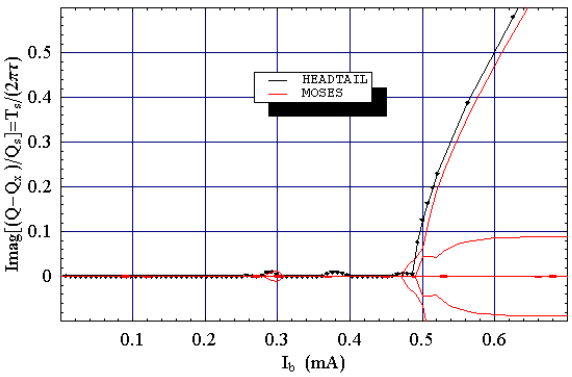

Figure 3: Comparing HEADTAIL (black full line with dots) and MOSES (red full line) growth rates as a function of bunch intensity.

Apart from a small non-zero growth rate at $I_b = 0.38$ mA, and a slightly lower growth rate in the range $I_b \in [0.45; 0.5]$ mA, HEADTAIL simulations clearly reproduce the instability growth rates predicted by MOSES calculations for the explored range of bunch intensities. However, this observation is necessary but not sufficient to prove that the transverse instability predicted by HEADTAIL is of the same nature as the one predicted by MOSES, i.e. a TMCI. To learn more about the nature of the fast transverse instability predicted by HEADTAIL, the behaviour of the transverse modes is analyzed in the frequency domain in the next section.

Tune shift of the bunch coherent modes

For each of the bunch intensities, the mode spectrum is obtained by applying a frequency analysis to the bunch transverse coherent oscillations as a function of time, which is an output of the HEADTAIL code. Two frequency analysis techniques were used to process the raw simulation data into normalized mode spectra: the Fast Fourier Transform (FFT) algorithm or the SUSSIX program [7]. The theory behind SUSSIX can be found in [8, 9]. A comparison between these two techniques for $I_b = 0.02$ mA is displayed in Fig. 4. The SUSSIX program is applied to the complex phase space normalized coordinate x-$j.p_x$ in the phase space whereas simple FFT is only applied to the coherent transverse position x of the bunch centroid, the transverse momentum p_x being left unused. It can be observed in the example in Fig. 4 that the coherent motion analyzed with SUSSIX enables to recognize azimuthal modes "-2" (2 separate radial modes), "-1", "0" (2 separate radial modes), "1", and "2" (2 separate radial modes). The same coherent motion analyzed with a classical *Mathematica* FFT algorithm only enables to observe 2 separate radial modes of azimuthal mode "0". More generally, the SUSSIX algorithm is found to be more powerful to analyze the behaviour of simulated transverse modes than a classical FFT.

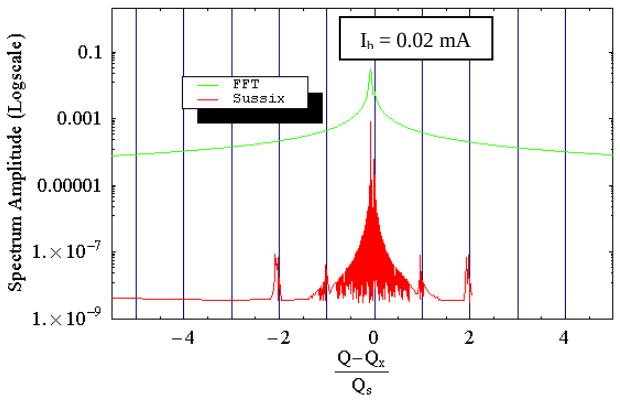

Figure 4: Comparing the performance of two frequency analysis algorithms applied to the coherent transverse oscillations simulated with HEADTAIL: FFT (green line) and SUSSIX (red line).

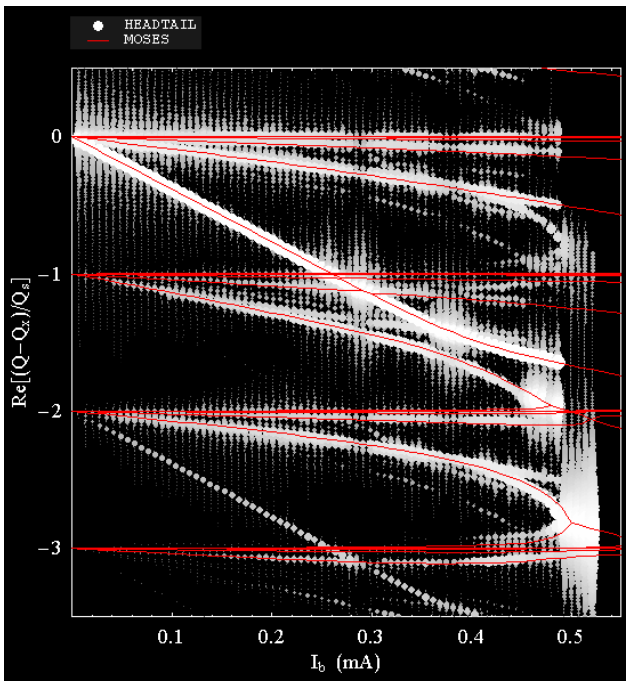

Figure 5: Comparing HEADTAIL (white dots) and MOSES (red lines). The transverse modes "0", "-1", "-2" and "-3" behaviour is plotted as a function of bunch intensity. The coherent motion as simulated with HEADTAIL was post-processed with SUSSIX and displayed using white dots, whose size and brightness are both non-linear functions of their spectral amplitude (bigger brighter dots have a higher amplitude than smaller darker dots).

The mode spectra obtained from a large number of simulations with bunch intensities ranging from $I_b = 0.01$ mA to $I_b = 0.55$ mA are displayed as a flattened 3-D plot in Fig. 5, and compared with MOSES mode spectra. From this comparison, it can be concluded that MOSES and HEADTAIL quantitatively agree in predicting most of the transverse modes shifting with increasing intensity, and transverse mode coupling at bunch intensities $I_b \sim 0.3$ mA (modes "0" and "-1"),

$I_b \sim 0.47$ mA (modes "-1" and "-2") and $I_b \sim 0.5$ mA (modes "-2" and "-3"). This latter coupled mode between modes "-2" and "-3" is clearly the main contribution to the spectrum amplitude for $I_b > 0.5$ mA, whereas the azimuthal mode "0" – also referred to as the transverse tune - carries most of the spectral power for $I_b < 0.5$ mA. This swift power swap between these two spectral lines, along with the large instability growth rate observed in the time domain (see Fig. 3), which both occur at $I_b = 0.5$ mA, proves that the resulting instability observed in HEADTAIL is indeed a TMCI.

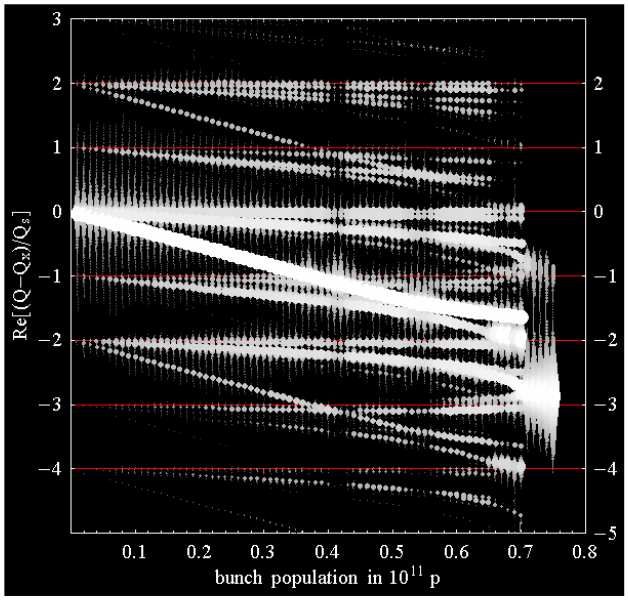

Figure 6: HEADTAIL (white dots) transverse modes "2", "1", "0", "-1", "-2", "-3", "-4" behaviour as a function of bunch population (N_b). Bunch intensity (I_b) and bunch population (N_b) are related by $I_b = N_b\, e\, f_0$, with e the proton charge and f_0 the revolution frequency. In the case of the SPS, I_b [mA] ~ 0.7 N_b [10^{11} p] .

However, the agreement between the two codes is not perfect as it can be seen in Fig. 5 that some simulated transverse modes from HEADTAIL are not predicted by MOSES. In particular, a "-2" spectral line undergoes a shift with intensity that is comparable to the shift of the main tune. Along with other features of the HEADTAIL simulated mode spectrum - see Fig. 6 -, this tends to indicate that the mode spectrum contains echoes of the main lines translated by +/- $2Q_s$, which do not seem to couple with other modes. Besides, as opposed to MOSES, the main tune couples twice with two different radial modes "-1" at $I_b \sim 0.38$ mA in HEADTAIL, which explains the non-zero growth rate at this current in Fig. 3. Work on understanding the reasons behind these discrepancies is still ongoing.

SIMULATIONS WITH HEADTAIL FOR A FLAT CHAMBER

Now that the simulations with HEADTAIL have been benchmarked with MOSES calculations for the round chamber case, we feel more confident to simulate the case of the flat chamber, i.e. two infinite horizontal parallel plates. This flat chamber case is closer to the real elliptic chamber of the CERN SPS, but it is not yet possible to solve it with MOSES. The simulation parameters in Table 2 were left unchanged. The comparison between the simulated growth rates for both horizontal and vertical planes of the flat chamber, and the growth rate for the round chamber simulated in the previous section, is shown in Fig. 7.

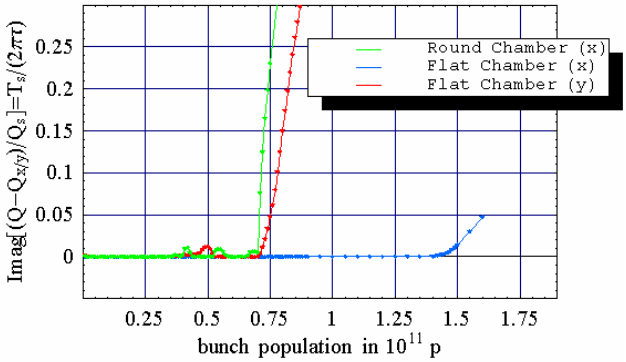

Figure 7: Comparison of HEADTAIL simulated growth rates for round chamber (green), horizontal plane of a flat chamber (blue) and vertical plane of a flat chamber (red) as functions of bunch population, for a shunt impedance $Z_s = 10$ MΩ/m.

These results are consistent with other HEADTAIL simulations presented in [10], in which the shunt impedance was set to $Z_s = 20$ MΩ/m. The instability threshold for the vertical plane of the flat chamber is slightly higher than the threshold for the round chamber case, and an instability threshold is found for the horizontal plane of the flat chamber a factor 2 higher than that of the vertical plane. As already mentioned in [10], the thresholds for the vertical and horizontal planes of the flat chamber are scaled from the round chamber threshold by the respective vertical ($\pi^2/12$) and horizontal ($\pi^2/24$) dipolar factors obtained by K. Yokoya [11].

Besides, simulated mode spectra as a function of bunch population (N_b) for both horizontal and vertical planes are presented in Fig. 8. A coupling between modes "-2" and "-3" in the vertical plane is observed. In the horizontal plane, the origin of the instability can not be proven, but a coupling between azimuthal modes "-1" and "-2" can be guessed. Moreover, the slope of the tune shift with intensity (main radial mode "0") for the vertical plane of the flat chamber case is observed to be higher by a factor $\pi^2/8$ than for the round chamber case. The slope of the tune shift with intensity for the horizontal plane of the flat chamber case is observed to be zero. These observations can be understood if we assume that both dipolar and quadrupolar parts of the flat chamber impedance have an impact on the tune shift [12]. Actually, for the vertical plane the two contributions add up resulting in a factor $\pi^2/12+\pi^2/24 = \pi^2/8$ with respect to the round chamber, whereas for the horizontal plane, the two contributions are subtracted and, in this specific case, they cancel out ($\pi^2/24-\pi^2/24=0$).

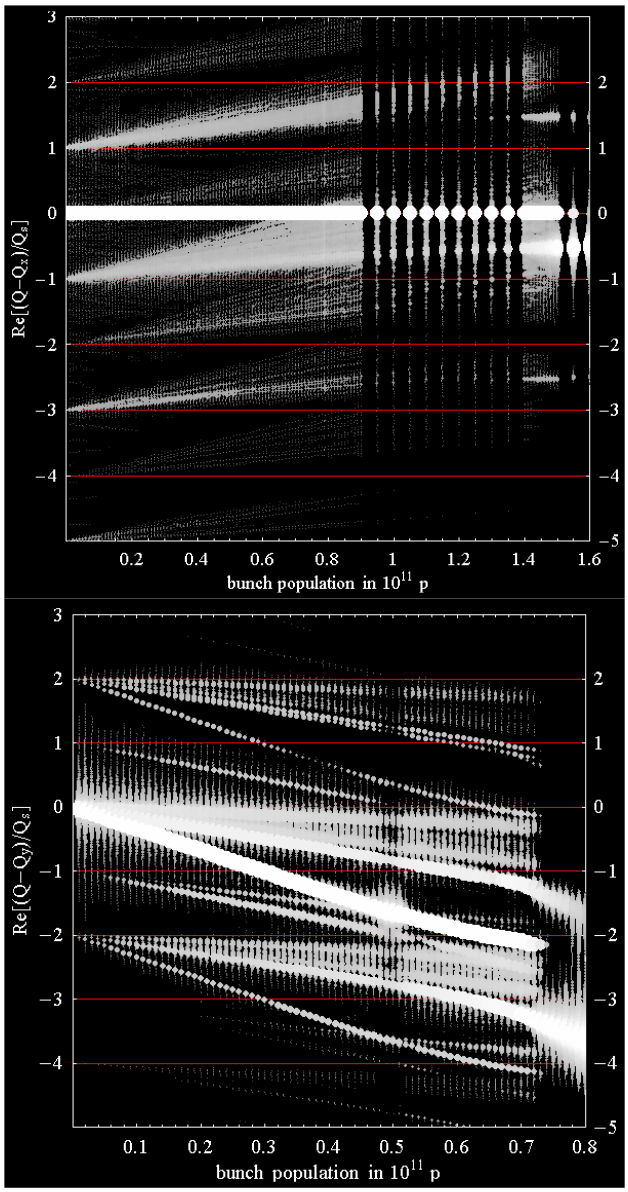

Figure 8: HEADTAIL horizontal (top) and vertical (bottom) modes behaviour as a function of bunch population for a flat chamber and a shunt impedance Z_s = 10 MΩ/m. It is important to notice that the horizontal scale range is larger, and that the density of simulations covering the population range $N_b \in [0.9;1.6]\ 10^{11}$ protons is reduced.

SIMULATIONS WITH HEADTAIL FOR A FLAT CHAMBER WITH LINEAR COUPLING

In the HEADTAIL simulations performed in [10], linear coupling between the transverse planes was observed to increase the TMCI threshold in the case of a flat chamber, when the transverse tunes are set to Q_x = 26.18 and Q_y =26.185. A threshold increase is indeed obtained with a linear coupling coefficient set to K=0.005 m^{-1} (see Fig. 9).

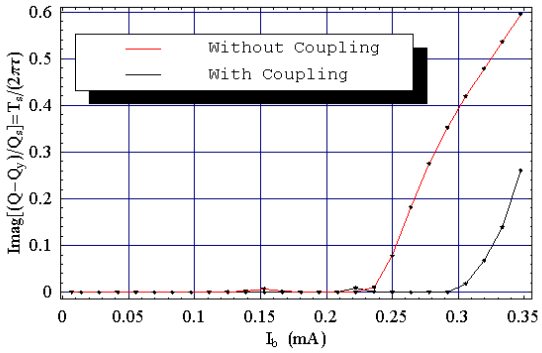

Figure 9: Comparison between HEADTAIL simulated growth rates for the vertical plane of a flat chamber without linear coupling between the two transverse planes (red), and with linear coupling (black) as a function of bunch intensity, for a shunt impedance Z_s = 20 MΩ/m.

The mode spectrum obtained in Fig. 10 is not normalized, so that the coupled tunes can be observed. Mode coupling is again observed to take place between mode "-2" and mode "-3" when linear coupling is present.

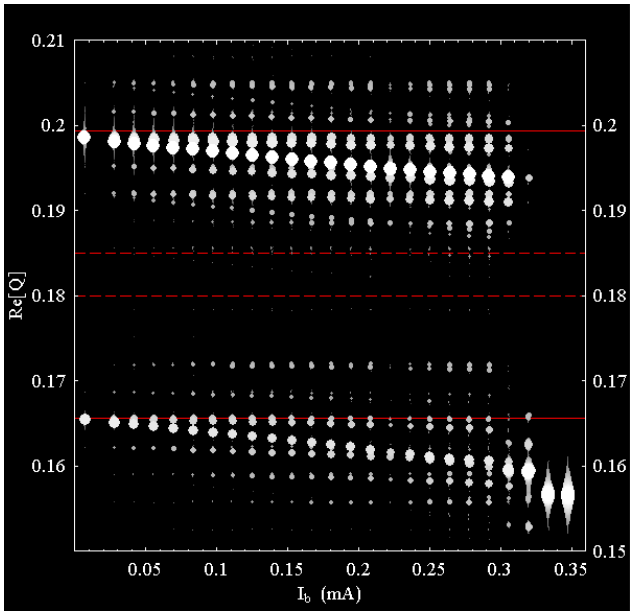

Figure 10: HEADTAIL mode behaviour as a function of bunch intensity for a flat chamber in the vertical plane, for a shunt impedance Z_s = 20 MΩ/m, and in the presence of linear coupling between the transverse planes. Dashed red lines are the uncoupled fractional parts of the vertical (0.185) and horizontal tunes (0.18). Full red lines are the coupled tunes predicted in [13].

CONCLUSION

Coupling between azimuthal modes "-2" and "-3" is observed to be the cause of the instabilities simulated with HEADTAIL, both in the case of the round chamber and of the vertical plane of the flat chamber (with and without linear coupling between transverse planes).

Besides, HEADTAIL simulations were benchmarked with MOSES in the case of the round chamber, and both

codes agree for the behaviour of most of the spectral lines with increasing bunch intensity. Minor discrepancies remain and work is ongoing to understand them.

The next step is to compare these simulations with measurements acquired in the SPS machine during the 2007 run.

ACKNOWLEDGMENTS

We would like to thank G. Arduini, T. Bohl, R. Calaga, and G. Papotti for their contributions to the preliminary measurements in the SPS, J. Jowett for useful tips on *Mathematica*, as well as D. Brandt, Y. H. Chin, A. Hofman, Y. Papaphilippou, L. Rivkin, E. Shaposhnikova, Y. Shobuda, and B. Zotter, for fruitful discussions and advice.

REFERENCES

[1] T. Bohl, *et al.*, "Impedance Reduction in the CERN SPS as seen from Longitudinal Beam Measurements", EPAC'02, Paris, France, 2002.

[2] E. Métral, *et al.*, "Transverse Mode Coupling Instability in the CERN Super Proton Synchrotron", ICFA Beam Dynamics Workshop, "High Intensity and Brightness Hadron Beams", Bensheim, Germany, 2004.

[3] G. Arduini, *et al.*, "Fast Vertical Instability at Injection in the CERN SPS – An Update", PAC'07, Albuquerque, NM, USA, 2007.

[4] E. Métral, *et al.*, "The Fast Vertical Single-Bunch Instability after Injection into the CERN Super Proton Synchrotron", EPAC'06, Edinburgh, UK, 2006.

[5] Y. H. Chin, "User's guide for new MOSES version 2.0 : MOde-coupling Single bunch instability in an Electron Storage ring", CERN/LEP-TH/88-05, 1988.

[6] G. Rumolo and F. Zimmermann, "Practical user guide for HEADTAIL", CERN-SL-Note-2002-036-AP, 2002.

[7] R. Bartolini, F. Schmidt, "Computer Code for Frequency Analysis of Non-Linear Betatron Motion" SL-Note-98-017-AP. CERN, 1998.

[8] R. Bartolini, F. Schmidt, "Normal form via tracking or beam data", Part. Accel., 59, pp. 93-106, 1998.

[9] J. Laskar, "Frequency analysis for multi-dimensional systems. Global dynamics and diffusion", Physica D: Nonlinear Phenomena, 67, Issue 1-3, pp. 257-281, 1993.

[10] E. Métral and G. Rumolo, "Simulation study of the beneficial effect of linear coupling for the transverse mode coupling instability in the CERN Super Proton Synchrotron", EPAC'06, Edinburgh, UK, 2006.

[11] K. Yokoya, "Resistive Wall impedance of beam pipes of general cross section", Particle Accelerators, vol. 41, 3-4, p.221, 1993.

[12] A. Burov and V. Danilov, "Suppression of Transverse Bunch Instabilities by Asymmetries in the Chamber Geometry", Phys. Rev. Lett. Vol. 82, 2286, 1999.

[13] G. Guignard, "The general theory of all sum and difference resonances in a three-dimensional magnetic field in a synchrotron", CERN-76-06, CERN, Geneva, 1976.

Francesco Ruggiero

Memorial Symposium

Francesco Ruggiero 1957–2007

O.S. Brüning, S. Myers, E. Picasso, W. Scandale, F. Zimmermann (editor), B. Zotter, CERN, Geneva, Switzerland; J.S. Berg, BNL, Upton, U.S.A.; C. Biscari, INFN, Frascati, Italy; W. Chou, FNAL, Batavia, U.S.A.; M.A. Furman, LBNL, Berkeley, U.S.A.; K. Hirata, KEK, Tsukuba, Japan; A. Mostacci, L. Palumbo, U. La Sapienza, Roma, Italy; S. Petracca, U. Sannio, Benevento, Italy; Q. Qin, IHEP, Beijing, China

Abstract

Francesco Ruggiero (1957–2007) was a brilliant accelerator physicist, an inventive researcher, a great collaborator, an excellent mentor, and a true gentleman. We here take a look at Francesco's scientific work, and highlight some of his contributions to accelerator physics. More details can be found in the slides presented by the speakers of the Francesco Ruggiero Memorial Symposium held at CERN on 3 October 2007 [2].

Figure 1: Francesco Ruggiero, 6. December 2003

1 BEFORE CERN

Francesco Ruggiero was of Neapolitan origin. Interestingly, he received his first diploma from the "Instituto Nautica di Piano di Sorrento" (a nautical school), which was later followed by a diploma thesis in physics on gravitational wave detection for the title of "Laurea" at the University of Pisa in 1980 [1]. After obtaining his diploma, he spent a few months at the University of Stuttgart with Prof. H. Haken, who had written several books on synergetic models in natural science. Emilio Picasso, the LEP Project Director who at the same time also was an expert of gravitational waves, had been much impressed with the thesis work which Francesco had performed for the title of Laurea [1], and he introduced him to Steve Myers to find a topic for a doctoral thesis. By then Francesco had moved on to the prestigious Scuola Normale in Pisa, where Prof. Luigi Radicati agreed to supervise a second (doctoral) thesis "di perfezionamento" on which he wanted work at CERN, where he became a thesis student in the ISR (later LEP) division. Prof. Francesco Pegoraro was a second thesis supervisor in Pisa. In 1985, Francesco received his PhD in accelerator physics from the the Scuola Normale Superiore.

2 CAREER AT CERN

Francesco first came to CERN as a summer student, from July to September 1981.

At the time he contributed to beam-beam studies for LEP under the supervision of Steve Myers. He was 24 years young. Intrigued by this experience, he soon started a doctoral thesis on collective instabilities in high energy particle storage rings, about which we will say more in the following section.

From January 1984 to July 1986 Francesco worked at CERN as a fellow, in the LEP Theory Group, at the same time as Luigi Palumbo. Luigi and Francesco were both from Naples, albeit from different parts of the city, and they shared the habits of people coming from south: late start in the morning, and late stop in the evening, often in the night. Francesco next became staff member in the LEP Theory Group from July 1986 to the end of 1989, during which time he participated in the commissioning of LEP. In 1990 he joined the accelerator physics group in the former SL division (SL-AP). In the SL-AP group Francesco made numerous invaluable contributions to the design of the LHC, in particular on collective effects, machine impedance, and beam-beam interaction. In 1997 Francesco recognized the potential danger from an electron cloud in the LHC and he launched an important remedial crash program. In 2000 he became SL-AP group leader. From 2000 onwards Francesco was the driving force behind the LHC accelerator upgrade studies, e.g., as coordinator of the CARE-HHH network. His final position was one as a section leader and deputy group leader in the newly formed AB/ABP group.

Under Francesco's wonderful and caring guidance many bright young accelerator physicists were trained or recruited at CERN, including Giulia Bellodi, Scott Berg,

Oliver Brüning, Alex Koschik, Andrea Mostacci, Yannis Papaphilippou, Giovanni Rumolo, Rogelio Tomas, Hiroshi Tsutsui, Xiaolong Zhang, Frank Zimmermann, and Mari-Paz Zorzano.

3 PHD THESIS

The first part of Francesco's PhD thesis concerned the Transverse Mode Coupling (TMC) instability due to localized impedances, studied under supervision by Bruno Zotter, while the second topic was the beam-beam effect in electron-positron colliders, supervised by Emilio Picasso, who was the LEP Project Director from 1981 to 1989.

Francesco's thesis or "tesi di perfezionamento" on "Theoretical Aspects of Some Collective Instabilities in High-Energy Particle Storage Rings" was published as a CERN Yellow Report [3] (see Fig. 2). In the extensive introduction of his thesis Francesco first gave a short and concise Hamiltonian formulation of single particle dynamics in storage rings, followed by a clear definition of the "smooth approximation" which had often been used by other authors without much further justification.


CERN 86-06
LEP Main Ring Division
8 August 1986

ORGANISATION EUROPÉENNE POUR LA RECHERCHE NUCLÉAIRE
CERN EUROPEAN ORGANIZATION FOR NUCLEAR RESEARCH

THEORETICAL ASPECTS
OF SOME COLLECTIVE INSTABILITIES
IN HIGH-ENERGY PARTICLE STORAGE RINGS

Francesco Ruggiero

GENEVA
1986

Figure 2: The cover page of Francesco's PhD thesis.

He also investigated the effects of noise in electron storage rings, using a renormalized Fokker-Planck equation which he solved with the techniques of stochastic differential equations. He later applied the same approach to analyze the beam-beam effect in colliders. Here he treated the beam-beam encounters as periodic kicks which can be considered to constitute an additional source of noise and thus lead to an increase of beam size above a threshold usually called beam beam limit.

The Transverse Mode Coupling Instability (TMC), sometimes called the fast-head-tail effect in the USA, was originally observed by R. Kohaupt at DESY when he tried to identify the cause of rapid beam loss which had occurred in the DESY electron storage ring PETRA in 1980, which he had originally called "Transverse Turbulence".

However, it soon became clear that this type of instability was actually caused by coupling of neighboring head tail modes, and its threshold current was found to be inversely proportional to the total transverse impedance around the machine circumference. Hence it would be especially dangerous for very large storage rings such as LEP which was then just being designed at CERN. A good understanding of beam stability in the presence of the rather large number of unavoidable structures surrounding the beam – such as RF cavities, kickers, bellows, pick-ups etc. – was therefore important in order to choose the best design parameters and to optimize future machine performance. In all previous analytic work distributed impedances had been assumed, mainly due to a large number of small cross section variations of the vacuum chamber, and often globally described by "broad-band impedances". In addition to analytical work, computer simulation codes in time domain were then being developed both at CERN (e.g. SIMTRAC by D. Brandt) and in other accelerator laboratories (SLAC, DESY) to include the effects of large, localized structures. Their impedances or wake fields could be measured or computed with numerical codes. This was in particular important for LEP where the major contribution to the impedance was expected to come from numerous large copper and superconducting RF cavities required to compensate the large synchrotron radiation losses.

To compare the results of the two methods, it was necessary to perform an analysis also using impedances of localized structures as assumed in the simulations. Francesco was able to develop a new and original approach leading to an integral equation for the dipole moment of the bunch oscillations. From this he obtained an eigenvalue problem which then allowed calculation of threshold currents and also led to a dispersion relation [4].

For Gaussian bunches, the usual shape of electron beams, explicit solutions in terms of Hermitian polynomials were found. The resulting expressions for the threshold current were in general agreement with those for distributed impedances, but the latter were shown to be valid only for tunes far from synchro-betatron resonances, while they could become drastically lower near those resonances. Francesco made numerical predictions for LEP which agreed quite well with results from computer simulation and were later verified by measurements on the machine (Fig. 3).

We now consider in some detail the effect of a localized impedance discussed in Francesco's thesis. Take a beam which passes through a localized object (at location s), and which induces a charge distribution on the object's walls, that depends on the beam distribution at s. The charge dis-

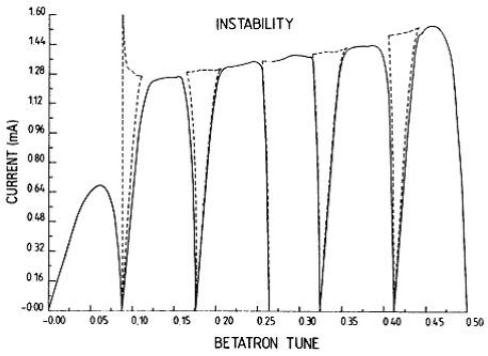

Figure 3: TMC threshold current vs. betatron tune with localized impedances, from Francesco's PhD thesis.

tribution affects the subsequent beam arriving at location s The effect arises from the wall charges at s. The distribution at s versus the turn number is to be analyzed. To this end one finds the eigenvalues of the Vlasov equation, and looks for instabilities. A Fourier transform is applied in s, with corresponding integer index k. The observation location chosen for the distribution can be taken to equal an impedance location. The Vlasov equation couples mode k to another mode $\bar{k}$, resulting in the impedance mode $k - \bar{k}$.

Normally accelerator physicists apply a smooth approximation and assume a uniform effective impedance. Francesco noticed that there would be no coupling between different modes k in such a case, i.e. for an effective impedance independent of s, while there would still be coupling between internal bunch modes and multibunch modes. Francesco looked at a different limit, namely the limit where all the ring impedance is concentrated at a single location. In this case only the fractional tunes can be relevant, and all modes k defined above are strongly coupled. Instead one can use a different mode basis, localized at a point s. The result then is a mode coupling between non-adjacent azimuthal mode numbers m, e.g. between $m = 0$ and $m = 4$. Fortunately, this coupling is typically weak. After a rather narrow stop band for higher intensity the motion is stable again. And the final strong instability can arise from the coupling between the modes $m = 0$ and $m = -1$, in a standard fashion. Mode parity explains why the approach of some of the modes does not result in a stop band.

4 LEP & TRISTAN

Francesco actively participated in "LEP-MDs" (machine development sessions), which was particularly valuable as he had been sent for a few weeks to KEK in Japan to participate in the commissioning of the world's second largest electron-positron collider "TRISTAN". During his stay in Japan, Francesco discussed many issues related to TRISTAN and to beam-beam effects with Kohji Hirata, whom he knew from an earlier correspondence on the correct treatment of a local impedance. Francesco's experiences at KEK are summarized in a LEP note [5], which he also sent to his friends and colleagues at KEK, where it was much appreciated. Shortly after his return to Geneva, Francesco invited Kohji Hirata to visit CERN and to profit from its exciting environment during the start up of LEP, in a letter dated 7 July 1987. At that time, TRISTAN had stopped using the electrostatic separators during injection and acceleration because of discharge problems and because they appeared to be unnecessary. Francesco wanted to know more details about the separator-free operation. Following Francesco's advice, Kohji Hirata decided to go to CERN as a scientific associate. His office was next to that of Francesco in building 30 and the two discussed and talked a lot in the offices and in the cafeteria of the 7th floor, leading in particular to the development of the "synchrobeam mapping", which we will recall in a later section on the "beam-beam" interaction.

5 CLIC AND BEAMSTRAHLUNG

In addition to his work on LEP Francesco also took an interest in the linear collider project CLIC, which was then proposing collisions of extremely small and dense bunches in order to achieve the very high luminosities desired by the experimenters. As classical physics seemed to predict that the energy loss in to the collision could become higher than the particle energies, it was then suspected that a quantum mechanical description would be required for these extreme particle densities. Several leading quantum physicists had already started to work on this problem.

With Claudio Pellegrini, who was then visiting CERN for several months, Francesco could show that this paradox was avoided when the "radiation reaction" was properly taken into account [6]; see Fig. 4. Following this study he further proposed the use of opposing bunches as focusing elements which could form an achromatic system without sextupole correction elements as required by conventional quadrupole channels [7].


CERN LEP-TH/86-03
CLIC Note No 9

RADIATION REACTION EFFECTS IN HIGH ENERGY ELECTRON-POSITRON LINEAR COLLIDERS

C. Pellegrini*) and F. Ruggiero

ABSTRACT

We discuss the electromagnetic interaction of electron and positron bunches at the focal point of a linear collider. Using classical electrodynamics and including the effect of the radiation reaction force, which plays a dominant role in the energy loss of the particles and influences their trajectories, we derive an expression for the beamstrahlung parameter which is consistent with energy conservation. In the limit of small losses, our results coincide with those obtained previously. We also discuss the conditions for which the classical description is no more valid and a quantum mechanical calculation is needed.

Figure 4: Paper with Claudio Pellegrini on "radiation-reaction effects" in linear colliders.

6 SYNCHROTRON RADIATION

In 1988 Kohji Hirata and Francesco studied the treatment of synchrotron radiation in electron storage rings, starting from basic principles [8].

Together with his former professors E. Picasso and L. Radicati Francesco also published a profound paper on the kinetic description of electron beam behavior in the presence of incoherent synchrotron radiation [9], as well as a lecture note on a statistical description of nonlinear phenomena in a charged-beam plasma [10]. With Emilio Picasso, Francesco also published an encyclopaedic article on particle accelerators [11] and some considerations on LEP [12]. Francesco also analyzed the effects of the discontinuous replacement of energy losses by RF cavities in LEP [13], and studied the proper inclusion of this radiation in simulation programs [14].

Later, for LEP, Francesco also derived a "correct" formula for the longitudinal quantum lifetime in electron storage rings [15], which differs from the classical formula of Matt Sands [16]. Francesco obtained his revised expression by applying a formalism developed much earlier by S. Chandrasekhar for problems involving diffusion across potential barriers in astrophysics [17]. After publishing his report Francesco received a phone call from Matt Sands in California. It is not clear whether that conversation came to a conclusion about the right expression.

7 OPTICS

Francesco published novel fundamental papers on many subjects of accelerator physics. Not quite as well known as his work on collective effects are his ingenious contributions to optics.

Together with Bob Gluckstern, Francesco derived the equation for the betatron function, the betatron phase advance, and the dispersion from variational principles [18]. These were recognized to be special cases of a general principle concerning the eigenvalues of a symplectic matrix.

For LEP Francesco also studied the subtle implications of a novel method to measure the dispersion dynamically via exciting longitudinal oscillations in the presence of spurious dispersion at the rf cavities [19], as well as, together with Alexander Zholents, a way to correct the residual dispersion in LEP resonantly [20].

Francesco wrote several novel and important modules of the accelerator design code MAD [21]. For a while Francesco's extended version of the code was called "rgomad", prior to its integration into the standard MAD code. The features introduced by Francesco were documented in [22]. They include an automatic search for the dynamic aperture "DYNAP", the calculation of early indicators of instability, like Lyapunov exponent or frequency detuning, and a global matching command "global" that could minimize any user-defined function. These tools were, and are still being, widely used, all over the world, for example in the design of BEPC-II at IHEP in China.

All his optics studies exhibited original approaches, novel methods, and a deep understanding of accelerator physics, which were, and remained, a key trademark of Francesco's work through his entire career in physics.

8 BEAM ECHOES

For many years Francesco was intrigued by beam echoes, which he considered a potentially highly efficient tool for measuring diffusion rates inside the beam. Early echo studies under his guidance were performed by Oliver Brüning [23], who joined Francesco's "collective effects" section in the SL-AP group as a fellow in 1995. Francesco's first assignment for Oliver was to study a paper by Pat Colestock, Francois Ostiguy and Linda Spentzouris on Beam Echo measurements in the Tevatron [24] and to explore the potential application of measuring small diffusion processes in an accelerator. Related echo phenomena had been studied earlier since the 1950's, for example spin echoes by E. Hahn in 1950 [25], plasma wave echoes by O. Neil in 1965 [26], or echo effects in hadron colliders by G. Stupakov and K. Kauffmann in 1992 [27], involving a dipole kick followed by a quadrupole kick. The beam echo studies at the CERN SPS in 1995 continued this type of research.

The longitudinal echo response in the beam current is of the form [23]

$$I(t) = A_{\mathrm{form}}(\rho) A_{rmenv}(t_1, t_2) A_{\mathrm{diffusion}}(D, t) \; , \qquad (1)$$

where the last term depends on the diffusion coefficient D. Francesco and Oliver realized that the echo response can be used for measuring small diffusion coefficients in relatively short time scales. The work at CERN clarified the correct interpretation of the diffusion term and provided the prerequisite for using this technique in a storage ring. The echo studies of the mid-90's proceeded via a strong collaboration within CERN between the accelerator physics (AP), RF and operation (OP) groups, as well as through a strong international collaboration performing and comparing measurements in several hadron machines: AGS, RHIC, HERA, Tevatron and SPS.

In 2000, a discussion of Francesco with Walter Scandale gave rise to the idea that it should be possible to generate transverse echoes in an unconventional way, namely by successively applying two dipole kicks of different magnitude rather than a single dipole kick followed by a quadrupole kick (transverse quadrupolar kickers are not available in most, if not all, machines). Francesco performed first simulations, and guided the parameter optimization for an SPS machine experiment in this new approach. The SPS study was immediately successful and led to the first ever observation of transverse beam echoes in good agreement with more advanced simulations [28]; see Fig. 5.

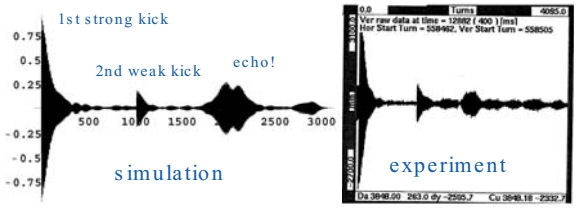

Figure 5: First observation of transverse beam echo induced by two successive dipole kicks at the SPS (right) compared with the corresponding simulation (left) [28].

9 LEP IMPEDANCE AND ZBASE

When Oliver Brüning joined the collective effects team Francesco also asked him to evaluate the LEP impedance as the Cu cavities were replaced by SC cavities and to estimate the TMCI threshold as a function of the installation progress. This task implied collecting the impedance data for different items from various groups, e.g. radiofrequency (RF), vacuum (VAC) etc., and to re-evaluate the wake fields and loss factors for shorter bunch length (requiring access to various computer tools: MAFIA, ABCI, etc.). The data was not always easy to get (e.g. geometry and wake potentials) and was generally not in a consistent format. This triggered the idea of building a data base "ZBASE" that ensured:

- a common data format (e.g. for measured data and for data from simulation or theoretical formulas);
- links to the programs that were used for calculating the impedance or wake potentials;
- the provision of tools for summing impedance and wake potential data of different items and converting from one to the other;
- including information of the relevant beam and optics data;
- the provision of tools for evaluation some of the key threshold values (e.g. TMCI and multi-bunch instability thresholds)

For this task to become a success, the work had to be done in the framework of a broad collaboration at CERN (e.g. including the RF and VAC groups), and in a close collaboration with external colleagues from other laboratories (e.g. Scott Berg and M. Dyatchkov); the data base had to be accessible from anywhere at CERN and in the world (leading to the choice of implementation on 'afs'); the data base had to be accessible from any platform (therefore the choice of an interpreted language: TclTk); and ZBASE had to be expandable to machines other than LEP, e.g. it included the LHC from the start.

It was not an easy task. A strong collaboration at CERN (e.g. between AP and RF) and beyond deserves credit for the successful outcome of the LEP ZBASE programme. Presently, we are at the 3rd generation of ZBASE (and there is no end in sight), which is being filled with updated data for the LHC and the SPS. The fact that the data base is still being developed demonstrates that there is a clear need for such a data base, which in turn shows that Francesco had the right vision when he asked Oliver to start this work.

10 LHC IMPEDANCE

10.1 LHC Beam Screen

After completion of his thesis Francesco remained in the LEP division of CERN as a fellow and later became a full staff member. One of his first tasks was the calculation of the impedance of the extremely large number of holes in the "liner" for the LHC. Such an inner vacuum chamber, held at an intermediate temperature, had been proposed for the LHC in order to reduce the cryogenic power required to keep the outer vacuum chamber near the very low magnet temperature of 2 degrees Kelvin by shielding it from the powerful synchrotron radiation of the beam. A similar idea had also been developed for the SSC which was then still planned to be built in Texas. Francesco started a collaboration with that laboratory, which was later extended to include accelerator physicists from the Budker Institute in Novosibirsk.

Francesco had found that the basic formulae for the electro-magnetic fields induced by a charged particle beam in a hole of a surrounding wall had already been derived many years earlier by the Nobel Laureate Hans Bethe. He extended this technique to estimate the impedance of the very large number of holes in a liner required to permit good pumping. He varied the hole shape, size, and number, and proposed random arrangements to reduce resonant effects on the beam occurring due to periodicities in regular arrangements. Over the next years the proposed shape of the liner was changed many times for mechanical reasons and many papers were written on this subject.

By 1995 the LHC pipe design had assumed the following features: rounded corners (manufacturing limitations), stainless steel pipe (pure Cu would not sustain the quenching forces due to magnetic field penetration & parasitic currents), copper-coated surface (uncoated SS would give excessive parasitic losses; the coating was restricted to flat faces, where fields and loss would be largest), and pumping holes (removal of desorbed gas molecules by synchrotron radiation). Beam-coupling impedances for this liner were computed by invoking a reciprocity theorem which can be applied if an unperturbed potential is known and using Leontòvich boundary conditions for the perturbed potential [29]. Stefania Petracca, closely collaborating with Francesco, used this reciprocity theorem for computing the longitudinal and transverse coupling impedances of a square liner with rounded corners [29].

The Leontovinch boundary condition [30]

$$\vec{n} \times \left(\vec{n} \times \vec{H} \right) = \sqrt{\frac{j\sigma}{\omega \mu_0}} \vec{n} \times \vec{E} \, , \qquad (2)$$

was originally formulated for a planar surface, bounding some highly reflecting transversely homogeneous lossy half-space. But in fact it is much more versatile than this, and it can also be applied to (1) lossy stratified media, e.g., by repeated use of the transmission-line impedance transport formula, (2) curved surfaces, and (3) inhomogeneous media, etc [31, 32].

The coupling impedance of perforated walls was computed starting from this boundary condition [29], and the impedance expressed through hole polarizabilities. The formulae obtained were consistent with earlier findings of Kurennoy [33] and Gluckstern et al [34]. Hole polarizabilities are available for a variety of hole shapes [35]. Corrections for hole-hole coupling were worked out [36] in the quasi-static approximation [37]. Corrections to Bethe's formula for polarizabilities beyond the underlying quasi-static ($kD \ll 1$) assumption (very short bunches) can be found in Ref. [38]. Stefania Petracca calculated the LHC parasitic losses on the beam screen analytically, adding the Ohmic and hole contributions. The final numbers were in good agreement with measurements by Fritz Caspers, Michele Morville, and Francesco.

Several calculations of beam-screen impedance were done in collaboration with Weiren Chou from the SSC, in particular, on how to minimize it in the slot design. Weiren and Francesco compared different lengths, shapes and distributions of slots and concluded that the short, racetrack-shaped, randomly distributed slots would be the best choice. This design was eventually adopted by the LHC. Figure 6 compares impedances for periodic and random slots produced in the course of a similar study for the SSC. Weiren Chou had extensive discussions with Francesco on this topic during his visit to CERN in 1995 because of the similarity between the SSC liner and LHC liner.

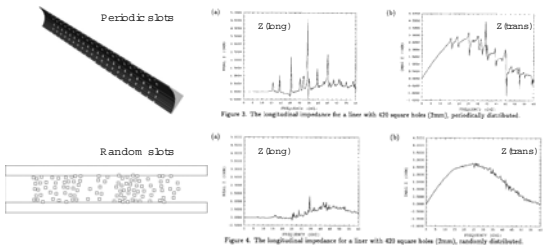

Figure 6: Longitudinal and transverse impedance of a beam screen with periodic (top) or random pumping slots (bottom) [39, 40] [Courtesy W. Chou].

In 1995 Weiren Chou tried to offer an alternative to the copper coated stainless steel pipe by an extruded aluminum pipe [41], which would have avoided the slots in the screen that might potentially generate TEM wave coupling between the beam and pipe. But Francesco refused to promote this proposal. And he was definitely right, especially in view of the later found electron cloud effect.

Detailed and advanced calculations on the beam pipe impedance were performed in the PhD thesis of Andrea Mostacci under the supervision of Francesco [42]. Andrea's thesis covered several aspects: (1) refined impedance calculations for the pumping slots, involving an analysis of the electromagnetic coupling through holes between a cylindrical and a coaxial waveguide; (2) the impedance effects of an artificial sawtooth roughness that had been added in 1997/98 to reduce the heat load from electron cloud, which required a study of the interaction between the beam and a surface (synchronous) wave in a (rectangular) beam pipe with "small" periodic corrugations; and (3) the effect of weldings, i.e. an investigation of the current distribution in a (metallic) beam pipe whose conductivity varies with the azimuth (for an ultrarelativistic beam).

With guidance from Francesco, Andrea Mostacci showed that randomizing the position of the holes does not affect the loss factor, and he calculated this (geometric) loss factor for N equispaced holes at distance D, in the limit of negligible Ohmic losses to be [42]

$$k(\sigma) = \frac{Z_0\sqrt{\pi}c(\alpha_m+\alpha_e)^2}{128\pi^4 b^4 \ln(d/b)\sigma^3}\left[N^2 + \left(\frac{\sigma}{D}\right)^2 \frac{(\alpha_m-\alpha_e)^2}{(\alpha_m+\alpha_e)^2}\right] , \tag{3}$$

with α_m and α_e denoting the magnetic and electric polarizability of the holes, respectively. Andrea also derived analytical expressions for the Ohmic losses in the coaxial region.

Depending on the length of the beam screen under consideration, one transits from a region where the losses per unit length increase linearly with the length of the beam screen to an asymptotic regime of constant loss per unit length. For LHC parameters, the transition occurs around a length of 100 m (roughly one arc FODO cell). Andrea Mostacci, Luigi Palumbo and Francesco together derived the exact formula which connects the two limiting regimes [43]. Around the nominal LHC values the (asymptotic) losses are described as [44]

$$P_\infty \approx P_0 \exp\left(-1.75\pi T/W\right) , \tag{4}$$

with

$$P_0 \approx 42\frac{\mathrm{mW}}{\mathrm{m}}\left(\frac{\mathrm{W}}{1.5\mathrm{mm}}\right)^4 , \tag{5}$$

where W denotes the slot width and T the wall thickness. A primary result of these investigations was that the power loss per unit length is negligible for holes of the nominal dimensions.

10.2 Resistive Wall Impedance

In addition to the impedance due to holes and other geometric obstacles, also the impedance arising from the resistivity of the liner should be included in the calculations. Francesco found a novel method to calculate the resistive wall impedance for pipes of arbitrary cross section, which he could express as derivative of their electric capacitance [45]. More specifically, Francesco showed that the longitudinal impedance is proportional to the "normal derivative"

of the electrostatic energy stored in the region between the beam and the surrounding beam pipe:

$$\frac{Z_L}{L} = Z_w \frac{\delta}{\delta n} \left(\frac{\epsilon_0}{\mathcal{C}} \right) , \quad (6)$$

where $\mathcal{C}$ denotes the "specific capacitance," and Z_w the surface impedance. He applied this new method of impedance computation to the LHC liner. From his equation he also deduced that for a centered beam pipe and for a given wall resistivity, a square pipe has the same longitudinal impedance as the inscribed circular pipe.

In the summer of 1995, while Weiren Chou visited CERN, he worked with Francesco not only on alternative beam screens, but foremost on the resistive wall heating of the LHC beam screen. Their joint study discussed for the first time the combined effect of wall resistance under three extreme conditions:

- at low temperature (a few °K);
- in a strong magnetic field (several Tesla); and
- for high frequency (fraction of GHz or above).

The result was published in the LHC Project Note no. 2 [46]. It led to a revision of the LHC cryogenic heat load budget, since the surface resistance of copper at cryogenic temperatures was found to be about a factor two larger than previously estimated. Further experimental and theoretical studies on this subject followed, under the leadership of Francesco [47, 48, 49]. Weiren Chou and Francesco had the chance to continue their discussions during Snowmass 1996 (Fig. 7).

Figure 7: Steve Holmes, Francesco Ruggiero, Hajime Ishimaru, Weiren Chou, Eberhard Keil, and Dave Finley at Snowmasss 1996 [Courtesy W. Chou].

Andrea Mostacci studied a beam pipe with azimuthally varying conductivity, using the calculation approach that had been described by Francesco in Ref. [45]. The current distribution and resulting azimuthal magnetic fields were obtained as a function of the azimuth for room temperature and cryogenic conditions at different frequencies. The main conclusions for LHC were that the surface currents are constant over the azimuth at all relevant frequencies. The losses in the welding equal 5% of the ones in the copper at room temperature or 50% of the copper losses at cryogenic temperatures.

An interesting exploration in this same context concerned the validity of the Leontovich boundary condition (2), which is a "first order" condition, or surface impedance boundary condition. A higher frequency limit arises from the requirement that the wave length be much larger than the skin depth. For stainless steel this gives a limit at 200 THz. At low frequencies two different effects limit the applicability of the Leontovich boundary condition at room temperature and at cryogenic temperature: the variation of the material properties should be small on the scale of the skin depth, and the beam pipe curvature should be much-larger than the skin depth. For LHC the resulting lower-frequency limits are 20 kHz and 5 kHz, respectively.

Both simulations by HFSS and laboratory Q measurements on a coaxial resonator comparing steel and brass bars [50] were used to corroborate the analytical results.

10.3 IR Y Chamber

For the LHC IR recombination chamber, or "Y chamber", MAFIA simulations demonstrated the importance of smooth transitions between the chambers to avoid unacceptable power deposition due to modes trapped in the structure [51].

For the LHC Y-chamber design, the trapped modes were not eliminated, but only damped, and further study was needed to see whether these modes could be either completely removed or damped to even lower values. Simulations by MAFIA and HFSS were benchmarked by measurements on a rectangular scaled model. These studies were performed in a collaboration which Francesco organized between CERN, LBNL, INFN, and the University La Sapienza. The joint studies demonstrated that tapering the transition, as in the actual geometry, strongly reduces the effect of the trapped modes [52, 53].

10.4 COLDEX

The COLD bore EXperiment (COLDEX) in the SPS machine uses an LHC-like cryogenic vacuum chamber to study the interaction with proton beams, with particular attention to the electron cloud effect. Its impedance was calculated in a collaborative effort [54]. For the upgraded COLDEX vacuum chamber studies with MAFIA indicated that the chamber heating due to the beam coupling impedance was reduced by two orders compared with an earlier version of COLDEX, and that, as a consequence, this heating should represent a negligible part of the measured total dissipated power [55], a large part of which could instead be attributed to the electron cloud.

10.5 Collimators

Invoking simple scaling arguments for the dependence of the resistive-wall impedance on length, resistivity, and aperture, Francesco was the first to point out that the LHC collimators had an impedance problem [56].

Some of the collimators in the LHC are not horizontal or vertical ones, but tilted in the transverse plane. Francesco readily showed how to deal with such cases using a tensor transformation [57], as sketched in Fig. 8.

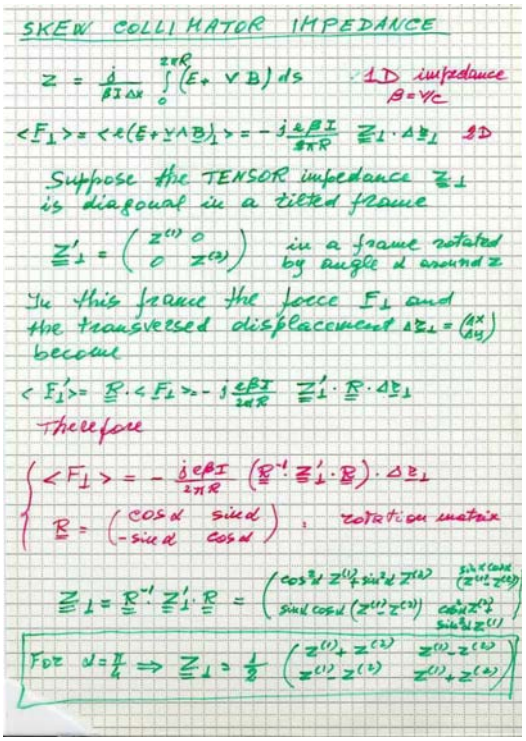

Figure 8: First slide from Francesco's presentation on the tensor impedance of tilted collimators [57].

For a skew collimator titled at $\pi/4$ the expression for the resulting tune shift is particularly simple. Noting that the impedance in the non-collimating direction $Z^{(2)}$ is equal to one half that in the collimating direction $Z^{(1)}$ (so-called Yokoya coefficient), the tune shifts induced by a skew collimator in either plane are [57]

$$\Delta Q_x = j\frac{N_b r_p}{2\pi\gamma}\frac{\beta_x}{Z_0 R}\frac{3}{4}Z_{(1)}\,, \qquad (7)$$

$$\Delta Q_y = j\frac{N_b r_p}{2\pi\gamma}\frac{\beta_y}{Z_0 R}\frac{3}{4}Z_{(1)}\,, \qquad (8)$$

Where Z_0 denotes the vacuum impedance, r_p the classical proton radius, and the beta functions are taken at the location of the collimator. In addition to these tune shifts the skew collimator also induced a cross term, i.e., a coherent horizontal motion will change the vertical focusing and vice versa, of strength [57]

$$\Delta Q_{xy} = j\frac{N_b r_p}{2\pi\gamma}\frac{\beta_x}{Z_0 R}\frac{1}{4}Z_{(1)}\,. \qquad (9)$$

10.6 Analytic Approximations of Tune Shifts and Beam Coupling Impedances

Together with Stefania Petracca, Francesco worked towards an analytical description of tune shifts and beam coupling impedances for the LHC.

The general tune shifts of the two transverse betatron modes are described by a tensor which is related to the tensor of Laslett coefficients. Both coherent and incoherent normal modes can be derived for square and circular pipes or liners. For a twin-beam toy model of an LHC dipole (Fig. 9) Stefania considered different regimes: incoherent-incoherent, coherent-coherent, and mixed. Both high-frequency non-penetrating modes and low-frequency penetrating modes were included. Different coherent and mixed dynamics were obtained [58]. The Al collars holding the beam pipes in the LHC design considered at the time would prevent the dynamic magnetic field from coupling the two beams, even at the lowest frequency associated with collective beam oscillations. As a result, the two beams are dynamically uncoupled. Neglecting space-charge effects, all regimes (incoherent, coherent, & mixed) merge in the limit $\beta \to 1$, yielding for both pipes the same general expression for the Laslett tensor.

Figure 9: Francesco Ruggiero, Massimo Placidi, Flemming Pedersen, and Karl-Heinz Schindl with an LHC dipole cold bore.

For analyzing real-world geometries, various numerical approaches were explored.

One of them is the *Method of Moments*. Using this method, rounded corners and shape variations were treated based on an efficient representation of the (exact) Green's function for rectangular and circular domains, allowing one to shrink the unknown charge density support (and related number of unknown charge expansion coeffecients) to a minimum [59]. This technique was used to compute the Laslett coefficients as a function of round-corner radius, and for a hard-cut circle model of the LHC beam screen, as in the final shape.

In the *random path* approach one computes the (complex) potential only on a circle, using stochastic calculus, and then uses the Cauchy integral formula for computing the Laslett coefficients without the need of approximating derivatives with finite differences [60]. Random paths were employed to compute the higher-order modes extending to the cold bore.

10.7 LHC Impedance Budget

The basic approach used for LHC impedances was to first identify the devices mostly affecting the machine impedance, and to make an impedance budget estimation for these devices: strip-line monitors, kickers, beam screen, Following the teaching of Bruno Zotter, Francesco and Luigi Palumbo perfected the impedance-wise design of LHC components. The fundamental guiding principle set up by Francesco was that the coupling impedance of each device must be estimated by means of at least two out of three methods: (1) theoretical estimation, (2) numerical simulation, and (3) bench measurements. Similar work was done for the impedance of DAFNE at LNF.

Examples of LHC impedance-wise designs, many of which were done in collaboration with Luigi Palumbo plus his students at the University La Sapienza in Rome, include (1) the LHC beam screen (vacuum pumping slots, artificial roughness, welding) [42]; (2) the anomalous skin effect [46, 47, 48, 49]; (3) the LHC IR [Y chamber] [51], and (4) the COLDEX chamber.

11 COLLECTIVE EFFECTS

Francesco had a deep understanding of collective phenomenona, which he demonstrated in his treatments of (1) the effect of a localized impedance treated in his thesis, (2) the two-dimensional transverse Landau damping, (3) electron cloud instability, and (4) space charge at high energy.

The effect of a localized impedance was discussed above. "Landau damping" can arise if the single-particle tune depends on the oscillation amplitude, together with a finite beam size. Due to the spread in frequencies an oscillation involving the entire beam will decohere, if the frequency of the oscillation lies within the beam frequency spread. Stability diagrams can be drawn so that any complex oscillation frequency within the boundary described by the diagram is stabilized. The boundary is a measure of the tune spread in the beam.

The LHC will have little radiation damping, but Landau damping is an important damping mechanism. When investigating the Landau damping caused by tune spread with amplitude one must take into account the betatron tune spreads in two directions. The calculation had only been done in one direction until Francesco looked at this problem. So he and Scott Berg computed it for two dimensions, with the tune shift as a function of the two transverse amplitudes pointing either into the same or in opposite directions [61]. Francesco found that if the tune shifts are in the same direction larger instabilities can be damped, but for tune shifts in opposite direction real mode shifts in both directions are allowed, which could be interesting in the presence of a modest space charge. The expected Gaussian tails must be truncated. Francesco worked out a model with cuts at 3σ; later Scott and Francecsco derived the solution for arbitrary cuts [61]. Afterwards, together with Elias Métral, Francesco extended the two-dimensional Landau damping formalism to explicitly include the combined effect of octupoles and nonlinear space charge, and the two applied this to the LHC at injection [62].

On many occasions, Francesco questioned whether space charge should be treated just as an impedance. He highlighted the difference that in case of space charge the beam itself, not a wall, mediates the force. The question was important for the LHC, where a large coherent space-charge tune shift might be favorable for Landau damping (it opposes the inductance). It induces a large incoherent tune spread, but does or can the space-charge tune shift with amplitude provide the naively expected Landau damping?

Based on work by himself, Luigi Palumbo, and other collaborators, Francesco wrote a comprehensive assessment of collective effects and the resulting impedance budget in the LHC, covering a large number of possible instabilities and space-charge effects, including fundamental questions about the role of space charge and particularities related to the large circumference of the LHC [63]. This report has become the "bible" of collective effects in the LHC.

Francesco also worked with K. Hirata and S. Petracca on bunch lengthening, using mathematical catastrophe theory [64].

12 ELECTRON CLOUD

A new type of collective effect is the electron cloud. In 1995-96 some concerns about the effect of "beam-induced multipacting" on the LHC vacuum were expressed by Oswald Gröbner, based on the ISR experience [65]. In response to instability observations at the KEK Photon Factory [66], and their interpretation as due to photoelectrons, the so-called "Ohmi effect" [67], a decision to add an antechamber to the arc vacuum chambers of the PEP-II Low Energy Ring (LER) was taken by Mike Zisman, and a last minute TiN coating effort for the final PEP-II LER arc chambers was launched by both John Seeman and Mike Zisman at the end of 1996. Following an invitation by Francesco after Snowmass 1996 (Fig. 10), Frank Zimmermann, who was involved in the PEP-II enterprise, visited CERN for two weeks in February 1997.

Frank realized that the number of synchrotron-radiation photons emitted per turn per proton in the LHC is the same as in the PEP-II positron ring. Therefore, in the LHC, photoemission, with a critical photon energy of 44 eV, would provide a formidable source of photoelectrons that could further be amplified by secondary emission via a "multipacting" process. During his stay at CERN Frank wrote a simulation code "ECLOUD" to model the electron-cloud generation in the LHC, including both photoemission and secondary emission. The simulations showed a run-away build up of electrons over a wide range of realistic surface parameters. Inspired by discussions with Francesco he added the electron space charge to limit the build up and obtained an equilibrium at rather high electron levels which could give rise to significant multibunch instabilities. Francesco also proposed to treat electrons spiraling in

Figure 10: Francesco Ruggiero and Frank Zimmermann during Snowmasss 1996.

a magnetic field as permanent magnetic dipoles. The result of Frank's study was published as an LHC Project Report [68].

Frank's work indicated various possible limitations for the beam intensities in the LHC due to the electron cloud. Francesco soon drew a schematic which nicely illustrated and summarized the process by which an electron cloud builds up in the LHC. It is shown in Fig. 11. The label "reflected" electrons was added by Francesco a couple of years later after the importance of elastic reflection had become clear [69]. Following Frank's visit, in 1997 and 1998, Francesco encouraged simulations at CERN by Oliver Brüning [70] and at LBNL by Miguel Furman [71], respectively, which highlighted that a main concern for the LHC is the energy deposition by the electrons given the limited cooling capacity of the LHC beam screens. LHC is the first storage ring ever in which this is a potential problem. The initial estimates for the resulting heat load were of order of several W/m, which would exceed the available cooling capacity of the LHC cryogenic system. The cryogenic system had been designed before the effect was discovered. At face value, one would have had to cut the bunch intensity or increase the bunch spacing by factors of a few to stay within the available cooling capacity of the cryogenic system.

Francesco recognized the importance of this potential threat and initiated a crash program at CERN that studied the implications of this effect for the LHC operation and looked at possible remedies for the LHC before all hardware designs were frozen. The crash programme was executed via a strong collaboration between different groups and departments at CERN (e.g. AB, AT and TS) and with the help of several other laboratories world wide

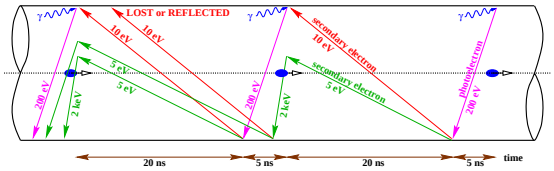

Figure 11: Schematic of electron-cloud build up due to photemission and secondary emission in the LHC, drawn by Francesco Ruggiero around 1997.

(e.g. LBNL, SLAC and BNL as part of US-LARP). Further studies and experimental evidence over the following years showed that the electron cloud effect is not only a problem for the LHC, but may also be one for the LHC injectors, SPS and PS, when operated with LHC beams.

At times there was skepticism about the electron cloud effect. Francesco looked at the calculations of others, saw its potential importance for LHC, and he vigorously started and led the crash program to address it. People involved in the LHC electron-cloud crash programme included Gianluigi Arduini, Vincent Baglin, Scott Berg, Christofore Benvenuti, Oliver Brüning, Fritz Caspers, Roberto Cimino, Ian Collins, Miguel Furman, Oswald Gröbner, Noel Hilleret, Ubaldo Iriso, Miguel Jimènez, Tom Kroyer, Mauro Pivi, Giovanni Rumolo, Daniel Schulte, Gennady Stupakov, Xiaolong Zhang, Frank Zimmermann, further colleagues of the LHC vacuum group, and many others.

The first simulation studies by Oliver Brüning aimed at a consolidation of Frank's code and an estimate of the parameter dependence of the expected heat-load [70]. Indeed the heat load in the magnets from the electron cloud was found to be a crucial issue. The heat arises via an energy transfer from the beam to the electron cloud. Francesco guessed that this could be approximated analytically assuming a known initial distribution. The analytical and approximate calculations of the electron energy gain for several longitudinal bunch profiles was accomplished by Scott Berg [72]. As a by-product, Scott's analytic computation also determined the minimum number of build-up simulation steps during a beam passage needed, so that the simulated electrons would correctly be trapped in the beam field.

Further studies looked at surface properties (secondary emission yield, energy spectrum of emitted electrons and surface conditioning due to synchrotron light and electron bombardment) and the impact of the low temperatures in the LHC with the help of laboratory setups (e.g. COLDEX installed in the EPA, and a dedicated coaxial resonator). Later studies used the SPS as a test bed and employed measurements with a real LHC-type proton beam (e.g. in-situ secondary electron yield measurements as a function of exposure time; spatial distribution of multipacting, and multipacting signals as a function of filling pattern).

Accomplishments either directly from the LHC crash programme or strongly inspired by it include: careful measurements of quantum efficiency and SEY in technical ma-

terials; the identification of TiZrV as a novel low-SEY coating for suppressing elecron-cloud effects; the development and deployment of several types of in-situ electron detectors; the measurement of electron flux and energy spectrum at SPS and RHIC with these detectors; the measurement of correlation of vacuum pressure with electron activity; the development of new mitigation mechanisms (e.g., grooved surfaces, high chromaticity mode, multibunch feedback for SPS in x-plane); the first observations of the electron cloud with LHC beam in SPS (1999) and in the PS (2001); the practical demonstration of self-conditioning of the electron-cloud effect at the SPS (within a few days); the development of careful secondary emission models; the understanding via analytical models; great developments in simulation codes, their validation, and benchmarking; the prediction of electron-cloud density and power deposition for LHC; the investigation of electron-cloud effects in other types of machines (eg., heavy-ion linacs); the investigation of the severity of the electron-cloud effect against fill pattern, bunch intensity, etc.

As a result of Francesco's concerted crash effort for the LHC, baffles were added behind the beam-screen pumping slots to prevent any direct impact of electrons on the cold magnet bore, and a sawtooth pattern was imprinted on the beam screen in the horizontal plane to minimize the photon reflectivity. In addition, LHC scrubbing and commissioning scenarios were developed, and other countermeasures, e.g. satellite bunches, were proposed [73] and tested in the SPS.

A further set of activities around the electron cloud concerned the single- and multi-bunch instabilities driven by the electron cloud. Francesco encouraged and guided the pertinent work of Elena Benedetto, Giuliano Franchetti, Giovanni Rumolo, Daniel Schulte, and Frank Zimmermann plus external collaborators like Kazuhito Ohmi and Eugene Perevedentsev [74, 75, 76, 77, 78, 79, 80], and in particular helped to establish a collaboration with Tom Katsouleas' group at USC [81].

Another outcome of the LHC electron-cloud effort is the CERN electron-cloud web site [82], which links to a simulation code repository [83, 84], code comparisons (e.g., for electron cloud [85]), experimental data, news, summaries of CERN meetings, workshop announcements and proceedings, links to related activities elsewhere, and, most importantly, an electron-cloud publications archive with about 200 articles at last count.

Much of the progress in electron-cloud R&D world-wide for the past $\sim$10 years is owed to, or has significantly benefited from, the LHC "Electron-Cloud Crash Program". Francesco Ruggiero deserves much of the credit for his strong and steady leadership.

The electron-cloud effect has meanwhile been recognized as an important limitation in all accelerators operating with positively charged intense particle beams. Electron-cloud effects have been observed at PEP-II, KEKB, BEPC, PS, SPS, APS, RHIC, Tevatron, MI, SNS, DAFNE, etc. They often diminish the accelerator performance. In some instances electron-cloud phenomena were generated in dedicated experiments. For the two B factories, PEP-II and KEKB, controlling the electron cloud proved essential to achieve and exceed the luminosity goals. At the Los Alamos PSR an electron cloud leads to high-current instability, and beam losses. At RHIC, fast vacuum pressure rise and instability at high current forces beam dump (in some fill patterns). Electron cloud is a major concern for future machines (LHC, LHC upgrade, LHC injector upgrades, CLIC and ILC damping rings, FNAL Main Injector upgrade,...).

For the LHC, the current consensus is that the electron-cloud heat load will cease to be a problem for the LHC when the peak secondary emission yield falls below $\sim$1.2–1.3. Probably this will be achieved after a relatively brief conditioning time. But, there is no clear experimental demonstration yet of this conditioning effect for a long, closed, cold Cu chamber. Concerning the effect of the electron cloud on the beam, difficult simulations are required, both below and above the threshold of strong electron-driven instability, and work is continuing. Much of the present R&D effort focuses on the proposed upgrades of both the LHC and its injectors.

13 BEAM-BEAM

A very important and fundamental contribution to the modeling of the beam-beam interaction is the "synchro-beam mapping", developed with Kohji Hirata, Herbert Walter Moshammer and Mario Bassetti [86, 87]. Work started at around the end of November 1989 (see the sketch from Francesco's discussion with K. Hirata dated 22 November in Fig. 12) and was completed basically at the end of January 1990. The main ingredients were: floating collision point, electric field due to focusing bunch, and an energy change due to a trajectory slope x; see the original slide in Fig. 13. The map was expressed by a product of several non-symplectic mappings. Symplecticity was the problem. H. Moshammer finally found that the map is symplectic using the code REDUCE. The map could be expressed in Lie algebraic form as $\exp(-H_{bb})x \rightarrow (\tilde{x} \equiv x - x'z/2))$. The result was first presented at a Workshop in Berkeley held 12–16, February 1990. It was later used, combined with Lorentz transformation, to verify the crossing angle option for the B factories.

In the early days of the US-CERN collaboration on the LHC, Weiren Chou worked with Francesco on dynamic aperture in the presence of the beam-beam effect. When Weiren presented him tracking results of the LHC dynamic aperture including the effect of long-range beam-beam collisions, Francesco immediately realized the seriousness of the problem and launched a simulation study at CERN. As a result, it was proposed to change the crossing angle in the baseline design from 200 to 300 μrad, which was later approved.

In 2001 Francesco and Frank Zimmermann recognized that the luminosity of a hadron collider can be pushed in an

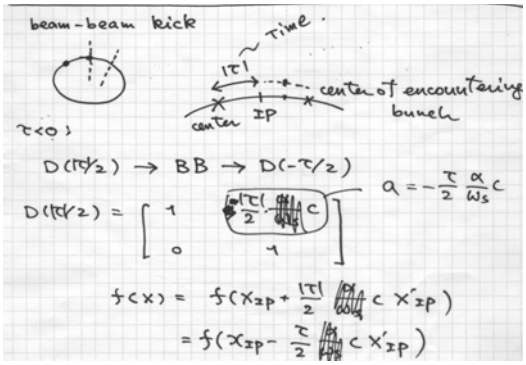

Figure 12: Initial work on the synchrobeam mapping; original sketch by Francesco during discussions with Kohji Hirata on 22/11/1989.

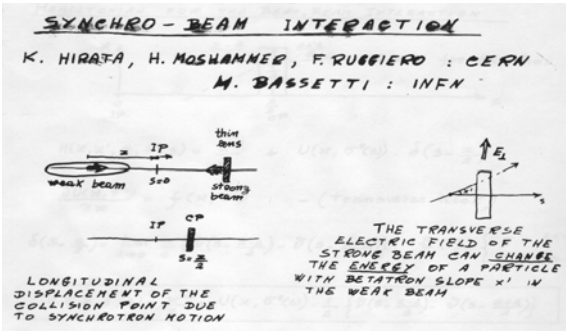

Figure 13: Slides from Francesco's first presentation on the synchro-beam interaction.

unconventional way by operating in a regime of large Piwinski angle and alternating planes of crossing at two collision points, which introduces the same geometric reduction factor both for the peak luminosity and, importantly, for the beam-beam tune shift [88]. At the beam-beam limit the luminosity can be re-expressed in the following form [88]:

$$L \approx \gamma \Delta Q_{\rm tot}^2 \frac{\pi \epsilon_N f_{\rm rep}}{r_p^2 \beta^*} \sqrt{1 + \left(\frac{\theta_c \sigma_z}{2\sigma^*}\right)^2}\,, \qquad (10)$$

where $\Delta Q_{\rm tot}$ signifies the total beam-beam tune shift, and ϵ_N the normalized emittance. The luminosity is proportional to the collision energy and to the normalized emittance which could be increased by a higher injection energy (accompanied with higher bunch intensity and constant beam brightness).

This approach to optimizing the collider luminosity has led to one of today's LHC upgrade scenarios which comprises intense bunches with 25-ns spacing and large Piwinski angle [89].

14 LHC UPGRADE

Francesco was the driving force behind the LHC upgrade studies. In 2001—2002 he chaired the first feasibility study for an LHC accelerator upgrade, which, on the request of the large physics experiments, aimed at an increase of the LHC luminosity by a factor 10, and he also edited its seminal summary report [90]. Later Francesco prepared, organized and led the European Network for high-energy high-intensity hadron beams, whose principal objective was to boost the luminosity performance of the LHC via a multi-pronged approach, including (1) an increase in beam intensity to ultimate or beyond, (2) an upgrade of the interaction regions in IP1 and 5, allowing for a reduced β^*, (3) the tailoring of LHC beam parameters for optimum luminosity at the beam-beam limit, (4) a possible installation of auxiliary components, e.g. long-range beam-beam wire compensators or crab cavities, and (5) an upgrade of the entire LHC injector complex, in order to raise the LHC beam intensity and brightness, as well as to reduce the LHC turnaround time.

Most, if not all, of Francesco's ideas have later been adopted by the CERN top management. They have meanwhile become the objects of several official projects, numerous working groups (PAF, SPL, PS2, SPSU, LIUWG, etc), the CERN DG White Papers, etc.

Francesco's efforts on the LHC luminosity upgrade have paved the way towards a brilliant future for CERN and for high-energy physics in general.

15 DAFNE UPGRADE

Around 2002–03 the Frascati laboratory started to discuss numerous intriguing ideas for an upgrade of DAFNE with at least 100 times higher luminosity, in which Francesco took an active interest. One of the new ideas for the DAFNE upgrade, proposed by Alessandro Gallo, Francesco Raimondi and Mikhail Zobov, was to arrange for a varying bunch length along the ring by providing for a large longitudinal phase advance so that the bunch would be short at the collision point, allowing for a small β^*, and large over most of the rest of the storage ring, — a scheme which was soon called "strong rf focusing" [91]. Initially a monotonic increase of the "momentum compaction" integral around the ring,

$$R_1(s) \equiv \int_s^{s_{rf}} \frac{D(s')}{\rho(s')} ds'\,, \qquad (11)$$

with s_{rf} the longitudinal location of the ring rf cavity, was considered for the strong rf focusing, which led to a large synchrotron tune that was not necessarily desirable. Later it was found that with a non-monotonic integral $R_1(s)$ around the ring a synchroton tune could be obtained while still retaining the strong focusing character of the longitudinal bunch evolution over one turn. The phase-space evolutions for the monotonic and non-monotonic R_1 integrals are compared in Fig. 14.

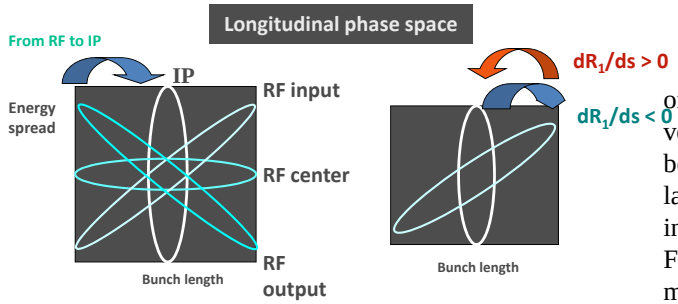

Figure 14: Schematic beam evolution in phase space for strong RF focusing with monotonic R_1 plushigh synchrotron tune (left) and non-monotonic R_1 plus low synchrotron tune (right) [92]

In September 2003 a workshop on the DAFNE upgrade was held in Alghero, Sardinia. Francesco took a vacation from CERN in order to participate in this event with his own money. Together with Mikhail Zobov, he chaired the session on "High Luminosity Issues". He reviewed the beam-beam scaling laws, plus luminosity constraints, and derived a strategy for optimizing the luminosity of the DAFNE upgrade, consisting of six ingredients. In parallel he collected other (alternative) new ideas for high luminosity, for example the collision of beams with much higher energy at a large crossing angle proposed by Pantaleo Raimondi, neutralized four-beam collisions with feedback, and ring-linac colliders, etc. Francesco's main conclusion from this workshop was that reaching a luminosity of 10^{35} cm^{-2}s^{-1}, about 1000 times higher than what DAFNE had so far achieved, required combining many new ideas and technologies, implying a higher risk and longer time scale than a more moderate upgrade target of 10^{34} cm^{-2}s^{-1}.

16 NUCLEAR FUSION IN LHC

The last scientific paper of Francesco, written together with Hans Braun and Frank Zimmermann, concerned the possibility and rate of nuclear fusion events occurring inside LHC proton or ion bunches and the resulting limit on the beam lifetime [93]. Quoting his own words, "... my original motivation was to understand whether "clean" nuclear fusion can be achieved in a high energy hadron machine, thus overcoming difficult problems of confinement in plasma fusion. It would be interesting to push the LHC ion beam intensity, for oxygen or other ions species (deuterium?), and set limits on the residual vacuum density and other machine parameters (e.g. space charge) such that nuclear fusion and the associated energy production becomes the dominant process" [94].

17 SEMINARS AND CULTIVATION

From 1982 to 1985, as a fellow at CERN, Francesco organized seminars for and from young scientists on diverse topics like particle detectors, RFQ design, TMCI and beam-beam interaction, gravitational waves, etc. Much later, in both the SL-AP and the AB-ABP group, Francesco initiated and scheduled the regular "Accelerator Physics Forum," which again covered a wide range of topics, mostly related to accelerator physics. He also created an informal series of accelerator physics publications meant to trigger and foster discussions, which could be rapidly published without any management approval, called the "Beam Physics Notes".

Francesco was always looking for the physical insight of results, the first condition for them to be correct. His initial step to assess a result was to always look for a counterexample. By way of his example he taught students and colleagues the need (and the pleasure) to understand in depth the issues that we were dealing with.

Francesco believed in the need of the SL-AP group of preserving and transmitting AP know-how. When he became group leader, training of students was explicitly declared in the SL-AP group mandate.

18 INTERNATIONAL COMMITMENTS

A member of the EPS Accelerator Group, Francesco helped in preparing the scientific programmes for several European Particle Accelerator Conferences (EPACs). He coordinated the sessions on "Beam Dynamics and Electro-Magnetic Fields" for the EPAC in Paris 2002, and for the EPAC in Lucerne 2004, as well as the session on "Circular Colliders" for the EPAC in Edinburgh 2006.

He contributed to PRST-AB, the refereed journal for accelerator physics and technology, as Associate Editor for Europe, and he belonged to the editorial board of the Springer series on *Particle Acceleration and Detection*. Since 2004 he was the coordinator of the European CARE-HHH (high energy high brightness hadron beams) accelerator network, as well as of its work package on "Accelerator Physics and synchrotron Design" (CARE-HHH-APD). It was thanks to his initiative that CARE-HHH created an accelerator-physics simulation codes web repository [83, 84] featuring programmes from many areas of beam physics, like beam-beam interaction, collimation, optics, instabilities, space charge, intrabeam scattering, cooling, nonlinear dynamics, vacuum, ions, electron cloud, etc.

19 BEYOND ACCELERATOR PHYSICS

Francesco loved the sea and its contemplation, animals as well as women loving animals, technological gadgets, and books about history, classical music and jazz. He was particularly fascinated by Einstein, the paradoxes of quantum mechanics, and by Pythagoras' vision of the world as a numeric harmony. In 2003 he gave two public lectures in

the Comune di Pergine Valdarno on "the relativity of Einstein" and "Einstein, Bohr, and the paradoxes of quantum theory". His 2005 article in "La Gazzetta dello Sport" explained to a general audience why boat weights measured in Valencia and Malmo differ by some 35 kg, addressing a mystery that arose during the weighing of boats between different races of the America's Cup.


BIBLIOTECA COMUNALE
DI PERGINE VALDARNO

Incontri sulla scienza

Centro Sociale di Pergine Valdarno
Venerdì 16 Maggio 2003 - ore 21,00

FRANCESCO RUGGIERO
Ricercatore fisico presso il CERN di Ginevra

la **Relatività di Einstein**

Tutto quello che avreste voluto sapere sulla relatività di Einstein ma non avete mai osato chiedere
I misteri della velocità della luce, spazio, tempo, piramidi e igloo
(con animazioni digitali)

Presentazione di **STEPHEN KATZ**
Responsabile del servizio divulgazione dati e informazioni della FAO

Iniziativa in collaborazione con la Scuola Media di Pergine Valdarno
e con l'Associazione Astrofili di Pergine V.no.

Figure 15: Announcement of Francesco's public lecture on "the relativity of Einstein" in Pergine 2003.


COMUNE DI PERGINE VALDARNO
(Provincia di Arezzo)

La Biblioteca Comunale di Pergine Valdarno
in collaborazione con la **Scuola Media di Pergine Valdarno**

organizzano per

Venerdi 21 Maggio alle ore 21,00

presso il Centro Sociale di Pergine Valdarno il **secondo incontro sulla scienza**

FRANCESCO RUGGIERO

Ricercatore fisico presso il CERN di Ginevra illustra

"EINSTEIN, BOHR, E I PARADOSSI DELLA TEORIA DEI QUANTI"

"Dal principio di indeterminazione al teletrasporto"

Niels Bohr Archive

Figure 16: Announcement of Francesco's public lecture on "Einstein, Bohr, and the paradoxes of quantum theory" in Pergine 2003.


ULTIMA

VELA | VUITTON IN SVEZIA

Malmoe, giallo sulla bilancia

Nessuna modifica ma barche più pesanti che a Valencia: colpa della gravit

LA GIULIA

DOMANI ACT 6 COI MATCH RACE

LO SCIENZIATO

Perché ai poli pesiamo di più

Figure 17: Francesco's article on boat weights at the America's cup in the Gazzetta dello Sport, August 2005

20 EPILOGUE

Francesco Ruggiero has contributed to many more scientific studies than mentioned in this paper. The examples above represent a set of projects where we had the chance and privilege to work together with him. All examples presented in this article underline Francesco's remarkable ability to bring people together and to work with a team for a common goal. Thereby Francesco contributed much more to our community than with his direct scientific studies alone.

But of course, Francesco's studies, publications, and seminars, have also greatly advanced accelerator physics. Francesco deeply understood collective phenomena. He always went far beyond simple repetition of previous work, and he encouraged those around him to do so too. He gave us many great ideas, and produced a multitude of interesting results.

His papers and reports remain extremely useful for the design and optimization of future particle accelerators and colliders.

Francesco was humble and rigorous in the research work, open minded, ready to listen to any other's opinion, an excellent mentor for young bright physicists, and a true gentleman. He respected and promoted the work of young people. He had the rare ability to make meaningful comments or suggestions on many technical aspects of any accelerator physics problem. He loved physics, and he was full of passion and energy, often working in his office until dawn.

During his long fight with cancer, he never gave up hope to fully recover and return to work. We are deeply saddened by his much too early death. Francesco will not only

be missed as a knowledgeable scientist but also as a great colleague and friend, by us and by the worldwide accelerator community.

We take some comfort in Hirata's thought that the memory of the creative moments enjoyed together with him will not damp nor diffuse, just like a constant of motion.

21 REFERENCES

[1] F. Ruggiero, "Alcuni Problemi Relativi allo Rivelazione delle Onde Gravitazionali," Anno Academico 1997–1980, Università degli Studi di Pisa e Scuolo Normale Superiore di Pisa pg. 1–180 (1980).

[2] The Francesco Ruggiero Memorial Symposium was organized at CERN on 3 October 2007, as part of the CARE-HHH BEAM'07 workshop; web site with talks: *http://indico.cern.ch/conferenceOtherViews.py?view=cdsagenda&confId=20082*

[3] F. Ruggiero, "Theoretical Aspects of Some Collective Instabilities in High-Energy Particle Storage Rings," Tesi di Perfezionamento preggo Scuola Normale Suepriore di Pisa (Tesi di Dottorato), CERN 86-06 (1986).

[4] F. Ruggiero, "Transverse Mode Coupling Instability due to Localized Structures," CERN-LEP-TH/84-21 (1984), published in Part. Accel. 20:45 (1986).

[5] F. Ruggiero, "Report on my Visit to KEK: 15 to 28 May 1987," LEP Theory Note 50 (1987).

[6] C. Pellegrini and F. Ruggiero, "Radiation Reaction Effects in High Energy Electron-Positron Linear Colliders," CLIC Note No. 9, CERN-LEP-TH-86-03 (1986).

[7] F. Ruggiero, "Achromatic Dissipative Focusing," CLIC Note 33 and LEP-TH/87-11 (1987).

[8] K. Hirata and F. Ruggiero, "Treatment of Radiation in Electron Storage Rings," CERN Report, LEP Note 611 (1988).

[9] F. Ruggiero, E. Picasso, L.A. Radicati, "Kinetic Description of the Beam Relaxation Caused by Incoherent Synchrotron Radiation in High-Energy Electron Storage Rings," Annals of Physics 197, pp. 396-438, Feb. 1990, and LEP-TH/89-40 (1989).

[10] F. Ruggiero, E. Picasso, L.A. Radicati, "Consideration on the Statistical Description of Charged-Beam Plasma," 1st US-CERN School on Particle Accelerators - Nonlinear dynamics aspects of particle accelerators Topical Course on Nonlinear Dynamics, Santa Margherita di Pula, Sardinia, 31 Jan - 5 Feb 1985, published in Lecture Notes in Physics Vol. 247, pp. 1–11, Springer Verlag (1986).

[11] E. Picasso, F. Ruggiero, "Gli Acceleratori di Particelle," in Storia della Scienza, Vol. IX, 145–159, Istituto Enciclopedia Italiana, Treccani (2003).

[12] E. Picasso, F. Ruggiero, "Alcune Considerazioni relative all Costruzione del LEP," Il Nuovo Saggiatore, Vol.'4, 16–50 (1988).

[13] F. Ruggiero, "Consequences of the Discontinuous Replacement of Radiated Energy on the Performance of LEP200," Report CERN-LEP-TH-89-19 (1989).

[14] K. Hirata and F. Ruggiero, "Treatment of Radiation for Multiparticle Tracking in Electron Storage Rings," CERN/LEP-TH/89-43 (1989).

[15] F. Ruggiero, "A Correct Formula for the Longitudinal Quantum Lifetime in Electron Storage Rings," CERN SL/93-05 (AP) (1993).

[16] M. Sands, "The Physics Of Electron Storage Rings: An Introduction." SLAC-0121 (1970).

[17] S. Chandrasekhar, "Stochastic Problems in Physics and Astronomy," Rev. Mod. Phys. 1943 (1943).

[18] R.L. Gluckstern, F. Ruggiero, "Variational Formulation for Linear Optics in a Periodic Focussing System," Part. Acc. 39, 125136 (1992).

[19] F. Ruggiero, "Effect of Residual Dispersion at the RF Cavities on the Dynamic Measurement of Dispersion in LEP," CERN SL/91-38 (AP).

[20] F. Ruggiero and A. Zholents, "Resonant Correction of Residual Dispersion in LEP," SL-MD Note 26 (1992).

[21] H. Grote, C. Iselin, "The MAD Program (Methodical Accelerator Design): Version 8.10; User's Reference Manual - 3rd ed.," CERN-SL-90-13-AP-rev-3 (1993).

[22] C. Iselin and F. Ruggiero, "A Modified Version of the Program MAD to Improve the Efficiency of Tracking Studies", CERN-SL-96-011 AP (1996).

[23] O. Brüning, T. Linnecar, F. Ruggiero, W. Scandale, E. Shaposhnikova, "Measuring Diffusion Coefficients and Distribution Functions Using a Longitudinal Beam Echo," 12th Advanced ICFA Beam Dynamics Workshop on Nonlinear and Collective Phenomena in Beam Physics, Arcidosso, Italy, September 1996, AIP Conf. Proc. 395, 155–162 (1996).

[24] P.L. Colestock, L.K. Spentzouris, F. Ostiguy, "Nonlinear wave phenomena in coasting beams," Proc. 16th IEEE Particle Accelerator Conference (PAC 95), Dallas, Texas, 1-5 May 1995, pp 2757-2761 (1995).

[25] E.L. Hahn, Phys. Rev. 80, 4 (1950).

[26] T.M. O'Neil, Phys. Fluids, 8, 12, (1965).

[27] G.V. Stupakov and K. Kauffmann, "Echo Effects in Accelerators," SSCL-587 (1992).

[28] G. Arduini, F. Ruggiero, F. Zimmermann, M.-P. Zorzano, "Transverse Beam Echoe Measurements on a Single Proton Bunch at the SPS," SL-Note-20000-048 MD (2000).

[29] S. Petracca, "Reciprocity Theorem for Coupling Impedance Computation in the LHC Liner," Part. Accel., 50, 211 (1995).

[30] L.D. Landau and E. Lifshitz, "Electrodynamics of Continuous Media," Course of Theoretical Physics, Vol. 8 (Pergamon, London, 1960), 2nd ed. (1960).

[31] T. Senior, J. Volakis, "Approximate Boundary Conditions in EMtics, IEE Press (1995).

[32] L.N. Trefethen, L. Halpern, "Well-Posedness of One-Way Wave Equations and Absorbing Boundary Conditions," Math. Comput. 47, 421 (1986).

[33] S. Kurennoy, "Impedance Issues for LHC Beam Screen," Workshop on Collective Effects in Large Hadron Colliders, Montreux, 17–22 October 1994, published in Part. Accel. 50, 167 (1995).

[34] R. Gluckstern, J. Diamond, "Penetration of Fields Through a Circular Hole in a Wall of Finite Thickness," IEEE Trans. MTT-39, 274 (1991).

[35] F. de Meulenaere, J. Van Bladel, IEEE Trans. AP-25, 198 (1977); R. de Smedt, J. van Bladel, IEEE Trans. AP-28, 703 (1980).

[36] S. Petracca, "Coupling Impedances for Perforated Beam Pipes with General Shape from Impedance Boundary Conditions," Phys. Rev. E60, 6030 (1999).

[37] R.E. Collin, Field Theory of Guided Waves, IEEE Press, New York (1991).

[38] J. Van Bladel, "Field Penetration Through Small Aperture: The First Order Correction," Radio Sci. 14, 319 (1979).

[39] W. Chou, T. Barts, "Wake Field and Impedance Studies of a Liner Using MAFIA," SSCL-PREPRINT-204, Proc. Computational Accelerator Particles Conference, "CAP'93," Pleasanton, February 22-26, 1993 (1993).

[40] W. Chou, T. Barts, "Ipedance of a perforated liner and its impact on the SSC collider," SSCL-PREPRINT-425, Proc. 1993 IEEE Particle Accelerator Conference (PAC 93), Washington, DC, 17-20 May 1993, pp. 3444-3446 (1993).

[41] W. Chou, "Feasibility Study of Using aluminium Alloy for the LHC Beam Screen," LHC-Project-Note-3 (1995).

[42] A. Mostacci, "Beam-Wall Interaction in the LHC Liner," PhD Thesis, U. La Sapienza, Roma, and CERN-THESIS-2001-014 (2001).

[43] A. Mostacci, L. Palumbo. F. Ruggiero, "Impedance and Loss Factor of a Coaxial Liner with Many Holes: Effect of the Attenuation," Phys. Rev. ST Accel. Beams 2:124401 (1999).

[44] A. Mostacci, F. Ruggiero, "Pumping Slots and Thickness of the LHC Beam Screen," LHC Project Note 195 (1999).

[45] F. Ruggiero, "Resistive Wall Impedance as Derivative of the Electric Capacitance for a Beam Pipe of Arbitrary Cross Section," Report CERN-SL-95-95 (1995), and Phys. Rev. E 53,3 (1996).

[46] W. Chou and F. Ruggiero, "Anomalous Skin Effect and Resistive Wall Heating," LHC Project Note 2 (SL/AP) (1995).

[47] F. Caspers, M. Morvillo, F. Ruggiero, "Surface Resistance Measurements for the LHC Beam Screen," LHC-Project-Report-115 (1997).

[48] F. Caspers, M. Morvillo, F. Ruggiero, J. Tan, "Surface Resistance Measurements and Estimate of the Beam-Induced Resistive Wall Heating of the LHC Dipole Beam Screen," LHC-Project-Report-307 (1999).

[49] F. Caspers, M. Morvillo, F. Ruggiero, J. Tan, H. Tsutsui, "Surface Resistance Measurements of LHC Dipole Beam Screen Samples," LHC-Project-Report-410 (2000).

[50] F. Caspers, A. Mostacci, L. Palumbo, F. Ruggiero, "Image Currents in Azimuthally Inhomogeneous Metallic Beam Pipes," LHC Project Report 493 (2001).

[51] B. Spataro, F. Ruggiero, D. Brandt, L. Vos, A. Mostacci, M. Migliorati, L. Palumbo, "Impedance of the LHC Recombination Chambers," LHC-PROJECT-NOTE-254 (2001).

[52] B. Spataro, F. Ruggiero, D. Brandt, L. Vos, A. Mostacci, M. Migliorati, L. Palumbo, D. Li, "On Trapped Modes in the LHC Recombination Chambers: Numerical and Experimental Results," Nucl. Instrum. Methods Phys. Res. A 517, 19-27 (2004).

[53] B. Spataro, F. Ruggiero, M. Migliorati, A. Mostacci, L. Palumbo, "Coupling Impedances of LHCb Recombination Chamber (IR8)," LHC-PROJECT-NOTE-348 (2004).

[54] B. Spataro, D. Alesini, M. Migliorati, A. Mostacci, L. Palumbo, V. Baglin, B. Jenninger, F. Ruggiero, "Impedances of the Cold Bore Experiment, COLDEX, Installed in the SPS Machine,' Nucl. Instrum. Methods Phys. Res. A 564, 38-43 (2006).

[55] B. Spataro, D. Alesini, M. Migliorati, A. Mostacci, L. Palumbo, V. Baglin, B. Jenninger, F. Ruggiero, "Coupling Impedance Studies and Power Loss Measurement of the COLDEX Upgraded Vacuum Chamber," to be published in Nucl. Instrum. Methods Phys. Res. A.

[56] F. Ruggiero, "Transverse Resistive Impedance of LHC Collimators Versus Impedance of Cold Beam Screen in the Arcs," CERN AB-LCE Meeting 14 February 2003.

[57] F. Ruggiero, "Tensor Transformation for Skew Collimators," CERN AB-LCE Meeting 3 October 2003.

[58] S. Petracca, "Normal Mode Laslett Coefficients for One (Coaxial) and Two (Offset) Liners in a Circular Magnetic Yoke," Part. Accel. 62, 241 (1999).

[59] S. Petracca, V. Galdi, I.M. Pinto, "Efficient Computation of Electrical Laslett Coefficients for Rounded-Rectangular Pipes," Part. Accel. 63, 37 (1999).

[60] S. Petracca, F. Ruggiero, V. Galdi, I.M. Pinto, "Path Integral Computation of Laslett Coefficients in Pipes with Arbitrary Transverse Geometry," Proc. PAC-97, 1753 (1997).

[61] J.S. Berg, F. Ruggiero, "Landau Damping with Two-Dimensional Betatron Tune Spread," CERN-SL-96-071-AP (1996).

[62] E. Métral, F. Ruggiero, "Stability Diagrams for Landau Damping with Two-Dimensional Betatron Tune Spread from Both Octupoles and Nonlinear Space Charge Applied to the LHC at Injection," CERN-AB-2004-067 (2004).

[63] F. Ruggiero, "Single-Beam Collective Effects in the LHC," CERN SL/95-09 (AP) (1995).

[64] K. Hirata, S. Petracca, and F. Ruggiero, "New Type of Bunch Lengthening with Cusp Catastrophe in Electron Storage Rings," Physical Review Letters 66, 1693 (1991), and CERN report CERN-SL-90-96 (1990).

[65] O. Gröbner, "Technological Problems Related to the Cold Vacuum System of the LHC", Vacuum, vol. 47, pp. 591-595 (1996).

[66] M. Izawa, Y. Sato, T. Toyomasu, "The Vertical Instability in a Positron Bunched Beam," Phys. Rev. Lett. 74:5044–5047 (1995).

[67] Kazuhito Ohmi, "Beam and Photoelectron Interactions in Positron Storage Rings," Phys. Rev. Lett. 75:1526–1529 (1995).

[68] F. Zimmermann, "A Simulation Study of Electron Cloud Instability and Beam Induced Multipacting in the LHC," CERN-LHC-PROJECT-REPORT-95, SLAC-PUB-7425 (1997).

[69] R. Cimino, I.R. Collins, M.A. Furman, M. Pivi, F. Ruggiero, G. Rumolo, F. Zimmermann, "Can low energy electrons affect high energy physics accelerators?," Phys. Rev. Lett. 93:014801, also SLAC-PUB-10350, CERN-AB-2004-012-ABP, LBNL-54594 (2004).

[70] O. Brüning, "Simulations for the Beam-Induced Electron Cloud in the LHC Beam Screen with Magnetic Field and Image Charges," LHC-Project-Report-158 (1997).

[71] M.A. Furman, "The Electron cloud effect in the arcs of the LHC," CERN-LHC-PROJECT-REPORT-180 (1998).

[72] S. Berg, "Energy Gain in An Electron Cloud During the Passage of a Bunch," LHC-Project-Note-97 (1997).

[73] F. Ruggiero and X.-L. Zhang, "Collective Instabilities in the LHC: Electron Cloud and Satellite Bunches," Proc. Workshop on Instabilities of High Intensity Hadron Beams in Rings, BNL, 28 June-1st July 1999, '¡eds. T. Roser and S.Y. Zhang, AIP Conf. Proceedings 496 (1999), pp. 40-48 (1999)

[74] F. Ruggiero, G. Rumolo, F. Zimmermann, "Simulation of the electron cloud buildup and its consequences on heat load, beam stability and diagnostics," ICAP 2000 Darmstadt, Phys. Rev. ST Accel. Beams 4:012801 (2001).

[75] K. Ohmi, F. Zimmermann, "Head-Tail Instability Caused by Electron Cloud in Positron Storage Rings," Phys. Rev. Lett. 85:3821-3824 (2000).

[76] K. Ohmi, F. Zimmermann, E. Perevedentsev, "Wake-Field and Fast Head-Tail Instability Caused by an Electron Cloud," Phys. Rev. E65:016502 (2002).

[77] E. Benedetto, G. Rumolo, D. Schulte, F. Zimmermann, "Simulation of Transverse Single Bunch Instabilities and Emittance Growth Caused by Electron Cloud in LHC and SPS," Proc. 31st ICFA Beam Dynamics Workshop: Electron Cloud Effects (ECLOUD04), Napa, California, 19-23 April 2004.,

[78] G. Rumolo, F. Zimmermann, "Practical User Guide for HEADTAIL," SL-Note-2002-036-AP (2002).

[79] E. Benedetto, "Emittance Growth Induced by Electron Cloud in Proton Storage Rings," PhD Thesis Politecnico di Torino (2006).

[80] E. Benedetto, G. Franchetti, F. Zimmermann, "Incoherent Effects of Electron Clouds in Proton Storage Rings," Phys. Rev. Lett. 97:034801 (2006).

[81] G. Rumolo, F. Zimmermann, F. Ruggiero, A.Z. Ghalam, T. Katsouleas, C.K. Huang, V.K. Decyk, C. Ren, W.B. Mori, "Electron Cloud Effects on Beam Evolution in a Circular Accelerator," Phys. Rev. ST Accel. Beams 6:081002 (2003).

[82] The CERN electron-cloud web site is *http://ab-abp-rlc.web.cern.ch/ab-abp-rlc-ecloud/*.

[83] F. Zimmermann et al., "Accelerator physics code web repository," EPAC'06 Edinburgh (2006).

[84] Web site of CARE-HHH accelerator physics simulation codes web repository is *http://oraweb.cern.ch:9000/pls/hhh/code_website.startup*

[85] E. Benedetto, F. Ruggiero et al., "Review and Comparison of Simulation Codes Modeling Electron-Cloud Build Up and Instabilities," EPAC 2004, Lucerne (2004).

[86] K. Hirata, H. Moshammer, F. Ruggiero and M. Bassetti, "Synchro-Beam Interaction," AIP Conference Proceedings No. 214 "Beam Dynamics Issues of High-Luminosity Asymmetric Collider Rings," (Ed. A.M. Sessler) p. 389 (1990)

[87] K. Hirata, H. Moshammer and F. Ruggiero, "A Symplectic Beam-Beam Interaction with Energy Change, Particle Accelerators," 40, 205 (1993).

[88] F. Ruggiero and F. Zimmermann, "Luminosity Optimization near the Beam-Beam Limit by Increasing Bunch Length or Crossing Angle," CERN SL-2002-005-AP (2002) and Phys. Rev. ST Accel. Beams. 5, 061001 (2002).

[89] F. Zimmermann, "LHC Upgrade Scenarios," PAC07 Albuquerque (2007).

[90] O.S. Brüning et al, F. Ruggiero (ed.), "LHC Luminosity and Energy Upgrade: A Feasibility Study," LHC-Project-Report-626 (2002).

[91] A. Gallo, P. Raimondi, M. Zobov, "Strong RF Focusing for Luminosity Increase," DAFNE-TECHNICAL-NOTE-G-60, e-Print: physics/0309066 (2003).

[92] C. Biscari, "Bunch Length Modulation in Highly Dispersive Storage Rings," Phys. Rev. ST Accel. Beams 8:091001 (2005).

[93] H.H. Braun, F. Ruggiero, F. Zimmermann, "Lifetime Limit from Nuclear Intra-Bunch Scattering for High-Energy Hadron Beams," Proc. EPAC06 Edinburgh and LHC Project Report 942 (2006).

[94] Last scientific email of F. Ruggiero to F. Zimmermann, 24 June 2006.

FRANCESCO AND MAD

Q. Qin#

Institute of High Energy Physics, CAS, Beijing 100049, P.R. China.

Abstract

A new version of the accelerator design code, MAD, was developed by Francesco Ruggiero in 1996. It can provide the function of automatically searching for the dynamic aperture of a synchrotron. With this MAD, we optimized the dynamic aperture of the upgrade project of Beijing Electron Positron Collider (BEPCII) at its R&D stage.

INTRODUCTION

As we all know, MAD (Methodical Accelerator Design) [1] is a code for circular synchrotron design, developed in 1980's by H. Grote and F. C. Iselin. With the code MAD, people can match a linear lattice of a circular synchrotron, correct chromaticity, optimize dynamic aperture with or without magnetic field errors, calculate synchrotron radiation related parameters, simulate beam-beam effects and beam lifetime, etc. Numerous circular machines were designed by using MAD. The language used in its input file became gradually the normal format in the later codes. In this paper, the new features introduced by Francesco are listed and the application on the BEPCII storage ring is explained.

NEW FEATURES OF MAD INTRODUCED BY FRANCESCO

It was 1989 when I first used MAD in my work on the Beijing Electron-Positron Collider (BEPC) in the Institute of High Energy Physics (IHEP). After that time, MAD became the main tool of mine to do accelerator study and design. In 1995, I worked in the SL/AP group of CERN as a visiting associate on the dynamic aperture optimization of the Large Hadron Collider (LHC). Dynamic apertures study was one of the most important topics of the LHC design. How to eliminate the effect of sextupolar and decapolar magnetic errors was the key point of the optimization of the LHC lattice. One of my tasks was to investigate the effect of each higher order component of the magnet fields of dipoles and quadrupoles installed around the LHC ring. At that time, I could only use MAD to do tracking one by one particle launched in the machine with different initial positions or divergences. It took the CPU of the SPARC computer about 12 hours for one particle tracking for one million turns of the LHC. When magnetic field errors were introduced, particles with different initial conditions were tracked with 60 random seeds in Gaussian distribution. So, this work was very much time-consuming. It took me about 3 months to get the results of different normal and skew field components for the version 4.1 of the LHC injection lattice.

A new version of MAD called "rgo mad" [2] was delivered to the users in the SL/AP group in April, 1996. In this new version, the new command *dynapstart* has attributes common to the MAD commands start and run. It defines the initial conditions of *xstart*, *pxstart*, *ystart*, *pystart*, *tstart*, *ptstart* and tracking options for a single particle. Together with the conventional MAD variables, such as normal mode chromaticities and anharmonicities, these new quantities could be saved in special tables and generated correlation plots. A subsequent call *dynap* is used to invoke tracking, performing an automatic search of dynamic aperture and can then compute several auxiliary quantities according to the additional attributes of *dynapstart*. A fraction *dynapfrac* of the initial betatron conditions gives the final result of the dynamic aperture. In the "rog mad" version, a new command *global* was added to have more capabilities of matching. The newly introduced variables can be used as the global matching constraints for a numerical optimization of machine parameters related to the dynamic aperture.

To my regret, I didn't use these new features of "rgo mad" for the dynamic aperture study of the LHC when I worked at CERN, since I returned my home institute on May, 1996.

APPLICATION OF THE "RGO MAD" IN IHEP

After I retuned the IHEP, Beijing, China, I was involved in the feasibility study of the project Beijing τ-Charm Factory, which started in 1996 and ended in 1998. This project was not approved by the government at that moment. In late 1998, the upgrade project of the Beijing Electron Positron Collider (BEPC), which is called BEPCII, started with its conceptual design of the storage ring. As an upgraded project, it was hoped to keep the original BEPC tunnel and all the synchrotron radiation beam line exit ports unchanged when it provided beam to synchrotron radiation users in addition to high energy physics experiments. It changed its design from a single-ring machine to a double-ring factory like collider in 2001, shown as Fig. 1. The current BEPCII locates in the original BEPC tunnel, with a crossing angle of 11mrad×2 at its interaction point, when it runs as a collider. A third ring, which is composed of the two halves of outer rings, can deliver beam to the synchrotron radiation users at a higher energy compared to the collision.

In the design of this project, I was in charged of the dynamic aperture optimization for the non-linear lattice of the BEPCII storage ring. According to the experiences got

#qinq@ihep.ac.cn

in the work at CERN, I chose MAD as a tool to study the dynamic aperture of the BEPCII storage ring in the R&D stage.

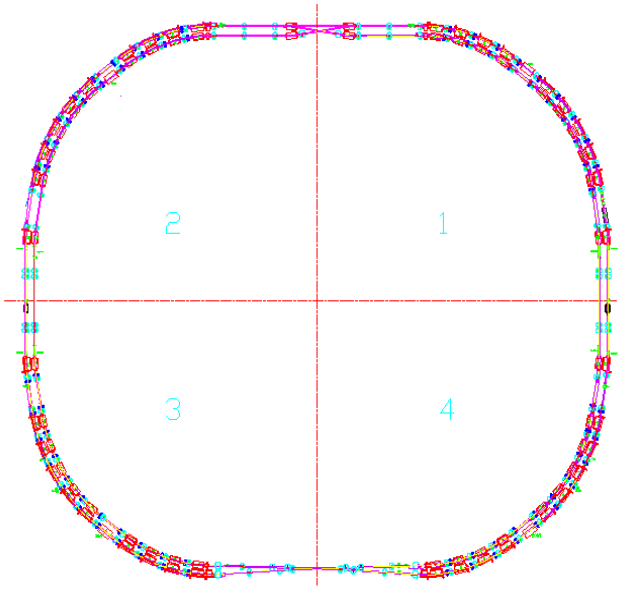

Figure 1: Layout of the BEPCII storage ring

It was naturally for me to have an idea on using the "rgo mad" to do simulation on the dynamic aperture automatically. Fig. 2 gives some of the results of particle tracking with the MAD version of "rgo mad".

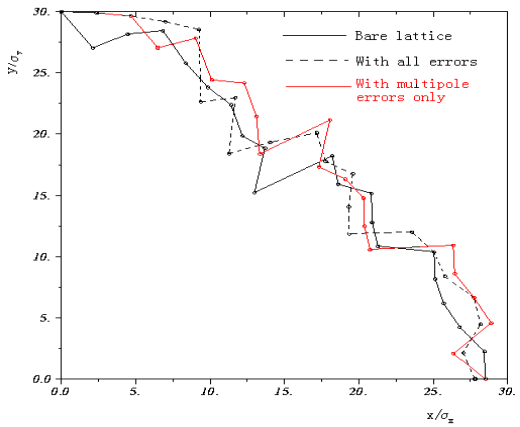

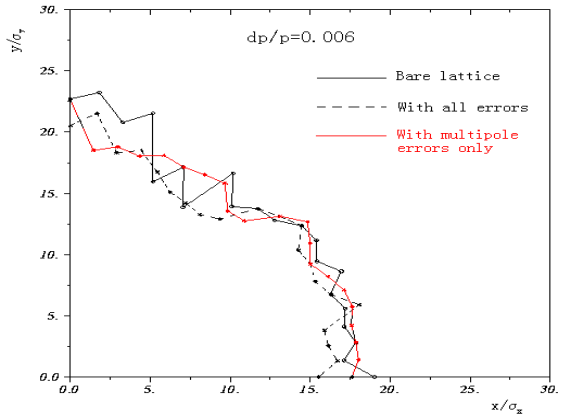

Figure 2: Dynamic aperture results got with rgo mad. Upper: on-momentum, lower: off-momentum

With these new features of the MAD, I did the simulation of the dynamic aperture for the BEPCII storage ring much faster than before. And the project also got the benefits from the contribution of Francesco.

SUMMARY

It is my honour to know Francesco Ruggiero when I worked at SL/AP, CERN. What impressed me most were his diligence shown in his work, intelligence reflected in his papers, humorous manner to life, and heartiness to everyone. I also benefited from his contributions on accelerator physics. What he did in the field of accelerator physics is forever.

REFERENCES

[1] H. Grote and F.C. Iselin, The MAD Program, CERN/SL/90-13(AP), 1990.

[2] F.C. Iselin and F. Ruggiero, A Modified Version of the Program MAD to Improve the Efficiency of Tracking Studies, CERN-SL-96-011 AP, 1996.

Mini-Workshop on Upgrades of LHC Injector Complex

THE LOW-POWER SPL

F. Gerigk for the SPL study group, AB/RF, CERN, Geneva, Switzerland

Abstract

This paper describes the basic parameters and the machine layout of the Low-Power SPL (LP-SPL), a 4 GeV superconducting H^- linac. In the first stage this machine is only designed to replace the PS booster (PSB) and to inject into a new proton synchrotron (PS2) at CERN. At the same time the components are designed such that the machine can be upgraded to become a high-power proton driver (5 GeV, $>$ 4 MW) for future radioactive ion beam (RIB) facilities or for various neutrino production schemes at CERN. The consequences for the low-power design are explained together with the possible upgrade paths.

INTRODUCTION

The aim of the LP-SPL [1] (together with PS2) is i) to remove any reliability concerns of the ageing LHC injector chain, specifically to replace Linac2, PSB, PS and ii) to provide a proton beam that is suitable for all foreseen LHC upgrade scenarios (compare [2]). After a recent cost and performance comparison [3] between an RCS (Rapid Cycling Synchrotron) based PS2 injector and the LP-SPL, the CERN management endorsed the SPL despite the 30% higher cost of the installation. Since then the LP-SPL together with the PS2 are considered as the baseline scenario for an upgrade of the CERN proton injector chain.

PS2 requires the injection of 1.5×10^{14} particles per pulse with a 1 Hz repetition rate at an energy of 4 GeV. This beam will be provided by the LP-SPL as a 1.2 ms long pulse with an average pulse current of 20 mA. In case of the High-Power SPL (HP-SPL) the average pulse current in the linac will be doubled to 40 mA, reducing the PS2 injection period to 0.6 ms. At the same time the repetition rate will be increased to 50 Hz.

THE SPL PROJECT AT CERN

The HP-SPL has to deliver beams with different time structures to a variety of users. This necessary flexibility is achieved by augmenting the linac with a combination of an accumulator and compressor ring. These first compress the pulse length of the linac pulse from the ms to the μs range and then rotate the bunches to lengths in the ns range. Since the requirements for the time structure of a future neutrino driver are still evolving, we foresee the following construction stages (taken from [5]), which can be matched to a growing number of applications and to evolving time structure requirements for future users:

1. **Construction of Linac4** [6]: the 160 MeV normal conducting front-end of the SPL. This machine is approved and is expected to be operational in 2013. It will replace the present Linac2 (50 MeV) and will inject at 160 MeV into the PSB. It is also the first step towards reaching the full luminosity potential of the LHC. The location of Linac4 on the CERN site is such that a straight prolongation of Linac4 is tangential to the SPS, with enough space between the two machines to construct the SPL and a new proton synchrotron (PS2), which will replace the aging PS machine. This layout allows to use the Linac4 beam for the commissioning of SPL and PS2, while maintaining the operation of the present LHC proton injector chain (PSB - PS - SPS). This approach minimises any interruption to LHC operation until the new injector chain is fully operational. Figure 1 shows a block diagram of Linac4/SPL and Fig. 2 shows the layout of the new injector chain on the CERN site.

2. **Low-power SPL (LP-SPL)**: installation of a 4 GeV superconducting linac, producing 200 kW of beam power with a repetition rate of 2 Hz. Two families of superconducting cavities ($\beta = 0.65$ and $\beta = 1.0$) are used to accelerate the beam to its top energy. This machine will replace the PSB and will inject directly into PS2. The R&D for this machine is partly covered by the recently approved "white paper", an initiative by CERN director general, which also provides the funding for Linac4.

3. **High-power SPL (HP-SPL)**: extension of the LP-SPL to 5 GeV and increase of the repetition rate to 50 Hz, producing 4 MW (or more) of proton beam power. At this stage the beam can be used for the production of neutrinos via beta-beams [7] and to drive a pulsed RIB facility [8].

4. **Accumulator ring**: in this configuration the SPL can drive a beta-beam facility and produce a so-called Superbeam at the same time, which is considered to be a promising combination for neutrino physics [9]. The capability to drive a RIB facility and the LHC injector chain remains unchanged.

5. **Compressor ring**: this enables the SPL to produce bunches in the nanosecond range, which are nowadays recommended for a neutrino factory target. In case further target studies prove the need for higher proton energies it seems realistic to extend the SPL to

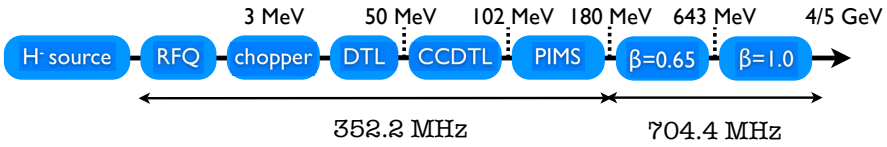

Figure 1: Block diagram of Linac4 and SPL.

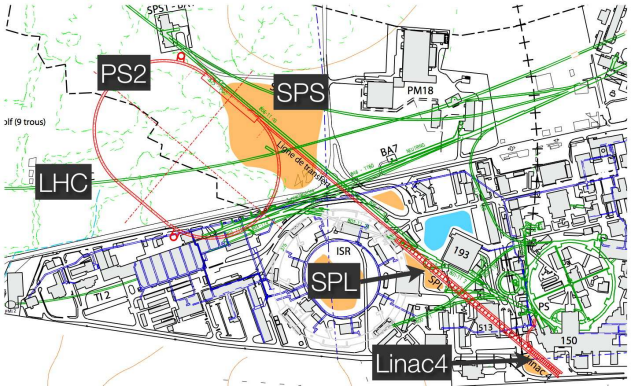

Figure 2: Layout of the SPL on the CERN site.

the 10 GeV range. A similar approach is proposed at FNAL in the 8 GeV proton driver project [10]. Energies beyond 10 GeV do not seem practical, since H^- stripping due to magnetic fields and black-body radiation becomes a serious problem [11, 12, 13].

It should be noted that the optimum energy and time structure for neutrino factory targets has not yet been experimentally determined. In this context the flexibility of the linac-based solution may ease the task of adapting the proton driver time structure to an evolving set of input parameters for a neutrino factory. The main parameters of Linac4, LP-SPL, and HP-SPL are summarised in Table 1.

Table 1: Parameter list for the machine evolution from LP-SPL to HP-SPL.

	LP-SPL	*HP-SPL*
Energy [GeV]	4	5
Beam power [MW]	0.192	> 4
Repetition rate [Hz]	2	50
Av. pulse current [mA]	20	40
Chopping ratio [%]	62	62
Beam pulse [ms]	1.2	0.4 - 0.6
Protons p. pulse [10^{14}]	1.5	1.0-1.5
Filling time PS2 [ms]	1.2	0.6
Beam duty cycle [%]	0.24	2.0
No. SC cavities	194	234
No. klystrons (352 + 704 MHz)	19+28†	19+57
RF peak power [MW]	100	219
Av. power consumption [MW]	4.5	38.5
Length [m]	459	534

SUPERCONDUCTING LINAC DESIGN

The superconducting section of the SPL is based on only two families of cavities with a geometrical beta of 0.65 and 1.0, respectively (see Table 2). The accelerating gradients of 19 and 25 MV/m have been chosen after considering the peak surface fields already achieved in tests with various cavities, which are summarised in Fig. 3. The chosen gradients correspond to a peak surface field of 50 MV/m, which is challenging but which seems realistic assuming that one can invest several years of R&D in the engineering of cavities and cryo-modules. Another conclusion to be drawn from Fig. 3 is that the maximum gradient does not seem to have a strong frequency dependance. Figure 4 shows a similar graph for the maximum surface magnetic field, which was limited to 100 mT in the case of the SPL.

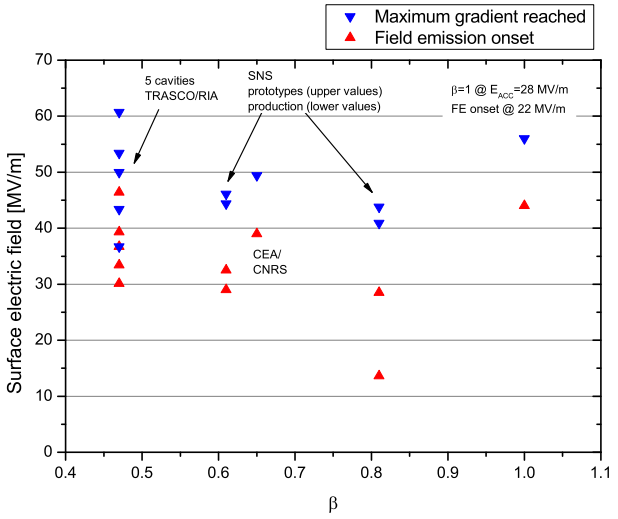

Figure 3: Peak surface electric fields corresponding to the maximum gradients reached in cavity tests (down triangle) and to the onset field emission (up triangle). From left to right: TRASCO/RIA (704/805 MHz), SNS (805 MHz), CEA/CNRS (704 MHz), SNS, TTF (1.3 GHz).

The cryo-module design will be based on the ILC/XFEL approach, using long interconnected cryo-modules with superconducting quadrupoles to minimise the number of cold-warm transitions. An appropriate R&D effort to redesign the ILC/XFEL cryo-modules for the SPL is planned until 2012, when a decision regarding the construction of the LP-SPL is expected. Until this date the SPL study group is preparing a technical design report, which will be the basis for a decision of the CERN management on construction.

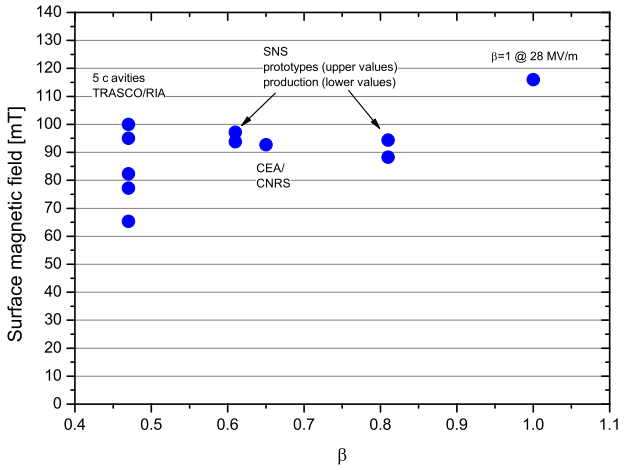

Figure 4: Peak surface magnetic fields corresponding to the maximum gradients reached in cavity tests. From left to right: TRASCO/RIA (704/805 MHz), SNS (805 MHz), CEA/CNRS (704 MHz), SNS, TTF (1.3 GHz).

Table 2: Characteristics of the two families of superconducting cavities.

section	$\beta = 0.65$	$\beta = 1.0$
accelerating gradient [MV/m]	19	25
el. peak surface field [MV/m]	50	
mag. peak surface field [mT]	100	
R/Q [Ω]	290	570
quality factor at 2 K	$\geq 10^{10}$	
cells per cavity	5	
cavities per module	6	8
focusing periods per module	2	1
module length [m]	11.45	14.26
focusing period length [m]	6.13	15.06
aperture radius [mm]	42.5	45

CIVIL ENGINEERING

While Linac4 is installed horizontally, the SPL tunnels will have a slope of $\approx 1.6\%$, to avoid crossings with existing tunnels and to ensure sufficient distance to tunnel areas which need to be accessed during operation. Furthermore the slope is necessary to reach the depth for the injection into the PS2, which is approximately 50 m under ground. The civil engineering effort for the LP-SPL is made in view of the full power operation of the machine. In particular this means:

i) keeping a distance of ≥ 8 m of earth between the SPL accelerating tunnel and areas that must be accessible during the operation of the machine. This distance ensures a radiation dose suitable for public access for instance for overground parking areas or basements of buildings.

ii) providing enough tunnel space for the HP-SPL infrastructure, comprising klystron, klystron modulators, cooling water pipes, air conditioning, etc.

Based on the above points a first layout of the tunnel cross sections is shown in Fig. 5. The klystron gallery and the accelerating tunnel have diameters of 6 m and 4.5 m, respectively. The distance between the tunnels is 9 m to ensure safe access to the klystron gallery during the SPL operation. The size of the klystrons is based on estimates using existing devices with similar specifications. The dimensions of klystron modulators was estimated by the CERN Power Group, which is now developing the modulators for Linac4, and the requirements of the services have been taken from [1].

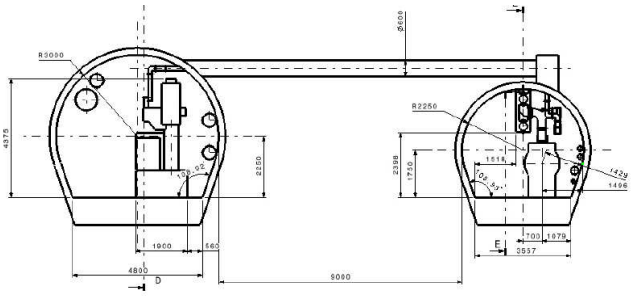

Figure 5: Cross-section of the accelerator tunnel (right) and klystron gallery (left).

As one can see from Fig. 6 most of the klystron tunnel volume is taken by the klystron modulators, despite the fact that approximately half of the modulator equipment is already housed on the surface. In the accelerating tunnel considerable space is taken by the RF distribution network, which splits the power from the klystrons to the single cavities.

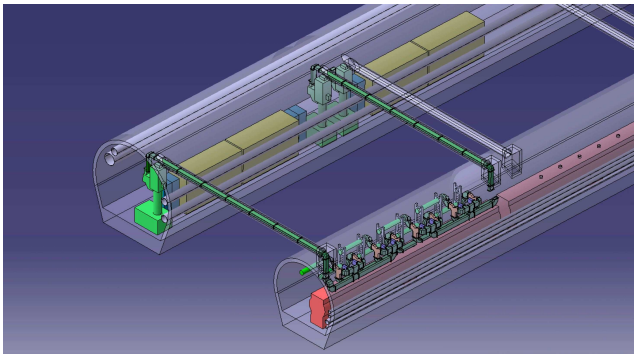

Figure 6: 3D layout of accelerator tunnel (right) and klystron gallery (left).

RCS VERSUS LINAC

Following a request of the CERN Scientific Program Committee (SPC) a comparison was made between a

synchrotron-based and linac-based proton driver for PS2 (see also [5]). The goal was to outline the pros and cons of each solution and to compare with the findings of the FNAL proton driver study II [10] which compared a 8 GeV full-energy superconducting linac with a 600 MeV linac plus an 8 GeV synchrotron. The FNAL aim was to achieve initially 0.5 MW beam power and to have the possibility to upgrade the power to 2 MW. It was found that the linac-based solution is approximately 30% more expensive than the synchrotron-based solution. Nevertheless the linac solution was preferred due to: i) its upgrade potential and its adaptability to future proton needs at FNAL, and ii) the possibility to construct a test bench for the International Linear Collider (ILC), making use of TESLA-style SC cavities and cryo-modules.

The CERN study compared the low-power SPL (4 GeV, 0.2 MW) with a rapid cycling synchrotron [3]. Both machines have to provide $1.5 \cdot 10^{14}$ particles per pulse with a 1 Hz repetition rate for injection into PS2 with 4 GeV injection energy. In accordance with the FNAL study it was found that the linac solution demands a 28% higher initial investment. However, due to its upgrade potential and its expected performance advantages, the linac solution was endorsed by the management and represents now the base line for the planned upgrade of the CERN proton injector chain. The relative merits of each solution are summarised in Table 3.

Table 3: Relative merits of RCS and SPL options for the injection into the proposed CERN PS2, see [3].

	SPL	*RCS*	*Advantage*
Filling time PS2	0.6 ms	1.3 s	SPL
Time struct. LHC	inherent	different	SPL
Rel. proton rate	2.5	1	SPL
Fixed target phys.	ideal	acceptable	SPL
Ions	acceptable	ideal	RCS
Upgrade potential	high	low	SPL
Relative cost†	1.28	1	RCS

† the relative cost considers only the items that differ between both solutions

SUMMARY

The normal conducting part of the SPL (Linac4) is approved and is planned to deliver protons in 2013. The LP-SPL together with PS2 is now the baseline scenario for upgrading the LHC proton injector chain. A new layout for whole proton injector complex has been found which allows the staged construction of Linac4 and SPL with minimum interruption of LHC operation. The first stage of the SPL, the LP-SPL is designed such that it can be upgraded to a multi MW proton linac for a reasonable cost. A civil engineering feasibility study including a cost estimate for the construction of the SPL is in preparation.

ACKNOWLEDGEMENTS

This paper results from the work of the SPL study group, the TS Civil Engineering group, the Safety Commission, and our collaborators in CEA Saclay (France), INFN Milano (Italy), and LPSC Grenoble (France). We also whish to thank Thales, CPI, Toshiba, AFT, and ACCEL for providing valuable data for the estimation of component performance and characteristics.

REFERENCES

[1] F. Gerigk (*Ed.*), Conceptual design of the SPL II, a high-power superconducting H^- linac at CERN, CERN-2006-006.

[2] R. Garoby, LHC injector upgrade plan, this workshop.

[3] R. Garoby, M. Benedikt, A. Fabich, and F. Gerigk, *et al.*, Comparison of options for the injector of PS2, CERN-AB-2007-014-PAF.

[4] F. Gerigk and R. Garoby, Operational flexibility of the SPL as proton driver for neutrino and other applications, HB'06, Tsukuba, Japan.

[5] F. Gerigk, Future high-intensity proton accelerators, SRF'07, Beijing, China.

[6] R. Gerigk and M. Vretenar (*Eds.*), Linac4 technical design report, CERN-AB-2006-084.

[7] P. Zucchelli, A novel concept for a $\bar{\nu_e}/\nu_e$ neutrino factory, *Phys. Lett* **B 532** (2002) 166.

[8] E. Noah *et al.*, EURISOL target stations operation and implications for its proton linac driver beam, EPAC'06, Edinburgh, UK.

[9] J.E. Campagne and A. Caze, The θ_{13} and δ_{CP} sensitivities of the SPL-Fréjus project revisited, CERN-NUFACT-NOTE 142 (2004).

[10] G.W. Foster, W. Chou, and E. Malamud (*Eds.*), Proton driver study II, FERMILAB-TM-2169 (2002).

[11] L.R. Scherk, An improved value for the electron affinity of the negative hydrogen ion, *Can. J. Phys.* **57** (1979) 558.

[12] W. Chou *et al.*, 8 GeV H^- ions: transport and injection, PAC'05, Knoxville, USA.

[13] H.C. Bryant and G.H. Herling, Atomic physics with a relativistic H^- beam, *J. Modern Optics* **53** (2006) 45.

SNS EXPERIENCE WITH A HIGH ENERGY SUPERCONDUCTING PROTON LINAC*

J. Galambos, I. Campisi, S. H. Kim SNS, Oak Ridge, TN 37831, U.S.A.

Abstract

The Spallation Neutron Source (SNS) requires a high power (> 1 MW) 1 GeV proton beam to produce an intense source of neutrons. The proton beam acceleration is primarily provided by a Superconducting Cavity Linac (SCL). This SCL is the first use of superconducting cavities to accelerate protons to energies this high and is also the first application of pulsed SRF with proton beams. The SCL has been in operation for over two years now. The experience in commissioning and operating the linac are discussed in this paper.

1 INTRODUCTION

Early in the course of the SNS construction project a decision was made to switch from an entirely copper structure linac to using Superconducting RF technology for the majority of the beam acceleration [1]. The SCL portion of the accelerator was provided by Thomas Jefferson National Lab (TJNL). The cavities were fabricated by industry, the cryomodules were assembled by TJNL, and shipped to SNS for installation in the tunnel. Cavity testing at SNS began in the spring of 2005, and proceeded along with cryomodules installation through July 2005. Beam commissioning of the linac occurred in August 2005, after which the machine was shutdown for three months to prepare for the downstream Ring and transport line commissioning. The SCL was quite stable for the initial Ring commissioning, and over the past 1.5 years the linac has been used for beam studies and neutron production, with an increasing fraction of the time being spent of neutron production as the facility matures. Table 1 shows the progression of pulse length and duty factor over the course of the startup of the SNS facility.

Section 2 briefly describes the design parameters of the SCL [2,3] and section 3 describes the cavity operational experience with a comparison to expectations and Section 4 describes the beam commissioning and operation.

2 SCL DESIGN

The SNS SCL is designed to accelerate the beam from 186 MeV to 1000 MeV. Two geometrical beta cavities are used, medium beta cavities (β_g=0.61) and high beta cavities (β_g=0.81). The medium beta cavities are packaged 3 per cryomodules and the high beta cavities are packaged 4 per cryomodule. Some of the design parameters are shown in Table 2-1. An important facet of the design is a single klystron powering each cavity. Also, the expected range in the SCL cavity performance was +15%, -5% range about the design value [2].

Table 1 Chronology of SNS SCL beam energy and pulse structure operational parameters

	Repetition Rate (Hz)	Flattop pulse length (μSec)	Energy (MeV)
Summer 2006	2	500	855
Fall 2006	5	500	890
Winter/Spring 2006	15	500	885
Summer 2007	30	600	885

Table 2. SNS SCL cavity and cryo-module parameters.

Cryomodule parameter	Medium Beta Section	High Beta Section
Output energy (MeV)	387	1000
No. of cryomodules	11	12
No. of cavities per cryomodule	3	4
Cryomodule length (m)	4.89	5.84
Warm section length (m)	1.6	1.6
Cavity Parameter	**Medium Beta Cavity**	**High Beta Cavity**
Geometric beta	0.61	0.81
EoT (MV/m)	10.1 at β=0.61	15.9 at β=0.81
Epeak (MV/m)	27.5	35.0
Hpeak (kA/m)	46.2 (580 Oe)	59.7 (750 Oe)
Q*Rs (Ω)	176	228
r/Q at design beta	279	483
Qex	7.3×10^5 (±20%)	7.0×10^5(±20%)
Stored energy (J) at design EoT	33	85
Inter-cell coupling (%)	1.6	1.6
Available klystron power (kW)	550	550
Bore radius (mm)	43	48.8
Equivalent Cavity Length (cm)	68.2	90.6

* ORNL/SNS is managed by UT-Battelle, LLC, for the U.S. Department of Energy under contract DE-AC05-00OR22725.

3. CAVITY PERFORMANCE

The initial experience in operating the SNS SCL has indicated several unexpected features. First cavity performance has proven to be much more varied from cavity to cavity than expected. In addition to higher than expected variations in the individual cavity superconducting characteristics sometimes peripheral equipment limits individual cavity performance. Also the linac has proved to be remarkably robust to running in conditions far from the design values. These issues are discussed below.

3a. Cavity Limits

The primary cavity limit is operating safely below any field emission quench limits. For most cavities radiation levels during the RF pulse are proportional to the field level in the cavity, as seen in Fig. 1a. However, some cavities exhibit behaviour with radiation spikes during the rise and fall of the field in the cavity, which is also mirrored in independent nearby electron probe measurements. While not completely understood, it is believed that this behaviour is related to electron generation near the ends of the cavities during the period with travelling wave conditions. The thermal cooling in the end group region is not designed to tolerate high electron heating loads, and some cavities are limited in gradient by this effect.

(a)

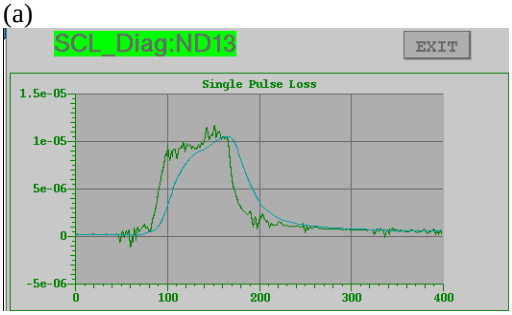

(b)

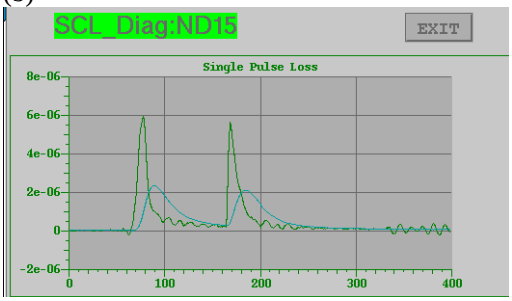

Fig. 1 a) Radiation vs. time signature adjacent to a normal cavity. This shape is similar to the RF forward power profile. B) Radiation signature of a cavity with end-group electron activity, exhibiting spikes during the rise and fall of the cavity field.

Another effect that limits some cavity gradients is the Higher Order Mode (HOM) coupler power. These couplers were added to remove HOM power and alleviate the remote possibility of cavity heating from HOM effects. They include a notch filter to inhibit fundamental power coupling, but some cavities show evidence of some fundamental power leaking into the HOM coupler. Since the HOM couplers have a limited power capability, this unexpected effect limits some cavities' performance.

Other peripheral cryomodule equipment has also affected the SCL operation in unanticipated ways. The Cold Cathode Gauges (CCG) used to measure vacuum in the SCL sometimes have long response times at the extreme vacuum levels of the cryogenic environment, and required intervention to evoke a response sufficient for the RF interlock to have confidence they are working. Cavity turn on procedures were developed to ensure safe operation while avoiding un-necessary protective measures. Another unexpected behaviour is the failure of piezo-tuners installed to correct the dynamic Lorentz force detuning. Several of these have failed requiring intervention to recover the use of the cavities. Because the present piezo-tuner implementation design is not optimal, and we have never used them in operation, we are removing these tuners from cryomodules that are worked on.

3b. Collective Cavity Limits

An unanticipated observation on the determination of reliable operating gradients is a dependency on neighbouring cavity conditions. Beam pipe temperature in one cavity can be affected by changes in a neighbouring cavity's phase or amplitude setting. Figure 2-1 shows an example for cryo-module number 13, indicating the various places where local heating is affected for each cavity, in addition to the cavity itself. This collective behaviour becomes more pronounced at higher pulse repetition rates. For reliable operations the cavities must be set at a gradient that not only is safe for the cavity itself, but also for neighbouring cavities.

3c. Overall SCL Cavity Performance

Figure 3 shows the operational gradients for all the SNS SCL cavities at the present time. The blue line indicated the design value, the green line is the average cavity gradient at 10 Hz and the red line is the average gradient for 60 Hz. The averages are indicated separately for the medium beta cavities (1a-11c) and high beta cavities (12a-23d). Some observations are: 1) there is a large spread in the cavity to cavity performance, 2) the medium beta cavities perform better than expected on average, 3) the high beta cavities perform worse than expected on average, 4) the 60 Hz limits are about 10% lower than the 10 Hz limits. The gradients shown in Figure 3 are for the present time. Over the past two years the operating gradients have changed as understanding of the limiting effects is better understood and the operational repetition rate has increased.

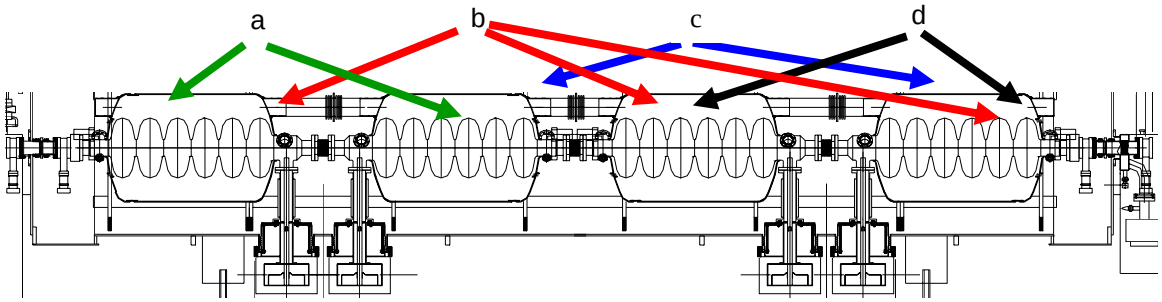

Figure 2. Local heating locations for the different cavities a, b, c and d in cryo-module 13. Each cavity affects multiple cavities within the same cryo-module.

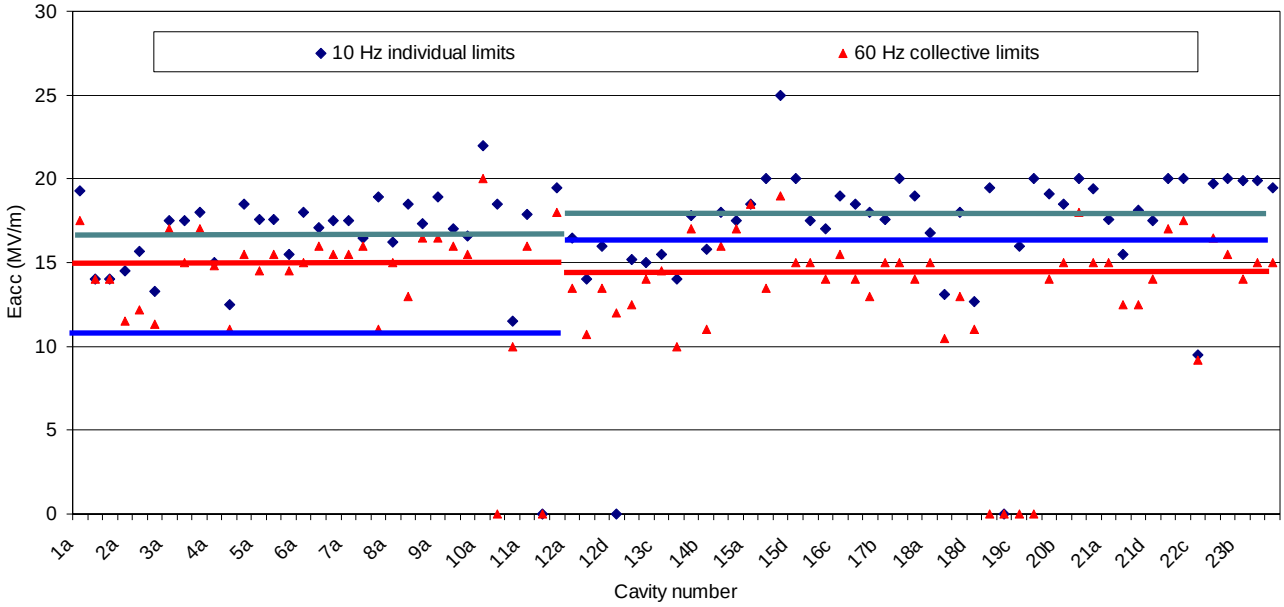

Figure 3. Operational gradients for the SNS cavities. The blue line indicated the design value, the green line is the average cavity gradient at 10 Hz and the red line is the average gradient for 60 Hz. The averages are indicated separately for the medium beta cavities (1a-11c) and high beta cavities (12a-23d). The medium beta cavities perform better than expected, and the high beta cavities have lower operational gradients than expected. The net effect is lower operational output beam energy than expected.

4. BEAM COMMISSIONING AND OPERATION

4a. Tools

The method of SCL cavity use at SNS is to operate each cavity at its maximum safe gradient and set its phase relative to the beam. We have used constant phase and constant focusing schemes. A key issue in this area is the tool used to set the cavity phase relative to the beam. We use a phase scan technique to determine the phase setpoint (shown schematically in Figure 4. A cavity phase is varied, and its arrival time measured at two downstream positions (using beam position monitors). All intervening cavities are set to not affect the beam during the pulses when the measurements occur. Each cavity has only 6 cells and the net effect of cavity acceleration on the beam is much like an ideal RF gap (β changes only slightly in each cavity). As a result, this phase scan can be employed throughout a 360 degree range and the measurement data is easily matched to model predictions to determine the input beam energy, cavity amplitude and klystron phase offset from the synchronous phase [4,5]. Figure 5 shows a typical scan for an SCL cavity. The resulting phase scan is much like the sinusoidal result expected from an ideal RF-gap, and all cavities show a similar behaviour. The line represents measured data and the dots are model predictions after solving for the input beam energy, cavity gradient and klystron phase offset. A standard drift-kick-drift longitudinal acceleration model is used [5]. As it is important to ensure there is no RF affecting the beam in between the cavity being varied and the two BPMs used to measure the Time-of-Flight. For the SNS arraignment of cavities and diagnostics there can be up to 7 intervening cavities, and in order to proceed through the 81 cavities quickly we have implemented a LLRF feature to allow "blanking" of the RF whenever beam pulses are triggered for these measurements. This allows the entire SCL RF system to be turned on and left on at a typical 30-60 Hz rate, with beam pulses periodically applied at 1 Hz for the phase setting studies. It still requires at least 5-10 hours to measure and set all cavities, from a cold start.

To avoid having to redo beam base measurements to set the SCL cavity phases whenever an upstream cavity phase or voltage changes a model based technique has been developed to calculate the changes in beam arrival time in downstream cavities when a cavity fails and to automatically adjust the downstream cavity phase setpoints [5]. Turning off an upstream cavity can result in changes in the arrival time at the downstream end of the linac equivalent to over 1000 degrees. Checks show that the recovery technique is accurate to within a few degrees. This technique has been used often to compensate for changes in SCL operating levels and for beam studies.

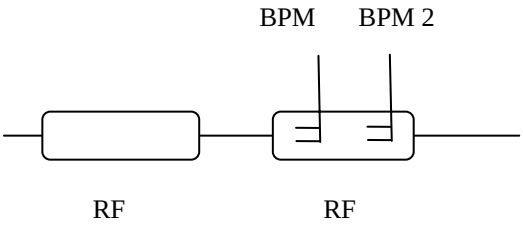

Fig.4. Schematic of the device layout used in the measurement to determine the SCL RF phase setting.

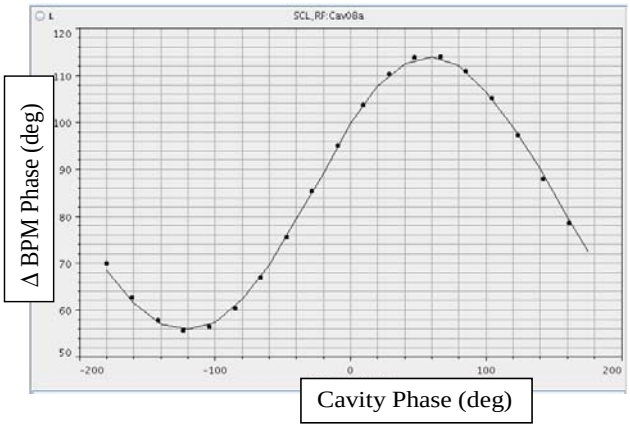

Fig.5 Example BPM phase difference vs. RF phase scan for a SCL cavity. The solid lie is a measurement and the dots are model predictions after matching the input beam energy, cavity voltage and RF phase offset.

Another technique that can be used to measure the cavity phase setpoint relative to the beam and also the cavity amplitude is the drifting beam technique [6]. This technique involves drifting the beam through an unpowered cavity. The beam readily excites the cavity and by comparing the measured cavity excitation with model based predictions it is possible to determine the proper cavity phase setpoint and the cavity amplitude. This technique requires knowledge of the beam energy and a good measurement of the beam current.

4b Beam Performance

Table 3 shows the SNS SCL high level beam performance parameters. All the design parameters have been met individually except beam power. The maximum beam power used during a neutron production run to date has been 200 kW. While this is a significant beam power, there is still a factor of 7 increase required for the beam power. This increase will be achieved by increasing the beam current, pulse length and beam energy. Some of this increase is

possible with existing hardware capabilities. Hardware improvements are also envisioned for the RF, High Power Converter Modulators, ion source and cavities to reach the final beam power. At present we observe some residual radio-activation in the warm sections separating the cryomodules (and containing the focusing quadrupoles) of about 10 mRem/hr measured 30 cm from the beam pipe 12 hrs after shutdown. This level of activation represents a small beam loss fraction (< 1 part in 1000) and is believed to be longitudinal in nature. There do not appear to be any fundamental beam dynamic issues to prevent attaining the expected final beam power.

Table 3. Summary of SNS SCL beam parameters achieved.

	Design	Highest Ever (Individual)	Highest Beam Power (Simultaneous)
Energy (GeV)	1.0	1.01	0.85
Rep Rate (Hz)	60	60	60
Pulse Length (mSec)	1	1	0.27
Avg. Beam Current (mA)	26	20	15
Beam Power (MW)	1.5	0.20	0.20

5 SUMMARY

The SNS SCL is the first high energy (~ 1 GeV) superconducting RF pulsed proton linac. Operation of the SNS SCL over the first two years has turned out quite different than expected during the design period. Cavity operational gradients are more varied than expected, often limited by the performance of auxiliary equipment such as HOM couplers. The behaviour of the SCL as an overall system, governed by many components, has become better understood during the initial operational period. As the understanding of the cavity performance improves, operational limits change. Operation of the linac under these unexpected and dynamic conditions has proven to be remarkably robust. An advantage of the SNS accelerator complex is that it can tolerate different output energies of the linac. So for example, energy reduction due to removal of a cryo-module for repair is tolerable. Tools have been developed to rapidly tune up the SCL, with its many cavities. Also tools have been created to rapidly adapt to failed cavities or changes in the cavity operational limits.

Acknowledgements

The material presented here is a collection of work provided by many groups. The RF, cryogenic, controls and the mechanical groups in particular played important roles in the work presented here. Also A. Aleksandrov, Y. Zhang, D. Jeon, S. Henderson, and A. Shishlo helped in the development of the beam based measurements and analysis tools.

REFERENCES

[1] Y. Cho, et al, Preliminary Design Report of Superconducting Radio Frequency Linac for the Spallation Neutron Source, SNS-SRF-99-101, December (1999)

[2] J. Stovall, et al, "Superconducting Linac for the SNS," Proceedings of LINAC 2000, pp.605-607, Monterey, California, 21-25, August, 2000

[3] J. Stovall, et al, "Expected Beam Performance of the SNS Linac," Proceedings of Particle Accelerator Conference 2001, pp.446-450, Chicago, Illinois, 18-22, June, 2001

[4] J. Galambos, A. Aleksandrov, C.K. Allen, S. Henderson, A. Shishlo, T. Pelaia, Y. Zhang, C. P. Chu, "Software Tools for Commissioning of the SNS Linac",Proceedings of PAC07, Albuquerque, New Mexico, USA http://accelconf.web.cern.ch/AccelConf/p07/PAPERS/TUOCC01.PDF

[5] J. Galambos, S. Henderson, A. Shishlo, Y. Zhang, "Operational Experience of a Superconducting Fault Recovery System at the Spallation Neutron Source", Procedings of the Fifth International Workshop on the Utilisation and Reliability of High Power Proton Accelerators, Mol Belgium, May 2007.

[6] Y. Zhang et al., Nucl. Inst. Meth. A 571 (2007) 574.

ESS PLANS AND SYNERGY WITH CERN

K.Bongardt, IKP, Forschungszentrum Juelich, D-52425 Juelich, Germany

Abstract

Summarized are properties of 10 MW ESS H^- SC Reference Linac, as described in ESS Update Report 2003. Particles are either injected into 2 accumulator rings, resulting in 1.4 μs pulses sent to a short pulse target station, or 2 ms long pulses directed to a long pulse target station. The 10 MW, 1.334 GeV ESS H^-linac is 570m in length, modular cryomodules are used above 400 MeV with separated warm quads.

After winding up the ESS Council and the Technical Team by the end of 2003, the neutron scattering community wanted to keep ESS on the political table and demonstrate to young scientist that the struggle for ESS goes on. For this purpose, the ESS-Initiative (ESS-I) was formed to include the European Neutron Scattering Association (ENSA), various consortia for site candidatures and some key European laboratories.

A major highlight was the successful promotion of ESS to be as a high maturity project on the European Road Map of Research Infrastructures, published in October 2006 by the European Strategy Forum on Research Infrastructures (ESFRI). The ESS Preparatory Phase project has been accepted in the meanwhile after a very positive assessment and has been allocated 5 M€ EU support to investigate site independent technical items and answer legal, financial and governance questions, starting January 2008.

ESS 07 will be a 5 MW LP source, the worlds first one to offer the unique capabilities of novel long pulse instruments for almost all of the most interesting areas of science and technology. ESS will be built in such a way that governments can decide later on during its lifetime to increase power and add more target stations, as the future scientific need would arise.

The 5 MW, 1 GeV ESS H^+ linac is similar to the ESS H^- SC Reference Linac, but only 464m in length, as more intense H^+ sources are available. ESS's world lead would become even more pronounced, even when SNS would upgrade its power to, say, 3 MW, if the ESS beam power would be increased to 7.5 MW. This goal is achievable by enlarging the linac tunnel by 115m, which allows to add later on 16 cyromodules, and increasing the accelerating gradient in all SC cavities by 15 %. The H^+ linac length of 579 m in this case would still not be larger than the ESS H^- SC Reference Linac.

Synergy with the CERN plans would require to avoid the funnel section at 20 MeV, leading to a 5 MW LP power at 2 GeV.Linac length is unchanged by using accelerating high gradient in SC cavities. SPL frequencies can be used, but components will differ, as ESS LP source requires high current and long pulses, whereas SPL linac is designed for high energy and high rep. rate.

ESS UPDATE REPORT, 2003

The European Spallation Source (ESS) project, as defined by the four volumes ESS Report 2002[1], was presented to the public, the general neutron user community and European decision makers at a meeting in the former house of parliament in Bonn, May 2002.

In January 2003 it became clear, that a decision to built ESS would not be likely forthcoming by the end of early 2004. The ESS council therefore decided to wind down all technical & project planning activities and limit the ESS efforts to documenting the technical and planning status.

The ESS Update Report, Dec 2003[2], is a summary of the amount of work, technical definition & progress achieved during the period from May 2002 to early 2003. Main new items are description of SC Reference Linac and improved chapter on Safety and Licensing

Full ESS facility consists of a 10 MW, H^- accelerator capable of delivering 5 MW, 1.4 μs pulses to a short pulse (SP) target at 50 Hz & 5 MW, 2 ms pulses to a long pulse (LP) target at 16 2/3 Hz.

In order to deliver 5 MW power in about 1.4 μs to the SP target, the ESS facility needs two accumulator rings with 35 m mean radius in a shared tunnel. Two accumulator rings are necessary to keep temperature rise of H^- stripping foils within reasonable limits. Prototype laser striping experiments are performed at SNS, up to now not scalable for MW beam power values[3].

Both targets have 22 beam lines and liquid Hg is chosen as target material. Required area for full ESS facility is 1150 m x 850 m.

SC Reference Linac:114 mA,1.334 GeV, 10 MW

Layout of ESS H^- SC Reference Linac is shown in Figure 1. 2 x 65 mA H^- beams are combined together at 20 MeV in a funnel section. High frequency Superconducting (SC) cavities accelerate the beam from 400 MeV on. Moderate gradient of 10.2 MV/m in SC linac is used to keep RF power couplers within reasonable limits, 11 % RF duty cycle. After reducing energy spread by bunch rotation (BR) to ±2 MeV, either halo scraping in large 180° achromatic section before injecting into both accumulator rings or 99 m transport to LP target.

The 1.334 GeV H^- linac is 570 m in length, 748 m from ion source to LP target, 95 m in length. Linac energy is determined by loss free ring injection. Chopper line needs low frequency to absorb 10 kW power at 4 locations, high frequency SC cavities have large bandwidth and stiffening.

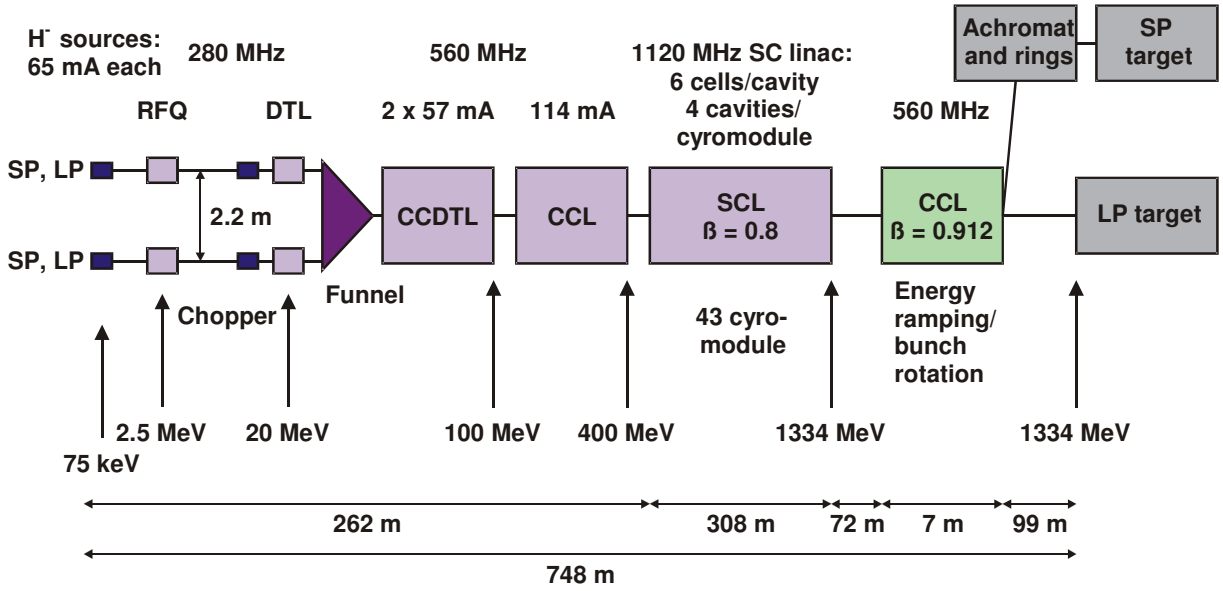

Figure 1 : ESS H- SC Reference Linac, serving SP&LP targets

ESS H- linac: double pulse for SP&LP targets

Two ESS accumulator rings get 2 x 0.48 ms long pulses, 600 turns per ring, with 70% chopping to leave a time gap for the ring extraction kicker magnets. A 100 µs gap is required for vertical deflection of the linac pulse between the rings. LP target get 2 ms pulse, no chopping, which requires 50% more power in SC coupler.

ESS double pulse sequence requires 2 ms unchopped pulse and only 7.7 ms time gap to next 1ms chopped pulse, shown in Figure 2. Not shown is voltage stabilization before beam arrival, done by closing RF loops and reducing RF power, and two other chopped pulse, send to SP target .As consequence, wall deformations are still present at beginning of next chopped pulse[4], requiring sophisticated RF control system, being easy at high frequency, as cavity bandwidth & stiffness are increased.

The ESS facility unique in its neutron scattering performance, but is challenging for same ESS linac components: the front end with its chopper/collector system and layout/RF control of pulsed SC cavities.

The chopping line must be able to switch the beam on and off between RF bunches resulting in elements with a rise time of less than 2 ns to avoid beam loss further down the accelerator. The beam collection system must be able to cope with up to 10 kW power, since both the SP and LP beam will be chopped initially.

The 280 MHz low frequency front end houses the ESS chopper line with its 2 innovative chopper/ collector systems[2,5], collecting up to 10 kW beam power in total 4 different positions. The 57 mA H- bunch is kept focused in all 3 directions by using combined function elements between the deflectors. The complete chopper line from RFQ to DTL entrance is about 3.5 m in length.

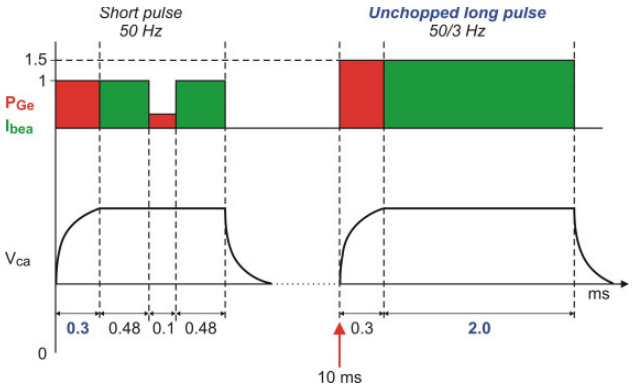

Figure 2: ESS double pulse sequence in SC cavities V_{ca} = cavity voltage, P_{ge} =RF generator power I= beam current, normalized to 70 % chopping .

For Gaussian test bunch at RFQ exit, particle tracking was performed up to 20 MeV DTL end, leading to very small filamentation. [6].

The main concern, however, are RF phase & amplitude jitter due to ringing of the power supplies. First simulations are indicating much smaller energy, phase deviation of the beam at 20 MeV [6], than used for the particle tracking along the SC linac, see beam dynamics section afterwards.

1120 MHz ESS SC high ß linac

Above 400 MeV, 1120 MHz SC cavities accelerate the ESS beam up to its full 1334 MeV final energy. SC structures offer a reduction in operating costs compared to warm NC ones, but it requires a careful look at the pulsed RF control system especially fore the double pulse to SP&LP targets.. Higher frequency SC structures are beneficial for the demanding ESS requirements and offer headroom for capital cost saving. As the ESS front end prefers low frequencies, a change in frequency from 560 MHz to 1120 MHz at 400 MeV is foreseen for the ESS SC Reference Linac.

Schematic drawing of a lattice period of the ESS SC linac is shown in Figure 3, adapted from SNS high ß SC linac. SNS high ß cryomodule can be quickly disconnected from the beam line , energy upgrade is planned by adding cryomodules afterwards[7].

The SC part of the ESS linac uses 43 cryomodules, each housing 4 elliptical bulk Nb SC cavities, 4cm iris aperture, 0.7 m cavity to cavity spacing. Large aperture minimize the risk of inadequate damping of higher order dipole modes which could be excited by the beam. Each cavity consists of 6 cells of ß=0.8 equipped with one SC main coupler. Doublets in the warm intersections provide the transverse focusing, see Figure 3. Each quadrupole is 30 cm in length, has 14 T/m focusing strength and 4 cm aperture radius.

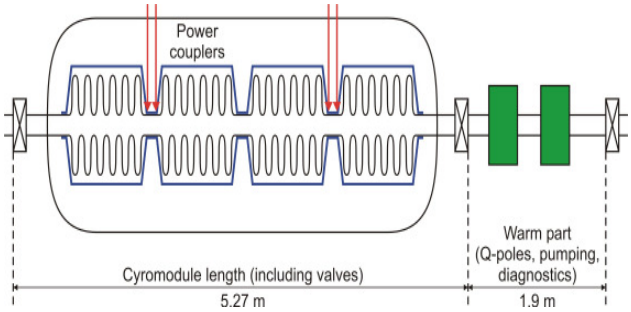

Figure 3:Schematic drawing of a lattice period of ESS SC linac

As the overall RF duty cycle is about 11%, we limited ourselves to only 0.85 MW peak power for the 114 mA LP beam, included are 30% surplus for RF control, leading to 80 kW SP&LP averaged power. Not planned was use of two couplers / cavity, as major concern about voltage stabilisation by RF vector-sum , lack of individual knobs for both couplers.

Only 10.2 MV/m accelerating gradient at $Q_0 = 10^{10}$ (2K) is required, keeping peak surface peak magnetic / electric field well below 50 mT / 25 MV/m. Matched 3 db cavity bandwidth is ±2 kHz for the 114 mA LP beam and R/Q=440Ω/m, linac definition. For the 1 ms, 70% chopped pulse to SP target, Figure 2, voltage fluctuation due to mismatch can be compensated by the foreseen 40% RF control power. Cavity stiffening methods for reducing the Lorentz-force frequency detuning are under investigation, absolutely necessary even for the envisaged 10.2 MV/m accelerating gradient due to the ESS double pulse,Figure 2. Sufficient cell-to-cell coupling is required.

Symmetric arrangement of power couplers leads to only 2 feed through per cryomodule. No power spitting between cavities, but combined High Voltage Power Supplies (HVPS) with central energy storage. Klystron peak power varies only by 25% along the SC linac.

Beam Dynamics in 1120 MHz SC high ß linac

Detailed Monte Carlo simulations with complete 3d space charge have been performed to demonstrate the capability of the 1120 MHz ESS SC linac to handle the 228 mA bunch current (114 mA pulse current) from 400 MeV onwards by using ß=0.8, 6 cell cavities only. Figure 4 shows the phase slip of the bunch centre for each cell of the total 172 cavities. The phase is always between ±90°, which means energy gain in each cell and therefore stable synchrotron oscillations. Figure 5 show quite small longitudinal filamentation at ring injection.

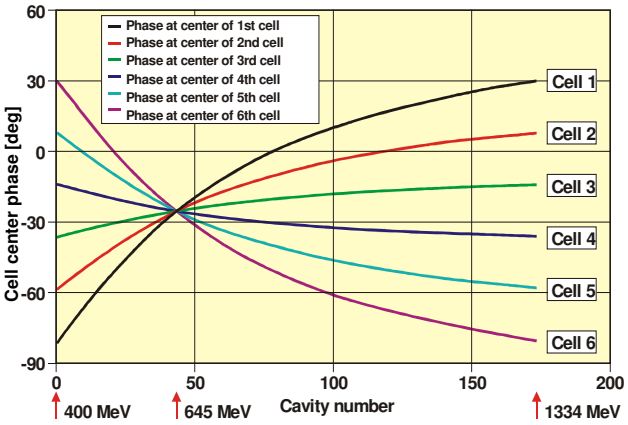

Figure 4 :Phase slip of the bunch centre in each of the six cells for all 172 SC cavities.

Maximal energy gain of 5.65 MeV/cavity occurs at 645 MeV, ß=0.8, 5% higher than average gain of 5.43 MeV/cavity. Minimal energy gain of 4.24 MeV occurs at 1.334 GeV final energy [8].

The transverse full current tune is set to be 45° all along the ESS linac. Tune depressions are above 0.55 and the transverse / longitudinal temperature ratio varies between 0.3 and 1.3 [9],avoiding emittance exchange during acceleration, see Figure 5. Less than 10 % rms emittance increase.

For high current linacs, onset of envelope instabilities must be avoided, limiting longitudinal zero current tune below 90° [10], being in conflict with high accelerating fields and long SC lattice periods. For the 7.17 m long ESS SC lattice and at 400 MeV, accelerating gradient has to smaller than 16 MV/m.

For a matched 6d Gaussian "control" beam as input to the SC linac and in the absence of RF field errors, very little filamentation is seen at 1334 MeV and the energy spread at the ring injection point, 71 m behind the BR cavity, is limited to ±0.5 MeV, only a quarter of the ±2 MeV constraint for loss free ring injection, red lines are ±0.5 MeV boundaries .Transverse & longitudinal rms emittances at 400 MeV are assumed to be 20% larger than those at 20 MeV. Beam radii are smaller than 1 cm all along the SC linac, maximal phase extend is about ±30° (1120 MHz), position of BR cavity.

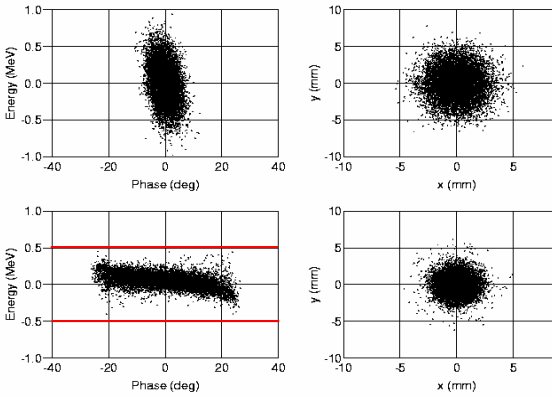

Figure 5 Longitudinal phase space & beam radii along the ESS SC linac for a matched 6d Gaussian "control "beam and without RF errors. 1.row is at 400 MeV injection, 2.row at 1334 MeV ring injection.

Energy spread reduction is obtained by placing warm ß=0.912 CCL structures 78 m downstream the SC linac, delivering a 13 MV rotation voltage to the beam, see Figure1. Due to 228 mA bunch current, rms energy spread increases by more than a factor 2 between linac end and position of BR cavity.

As accumulated errors in the NC part of the ESS linac leads to mismatch and phase space filamentation at injection into the SC part, we carefully checked the design of the 228 mA SC linac to be insensitive against strong initial mismatch and different input distributions. As an example we excited a pure "low" mode (radial by +15%, axial by –30% change in initial radii) at 400 MeV for a 6d Gaussian "control" beam in an error free SC linac. Both radii are oscillating out of phase with the bunch length (rms phase width), as expected [11]. In phase oscillations of the transverse beam radii are visible all along the linac and up to ring injection. The beam is kept transversely focused.

Resulting phase space and radii plots show much larger axial than radial filamentation compared to the matched case of Figure 5. This is as predicted for the "low" mode excitation, as at input only longitudinal halo particles can be in resonance with the oscillating beam core [11].The energy spread at the ring injection point is limited to ±1 MeV, still only half of the ±2 MeV constraint for loss free ring injection. About 10^{-3} particles are outside ±0.5 MeV.

Exciting the "low" mode or another bunched beam eigenmode [11] for a 6d Waterbag instead of a Gaussian beam at 400 MeV leads to almost the same phase space plots at ring injection, indicating the insensitive of the 228 mA ESS design against details of the input distribution.

RF field errors along the ESS linac will lead to a shift of the beam centre in energy and phase/time, possibly leading to unacceptable large energy shifts after final bunch rotation. The input values at 400 MeV of ±4.5° (1120 MHz) phase resp. ±1.3 MeV energy deviation of the beam centre, accumulated from RF errors in the preceding warm structures, are about 10 times larger than obtained after the DTL at 20 MeV [6].

Assuming ±1%, ±1° RF amplitude and phase errors in each SC cavity, randomly distributed along the 172 SC cavities, and applying the same bunch rotation voltage as used for the Gaussian "control" beam, energy deviation of the bunch centre is reduced by a factor 2, ±1 0 MeV after bunch rotation in about 1 in 10^3 cases, see Figure 6.The red curves represent 10^{-3} error boundary, increased by more than factor 2 due to RF random distributed RF errors in the SC cavities. Red lines are ±1 MeV boundaries.

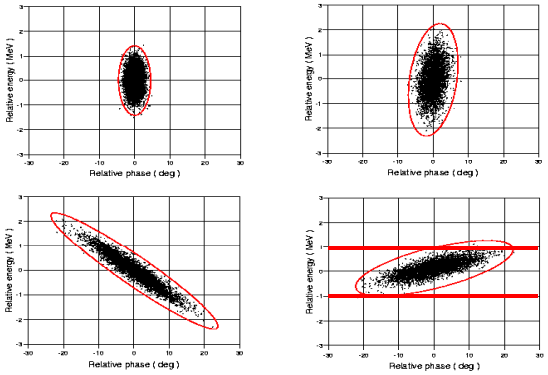

Figure 6 :Scatter plot along the ESS SC linac

Phase displacement of bunch centre is increased to ±25° (1120 MHz), result of accumulated RF amplitude and phase errors. As consequence, single particles can be ±50° (1120 MHz) away from design phase , excluding use of a SC ß=0.8, 6 cell cavity for energy spread reduction. There is no phase slip by using 560 MHz CCL, ß=0.912, and maximal single particle phase deviation is only ±25° (560 MHz).

ESS INITIATIVE (ESS-I) AND ESFRI REPORT 2006

After winding up the ESS Council and the Technical Team by the end of 2003, the neutron scattering community wanted to keep ESS on the political table and demonstrate to young scientist that the struggle for ESS goes on.

For this purpose, the ESS-Initiative (ESS-I) was formed [12] to include the European Neutron Scattering Association (ENSA) [13], various consortia for site candidatures and some key European laboratories.

ILL Grenoble is hosting ESS-I, and it is lead by an independent chair. The overview given here borrows from what Peter Tindemans, chair of ESS-I, presented at ICANS XVIII, Dongguan, April 2007[14].

A major highlight was the successful promotion of ESS to be as a high maturity project on the European Road Map of Research Infrastructures, published in October 2006 by the European Strategy Forum on Research Infrastructures (ESFRI) [15]. In doing so, ESFRI has both honoured and vindicated the effort of all major neutron

labs and more than 100 leading scientists all over Europe who for the past 13 years have developed the ESS project.

ESS will be a 5 MW LP source, the worlds first one to offer the unique capabilities of novel long pulse instruments for almost all of the most interesting areas of science and technology. The intention is that ESS will be built in such a way that governments can decide later on during its lifetime to increase power and add more target stations, as the future scientific need would arise.

ESS's world lead would become even more pronounced, even when SNS would upgrade its power to, say, 3 MW, if the ESS beam power would be increased to 7.5 MW.

ESS PREPARATORY PHASE PROJECT& 3 SERIOUS SITE CANDIDATES

A special call was issued by the EU for projects on the ESFRI Road Map to submit ESS EU FP 7 Preparatory Phase projects. ESS has done so and asked for financial support to site independent technical items and answer legal, financial and governance questions concerning ESS. The ESS Preparatory Phase project has been accepted in the meanwhile after a very positive assessment and has been allocated 5 M€ EU support to investigate all the issues mentioned above, starting January 2008.

A coordination team involving members of all 3 site candidates leads the ESS Preparatory Phase project.

Sweden: Lund

Sweden proposes to locate ESS in Lund[16], and offers to pay about 30% of construction costs. A new organization has been set up temporarily at Lund University, to be transformed later as a national structure. 10 M€ is available till the end of 2008. ESS will have a carbon-neutral, energy-efficient concept. In March 2007, ESS-S organized a well attended target workshop at Lund. Negotiations have now started with various countries and a series of Round Tables is being organised.

Spain / Basque Country: Bilbao

Spain has put forward a bid to host ESS near Bilbao[17]. It too offers around 30% of construction costs, and has made available funds for the current phase. It has recently joined forces with Hungary by concluding an MoU to coordinate the search for international partners. Spain and Hungary will appoint a joint Project Director and a joint International Advisory Board. The Spanish, as well as the joint Spanish/Hungarian financial bid are based on the idea that shares will be issued which provide use rights. Two sites are being discussed, both close to Bilbao.

Hungary: Debrecen or Székesfehérvár

Hungary too offers to host ESS[18], and is willing to pay a substantial share of the construction costs. Spain and Hungary have agreed on a procedure to select the site, if ESS goes their way. For Hungary, the first phase of the site selection has reduced 6 candidates to 2, one site in Debrecen, the other in Székesfehérvár, some 50 km from Budapest. Hungary has a financial scheme quite similar to the Spanish one.

The aim is now to arrive at a site decision early 2008, and a full financial governmental agreement by the end of 2008. In that case the ESS facility can deliver its first neutrons by the end of 2017 with full operational mode in 2019/2020. For all the three sites, the ESS facility will not be regarded as a nuclear facility.

ESS 07: 5 MW LP SOURCE, POSSIBLE FOR UPGRADE

improved neutron performance

Stimulated by the ESFRI 2003 findings [19], beginning 2003 discussions started about the scientific relevance of pure LP facility, compared to full ESS facility, SP&LP target stations.

In response to these discussions, layout of 15 MW, 3 GeV H^+ linac was included in ESS Update Report 2003.

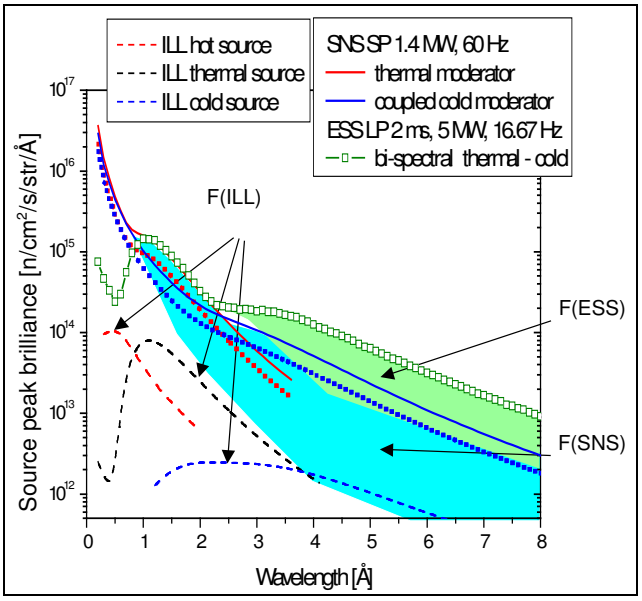

Figure 7 : neutron flux, figure of merit (F) for proposed ESS 5MW LP source compared to most powerful reactor & SP facility

Since than, neutron instrument experts and instrument modellers discussed and assessed potential gains expected from the ESS LP target station with bi-spectral thermal-cold moderators. Results were accepted at the ESS-I Rencurel workshop, Sep2006 [20]. Confirmed was multi-spectral beam extraction scheme, mentioned in ESS Update Report, meanwhile successfully implemented and tested at BENSC EXED beamline [21]. Improved neutron fluxes for 5MW ESS LP source are shown in Figure 7 [22].

Compared to fully upgraded ILL reactor at Grenoble or to 1.4 MW SNS SP facility, most powerful existing ones, proposed 5 MW ESS LP source will leap in neutron performance, as for thermal neutrons: 20x ILL & (1-5)x

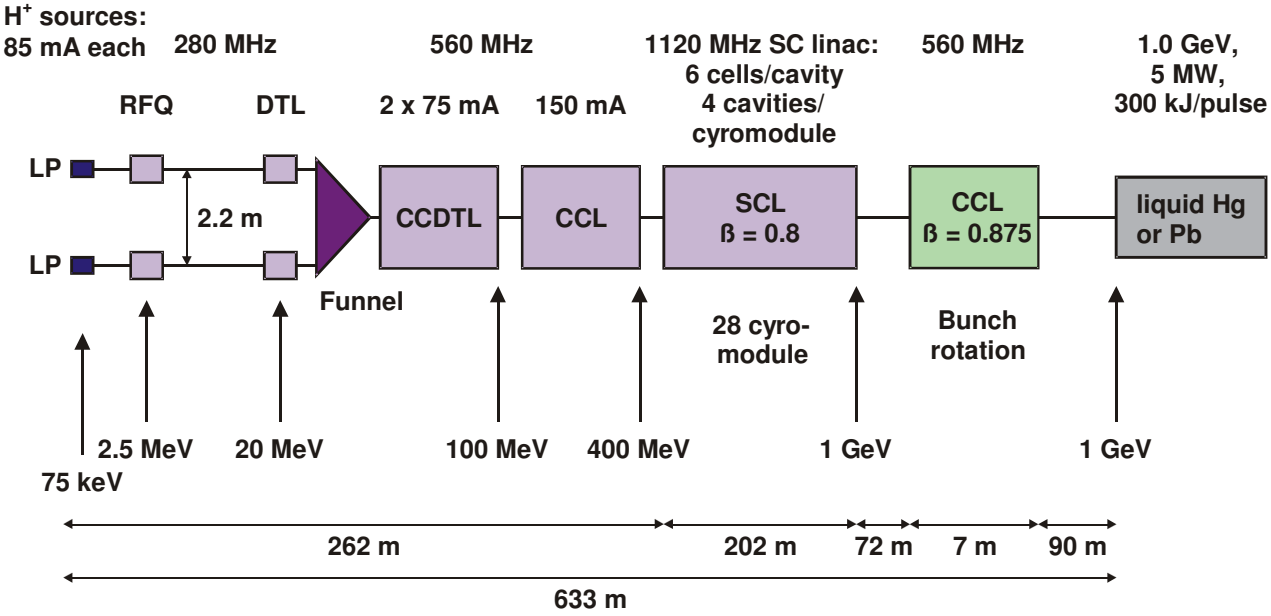

Figure 8: ESS H^+ SC linac, serving only LP target

SNS, whereas for cold neutrons: (10-40)x ILL & (3-15)x SNS. Hot neutrons (wavelength <0.7 Å, 100 meV to beyond 1eV) are relatively small chapter of neutron research, well served by existing reactors with hot source and SP sources.

ESS H^+ linac layout & target options

Layout of 5MW ESS H^+ LP facility is shown in Figure 8, based on the ESS H^- SC Reference Linac, using more powerful H^- beam instead, but without 2.5 MeV chopper line and achromatic bending section. Serving only LP target station, 2 ms pulse every 60 ms, 16 2/3 Hz, allows to have 150 mA current after 20 MeV funnel section. Reduced linac energy of 1 GeV requires only 28 cryomodules from 400 MeV on, 202 m in length,for unchanged moderate accelerating gradient of 10.2 MV/m

Peak power in SC main coupler is less than 1.15 MW, including 30% surplus for RF control, whereas average power is reduced to less than 45 kW, as only 4% RF duty cycle, 2.3 ms every 60 ms. 262 m NC 400 MeV linac is unchanged in length, but with reduced structure cooling. Two more 5 MW peak power klystrons are needed for CCL section, as increased linac current. Linac length is 464 m, whereas 633 m is total length from H^+ source to LP target, about 95 m in length.

Similar to layout of ESS H^- SC Reference Linac, energy spread is reduced by 560 MHz BR cavity, 20 MV rotation voltage & 3.5 MW peak RF power, needed to install dipol magnet before LP target in order to reduce backstreaming neutrons in 90 m long transport line. BR cavity is placed 72 m behind linac end, same distance as for ESS H^- SC Reference Linac. Larger increase in energy spread for 150 mA, 1 GeV H^+ beam, compared to more than factor 2 for 114 mA, 1.334 GeV H^- beam, is tolerable, as less restrictions for H^+ beam, but has to be studied.

Liquid metal target are preferred choice for ESS LP target station, either with Hg or Pb eutectics. Pb/Bi Megapie target at PSI Zürich was successful operated with 1600 MWh accumulated power during 4 month period, August to December 2006 [23].After stop of the beam, Pb/Bi eutectic in the target has been solidified. After extraction from SIN-Q facility, the target will be stored for about one and a half years. It will than be opened and the status of the internal components and structural materials will be analysed.

Thermal-hydraulic studies are required for both target materials. ESS LP target station has 22 beam holes, but multi-spectral beam extraction scheme allow to install up to 44 instruments afterwards. In terms of capacity, ESS plant will than provide twice as many beamlines for experimental work as SNS and J-PARC.

Performance & power upgrade

The 1 GeV, 5 MW ESS H^+ linac is a cost effective and power efficient accelerator for a LP neutron facility, therefore decided to be the basis of the ESS EU FP 7 Preparatory Phase project. Scientific capability is doubled by installing additional instruments afterwards.

In order to pronounce ESS facility as the world leading neutron source, even when 3 MW SNS, Japanese MW J-PARC facility [24]and fully upgraded ILL are ready, ESS beam power should be 7.5 MW, 50% increase. As 2 ms pulse length and 60 ms rep. time are fixed parameters for LP target, either current or energy must be increased. Increase of H^+ source current is not considered, as two almost identical high current H^+ sources are required.

As accelerating gradient in NC structures is also fixed, only enlarged can either linac tunnel and / or accelerating gradient in SC cavities. High ß bulk Nb SC cavities are tested for much higher gradients than assumed10.2 MV/m, but not for 2 ms pulse length. In addition, shortening rep. time limits accelerating gradient in high ß

SNS SC cryomodules, as cross-talk of the 4 cavities inside one cryomodule [25]. But as ESS LP source has 60 ms rep. time, almost factor 4 longer than SNS value, latterly 15% increase of accelerating gradient leads to 700 MeV energy gain instead of 600 MeV. Klystrons and SC couplers are designed for 30% surplus in peak power, reducing RF control power from 30% to 15% is possible after extended learning period.

Enlarging linac tunnel by 115m allows to add latterly 16 cryomodules, leading to additional 400 MeV energy gain, also operating at 15% higher gradients. Total length from H^+ source to 7.5 MW LP target is 748 m, almost the same as for 5 MW ESS H^- SC Reference Linac. Without 15% larger gradients in SC cavities, 6.7 MW beam power is reached at 1.35 GeV. BR cavity can still be placed 72 m behind linac end, maybe improved adjustment of linac bunch is necessary by phase shifting of same previous SC cavities. 90 m long transfer to LP target is adequate even for a 1.5 GeV beam.

For optimal neutron production rate, maybe moderators in LP target must be changed for going from a 1 GeV, 5 MW beam to a 1.5 GeV, 7.5 MW beam. Enlarged pulse content of 450 kJ must be considered.

Adding latterly dedicated low power target station, like proposed long wavelength one for SNS[26], is possible by adding pulsed dipol after BR cavity. Innovative chopper collector systems can be easily added into 2.5 MeV transfer line from RFQ to DTL.

As higher accelerating gradients are possible for the ESS H^+ linac, changing from 6 cells, ß=0.8 SC cavity to 5 cells, ß=0.85 SC cavity gives less phase slip at 400 MeV and improved energy gain up to 1.5 GeV, as maximal efficiency is shifted towards 850 MeV, see Fig4. Symmetric 5 cell cavity maintain field flatness over a wide tuning range by providing an identical deformation of both end-cells. Cryomodule and SC linac length are unchanged in length, if accelerating gradient is increased by less than 12%.

SYNERGY WITH CERN

The 1 GeV, 5 MW ESS H^+ linac is a cost effective and power efficient accelerator for a LP neutron facility, but needs 3 different frequencies due to 20 MeV funnel. Low energy, but high beam current requires moderate accelerating gradient in SC cavities to limit peak values in SC power couplers.

Layout of 1 GeV, 5 MW ESS H^+ linac is unique, as most other pulsed high power linacs need high energy, less current. But ESS H^+ linac can also operate at slightly modified frequencies, 325/650/1300 MHz, to more overlap with CERN & DESY, leading labs for NC&SC parts.

Planned CERN Linac4 operates at 350 MHz, the 1st NC H^+ linac to be built in Europe after 30 years[27].Construction of Linac4 (160MeV,H^-) is approved as a high priority project intended to start in January 2008 and last 4 years(2008-2011).The 2012 PS Booster start-up is foreseen with the new Linac4 beam.

Tesla Test Facility at DESY has produced more than 100 ß=1 multi-cell 1.3 GHz SC cavities, reaching gradients well above 20 MV/m, .installed in long cryomodules[28]. Multi-beam klystrons with more than 10 MW peak power are driving string of cavities, 1 ms pulse and 5 Hz rep. rate.

Using 5 cells, ß=0.85 1.3 GHz SC cavity above 400 MeV for the ESS H^+ linac require accelerating gradient below 15.3 MV/m to preserve 748 m length of ESS 7.5 MW H^+ facility.. Matched 3db cavity bandwidth is ±1.5 kHz for the 114 mA LP beam and R/Q=440 Ω/m, linac definition. Investigated must 1.3 GHz SC main couplers, 1.15 MW peak power for 2.3 ms and average power of 45 kW.

Avoiding 20 MeV funnel section will give 5MW LP power at 2 GeV. For the ESS SC lattice period, shown in Figure 3,linac length is unchanged by using about 25MV/m accelerating gradient in SC cavities. In Table 1, main linac parameters are shown for 2 GeV, 5 MW ESS H^+ linac, compared to 5 GeV, 4 MW CERN SPL one [29].

Table 1: 5 MW ESS compared CERN-SPL

	ESS: 5 MW LP	**CERN-SPL: 4 MW**
Energy, length	2 GeV, 464 m	5 GeV, 534 m
Pulse current	75 mA	40 mA
Pulse length, rep. rate	2 ms, 16.67 Hz	0.4 ms, 50 Hz
Klystrons, cavities in high ß SC part	112, 112: no power splitting	32, 136: up to 8 fold power splitting

Synergy with the CERN plans would require to avoid the funnel section at 20 MeV, leading to a 5 MW LP power at 2 GeV.Linac length is unchanged by using high gradient in SC cavities. SPL frequencies can be used, but components will differ, as ESS LP source requires high current and long pulses, whereas SPL linac is designed for high energy and high rep. rate. SPL design report, including costs, will be available in 2011 / 2012.

SUMMARY

After completing ESS Update Report by end of 2003. aiming for 10 MW H^- facility with SP and LP targets, neutron scientist have gained improved understanding for unique capabilities of novel long pulse instruments.. ESS 07 will be a 5 MW H^+ facility serving only LP target, built in such a way that governments can decide later on its lifetime to increase power and add more target stations, as the future scientific need would arise.

Later on, goal of 7.5 MW beam power is achievable by enlarging linac tunnel by 115m, allows to add latterly 16 cyromodules, and increasing accelerating gradient in all SC cavities by 15%.

Avoiding 20 MeV funnel section will give 5 MW LP power at 2 GeV. Linac length is unchanged by using high accelerating gradient in SC cavities. SPL frequencies can be used, but components will differ,as ESS LP source

requires high current and long pulses, whereas SPL linac is designed for high energy and high rep. rate.

ACKNOWLEDMENT

Grateful acknowledged is fruitful cooperation with former ESS linac team, providing for many years lot of help and enormous amount of informations. Expressed are many thanks to P.Tindemans and F Mezei, providing details about ESS 07 plans and improved neutron performance for LP sources.

REFERENCES

[1] The ESS Project Volumes I, II, III, and IV, 2002
[2] The ESS Project Volumes III Update 2003, http://neutron.neutron-u.net/n_documentation/n_reports/n_ess_reports_and_more/106
[3] V. Danilov et al, PRSTAB, Vol 10, 2007, p.053501, V. Danilov et al, PAC 07, Albuquerque, USA, p.2582
[4] K.Bongardt, M.Pabst, A.Letchford, NIM A, 2000, Vol 451, p. 287
[5] M.A. Clarke-Gayther, G. Belodi, F. Gerigk, Proc. EPAC 2006, Edinburgh, Scotland, p. 300
[6] F. Gerigk, "Revised ESS front End, 2.5-20 MeV ", internal note, ESS-03-138-A, December 2003
[7] Proposed Power Upgrades for SNS http://neutrons.ornl.gov/facilities/proposed_upgrades.shtml
[8] M. Pabst, K. Bongardt, "Analytical Approximation of the Transit Time Factor in SC Cavities ", internal note, ESS-02-128-L, July 2002
[9] M. Pabst, K. Bongardt, Proc. Linac 2002, Gyeongju, Korea, USA, 2002, p. 392
[10] M. Pabst, K. Bongardt, A.Letchford Proc. EPAC 1998, Stockholm, Sweden, p. 147
[11] A. Letchford, M. Pabst, K. Bongardt, Proc. PAC 1997, New York, USA, p. 1767
[12] ESS-Initiative: http://essi.neutron-eu.net/essi/
[13] ENSA: http://neutron.neutron-eu.net/n_ensa/
[14] ICANS XVIII, Dongguan, China, April 2007 http://www.icans-xviii.ac.cn/
[15] ESS-I press release about ESFRI evaluation: http://essi.neutron-eu.net/essi/news_essi/#news1199
[16] ESS-S: http://www.ess-scandinavia.org/new/source/index.asp
[17] ESS-Bilbao: http://www.essbilbao.com/
[18] coordinating team for ESS-Hungary: http://www.kfki.hu/indexeng.html
[19] ESFRI 2003: http://neutron.neutron-eu.net/n_documentation/n_reports
[20] ESS-I press release about Rencurel2006 workshop: http://essi.neutron-eu.net/essi/news_essi/#news1199
[21] BENSC EXED beamline: http://www.hmi.de/bensc/reports/2004/pdf-files/EF_38.pdf
[22] F. Mezei, New perspectives from new generation of neutron sources, in press C. R. Physique, 2007 F.Mezei, ECNS 2007 conference, Lund, Sweden, June 2007
[23] PSI press release, Jan 2007: http://www.psi.ch/medien/Medienmitteilungen/mm_megapie_jan07/PSI_MM_Megapie_Jan07_BgInfo_E.pdf
[24] J-PARC: http://j-parc.jp/en/message.html
[25] S. Henderson et al, PAC 07, Albuquerque, USA, p. 7 I.E. Campisi et al., PAC 07, p.2502
[26] J.M. Carpenter, T.E. Mason, NIM A545, 2005, p. 1
[27] F. Gerigk, M. Vretenar (Editor), "Linac4 Technical Design Report", CERN-AB-2006-084-ABP/RF, December 2006
[28] TTF: http://tesla-new.desy.de/
[29] F. Gerigk (Editor), "Conceptual Design of the SPL II", CERN Yellow Report 2006-006, July 2006

LINEAR OPTICS DESIGN FOR PS2

Y. Papaphilippou, W. Bartmann, M. Benedikt, C. Carli,
B. Goddard, S. Hancock, J. M. Jowett, A. Koschik,
CERN, Geneva, Switzerland

Abstract

The design considerations and key parameters for the replacement of the CERN Proton Synchrotron (PS) with a new ring (PS2), as part of the upgrade of the LHC injector complex are summarized. Classical linear optics solutions including standard FODO, doublet and triplet cells with real transition energy, are studied. Particular emphasis is given to the tuning and optimisation of Negative Momentum Compaction (NMC) cells with imaginary transition energy. The optics of the high energy transfer line is also presented.

INTRODUCTION

Motivation

The replacement of the ageing CERN Proton Synchrotron (PS), which was constructed half a century ago, with a new ring (PS2), plays a key role in the overall upgrade strategy of the Large Hadron Collider (LHC) [1, 2]. The main purpose of the new ring is to ensure reliable operation over the coming decades and to enable the transmission of the ultimate beam needed for the LHC luminosity upgrade. The increased beam brightness and intensities should also enhance the opportunities of CERN's fixed target physics program.

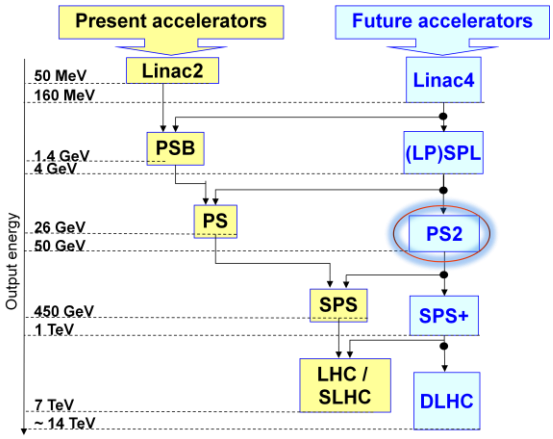

Figure 1: Output energy flowchart of the LHC injectors and collider at present and in the future, following a staged upgrade strategy [1].

Requirements

The PS2 should have the versatility of the existing PS, providing many different proton and ion beams, with various bunch patterns, for downstream accelerators or directly for physics experiments. In this respect, several injection and extraction systems must be implemented, including H^- charge exchange and fast ion injection, conventional fast extraction for LHC, multi-turn extraction for SPS fixed target experiments and slow extraction for PS2 physics. Furthermore, the PS2 has to be integrated into the existing complex as part of a staged upgrade plan, presented schematically in Fig. 1 [1]. The upgrade scenario foresees the injection of proton beams into the PS2, directly from the Super-Conducting Proton Linac (SPL) [3, 4]. The low energy part of the SPL, called Linac4, will be constructed sooner, close to the PS complex, to provide 160 MeV H^- for the PS Booster [5]. The ion beams should be injected from the existing ion complex.

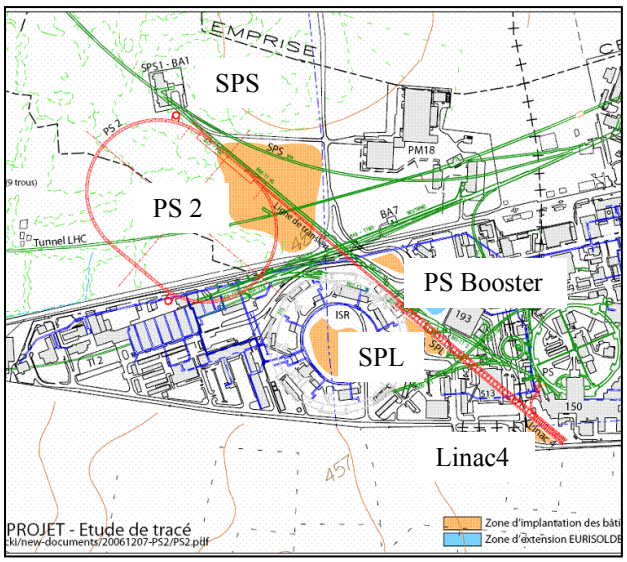

Figure 2: Layout of the PS2 integrated into the CERN accelerator complex.

A tentative layout of the PS2, integrated into the CERN accelerator complex, is shown in Fig. 2. The racetrack shape of the ring was dictated by the assumption that the SPL will be the proton injector for the PS2. In this respect, the injection and extraction systems are installed in one straight section [6]. The advantage of the racetrack shape is that the number of dispersion suppressors is reduced, which increases the bending filling factor and thereby the energy range that the synchrotron can reach. On the other hand, a racetrack shape with super-periodicity of only 2 will be quite susceptible to systematic linear and non-linear resonances, making the working point choice difficult. A supplementary constraint is imposed by the necessity to reduce H^- beam losses due to Lorentz stripping. Hence, the bending radius of the PS2 injection transfer line must be large and unnecessary bending must be avoided. Finally, the installation of the PS2 close to the SPS minimises the

length of the high-energy transfer line, but the optics constraints to be achieved become more difficult.

OPTICS DESIGN CONSTRAINTS

Some basic parameters that constrain the optics design of PS2 are displayed in Table 1, as compared to the ones of the present PS [7]. The kinetic energy at the PS2 extraction should be at least doubled in order to reduce the losses in the present SPS and limit the energy swing of a future machine with extraction energy of close to 1TeV. For reaching a 50 GeV kinetic energy with iron dominated magnets providing maximum bending field of 1.8T [8], the circumference of the ring should be at least doubled with respect to the 200π circumference of the PS. For optimum filling of the SPS for fixed target experiments with a 5-turn extraction from the PS2 and leaving some space for the SPS dump kicker, C_{PS2} should be less than one fifth of C_{SPS}, i.e. a bit longer than twice the circumference of the PS. Finally, the bunch patterns needed impose additional constraints in the circumference which was fixed to $C_{PS2} = \frac{15}{77} C_{SPS} = \frac{15}{7} C_{PS} = \frac{3000}{7}\pi$ [9].

Table 1: Basic beam parameters for PS2 as compared to the actual PS. Note that the PS is uses combined function magnets.

Basic beam parameters	**PS**	**PS2**
Injection kinetic energy [GeV]	1.4	4
Extraction kinetic energy [GeV]	13 / 25	50
Circumference [m]	200π	3000π/7
Transition energy [GeV]	6	~10/10i
Max. bending field [T]	1.2	1.8
Max. quadrupole gradient [T/m]	5	17
Max. beta functions [m]	23	60
Max. dispersion function [m]	3	6
Min. drift space for dipoles [m]	1	0.5
Min. drift space for quads [m]		0.8
Max. arc length [m]		510

The kinetic energy at injection is constrained by the maximum acceptable incoherent space charge tune-shift, which is scaled as $\Delta Q_{S.C.} \propto \frac{N_b}{\varepsilon_n \beta\, \gamma^2 B_f}$, i.e. proportional to the bunch population and inversely proportional to the normalised emittance ε_n, the bunching factor B_f and the square of the energy. In the PS, the space charge tune shift is around 0.2 for LHC-type beams at the 1.2ms injection plateau, a value considered as the maximum acceptable limit, for avoiding high beam losses due to resonance crossing. Considering that the number of protons per bunch for the LHC upgrade will be 4×10^{11} with respect to 1.7×10^{11} in the PS, the same normalised emittance and a bunching factor which is doubled due to the increase of the circumference of the ring, the injection energy should be increased accordingly from 1.4 to around 4GeV.

The increase of both injection and ejection energies tends to slow down motion in longitudinal phase space and to increase longitudinal acceptances [10]. The choice of the main RF systems can be either a low-frequency large-bandwidth one, as in the actual PS, or a 40MHz system compatible with a pre-chopped beam coming from the SPL, but incompatible with the present scheme of heavy ion beam acceleration. The former system has the advantage of allowing different type of longitudinal manipulations, but it implies the increase of longitudinal acceptance and time needed for RF gymnastics, especially at high energy. The choice of the momentum compaction factor $\frac{1}{\gamma_{tr}^2} \approx \pm 0.01$ limits the aforementioned increase. Nevertheless, it constrains the transition energy to a real or imaginary value of around 10. The real transition energy is relatively straightforward to obtain with standard cells but necessitates the development of a low loss transition crossing scheme. The optics design of a Negative (or Flexible) Momentum Compaction (NMC) lattice leading to low imaginary transition energy is more challenging but has the obvious advantage of avoiding the problems of transition crossing and thus simplifying the whole acceleration process.

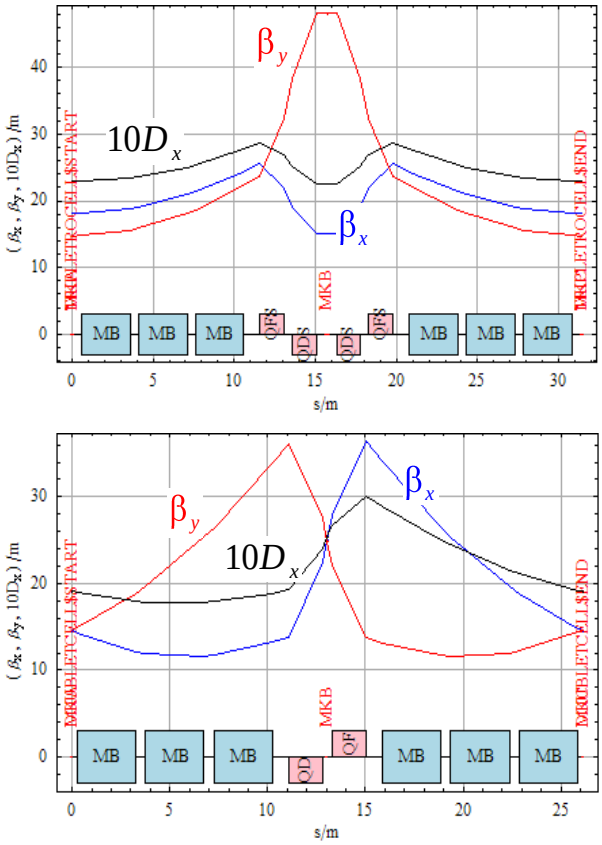

Figure 3: Optics functions for arc cells based on quadrupole doublets (bottom) and triplets (top).

The maximum quadrupole gradient is limited to below 17T/m giving a pole tip field of 1.3 T with 75mm pole radius [11], which leaves enough clearance for the

maximum beam sizes considered, taking into account the maximum optics functions quoted in Table 1.

The minimum drift lengths are set so as to leave enough space for placing other magnets such as orbit correctors, chromaticity sextupoles and instrumentation. Finally, the maximum arc length is set to around 510m, in order to leave enough space for the injection and extraction elements placed in the long straight sections.

LATTICE CONSIDERATIONS

Doublet and Triplet Lattices

Lattices based on quadrupole doublets and triplets (Fig. 3) allow longer drift sections for injection and extraction insertions. The triplet cells offer the additional feature of significantly reducing betatron functions in the long drift, which is an advantage for dipole apertures.

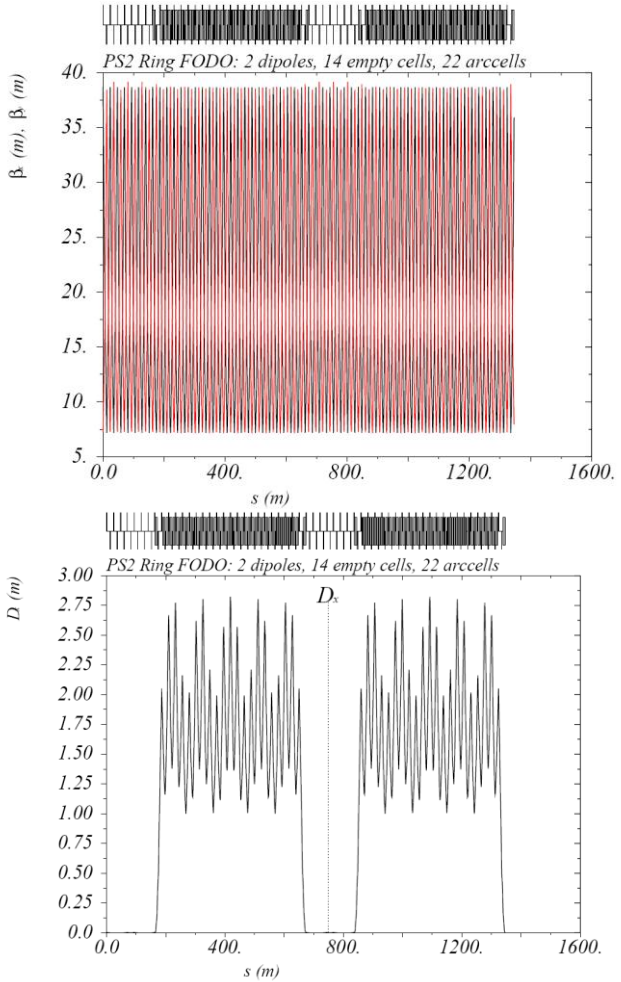

Figure 5: Lattice functions for the PS2 FODO lattice. Horizontal and vertical beta functions (top) and dispersion functions (bottom).

The main disadvantage of these lattice types is the strong focusing strength needed due to the small distance between adjacent quadrupoles, which exceeds the imposed gradient limit or requires longer quadrupoles, reducing the bending magnet filling factor. In consequence, there is insufficient space for the injection and extraction systems for the imposed circumference and top energy.

FODO Lattice

The simplest lattice is based on plain FODO cells with two quadrupole families. With a phase advance of close to $\pi/2$ per cell, the dispersion can be suppressed naturally by a missing dipole scheme. The ring consists of 22 arc cells with four 3.8m-long dipoles per regular cell. The quadrupoles have all 1.5m length and their strength is within the imposed limit. The total length of the arc is around 510m. The optics functions' evolution along the whole ring is displayed in Fig. 5. Their maximum values are comfortably within the upper limits set in Table 1. The chosen phase advance per cell allows simple design of the transfer channels which can be located within the 7 cells of one of the long straight sections, as indicated in Fig. 6. This lattice achieves transition energies of around 11GeV for working points between 14.1 and 14.9 in both planes. The limited tunability of the lattice is its main drawback, as the two quadrupole families do not provide enough flexibility for exploring other working points. In this respect, an alternative FODO lattice with 10 quadrupole families has been also studied, with around 80º phase advance per cell, providing similar results with respect to optics functions, space constraints and transition energies reached.

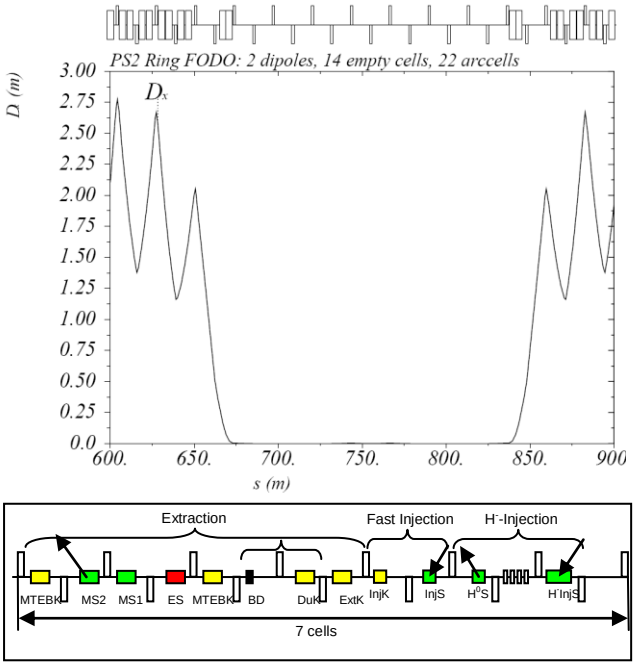

Figure 6: Dispersion suppression in the long straight section (top) and layout of all injection and extraction channels (bottom).

NMC Modules

NMC modules similar to the ones studied in detail in the 90's [13,14] and built recently for the high energy synchrotron of the J-PARC project [15] have been investigated [16]. The first module studied for PS2 starts

from an almost regular FODO focusing structure shown in the upper part of Fig. 7, with one special cell without bends surrounded by two filled cells. The phase advance per cell is matched to the desired value. The plot corresponds to phase advance of 90º, bringing the dispersion at the beginning and at the end of the module to zero. The drifts in the central cell are then reduced and the quadrupole strengths of the centre are rematched to the desired average phase advance per cell to obtain the lattice in the lower plot. Following this method, the low imaginary transition energy of 10i can be obtained. The main disadvantage is that the vertical beta function exceeds by far the imposed limit (it gets close to 80m).

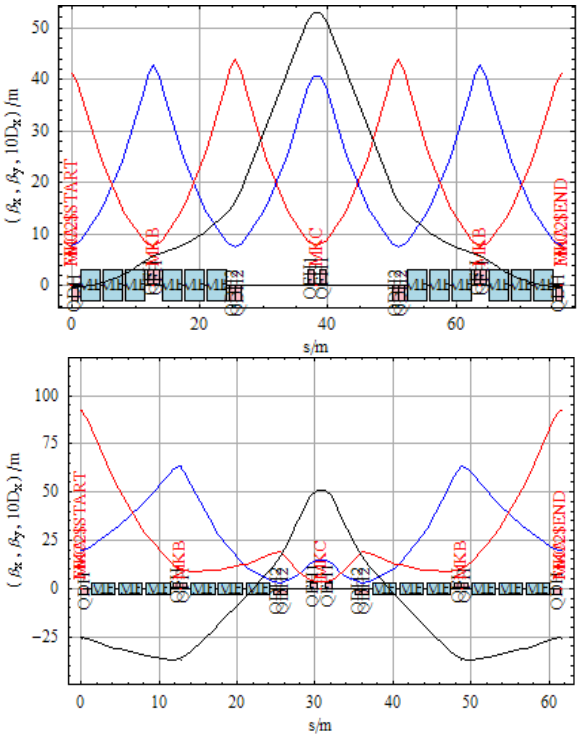

Figure 7: Horizontal (blue), vertical (red) beta functions and dispersion (black), for NMC module starting from regular FODO cells (top) and reducing central drifts (bottom).

Another NMC module is shown in Fig. 8. The bending filling factor is improved by increasing the number of FODO cells from 3 to 4, i.e. adding a half FODO cell with bends from either side of the previous module. In that way, the phase advance per cell can be lowered and, at the same time, a very low imaginary gamma transition can be obtained.

The functioning of the module is depicted in the upper plot showing the trace of the normalised dispersion vector $(\frac{D_x}{\sqrt{\beta_x}}, D_x'\sqrt{\beta_x} + D_x\frac{\alpha_x}{\sqrt{\beta_x}})$, for one module. The effect of the cells filled with bends is indicated by a single jump in the dispersion invariant and in thin lens approximation (the correct evolution of the dispersion vector is plotted as a dashed line). The radius of the induced dispersion beating can be adjusted with the overall phase advance inside the module. Large radii and thus negative contributions to the momentum compaction can be obtained with a phase advance slightly smaller than 2π.

By choosing appropriate phase advances tuned by 4 families of quadrupoles, the module can give relatively low imaginary transition energy. In the example presented on Fig. 9, for horizontal and vertical phase advances of 280º and 320º, respectively, imaginary transition energy of 8.2i can be obtained. The main drawback of this module is its length of around 96m which leaves very little space for the long straight section.

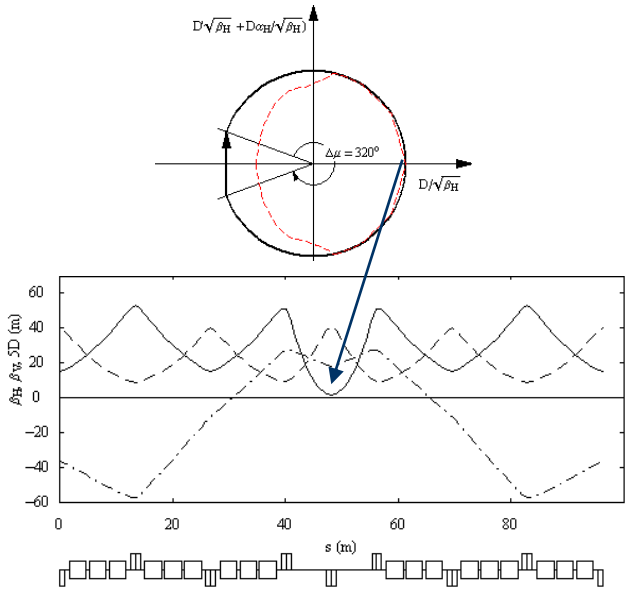

Figure 8: NMC module with increased filling factor.

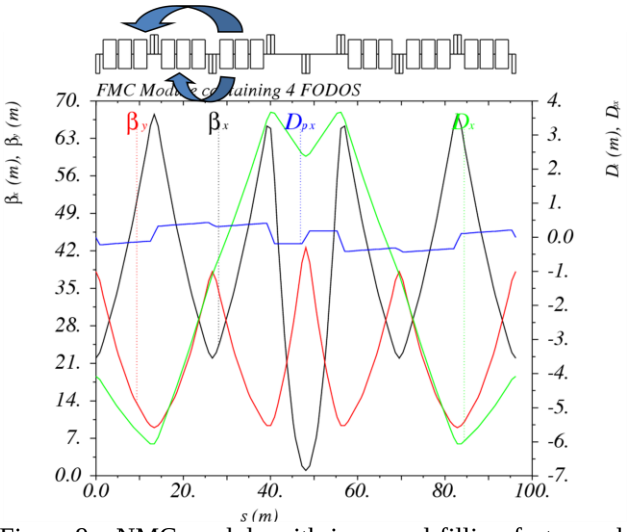

Figure 9: NMC module with increased filling factor and low imaginary transition energy.

A modified module can be obtained by moving the bending magnets of the most internal half cell towards the exterior parts of the module. The momentum compaction factor defined as $\alpha_c = \frac{1}{C}\oint\frac{D(s)}{\rho(s)}ds$ will become even smaller, as the bending magnets are pushed to areas where the dispersion is negative. At the same time, the space between the bend-free cells can be further squeezed, thus diminishing drastically the size of the

whole module. An example of the NMC described above is given on the top of Fig. 10, consisting of one FODO cell with four bending magnets per half cell and a quadrupole doublet. All quadrupoles in half of the module are powered individually setting the total number to 5 families. For phase advances of 320º, in both planes, imaginary transition energy of around 6i can be achieved. For driving the momentum compaction factor to such low negative values in a limited space while keeping the beta functions below 60m, the dispersion has big excursions from -8 to 6m. The arc can be built with 5 of this modules plus a dispersion supressors of around the same length giving an estimated total length of 560m, which still does not leave enough space for the long straight section elements.

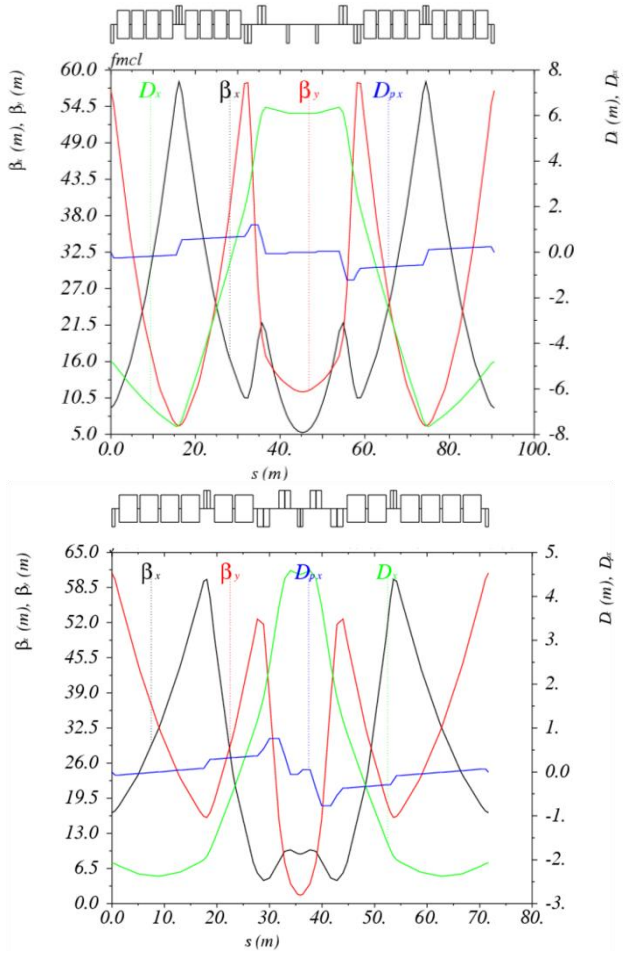

Figure 10: Optics functions of short NMC modules with high filling factor and low imaginary transition energy, leaving reasonable space for the long straight sections.

In order to shorten this module, one could first cut down the number of dipoles in the second FODO half cell and than reduce the space in the center of the module, having one instead of two central quadrupoles (bottom of Fig.10). This assymetric FODO cell module satisfies all the criteria from the point of view of optics functions maxima. For phase advances of around 270º and 260º degrees in the horizontal and vertical plane, it provides imaginary transition energy of 10i. The clear advantage of this module is its length, which is around 70m. With 7 modules of this type plus dispersion suppressors having equal length in total, the arc length can be below the required 510m.

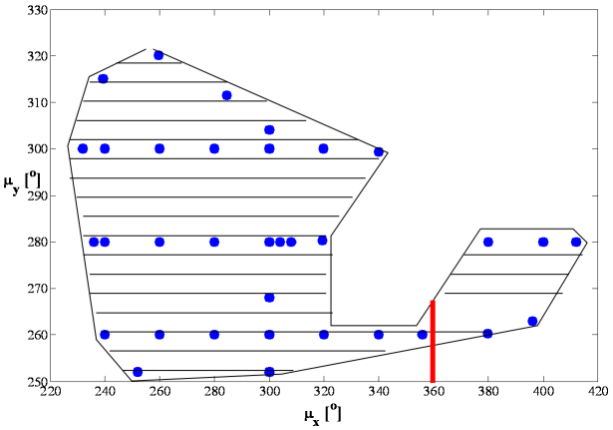

Figure 11: Phase advances achieved from the short high-filling-factor NMC module.

In Fig.11, the possible phase advances achieved by this module are shown. The blue dots are a few matched cases, for which all the imposed optics, gradient and length constraints are satisfied, but the tuning of the module is pretty flexible and it covers all the shaded area, i.e. phase advances of 240º to 420º in the horizontal plane and 250º to 320º in the vertical plane. The red dash marks the 360º horizontal phase advance which cannot be reached, as the optics become unstable.

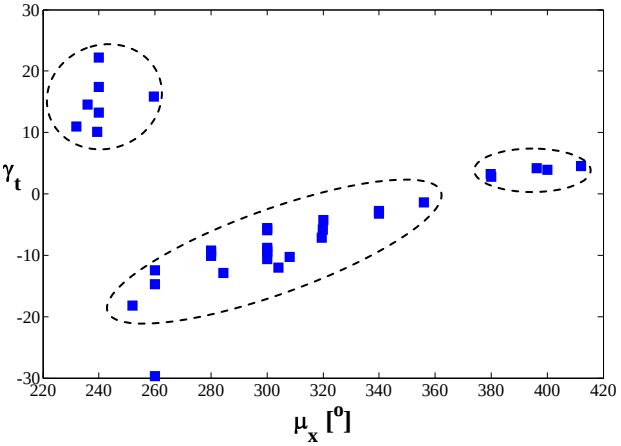

Figure 12: Phase advances achieved from the short high-filling-factor NMC module. The negative part of the vertical axis corresponds to imaginary transition energies.

All the matched phase advances do not necessarily correspond to imaginary transition energies. In Fig. 12, the horizontal phase advance is plotted versus the transition energy. Imaginary transition energies correspond to the negative part of the vertical axis for plotting simplicity. The diagram can be roughly divided in three parts. The upper left part, for which the horizontal phase advance is particularly low, corresponds to real transition energies. The middle part corresponds to imaginary values going from 20i down to 2i for horizontal

phase advances very close to 2π. Above 360º, solutions with very low real transition energies can be achieved.

Apart from the dependence of the transition energy on the phase advance, there is also an almost linear dependence of the momentum compaction factor (inverse square of the transition energy) to the extremum value of the dispersion as shown in Fig. 13, where the transition energy is plotted against the maximum and minimum values of the dispersion function. For low imaginary or real transition energy the excursion of the dispersion function is getting to very high values and certainly above the imposed 6m limit. The dispersion function is getting much more relaxed for high transition energies.

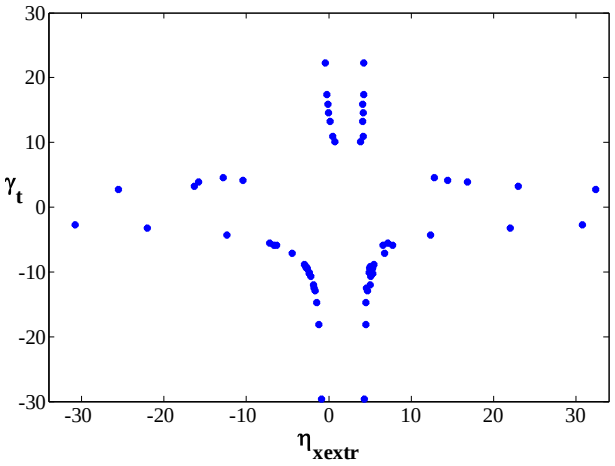

Figure 13: Transition energy versus dispersion minimum and maximum values. The negative part of the vertical axis corresponds to imaginary transition energies.

Finally, the dependence of the chromaticity on transition is plotted in Fig. 14, where the blue dots correspond to horizontal and red to the vertical plane. For lower transition energies, the horizontal chromaticity tends to become higher. The vertical chromaticity is certainly independent of the transition energy. It is mostly restricted by the matching conditions to achieve the vertical phase advance of the different options.

The challenge of this type of modules is to construct a dispersion suppressor that would also match the optics' functions in the long straights. The structure along with the lattice functions of a possible dispersion supressor are depicted in Fig. 15. The first half module is exactly a copy of the arc NMC module. The second part of the module where the dispersion is matched to zero while keeping the beta variation under control uses 4 independent quadrupole families and it is necessary to add a fifth dipole in the last half FODO cell. With this dispersion supressor the whole arc has the required length of 510m and the long straight section can be matched without difficulty to form the rest of the ring. The main drawback is the high horizontal beta function of around 70m, that has to be reduced by relaxing some space contraints or by accepting a slighlty higher imaginary transition energy.

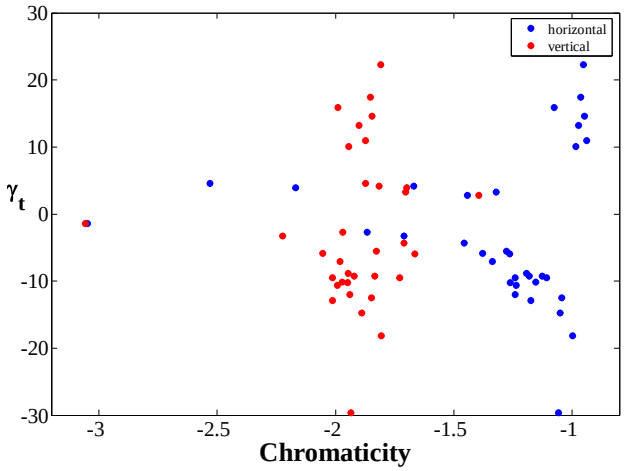

Figure 14: Transition energy versus horizontal (blue) and vertical (red) chromaticity. The negative part of the vertical axis corresponds to imaginary transition energies.

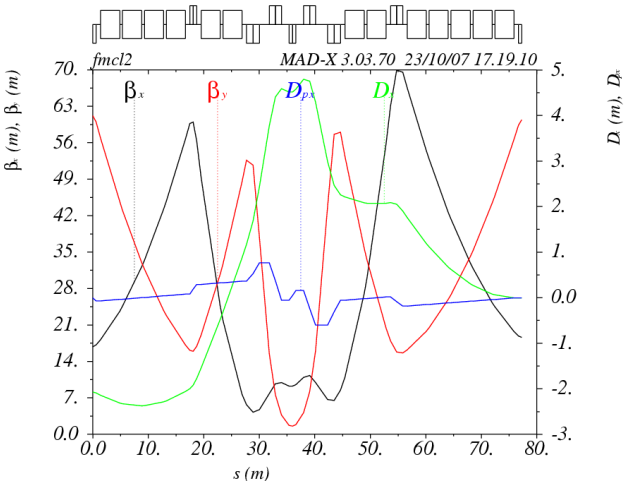

Figure 15: Optics functions evolution along the NMC module dispersion suppressor.

HIGH ENERGY TRANSFER LINE

The high energy transfer line has to match the PS2 optics into the SPS with the tight geometry and length requirements of the proposed layout (see Fig. 16). It should also accommodate a stripping foil for Pb ions, which necessitates a low beta insertion. The use of normal conducting magnets with adequate fields and gradients is a reasonable choice. The transfer line may necessitate an emittance exchange scheme as in the present PS to SPS transfer line and a branch to serve the future experimental areas of the PS2. Vertical bending magnets are not necessary as the PS2 will be constructed at the same level as the SPS.

Studies of possible solutions were made using two main achromat bends in the middle of a 360m-long line. This design provides the adequate separation required between the PS2 machine and the existing transfer tunnels. A matching section with a low beta insertion for the stripping foil location was designed near the SPS. The emittance exchange scheme remains challenging due to the space constraints (additional cells have to be

added). The design of the injection and experimental area transfer lines are in progress.

SUMMARY AND PERSPECTIVES

Optics considerations to define a suitable lattice for the proposed PS2 machine were presented. The plain FODO lattice is a good candidate and a straightforward choice. A transition crossing scheme should be implemented to complete the linear lattice design.

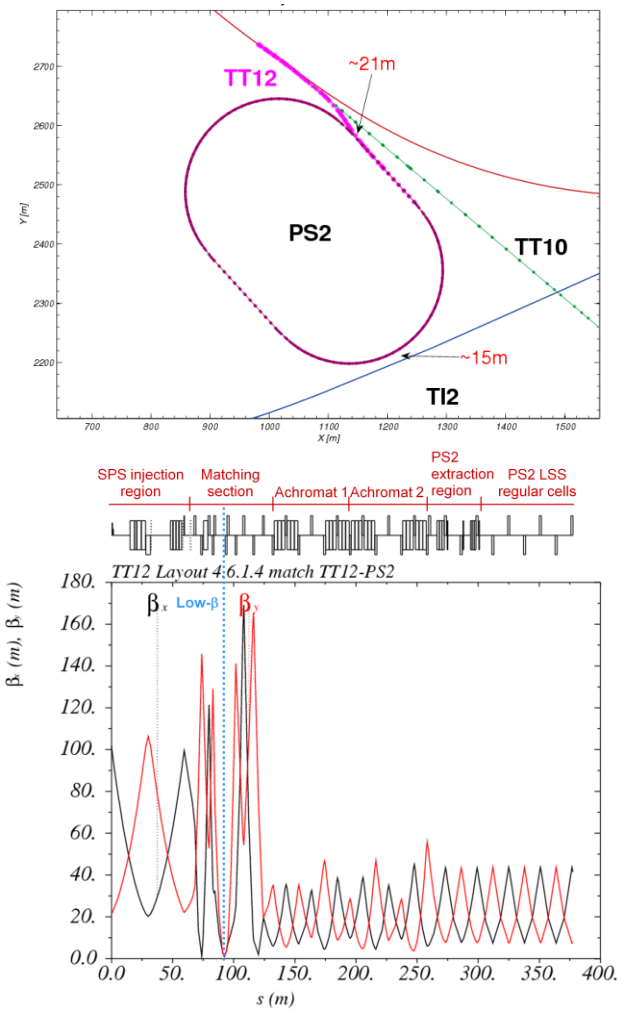

Figure 16: Layout of the PS2 to SPS transfer line (top) and beta function evolution for a proposed optics design solution (bottom).

Alternative negative momentum compaction lattices were investigated. In particular, a short high-filling-factor module satisfies all optics constraints. An optics parameter scan demonstrated the difficulty to keep the low imaginary transition energy of 10i, while keeping the optics functions (especially dispersion) below the imposed limit of 6m. A dispersion suppressor for arc cells based on this module was designed giving a total arc length which is short enough to accommodate the long straight section injection and extraction insertions.

The study will be completed including chromaticity correction, orbit, gradient, coupling and non-linear multipole error analysis and dynamic aperture simulations. The detailed comparison between the two options (real or imaginary transition energy) should be based on the performance of the lattices against beam losses, which implies a careful design of a collimation system and non-linear dynamics considerations including the impact of space charge and other collective effects.

ACKNOWLEDGEMENTS

We would like to thank all the members of the PS2 study group for fruitful discussions and in particular G. Arduini for his constructive comments and corrections to a draft version of this paper.

REFERENCES

[1] R. Garoby, these proceedings.
[2] M. Benedikt, R. Garoby, F. Ruggiero, R. Ostojic, W. Scandale, E. Shaposhnikova, J. Wenninger, "Preliminary Accelerator Plans for Maximising the integrated LHC Luminosity", CERN-AB-2006-018-(PAF).
[3] R. Garoby, M. Benedikt, A. Fabich, F. Gerigk, "Comparison of Options for the Injector of PS2", CERN-AB-2007-014 (PAF).
[4] F. Gerigk, these proceedings.
[5] M. Vretenar, these proceedings.
[6] M. Barnes, M. Benedikt, J. Borburgh, T. Fowler, B. Goddard, "PS2 Beam Transfer Systems: Conceptual Design Considerations", CERN internal AB-Note-2007-001.
[7] M. Benedikt, "General Design Aspects for the PS2", Proceedings of LUMI'06 Valencia, CERN-2007-002.
[8] T. Zickler, "Design study of normal-conducting magnets for the CERN PS2", CERN internal AT-MEL Technical Note, edms:855337.
[9] R. Garoby, "RF Constraints on the Size of PS2", CERN internal AB-Note-2007-020.
[10] S. Hancock, "Gamma at Transition of the proposed PS2 Machine", CERN internal AB-Note-2006-39.
[11] M. Benedikt, "Preliminary requirements for the design of PS2 magnets", CERN internal AB-Note-2007-29.
[13] S. Y. Lee, K. Y. Ng, D. Trbojevic, "Minimising dispersion in flexible–momentum-compaction lattices", Physical Review E, Vol.48, No 4, p. 3040-3048.
[14] U. Wienands, et al., "The High-γ_t lattice for the SSC low energy booster", Proceeding of HEACC'92, Hamburg.
[15] "Accelerator Technical Design Report for JPARC", KEK Report 2002-13.
[16] W. Bartmann, M. Benedikt, C. Carli, B. Goddard, S. Hancock, J.-M. Jowett, Y. Papaphilippou, "Optics considerations for the PS2", Proceedings of 2007 Particle Accelerator Conference, Albuquerque, NM, USA, 25 - 29 Jun 2007, p.739-741.

IMPEDANCE ESTIMATES AND REQUIREMENTS FOR THE PS2*

V. Lebedev#, FNAL, Batavia, IL 60510, U.S.A.

Abstract

The small ring impedance required for beam stability and the fast ramping rate required to boost the integrated particle flux in a fast ramping syncrotron are contradictory to each other. The paper discusses possible aproaches to the choice of PS-2 vacuum chamber and major limitations on the ring impedance and the beam stability.

1. RING PARAMETERS

There is a similarity between PS-2 parameters and parameters of FNAL's Project-X [1]. Both projects are based on the multi-turn injection from a SC linac. Unlike the PS-2 which will be a new ring in CERN, FNAL plans to upgrade the existing Main Injector (MI) for Project X The MI has higher injection and extraction energies than are presently considered for the PS-2. Parameters for both synchrotrons are presented in Table 1.

Table 1: Tentative PS-2 and MI parameters

	FNAL MI		PS-2
	Present	Project X	
Injection energy, GeV	8		5
Extraction energy, GeV	120(max. 150)		50
Circumference, m	3319.42		1346
Particles per bunch	$0.7\cdot10^{11}$	$3.1\cdot10^{11}$	$4\cdot10^{11}$
Beam current at inj., A	0.49	2.45	2.5
Cycle duration, s	2.2	1.4	1.5
Norm. 95% emit., mm mrad	15/15	25/25	18
Norm. acceptance at inj., mm mrad	40/40	40/40	100
90% long.emit., eV s/bunch	0.4	0.5	0.5
Total number of particles	$3.4\cdot10^{13}$	$1.7\cdot10^{14}$	$6.5\cdot10^{13}$
Betatron tunes, Q_x/Q_y	26.42/ 25.41	26.45/ 25.46	~15
Maximum Coulomb tune shifts, $\Delta Qx/\Delta Qy$	0.033/ 0.038	0.043/ 0.046[1]	0.07/ 012
Harmonic number	588	588	180
Accelerating freq., MHZ	53	53	40

2. MAGNETIC FIELD SCREENING BY VACUUM CHAMBER

To achieve reliable operation of the synchrotron with the required beam current it is highly desirable to reduce the ring impedances. That is normally achieved by minimizing the number of discontinuities of the vacuum chamber and making the vacuum chamber from high conductive material (aluminum, copper). Nevertheless the high conductivity of the walls results in the magnetic field screening by the vacuum chamber walls due to eddy currents. For the planned ramping frequency (f~0.5-0.3 Hz) the skin-depth in the vacuum chamber walls, δ, is much larger than the wall thickness, d, and the correction to the dipole magnetic field in the vacuum chamber center is:

$$\left.\frac{\delta B}{B}\right|_y = i\frac{a_x d}{\delta^2}F(a_x,a_y) \quad . \qquad (1)$$

For elliptic vacuum chamber with half sizes a_x and a_y and the constant thickness of the wall, $d << a_x, a_y$, the form-factor in Eq. (1) is equal to:

$$F(a_x,a_y)=\frac{4a_y}{\pi}\int_0^{\pi/2}\frac{\sqrt{a_x^4\sin\varphi+a_y^4\cos\varphi}}{\left(a_x^2\sin\varphi+a_y^2\cos\varphi\right)^{3/2}}(\cos\varphi)^2\,d\varphi \quad . \qquad (2)$$

One can see that it depends only on the ratio of the sizes, $x=a_x/a_y$. Figure 1 presents corresponding plot.

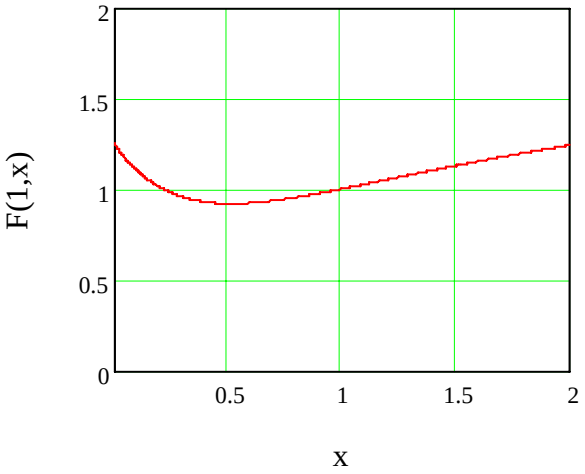

Figure 1. Dependence of Eq. (1) form-factor on the ratio of vacuum chamber sizes, $x = a_x / a_x$.

The vacuum chamber sizes are set by the machine acceptances. For the maximum of beta-function of ≈40 m and the normalized acceptances: $\varepsilon_{xn} \approx \varepsilon_{yn} \approx 100$ mm mrad one obtains typical sizes: $a_x \approx 6.2$ cm, $a_y \approx 2.5$cm (horizontal size is increased to accept of momentum particles). Those are the same dimensions as for FNAL MI. It is expected that the actual PS-2 vacuum chamber will be very similar. For stainless steel with $d = 1.3$ mm (FNAL MI) and $f = 1$ Hz one obtains $\delta B/B \approx 2\cdot10^{-4}$. Aluminum is less rigid material and should have thicker walls. For $d = 3$ mm one obtains $\delta B/B \approx 10^{-2}$ which is too large value to be accepted for a fast cycling synchrotron. The problem is exacerbated by the fact that the field is not-uniform across the aperture as shown in Figure 2.

Note that if the field correction would be constant across the aperture its value could be easily corrected by

* Work supported by Fermi Research Alliance, LLC., under contract DE-AC02-76CH03000 with the U.S. Dept. of Energy.
#val@fnal..gov

[1] Flat transverse and longitudinal distributions are achieved by painting the small emittance linac beam at injection to synchrotron.

minor adjustment of the quad currents relative to the dipole current. The uniformity of field correction can be achieved by using a vacuum chamber with specially profiled thickness so that the inner and outer boundaries are similar ellipses, $\Delta a_x / a_x \equiv \Delta a_y / a_y$. In this case the field correction is:

$$\frac{\delta B}{B} = i\frac{2a_x a_y \Delta a_x}{\delta^2 (a_x + a_y)} \quad , \tag{3}$$

and it is uniform across the aperture.

Figure 2 presents comparison of field variation along *x*-axis for the cases of equal wall thickness and similar elliptic boundaries. Such a choice, in principle, allows one to use an extruded aluminum vacuum chamber which is inexpensive to manufacture. Nevertheless to have a good uniformity of the field correction one needs to have high accuracy in the chamber profile, and uniformity of material (no cracks, etc.). Although such a choice does not look too attractive from operational point of view, because of the imbalance in the quad and dipole magnetic fields, it could significantly reduce resistive wall impedance. Note that the field correction inside quads is non–uniform with the exception of the round vacuum chamber case.

3. TRANSVERSE IMPEDANCE DUE TO WALL RESISTIVITY

For an estimate of the transverse impedance, we will use the expression describing the transverse impedance of a round vacuum chamber (see details in Ref. [2]) ($d << a$, $b = a + d$):

$$Z_\perp = -i\frac{Z_0 (2\pi R)}{2\pi a^2}\left[\frac{2e^{kd}(1+kb) - e^{-kd}(1-kb)}{e^{kd}(1+ka)(1+kb) - e^{-kd}(1-ka)(1-kb)} + \frac{1}{\beta} - 1\right], \tag{4}$$

where a and b are the inner and outer radii of the chamber, R is the ring radius, Z_0=377 Ω, $k = (1-i)/\delta$, and βc is the beam velocity. Its asymptotical behavior can be presented by the following expression:

$$Z_\perp = (2\pi R) Z_0 \begin{cases} \dfrac{c(1-i)}{2\pi a^3 \sqrt{2\pi\sigma_R \omega}} - \dfrac{i}{2\pi a^2}\left(\dfrac{1}{\beta} - 1\right) & , \quad \delta \le d \\ \dfrac{c^2}{4\pi^2 \sigma_R \omega a^3 d} - i(...) & , \quad \sqrt{ad} \ge \delta \ge d \\ \dfrac{\sigma_R \omega d}{c^2 a} - i\dfrac{1}{2\pi a^2 \beta} & , \quad \delta \ge \sqrt{ad} \end{cases} \tag{5}$$

The corresponding plot for the expected PS-2 resistive wall impedance is presented in Figure 3. One can see that at the lowest betatron sideband accounting the finite thickness of the vacuum chamber results in small correction (~20-30%) for the resistive part of the impedance and in the most of cases can be neglected. Consequently, an approximation of $\delta < d$ (top equation in Eq. (5)) can be used for the impedance calculations. The impedance of elliptical vacuum chamber with large ratio of sizes, a_x/a_y>>1, is close to the impedance of a flat vacuum chamber. In this case the resistive part of vertical impedance is $\pi^2/12 \approx 0.822$ times smaller than the resistive part of impedance for round vacuum chamber with the radius equal to the half gap [3]. The horizontal impedance is half of the vertical one.

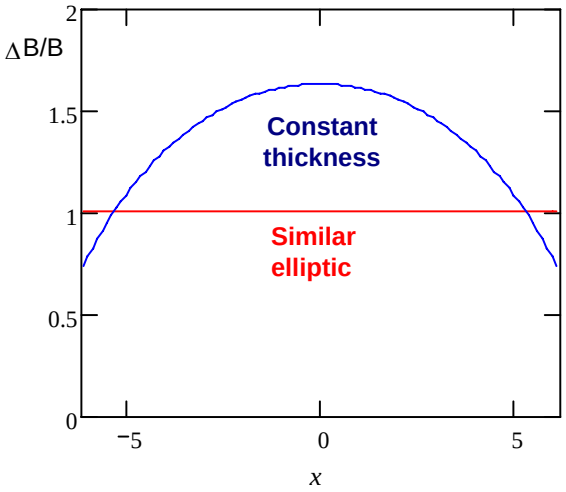

Figure 2. Dependence $\Delta B_y(x,0)$ for similar elliptic and constant width vacuum chambers, arbitrary units, $a_x \approx 6.2$ cm, $a_y \approx 2.5$cm, $\Delta a_x = d$.

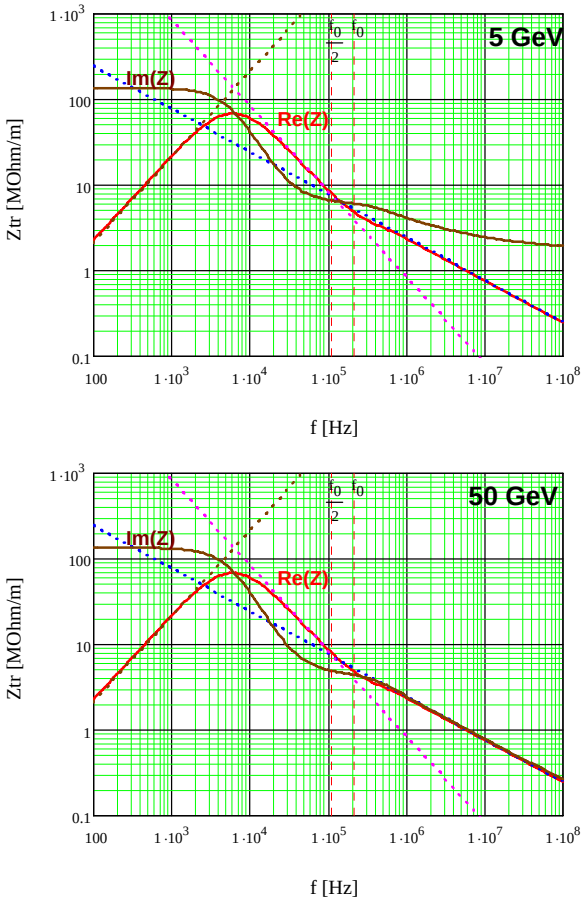

Figure 3. Transverse impedance per unit length of round stainless steel vacuum chamber, r = a = 25 mm, d=1.3 mm; top - 5 GeV, bottom - 50 GeV.

A detailed analysis carried out for Tevatron [4] showed

that in the case of stainless steel vacuum chamber the impedance is dominated by wall resistivity at frequencies below ~100 MHz. With a properly built vacuum chamber the similar relationship should be justified for the PS-2 vacuum chamber.

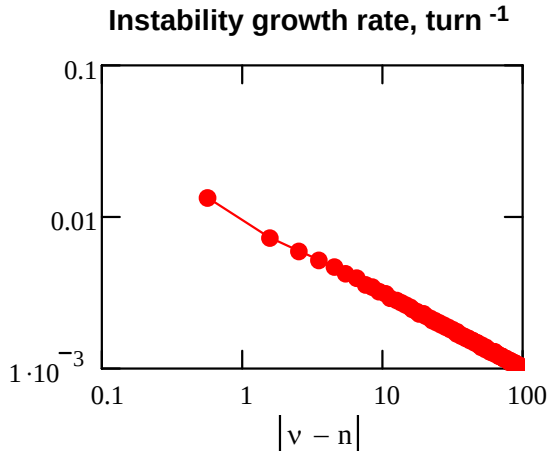

Figure 4. Instability growth rate for different transverse modes at the injection energy of PS-2.

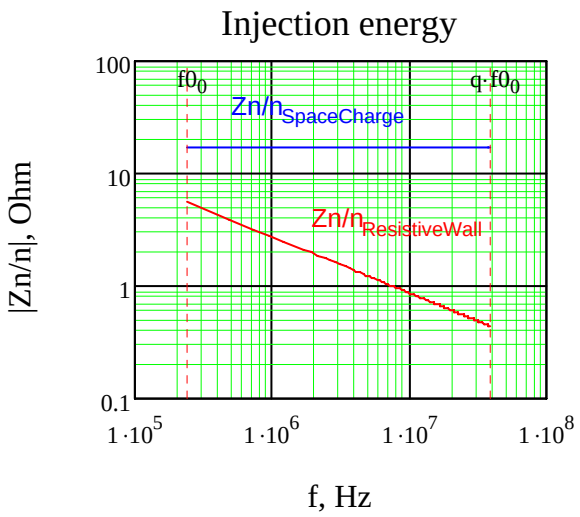

Figure 5. Dependence of the space charge and resistive wall longitudinal impedances on frequency for the PS-2 parameters and stainless steel vacuum chamber.

To estimate an effect of ring impedance on the transverse beam stability we consider the betatron tune shift due to the wall resistivity where we will be using the top equation of Eq. (5) for the impedance and the mentioned above $\pi^2/12$ correction for flat vacuum chamber. That results in:

$$\Delta\nu_{y\,n} = -\frac{1+i}{96\pi}\frac{r_p\left(I_0/e\right)(2\pi R)^{5/2}}{\gamma\beta^2\nu a_y{}^3\sqrt{\sigma_R c(n-\nu)}}\quad , \qquad (6)$$

where ν is the betatron frequency, σ_R is the conductivity of vacuum chamber walls (σ_R =1.1·10^{16} s^{-1} – for stainless steel), and I_0 is the beam current. In the case of zero chromaticity the imaginary part of the tune shift coincides with the instability growth rate. Figure 4 presents the instability growth rates computed with Eq. (6) for the PS-2. The growth rate of the lowest betatron sideband observed at the operating parameters of the FNAL MI is ~0.01 turn^{-1}. As one can see this number is close to the expected growth rates at the PS-2. FNAL uses a digital damper to control the instability. Thus, the usage of similar damper at PS-2 should address the beam stability problem. Note that because of larger ring circumference the instability growth rate at the MI for the Project-X parameters is expected to be ~0.1 turn^{-1} and presents a significant challenge. In both cases the stability at high frequencies should be achieved by using large chromaticity.

Although the use of stainless steel significantly increases the impedance, its value is still at an acceptable level. Thin well-conductive layer (copper or silver) can reduce the impedance at high frequencies but it will not change the impedance significantly at the lowest betatron sideband because its thickness is limited by the field screening discussed in Section 2.

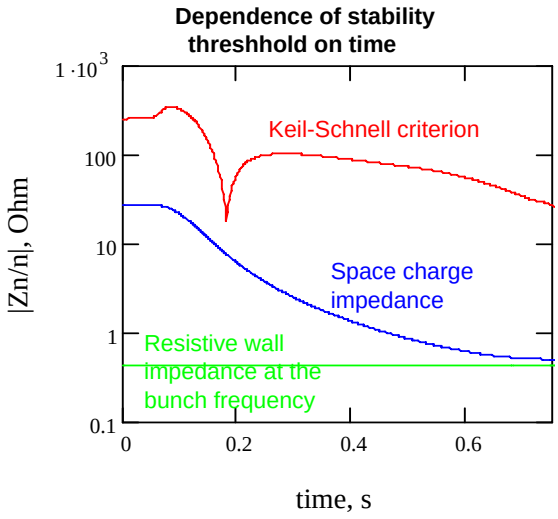

Figure 6. Dependence of the stability criteria on time within accelerator cycle for PS-2 parameters and the stainless steel vacuum chamber.

4. WIDEBAND LONGITUDINAL IMPEDANCE

At low energy and transition crossing, the longitudinal impedance is dominated by the space charge:

$$\frac{Z_n}{n} = i\frac{Z_0}{\beta\gamma^2}\ln\left(\frac{a_y}{1.06\sigma}\right)\quad . \qquad (7)$$

The wall resistivity makes the second largest contribution at small frequencies, f ≤100 MHz,

$$\frac{Z_n}{n} = (1-i)\kappa\frac{Z_0}{4\pi a_y}C\sqrt{\frac{n\omega_0}{4\pi\sigma_R}}\quad . \qquad (8)$$

where κ = 1 and κ = 0.8 for the round and flat vacuum chambers, correspondingly. Figure 5 presents dependence of these impedances on the frequency for the PS-2 parameters and stainless steel vacuum chamber. At high frequencies (f ≥ 100 MHz), similar to the transverse case,

the vacuum chamber discontinuities begin dominating the impedance

The wide band longitudinal impedance is sufficiently small and should limit the single bunch longitudinal beam stability as presented in Figure 6.

CONCLUSIONS

There is no doubt that to ensure a reliable operation of the PS-2 with beam current of ~2.5 A one needs to minimize the machine impedances. Nevertheless taking into account that for comparatively short cycle time of ~(1-3) s the eddy currents limit the vacuum chamber conductivity and thickness, and taking into account the mechanical stability of the vacuum chamber, the elliptical stainless steel vacuum chamber still looks as a reasonable choice. Covering it with thin layer of better conducting material (gold, silver or copper) would be helpful but is rather a question of choice than a necessity. To prevent the domination of bending field screening by this layer its thickness should not exceed 30-50 μm. That results in that the full gain in the impedance proportional to $\sqrt{\sigma_1/\sigma_2}$ will only be observed at high enough frequencies, ≥20 MHz. The impedance value at the revolution frequency will be rather set by the limitation on the bending field screening than by conductivity of the material.

To keep the impedance at minimum the standard practice, for reducing discontinuities of the vacuum chamber, needs to be used: good electromagnetic screening of bellows and other discontinuities of the vacuum chamber, careful design of kicker and septum magnets, *etc*.

To guaranty multibunch stability the transverse and longitudinal bunch-by-bunch dampers have to be used.

ACKNOWLEDGEMENTS

The author is grateful to N. Gelfand for careful reading of manuscript and suggestions for its improvements.

REFERENCES

[1] Accelerator Issues of Project X, Fermilab, August 2007; http://projectx.fnal.gov/AACReview/ProjectXAacReport.pdf

[2] A. Burov and V. Lebedev, "Transverse resistive wall impedance for multi-layer round chambers," EPAC-2002.

[3] A. Burov and V. Lebedev, "Transverse resistive wall impedance for multi-layer flat chambers," EPAC-2002.

[4] "Run IIA handbook", FNAL, 2001.

THE LATTICE WITH IMAGINARY γ-TRANSITION FOR THE CERN PROTON SYNCHROTRON PS2

Yu. Senichev*, Institute of Nuclear Physics, FZJ, Germany, D-52425, Juelich, Germany

Abstract

At present the new proton synchrotron PS2 with the energy range 4-50 GeV is discussed to upgrade LHC injector's complex [1]. Two lattices with and without the transition energy crossing are considered. In second option the momentum compaction factor must be kept low enough or negative. On the basis of the theory of "resonant" lattices for synchrotrons with complex transition energy developed in [2], the lattice with imaginary gamma-transition γ_{tr} for construction of PS2 lattice is proposed. Additionally the lattice should meet a number of important requirements, e.g., dispersion-free straight sections, a flexible scheme of chromaticity correction, a large enough dynamic aperture, etceteras.

INTRODUCTION

Since the longitudinal oscillation frequency is proportional to a root square of the slip factor $\eta = 1/\gamma_{tr}^2 - 1/\gamma^2$, the longitudinal stability at the transition $\gamma = \gamma_{tr}$ is lost. Therefore the acceleration through transition is considered a major problem, and the momentum compaction factor $\alpha = 1/\gamma_{tr}^2$ is one of the most important characteristics of any synchrotron. With regard to this problem, many methods have been developed for crossing the transition energy with minimum particle loss. However, in a high-intensity proton accelerator, the transition-energy crossing must be completely avoided because of the need for extremely low losses at the $10^{-3} - 10^{-4}$ level. Moreover, the slip factor should be as high as possible in order to increase the collective instability threshold. Besides the absolute value of slip factor can be used as additional factor for matching between two accelerators or/and control of beam sizes during acceleration.

To eliminate the transition energy crossing in anew designed PS2 synchrotron the gamma-transition must be moved away from acceleration range $\gamma \approx 5 \div 50$. For this purpose we use the theory of "resonant" lattices. With specially correlated modulation of quadrupoles gradient and orbit curvature and a particular choice of betatron oscillation frequencies, the theory of "resonant" lattices developed in [2] makes it possible to get interrelated dispersion variations D(s) and $1/\rho(s)$ along the equilibrium orbit and a negative momentum compaction factor

$$\alpha = \frac{1}{C}\oint^{C} \frac{D(s)}{\rho(s)} ds \le 0 \qquad (1)$$

A lattice like this should eliminate transition energy crossing by accelerated particles since the transition energy takes imaginary values $\gamma_{tr} = -i/\sqrt{|\alpha|}$. In addition, the PS2 lattice must meet a number of physical and technical requirements, such as independent tuning of the momentum compaction factor and betatron frequencies of arcs, zero dispersion in straight sections, effective chromaticity correction by the smallest possible number of quadrupole families, a large dynamic aperture. The latter implies first of all mutual compensation of the nonlinear effect of chromatic sextupoles on the motion of particles in the accelerator in the first order of the perturbation theory.

In this article we propose the imaginary γ_{tr} lattice for PS2 complying with the above conditions and discuss which lattice is optimal in view of the possible technological features of a particle accelerator.

The "resonant" lattice was first proposed for the Moscow Kaon Factory [3]. This lattice was then adapted for the TRIUMF KAON Factory (Canada) [4]. Later it was considered as the best candidate for the Superconducting Super Collider (SSC) Low Energy Booster (USA) [5], then was adopted for the main accelerator of the Neutrino Factory at CERN (Switzerland) [6], and ultimately was implemented in the JPARC (Japan Protons Accelerator Research Center), accelerator complex [2,7]. In the High Energy Storage Ring (HESR) lattice of the FAIR project, the same idea is also accepted [8].

The distinguishing features of this lattice are:

- ability to achieve the negative momentum compaction factor using the resonantly correlated curvature and gradient modulations;
- gamma transition variation in a wide region from $\gamma_t \approx \nu_x$ to $\gamma_t \approx i\nu_x$ (ν_x is the horizontal tune) with quadrupole strength variation only;
- dispersion-free straight section;
- independent optics parameters of arcs and straight sections;
- two families of focusing and one of defocusing quadrupoles;
- separated adjustment of gamma transition, horizontal and vertical tunes;
- convenient chromaticity correction method using sextupoles;
- first-order self-compensating scheme of multipoles and a large dynamic aperture;
- low sensitivity to multipole errors.

Hereinafter we will denote the horizontal tune ν_x as ν, since the vertical tune does not affect on the momentum compaction factor.

* On leave from Institute for Nuclear Research, RAS, Moscow, e-mail: y.senichev@fz-juelich.de

MAIN PROPOSITIONS OF THE "RESONANT" LATTICE THEORY

General principles of construction of "resonant" lattices detailed in [2] are based on the solution of the equation for the dispersion D(s) in the biperiodical structure.

$$\frac{d^2D}{ds^2}+[K(s)+\varepsilon\, k(s)]D=\frac{1}{\rho(s)} \qquad (2)$$

Here the gradient G(s) and the orbit curvature ρ(s) related to each other through the functions

$$K(s)=\frac{eG(s)}{p},\ \varepsilon\, k(s)=\frac{e\Delta G(s)}{p},$$

where $p=m_0\gamma v$ is the particle momentum, should be modulated resonantly and in correlation with each other.
In what follows we will use harmonics of the modulated function of gradients

$$\varepsilon\cdot k(\phi)=\sum_{k=0}^{\infty} g_k\cos\ k\phi \qquad (3)$$

where

$$g_k=\frac{e}{p}\cdot\frac{1}{\pi}\int_{-\pi}^{\pi}\Delta G\cos k\phi\, d\phi$$

is the k-th harmonic of the Fourier series of gradients function and

$$\phi=2\pi\cdot s/L_s$$

is the longitudinal coordinate normalized to the superperiod length L_s, and harmonics in the expansion of the curvature function

$$\frac{1}{\rho(\phi)}=\frac{1}{\overline{R}}\left(1+\sum_{n=1}^{\infty} r_n\cos n\phi\right) \qquad (4)$$

where

$$r_n=\frac{\overline{R}}{\pi}\int_{\pi}^{-\pi}\frac{\cos n\phi}{\rho(\phi)}d\phi$$

is the n-th harmonic of the Fourier series of the orbit curvature function and

$$\overline{R}=L_s\cdot S/2\pi$$

is the average curvature radius of the equilibrium orbit in the superperiod, S is the total number of superperiods.
Since mirror symmetry of the superperiod is one of the conditions for the construction of the "resonant" lattice, expansions of the functions $\varepsilon\, k(\phi)$ and $1/\rho(\phi)$ in the Fourier series involve only terms with cosines.
According to (1), the momentum compaction factor is the average value of the function $D(\phi)/\rho(\phi)$. In the general form, the dispersion $D(\phi)$ and the orbit curvature $\frac{1}{\rho(\phi)}$ can be represented in terms of the averages $\overline{D}$ and $\overline{R}$ and the functions $\tilde{D}(\phi),\tilde{r}(\phi)/\overline{R}$ oscillating about these averages:

$$D(\phi)=\overline{D}+\tilde{D}(\phi)\ \text{ and }\ \frac{1}{\rho(\phi)}=\frac{1}{\overline{R}}(1+\tilde{r}(\phi)).$$

Then the momentum compaction factor can be written as the sum

$$\alpha=\frac{\overline{D}}{\overline{R}}+\frac{\overline{\tilde{D}(\phi)\cdot\tilde{r}(\phi)}}{\overline{R}} \qquad (5)$$

In an ordinary regular FODO lattice without gradient and orbit curvature modulation the oscillating components are equal to zero, $\tilde{D}(\phi)=0$, $\tilde{r}(\phi)=0$, and the momentum compaction factor is governed by the first term in (5). Considering that the average dispersion in classical lattices is

$$\overline{D}=\frac{\overline{R}}{\nu^2}$$

we find that the minimum value of the momentum compaction factor

$$\alpha=\frac{\overline{D}}{\overline{R}}=\frac{1}{\nu^2}$$

is limited by the total number of horizontal betatron oscillations ν in the magnetic optical structure of length $S\cdot L_s$. In the "resonant" lattice, the functions of gradients and/or orbit curvature can be modulated jointly or individually. In [2] general expressions were obtained for the momentum compaction factor for one superperiod

$$\alpha_s=\frac{1}{\nu^2}\left\{1+\frac{1}{4}\left(\frac{\overline{R}}{\nu}\right)^4\sum_{k=-\infty}^{\infty}\frac{g_k{}^2}{(1-kS/\nu)[1-(1-kS/\nu)^2]^2}\right.$$
$$+\frac{1}{4}\sum_{k=-\infty}^{\infty}\frac{r_k^2}{1-kS/\nu}-\frac{1}{2}\left(\frac{\overline{R}}{\nu}\right)^2\sum_{k=-\infty}^{\infty}\frac{r_k g_k}{(1-kS/\nu)[1-(1-kS/\nu)^2]}$$
$$\left.-\frac{1}{2}\left(\frac{\overline{R}}{\nu}\right)^2\sum_{k=-\infty}^{\infty}\frac{r_k g_k}{[1-(1-kS/\nu)^2]}+O(g_k^i\cdot r_k^j, i+j\ge 3)\right\} \qquad (6)$$

and for the dispersion function maximum in a superperiod

$$D_{\max}=\frac{\overline{R}}{\nu^2}\,\hat{f}\cdot\left\{1-\frac{1}{2}\left(\frac{\overline{R}}{\nu}\right)^2\sum_{k=-\infty}^{\infty}\frac{g_k}{(1-kS/\nu)[1-(1-kS/\nu)^2]}\right.$$
$$\left.-\frac{1}{2}\left(\frac{\overline{R}}{\nu}\right)^2\sum_{k=-\infty}^{\infty}\frac{g_k}{[1-(1-kS/\nu)^2]}+\frac{1}{2}\sum_{k=-\infty}^{\infty}\frac{r_k}{1-kS/\nu}\right\}$$
$$+O(g_k^i\cdot r_k^j, i+j\ge 2) \qquad (7)$$

where kS is the modulation frequency of the k-th harmonic in the expansion of the gradient and curvature

functions, $\hat{f}$ is the function describing beam envelope oscillations, which is normalized to its average value. We will call the harmonic closest to ν (with the minimum possible difference $kS-\nu$) and producing the maximum effect on the momentum compaction factor the fundamental harmonic. This harmonic has kS oscillations over the entire lattice in question. In most cases under our consideration the frequency of the k-th harmonic coincides with the number of superperiods, i.e., k = 1 and $kS = S$. Indeed, if both the quadrupole gradient function and the orbit curvature function are modulated with an identical frequency (i.e., at k = n in (3) and (4)), the second term in (5) may make an appreciable contribution to the momentum compaction factor provided that the value $1-kS/\nu$ is small (see (6)).

In addition, from (6) there follows an obvious condition of antiphase modulation of the gradient and curvature function, which allows correlated variation of the momentum compaction factor with the aid of these functions. We call this lattice, based on the resonant and correlated perturbation of the magnetic optical channel parameters, the "resonant" lattice.

Thus, the following principles underlie the general approach to construction of a "resonant" lattice:

- the fundamental modulation frequency should be identical for the functions of the gradients and the orbit curvature and higher than the horizontal betatron frequency $kS > \nu$ with as minimum a difference $kS-\nu$ as possible;
- modulation of the orbit curvature should be in antiphase with modulation of the quadrupole gradients, $g_k r_k < 0$;
- amplitudes of each of the fundamental harmonics, g_k and r_k, should be as high as possible;
- exact equality of the frequencies $\nu = kS$ and $\nu = kS/2$ at which the dispersion and the β-function increase beyond limits should be eliminated.

A SUPERPERIOD OF THE "RESONANT" LATTICE

In common case there are two types of lattices used in accelerators with inserted straight sections, the so-called circular lattices with S identical superperiods and the lattice consisting of arcs with S_{arc} superperiods per each one separated by straight sections. In the former lattices the momentum compaction factor completely coincides with its value for one superperiod. In the lattices consisting of arcs with S_{arc} superperiods of length L_s and separated by straight sections of length L_{str}, the momentum compaction factor for the entire accelerator α_{total} and for a superperiod α_s are related by the equation

$$\alpha_{total} = \alpha_s \frac{S_{arc} \cdot L_s}{S_{arc} \cdot L_s + L_{str}}. \qquad (8)$$

Thus, knowing the momentum compaction factor for one superperiod, one can easily find its value for the entire accelerator.

For the proton synchrotron PS2 the racetrack lattice was adopted due to many reasons considered in [1]. On the straight sections several injection and extraction systems must be implemented [9]. Since the straight sections do not affect essentially on the momentum compaction value, just as a coefficient in expression (8), we concentrate our investigations on the arc structure for the most part. So, hereinafter we discuss the arcs structure only, assuming they can be easily matched with the designed straight sections. For the dynamic aperture calculation we take the straight section as regular FODO insertions between arcs.

The arcs are based either on the regular cell-periodical structure or on superperiods. A superperiod is usually formed by varying parameters of a regular lattice consisting of singlet FODO cells, doublet FDO cells, or triplet FDFO cells (F is the focusing quadrupole, D is the defocusing quadrupole, and O is the drift space), each having its advantages and drawbacks. However, considering the chromaticity compensation requirement, the FODO lattice is most preferable because the other two lack good separation of the horizontal and vertical β-functions, which results in a decreased efficiency of the sextupoles and accordingly in a decreased dynamic aperture. In addition, the FODO superperiod with mirror symmetry about its centre provides most favourable conditions for independent control of the betatron frequencies, chromaticity in both planes, and momentum compaction factor, which makes a lattice like this superior to any other.

The number of cells in a superperiod N_{cell} is dictated by the required phase advance of radial oscillations. Following the theory of resonant lattices, we will try to construct a lattice with the horizontal frequency ν_{arc} as close to the number of superperiods S_{arc} as possible [2]. In this case, the phase advance of horizontal oscillations per cell will be about $2\pi \frac{\nu_{arc}}{S_{arc} \cdot N_{cell}}$. At the same time it is known that from the point of view of minimization of the β-functions for a cell the phase advance of radial oscillations should fall within the range 60°–100°. Thus, in a lattice with the fundamental harmonic of the modulation of the superperiod parameters k = 1 and with $\nu_{\text{arc}} < S_{arc}$ the number of cells turns out to be 3–5 per superperiod.

Since an increase in the number of cells requires greater splitting of the superperiod and entails an increase in the number of magnetic optical elements, we exclude the five-cell option from consideration and confine ourselves to analysis of a superperiod comprising 3–4 cells.

Figures 1and 2 show the behavior of the function $\beta_{x,y}$ and D_x in a regular arc based on plain FODO cells, where each drift space accommodates a bending magnet. Taking into account the PS2 parameters [1], the magnetic rigidity

$p/e \approx 170$ $m{\cdot}T$, the cells number 22, the maximum field in magnet 1.8 T and the maximum gradient in quadrupole

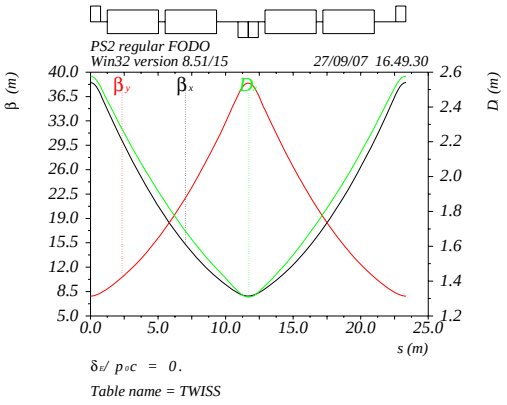

Figure 1: FODO cell

17 T/m the arc total length together with two missing magnet suppressors at edges is to be 513.5 m. Obviously, strict periodicity of cells does not make it possible to get the required value of the momentum compaction factor which is fixed by the value of the horizontal betatron frequency in this case $\gamma_{tr} \approx 10$.

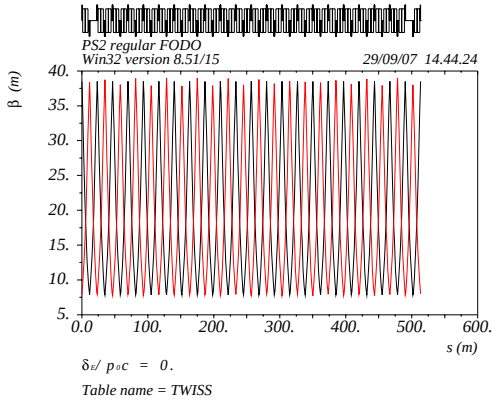

Figure 2: Arc based on FODO with dispersion suppressors located at edges of arcs

As a remark to make the gamma-transition higher than 50 the total number of FODO cells has to be increased up to 110 per arc. Therefore the only possible solution to eliminate the gamma-transition crossing is the "resonant" lattice.

Figure 3 shows a superperiod made up of three FODO cells with gradient modulation alone and mirror symmetry about the center, where two quadrupole families form the required fundamental harmonic $k = 1$. The arc is supposed to consist of 8 superperiods with the same total length of arc 513.5 m. However, to get the required gamma-transition $\gamma_{tr}=i10$ [1] this modulation method requires a great change of the field in the quadrupoles. Note that strong modulation of the gradients leads to a considerable increase in β-functions, in our case $\beta_x \sim 100$ m, and chromaticity of the entire accelerator, which results in a reduced dynamic aperture, and therefore this version of the resonant lattice is left out of consideration.

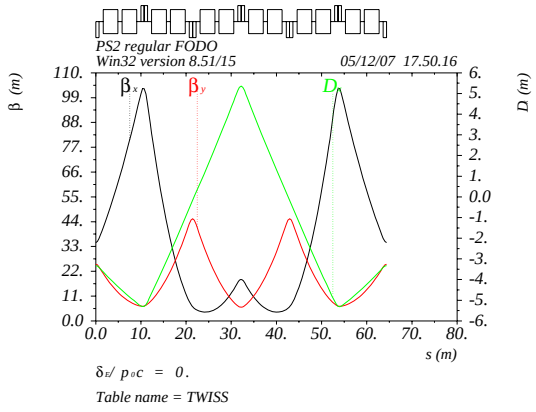

Figure 3: Superperiod with gradient modulation

Figure 4 correspond to the lattices where a superperiod is made up of three cells and the fundamental harmonic $k = 1$ is produced by modulation of the orbit curvature through using empty central cells called missing magnets (or missing magnet cells). In these curvature-varying lattices β-functions became smaller and chromaticity is kept lower. But unfortunately, the orbit curvature modulation method does not always provide the required value of gamma-transition. In our case under arc length restricted by 513.5 m it is about $\gamma_{tr} \approx 12$, which one is absolutely not enough.

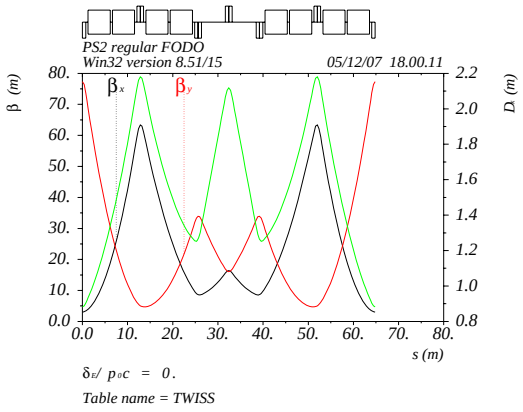

Figure 4: Superperiod with orbit curvature modulation

Thus, modulation of the orbit curvature and modulation of the quadrupole gradients can be used to get the required momentum compaction factor. The former method allows controlling the momentum compaction factor with the minimum increase in the β_x function and D_x and, compared with gradient modulation lattices, does not require strong sextupoles for chromaticity correction. However, the gradient modulation method is more flexible as it allows the momentum compaction factor of the already existing machine to be varied. In addition, it is often impossible to employ the factor $1/(kS_{arc}/\nu_{arc} - 1)$

and to increase it by making ν_{arc} approach kS_{arc}, which results in ineffectiveness of each method used separately. For example, in high-intensity accelerators one of the requirements is zero dispersion in straight sections. This means that the phase advance of radial oscillations in arcs should be a multiple of 2π and the condition $\min\{kS_{arc} - \nu_{arc}\} = 1$ should hold.

Based on the above reasoning, the "resonant" lattice method with simultaneous orbit curvature and quadrupole gradient modulation with an identical frequency of the fundamental harmonics and an approximately identical contribution of both modulations to the final value of the momentum compaction factor is most effective. From (6) it is easy to derive the following equality for an arbitrary fundamental harmonics g_k and r_k giving $\alpha \approx -1/\nu^2$:

$$\left(\frac{\overline{R}}{\nu}\right)^2 \cdot \frac{g_k}{1-\left(1-kS_{arc}/\nu_{arc}\right)^2} - r_k = \pm 2^{3/2}\left(kS_{arc}/\nu_{arc} - 1\right)^{1/2}$$

and (9)

$$|r_k| \le \left(\frac{\overline{R}}{\nu}\right)^2 \left|\frac{g_k}{1-(1-kS_{arc}/\nu_{arc})^2}\right|$$

As was already mentioned, modulation of gradients and modulation of the orbit curvature should be in antiphase and the reasonable location of the missing magnet cell is at the centre of the superperiod. This means that the amplitude of the fundamental harmonic of the orbit curvature modulation should be negative, $r_n < 0$, and therefore the amplitude of the gradient modulation will be positive. At these conditions the gamma-transition varies in a wide region from $\gamma_{tr}=\nu$ to $\gamma_{tr}=i\nu$ with quadrupole gradient modulation only. As an example of a lattice with both modulations, you can see figure 5.

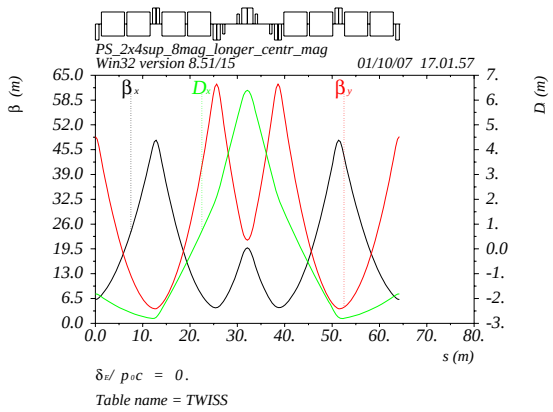

Figure 5: Superperiod of "resonant" lattice with simultaneous orbit curvature and quadrupole gradient modulation

However under the PS2 arc length restriction 513.5 m the central drift has to be shorter, and the zero momentum compaction factor can be obtained with additional modulation of gradients at a level of approximately 20% (see Fig. 6). In result the horizontal β_x-function on 10 % above in comparison with regular structure.

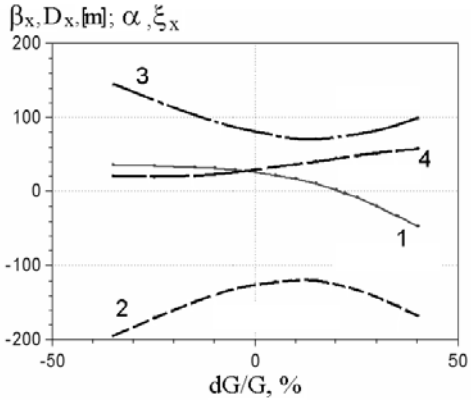

Figure 6: The α (1), ξ_x (2), β_x (3) and D_x (4) versus the gradient modulation

Figures 7 and 8 show the results yielded by various modifications of the method. In the first case (Fig. 7) the central quadrupole is "cut" in two slices and a sextupole is inserted between the slices, as was done, for example, in the JPARC project [7].

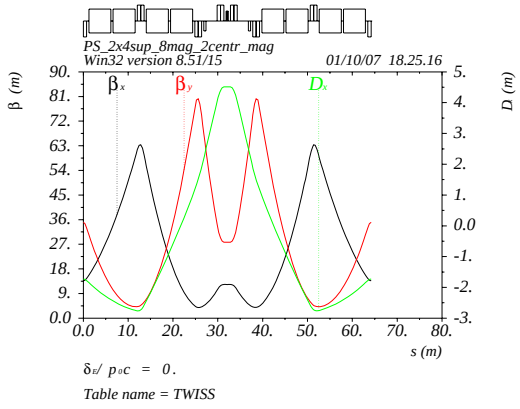

Figure 7: Superperiod with the central quadrupole sliced

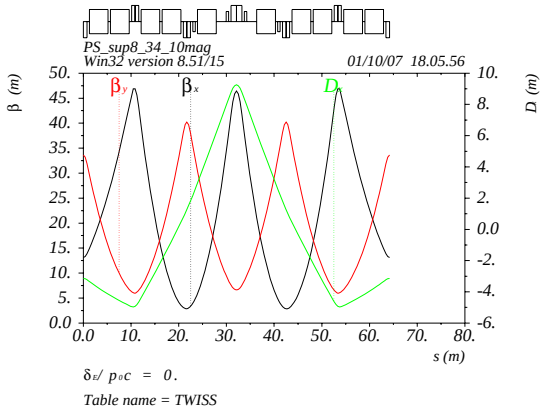

Figure 8: Superperiod with 10 magnets

On the one hand, positioning of the sextupole at a point where the horizontal β-function has a large value

increases its efficiency and thus the total number of focusing sextupoles can be reduced. On the other hand, division of a quadrupole into two halves increases their number. To our mind, this design does not give any significant advantages and is only a modification of the universally accepted resonant lattice. In the second case (Fig. 8) the orbit curvature is varied without a decrease in the total number of magnets, by varying the central cell length alone. This option may be advantageous for a magnetic optical lattice with rectangular magnets because the magnet sagitta is considerably decreased.

STRUCTURE OF ARCS

Now let us consider the magnetic optical structure of the entire accelerator, i.e., lattices of its arcs and straight sections. The straight sections will be added as the FODO insertions between arcs without details, since their structure do not affect on the momentum compaction factor and is specified and designed in [9]. Considering that physics equipment is to be installed in straight sections, let us formulate additional requirements to the resonant lattices:

- independent tuning of arcs and straight sections;
- controllable variation of the momentum compaction factor within the range $\alpha \sim 1/\nu^2$ to $-1/\nu^2$;
- ability to correct chromaticity of the entire accelerator by sextupoles located in the arcs;
- a sufficiently large dynamic aperture with allowance for all nonlinearities;
- zero dispersion in straight sections.

The first condition determines the macrostructure of the accelerator, namely, separation in functions between arcs and straight sections. Arcs fulfill bending functions and functions governing the main magnetic optical characteristics of the lattice, such as the momentum compaction factor, suppression of chromaticity, zero dispersion in straight sections, and correction of higher-order nonlinearities. Straight sections fulfill functions associated with accommodation of experimental equipment and final tuning of betatron oscillation frequencies of the entire accelerator. In addition, the optics of the arcs should be independent of the optics of the straight sections to allow more convenient work and minimum preparation for experiments. The number of arcs and straight sections is dictated by many parameters, first of all by the required architecture of the ring and the projected experiments, and for the PS2 it is two [1,9].

For the dispersion in straight sections to be zero, the arc consisting of S_{arc} superperiods should have a phase advance of radial oscillations that is a multiple of 2π, i.e., ν_{arc} should be an integer. This means that the phase advance in one superperiod should be $2\pi\nu_{arc}/S_{arc}$. On the other hand, for the momentum compaction factor to be controlled, the betatron frequency of horizontal oscillations should be smaller than the number of superperiods multiplied by the number of the fundamental harmonic. From this point of view it is reasonable to take the minimum possible difference

$$\nu_{arc} - kS_{arc} = -1 .$$

Thus, there exist many ratios between S_{arc} and ν_{arc}:

(4:3), (6:5), (8:7), (10:9), ….

Besides, there is another possibility. The arc may be divided into an equal integral number of superperiods within which the above ratios hold, for example, the ratio can be

$$S_{arc} : \nu_{arc} = 8 : 6 = 2 \text{ x } (4:3)$$

Actually, the arc is divided into two arcs in the ratio 4 : 3 without a straight section, and the zero dispersion condition is met not only at the edges but also in the middle of this double arc. As is seen, in all ratios the number of superperiods S_{arc} is taken to be even while the betatron oscillation frequency takes on integral odd values. In this case, the phase advance of the radial oscillations between the cells located in different superperiods and separated by $S_{arc}/2$ superperiods is obviously

$$2\pi \cdot \frac{\nu_{arc}}{S_{arc}} \cdot \frac{S_{arc}}{2} = 2\pi \cdot \frac{\nu_{arc}}{2} = \pi + 2\pi m ,$$

which corresponds to the condition of first-approximation compensation for the nonlinear effects of sextupoles located in these cells. This remarkable property also applies to higher multipoles in bending magnets and quadrupoles because each of them has a partner in the other quarter of the arc at a distance of odd integral π of radial oscillations (see Fig. 9).

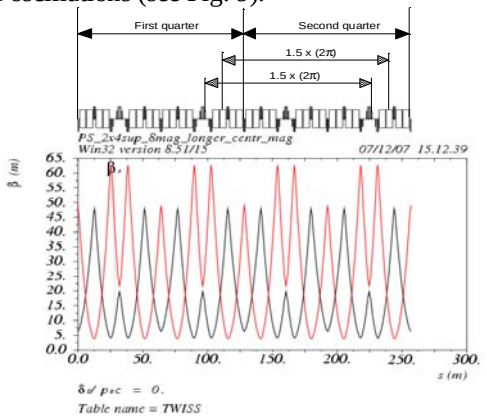

Figure 9: Half of arc with (S_{arc}:ν_{arc})=8:6

Thus, choosing S_{arc}, k, and ν_{arc}, we determine the lattice of the arc and the number of arcs. On the one hand, we are limited by strict rules for the choice of these parameters, on the other, the choice is quite wide and we may speak about a certain class of accelerators with such arcs.

By way of example, let us consider two versions of the lattice for the PS2 accelerator with an identical number of arcs and identical transition energy $\gamma_{tr} = i10$. In the first version the arc has the number of superperiods S_{arc} = 8

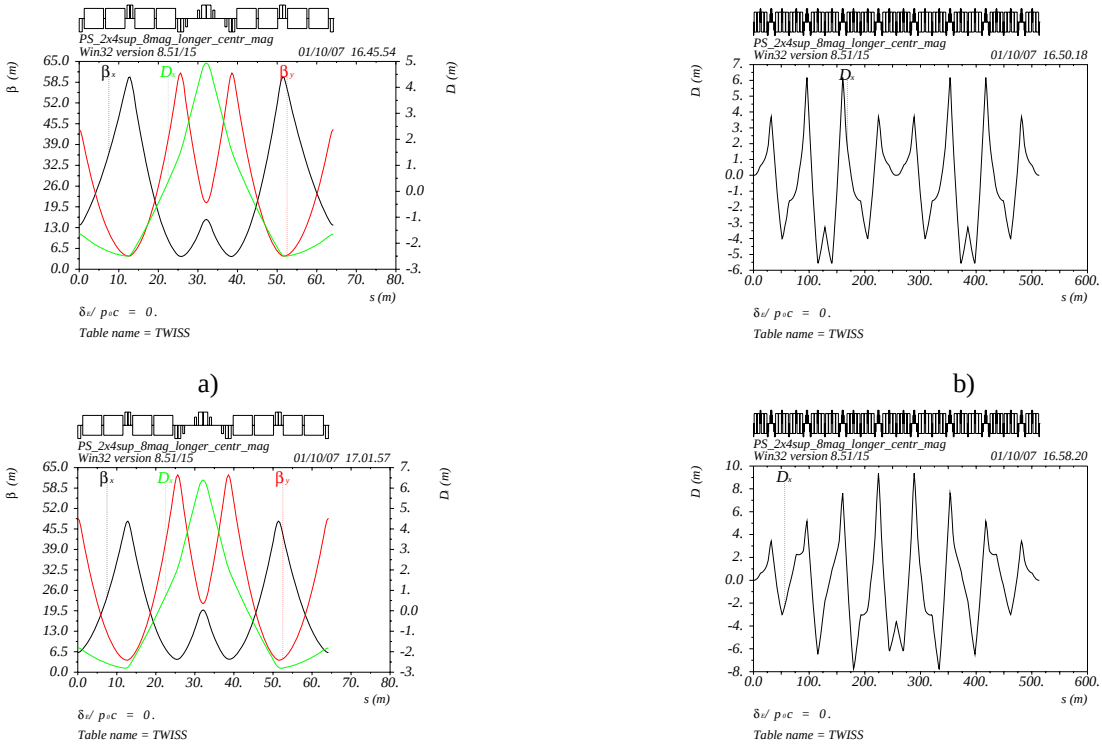

Figure 10: Dependence of the β-functions (a, c) in one superperiod and the dispersion (b, d) in the 8-superperiods arc with the horizontal tune ν_{arc}=6 (a, b) and ν_{arc}=7 (c, d) and 8 magnets per one arc.

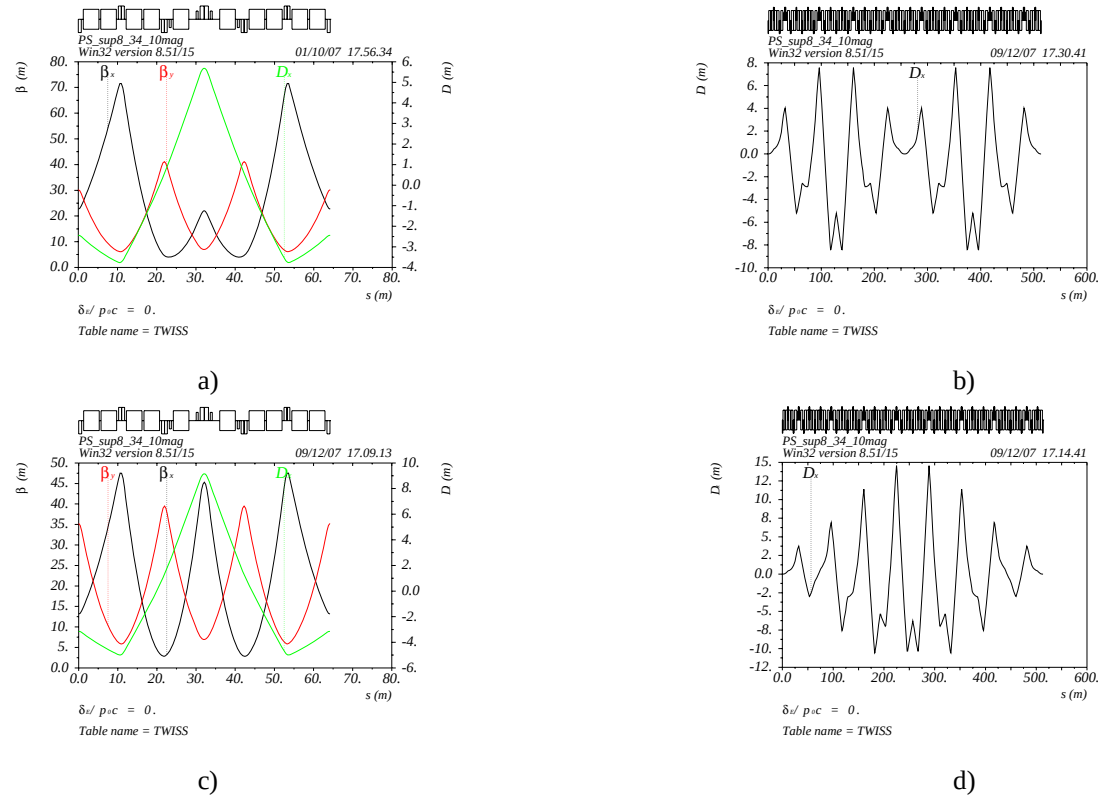

Figure 11: Dependence of the β-functions (a, c) in one superperiod and the dispersion (b, d) in the 8-superperiods arc with the horizontal tune ν_{arc}=6 (a, b) and ν_{arc}=7 (c, d) and 10 magnets per one arc.

Table 1: TWISS parameters of regular FODO lattice and "resonant" lattices with 8 superperiods per arc

Options(arc length=513.5 m)	γ_{tr}	$\beta_x$max	$\beta_y$max	$D_x$max
Regular lattice with 22 FODO cells (84 magnets per arc)	~10	39	39	3.5
Resonant lattice with ν_x=6; ν_y=6; longer central quadrupole, 8 magnets per superperiod	~i8÷10	60	61	6.2
Resonant lattice with ν_x=6; ν_y=6; two central quadrupoles; 8 magnets per superperiod	~i8÷10	62	69	6.0
Resonant lattice with ν_x=7; ν_y=6; longer central quadrupole; 8 magnets per superperiod	~i8÷10	48	62	9.4
Resonant lattice with ν_x=7; ν_y=6; two central quadrupoles; 8 magnets per superperiod	~i8÷10	49	71	9.0
Resonant lattice with ν_x=6; ν_y=6; longer central quadrupole; 10 magnets per superperiod	~i8÷10	71	41	7.9
Resonant lattice with ν_x=7; ν_y=6; longer central quadrupole; 10 magnets per superperiod	~i8÷10	47	40	14.5

Table 2: Magnito-optic elements of regular FODO lattice and "resonant" lattices with 8 superperiods on arc

One arc: length=513.5 m	N_{mag}	L_{mag}	N_{quad}	L_{quad}	N_{sext}	L_{sext}
Regular with 22 FODO cells (84 magnets per arc)	84	3.7	44	1.5	44	0.5
Resonant lattice with ν_x=6; ν_y=6; longer central quadrupole, 8 magnets per superperiod	64	4.9	48	1.5;2.3	32	0.5
Resonant lattice with ν_x=6; ν_y=6; two central quadrupoles; 8 magnets per superperiod	64	4.9	56	1.5	32	0.5
Resonant lattice with ν_x=7; ν_y=6; longer central quadrupole; 8 magnets per superperiod	64	4.9	48	1.5;2.3	32	0.5
Resonant lattice with ν_x=7; ν_y=6; two central quadrupoles; 8 magnets per superperiod	64	4.9	56	1.5	32	0.5
Resonant lattice with ν_x=6; ν_y=6; longer central quadrupole; 10 magnets per superperiod	80	3.9	48	1.5;2.3	32	0.5
Resonant lattice with ν_x=7; ν_y=6; longer central quadrupole; 10 magnets per superperiod	80	3.9	48	1.5;2.3	32	0.5

and the frequency of horizontal oscillation in the arc ν_{arc} = 6, in the second version S_{arc} = 8 and ν_{arc} = 7 (see Fig. 10). Besides, both versions have two options with 8 and 10 magnets per one superperiod (see Fig. 11). In tables 1 and 2 parameters of the considered structures are placed. In spite of all structures have identical properties, it is reasonable to take finally the structure with the minimal values of $\beta_{x,y}$ and D_x as optimum structure.

For the dispersion in the straight sections to be zero, the phase advance of radial oscillations should be a multiple of 2π and the dispersion should begin with the zero value at the entrance of the arc. Therefore, the dispersion oscillates with a double frequency: the superperiod frequency and the arc periodicity. This leads to an additional increase in the maximum dispersion in the arc. Obviously the longer arc, the bigger amplitude of second periodicity. For example, in the arc with S_{arc}: ν_{arc}=8:6 the dispersion increases from 6 m for superperiod to 8 m for arc, which is a ~30% increase, and in the arc with S_{arc}: ν_{arc}=8:7 the maximum dispersion increases from 6.5 m to 9.5 m correspondingly, which is a ~45% increase. In the latter case the arc period is longer and thus the arc periodicity causes a larger increase in dispersion. Note that in both cases the arc periodicity of the dispersion function does not lead to variation in the momentum compaction factor because integral (1) remains unchanged. The behavior of the $\beta_{x,y}$-functions also remains unchanged because the initial zero dispersion values do not affect them. Since arcs and straight sections are separated in functions, the betatron oscillation frequencies $\nu_{x,y}$ in the arcs do not change in any mode of operation and therefore quadrupoles specially inserted in the straight sections and providing the desired fraction value of the betatron frequency of the entire machine are responsible for the control of the working point position. However, in the case of retuning of the momentum compaction factor, the arc edge values of

the $\beta_{x,y}$-functions change. Therefore, special matching sections are inserted in the straight sections, which, with their four quadrupoles, allow matching of the arcs and straight sections to be retained. As a result, arcs are fully independent of straight sections and correction of the momentum compaction factor does not affect the values of the $\beta_{x,y}$-functions set for the straight section's facilities. If there are no special requirements to the behavior of the $\beta_{x,y}$-functions in the straight sections, the straight section lattice is usually mirror symmetrical about its middle, and therefore all quadrupoles of the straight sections can be directly used for matching arcs and straight sections. This considerably simplifies tuning of the entire accelerator due to minimization of the number of quadrupole families in the straight sections.

CONTROL OF MOMENTUM COMPACTION FACTOR AND ARCS TUNE

As we know in the "resonant" lattice in order to achieve the required momentum compaction factor, we modulate the quadrupole gradients on arcs correlated with a fixed orbit curvature modulation. In practice, we should know exactly which element controls the momentum compaction factor and arc tunes. Moreover, the element responsible for one function should be minimally correlated with the element responsible for another function. Due to the special features of the "resonant" lattice, this principle can be realized. From formulas (6) and (7), we can derive that at the mirror superperiod symmetry, the dispersion and the β functions are modulated by factors:

$$D(\phi) \propto \left\{1-\frac{1}{2}\left(\frac{\overline{R}}{\nu_{total}}\right)^2 \times \right.$$

$$\left. \frac{g_k \cos k\phi}{(1-kS_{arc}/\nu_{arc})[1-(1-kS_{arc}/\nu_{arc})^2]} + \frac{1}{2}\frac{r_k \cos k\phi}{1-kS_{arc}/\nu_{arc}} \right\}$$

$$\beta_{x,y} \propto \cos \mu\phi \left[1-\frac{1}{2}\left(\frac{\overline{R}}{\nu_{total}}\right)^2 g_k \frac{\cos k\phi}{1-(1-kS_{arc}/\nu_{arc})^2}\right] \quad (10)$$

On condition that ratios $kS_{arc} > \nu_{arc}$, $g_k > 0$ and $r_k < 0$ are fulfilled for the fundamental harmonic k=1, the maximum dispersion will be at the superperiod center $\phi = 0$, and the maximum horizontal β-function beginning at $\phi = -\pi$ and ending at $\phi = \pi$ on the superperiod.

Figure 12 shows the functional control of all quadrupoles. In the "resonant" lattice, the central focusing quadrupole QF2 is placed in the maximum dispersion giving it the main role in controlling the fundamental harmonic. Another focusing quadrupole QF1 is placed in the maximum β_x-function, which makes it effective at controlling the horizontal tune.

Due to FODO features, the $\beta_{x,y}$ - functions are very well separated and two defocusing quadrupoles independently affect the vertical tune. To prove independent controllability of the momentum

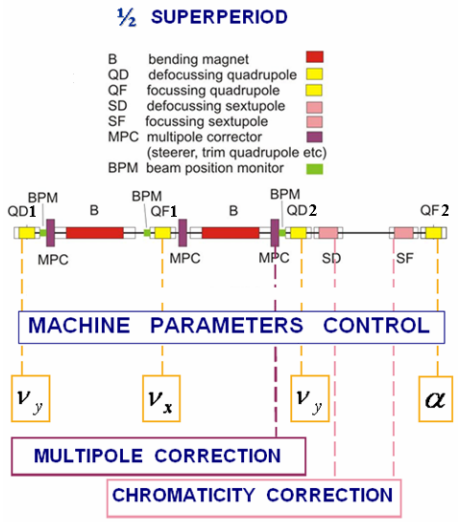

Figure 12: Functional control scheme of elements in a half superperiod

compaction factor on both horizontal and vertical arc tunes, we performed a numerical simulation of such control in the lattice with originally installed maximum possible negative $\alpha = -0.02$ ($\gamma_{tr} \approx i7$).

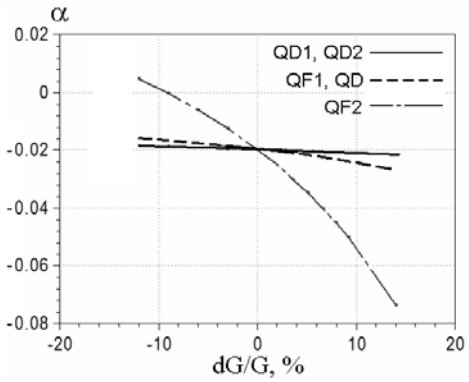

Figure 13: Momentum compaction factor vs quadrupoles gradient

Figure 13 shows how the gradient of quadrupoles QF1, QF2, QD1, QD2 and QD (QD1=QD2) changes the momentum compaction factor in the vicinity of working meaning $\alpha = -0.02$. In the case where QD1=QD2, there is one family of defocusing quadrupoles, and both quadrupoles are feed by one power source.

From these results we can see that the derivatives of momentum compaction factor with a gradient in the quadrupoles are in the relation:

$$\frac{\partial\alpha}{\partial G_{QF2}} >> \frac{\partial\alpha}{\partial G_{QF1}} \approx \frac{\partial\alpha}{\partial G_{QD1}} \approx \frac{\partial\alpha}{\partial G_{QD2}} \qquad (11)$$

Thus, the momentum compaction factor can be very flexibly controlled by the focusing quadrupole QF2 alone. Simultaneously, the QF1 gradient is expected to impact effectively on horizontal tune. Figures 14 and 15 show the numerical simulation of how each family of quadrupoles changes the horizontal and vertical tunes for one half-arc in the vicinity of working points $\nu_{arc\,x} = 2\times 3.0$ and $\nu_{arc\,y} = 2\times 3.0$.

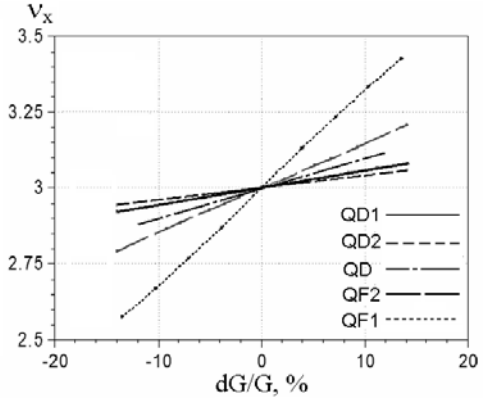

Figure 14: Horizontal tune vs quadrupoles gradient

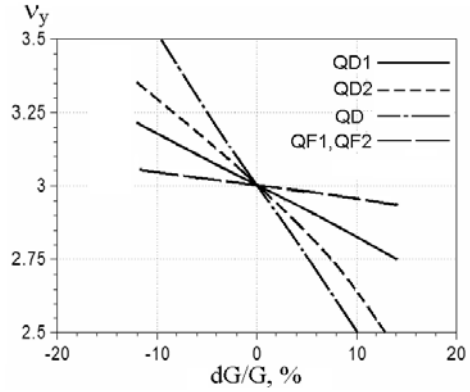

Figure 15 : Vertical tune vs quadrupoles gradient

From these results, we can see that the derivatives of horizontal and vertical tunes with a gradient in the quadrupoles are in the relation:

$$\begin{aligned} &\frac{\partial\nu_{arc\,x}}{\partial G_{QF1}} > \frac{\partial\nu_{arc\,x}}{\partial G_{QF2}} >> \frac{\partial\nu_{arc\,x}}{\partial G_{QD1}} \approx \frac{\partial\nu_{arc\,x}}{\partial G_{QD2}} \\ &\frac{\partial\nu_{arc\,y}}{\partial G_{QD1}} \approx \frac{\partial\nu_{arc\,y}}{\partial G_{QD2}} >> \frac{\partial\nu_{arc\,y}}{\partial G_{QF1}} \approx \frac{\partial\nu_{arc\,y}}{\partial G_{QF2}} \end{aligned} \qquad (12)$$

After readjusting the momentum compaction factor using the QF2 quadrupole family, the required tunes value $\nu_{arc\,x,y}$ are returned by two-three iteration steps using another quadrupole family QF1 and QD, which in turn weakly influence the momentum compaction factor.

Thus, we have separated internal arc functions:

- momentum compaction factor is controlled by central focusing quadrupole QF2,
- horizontal tune is controlled by focusing quadrupole QF1,
- vertical tune is controlled by defocusing quadrupoles QD1 and QD2 or QD.

Since derivatives $\frac{\partial\nu_{arc\,y}}{\partial G_{QD1}}$ and $\frac{\partial\nu_{arc\,y}}{\partial G_{QD2}}$ have approximately equal values, it is reasonable to use one family of defocusing quadrupoles, QD, only. This allows us to control the vertical tune more easily and more effectively, and does not influence the controllability of other parameters.

CHROMATICITY CORRECTION

The chromaticity is created by the quadrupole and defined as the variation of the betatron tune $\nu_{x,y}$ with the relative momentum deviation $Q'_{x,y} = \frac{d\nu_{x,y}}{d\delta}$, where $\delta = \frac{\Delta p}{p}$. The special optic elements, the sextupoles, are installed into the lattice to correct the chromaticity. Their integrated contribution over the whole ring circumference C on the chromaticity is:

$$\frac{\partial\nu_{x,y}}{\partial\delta} = \pm\frac{1}{4\pi}\int_0^C \beta_{x,y}(s)\cdot D(s)\cdot S(s)ds \qquad (13)$$

Obviously, to strengthen the sextupole efficiency, they have to be allocated in maximum dispersion and with different β_x and β_y values to split the chromaticity correction in the horizontal and vertical planes. With regard to the last point, the "resonant" lattice based on the singlet FODO structure is preferred above other lattices based on doublet or triplet structures. In the "resonant" lattices, the empty space of magnet-free cells is used for the sextupole location (see Fig. 12). In some projects, for instance in JPARC, the focusing sextupole is inserted into the splintered central focusing quadrupole (see Fig. 7). Two families of sextupoles, two focusing and two defocusing sextupoles, are used.

In order to prove independent controllability of chromaticity on both focusing and defocusing sextupoles, we performed a numerical simulation of such control in the lattice with initially installed zero chromaticity $\xi_{x,y} = 0$. Figures 16 and 17 show the numerical simulation results and how the focusing and defocusing sextupoles SF and SD change the horizontal and vertical chromaticity correspondingly. From these results, we can see that the derivatives of horizontal and vertical chromaticities with gradient in the sextupoles can be related as follows:

$$\left|\frac{\partial\xi_x}{\partial G_{SF}}\right| > \left|\frac{\partial\xi_x}{\partial G_{SD}}\right| \text{ and } \left|\frac{\partial\xi_y}{\partial G_{SD}}\right| > \left|\frac{\partial\xi_y}{\partial G_{SF}}\right| \qquad (14)$$

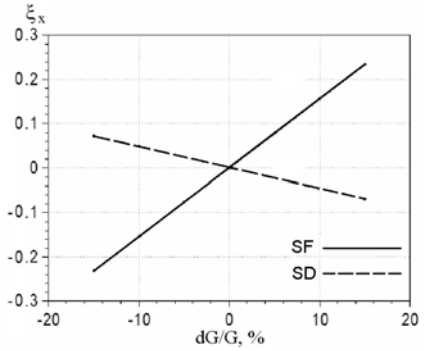

Figure 16: Horizontal chromaticity vs focusing and defocusing sextupole gradient

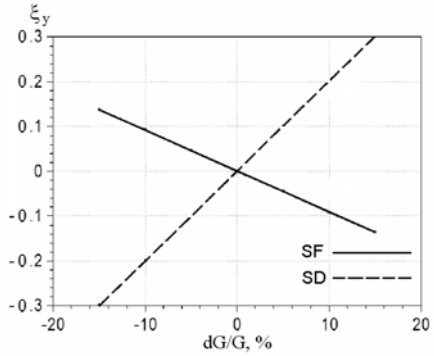

Figure 17: Vertical chromaticity vs defocusing and focusing sextupole gradient

Thus, two sextupole families can control both horizontal and vertical chromaticities independently and successfully.

COMPENSATION OF SEXTUPOLE NONLINEARITY

In the common case, the lattice has nonlinear optics. Usually, the strongest contribution to the nonlinearity is made by the chromatic sextupoles. In order to investigate the nonlinear optics, we use the Hamiltonian formalism. In the variable "action-angle", $I_{x,y}, \vartheta_{x,y}$ coordinates

$$I_x = (1+\delta)\frac{x^2}{2\beta_x(s)}\sec^2\vartheta_x, \quad I_y = (1+\delta)\frac{y^2}{2\beta_y(s)}\sec^2\vartheta_y \tag{15}$$

the Hamiltonian is presented as:

$$H(I_x,\vartheta_x,I_y,\vartheta_y) = \nu_x I_x + \nu_y I_y + \frac{1}{2}\sum_{j,k,l,m} E_{lm}^{jk}\cdot I_x^{j/2}\cdot I_y^{k/2}\exp i(l\vartheta_x + m\vartheta_y), \tag{16}$$

where the coefficients E_{lm}^{jk} depend on the value and distribution of the nonlinear elements, and they have the periodicity 2π with the new "time" coordinate $\theta = \frac{1}{R}\cdot s$:

$$E_{lm}^{jk} = \sum_p h_{jklmp}\exp ip\theta \tag{17}$$

So, the nonlinear part of Hamiltonian is:

$$V = \frac{1}{2}\sum_{j,k,l,m}\sum_{p=-\infty}^{\infty} h_{jklmp}\cdot I_x^{j/2}\cdot I_y^{k/2}\exp i(l\vartheta_x + m\vartheta_y - p\theta) \tag{18}$$

with the Fourier coefficients:

$$h_{jklmp} = \frac{1}{2\pi}\int_0^{2\pi} E_{lm}^{jk}\exp ip\theta\,. \tag{19}$$

In case two conditions are fulfilled, namely the harmonic value $h_{jklmp}\neq 0$ for some of the nonlinear elements M_{j+k}, and $k_x\nu_x + k_y\nu_y = p$, where $k_x = l$ and $k_y = m$, we have nonlinear resonance, and on the contrary, when we wish to exclude the resonance influence, we should minimize the harmonic amplitude h_{jklmp}. The only condition, which cancels all coefficients E_{lm}^{jk} is the zero value of $h_{jklmp}=0$ for all j,k,l,m. In particular, where the chromaticity correction on arcs with S_{arc} superperiods is performed, the sextupoles must be placed with the phase advances μ_x, μ_y per superperiod, when the harmonic is $h_{jklmp}=0$ for all above-mentioned combinations of j,l,k,m in (19), and the total multipole of the third order is canceled:

$$M_3^{total} = \sum_{n=0}^{N} S_{x,y}\beta_x^{l/2}\beta_y^{m/2}\exp in(l\mu_x + m\mu_y) = 0\,, \tag{20}$$

where $S_{x,y}$ are the sextupoles gradient. In the "resonant" lattice, the superperiod number S_{arc} is even and the arc tune ν_{arc} is odd, then the phase advance between similar sextupoles of $n-th$ and $\left(n+\frac{S_{arc}}{2}\right)-th$ superperiods equals $l\cdot\mu_x\cdot\frac{S_{arc}}{2} = l\cdot\frac{2\pi\nu_x}{S_{arc}}\cdot\frac{S_{arc}}{2} = \pi\nu_x l$ (see Fig. 9). In the first order of the perturbation theory, the sextupole excites four resonances $\{l,m\}=\{1,0;3,0;1,\pm2\}$. Taking into account that sextupole takes the odd integer l, we have the conditions required to compensate for each sextupole's nonlinear action with another one.

The same can be inferred for the sextupole components in the magnets, since each magnet has its twin located

on $\pi\nu_x l$ phase advance, where the nonlinear kick is compensated.

In case of essential chromaticity contribution from the straight section a method of the second order non-linearity compensation has to be foreseen as well. Solving the nonlinear equation and deriving the Hamiltonian (16) in the first order of the perturbation theory, the value h_{jklmp} is taken as the small parameter, and all non-resonant terms are omitted. Thus, in the first order of the perturbation theory, the sextupoles can be canceled. However, in the second order, the nonlinear perturbation already contains the higher order of h_{jklmp}, which gives nonlinear tune shifts, such as octupoles [10]. In principle, the sextupole nonlinear tune cannot be controlled after the sextupole location has been fixed. Therefore, the sign of total chromaticity is controlled by the octupoles, which are located in the multi-pole correctors. Thus, after chromaticity correction, the nonlinear tune shift is measured and then using the correcting octupole, we adjust the required sign and value of the nonlinear tune shift, as described in [10].

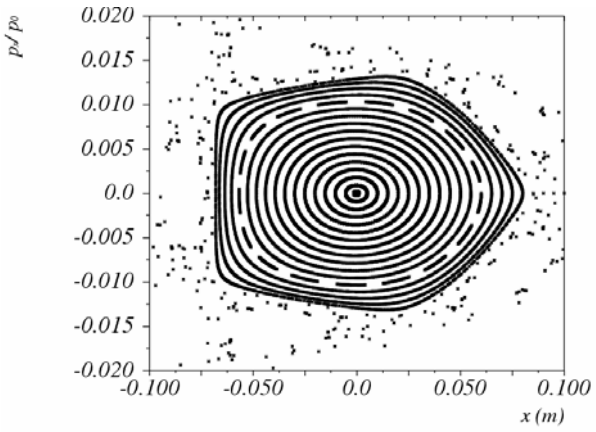

Figure 18: PS2 dynamic aperture after chromaticity correction at Δp/p=1%

After all corrections have been made, we have done the tracking for the maximum momentum spread beam $\Delta p / p = 1\%$. Figure 18 shows the results of dynamic aperture calculations after chromaticity correction. For horizontal plane it is ~600 *mm·mrad* and for vertical plane it has approximately the same meaning ~500 *mm·mrad*.

CONCLUSION

The PS2 imaginary gamma-transition lattice was developed with features:

- ability to achieve the negative momentum compaction factor using the resonantly correlated curvature and gradient modulations;
- gamma transition variation in a wide region from $\gamma_{tr}=\nu_x$ to $\gamma_{tr}=i\nu_x$ with quadrupole strength variation only;
- integer odd 2π phase advance per arc with even number of superperiod and dispersion-free straight section;
- independent optics parameters of arcs and straight sections;
- two families of focusing and one of defocusing quadrupoles;
- separated adjustment of gamma transition, horizontal and vertical tunes;
- convenient chromaticity correction method using sextupoles;
- first-order self-compensating scheme of multipoles and as consequence low sensitivity to multipole errors and a large dynamic aperture

ACKNOWLEDGMENTS

Author is grateful to M. Benedict and E. Shaposhnikova for scientific discussion of specific problems and parameters of the proton synchrotron PS2.

REFERENCES

[1] W. Bartmann, M. Benedikt, C. Carli, B. Goddard, S. Hancock, J.M. Jowett, Y.Papaphilippou, Optics Considerations for the PS2, Proceedings of Particle Accelerator Conference 2007, Albuquerque, p.739, http://accelconf.web.cern.ch/accelconf/p07/PAPERS/TUODKI02.PDF;
W. Bartmann, M. Benedikt, C. Carli, B. Goddard, S. Hancock, J.M. Jowett, A. Koschik, Y. Papaphilippou,http://indico.cern.ch/getFile.py/access?contribId=66&sessionId=16&resId=2&materialId=slides&confId=20082

[2] Yu.Senichev, A «resonant» lattice for a synchrotron with a low or negative momentum compaction factor, submitted in Particle Accelerator, KEK Preprint 97 40, 1997, 27 pages, http://doc.cern.ch/tmp/convert_SCAN-9711073.pdf

[3] N. Golubeva, A. Iliev, Yu. Senichev, The new lattices for the booster of Moscow Kaon Factory, Proceedings of International Seminar on Intermediate Energy Physics, Moscow 1989, vol. 2, p. 290, INR, Moscow, November 1989

[4] U. Wienands, R. Servranckx, N. Golubeva, A. Iliev, Yu. Senichev. A racetrack lattice for the TRIUMF Kaon Factory Booster, Proceedings of the 15-th International Conference on High Energy Accelerators, Hamburg, 1992

[5] E. Courant et al., Low Momentum Compaction Lattice Study for the SSC Low Energy Booster, Proceeding IEEE Particle Accelerator Conference, San Francisco, CA,1991, http://accelconf.web.cern.ch/accelconf/p91/PDF/PAC1991_2829.PDF

[6] H. Schönauer, B. Autin, R. Cappi, J. Gareyte, R. Garoby, M. Giovannozzi, H. Haseroth, M. Martini, E. Métral, W. Pirkl,C.R. Prior, G.H. Rees, RAL, Chilton, Didcot, I. Hofmann, Yu. Senichev, A slow-cycling proton driver for a Neutrino Factory, Proceedings of EPAC, Vienna, 2000, http://accelconf.web.cern.ch/AccelConf/e00/PAPERS/THP2A09.pdf

[7] Y. Ischi, S. Machida, Y. Mori_, S. Shibuya, Lattice design of JHF synchrotrons, Proceedings of APAC, Tsukuba, 1998, http://hadron.kek.jp/jhf/apac98/5D002.pdf

[8] Yu. Senichev, S. An, K. Bongardt, R. Eichhorn, A. Lehrach, R. Maier, S. Martin, D. Prasuhn, H. Stockhorst, R. Toelle, Lattice Design Study for HESR, Proceedings of EPAC, Lucerne, 2004, p.653, http://accelconf.web.cern.ch/accelconf/e04/PAPERS/MOPLT047.PDF

[9] W. Bartmann, M. Benedict, B. Goddard, T. Kramer, A. Koschik, PS2 injection, extraction and beam transfer concepts, Proceedings of PAC 2007, Albuquerque, p.1598, http://accelconf.web.cern.ch/accelconf/p07/PAPERS/TUPAN094.PDF

[10] A. Chechenin, E. Senicheva, R. Maier, Yu. Senichev, The high order non-linear beam dynamics in High Energy Storage Ring of FAIR, Proceedings of EPAC, Edinburg 2006, pp.2083-2085 http://accelconf.web.cern.ch/accelconf/e06/PAPERS/WEPCH072.PDF

SPS CHALLENGES

E. Shaposhnikova, CERN, Geneva, Switzerland

Abstract

In future the SPS should be able to transfer to the LHC the beam produced by a completely new pre-injector chain and required by the LHC for different upgrade scenarios. The issues related to this extremely challenging task are presented together with some possible ways of overcoming the problems that arise. Besides an increase in injection energy provided by PS2, these measures can include both an SPS vacuum chamber upgrade against the e-cloud and operation with larger longitudinal emittance for beam stability. As a result the power plant of the SPS RF system must be doubled. The SPS upgrade will also need the improvement or replacement of many other machine elements.

MOTIVATION

The SPS is challenged by two main LHC upgrade scenarios which are presently under consideration [1]. One of them is based on the ultimate LHC beam having bunches with intensity of 1.7×10^{11} spaced at 25 ns. Difficulties expected in producing this beam are discussed in [2]. Another scenario, which seems to be more acceptable for the LHC experiments, requires bunches spaced by 50 ns with 5×10^{11}/bunch.

At the same time, possibilities which could be offered by a completely new SPS injector chain (Linac4-SPL-PS2) are even more challenging for the SPS [3], [4]. Indeed, for the LHC beam 168 bunches spaced by 25 ns with 4×10^{11}/bunch could be injected at 50 GeV/c at 2.4 s intervals. For the FT/CNGS beam - a total intensity of 10^{14} per injection could also become available (full SPS ring).

At the moment the SPS is able to deliver at top energy the nominal LHC beam (1.2×10^{11} p/bunch) with the required transverse and longitudinal emittances. The maximum intensity in the SPS has been obtained for the CNGS type beam in 2004 [5]. A single bunch with 1.8×10^{11} (ultimate LHC intensity) was seen in the SPS at 26 GeV/c in 2006.

The present achievements and future needs in the SPS are summarised in Table 1. It is clear that the SPS upgrade is also required to provide the beam necessary for the LHC upgrade and as well as to make optimum use of the possibilities offered by the new injectors both for the LHC and for other users (FT, CNGS...). Initial studies, done in the framework of PAF [3], were continued in 2007 in the specially created inter-departmental Study Team, PAF-SPSU, [6].

In this paper the problems related to the LHC beam with 5.5×10^{11}/bunch and 50 ns spacing, the most demanding for the SPS, will be analysed, assuming that the way to produce this beam has been found in the PS2 [7].

	SPS record at 450 GeV	LHC request at 450 GeV	PS2 offer at 50 GeV/c
$N_b/10^{11}$	1.2	1.7/5.5	$3.6/7.2^{**}$
$N_{tot}/10^{13}$	3.5(5.3*)	9.2	12.0
I_{RF} [A]	1.5	3.5	4.6

Table 1: Maximum intensities achieved in the SPS up to now and future requests. 10% beam loss assumed for PS-SPS and SPS-LHC beam transfer. * CNGS beam at 400 GeV with 5 ns spacing and full ring. ** Intensity for 25/50 ns bunch spacing.

MAIN INTENSITY LIMITATIONS

The main intensity limitations for a single bunch are space charge and TMCI. The e-cloud, generated by the presence of many bunches in the ring, is at the origin of the single bunch vertical instability. Other multi-bunch limitations in the list are coupled bunch instabilities, beam losses, beam loading in the TW 200 MHz and 800 MHz RF systems as well as heating of different machine elements (e.g. MKE kickers). For future high intensity beams the measures to overcome these limitations include:

- Higher injection energy with PS2: 50 GeV/c instead of 26 GeV/c, see [8].
- New campaign for impedance reduction after its identification [9].
- Active damping of coupled bunch instabilities will need a beam control upgrade (transverse and longitudinal feedbacks) [10].
- Passive (Landau) damping from increased nonlinearity (synchrotron frequency spread) with

  - the 4th harmonic RF system (800 MHz) and

  - increased longitudinal emittance .

As we will see below, an increased longitudinal emittance is one of the most efficient and appropriate cures. It is already used now and can be more extensively applied in the future.

Single bunch

The tolerable limit for the space-charge tune spread in the SPS from past experience (ppbar) is believed to be $\Delta Q_{sc} < 0.07$. For the LHC bunch at 26 GeV/c ΔQ_{sc} is 0.05 for the nominal intensity and 0.07 for the ultimate intensity [11]. The bunch intensity for the upgrade scenario will increase this value to 0.23. One can expect

the improvement ($\propto 1/\gamma^2$) from the higher injection energy, see Fig. 1, to be sufficient to counteract this. Indeed for the planned increase of injection energy to 50 GeV/s, $\Delta Q_{sc} = 0.06$, so that the tune shift is almost back to its present value.

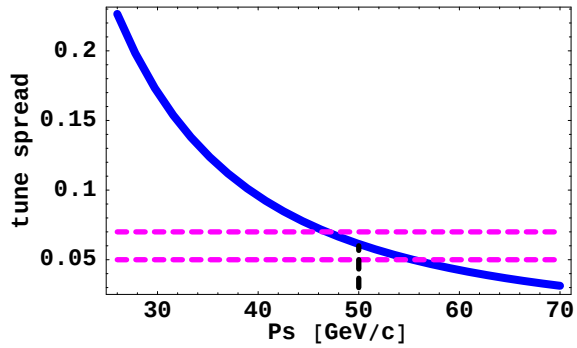

Figure 1: The value of ΔQ_{sc} for 5.5×10^{11}/bunch as a function of the SPS injection momentum.

Another possible bunch intensity limitation is the TMCI, transverse mode coupling instability, observed in the SPS with longitudinal emittance smaller than nominal [12], [13]. With an impedance model obtained from a best fit to measurements for the LHC bunch at 26 GeV/c (2006) the threshold intensity is $N_{th} \sim 1.4 \times 10^{11}$ [8]. For the matched voltage the threshold intensity scales as

$$N_{th} \propto |\eta|\varepsilon.$$

At 50 GeV/c the TMCI threshold will already be higher than at 26 GeV/c by a factor 2.5, see Fig. 2. Therefore the stability of a bunch with intensity of 5.5×10^{11} can be provided by an increase of emittance to 0.6 eVs. Other possible cures for this instability are increased vertical chromaticity and capture voltage (also needed for larger emittance).

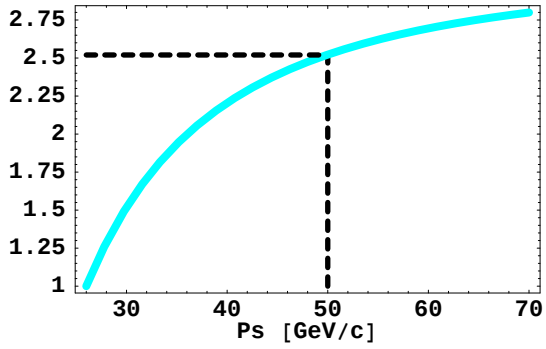

Figure 2: Relative change in the TMCI threshold as a function of the SPS injection momentum.

e-cloud

At the moment the effects connected with e-cloud give the main intensity limitation in the SPS for the nominal LHC beam. It leads to transverse emittance blow-up and instabilities - coupled bunch in the horizontal plane (seen at a few MHz) and single bunch in the vertical plane in the batch tail ($\sim$ 700 MHz). Present cures include an annual scrubbing run at the end of each SPS shutdown, operation with high chromaticity in the vertical plane and use of the transverse damper in the horizontal plane. Studies done with 1.1×10^{11} p/bunch for the coupled-bunch instability in H-plane at different energies [2] suggest that the instability growth rate scales as $\sim 1/\gamma$ and improvement can be expected at a higher injection energy.

On the other hand, in the vertical plane, simulations predict a threshold reduction with energy [14]. The results of the intensive MD studies in 2007 of the vertical e-cloud instability at different SPS energies are presented in [15].

Possible SPS chamber modifications as measures against e-cloud effects are now under extensive investigation by the SPSU Study Team [6]. They include

(1) TiN, graphite or other surface coatings [16],

(2) cleaning electrodes [17],

(3) grooves (in collaboration with SLAC, [18]).

The solution should satisfy the following main requirements: the possibility of application onto the existing vacuum pipe inside the magnets, stability over long-term, resistance to venting in the absence of baking, low beam-coupling impedance and no significant aperture reduction (< 1 mm). It is planned to install three different samples in the SPS e-cloud measurement set-up (M. Jimenez, K. Cornelis et al.) during the 2007/2008 machine shutdown for beam tests in 2008.

Some improvement should be also expected for the 50 ns bunch spacing as is the expected case for the LHC itself [19]. This can be confirmed by HEADTAIL simulations.

Longitudinal coupled bunch instabilities

The longitudinal coupled-bunch instability of the LHC beam in the SPS is characterised by a very low intensity threshold [20]. A single LHC batch with 2×10^{10} per bunch becomes unstable during acceleration at $\sim$ 280 GeV/c. Possible impedance sources of this instability are the fundamental and HOMs (at 629, 912 MHz...) of the 200 MHz and 800 MHz RF systems. To stabilise the beam controlled emittance blow-up is performed twice during the cycle, in addition to the use of the 800 MHz RF system as a Landau cavity in bunch-shortening mode throughout the cycle. The first blow-up is with mismatched voltage at injection; due to filamentation the initial emittance of 0.35 eVs is increased to 0.42 eVs. The second takes place at around 200 GeV/c, with band-limited noise which blows up the emittance to 0.6 eVs.

At injection the coupled-bunch instability is observed at $\sim 1.1 \times 10^{11}$/bunch (with 800 MHz off). No significant

change in threshold due to injection at 50 GeV/c is expected. Taking into account that the instability threshold scales as [21]

$$N_{th} \propto \varepsilon^2,$$

an emittance of 0.6 eVs will be required at injection for stability of a beam of 5.5×10^{11} per bunch and 50 ns bunch spacing.

Later in the cycle (above 250 GeV) controlled emittance blow-up to at least 0.9 eVs will be needed to stabilise the "50 ns scenario" beam. This in turn will require an upgrade of the SPS RF system as demonstrated in the next section.

SPS ACCELERATION CYCLE WITH PS2

To analyse the voltage and power requirements for high intensity beams injected at 50 GeV/c from future PS2 we need to have the corresponding magnetic cycle. An example of an acceleration cycle (synchronous momentum and its derivative) designed for this purpose is shown in Fig. 3. It is based on the present magnetic cycle for the LHC beam in the SPS and differs from it only below 150 GeV/c.

To avoid (or minimise) beam loss during acceleration the voltage programmes used in operation in the SPS usually provide a bucket area $A \simeq 1.4\,\varepsilon$. Therefore for $\varepsilon_{inj} = 0.6$ eVs at the beginning of the ramp we need $A = 0.85$ eVs (or 0.75 eVs with a filling factor in area of 0.9 and in momentum of 0.95). The voltage programmes for the 200 MHz RF system, corresponding to the magnetic cycle shown in Fig. 3, and found for longitudinal emittances of 1.0, 0.75 and 0.5 eVs are presented in Fig. 4 (top). The voltage for the smallest emittance value reflects the present situation with the LHC beam in the SPS and is shown for comparison. Due to the required controlled emittance increase to 1 eVs during acceleration, two voltage programmes are presented - for injected and extracted emittance values with transition between them (emittance blow-up) somewhere around 200 GeV/c. As one can see, for large emittances the maximum required voltage is close to the value at flat bottom and can only slightly be reduced by slowing down the acceleration ramp.

The matched voltage at injection as a function of injection momentum at constant longitudinal emittance is shown in Fig. 5. The required voltage is proportional to $|\eta|/\gamma$. As one can see the matched capture voltage is higher for injection above 26 GeV/c. For injection at 50 GeV/c with the available $V_{max} = 7.5$ MV at 200 MHz the injected emittance ε_{inj} should not exceed 0.8 eVs ($V_{inj} \propto \varepsilon_{inj}^2$). Even only lower ε_{inj} would be allowed for injection in the range (30-50) GeV/c. From this point of view the PS2 energy should not be much below 50 GeV.

If the voltage presently available is sufficient to accelerate high intensity beams with large longitudinal emittances, the RF power required for beam loading compensation is significantly higher than actually possible [22]. The power per 200 MHz TW cavity for $V = 7.5$ MV is shown in Fig. 6 together with the present limitations for pulsing

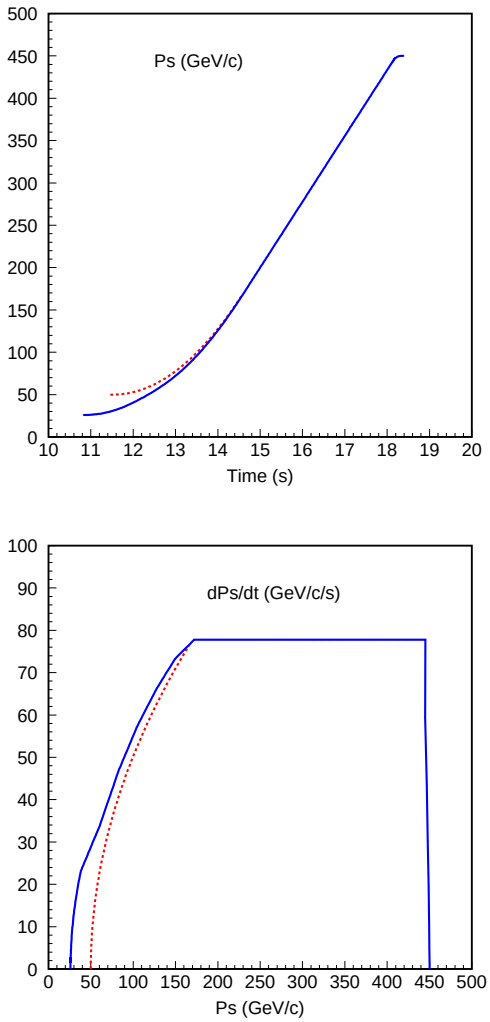

Figure 3: Synchronous momentum (top) and its derivative (bottom) for the LHC cycle now used operationally in the SPS (blue curve) and the cycle possible with the PS2 (red curve).

mode (LHC beam - half ring filled) and continuous operation (FT/CNGS beam - practically the whole ring is filled), for two values of beam current corresponding to the LHC upgrade scenario (top figure) and the maximum intensity available from PS2 (bottom figure). The effect of reducing the cavity length (number of sections) is also illustrated.

Following from this comparison of the power needed for future beams with the existing possibilities, it is clear that the 200 MHz and 800 MHz power plant should be doubled and R&D for the re-design of couplers and coaxial lines should start as soon as possible. Some reduction in required power can be achieved by optimisation of the cavity length ($5 \rightarrow 3$ sections) for high intensity operation [23], see Fig. 6.

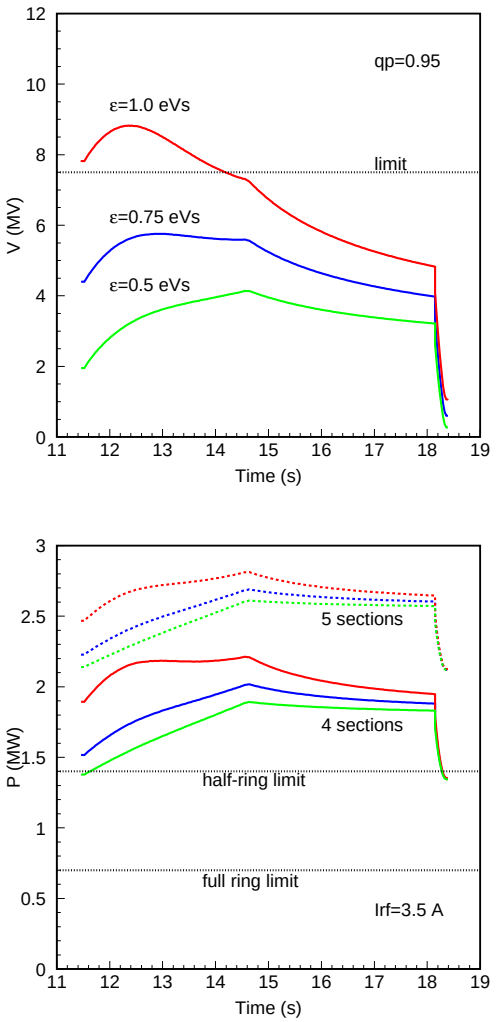

Figure 4: Top: voltage programme for the magnetic cycle from Fig. 3 for different values of longitudinal emittance together with present limit of 7.5 MV (dashed line). Bottom: corresponding power requirements for the SPS 200 MHz TW cavity with different number of sections for beam intensity for the LHC upgrade scenario with "50 ns spacing" together with actual power limitations.

Future CNGS/FT beam The voltage and power requirements for the LHC beam in the future can be compared with estimations [24] done for the future CNGS/FT beam and based on the possibilities offered by the new SPS injector - PS2 [4]. The maximum 200 MHz voltage required for accelerating a beam with an emittance of 0.7 eVs with acceleration times 3.0 s and 4.2 s (corresponding to an SPS cycle length of 4.8 s and 6.0 s) is shown in Table 2for filling the SPS from the existing PS injector and the future PS2.

The corresponding peak power per cavity needed for the total CNGS beam intensity of 4.8×10^{13} (nominal value), 7×10^{13} and 1×10^{14} (maximum available from PS2) is

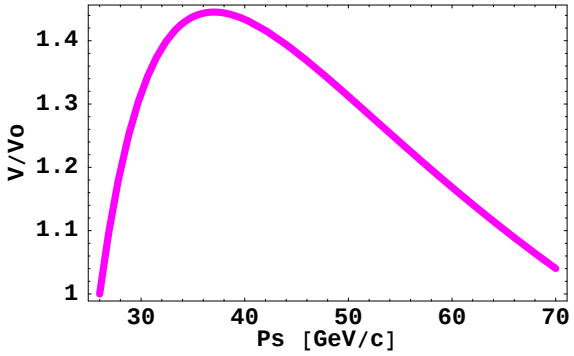

Figure 5: Matched capture voltage (normalised to the value at 26 GeV/c) required for $\varepsilon = const$ as a function of the injection momentum.

	SPS= 11 PS	SPS $\simeq$ 5 PS2	
t_{acc}	3.0 s	3.0 s	4.2 s
t_{cycle}	6.0 s	4.8 s	6.0 s
V_{max}	7.6 MV	10.5 MV	7.0 MV

Table 2: The 200 MHz voltage [MV] needed for accelerating the FT/CNGS beam in the SPS now and in the future with two different values of acceleration time - 3.0 and 4.2 s and an emittance of 0.7 eVs.

shown in Table 3 for two different SPS cycle lengths and different filling schemes.

	RF power [MW]		
N	SPS= 11 PS	SPS $\simeq$ 5 PS2	
[10^{13}]	$t_{acc} = 3.0$ s	3.0 s	4.2 s
4.8	0.65	0.75	0.5
7.0	0.85	1.0	0.7
10.0		1.4	1.1

Table 3: Peak RF power [MW] required per 200 MHz TW cavity to accelerate the nominal CNGS beam and the future FT/CNGS beam with different intensities and acceleration times.

As one can see, twice the RF power and 40% more voltage than available now are necessary for a short ($t_{acc} = 3.0$ s) acceleration cycle of 4.8 s. However in order to provide the same number of pot/year 25% more beam intensity should be accelerated in the SPS with the long cycle of 6 s ($t_{acc} = 4.2$ s). We can conclude that these RF requirements are also not very different from the needs for the LHC "50 ns spacing" upgrade scenario beam.

BEAM LOSS

In 2003 an LHC beam with nominal intensity and longitudinal parameters was accelerated in the SPS to top energy [20]. However this could be achieved only by inject-

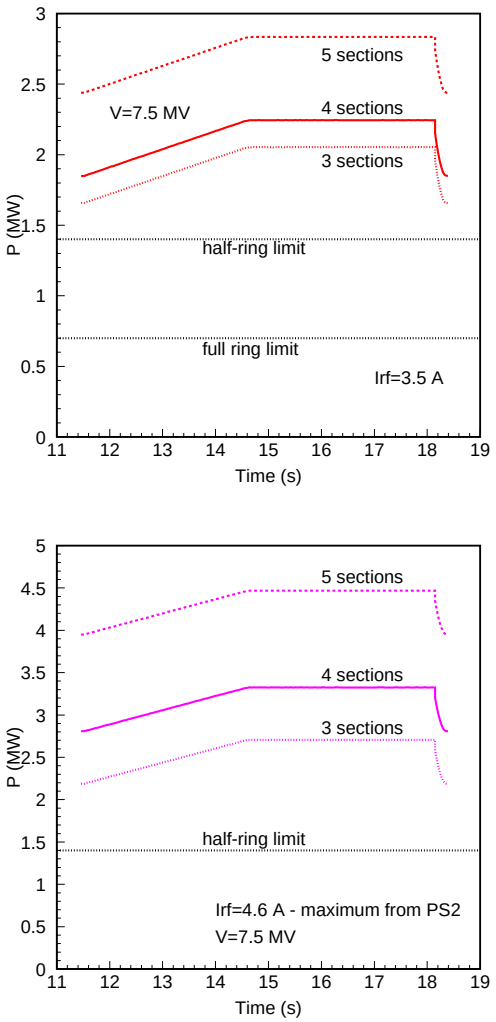

Figure 6: Power per SPS 200 MHz TW cavity having 3, 4 or 5 sections with $V = 7.5$ MV for LHC upgrade intensity from "50 ns spacing" scenario (top) and maximum PS2 intensity (bottom). The actual power limit in pulsing mode is believed to be 1.4 MW and for continuous operation 700 kW [22].

ing 15% more particles due to significant beam loss. After intensive MD studies, a reduction of losses to 7% was obtained at the end of 2004 with a new working point and additional RF gymnastics on the flat bottom [2], [26]. In general the injection and capture losses of the LHC beam in the SPS have a strong dependence on the batch intensity, Fig. 7. A reduction in relative loss to 3% was measured for a beam with 75 ns bunch spacing and nominal bunch intensity. Beam loss at high energies was also the main limitation for the intensity increase during the "record" CNGS run in 2004 [5].

Indeed, usually the relative beam loss increases with intensity due to different collective effects (space charge,

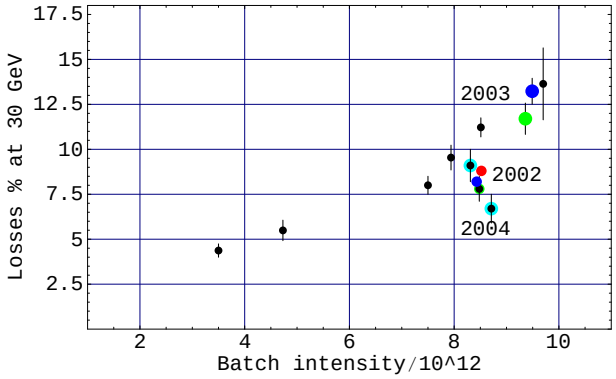

Figure 7: Relative capture loss for different batch intensities in the SPS.

beam loading, instabilities, increased beam size...):

$$\frac{\Delta N_{loss}}{N} \propto N.$$

However, to keep the same absolute loss ΔN_{loss}, responsible for the radiological impact, the relative loss should be reduced at higher intensity as

$$\frac{\Delta N_{loss}}{N} \propto 1/N.$$

As a result, for higher beam intensities, significantly improved machine performance and radioprotection will be required. The possible installation of beam collimation for beam loss control should also be considered.

SUMMARY AND DISCUSSION

The SPS must be significantly improved to match all other upgrades in the accelerator chain. Indeed, the present upgrade scenarios, both for the LHC itself and for its injector chain are very challenging for the SPS. Among them, the scenario with 50 ns bunch spacing and very high bunch intensity, is the most demanding in terms of required SPS upgrade. Nevertheless, the increased injection energy with PS2 ($\geq$ 50 GeV) should help to overcome certain single bunch limitations (such as space charge and transverse mode coupling instability - TMCI), and increased longitudinal emittance at injection (≥ 0.6 eVs) should cure multibunch effects (except e-cloud) and TMCI (completely). However in order to accelerate the "50 ns scenario" beam with large longitudinal emittance the RF system of the SPS must be upgraded: doubling the power plant with R&D for the most critical elements is indispensable.

The actual "bottle-neck" for the nominal LHC beam, the vertical e-cloud instability, will have even lower threshold at higher injection energy and studies of possible SPS vacuum chamber upgrade should be pursued now, taking into account the time which is necessary to find proper solutions in the laboratory and to test them with the beam in the SPS ring for long term effects. Resources are required so these studies can start now.

Control of the SPS impedance, and it's reduction when possible, is also essential for any future intensity increase.

Issues related to beam loss and radiation could become the most important limiting factors for future plans and should not be neglected.

There are other important components of the SPS upgrade for high intensity beams which were not discussed here:

- Injection kicker at 50 GeV/c
- Beam control:
  - longitudinal feedback, feed-forward and damper
  - transverse feedback/damper
- Beam dump
- Beam instrumentation
- Beam collimation

ACKNOWLEDGMENTS

The author would like to thank R. Garoby and T. Linnecar for useful discussions and suggestions.

REFERENCES

[1] W. Scandale, F. Zimmermann, Scenarios for the LHC upgrade, these Proceedings.

[2] G. Arduini, Ultimate LHC beam, these Proceedings.

[3] M. Benedikt et al., Preliminary accelerator plans for maximizing the integrated LHC luminosity, CERN PAF, January 2006. See also http://paf.web.cern.ch/paf/

[4] PS2 Working Group web page: https://paf-ps2.web.cern.ch/paf-ps2/

[5] E. Shaposhnikova et al., Recent intensity increase in the CERN accelerator chain, Proc. PAC05, Knoxville, USA, 2005.

[6] SPS Upgrade Study Team web page: http://paf-spsu.web.cern.ch/paf-spsu/

[7] R. Garoby, LHC injector upgrade plan, these Proceedings.

[8] G. Rumolo, E. Metral, E. Shaposhnikova, SPS performance with PS2, Proc. of LIMI'06, Valencia, 2006, CERN-2007-002.

[9] E. Metral et al., SPS impedance, these Proceedings.

[10] T. Linnecar, E. Shaposhnikova, J. Tuckmantel, LHC upgrade scenarios - preliminary estimations for the RF systems, AB-Note-2006-042 RF, 2006.

[11] G. Arduini, Beam Quality Preservation in the CERN PS+SPS Complex, Proc. EPAC 2004.

[12] G. Arduini, A. Verdier, AB-Note-2003-017 MD, 2003.

[13] B. Salvant et al., TMCI studies with HEADTAIL and MOSES, these Proceedings.

[14] G. Arduini, Proc. Workshop Chamonix XIII, 2004.

[15] G. Rumolo et al., Experimental studies on the SPS e-cloud, these Proceedings.

[16] P. Chiggiato, S Calatroni, SPS chamber upgrade: TiN coating, these Proceedings.

[17] F.Caspers, T.Kroyer, Clearing electrodes: Past experience, technological aspects and potential, these Proceedings.

[18] M Pivi, private communication, 2007

[19] F. Zimmermann, Generation and stability of intense long flat bunches, these Proc.

[20] P. Baudrenghien, T. Bohl, T. Linnecar, E. Shaposhnikova and J. Tuckmantel, Nominal longitudinal parameters for the LHC beam in the CERN SPS, Proc. PAC 2003.

[21] E. Shaposhnikova, CERN SL-Note-2001-031 HRF.

[22] E. Montesinos, private communication, 2007.

[23] T. Linnecar, private communication, 2007.

[24] M. Meddahi, E. Shaposhnikova, CERN-AB-2007-013-PAF

[25] T. Bohl et. al., Beam transfer functions and beam stabilisation in a double RF system, EPAC'05.

[26] T. Linnecar et al., 33rd ICFA Advanced Beam Dynamics Workshop, AIP Conf. Proc.: 773 (2005) pp. 345-349.

SPS IMPEDANCE

E. Métral, G. Arduini, T. Bohl, H. Burkhardt, F. Caspers, H. Damerau, E. Gaxiola, T. Kroyer, H. Medina, G. Rumolo, B. Salvant, E. Shaposhnikova, M. Schokker, J. Tuckmantel (CERN, Geneva, Switzerland), R. Calaga (BNL, Upton, NY, USA) and B. Spataro (INFN, Frascati, Italy)

Abstract

For many years several measurements of the beam coupling impedance have been performed each year in both longitudinal and transverse planes of the CERN Super Proton Synchrotron to keep track of the evolution of its hardware. Copious types of equipments had to be modified or added in the past to allow the SPS to produce the nominal LHC beam. The next challenge would be the operation of the SPS with higher intensity for the LHC luminosity upgrade, which requires a good knowledge of the machine impedance and in particular of its major contributors. The current understanding of the measurements performed over the last few years is presented in this paper. In particular, this analysis reveals that the longitudinal impedance is reasonably well understood, while the situation is less satisfactory in the transverse planes, where about half of the measured impedance still needs to be identified.

INTRODUCTION

Before 2001, the longitudinal single bunch (microwave) instability has been observed in the SPS in practically all operation modes: with leptons and protons, below and above transition energy, with RF on and RF off [1,2]. Even though in most cases the associated longitudinal emittance blow-up was not detrimental, it became a significant issue for the high-brightness beams required for LHC. Different solutions to avoid or cope with the uncontrolled emittance blow-up due to the microwave instability were studied. The most attractive cure was the removal or shielding of the elements concerned [3]. Different types of reference measurements were initiated in order to followup the impedance reduction program and to see the consequences on the beam. The global effect of the SPS impedance reduction in the longitudinal plane can be observed in Fig. 1, where the reference measurements done in 1999 (before impedance reduction) are compared to 2001 (after). Note that two mechanisms are expected to lead to an increase of the bunch length with intensity; firstly the potential-well distortion defined by the inductive part of the effective (i.e. taking into account the bunch spectrum) longitudinal impedance Im $[Z_l/n]_{eff}$) and then, above some threshold intensity the uncontrolled emittance blow-up induced by the microwave instability. The difference in the slopes of Fig. 1 is around a factor 7. It can also be concluded that in 1999 the microwave instability threshold was at or below 3×10^{10} p/b. In 2001 the smooth increase with intensity due to potential-well distortion can clearly be observed. Simulations showed that the impedance of the vacuum pumping ports was responsible for most of the uncontrolled emittance blow-up observed before 2001. The shielding of these elements (~ 1000 vacuum pumping ports) eliminated the microwave instability. Note that in addition several kickers were also removed (the total number of kickers in 2001 was 11) as well as the lepton RF cavities. It was deduced from measurements (as will be seen also later in this paper) that the impedance reduction factor was ~ 2.5 in the longitudinal plane, whereas it was only ~ 0.4 in the vertical one.

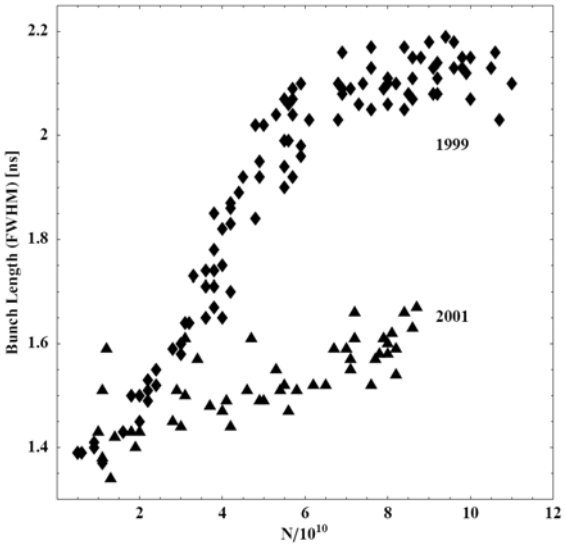

Figure 1: Bunch length measured 600 ms after injection as a function of bunch intensity in 1999 and 2001. Data taken at 26 GeV/c, with the RF voltage V_{RF} = 900 kV and the longitudinal emittance ε_L = 0.15 eVs [1].

To extract the beam towards the LHC, new extraction kickers (MKE) were required. In 2003, the first 5 MKE kickers (out of 9 in total) were installed in the sextant LSS4 (i.e. 16 kickers in total were present in the SPS). In 2006, the remaining 4 MKE kickers were added in sextant LSS6 (leading to a total of 20 kickers). Note that one of the MKE kicker was shielded on 2 cells. Finally, in 2007 one MKE kicker was removed and one MKE was "fully" shielded, leading to a total of 19 kickers. To be able to follow the impedance increase and to see the consequences for the beam, the same reference measurements had been continued. In parallel a lot of

work was devoted to estimate better the resistive-wall impedance [4] and the results were applied to the MKE kickers and compared to bench measurements (see later).

Detailed measurements were also performed in 2003 in the SPS right after injection at 26 GeV/c, where a fast single-bunch vertical instability develops when the longitudinal emittance of the beam is too small [5]. Figure 2 is an example of what was observed with a high-intensity single bunch ($\sim 1.2 \times 10^{11}$ p/b) of low longitudinal emittance (~ 0.2 eVs). The RF voltage was $V_{RF} \approx 600$ kV, which corresponds to the synchrotron period $T_s = 7.1$ ms. Keeping the chromaticity close to zero, the bunch was stabilized when the intensity was reduced to $\sim 6 \times 10^{10}$ p/b. A detailed comparison between the measurements and HEADTAIL [6] simulations was performed in the past. As can be seen in Fig. 3, a good agreement between the two was already revealed when the measured "equivalent" broad-band impedance model (with a shunt impedance $R_y = 20$ MΩ/m, a resonance frequency f_r = 1 GHz and a quality factor Q = 1) was used. In particular the analysis in the time domain revealed a travelling-wave pattern along the bunch, which is believed to be the signature of a transverse-mode coupling instability (the coupling of standing-wave patterns leads to a travelling wave). After having analysed the instability in the time domain, the next step consisted to analyse the instability in the frequency domain to try and observe a coupling between the azimuthal modes. A sensitive frequency analysis of the HEADTAIL simulations output was therefore done using SUSSIX [7], which brought to light the fine structure of the mode spectrum of the bunch coherent motion. A coupling between the azimuthal modes -2 and -3 was clearly observed to be the reason for this fast instability, which was in good agreement with the predictions from MOSES [8] for the case of a round geometry (see Fig. 4) [9]. The next steps consisted then on one hand to improve the model of the SPS transverse (vertical) impedance to make more realistic predictions from theory and/or HEADTAIL simulations and on the other hand to try and measure the mode coupling. The first step was started adding the computed contributions from all the kickers plus several other elements, and is discussed later in the present paper, whereas the measurements still have to be analysed in detail.

In addition to coherent instabilities, the real part of the longitudinal impedance of the ferrites installed in the MKE extraction kickers lead to significant beam-induced heating of the magnets. The temperature variation is usually measured on the ceramic spacers, which touch the ferrites. If a part of the ferrite itself happens to reach temperatures above the Curie temperature, around 125°C, it loses its magnetic properties and the magnetic field strength is reduced. Structural damage to the kicker magnets cannot be excluded for temperatures above 150°C. Presently the beam in the SPS is aborted if the measured MKE temperature reaches 90°C.

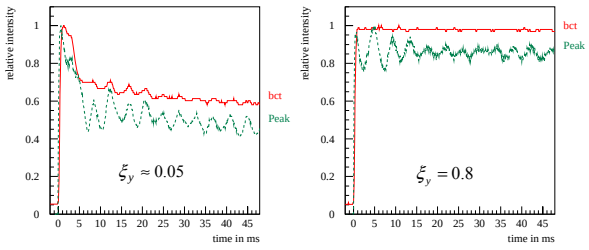

Figure 2: Measured relative (normalized to the value at injection) bunch intensity vs. time in the SPS machine in 2003. bct stands for beam current transformer and Peak stands for peak intensity. The bunch, which is unstable when $\xi_y \approx 0.05$ (left) is stabilized by increasing the (relative) chromaticity to $\xi_y = 0.8$ (right).

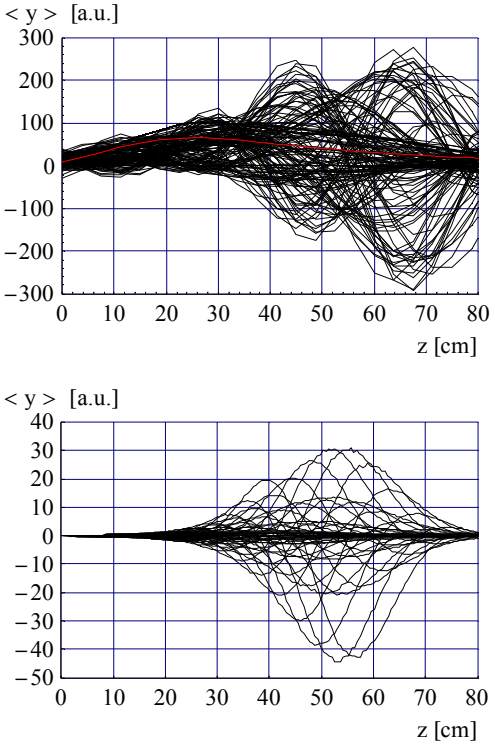

Figure 3: (Upper) Measured evolution of the vertical centroid position along the bunch $< y > = N(z) \times y_{av}(z)$, where N (z) is the longitudinal bunch profile, using the "Head-Tail" monitor [10] (with the traces of all the 150 turns superimposed), for a vertical (relative) chromaticity close to zero (see Fig. 2). The first turn after injection is shown in red. The head of the bunch (truncated at $\pm 2\sigma_z$) is on the left and the tail on the right. (Lower) Simulated evolution of the vertical centroid position along the bunch using the HEADTAIL code (with the traces of all the turns superimposed). The head of the bunch (truncated at $\pm 2\sigma_z$) is on the left.

The outline of the present paper is the following: the first section deals with the resistive-wall formula used to estimate the impedance of all the SPS kickers. The second section is devoted to the detailed comparison between measurements and theoretical predictions. Finally, new HEADTAIL simulations in the longitudinal plane are discussed.

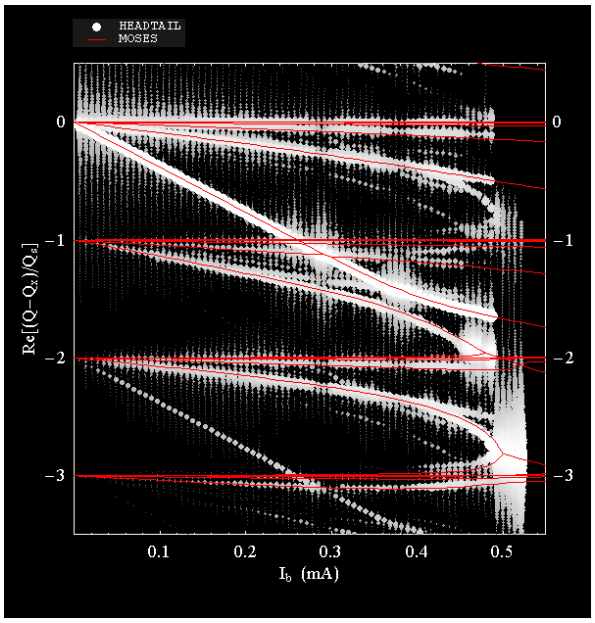

Figure 4: Head-tail modes vs. bunch intensity for ε_L = 0.2 eVs, σ_t = 0.67 ns, V_{RF} = 600 kV and ξ_x = 0. MOSES (red lines) vs. HEADTAIL (white dots) results analyzed with SUSSIX. The impedance used here is a broad-band impedance with a shunt impedance R_y = 10 MΩ/m (instead of 20 MΩ/m above), a resonance frequency f_r = 1 GHz and a quality factor Q = 1.

RESISTIVE-WALL IMPEDANCE OF THE MKE KICKERS

Figure 5 shows the real cross-section of a MKE magnet. From the impedance point of view, it can be approximated by the simpler geometry of Fig. 6. Detailed analytical studies revealed that for the computation of the transverse (vertical) impedance, the model of two infinite ferrite plates is well justified and Zotter's formula [4] should be used, as confirmed by measurements shown in Fig. 7. However, for the computation of the longitudinal impedance, it is mandatory to take into account the perfect conductor on both sides (left and right) and use Tsutsui's formula [11]. This was confirmed by measurements [12] as can be seen in Figs. 8 and 9. To get rid of the operational issue of the heating associated with the real part of the longitudinal impedance of the MKE kickers, it was suggested to print conducting strips directly onto the ferrite. This was done on the kicker MKE-L10 (see Fig. 10) and the effect on the impedance was measured (see Fig. 11). A more detailed description of the impedance measurements and of the approaches to reduce kicker heating can be found in Ref. [13]. It can be concluded from Fig. 11 that the real part of the impedance is indeed considerably reduced, even though resonances are created near 50 MHz and 1.7 GHz.

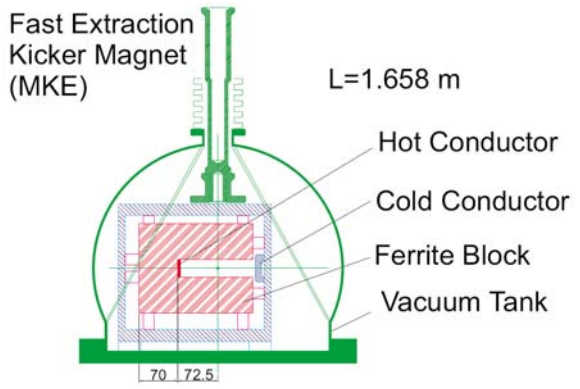

Figure 5: Cross-section of a MKE magnet.

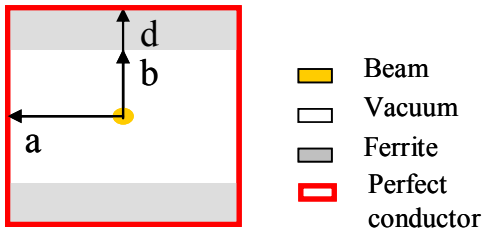

Figure 6: Simplified model for the computation of the MKE kicker impedance.

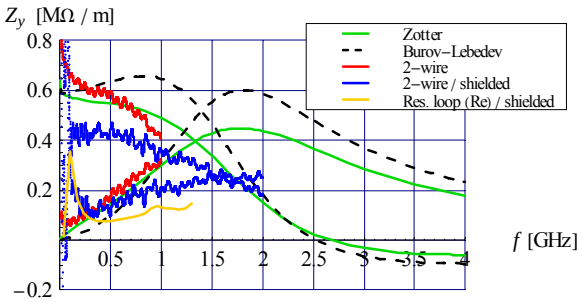

Figure 7: Measurement (with 2 wires, in red) of both real and imaginary parts of the vertical impedance of an SPS MKE kicker vs. frequency, compared to Zotter's [4] (in green) and Burov-Lebedev's [14] (in black) theories. The blue and yellow curves correspond to two different methods (with 2 wires and resonant loop) of measurement in the case of a "shielded" kicker with printed strips used to mainly reduce the real part of the longitudinal impedance and the associated heating (see Figs. 10 and 11).

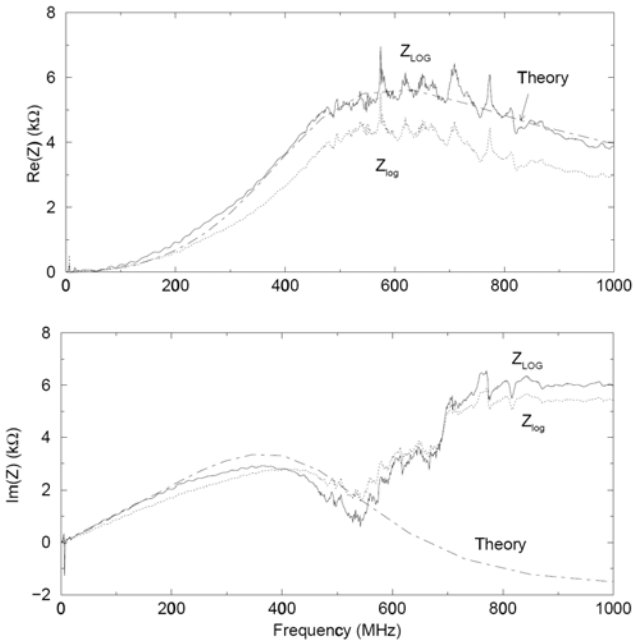

Figure 8: Measurement of the real (upper) and imaginary (lower) part of the longitudinal impedance of a SPS MKE kicker vs. frequency in 2000, compared to Tsutsui's theory [11]. The increase in the imaginary part after ~ 500 MHz was then understood as can be seen in Fig. 9.

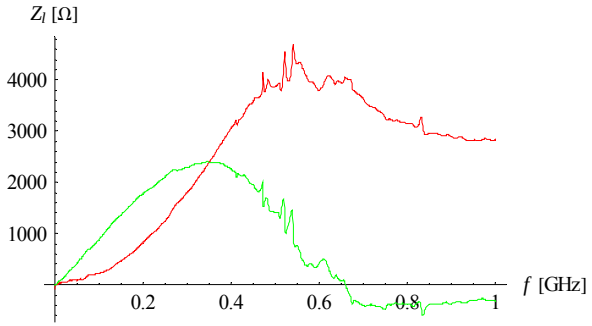

Figure 9: Measurement of the real (red) and imaginary (green) part of a SPS MKE kicker impedance vs. frequency in 2006.

In fact two resonances were also introduced below 100 MHz in the transverse plane (barely visible in Fig. 7). The effects of these resonances were studied both in the longitudinal and transverse planes, and it was concluded that they were not too harmful and that the impedance reduction campaign for the MKE kickers should be pursued by the deposition of conducting strips as this has a significant impact on the overall longitudinal impedance and on the kicker heating [15].

It was concluded from the above comparisons between analytical formulae and measurements of both longitudinal and transverse impedances that our theoretical estimates are quite satisfactory and that one could use them to estimate both longitudinal and transverse resistive-wall impedances of all the SPS kickers in the past few years. These estimates are compared to beam-based measurements in the next section.

Figure 10: Printed conducting strips directly on top of the ferrite of the MKE-L10 kicker.

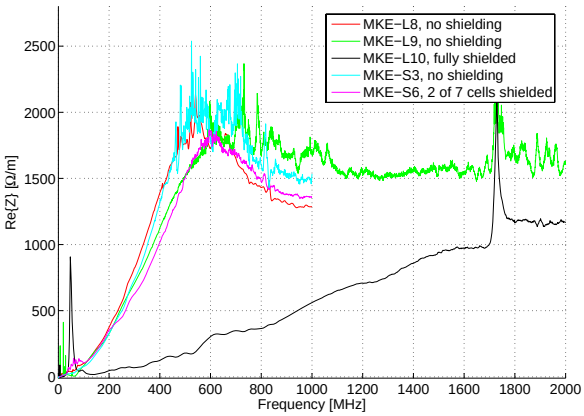

Figure 11: Measurement of the real part of the longitudinal impedance of different SPS MKE kickers vs. frequency, and in particular for the MKE-L10 (in black) fully equipped with printed strips to reduce the real part of the longitudinal impedance.

MEASUREMENT VS. THEORY

Transverse Coherent Tune Shift vs. Intensity

The measurements of the single-bunch transverse (vertical) coherent tune shift vs. intensity [16] over the last few years are depicted in Fig. 12 [17]. It can be first seen that in 2001 the measured "total" (i.e. dipolar plus quadrupolar [18]) effective impedance was reduced by 40% compared to the measured value in 2000 (as already mentioned in Introduction). Secondly, one can observe that the measured "total" impedance increase from 2001

to 2006 (i.e. due to the installation of the 9 MKE kickers) is 4.5 MΩ/m, which has to be compared to 5.2 MΩ/m expected from theory (see Table 1). Furthermore, a slight reduction of the impedance was expected in 2007 (due to the removal of one MKE kicker and shielding of another one). This seems also to be reflected in Fig. 12, even though one might reach the precision limit for the measurements and the exact predicted "total" impedance of the shielded kicker could not be given as the quadrupolar impedance is missing (only the dipolar impedance was measured in Fig. 7). This good agreement reveals that the impact of the hardware modifications can be well explained since 2001. Note that the imaginary part of the vertical effective dipolar impedance of the shielded kicker is $\mathrm{Im}[Z_{y,\mathrm{dip}}]_{\mathrm{eff}} = 0.24$ MΩ/m, whereas it was 0.27 MΩ/m before the shielding, revealing a small effect of the shielding in the vertical plane. Furthermore, the imaginary part of the vertical effective "total" impedance from space charge (which contributes to the coherent tune shift) is $\mathrm{Im}[Z_y]_{\mathrm{eff}} = 2.6$ MΩ/m (it is 0.04 MΩ/m in the horizontal plane).

The conclusions of these measurements are that (i) the contribution from all the kickers vs. time can be reasonably well explained, (ii) all the kickers in 2006 (and 2007) contribute to ~ 40 % of the total measured impedance and (iii) 13 MΩ/m (= 19.1 – 3.5 – 2.6) are still missing (already in 2001).

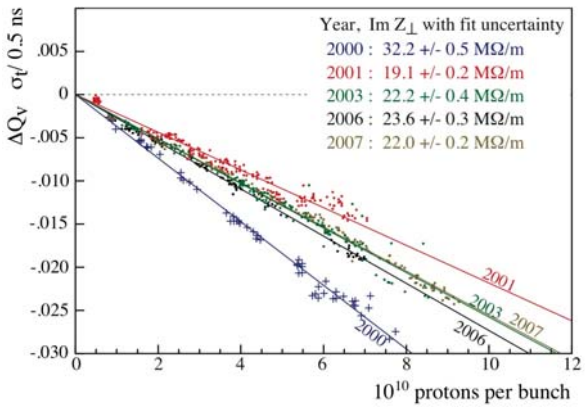

Figure 12: Measurements of the single-bunch vertical coherent tune shift vs. intensity over the last years [17].

Table 1: Summary and comparison between beam-based measurements (of the whole SPS ring) and theoretical predictions (considering only the contribution from all the kickers).

$\mathrm{Im}(Z_y)_{\mathrm{eff}}$ [MΩ/m]	Meas	delta	Theory (kickers)	delta	Error delta [%]
2001	19.1		3.5		
2003	22.2	3.1	6.4	2.9	7
2006	23.6	1.4	8.7	2.3	-39
2007	22	-1.6			

Fast Vertical Single-Bunch Instability Intensity Threshold at Injection

Taking into the contribution from all the (20) kickers in 2006, the vertical wake field has been obtained through ZBASE3 (which is a new version still under development of the impedance database ZBASE [19]). It is plotted in Fig. 13 together with the wake field of the broad-band resonator model (10 MΩ/m) used for the transverse mode coupling analysis (see Fig. 4). The HEADTAIL simulation code has been upgraded to be able to read the wake field from a table of data instead of using an analytical formula, and the result from the HEADTAIL simulations is depicted in Fig. 14. It reveals that the intensity threshold found with the same bunch parameters as above and the "real" (computed) impedance from all the (20) kickers in 2006 is $N_b^{th} \approx 1.1\times0^{11}$ p/b. In order to check that the results obtained with the recently upgraded

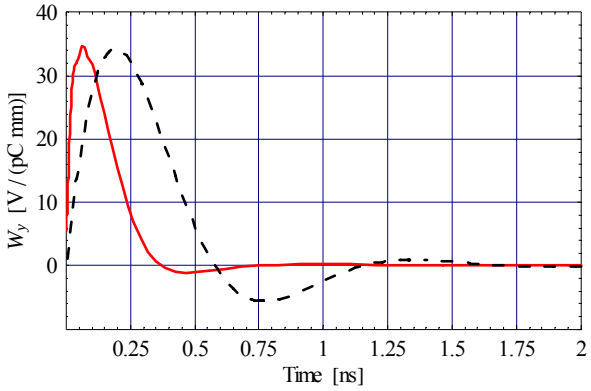

Figure 13: Theoretical wake field from all the (20) SPS kickers in 2006 (red curve) compared to the one from the broad-band resonator model (10 MΩ/m) used for the transverse mode coupling analysis (see Fig. 4) (dashed black curve).

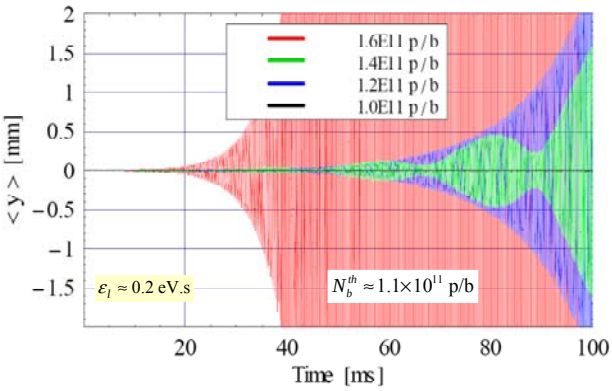

Figure 14: Evolution of the vertical centroid position (simulated with the HEADTAIL code) vs. time using the "real" computed wake field for all the (20) SPS kickers in 2006 (see Fig. 13). In the legend the numbers refer to the number of protons per bunch.

HEADTAIL code are correct, the wake field of Fig. 13 has been fitted by a broad-band resonator model (see Fig. 15) and the latter has been used to perform MOSES computation (see Fig. 16). The fitted resonator has a shunt impedance of 3.5 MΩ/m, a resonance frequency of 2.3 GHz and a quality factor of 0.6. As can be seen from

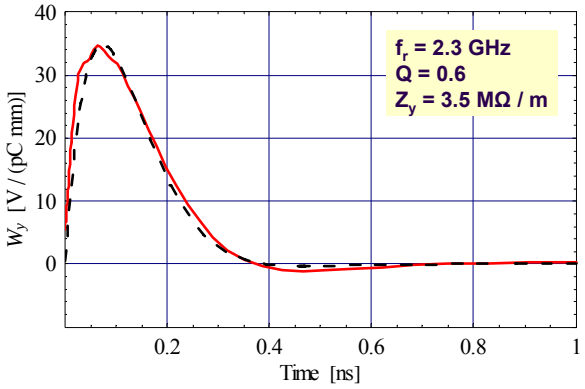

Figure 15: Fit (dashed black curve) of the wake field for all the (20) SPS kickers in 2006 (red curve).

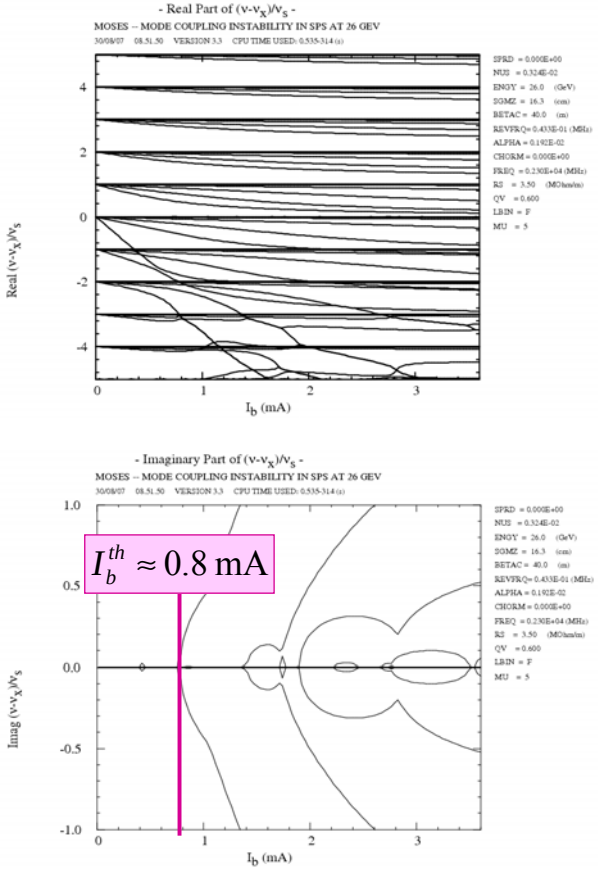

Figure 16: MOSES computation with the fitted resonator of Fig. 15. Real (upper) and imaginary (lower) parts of the normalised vertical tune shift vs. bunch intensity.

Fig. 16 (lower) the intensity threshold is $I_b^{th} \approx 0.8$ mA, which corresponds to a threshold in the number of protons per bunch of $N_b^{th} \approx 1.15\times10^{11}$ p/b. This value is therefore in very good agreement with the one previously found with HEADTAIL (~ 1.1×10^{11} p/b), which constitutes a satisfactory benchmark between the two codes.

The conclusion from these measurements is that predicted intensity threshold with the "real" computed wake field from all the (20) kickers in 2006 is about a factor 2 higher (~ 1.1×10^{11} p/b predicted compared to ~ 0.6×10^{11} p/b measured). Here again, this means that the contribution from the kickers to the vertical impedance is only ~ 50%.

Head-Tail Growth/Decay Rate

Changing the (vertical) chromaticity the growth or decay rates of the single-bunch head-tail instability (which depend only on the dipolar impedance) can be measured. This provides information about the real part of the vertical (dipolar) impedance. Using the fit of the "real" computed wake field for all the (20) SPS kickers in 2006 discussed in the previous section, the predicted head-tail growth/decay rates are compared to the measured ones in Fig. 17.

The conclusion from these measurements is also that the real part of the effective vertical impedance from all the (20) kickers in 2006 contribute to ~ 50% of the total measured impedance. Therefore, the three measurements of the vertical impedance are quite consistent.

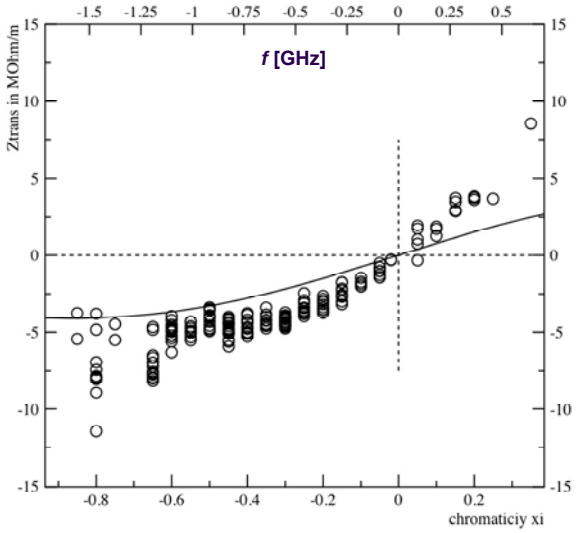

Figure 17: Comparison between the measured (dots) and computed (full black curve) real part of the effective vertical impedance vs. chromaticity. The computation was made using the fitted resonator for 2006, i.e. with a shunt impedance of 3.5 MΩ/m, a resonance frequency of 2.3 GHz and a quality factor of 0.6.

Quadrupole Oscillation Frequency Shift vs. Intensity

The inductive part of the effective longitudinal impedance can be assessed by measuring the quadrupole oscillation frequency shift vs. intensity. The results of these measurements over the last years can be found in Fig. 18 [20]. These estimates were based on the analysis of the data of Fig. 19. It can be first seen that in 2001 the measured effective impedance was reduced by a factor of ~ 2.5 compared to the measured value in 1999 (as already mentioned in Introduction). Secondly, one can observe that the effective impedance increase from 2001 to 2006 (i.e. due to the installation of the 9 MKE kickers) is 3 Ω, which has to be compared to 4 Ω expected from theory (see Table 2). The agreement is quite good if one keeps also in mind that these measurements are very sensitive to the bunch length (see Appendix E). Finally, a slight reduction of the impedance was expected in 2007 (due to the removal of one MKE kicker and shielding of another one). As can be seen in Figs. 18 and 19, contrary to the expectations, an increase of the impedance by ~ 40 % was observed. This issue still has to be investigated in detail. More measurements are planed at the end of the 2007 run to try and understand the reason of this unexpected and significant increase. Note that the longitudinal effective inductive impedance of the shielded kicker is $\mathrm{Im}[Z_l/n]_{\mathrm{eff}} = 0.1\ \Omega$, whereas it was 0.4 Ω before the shielding, which reveals the important effect of the shielding. Furthermore, the longitudinal effective inductive impedance from space charge (which contributes to the frequency shift) is $\mathrm{Im}[Z_l/n]_{\mathrm{eff}} \approx -1\ \Omega$, and it has already been subtracted from the above cited numbers (unlike the transverse plane).

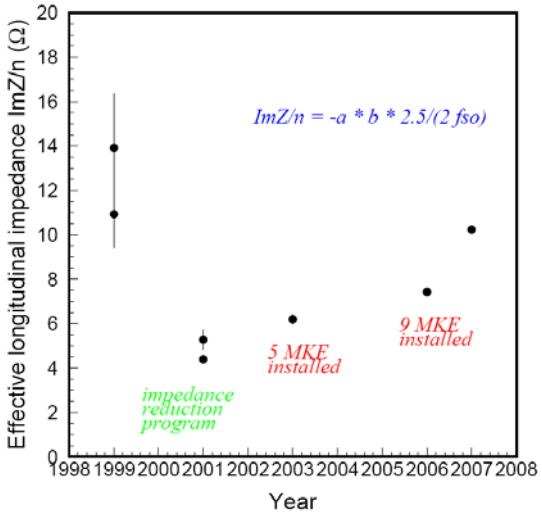

Figure 18: Longitudinal effective inductive impedance as deduced from the quadrupole oscillation frequency shift over the last few years (see Fig. 19).

The conclusions from these measurements are that (i) the contribution from all the kickers vs. time can be reasonably well explained until 2006, (ii) an increase by ~ 40 % was observed in 2007, which is not explained yet as a slight reduction was predicted.

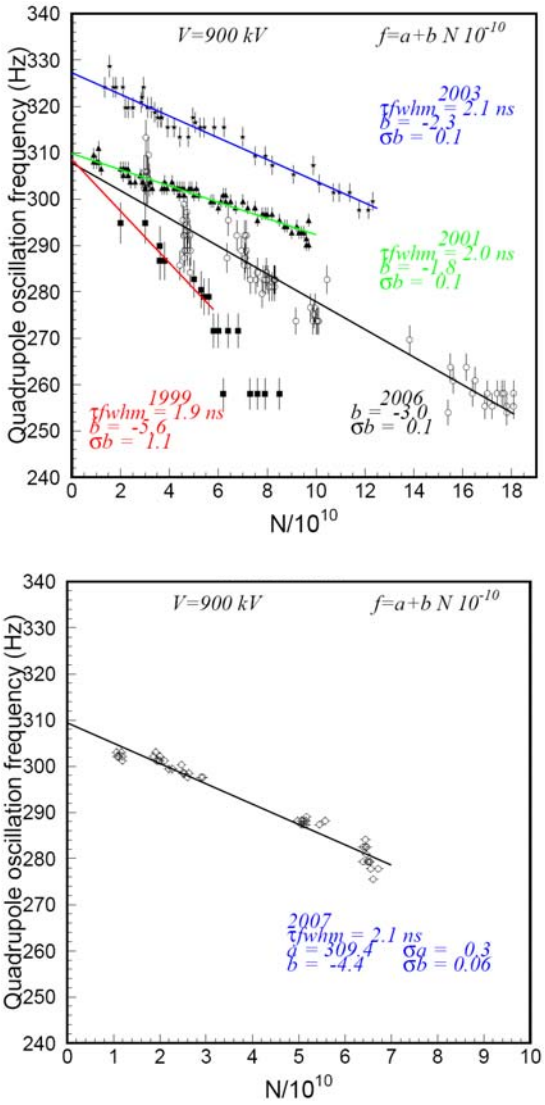

Figure 19: Quadrupole oscillation frequency vs. intensity from 1999 to 2006 (upper), and in 2007 (lower).

Table 2: Summary and comparison between beam-based measurements (of the whole SPS ring) and theoretical predictions (considering only the contribution from all the kickers).

$\mathrm{Im}(Z_l/n)_{\mathrm{eff}}$ [Ω]	Meas	delta	Theory (kickers)	delta	Error delta [%]
2001	4.4		1.2		
2003	6.2	1.8	3.4	2.2	-18
2006	7.4	1.2	5.2	1.8	-33
2007	10.2	2.8	4.4	-0.8	-450

Power Loss

All the measurements discussed above used the same kind of beam: a single bunch with low longitudinal and transverse emittances (compared to the nominal LHC bunches). Considering now the nominal LHC beam in the SPS, i.e. 4 batches of 72 bunches with 1.2×10^{11} p/b and an rms bunch length of 0.7 ns, yields the power losses shown in Table 3 over the last years. Note that the power loss for the shielded kicker is computed to be 407 W, whereas it is expected to be 1127 W without the shielding. This means that a reduction in the power loss by a factor of ~ 3 is predicted. This was confirmed by measurements as a reduction by a factor 3-4 was observed [21].

Table 3: Power loss computed with a nominal LHC beam in the SPS (4 batches of 72 bunches with 1.2×10^{11} p/b and an rms bunch length of 0.7 ns).

Power loss [W]	Theory	delta
2001	2085	
2003	8027	5942
2006	12742	4715
2007	10792	-1950

HEADTAIL SIMULATIONS IN THE LONGITUDINAL PLANE

As the longitudinal impedance was measured to have increased by ~ 40 % in 2007, HEADTAIL simulations were performed in the longitudinal plane to see where the longitudinal microwave intensity threshold stands. A modelled resonator impedance was first used with a shunt impedance of 10 Ω (as deduced from Table 2), a resonance frequency of 1 GHz and a quality factor of 1. The bunch parameters were taken to be the same as the ones used for the transverse mode coupling analysis. The rms bunch length vs. intensity is plotted in Fig. 20, where

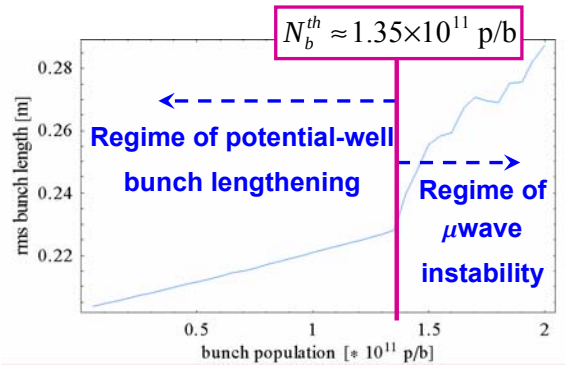

Figure 20: Rms bunch length vs. intensity simulated with the HEADTAIL simulation code. The same parameters as the ones for the transverse mode coupling analysis were used. A modelled resonator impedance was used with a shunt impedance of 10 Ω (as deduced from Table 2), a resonance frequency of 1 GHz and a quality factor of 1.

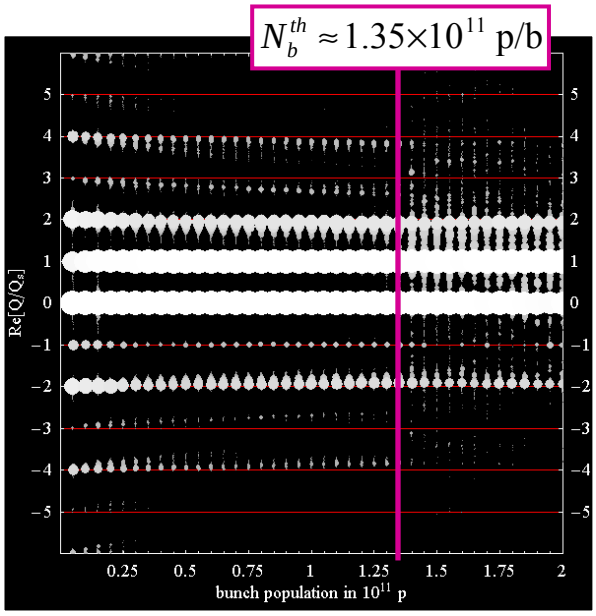

Figure 21: Longitudinal modes vs. bunch intensity for the same bunch parameters as the ones used in the transverse mode coupling analysis. However, the impedance used here is a modelled broad-band impedance with a shunt impedance of 10 Ω (see Table 2), a resonance frequency of 1 GHz and a quality factor of 1.

two regimes can be clearly distinguished. The first (almost) linear one corresponds to the potential-well bunch lengthening regime. The second is the regime of microwave instability. On this picture the intensity threshold can be deduced unambiguously and is $N_b^{th} \approx 1.35\times10^{11}$ p/b. Applying the same sensitive frequency analysis as was done previously for the transverse plane (with SUSSIX) of the HEADTAIL simulations output, the evolution of the longitudinal coherent frequency shifts vs. intensity is depicted in Fig. 21. No clear mode coupling as in the transverse plane is observed, which may be due to the fact that the frequency signals are largely dominated by the modes 0 and 1. However, close to the intensity threshold some activity can be seen around mode 2 (with modes 1 and 3), and this will be investigated in detail in the future.

To check the validity of the analytical formula for the prediction of the potential-well bunch lengthening, the longitudinal effective inductive impedance was deduced from the slope of Fig. 20, and compared to the known impedance introduced in HEADTAIL. From the usual 4th order equation [22], a simplified equation can be deduced in our case and is given by

$$\mathrm{Im}\left[\frac{Z_l}{n}\right]_{protons} \approx -\frac{4\cos\phi_s\,\pi^2\,V_{RF}\,h\,(f_0\,\tau_{b0})^2}{3\,e}\times\frac{d\,\tau_b}{d\,N_b}, \quad (1)$$

where ϕ_s is the RF phase of the synchronous particle ($\cos\phi_s > 0$ below transition and $\cos\phi_s < 0$ above), V_{RF} the peak RF voltage, h the harmonic number, f_0 the revolution frequency, τ_b the total bunch length in seconds (with τ_{b0} the value at zero intensity) and e the elementary charge. Applying Eq. (1) to the slope of Fig. 20 yields $\mathrm{Im}[Z_l/n]_{\mathrm{eff}} \approx 8.4\ \Omega$, whereas 10 Ω were used in HEADTAIL, which is in good agreement (the error is 16%).

The intensity threshold of the microwave instability has also been compared to the analytical formula of Ref. [23] given by

$$\frac{\left|Z_l^{BB}/n\right|}{1.2}\times\left[1-Sgn(\eta)\times\frac{3}{4}\left(\frac{\left|Z_l^{SC}/n\right|}{\left|Z_l^{BB}/n\right|}-1\right)\right]^{1/4} \leq \frac{(E/e)\beta^2|\eta|}{I_{p0}}\times\left(\frac{\Delta p}{p_0}\right)^2_{\mathrm{FWHH},0}, \quad (2)$$

where BB stands for Broad-Band and SC for Space Charge impedance, $\eta = \gamma_{tr}^{-2} - \gamma^{-2} = (\Delta T/T_0)/(\Delta p/p_0)$ is the slippage factor, $Sgn(\eta)$ denotes the sign of η (it is - below transition and + above), β is the relativistic velocity factor, E the total beam energy, $I_{p0} = 3\,e\,N_b/(2\,\tau_{b0})$ is the bunch peak current (without potential-well distortion) considering a parabolic line density, and $(\Delta p/p_0)_{\mathrm{FWHH},0}$ is the full width at half height of the relative momentum spread (without potential-well distortion). Note that in the present case,

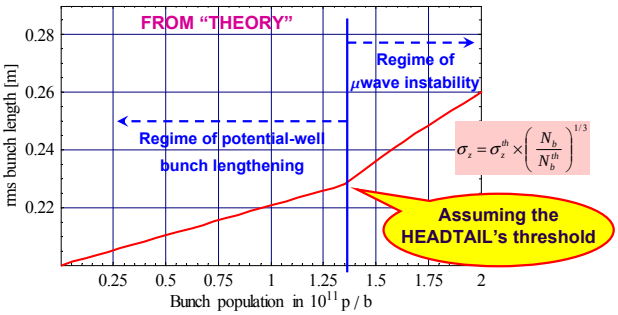

Figure 22: Rms bunch length variation vs. intensity as predicted from theory [22].

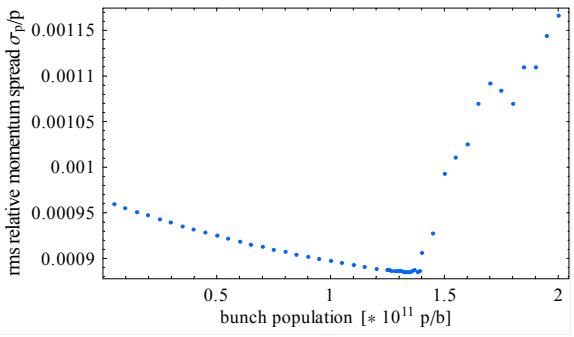

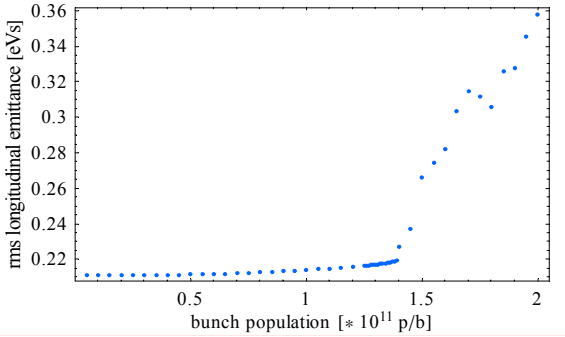

Figure 23: Rms relative momentum spread (upper) and rms longitudinal emittance (lower) vs. intensity from HEADTAIL simulations.

i.e. above transition and without space charge, Eq. (2) leads to the same result as the usual Keil-Schnell-Boussard approximation. Applying Eq. (2) yields $N_b^{th} \approx 0.7\times10^{11}$ p/b, i.e. the theoretical prediction is about a factor 2 lower than the simulated one ($N_b^{th} \approx 1.35\times10^{11}$ p/b). Furthermore, in the microwave instability regime the bunch length was estimated in Ref. [22] to vary with the power 1/3 of the intensity, which seems to underestimate the effect (see Fig. 22 from theory compared to measurements in Fig. 20). For completeness the evolution of both momentum spread and longitudinal emittance vs. intensity obtained from HEADTAIL is shown in Fig. 23.

The next steps would consist to improve the model of the SPS longitudinal impedance to make more realistic predictions from theory and/or HEADTAIL simulations and to try and measure the (possible) mode coupling.

CONCLUSION

All the comparisons performed so far between transverse analytical estimates and measurements of the effective impedance are in good agreement over the last few years, when relative values are discussed. All the kickers can only explain ~ 40% of the measured vertical impedance. Removing the contribution from space charge to the coherent tune shift, 13 MΩ/m are still unexplained. In addition to the kickers, the impedance of several other equipments has been computed or simulated, such as the 108 horizontal and vertical beam position monitors, ~ 1000 (shielded) vacuum pumping ports, the four Travelling-Wave (TW) 200 MHz cavities and the high-energy beam dump absorber (See Appendices). However, their contribution cannot explain the missing 13 MΩ/m. The next step will therefore consist in identifying additional sources of impedance.

In the longitudinal plane, the situation is different. Here again a good agreement between measurements and theory is obtained when relative values are mentioned (i.e. for the contribution from all the kickers). Furthermore, it seems that even for the absolute value the

agreement is relatively good as the main remaining part, ~ 3.2 Ω (= 4.4 Ω – 1.2 Ω) in 2001, could be mainly explained by the four TW 200 MHz cavities, whose inductive effective longitudinal impedance is predicted to be very close to this value (see Appendix F). This study still has to be finalized and the exact contribution from the other (800 MHz) RF system has to be computed. However, one major issue remains in our understanding: why did the longitudinal effective impedance measured in 2007 increase by ~ 40% compared to 2006, whereas a slight reduction was foreseen?

REFERENCES

[1] T. Bohl et al., "Impedance Reduction in the CERN SPS as seen from Longitudinal Beam Measurements", Proc. EPAC2002, Paris, France.

[2] LHC Design Report, CERN-2004-003, Chap. 17.

[3] P. Collier et al., "Reducing the SPS Machine Impedance", Proc. EPAC2002, Paris, France.

[4] E. Métral et al., "Resistive-Wall Impedance of an Infinitely Long Multi-Layer Cylindrical Beam Pipe", Proc. PAC2007, Albuquerque, New Mexico, USA, June 25-29, 2007.

[5] G. Arduini et al., "Observation of a Fast Single-Bunch Transverse Instability on Protons in the SPS", Proc. EPAC'04, Lucerne, Switzerland, 2004.

[6] G. Rumolo and F. Zimmermann, "Practical user guide for HEADTAIL", CERN-SL-Note-2002-036 AP.

[7] R. Bartolini and F. Schmidt, "SUSSIX : A Computer Code for Frequency Analysis of Non-Linear Betatron Motion", CERN SL/Note 98-017 (AP) updated June 29, 1998.

[8] Y. H. Chin, "User's guide for new MOSES version 2.0: MOde-coupling Single bunch instability in an Electron Storage ring", CERN/LEP-TH/88-05, 1988.

[9] B. Salvant et al., "Transverse Mode Coupling Instability in the SPS: HEADTAIL simulations and MOSES computations", these proceedings.

[10] D. Cocq et al., "The Measurement of Chromaticity via a Head-Tail Phase Shift" presented at BIW'98, Stanford, CA, USA, May 1998.

[11] H. Tsutsui, "Some Simplified Models of Ferrite Kicker Magnet for Calculation of Longitudinal Coupling Impedance", CERN-SL-2000-004 AP.

[12] F. Caspers et al., "Impedance Evaluation of the SPS MKE Kicker with Transition Pieces between Tank and Kicker Module", CERN-SL-2000-071 (AP).

[13] T. Kroyer et al., "Longitudinal and Transverse Wire Measurements for the Evaluation of Impedance Reduction Measures on the MKE Extraction Kickers", CERN-AB-Note-2007-028.

[14] A. Burov and V. Lebedev, "Transverse Resistive Wall Impedance for Multi-Layer Flat Chambers", Proc. of EPAC 2002, Paris, France.

[15] CERN APC meetings held on 27/04/2007 and 11/05/2007 (http://ab-div.web.cern.ch/ab-div/Meetings/APC/Welcome.html).

[16] H. Burkhardt et al., "Coherent Beam Oscillations and Transverse Impedance in the SPS", Proc. of EPAC 2002, Paris, France.

[17] H. Burkhardt, CERN APC meeting held on 17/08/07 (http://ab-div.web.cern.ch/ab-div/Meetings/APC/Welcome.html).

[18] A. Burov and V. Danilov, Phys. Rev. Lett. **82**, 2286-2289 (1999).

[19] O. Bruning, "ZBASE user's guide Version 1.1: an Impedance Data Base Program", CERN-SL-96-069-AP.

[20] E. Shaposhnikova, CERN APC meetings held on 11/05/07 and 03/08/07 (http://ab-div.web.cern.ch/ab-div/Meetings/APC/Welcome.html).

[21] L. Ducimetière, private communication (2007).

[22] J.L. Laclare, "Bunched Beam Coherent Instabilities", CERN Accelerator School, CERN 87-03, p. 264.

[23] E. Métral, "Stability Criterion for the Longitudinal Mode-Coupling Instability in the Presence of Both Space-Charge and Resonator Impedances", CERN/PS 2001-063 (AE).

[24] G. Arduini et al., "Localizing Impedance Sources from Betatron Phase Beating in the CERN SPS", Proc. EPAC'04, Lucerne, Switzerland, 2004.

[25] MAFIA, v.4.107, CST GmbH (Darmstadt, Germany), 2002; www.cst.de.

[26] G. Rumolo et al., "Tracking Study of the Effect of BPM Impedances in the SPS", CERN-AB-2005-088-RF.

APPENDIX A: MICROWAVE INSTABILITY WITH RF OFF

The unstable bunch spectrum when a single-bunch is injected into the SPS with RF OFF has been measured up to 2 GHz in 2001 and 2007 with similar beam parameters. The results are shown in Fig. A1. It can be seen that a resonance near 1.4 GHz, which was just visible in 2001, is clearly present in 2007.

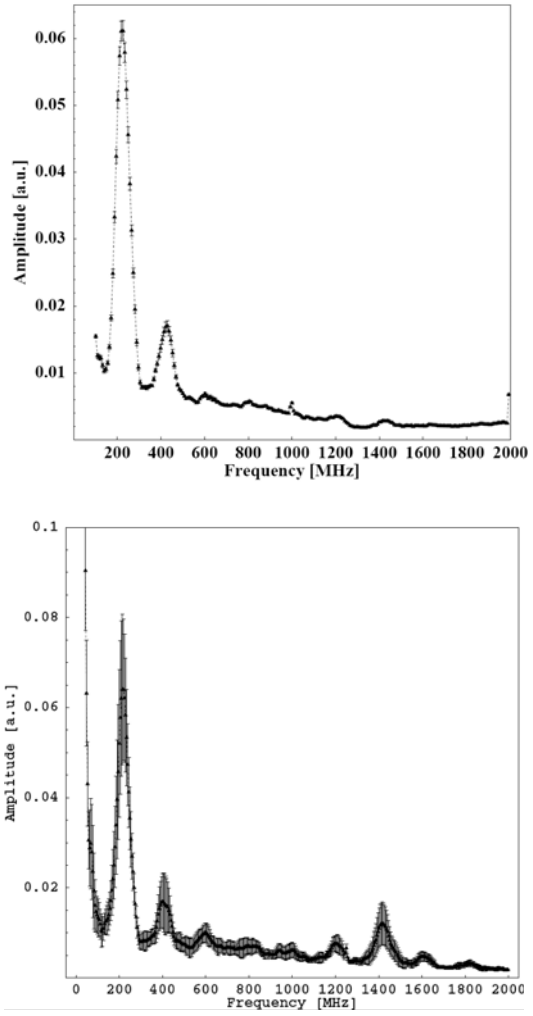

Figure A1: Unstable bunch spectra up to 2 GHz with RF OFF in 2001 (upper) and 2007 (lower), with similar beam parameters.

APPENDIX B: LOCALIZED SPS IMPEDANCE FROM PHASE BEATING VS. INTENSITY

By detecting the current-dependent phase advance between adjacent Beam Position Monitors (BPMs) localized impedances around the ring could be identified in principle. This method is very attractive as it could help us to identify the remaining 13 MΩ/m of vertical "total" impedance, which for the moment are still unknown. Measurements have been performed in 2007, but the data still have to be analyzed in detail, in particular to correctly take into account the effect of the detuning impedance. An example of what was obtained in 2003 is shown in Fig. B1 [24]. It was concluded that impedance is mainly concentrated in a few locations where the injection (MKP) kickers and extraction (MKE) kickers are, where the RF cavities are, and another location (in sextant 5) where the instrumentation is.

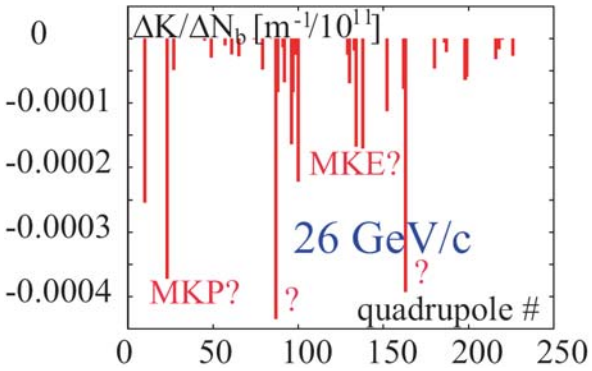

Figure B1: Local impedance distribution around the SPS ring from the measured current-dependent phase beating at 26 GeV/c in 2003.

APPENDIX C: BEAM POSITION MONITORS

The impedance of the 108 horizontal beam position monitors (BPMH) and 108 vertical beam position monitors (BPMV) have been simulated with MAFIA [25]. The resulting longitudinal and vertical broad-band impedances (for all the BPMs) are Im $[Z_l/n] = 0.02$ Ω and Im $[Z_y] = 0.07$ MΩ/m respectively, while the four most critical trapped modes (also for all the BPMs) are given in Table C1. It can be seen that the contribution of the BPMs to the broad-band impedance of the SPS machine is small. Furthermore, HEADTAIL simulations were performed with the four trapped modes and they revealed that the fast single-bunch vertical instability threshold was about one order of magnitude higher than the one measured [26]. The BPMs cannot therefore be held as the main responsible for the fast transverse instability observed in the SPS with low emittance bunches.

Table C1: Four most critical trapped modes for all the 108 horizontal and vertical beam position monitors (with the associated values of the betatron functions).

β_x [m]	β_y [m]	f_r [GHz]	R_y [MΩ/m]	Q
103	21	0.537	500	1951
103	21	1.836	254	3367
22	101	0.786	180	2366
22	101	2.270	222	5880

APPENDIX D: VACUUM PUMPING PORTS

The SPS machine comprises 216 main quadrupole magnets alternately focusing (QF) and defocusing (QD), in a classic FODO lattice, with a half cell length of 32 m. In the arcs, the space between the quadrupoles is occupied by 4 main bending magnets (MBA = dipole with large horizontal aperture and MBB = dipole with large vertical aperture) and a short straight section (SSS = Short Straight Section girder supporting BPM and correctors, together with, various multipole magnetic correction elements at different locations around the SPS).

Both longitudinal and transverse impedances of the (shielded) transitions [2,3] have been simulated with MAFIA. The resulting longitudinal and vertical broad-band impedances for the 96 transitions QD_MBB, 90 transitions MBB_MBA, 90 transitions QF_MBA, 180 transitions MBA_MBA and 192 transitions MBB_MBB (i.e. 648 transitions in total) are Im $[Z_l/n] = 0.02$ Ω and Im $[Z_y]$ = 0.2 MΩ/m respectively, which are small compared to the measured values. The next step will consist to examine in detail the remaining kickers and septa which do not have shielded transitions.

APPENDIX E: RF CAVITIES

There are four travelling-wave 200 MHz RF cavities, two with four sections and two with five sections, and each section is composed of 11 drift tubes. The real and imaginary parts of the (normalized) longitudinal impedance for all these cavities are plotted in Fig. E1. Due to the shape of the imaginary part of the impedance near 200 MHz, the effective impedance is very sensitive to the bunch length, as can be seen in Fig. E2. Over the last years measurements have been performed for total bunch lengths between ~ 2 ns and ~ 3 ns. It is seen from Fig. E2 that for a total bunch length of 3 ns the imaginary part of the effective (normalized) longitudinal impedance is higher than the one for a total bunch length of 2 ns by 1.7 Ω, which represents 23% of the measured impedance in 2006.

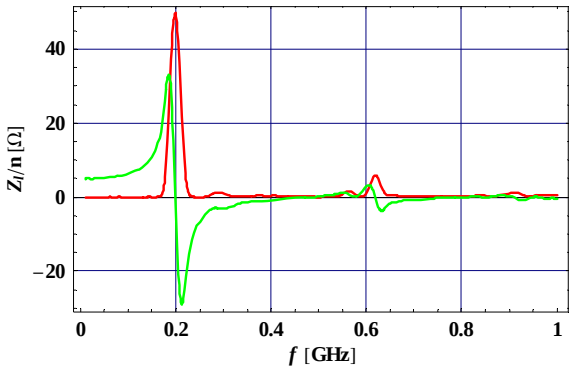

Figure E1: Real (red curve) and imaginary (green curve) parts of the longitudinal impedance vs. frequency for all the four travelling-wave 200 MHz RF cavities.

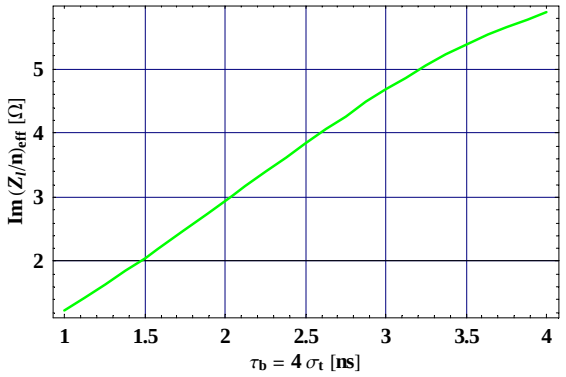

Figure E2: Imaginary part of the effective (normalized) longitudinal impedance vs. total bunch length τ_b (4 σ_t Gaussian fit).

APPENDIX F: HIGH ENERGY BEAM DUMP ABSORBER (TIDVG)

The TIDVG is the SPS high energy beam dump absorber with Graphite core installed in 1999. A titanium (Ti) coating of 1-2 microns was applied to the graphite blocks in order to prevent risk of polluting with graphite dust the downstream SPS injection kicker (~7 m downstream). As there was no high temperature treatment of the graphite applied, a poor condition of the graphite surface was obtained, which means that the Ti coating was very fragile. For this purpose, a Ti foil (with a thickness of ~ 50 μm) was installed as an additional protection.

A visual inspection in March 2004 of the TIDVG (removed for LSS1 re-cabling) revealed a deformation of the Ti foil, which was traced back to be the reason for the limitation of the SPS vertical aperture.

During the 2007 run there was no Ti foil. Preliminary computations of the longitudinal resistive-wall impedance with or without the Ti foil revealed that the imaginary part of the effective (normalized) longitudinal impedance is much smaller than 1 Ω, and that the absence of the Ti foil in 2007 cannot be responsible for the measured increase.

Experimental studies on the SPS electron cloud

G. Rumolo*, G. Arduini, E. Métral, E. Shaposhnikova,
E. Benedetto, R. Calaga[(a)], G. Papotti, B. Salvant[(b)]
CERN, Geneva, Switzerland, [(a)] BNL, Brookhaven, USA, [(b)] EPFL, Lausanne, Switzerland

Abstract

One of the most important limitations in the performances of the CERN-SPS is presently the Electron Cloud Instability (ECI). Hence, defining its dependence on energy with confidence is an indispensable asset to direct the efforts for all the upgrade studies.
Macroparticle simulations carried out with the HEADTAIL code [1] have shown that the ECI mechanism is subtle and the scaling laws valid for the Transverse Mode Coupling Instability cannot be applied to it [2]. The reason lies in the fact that the electron dynamics, while a bunch is going through an electron cloud, is heavily affected by the transverse beam size. In fact, transversely smaller beams can enhance the electron pinch and lower the intensity threshold for the bunch to be unstable. Hence, higher energy beams, though more rigid, can be more unstable due to their smaller transverse size (with constant transverse normalized emittance).
During the 2007 run a measurement campaign has been carried out at the CERN-SPS to prove experimentally the outcomes of macroparticle simulations.

INTRODUCTION AND MOTIVATIONS

Plans for the Large Hadron Collider (LHC) performance upgrade include the improvement of the existing LHC injectors and/or the design of possible new rings in the injector chain [3]. Several scenarios, aimed at overcoming the existing bottlenecks, are presently being taken into consideration. One option, based on the replacement of the Proton Synchrotron (PS) ring with the PS2 [4], foresees an increase of the injection energy into the existing SPS from the present 26 GeV/c to 50 GeV/c. This is believed to be beneficial for the machine in many regards (e.g., less space charge and intra beam scattering, more rigid beams against coupled bunch instabilities, no transition crossing, lower injection and capture losses) [2]. Furthermore, it would allow for an upgrade of the SPS to a 1 TeV extraction energy ring, with the related advantages for injection into the LHC.
However, the SPS upgrade plan crucially depends on the effect of a higher injection energy on the collective phenomena that are presently believed to be the real limitation in the SPS performance. One of them is TMCI, which was observed in the SPS for special intense bunches with low longitudinal emittance [5, 6]. Therefore, it could be a potential limiting factor in the future, especially taking into account the enhancement of the impedance of the SPS caused by the installation of 9 new extraction kickers in the ring since 2003 and the higher charge per bunch that should be injected into the SPS [7]. In addition, the vertical single bunch ECI has been limiting for a long time the number of batches that could be injected into the SPS and it could be overcome by beam scrubbing and subsequently operating the ring with a high vertical chromaticity (which nonetheless can be harmful for the beam lifetime) [8]. A detailed study on the energy dependence of the threshold for the onset of these instabilities is essential to assess a global beneficial effect of the pre-injector upgrade without unwanted side effects.
The scaling law of the TMCI threshold with energy was already addressed in [9]. Under conservation of the longitudinal emittance and assuming bunches always matched to their buckets, the TMCI threshold only depends linearly on the slip factor $|\eta|$, and therefore a higher injection energy would certainly help to operate the machine farther from this limitation. Besides, preliminary studies of the dependence of the ECI threshold on energy were done, which showed that the related scaling law cannot be trivially derived from the existing TMCI theories. In fact, a first attempt of analytical approach using a broad-band resonator with beam dependent parameters showed that it may become surprisingly unfavourable at high energies far from transition, under the further assumptions of conservation of the bunch length and the normalized transverse emittances. A comprehensive study of the effect of higher injection energy on the ECI has been therefore carried out numerically and experiments are being done in the CERN-SPS with an LHC-type beam to verify it.

SUMMARY OF SIMULATION RESULTS AND CODE-TO-CODE BENCHMARK

Table 1 shows a list of the essential parameters used for the numerical study (typical LHC-type bunch in the SPS). The main assumptions of our model are:

- The longitudinal emittance and the bunch length are kept constant. The momentum spread $\Delta p/p_0$ is re-scaled and the matched voltage re-adjusted accordingly when changing the energy. The matched voltage goes like $|\eta|/\gamma$ with energy. This constraint could be relaxed by increasing the longitudinal emittance.
- The normalised transverse emittances are constant.

* Giovanni.Rumolo@cern.ch

Consequently the transverse beam sizes are scaled down $\propto \sqrt{1/\gamma}$ when changing the energy. This constraint comes from the LHC requirements in terms of transverse emittance.

Table 1: Parameters used in our study

Parameter	Symbol	Unit	Value
Circumference	C	km	6.9
Momentum	p_0	GeV/c	14–450
Norm. transv. emitt.	$\epsilon_{x,y}$	μm	2.8
Long. emitt. (2σ)	ϵ_z	eVs	0.35
Bunch length	σ_z	m	0.3
Bunch population	N		1.1×10^{11}
Number of bunches	N_b		72
Bunch spacing	T_b	ns	25
Number of trains			4
Train spacing		ns	200
Vertical tune	Q_y		26.13
Momentum comp.	$\alpha = 1/\gamma_t^2$		0.00192
Av. cloud density	ρ_e	m^{-3}	10^{12}

HEADTAIL simulations

The dependence of the ECI threshold on energy has been simulated with the HEADTAIL code [1]. The kick approximation is used for the action of the electron cloud on the bunch, namely the action is lumped in one or more points along the ring. The N_{sl} slices of which the bunch is made, interact with the electrons (modeled as N_e macro-particles and uniformly distributed with zero initial speed in the cross-section of the pipe) after one another. Each slice sees the electron cloud as deformed by the interaction with the preceding slices. The distortion of the cloud distribution induced by the bunch traversing it, is the mechanism that couples body/tail motion of the bunch with the head motion and potentially causes instability. To gain an insight into the physical mechanism that determines the type of dependence of the instability threshold on energy, we have first looked for thresholds at different energies assuming an electron cloud with initial uniform density (and fixed average value) concentrated in the dipole regions of the machine (which is supported by the SPS experimental observations). Figure 1 shows that the ECI threshold drops down with energy like $1/\gamma$ under the given assumptions. A very weak dependence on $|\eta|$ seems to be hinted to by the two points at 20 and 26 GeV/c (equidistant from transition), which exhibit the same threshold. Our explanation for this unusual behaviour is that, although the bunch becomes more rigid at a higher energy, and therefore less sensitive to collective effects, it also becomes transversely smaller, which enhances the effect of the electron cloud pinch. As a result, the "head wake" of the EC (calculated as the response, in terms of electric field averaged over the beam cross section, to a small displacement of the bunch head) has a higher frequency and amplitude at higher energies. Besides, the matched voltage changes like $|\eta|/\gamma$, which causes a decrease of the synchrotron tune far from transition. This translates into a slower motion in the longitudinal plane and therefore larger time scales for natural damping.

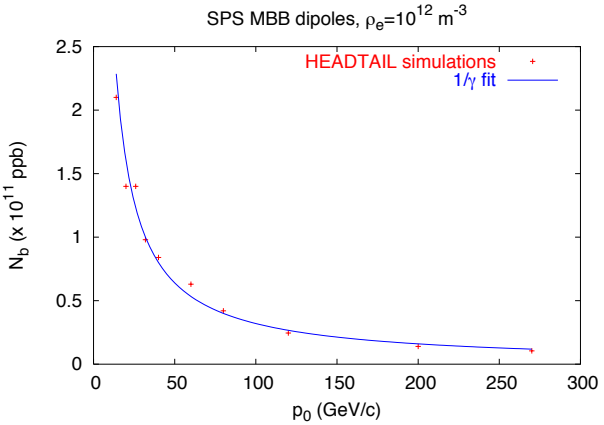

Figure 1: Simulated ECI threholds at different energies, study done with fixed e-cloud density.

The HEADTAIL code has been recently upgraded to deal with more realistic initial distributions of the electrons. The necessity of a more refined model to gain more confidence in the predictions was evident, because the average electron density over the full pipe cross section can significantly differ from the local density around the bunch, which is more directly related to the development of instabilities. Therefore, HEADTAIL can now load the 4D electron distribution as produced by the build up code ECLOUD [10] and use it for the instability simulation. The integration ECLOUD-HEADTAIL, though not completely self-consistent, is certainly a significant step forward with respect to the old model, which only interfaced the two codes through the value of the average density over the pipe section.
The result of a scan extending to 270 GeV/c over a few points is shown in Fig. 2 for a maximum SEY δ_{max} of 1.4. The decreasing trend of the threshold with increasing energy is confirmed. Nevertheless, the strong $1/\gamma$ decaying law found with the fixed density cloud model turns into a smoother decrease of the threshold with energy, which simply levels off to the threshold for electron cloud build up at energies higher than ≈ 100 GeV/c.

Comparison with the PEHTS code

To cross-check the validity of this result a benchmark was carried out with the PEHTS code [11], which was separately developed by K. Ohmi and can also simulate the interaction of a positively charged bunch with an electron cloud. Two reference cases from Fig. 1 (and parameters from Table 1), far apart from each other, were chosen to be simulated with the PEHTS code. The two values of beam energy used for the benchmark are 40 and 270 GeV/c. Figures 3 shows the beam vertical rms-size evolution for dif-

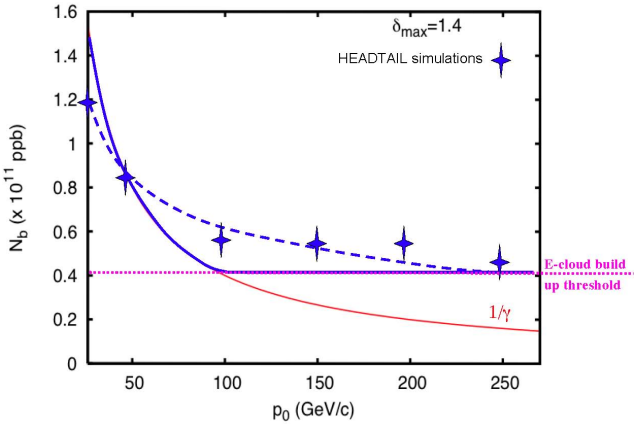

Figure 2: Simulated ECI thresholds at different energies, study done with quasi-self-consistent e-cloud distribution.

ferent bunch populations, as resulting from PEHTS simulations [12]. It can be deduced that the thresholds for instability lie at around 7×10^{10} and 2×10^{10} for 40 and 270 GeV/c, respectively. Therefore, these values are very close to those calculated with HEADTAIL and confirm the decreasing trend of the ECI threshold with energy, as was anticipated in our study.

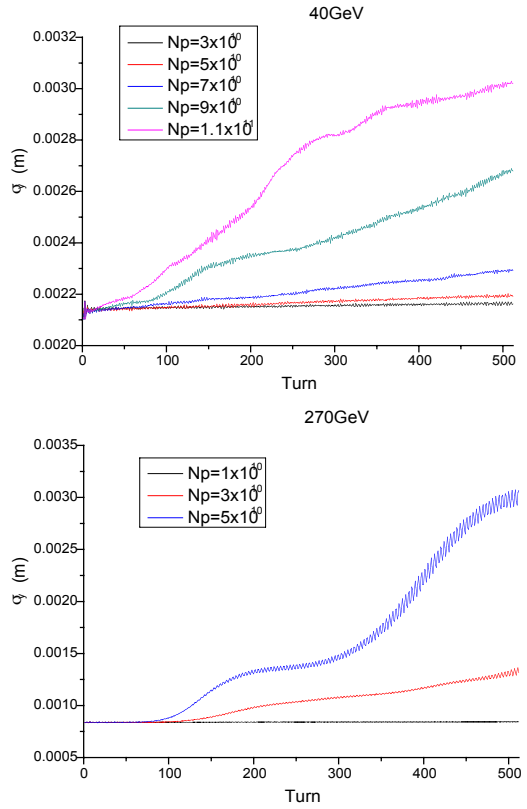

Figure 3: Emittance evolution for different bunch population at 40 (top) and 270 GeV/c (bottom). Courtesy of H. Jin and K. Ohmi

EXPERIMENTAL CAMPAIGN AT THE SPS (AS OF SEPTEMBER 2007)

An experimental study to prove the scaling law found by simulations has been carried out at the CERN-SPS during the 2007 run. The studies were essentially done using two possible SPS cycles (see Fig. 4). In the short MD1 cycle (top part of Fig. 4), parallel to physics, only one batch of the LHC beam was injected in the SPS at 26 GeV/c and then accelerated to 37 GeV/c. Two flat parts of about 1 s were available at bottom and top energy, during which it was attempted to induce ECI. With this cycle it was expected to see a larger effect before the scrubbing run, when the electron cloud could be potentially a problem already at the tail of one batch alone. In the long dedicated supercycle for MDs (bottom part of Fig. 4) we used an LHC-type beam made of 1 to 3 batches with 72 bunches each. The beam was injected into the SPS at 26 GeV/c during a flat bottom of 10.86 s, then accelerated to an intermediate plateau of 55 GeV/c (about 6 s) and eventually taken to 270 GeV/c and sent onto a dump. The 55 GeV/c flat portion would serve to show that the beam still suffers from ECI at this higher energy. Observing the beam behaviour at this energy would be specially interesting, because it lies close to a potential value as new SPS injection energy after the upgrade of the pre-injectors.

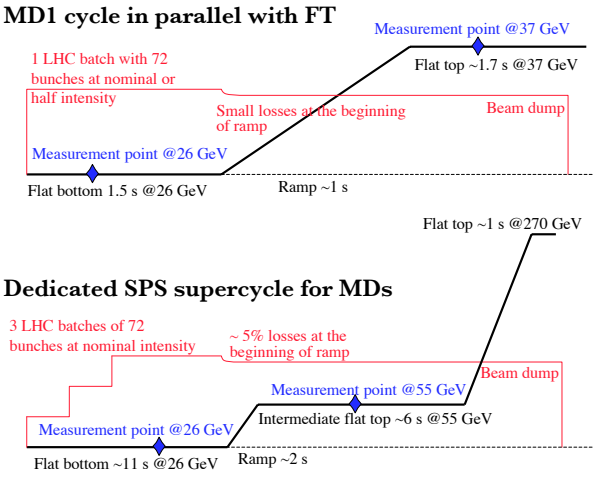

Figure 4: SPS cycles that were used to carry out ECI measurements at different energies in the SPS.

Measurements at 26 and 37 GeV/c

The experiment at 26 and 37 GeV/c was conducted using the short MD1 cycle. After having one batch injected into the SPS in stable conditions, a vertical chromaticity bump was created, which quickly lowered chromaticity in the middle of the flat bottom or of the flat top. No significant difference was observed between the measurement sessions that took place before scrubbing and those after the scrubbing run. Also the damper gain settings did not appear to influence the results. In this way we could deter-

mine the limit value of vertical chromaticity below which the beam would become unstable at both energies. Threshold chromaticity values were therefore identified to be 2.2 and 3.3 (in Q' units) at 26 and 37 GeV/c, respectively, and did not change over the different MD sessions done with this cycle. The instability manifested itself with beam loss in the tail of the batch at both energies. Figure 5 shows that, after the instability developed, the last part of the batch is quickly lost. This feature points to an electron cloud as possible source of the instability, but does not rule out possible coupled bunch instabilities caused by a long range wake field that can extend over one batch length but does not accumulate the effect turn after turn. Actually, the electron cloud signal as observed from the e-cloud monitor appears on the ramp, where the bunch gets shorter, and significantly extends to the flat top, as well (see Fig. 6). No strong signal is observed at 26 GeV/c in standard operation. However, during one of the MD sessions a successful attempt was made to trigger a stronger electron cloud at 26 GeV/c by means of a voltage bump, which causes a localized bunch shortening on the flat bottom (Fig. 7). No significant difference in the instability evolution at 26 GeV/c was observed under these conditions (nor depending on whether the chromaticity bump was created within the voltage bump or outside of it). This induced us to believe that the main driving force for the instability observed at 26 GeV/c was not electron cloud.

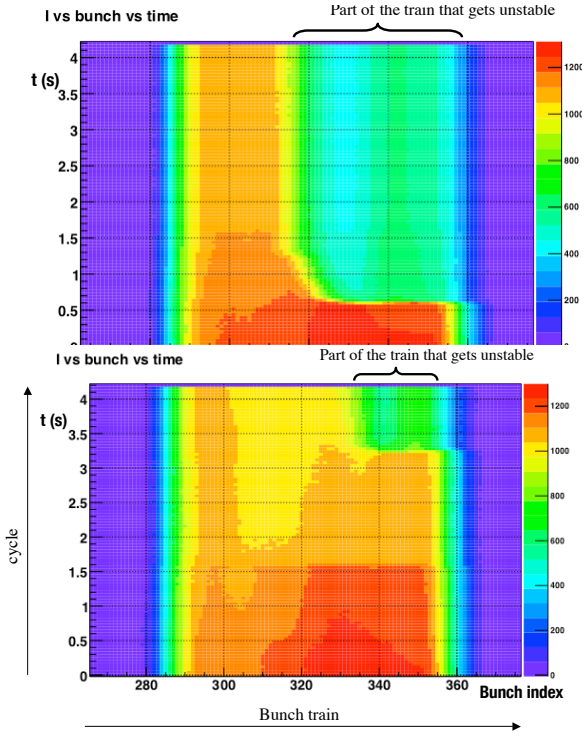

Figure 5: Bunch by bunch intensity evolution with an unstable beam. Top picture shows the intensity evolution when the instability is driven at 26 GeV/c, the bottom picture corresponds to an instability driven at 37 GeV/c

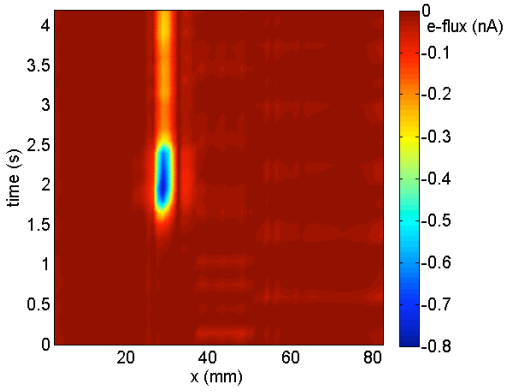

Figure 6: Measured electron cloud build up during the MD1 cycle.

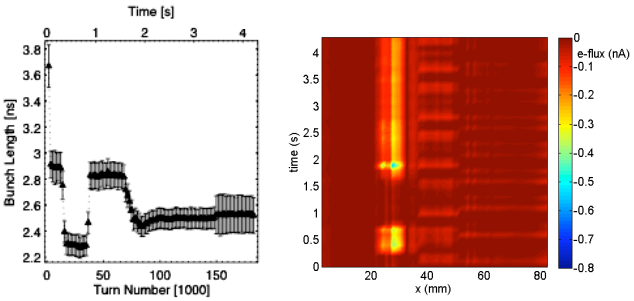

Figure 7: Bunch length (left) and measured electron cloud build up during the MD1 cycle (right) when a voltage bump is appled at the flat bottom in order to shorten the bunch and enforce the electron cloud at 26 GeV/c.

Figure 8 shows the typical bunch by bunch centroid evolution over 1000 subsequent turns, acquired with the LHC-BPMs (i.e., beam position monitors that can provide turn by turn and bunch by bunch measurements). It is evident that the intra-batch motion exhibits some correlation and a traveling wave pattern at 26 GeV/c, with a possible single bunch component at the very end of the batch. However, at 37 GeV/c there was no evident sign of coupled bunch motion and the unstable bunch by bunch motion at the tail of the batch looked uncorrelated, possibly induced by a single bunch effect. The difference between the two cases becomes more evident plotting the spectra of the LHC-BPM signals, Fig. 9. The upper pictures show the individual Fourier transforms of the time traces of each bunch separately (for 26 and 37 GeV/c), whereas the lower graphs are the complete 2D Fourier transforms of the signals. In the spectra of the bunch by bunch time traces, a coherent signal is obviously visible only in the tail of the batch, where bunches have acquired a coherent motion due to the instability. Two lines can be seen at 26 GeV/c, whereas one line (with possible side-bands) is visible at 37 GeV/c, which shifts upwards with the bunch number. The full 2D Fourier

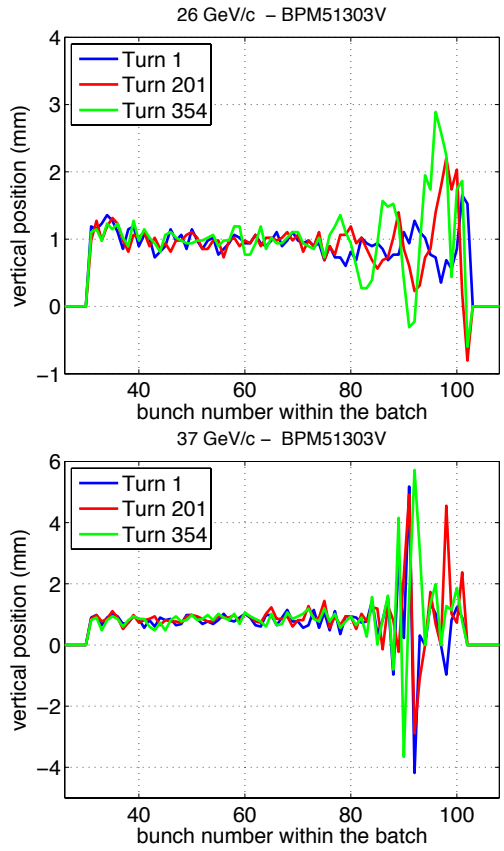

Figure 8: Bunch by bunch Δ_y signal of an unstable beam. Top picture shows three snapshots of the instability evolution along the batch at 26 GeV/c, the bottom picture corresponds to an instability driven at 37 GeV/c. Acquisition starts at turn 1.

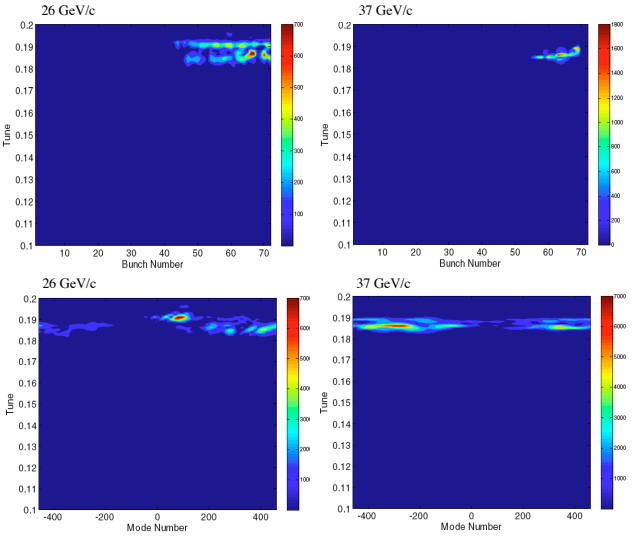

Figure 9: Fourier transforms of the bunch by bunch BPM signals from an unstable bunch at 26 (left) and 37 GeV (right). The top plots are the Fourier transforms of the bunch by bunch signals carried out indivudually over the acquisition time, whereas the bottom pictures represent the full 2D Fourier transforms of the 2D signal.

transform reveals one main peak at 26 GeV/c associated to the upper tune line (with a weaker component of the signal spread over all the bunch numbers and mainly associated to the lower tune line) and appears uniformly smeared over the bunch numbers at 37 GeV/c. The presence of a high peak in the 2D Fourier spectrum of the 26 GeV/c signal translates into a coupled bunch instability component dominant at this energy. The signal spread over all bunch numbers at 37 GeV/c indicates a dominant single bunch instability.

Measurements at 26 and 55 GeV/c

Using the LHC-type beam in the SPS on a long MD cycle as the one shown in the bottom illustration of Fig. 4, we tried to excite the ECI at 26 and 55 GeV/c. Figure 10 shows that, when injecting one (top) or 2 (bottom) batches into the SPS, a strong signal from the e-cloud monitor could be observed. The 2-stripe signal would be growing along the cycle. With 2 batches (Fig. 10, bottom picture) a sharp increase could obviously be seen at the flat bottom when the second batch got injected into the machine, but later on it would continue also over the ramp to the intermediate 55 GeV/c plateau, and become even more pronounced over the second ramp to 270 GeV/c. The reason could be a combined effect of bunch shortening and reduction of the transverse beam size. It is interesting to observe that, with one single batch inside the machine, the electron cloud evolution looks rather similar, but with one remarkable difference: the curious sudden appearance of a quite strong electron cloud signal after about 6 s from injection (Fig. 10, top picture). The reason of this puzzling behaviour was investigated, and it was found out that the signal appears when the uncaptured beam has completed a full turn and has smeared all over the machine. This coasting beam component can therefore trap the electrons between two subsequent passages of the batch through one section and allow a multi-turn electron cloud build up. The suspicion that this could be the cause was then easily confirmed by cleaning the gap with a kicker and thus observing the complete absence of any electron cloud signal all along the flat bottom.

To excite the instability, the chromaticity would be quickly reduced toward the end of the flat bottom (after all batches have been injected and possible transients have damped out) or in the middle of the intermediate plateau at 55 GeV/c. It was expected to observe ECI below some positive chromaticity value at both energy values. The transverse feedback system was kept on during these measurements. The outcome was that Q' could be set to a slightly negative at 26 GeV/c before an instability would set in, whereas at 55 GeV/c a Q' of about 4 units was the observed threshold for instability. The instability always started from the tail of the batch (or of the batches) and measurements with a different batch distribution (3 batches uniformly distributed around the ring) seemed to significantly stabilize

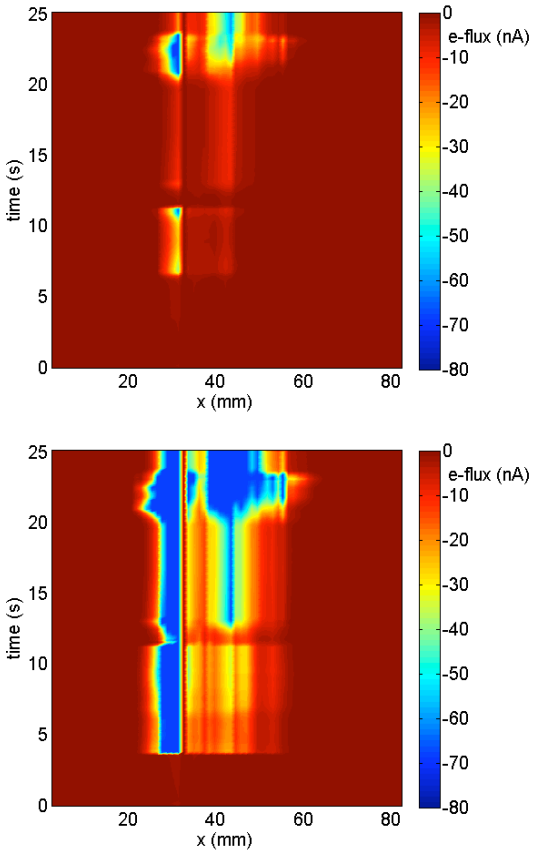

Figure 10: Measured electron cloud build up during the long dedicated MD cycle with only one batch (top picture) and with 2 batches injected into the SPS (bottom picture).

the beam at 55 GeV/c. Both elements pointed once again to either electron cloud or a coupled bunch phenomenon, or a combination of the two. A preliminary analysis of the bunch by bunch centroid evolution shows that the instability was of coupled-bunch type with a dominant low mode number both at 26 and 55 GeV/c. In some cases, a variety of modes could be seen, with a possible single bunch component. Nonetheless, these minor modes, where present, could not be easily disentangled from the dominant coupled bunch low number mode. Although these modes should have been damped by the transverse feedback, there is a strong suspicion that actually they appeared because they were induced by an incorrect setting of the damper.

CONCLUSIONS

In conclusion, experiments carried out at the SPS until September 2007 have given evidence of electron cloud inside the machine (depending on the operating conditions), but they are not conclusive on the scaling law of the instability threshold, because of the presence of other collective phenomena in most of the measurements, which made it difficult to isolate the contribution coming from the electron cloud.
In particular, the electron cloud was observed in the SPS with the e-cloud monitor

- At 26 GeV/c with a bunch shortening voltage bump or enhanced by uncaptured coasting beam
- A clear signal could be seen especially at higher energies (shorter bunch, smaller transverse sizes)

Concerning the instability, it can be concluded that the LHC beam was observed to be vertically unstable in the SPS at

- 26 GeV/c for vertical $Q' < 0$–2 (with 1 to 3 batches, and depending on the feedback system settings)
- 37 GeV/c for vertical $Q' < 3.3$ (with 1 batch)
- 55 GeV/c for vertical $Q' < 4$ (with 1 to 3 batches)

In most of these cases it was observed that only the tail of the bunch train(s) is affected by the instability. However, the pattern of the instability along the bunch train shows a coupled bunch instability (not excluding that single bunch effects were also present but not dominant) both at 26 and 55 GeV/c. In particular, the measurements conducted at 26 and 55 GeV/c were probably affected by a not optimum setting of the transverse feedback, which induced coupled bunch oscillations instead of damping them. Only at 37 GeV/c the principal instability seems to be of single bunch type and can be associated with electron cloud, since it only affects the last few bunches of the batch and does not seem to have any coherent bunch to bunch pattern.
Therefore, drawing conclusions on the dependence of the electron cloud instability on the beam energy is not straightforward from the data so far collected. It is foreseen in the next dedicated MD sessions to try to observe ECI at 55 GeV/c and assess its dependence on the beam transverse size by using controlled transverse emittance blow up with the transverse damper. This would be the easiest indirect proof of the mechanism responsible for the scaling law of the ECI threshold with energy, as was found with our simulations.

ACKNOWLEDGMENTS

The authors would like to thank T. Bohl, D. Quatraro, F. Roncarolo, R. Tómas and F. Zimmermann for inspiring discussions, help and support. Special thanks go to H. Jin and K. Ohmi for their availability in benchmarking our codes.

REFERENCES

[1] G. Rumolo, and F. Zimmermann, Phys. Rev. ST Accel. Beams **5**, 121002 (2002)

[2] G. Rumolo, E. Métral, and E. Shaposhnikova, in Proc. of the LUMI'06 Workshop, Valencia, Spain, 16-20 October 2006, edited by W. Scandale, T. Taylor and F. Zimmermann, published as CERN Yellow Report CERN-2007-002

[3] Proceedings of the LUMI'05 Workshop "Scenarios of the LHC Luminosity Upgrade", Arcidosso, Italy, 31 August-3 September 2005, http://care-hhh.web.cern.ch/CARE-HHH/LUMI-05/default.html

[4] M. Benedikt *et al.*. "Preliminary accelerator plans for maximizing the integrated LHC luminosity", PAF, January 2006, http://paf/web.cern.ch/paf

[5] G. Arduini and A. Verdier, "Poor man pilot and TOTEM bunches", CERN AB-Note-2003-017 (MD)

[6] G. Arduini, H. Burkhardt and E. Métral, "Observation of a fast single-bunch transverse instability on protons in the SPS", CERN AB-Note-2003-093 (MD)

[7] G. Rumolo, E. Shaposhnikova and V. G. Vaccaro, CERN-AB-2005-088-RF (2005)

[8] G. Arduini *et al.*, CERN-SL-2001-003-DI (2001)

[9] G. Rumolo, E. Métral, E. Shaposhnikova, "Simulation Study on the Energy Dependence of the TMCI Threshold in the CERN-SPS", in Proc. EPAC'06, Edinburgh, Scotland, June 26-30, 2006

[10] G. Rumolo and F. Zimmermann, CERN-SL-Note-2002-016-AP (2002)

[11] K. Ohmi and F. Zimmermann, Phys. Rev. Lett. **85**, 3821 (2000)

[12] H. Jin and K. Ohmi, private communication, 2007.

FAST CYCLED SUPERCONDUCTING MAGNETS FOR THE UPGRADE OF THE LHC INJECTOR COMPLEX

L. Bottura, G. Kirby, R. Maccaferri, C. Maglioni, V. Parma, G. de Rijk, L. Rossi, W. Scandale, L. Serio, D. Tommasini, A. Verweij, CERN, Geneva, Switzerland.

Abstract

An upgrade of the LHC injection chain, and especially the sequence of PS and SPS, up to an extraction energy of 1 TeV, is one of the steps considered to improve the performance of the whole LHC accelerator complex. The magnets for this upgrade require central magnetic field from 2 T (for a PS upgrade) to 4.5 T (for an SPS upgrade), and field ramp rate ranging from 1.5 to 2.5 T/s. In this paper we discuss under which conditions superconducting magnets are attractive in this range of operating field and field ramp-rate, and we list the outstanding issues to be adddressed by a dedicated R&D.

MAGNET NEEDS AND R&D TARGETS

Magnet requirements

The main motivation for a CERN R&D program on fast cycled superconducting magnets comes from the need to upgrade the LHC injector chain. A definition of the objectives of this R&D at CERN was initiated at the workshop ECOMAG [1], pursued in several proposals for specific magnet work [2], [3], and appeared among the declared Magnet R&D objectives of the medium term plan (2008-2011) for the Scientific Activities at CERN [4]. Following the discussion at the workshop LUMI-06 on luminosity upgrades for the LHC [5], and the outcome of the PS2 Study Group [6], the range of parameters identified for the relevant magnet designs has been narrowed to the values reported in Table I. Aperture requirements are defined for the PS upgrade option PS2a (rectangular, with height and width 60 mm x 84 mm [6]), but not yet finalised for the other magnets and in particular for an SPS upgrade (values quoted in Table I are estimates). The present baseline is a PS2 accelerating to 50 GeV, i.e. option PS2a in Table I. An SPS extraction around 1 TeV would already be desirable for the present LHC, and indeed necessary for an energy upgrade of the collider.

As discussed in [7] superconducting magnets could provide a compact and cost effective alternative to the normal conducting baseline considered for an upgrade of the PS with extraction energy of 50 GeV (maximum field of 1.8 T, option PS2a). Above 2 T, i.e. for an increased extraction energy at the PS, and for an energy upgrades in the SPS, superconducting magnets are *the* enabling technology, and, in practice, the only possible choice. We remark, however, that the present PS2 baseline makes an energy upgrade of the SPS up to 1 TeV quite challenging. The concern is the control of the field quality in superconducting magnets with low injection field (0.23 T) and large field swing (20). HERA, that had working conditions in the same range, was a very slow-ramping accelerator, and yet witnessed difficulties at the level of the compensation of field errors.

Table I. Range of magnet design parameters considered for an upgrade of the CERN injector chain, compiled from [5] and [6].

	PS2a	PS2b	SPS2a	SPS2b
Injection energy [GeV]	4	4	50	75
Extraction energy [GeV]	50	75	1000	1000
Injection field [T]	0.144	0.144	0.225	0.337
Extraction field [T]	1.8	2.7	4.5	4.5
Good field diameter [mm]	103	*≈100*	*≈75*	*≈75*
Ramp time [s]	1.1	1.1	3.0	3.0
Flat-top/-bottom time [s]	0.1	0.1	3.0	3.0
Field ramp-rate [T/s]	1.6	2.5	1.4	1.4

R&D issues

As far as operating conditions are concerned, the magnet parameters derived from the upgrade requirements of Table I, and in particular the maximum field and maximum ramp-rate, are *per se* not critical. Indeed, the peak field and aperture required for the SPS2 options are those produced routinely at Tevatron (4 T over 75 mm) and HERA (5.2 T over 75 mm), and largely surpassed at the LHC (8.3 T over 56 mm). The difficulty, however, is to achieve the required repetition rate (ramping 30 to 1000 times faster than at Tevatron, HERA and LHC), economically and reliably, as required by an injector. A detailed analysis of the R&D issues is reported in [8]. Technology demonstration is required in the following fields:

- AC loss. The control and reduction of AC loss has foremost importance to reduce the cryoplant investment and operation cost, and limit the temperature excursions in the conductor. This work implies material developments (superconducting strand and cable) as well as specific magnet design and optimization;
- Cooling. The heat loads on the magnet, and especially those originating from the AC loss and beam heating, must be removed efficiently to warrant a margin sufficient for stable operation. Suitable cooling schemes require design, optimization and test in relevant conditions;
- Quench detection and protection. Protection of superconducting magnets is especially demanding in case of fast ramping machines due to the relatively high inductive voltages in comparison to the voltage developed by a resistive transition. Voltage compensation and magnet protection must be proven in the presence of an inductive voltage

during ramps that can be as large as 1000 times the detection threshold;
- Field quality, in particular the contribution of eddy currents in the superconductor and iron yoke is difficult to predict, control and measure at the desired resolution during fast ramps;
- Material fatigue, over several hundreds million cycles, influencing material selection and, possibly, requiring dedicated testing;
- Radiation dose from beam losses, which requires careful material choice, and consideration on shielding and maintenance.

Targets for a magnet R&D

Rather than taking the single design parameters listed in Table I, and address feasibility and performance of each magnet variant, we have attempted to specify a more generic target for magnet R&D. As discussed in [8] and [9], it is possible to specify a generic R&D target for the magnet by taking as performance indicator the product of the maximum field and the maximum field ramp-rate. The envelope of needs for PS2, SPS2, as well as present developments at companion laboratories, recalled in a later section, tend to cluster along a line with B_{max} x $(dB/dt)_{max}$ = 7. This is shown in Fig. 1 (reproduced from Ref. [8]).

A suitable and scalable R&D target for the demonstration of the technology of fast-cycled superconducting magnets is then a magnet model of relevant length (typically longer than 1 m) that achieves:

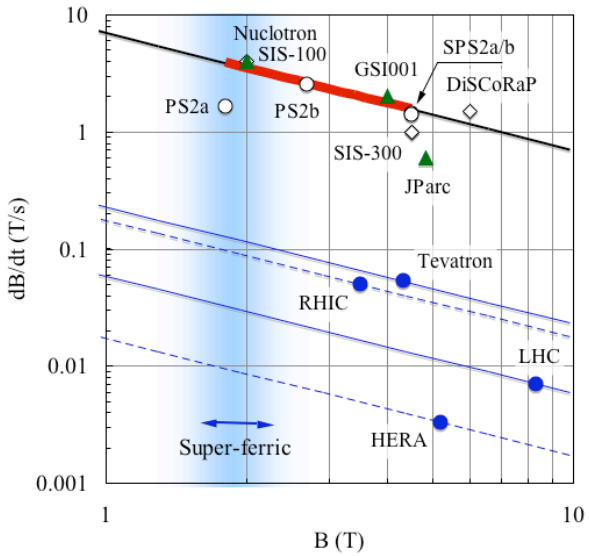

Figure 1. Scatter plot of $(dB/dt)_{max}$ vs. B_{max} for the magnet parameters of Table I (upgrade of the CERN injector chain), and various magnets from operating accelerators, demonstration prototypes and design studies, reproduced from [8]. The solid line represents the R&D target at B_{max} x $(dB/dt)_{max}$ = 7 T^2/s. The R&D range is the thick portion of the solid line. The shaded area of field around 2 T is the typical range of superferric magnets.

- nominal operating conditions of peak field and ramp-rate, such that B_{max} x $(dB/dt)_{max}$ = 7 T^2/s, cycling over long times (typically more than 12 hours) to prove periodic steady state operation relevant for an accelerator;
- AC loss below 5 W/m of magnet to provide an economic option to normal-conducting magnets (see the discussion in the next section);
- robustness and reliability, demonstrating stable operation in sequences of rapidly varying cycles (i.e. the equivalent of an accelerator supercycle), and a low rate of fake quench detection (typically below 10^{-6}), possibly undergoing an accelerated life tests to simulate the expected fatigue over 20 years of operation.

This target was specified in [9] at a bore field larger than 2 T (and specifically option PS2b in Table I) with the intention to focus on coil-dominated magnets, rather than iron-dominated magnets that would be the natural choice for a bore field below 2 T. As discussed in the next section, the result of magnet and system design studies have driven towards a reduction of the bore field, yet maintaining the overall objective outlined so far.

A SUMMARY OF DESIGN STUDIES

A number of design studies were pursued in 2007 to identify the preferred design options and quantify performance of fast cycled superconducting magnets for the upgrade of the LHC injectors.

The first study, described in [7], produced a design and cost evaluation of superconducting dipoles and quadrupoles for the PS2+a, comparing the cost figures to the estimates available for a normal conducting machine [10]. The design chosen, with cold iron, was such that the total magnet volume was minimised, thus reducing the material cost and overall mass. The result was spectacular in terms of saving: the mass of the 3 m long dipole could be reduced from about 15 tons (for the normal conducting design) to about 2 tons (for the superconducting option). For the quadrupoles a similar saving ratio was possible. This saving in capital costs for the magnets was however partially offset by the cost of the 15 kW cryogenic plant, and by the associated operation costs [11]. The reason is that on an accelerator of the scale of the PS2, and with the present cost of electricity (40 CHF/MWh) the trade-off between the costs of a resistive electrical load (absent for superconducting magnets) and that of cryogenic operation (to be considered for superconducting magnets) is around 10 W/m of heat load per unit magnet length. With an estimate AC loss of about 5 to 8 W/m of magnet, the design selected was too close to the point of trade-off.

A second study, originally motivated by the discussion at ECOMAG [1], and completed in [8], was performed on a class of cos-θ magnets with cold iron, in a range of bore field from 2.5 T to 5 T, covering the PS upgrade option PS2b (with high extraction energy), as well as both SPS2

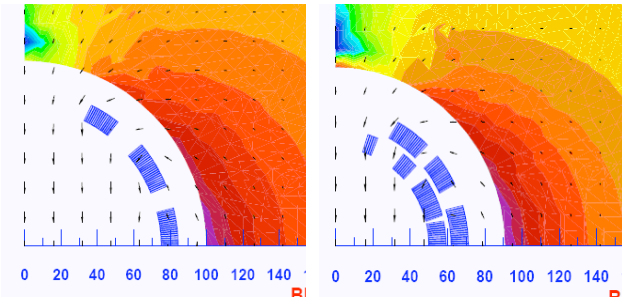

Figure 2. Cross section of the coils considered in the scaling study for PS2 (left) and SPS2 (right) superconducting, cos-θ magnets.

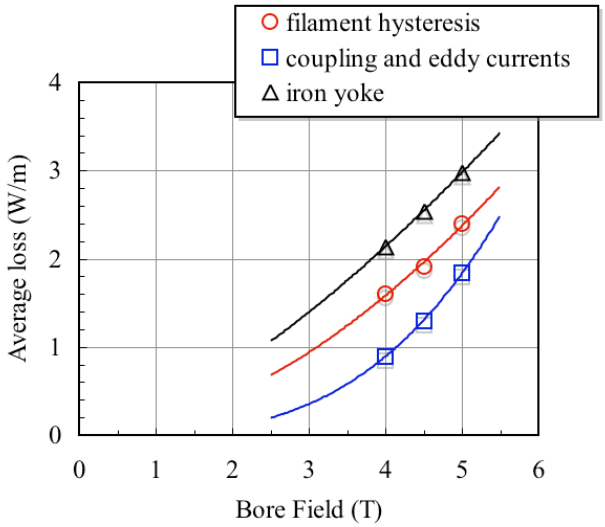

Figure 3. Dependence of AC loss contributions on the bore field in a cos-θ magnet with cold iron yoke. The calculations were performed for the magnet design detailed in [8], and refer to an SPS-like operation cycle lasting a total of 12 s.

options [8]. The typical cross esctions of single and double layer magnets is shown in Fig. 2. One of the main results of this study was a set of scaling law for the dependence of main magnet design parameters, such as volume, mass, inductance, energy and loss, on bore field and diameter. One such result is shown in Fig. 3, reporting the contribution of AC loss (hysteresis in the superconducting filaments, coupling in strands and cable, hysteresis in iron yoke) as a function of the bore field, having assumed a cycle reference as for SPS2 (3 s ramp-up and ramp-down, 3 s flat-top and flat-bottom, 12 s total). The level of loss at a bore field of 4.5 T is 5.7 W/m of magnet length, which in the case of a superconducting SPS2 would require a cryogenic installation of 34 kW @ 4.2 K. This translates to an electrical power need at the level of about 10 MW, which is a significant percentage of the total installed power for the present SPS (60 MW total power).

For a PS2 magnet, similar analysis and scaling by the reduced cycle time lead to the quoted value of 15 kW installed power @ 4.2 K. This corresponds to a required

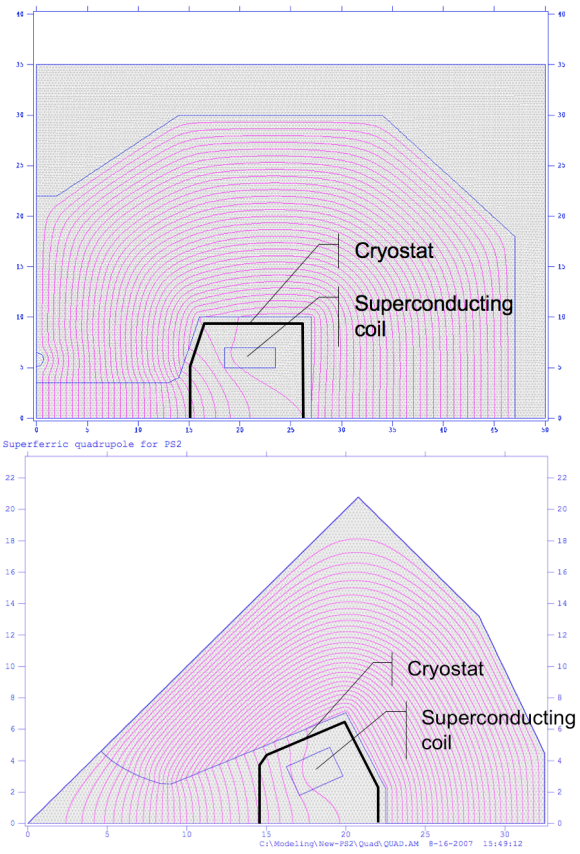

Figure 4. Schematic cross section of iron-dominated (*superferric*) designs of a dipole (top) and quadrupole (bottom) for the PS2.

electrical power of approximately 4.5 MW, which represents about half of the present power need for the PS, and tips the balance of operation costs in disfavour of a superconducting option, thus corroborating the results of [7].

An AC loss reduction with respect to the projected values is hence mandatory before a superconducting magnet option is attractive for use in the injectors. In addition, examining this result it is also evident that a large part of the loss takes place in the iron yoke. A corresponding saving could be achieved by intercepting these losses at temperature higher than the nominal operating point of 4.5 K, and especially in the case of a warm iron yoke. The drawback is the design complication in the thermal insulation and mechanical support of the coils.

This result motivated us to revisit the design study for a superconducting PS2 magnet, as discussed in [12]. Rather than aiming at the most compact magnet design, in this iteration we tried to achieve maximum efficiency in terms of power requirements and operation costs. This implied a reduction of AC losses to the minimum that can be reasonably achieved with available technology. For the specific conditions of the PS2, this criterion is best satisfied in the case of an iron-dominated magnet, of the type descibed in [13] and somewhat improperly named *superferric*. The iron is at room temperature (thus

removing the corresponding loss from the cryogenic load) and the superconducting coils provide the magneto-motive force, but can be placed in a location in the iron yoke where they are not exposed to the maximum field (thus reducing the field swing and ramp-rate, and the associated AC loss) nor the direct loss of beam particles. This choice also allows to minimise the variations with respect to the normal-conducting baseline magnet. The field quality is with good approximation identical in the two cases, being dominated by the shape of the iron pole, and the magnet bore is at room-temperature, with easy access (e.g. for beam pipe and collimation systems).

The main result was that we could produce a conceptual design of the main magnets (dipole and quadrupoles, shown schematically in Fig. 4) that would lead to a projected total power consumption of 7.6 MW, about half of the power required by a normal-conducting PS2, i.e. 14.6 MW. The operation costs would be in consequence significantly lower, by 1.6 MCH/year at the assumed electricity cost of 40 CHF/MWh. This advantage scales proportionally with energy cost, which is expected to increase in the near future. The additional cost for the construction of the magnet system, and associated auxiliaries (e.g. cryoplant) would amount to an estimate of 6 MCHF, which is a small fraction (a few %) of the total PS2 complex.

A *superferric* design with the above properties becomes an interesting option for an injector upgrade such as the PS2. In addition to a long term advantage for the cost of an operation that is projected over 20 years and longer, it provides operational flexibility in the duty cycle, as the absence of significant resistive losses allows long flat-tops, up to steady state.

ON-GOING R&D OUTSIDE CERN

The above R&D objectives and ideas are not isolated. Comparable to work is in progress at other European HEP and associated laboratories. Below is a summary of the relevant R&D on fast cycled superconducting magnets.

The Gesellschaft für Schwerionenforschung (GSI) in Darmstadt (D) is organizing the construction of a new Facility for Antiprotons and Ion Research (FAIR) [14]. The central part of this complex are the two rings SIS100 and SIS300 that will be built in the same tunnel and will have magnetic rigidity $B\varrho$ = 100 Tm and $B\varrho$ = 300 Tm respectively. To achieve this magnetic rigidity the dipoles of SIS100 will have a bore field of 2 T in a rectangular bore of 130 mm x 65 mm. The dipoles of SIS300 will require a peak field of 4.5 T in a round bore with a diameter of 100 mm. The magnets for these two rings are especially challenging because the operation mode of the complex foresees fast ramping of the energy. SIS100 should undergo a full cycle in 1 s, corresponding to a ramp-rate of 4 T/s. The ramp-rate requirements for SIS300, which will operate as a storage ring, are more soft, but still the aim is to ramp the ring at 0.5 to 1 T/s.

The SIS-100 R&D at GSI is supported by activities at the Joint Institute for Nuclear Research (JINR) in Dubna (R). A synchrotron similar to SIS-100, the Nuclotron, has been in operation at JINR since 1994 [15]. The Nuclotron dipole magnets are operated in the accelerator at a peak field of 1.5 T, ramping at 0.6 T/s, and have achieved a peak field of 2 T, ramping at 4 T/s.

For SIS-300, work has been performed in collaboration with Brookhaven National Laboratory (BNL). A prototype magnet, GSI001 with a single layer coil and similar in construction to the RHIC dipole, was built and tested successfully at BNL, demonstrating operation up to 4 T bore field in pulsed conditions up to 4 T/s. The magnet sustained short pulse sequences between 2 T/s (500 repeated cycles) and 4 T/s (3 repeated cycle) without quenching [16].

Since end 2006, Istituto Nazionale di Fisica Nucleare (INFN) has launched a prototype design and construction activity to demonstrate the feasibility and test the performance of a dipole for SIS-300 [17]. The INFN program, dubbed DiSCoRaP (Dipolo SuperConduttore Rapidamente Pulsato), originally aimed at a peak field of 6 T and a ramp rate of 1.5 T/s, is now focussing on the design and construction of a prototype with peak field of 4.5 T and ramp-rate of 1 T/s (compatible with the recent change of parameters for the SIS-300 dipoles).

The above magnet parameters have been reported in the scatter plot of Fig. 1 for comparison with the target of B_{max} x $(dB/dt)_{max}$ = 7 T^2/s.

Finally, CEA has proposed an R&D program (Supra Pulse) that aims at the realization of a demonstrator quadrupole magnet reaching 90 T/m over an aperture of 100 mm, ramping at 1 T/s on the coil.

PERSPECTIVE AND PLAN

From the discussion above, and given a realistic timeline of the upgrade of the injector complex, it is clear that an R&D on fast cycled superconducting magnets should be focussed in priority on PS2. For this reason we have defined as a primary objective the design, construction and test of a demonstration magnet that should achieve the operating conditions of PS2a (B_{max} = 1.8 T, $(dB/dt)_{max}$ = 1.6 T/s) with a thermal load per unit magnet length of the order of 2 W/m. The same magnet should be capable of operation at the same bore field, but increased ramp-rate $(dB/dt)_{max} \approx 4$ T/s to demonstrate scalability to the upper limit of present technology, i.e. B_{max} x $(dB/dt)_{max}$ = 7 T^2/s, with a thermal load per unit length of magnet well below 5 W/m. In addition to being directly relevant for the PS upgrade, this development is complementary to the work in progress in companion HEP laboratories, thus supplying an element of novelty in the picture. We expect the first results on this program by late 2008 (strand and cable) and during 2009 (magnet construction and test).

A significant portion of this R&D will be devoted to the development and procurement of suitable strand and cable [18]. This R&D is in practice common to all magnet options in the spectrum identified for the upgrade of the

LHC injectors, as well as the work at companion laboratories.

Finally, as a complement to the technology R&D for the PS2 demonstration, we plan to pursue the studies on superconducting options for an upgrade of the SPS by exploring magnet designs with the iron yoke at room-temperature, explicitly including the minimization of the cost of operation among the design targets.

REFERENCES

[1] L. Bottura, M. Buzio, D. Tommasini, Executive Summary, in Proceedings of ECOMAG HHH-AMT Workshop on Superconducting Pulsed Magnets for Accelerators, Frascati (Italy), 26-28 October 2005, CARE Conf-06-036-HHH, EDMS 819797.

[2] L. Rossi, Considerations on the Cost of the R&D and Construction for the Various Options for the Magnet Based Projects for CERN, under Request of PAF, November 2006, EDMS 754391.

[3] L. Rossi, Executive Summary of the White Paper Third Theme – Component 1: Magnet R&D, 28 November 2006.

[4] Scientific Activities and Budget Estimates for 2007 and Provisional Projections for the Years 2008-1010 and Perspectives for Long-Term, "White Paper", 5 October 2006.

[5] Proceedings of LHC LUMI 2006 - Towards a Roadmap for the Upgrade of the CERN & GSI Accelerator Complex, Valencia (Spain) 16 - 20 October 2006, available as draft at http://care-hhh.web.cern.ch/CARE-HHH/LUMI-06/Proceedings/proceedings_lumi06.htm

[6] M. Benedikt, Preliminary requirements for the design of the PS2 main magnets, CERN AB-Note-2007-029 OP, 13 June 2007.

[7] R. Ostojic, A Preliminary Analysis of the Options for the Magnet System of the PS2, AT-MEL Technical Note, 1 June 2007.

[8] G.A. Kirby, A. Verweij, L. Bottura, B. Auchmann, N. Catalan Lasheras, Fast Ramping Superconducting Magnet Design Issues for Future Injector Upgrades at CERN, Paper presented at MT-20, Philadelphia (USA), August 2007, to appear in IEEE Trans. Appl. Sup., 2008.

[9] L. Bottura, Proposal of a R&D Program on Fast Cycled Superconducting Magnets, June 28, 2007.

[10] Th. Zickler, Design Study of Normal Conducting Magnets for the CERN PS2, CERN AT-MEL Technical Note, EDMS 855337, June 25, 2007

[11] M. Benedikt, PS2 NC – SC comparison, Presentation to the CERN-PAF, September 7, 2007.

[12] L. Bottura, R. Maccaferri, C. Maglioni, V. Parma, G. de Rijk, L. Rossi, W. Scandale, L. Serio, D. Tommasini, Conceptual Design of Superferric Magnets for PS2, CERN AT-MCS Internal Note 2007-07, EDMS 871183.v3, CARE-Note-2007-019-HHH, November 5, 2007.

[13] W. Scandale, First Configuration of a Possible Superferric option for PS2+, CERN AT-MCS Internal Note 2006-07, December 2006.

[14] FAIR An International Accelerator Facility for Beams of Ions and Antiprotons, H. H. Gutbrod (Editor in Chief) , I. Augustin, H. Eickhoff, K.-D. Groß, W. F. Henning, D. Kraemer, G. Walter Editors, ISBN 3-9811298-0-6, EAN 978-3-9811298-0-9, September 2006.

[15] A.D. Kovalenko. Status of the Nuclotron, EPAC'94, London, June 1994. Proceedings, v.1, p.p. 161-164, 1995.

[16] P. Wanderer, et al., Initial Test of a Fast-Ramped Superconducting Model Dipole for GSI's Proposed SIS200 Accelerator, Proceedings of PAC 2003, 2162-2164.

[17] Memorandum of Understanding for Collaboration in the R&D of fast ramping high field dipole magnets for the SIS300 synchrotron of the FAIR facility, between The Facility for Antiproton and Ion Research (FAIR) and The National Institute of Nuclear Physics (INFN), 2006.

[18] L. Bottura, R&D Targets for Low-Loss Nb-Ti Strands and Cables for Fast Cycled Superconducting Magnets at CERN, AT-MCS Internal Note 2008-01, January 2008, EDMS 887688.

.

BEAM-BEAM AND COMPENSATION SCHEMES: CONCLUSIONS

J. P. Koutchouk, CERN, Geneva, Switzerland

Abstract

This paper attempts at giving the important conclusions from this session.

AGENDA OF THE SESSION

1. Summary of the SLAC beam-beam compensation workshop, W. Fischer, BNL
2. Head-on and pacman compensation with electron lens, V. Shiltsev, FNAL,
3. Beam-beam and emittance growth with wire compensation, U. Dorda, CERN & U. Vienna
4. Beam-beam and emittance growth with crab cavities, R. Calaga, BNL,
5. Beam-beam with a few long-range encounters at short distance, N. Abreu, BNL
6. Beam-beam with long flat bunches and large Piwinski angle, K. Ohmi, KEK.

CONCLUSIONS OF THE SESSION

- **On the US-LARP beam-beam workshop**: In the US-LARP beam-beam compensation meeting, the accent was different and nicely complementary with this session: the phenomenology of the beam-beam limit had been reviewed, to better identify a possible hierarchy in phenomena needing compensation. Actually all three beam-beam issues (head-on, long-range and pacman) need be addressed. The experimental program of RHIC is the key to improve the understanding, taking advantage of the wire compensators newly installed in the machine. The MD results, together with the former SPS results, had been not only analysed but as well evaluated in terms of reliability of the conclusions. The beam-beam experiments are indeed notoriously known for their complexity and sensitivity to details. All results tend to give a coherent semi-quantitative picture. With more MD time, RHIC has all the potential to reach precise conclusions in a critical field limiting machine performances.
- **On the electron lens:** The electron lens has proven its reliability as abort gap kicker in the Tevatron. As a linear bunch-by-bunch tune shifter, it demonstrated both its usefulness and the high quality of the electron current control that causes no detectable emittance growth over long periods. With this solid basis, the efficiency of more complex compensations can be attacked: head-on, long-range. Experiments are strongly encouraged and results eagerly awaited. The electron lens is a good candidate for long-range beam-beam compensation in situations where the wire would be too close to the beam (possibly for the early separations scheme).
- **On the wire compensation:** With experiments and very detailed simulations using various criteria for testing the regularity of the motion, the ability to compensate the long-range beam-beam effect by wires appears now established. The significant gain of about 2 sigma in dynamic aperture is appreciable for a relatively modest investment. A simple dc system mitigating the compensation for normal and pacman bunches appears already very valuable and should be scheduled for installation in the LHC. For an exact compensation of pacman bunches, a promising research line has been identified by using an RF waveform, reducing significantly the requirement of synchronization accuracy that was otherwise extreme.
- **On the cross-talk between chromaticity and long-range beam-beam:** Simulations confirms the RHIC observations showing that the allowed chromaticity range is reduced by the presence of the long-range beam-beam interactions.
- **On the importance of the triplet length:** depending on the technology (Nb-Ti or Nb_3Sn) and on the aperture requirements, the triplet length varies significantly. It was shown that the increase of the number of long-range beam-beam encounters at a given beam separation has a significant impact. For Nb-Ti and apertures of about 200 mm, the dynamic aperture becomes unacceptably small.
- **On the consequences of a large Piwinski angle:** Weak-strong simulation of the LPA (large Piwinski Angle) option for the LHC upgrade do not exhibit any evident pathology, except perhaps for horizontal-vertical crossing where the number of excited resonances is larger. To become conclusive, more studies and simulations are needed, e.g. to take into account long range and imperfections.
- **On the acceptable number of close encounters for an early separation scheme:** the experimental data collected seem to show that, contrary to what was feared, a small number of encounters at 5 sigma separation can be tolerated. Their exact number is not yet clear. Further experiments in RHIC are needed to establish quantitatively this number that is critical for the early separation scheme.
- **On crab cavities:** the potential in luminosity upgrade of weak angle crab crossing is very large and does not appear out of reach from the technology point of view. The various challenges (technology, collimation,…) will be addressed in a forthcoming US-LARP workshop.
- **Conclusion from the chairman:** for decades, the beam-beam effect had to be accepted as the ultimate limit of colliders. Since a relatively short time, three compensation concepts have been devised, simulated, partially implemented and experimented. Their potential is very high and they are thus of direct interest to the LHC upgrade, allowing a higher luminosity for a given beam current. Demonstrations in existing colliders are of highest value given the subtlety of the beam-beam effects.

Summary of Session on Beam Losses, Halo Generation and Collimation

G. Rumolo
CERN, Geneva, Switzerland

Abstract

The session on beam losses, halo generation and collimation is the first of two sessions of the BEAM07 Workshop, which were devoted to specific CERN-GSI subjects and were meant to be the follow up of last year's CERN-GSI Bilateral Meeting on Collective Effects, which took place on March 30-31, 2006 at the GSI-Darmstadt.

INTRODUCTION

The goal of the session on beam losses, halo generation and collimation was to identify the main loss mechanisms in ion or proton rings and the tools to model them.
During this session, specific beam loss issues in different existing machines (SIS18, PS, SPS, RHIC) were described and explained through simulations. Collimation systems have been proved necessary for future (or upgraded) machines to be able to localize and control the beam losses, which may become intolerable for high intensity/high energy beams, if randomly distributed over the machine. The design of efficient collimation systems strongly relies on the capability of the present simulation techniques to predict with high accuracy the loss distribution around a machine. Therefore, the successful benchmark of the so far developed simulation tools (containing particle tracking, scattering and secondary generation) is a necessary asset to establish their reliability and range of applicability. Most of the presentations of this session (R. Bruce, S. Gilardoni, C. Omet, S. Redaelli, G. Robert-Demolaize, P. Spiller) covered:

- Collimation and studies of loss localization in several machines (PS, SPS, LHC, SIS18, SIS100/300, RHIC)
- Code benchmark against measurements in running machines (PS, SPS, RHIC)

In two presentations (G. Franchetti, S. Sorge), some exotic loss mechanisms were explained in greater detail:

- Resonances induced by the electron cooler
- Trapping and loss induced by electron cloud in a dipole field

Several methods to track scattered and secondary particles and study loss distribution were outlined. The tools were optimized case by case according to specific needs and requirements:

- A combination of Sixtrack for particle tracking and K2 for modeling the interaction with matter is used for specific collimator studies (SPS, LHC, RHIC). It was also modified and adapted to study losses in the PS
- Generation of external distribution through MARS and tracking with MAD-X. It was applied to the PS
- ICOSIM, as a self-consistent package inluding tracking and ion-matter interaction. It uses MAD-X optics and nuclear interaction cross-sections from RELDIS and ABRATION/ABLATION routines. This tool has been widely used for studying ion losses in the SPS and predict those in the LHC
- STRAHLSIM (code developed at GSI) for full ion tracking including capture/recombination phenomena (cross sections available within 30% accuracy at the needed high energies), scattering and desorption. It was used to design the collimator system for the upgraded SIS18 and for the SIS100/300.

All these methods also need to depend on a detailed external aperture model (and detailed collimator geometry, where applicable) to predict the loss locations
The reasons why it is very important to develop powerful and robust tools to predict losses around a circular machine are:

- Assess the required cleaning performance of collimator systems for new superconducting machines with high stored beam energy (e.g. LHC has 360 MJ stored energy to be compared with typical quench limits for superconducting magnets of the order of few mW/m^2)
- Save surroundings from irradiation (CT extraction in the PS). If losses can be predicted, they can be also suppressed or relocated in order not to exceed the allowed irradiation doses in critical areas and to increase the transmission efficiency and performance of the machine
- Determine and steer the design of collimator systems in new machines (LHC, SIS100, PS2) or new collimator systems necessary for the upgrade of existing machines limited by loss induced vacuum instabilities (SIS18)

The reliability of these tools can be only assessed through direct benchmark with known loss patterns in running machines (PS, SPS, SIS18, RHIC) and their predicting power is the base on which the design of collimation systems is founded. In the specific case of LHC, there are at least three reasons why the collimation system is an unprecedented challenge: 1) losses have to be controlled 1000 time better than the present state-of-the-art, 2) collimation is needed at all machine states (injection, ramp, squeeze, store), and 3) the collimation system plays an important role for machine protection.

COLLIMATION SYSTEMS FOR THE LHC AND THE UPGRADED SIS18

S. Redaelli presented the basic scheme of the multi-stage collimation in the LHC. The primary halo of the circulating beam hits the primary collimators, so that the resulting hadronic showers and secondary halo will be intercepted by the secondary collimators. Some shower absorbers are placed further downstream. The tertiary beam halo will be finally intercepted by tertiary collimators which are situated just in front of the superconducting triplet. In addition, some protection devices are placed at intermediate settings in order to shield sensitive machine equipment (including some collimators) from full beam impact possibly induced by missteering. Collimation is needed in LHC from injection to collision, forcing the devices to be movable such that their position may be adjusted according to the beam size. All cleaning and protection devices have to be included in the simulations to assess the efficiency of the system.

In the SIS18 the main reason for vacuum runaway leading to beam loss is the charge exchange process. U^{28+} can be further ionized by collisions against the rest gas, so that the U^{29+} ions are lost in the bends because of the higher charge and start a vacuum instability process due to the high desorption yield values. Therefore collimators have to be inserted downstream from the dipoles to catch all the ions with the wrong charge and localize the loss. P. Spiller and C. Omet pointed out that losses should be peaked at location of the collimators (designed such as not to reduce the machine aperture), where the main beam and the products from charge exchange are well separated. The performance of SIS18 is expected to increase dramatically (and meet the requirements to become injector for SIS100) with the use of adequately placed absorbers along with NEG coating and pumping ports in the vicinity.

BENCHMARK OF SIMULATION PACKAGES WITH EXPERIMENTAL DATA

S. Redaelli showed the results of the comparison between the predicted loss maps (using a combination of Sixtrack for particle tracking, K2 for modeling the interaction with matter and BeamLossPattern for the detailed aperture model) and the measured ones. Measurements were taken at the SPS using the signals of the Beam Loss Monitors, when the circulating beam in the machine was scraped by an LHC collimator prototype. The agreement is remarkably good, because it can successfully reproduce not only the high peak at the collimator location, but also the other small peaks present in other locations of the machine (where the scattered or secondary particles hit some aperture limitation).

The same sets of data were used in the study presented by R. Bruce to benchmark the ICOSIM code against experimental data. The ICOSIM code is oriented to the ion collimation, which needs to be studied separately because, due to large probability of fragmentation in primary collimators, there is a high production of isotopes having Z/A which would not be intercepted by the secondary collimators as designed for protons.

The same tool as used for the SPS was also used by J. Barranco and S. Gilardoni to benchmark loss data in the PS machine. However, this required some modifications, in particular the halo had to be identified with the scattered particle distribution and the event cross sections had to adapted to the lower energy of the PS. The resulting loss pattern turned out to be in very good agreement with the measured one. Still based on this simulation tool, G. Robert-Demolaize presented a satisfactory comparison between simulated loss locations and live measurements from the RHIC BLMs, when the collimator jaws were moved in different positions.

GSI simulations are all based on the internally developed code, called STRAHLSIM, which can apparently well reproduce the loss patterns as presently observed in the SIS18.

MORE CONSIDERATIONS ON SOME LOSS MECHANISMS

Particle loss occurs at different stages due to several mechanisms. For example, there are usually injection and rf-capture losses in all machines, and particles can get lost on the accelerating ramp if they were not correctly captured in the buckets. The result of a GSI study presented by P. Spiller was that fast ramping can help to reduce the losses on the ramp, and an optimum can be found before the rf-capture losses take off. In the frame of the FAIR project, an SIS18 uppgrade program has been approved to improve all the known loss mechanisms. The most important points (some of which will be financed by the EU) are:

- New RF-System, h=2 acceleration cavity and bunch compression system (2009)
- Upgrade of the UHV System, with new, NEG coated dipole and quadrupole chambers (2006-2008). Next year the SIS18 will run with 30% of the chambers coated and a significant improvement in the storage and acceleration of U^{28+} is foreseen.
- Set-up of a of the previously described desorption collimation system (2007-2008)
- Upgrade of the Injection/Extraction Systems, with a new injection septum, power supply and large acceptance extraction channel (2007)
- Replacement of Main Dipole Power Supplies, to allow operation with 10 T/s up to 18 Tm (2010)

On top of that, to push the SIS18 performance and fight instabilities and halo formation, a crash program for the development of high current operation has been started in 2007, including studies on compensation of resonances and impedance reduction. Furthermore, longitudinal and transverse feedback systems are being designed for damping of

coherent oscillations, coupled bunch modes and for phase stabilization.

Beam losses also occur because particles move to large amplitudes in the transverse plane due to resonance crossing and eventually hit some aperture limitations. G. Franchetti developed an analytical model which explains why the stripe structure of the electron cloud inside a dipole field during the pinch can cause single particle detuning depending on the longitudinal position of the particle within a bunch. Trapping in the islands and growth to the large amplitude is therefore possible due to the synchrotron motion, which moves the particles in the longitudinal direction and causes them to see different detunings in a periodic fashion. This may result in emittance growth in rings like the SPS and the SIS100, if there is an electorn cloud and its density is high enough. S. Sorge studied the effect of the electron cooler on detuning and resonance crossing, which is relevant both for the SIS18 and for some of the future GSI storage rings that are planned to be equipped with an electron cooler. The resonances that can be excited by the electron cooler have been identified using MAD-X with a nonlinear kick, which models the electromagnetic interaction of the beam with the electron cooler. When the machine working point is such as to cross any of these resonance lines, emittance growth sets in.

CONCLUSIONS

Many tools have been developed to predict beam loss locations in rings and they have been successfully benchmarked against measurements. Based on these tools, collimation systems have been designed for new or upgraded rings. Furthermore, understanding the location of the losses gives a powerful tool to suppress or relocate them conveniently.

Electrons in a proton or ion machine (from an electron cooler or an electron cloud) may cause losses The odd distribution of a uniform electron cloud pinched in a dipole field can give rise to trapping and hence, to emittance growth. The electron cooler was found to excite resonances up to 6th order.

ACKNOWLEDGMENTS

I would like to thank all the speakers for the interesting and well structured presentations, and the organizers of the BEAM07 workshop for inviting me to chair this session. I also would like to thank Dr. Oliver Boine-Frankenheim for co-chairing with me the session and Dr. Stefano Redaelli for patiently proof-reading this summary.

List of Beam'07 Participants

Abreu	Natalia	BNL
Aiba	Masamitsu	CERN
Arduini	Gianluigi	CERN
Assmann	Ralph	CERN
Baglin	Vincent	CERN
Bane	Karl	SLAC
Barranco	Javier	CERN
Berg	J.Scott	BNL
Boine-Frankenheim	Oliver	GSI
Bongardt	Klaus	IKP-FZJ
Bottura	Luca	CERN
Bruce	Roderik	CERN
Bruning	Oliver	CERN
Buzio	Marco	CERN
Cai	Yunhai	SLAC
Calaga	Rama	BNL
Calatroni	Sergio	CERN
Carli	Christian	CERN
Caspers	Fritz	CERN
Catalan Lasheras	Nuria	CERN
Chanel	Michel	CERN
Chiggiato	Paolo	CERN
Damerau	Heiko	CERN
De Maria	Riccardo	CERN
Dorda	Ulrich	CERN
Fabbricatore	Pasquale	INFN
Fisher	Wolfram	BNL
Franchetti	Giuliano	GSI
Furman	Miguel	BNL
Galambos	John	ORNL-SNS
Garcia	Juan	CERN
Garoby	Roland	CERN
Gerigk	Frank	CERN
Gilardoni	Simone	CERN
Goddard	Brennan	CERN
Hasse	Rainer	GSI
Hirata	Kohji	Sokendai

Hoa	Christine	CERN
Jimenez	Jose Miguel	CERN
Jowett	John	CERN
Kornilov	Vladimir	GSI
Koschik	Alexander	CERN
Koutchouk	Jean-Pierre	CERN
Kozanecki	Witold	CEA-Saclay
Kroyer	Tom	CERN
Lebedev	Valeri	Fermilab
Linnecar	Trevor	CERN
Markiewicz	Thomas	SLAC
Metral	Elias	CERN
Mostacci	Andrea	La Sapienza, University of Rome
Mustafin	Edil	GSI
Ohmi	Kazuhito	KEK
Omet	Carsten	GSI
Ostiguy	Jean-Franois	FNAL
Palumbo	Luigi	La Sapienza, University of Rome
Papaphilippou	Yannis	CERN
Paret	Stefan	GSI
Parma	Vittorio	CERN
Peggs	Stephen	BNL
Petit-Jean-Genaz	Christine	CERN
Petracca	Stefania	INFN
Pieloni	Tatiana	CERN
Pierini	Paolo	INFN
Qin	Qing	IHEP
Redaelli	Stefano	CERN
Robert-Demolaize	Guillaume	BNL
Rumolo	Giovanni	CERN
Salvant	Benoit	CERN/EPFL
Scandale	Walter	CERN
Schmidt	Frank	CERN
Seiya	Kiyomi	Fermilab
Sen	Tanaji	Fermilab
Shaposnikova	Elena	CERN
Shiltsev	Vladimir	Fermilab
Sorge	Stefan	GSI
Spiller	Peter	GSI
Sterbini	Guido	CERN
Taborelli	Mauro	CERN
Tsesmelis	Emmanuel	CERN
Vretenar	Maurizio	CERN
Walckiers	Louis	CERN
Wienands	Uli	SLAC
Yan	Yiton	SLAC
Yurij	Senichev	FZJ
Zimmermann	Frank	CERN
Zotter	Bruno	CERN


At CERN
Contribution to the commissioning of LEP,
numerous invaluable contributions to the design of the LHC
collective effects,
machine impedance and
beam-beam interaction.
In 1997, he recognized the potential danger from an electron cloud in the LHC and he launched an important remedial crash programme.
Later in 1997 Francesco became leader of the accelerator-physics group in the former SL Division.
Since 2000 he drove the LHC accelerator upgrade studies.
Under his wonderful and caring guidance many bright young accelerator physicists were trained or recruited at CERN.
Walter Scandale
Two young people from south ....
Francesco started his thesis work in the same team: LEP-TH, in the same floor, the 5th of building 30.
We shared the habits of people coming from south:
- late start in the morning
- late stop in the evening ... often in the night
Francesco always won the game ... with the help of coffee, preferably with a good one, from Naples.
Outlook
- Laslett coefficients for Betatron Normal Modes
Square vs Circular Pipes
A Tiny Twin-Liner Model
Real-World Geometries, MoMs & Random Paths
- Beam Coupling Impedances from Reciprocity Theorems
Rounded corners and more
- Leontóvich Boundary Conditions and Beyond
Lossy Walls, Coated Walls, Pumping Holes, etc.
...What's it all for ?
Francesco Ruggiero Memorial Symposium
CERN, October 2 2007
Dear Hirata,
I think it is a good idea to visit other laboratories (even from the accelerator point of view) and CERN will probably be one of the most interesting ones in the near future, when LEP will be ready.
Francesco suggested me to work at CERN.
Experience with Francesco
is already an old story.
But the feeling of creative moment
will not damp nor diffuse
like a constant of motion.
hirata@soken.ac.jp
Francesco Ruggiero, 1957-2007
I met Francesco on many occasions during my career in accelerator physics. I feel honored to have met him and grateful for what I learned from him. I am indebted for his strong and steady support of the LARP program, especially on electron-cloud physics.


echoes with two dipole kicks
first observation of transverse beam echo
1st strong kick
2nd weak kick
echo!
simulation
experiment
New upgrade scenarios